NASA Conference Publication 2369

Nonlinear Constitutive Relations for High Temperature Application—1984

Proceedings of a symposium held at
NASA Lewis Research Center
Cleveland, Ohio
June 15-17, 1984

NASA

NASA Conference Publication 2369

Nonlinear Constitutive Relations for High Temperature Application—1984

Proceedings of a symposium held at
NASA Lewis Research Center
Cleveland, Ohio
June 15–17, 1984

NASA
National Aeronautics
and Space Administration

**Scientific and Technical
Information Branch**

1985

Page intentionally left blank

PREFACE

The Second Symposium on Nonlinear Constitutive Relations for High Temperature Applications, sponsored by the NASA Lewis Research Center, was held at Cleveland, Ohio on June 15-17, 1984. Some one-hundred participants and attendees representing NASA, other government agencies, universities, and industry were in attendance. The purposes of the symposium were (1) to review the state-of-the-art in nonlinear constitutive modeling of high-temperature materials, (2) to identify needs for future research and development in this area, and (3) to document and disseminate the research progress and new technology developed to date.

One of the specific goals of NASA is to foster technological development of analytical/experimental methodologies for improved design of gas turbine engine structures and components and space shuttle main engine structures. To support these technologies, both NASA and the aerospace industry recognize that there is considerable development work yet needed in the area of nonlinear constitutive relations for high-temperature applications. This has become an increasingly critical need with the recent advances in high-temperature materials technology in response to new demands on material performance. NASA Lewis, in cooperation with industry, universities, and other government agencies, is supporting this technology development, some of which is reported in this symposium publication. The Symposium then served not only to foster this technological development, but also act as a common forum for all industries with a commonality of interrelated activities and interests relating to nonlinear constitutive model/experimental development for material characterization at elevated temperature.

The Symposium was organized into the following six sessions:

I. Constitutive Modeling I
II. Constitutive Modeling II
III. Numerical Methods
IV. Material Testing
V. Structural Applications
VI. Panel Discussion

There were a total of twenty-one papers presented in the five technical sessions. The papers and the authors are grouped by session in the Contents.

I wish to thank the session chairpersons, authors and speakers, and panelists whose efforts contributed to the technical excellence and success of the Symposium. I am also grateful to the Lewis staff for their help before and during the Symposium.

R. L. Thompson
Symposium Chairman
NASA Lewis Research Center

Page intentionally left blank

CONTENTS

A SURVEY OF UNIFIED CONSTITUTIVE THEORIES*

K.S. Chan and U.S. Lindholm
Southwest Research Institute
San Antonio, Texas 78284

S.R. Bodner
Technion - Israel Institute of Technology
Haifa, Israel

K.P. Walker
Engineering Scientific Software, Inc.
Smithfiled, Rhode Island 02906

A literature survey has been conducted to assess the state-of-the-art of time-temperature dependent elastic-viscoplastic constitutive theories which are based on the unified approach. This class of constitutive theories is characterized by the use of kinetic equations and internal variables with appropriate evolutionary equations for treating all aspects of inelastic deformation including plasticity, creep, and stress relaxation. The review identifies more than ten such unified theories which are shown to satisfy the uniqueness and stability criteria imposed by Drucker's postulate and Ponter's inequalities. These theories are compared on the basis of the types of flow law, kinetic equation, evolutionary equation of the internal variables, and treatment of temperature dependence. The similarities and differences of these theories are first outlined in terms of mathematical formulations and then illustrated by comparisons of theoretical calculations with experimental results which include monotonic stress-strain curves, cyclic hysteresis loops, creep and stress relaxation rates, as well as thermomechanical loops. Numerical methods used for integrating these stiff time-temperature dependent constitutive equations are also briefly reviewed.

INTRODUCTION

Constitutive theories based on the classical concepts of plasticity and creep generally decompose the inelastic strain rate into a time-independent plastic strain rate and a time-dependent creep rate with independent constitutive relations describing plastic and creep behavior. While this approach can be rationalized on historical grounds and perhaps on computational convenience, experimental evidence collected on structural alloys at elevated temperature indicates inherent time-dependency and creep/plasticity interactions [1]. This suggests that inelastic deformation might be primarily controlled by a single overall mechanism and should be treated in a unified manner.

In recent years, a number of formulations of elastic-viscoplastic constitutive equations have been presented in the engineering literature. Such equations are sometimes referred to as "unified" since inelastic deformations are represented and treated by a single kinetic equation and a discrete

* This work was performed under NASA Contract No. NAS3-23925.

set of internal variables. In this context, creep, stress relaxation, and plastic flow are different manifestations of time-dependent inelastic deformations under particular loading conditions with consequently different response characteristics.

There are more than ten unified constitutive theories in the literature. These constitutive equations have some common properties and some essential differences which have been reviewed recently by Walker [2]. Since then, there have been more advances in the development of the unified theories. The purpose of this survey is to update Walker's previous work by reviewing the state-of-the-art and the numerical integration techniques for these unified theories. This survey also serves to identify areas for further model developments.

The unified theories which are reviewed in this survey include those of Walker [2], Bodner and Partom [3,4], Miller [5], Krieg, Swearengen and Rhode [6], Chaboche [7], Robinson [8], Hart and co-workers [9], Stouffer and Bodner [10], Lee and Zaverl [11], Ghosh [12], and Kagawa and Asada's modification of Miller's model [13].

GENERAL CHARACTERISTICS OF UNIFIED CONSTITUTIVE EQUATIONS FOR ELASTIC-VISCOPLASTIC MATERIALS

Constitutive equations for elastic-viscoplastic material could be formulated either with or without the use of a yield criterion. A basic assumption for this class of constitutive theories is that in the range where inelastic strains are present, the total strain rate $\dot{\varepsilon}_{ij}$ can be divided into elastic and inelastic components which are both nonzero, i.e.

$$\dot{\varepsilon}_{ij} = \dot{\varepsilon}_{ij}^{e} + \dot{\varepsilon}_{ij}^{p} \tag{1}$$

This equation is applicable for the small strain case and a similar decomposition is assumed to hold for the deformation rates in the case of large strains. Those are equivalent to strain rates if the strains are small.

For the small strain case considered here, the elastic strain rate is given by the time derivative of Hooke's Law. An important question related to Equation (1) is an appropriate definition of $\dot{\varepsilon}_{ij}^{p}$. One possibility is to define $\dot{\varepsilon}_{ij}^{p}$ as the total strain rate contribution that is both thermodynamically and geometrically irreversible , i.e., non-elastic in all respects. An alternative definition of the incremental plastic strain is the residual strain upon loading and unloading from a stress increment. This seems to be the definition adopted by E. H. Lee in his treatment of large plastic strains, see e.g. [14]. Since non-elastic strains are also generated during unloading, constitutive equations based on this definition would be different than in the former case. Each approach seems possible, but the proper definition and use of the $\dot{\varepsilon}_{ij}^{p}$ term should be indicated and be consistent with the constitutive equations.

The expression "unified" applied to such theories is generally taken to mean that all aspects of inelastic behavior such as plastic flow, creep, and stress relaxation are included in the $\dot{\varepsilon}_{ij}^{p}$ function and are particular response characteristics for different loading histories. This broad definition of "unified" would admit theories with and without a yield criterion and alternative specifications of $\dot{\varepsilon}_{ij}^{p}$. Separation of the non-elastic strain rate into geometrically reversible (anelastic) and non-reversible components could be a convenient procedure and does not detract from the "unified" concept.

Constitutive theories which are formulated without the use of a yield criterion include that of Bodner and his associates [3,4], Walker [2], Miller [5], and Krieg, Swearengen and Rhode [6]. Since these models do not contain a completely elastic regime, the function that describes the inelastic strain rate should have the property that the inelastic strain rate be very small for low stress levels.

For theories with a yield criterion, $\dot{\varepsilon}_{ij}^{p}$ is identically zero until an invariant function of the stress reaches a prescribed value; the function, by definition, is independent of strain rate. For stresses at or exceeding the yield value, Equation (1) applies and $\dot{\varepsilon}_{ij}^{p}$ and the stress σ_{ij} are functionally related. The fully elastic state, i.e. $\dot{\varepsilon}_{ij}^{p} = 0$, would apply only for stress states less than the rate independent yield value, and loading and unloading paths above that are controlled by the loading conditions through the constitutive equations. Theories of this type have been developed by Perzyna [15] for the case of isotropic hardening and by Chaboche [7], Robinson [8], and Lee and Zaverl [11] for the case of both isotropic and directional hardening.

All the unified models are formulated on the basis of internal variables which depend on the loading history. The essential features of these unified theories are: (1) a flow law which functional form depends on the method of treatment of directional (kinematic) hardening, (2) a kinetic equation which is the temperature dependent functional relationship between the strain rate and stress invariants and includes internal variables, and (3) a set of evolution equations for describing the growth of the internal variables. Here, the internal variables are used to represent the current resistance to inelastic flow of the deformed solid. Two deforming solids with identical values of their internal variables would have identical inelastic responses under the same imposed stress state. Both the choice and the number of internal variables vary with the unified models. Most of the unified models use two internal variables or one variable with two components: one to represent isotropic hardening and another to represent directional (kinematic) hardening. In most models, the isotropic hardening variable is represented by a scalar quantity, either the drag stress (K) or the yield stress (Y), while directional hardening is represented by a second order tensor Ω_{ij} or a scalar function of such a tensor.

Basic Flow Laws

Four basic forms of the inelastic flow law have been identified. Plastic incompressibility is always assumed and these flow laws are:

$$(1) \quad \dot{\varepsilon}_{ij}^{p} = \lambda_1 S_{ij} \qquad \dot{\varepsilon}_{kk}^{p} = 0 \tag{2a}$$

$$(2) \quad \dot{\varepsilon}_{ij}^{p} = \lambda_2 \Sigma_{ij} = \lambda_2 (S_{ij} - \Omega_{ij}) \;, \quad \dot{\varepsilon}_{kk}^{p} = 0 \tag{2b}$$

$$(3) \quad \dot{\varepsilon}_{ij}^{p} = \lambda_{ijkl} S_{kl} \;, \quad \dot{\varepsilon}_{iikl}^{p} = \dot{\varepsilon}_{ijkk}^{p} = 0 \tag{2c}$$

$$(4) \quad \dot{\varepsilon}_{ij}^{p} = \frac{\partial f}{\partial \sigma_{ij}} \;, \quad \dot{\varepsilon}_{kk}^{p} = 0 \tag{2d}$$

where S_{ij}, σ_{ij}, and Σ_{ij} are the deviatoric, direct and effective stresses, respectively. The tensor Ω_{ij} represents the "equilibrium stress" which has also been referred to as the "back stress" and the "rest stress." The parameter f is a yield function or a flow potential. It should be noted that the first three laws can be considered or can be derived from Equation (2d) if they are associated with a flow potential.

Equation (2a) is the Prandtl-Reuss flow law associated with the von Mises yield criterion. However, it can be considered as a basic material equation in its own right independently of a yield condition. As such, this equation is usually taken to be applicable for proportional loading conditions for which isotropic hardening would be appropriate. The equation states that the material response (i.e., the plastic strain rate) to stress is isotropic even though λ_1 could be stress history dependent. Since stress is directional, λ_1 could have a directional character within the context of incremental isotropy and thereby account for induced directional hardening effects.

Equation (2b) is the flow law obtained by introducing the kinematic hardening variable of Prager [16] into the classical plasticity formulation to account for directional hardening (the Bauschinger effect). In this context, the term Ω_{ij} would represent the new origin of a translating von Mises yield surface in deviatoric stress space, and Equation (2b) would be the associated flow rule. As before, Equation (2b) can be taken to be a basic material equation in a formulation without a yield criterion and the "equilibrium stress" tensor Ω_{ij} is generally intended to serve the following functions: (a) to account for directional hardening (the multi-dimensional Bauschinger effect), and for the non-coaxiality of $\dot{\varepsilon}_{ij}^{p}$ and S_{ij} under nonproportional loading histories (Figure 1); (b) to account for reversed plastic straining effects, e.g. reversed creep, relaxation through zero stress, when the effective stress Σ_{ij} is negative; (c) for theories without a fully elastic range (i.e., a yield criterion), to account for low plastic straining within a given range.

Equation (2c) is the generalized anisotropic form of the Prandtl-Reuss flow law which can be rewritten in a 6D stress and strain rate space to take the form,

$$\dot{E}_\alpha^p = \Lambda_{\alpha\beta} T_\beta \qquad \begin{matrix} \alpha = 1,\text{---}6 \\ \beta = 1,\text{---}6 \end{matrix} \tag{3}$$

where $\dot{E}_\alpha$ and T_β are related to the usual plastic strain rates and stresses in a simple manner, see [10], and $\Lambda_{\alpha\beta}$ is the 6x6 matrix of coefficients. If the material is initially isotropic and the law for plastically induced directional hardening does not lead to off diagonal terms, then $\Lambda_{\alpha\beta}$ is initially and remains diagonal. Under these conditions, Equation (2c) is equivalent to Equation (2b) since 6 material constants determine the anisotropic flow behavior. All the flow equations, Equations (2a,b,c), would be equivalent for the case of proportional loading, including cyclic conditions. The real differences in those equations would show up for nonproportional loading histories.

For constitutive theories with a flow potential, both the flow law and the growth law of the directional (kinematic) hardening variable Ω_{ij} are derivable from a single flow potential. The associated flow law of a basic form of such a flow potential is [8].

$$\dot{\varepsilon}_{ij}^p = \frac{1}{2\mu} F^{\frac{n-1}{2}} (\sigma_{ij} - \Omega_{ij}) \qquad \text{for inelastic loading} \tag{4a}$$

and $$\dot{\varepsilon}_{ij}^p = 0 \qquad \text{for elastic loading/unloading} \tag{4b}$$

where F is the von Mises yield function, n and μ are material parameters. The conditions for inelastic loading and elastic unloading have been identified in [8]. It can be easily seen that (4a) and (2b) are equivalent. In both cases, the direction of the inelastic strain rate vector is coaxial with the current effective stress vector (see Figure 1).

Kinetic Equations

The flow laws, Equations (2a) and (2b) can be squared to give respectively,

$$\lambda_1 = [D_2^p / J_2]^{1/2} \tag{5a}$$

$$\lambda_2 = [D_2^p / J_2']^{1/2} \tag{5b}$$

where D_2^p is the second invariant of the plastic strain rate, $D_2^p = (1/2)\ \dot{\varepsilon}_{ij}^p\ \dot{\varepsilon}_{ij}^p$, and J_2 and J_2' are the second invariants of the deviatoric stress and effective deviatoric stress, respectively,

$$J_2 = (1/2)\ S_{ij}\ S_{ij} \tag{6a}$$

$$J_2' = (1/2)\ (S_{ij} - \Omega_{ij})(S_{ij} - \Omega_{ij}) \tag{6b}$$

Fundamental to all "unified" viscoplastic formulations based on flow laws of the forms listed in Equations (2) is that inelastic deformations are governed by a functional relation between D_2^P and J_2 (or J_2') that could involve load history dependent variables. These variables are intended to represent properties of the inelastic state with respect to resistance to plastic flow, e.g. hardening, and damage. Some functions that have been suggested are the following.

$$(a) \quad D_2^P = D_o X^n \tag{7a}$$

$$(b) \quad D_2^P = D_o \exp\left[-\left(\frac{1}{X}\right)^n\right] \tag{7b}$$

$$(c) \quad D_2^P = D_o \left[\sinh(X)^m\right]^n \tag{7c}$$

where $X = 3J_2/K^2$, or $3J_2'/K^2$

and n, m, and D_o are constants. The inelastic strain rate components can then be obtained as a function of the stress by the use (2a) or (2b) and one of Equations (7). Expression (7b) would seem to have some advantage over (7a) or (7c) in theories without a yield criterion in that the value of D_2^P is almost zero for some range of J_2 regardless of the value of n. In (7b), Do is the limiting value of the inelastic strain rate in shear; (7a) and (7b) do not contain such a limit. These differences between the kinetic equations are illustrated in a normalized plot of log (D_2^P/D_o) vs X in Figure 2 for the case of n = 3 and m = 1.0.

In all the preceding equations (7a,b,c) the exponent n influences the slope of the D_2, J_2 relation and therefore has the major influence on strain rate sensitivity. That parameter also affects the overall level of stress-strain curves although the level also depends on the hardening parameter K.

Temperature (T) dependence of plastic flow is a first order phenomenon comparable to strain rate sensitivity and should appear directly in the kinetic equation. In the case of Equations (7a,b), this can be achieved by taking the exponent n to be a function of T, e.g. n = ck/T (k is Boltzmann's constant and c a material constant) which leads to strong temperature dependence of the stress parameter $X=3J_2/K^2$ (or $3J_2'/K^2$). Numerical results for this dependence are shown in Figure 3 for both the power law and exponential kinetic equations at different non-dimensionalized strain rates.

The method of including temperature dependence in Equations 7a,b is comparable to an activation energy formulation. Table I lists temperature-dependent kinetic equations based on four different functional expressions for the activation energy. Some of the consequences of the various relations are discussed in [17].

Another procedure for including temperature dependence in the kinetic equations is to multiply the stress function, the right hand side of equations (9) by a temperature function. The temperature factor can again be motivated by thermal activation considerations and the Arrhenius expression seems to be the reasonable function to use (Table I). This is the approach taken by Miller [5].

Evolutionary Equations for Internal Variables

The general framework of the evolutionary equations of internal variables is based on the now well-accepted Bailey-Orowan theory [18,19] which theorizes inelastic deformation to occur under the actions of two simultaneously competing mechanisms, a hardening process proceeding with deformation and a recovery or softening process proceeding with time. The evolution rate of an internal variable is then the difference between the hardening rate and the recovery rate as given by

$$\dot{X}_i = h_1(X_i)\,\dot{M}_1 - r_1(X_i, T) \tag{8}$$

where $\dot{X}_i$ is the evolution rate of the internal variable X_i, and h_1 and r_1 are the hardening and the thermal recovery functions, respectively. h_1 and r_1 are functions of X_i, temperature, T, and the hardening measure, $\dot{M}_1$ is either $\dot{\varepsilon}_{ij}^{p}$ or $\dot{W}_p$ depending on the model.

(1.) Isotropic Hardening

The quantity K in Equation (7) is usually interpreted as the isotropic hardening internal variable and is often referred to as the drag stress. Evolutionary equations for the isotropic hardening parameter generally follow the hardening/recovery format shown in Equation (8). A comparison of these hardening and recovery functions in various unified theories is shown in Table II. The rate of isotropic hardening is usually given by a function of the hardening variable K, which may saturate to a limiting value, shown as K_1 in Table II, multiplied by a measure of the hardening rate. Both the inelastic work rate and the effective inelastic strain rate have been proposed as the scalar hardening measure. On the other hand, the rate of softening or recovery is often taken to be a power function of K and a temperature-dependent constant K_0 which value represents the reference state for that particular temperature. This recovery model, sometimes credited to Friedel [20], theorizes that recovery occurs only when the current internal state exceeds the reference state.

(2.) Directional or Kinematic Hardening

Probably the main difference in the various unified theories is the treatment of directional or kinematic hardening. Differences exist not only in the choice of the flow law but also in the evolutionary equations. The general framework of these evolutionary equations follows the hardening/recovery formulation represented in Equation (8) with indexes to indicate the directions of hardening and recovery.

$$\dot{\Omega}_{ij} = h_2(\Omega_{ij})\dot{M}_{ij} - d(\Omega_{ij}, T)\dot{N}_{ij} - r_2(\Omega_{ij}, T)V_{ij} + \Theta(\Omega_{ij}, T)\dot{T}\,W_{ij} \tag{9}$$

where h_2, d, and r_2 are the hardening, dynamic recovery , and static thermal recovery functions, respectively. Θ represents hardening and/or recovery associated with the rate of temperature change. $\dot{M}_{ij}$, $\dot{N}_{ij}$, V_{ij} and W_{ij} are the directional indexes of h_2, d, r_2, and Θ, respectively. The main differences

among the various theories, as summarized in Table III, are in the choices of the directional index and the hardening and recovery functions.

As indicated in Table III, unified models based on the equilibrium stress utilize the inelastic strain rate as the directional index for hardening and contain a "dynamic recovery" term in the hardening function. The proposed hardening rule is thus similar to the Prager rule [16] in conventional plasticity which requires the translation of a yield surface to occur in the direction of the plastic strain increment. On the other hand, the evolutionary equation proposed in conjunction with Equation (2a) is based on the direct stress as the index for directional hardening [3,4]. This formulation avoids the cross-softening effect associated with inelastic strain rate as the index and the theory is more compatible with Ziegler's modification [21] of the Prager hardening rule. The directional index for "dynamic recovery" is generally in the opposite direction of the directional hardening variable Ω_{ij}. The "dynamic recovery" term is treated in [3,4] as a saturation term in the direction of the direct stress but the index has recently been modified to be in the direction of $-\Omega_{ij}$ also [22]. The unit vector which represents the direction cosines of the directional hardening variable is usually taken to be the directional index for static thermal recovery. Recovery always occurs in the opposite direction of the unit vector and tends to reduce the magnitude of the directional (kinematic) hardening variable. Most unified theories utilize Friedel's recovery model and take zero magnitude of Ω_{ij} as the reference state. Table III shows that a temperature rate term is also included in the theories of Walker and Chaboche. In principle, similar terms could be added to the other theories.

The temperature dependence of the internal variables is also important. The experience with the unified models to date indicates that all the material constants in the formulations would depend on temperature and must be evaluated at a number of base temperatures.

Uniqueness and Stability Criteria

For stability, unified theories with internal variables must, according to Ponter [23], obey the following inequality:

$$d\sigma_{ij}\, d\dot{\varepsilon}^{p}_{ij} - dXi\, d\dot{X}i > 0 \qquad (10)$$

where $d\sigma_{ij}$, $d\dot{\varepsilon}_{ij}$, dXi, and $d\dot{X}i$ represent incremental changes in stress, inelastic strain rate, the current value and the evolution rate of the internal variables. The inequality admits classical plastic flow, creep, and stress relaxation behavior. It also admits recovery phenomena involving negative inelastic work provided that the corresponding changes in the internal variables are sufficiently large to make the inequality in Equation (10) remain valid. The basic requirement of Equation (10) is that the dissipation rate must be nonnegative.

For a constant internal state, a small change in σ_{ij} results in a corresponding change in $\dot{\varepsilon}_{ij}^{p}$ so that [23]

$$d\sigma_{ij}\, d\dot{\varepsilon}_{ij}^{p} > 0 \quad , \quad \dot{X}_i = 0 \tag{11}$$

The inelastic work inequality is identical to Drucker's postulate [24] in classical plasticity that for a stable material flow the plastic work done must be nonnegative. For proportional loading the kinetic equations represented in Equation (7a) to Equation (7c) all yield convex "flow potentials" to which the inelastic strain rate vectors are normal. The consequence is that the inelastic work is always positive, and unified theories based on Equation (7a) to (7c) obey the inelastic work inequality.

For uniqueness, it appears that the inelastic strain rate must be a single-valued function of stress and internal variables. To satisfy the requirement for stable flow, Equation (10) dictates that stress-strain curves at constant strain rate must have positive slope but must decrease with increasing strain. On the other hand, stress-strain curves at constant plastic strain or plastic work must have positive slope, but the slope may either increase or decrease with increasing strain rate [23].

Most, if not all, of the unified theories listed in Table II satisfy the Ponter inequalities and met the uniqueness and stability requirements. The stability requirement is, however, not essential for constitutive theory developments. Unified theories admit unstable inelastic flow and are generally modeled by including softening mechanisms such as thermal softening and continuum damage in the evolution and/or kinetic equations.

NUMERICAL METHODS FOR INTEGRATING UNIFIED CONSTITUTIVE EQUATIONS

The unified constitutive equations can be characterized as mathematically "stiff." That is, in these equations, dependent variables are susceptible to large changes from small increments of the independent variables or from small time steps. This "stiff" behavior occurs usually with the onset of a significant amount of inelastic strains in the loading cycle and is due to the generally nonlinear nature of the functional forms that are employed in the kinetic equations of these theories.

A systematic comparison of a variety of approaches for integrating unified constitutive equations has been reported by Kumar, Morjaria, and Mukherjee [25]. This study concluded that for the constitutive theory of Hart, a relatively simple Euler integration method, together with a time step control strategy, was optimal when compared with the more sophisticated methods. The Walker constitutive theory has been integrated using the Euler single step approach usually without automatic time step control, but rather by determining an optimum step size for each problem. Efficiency obtained by using this approach has been acceptable and has shown considerable improvement over more sophisticated approaches such as higher order Runge-Kutta methods.

Tanaka and Miller recently developed a noniterative, self-correcting solution (NONSS) method for integrating stiff time-dependent constitutive equations [26]. In this approach, implicit quantities are removed by Taylor expansions of σ, $\dot{\varepsilon}$, and $\dot{X}$ through the incorporation of the integration operator α. The method which reduces to the explicit Euler method when $\alpha = 0$ and to the implicit Euler method when $\alpha > 0$ is unconditionally stable for $\alpha \geq 1/2$ and is noniterative. Accuracy is maintained through self-adaptive time control and by correcting previous errors at the current step.

A summary of these various numerical techniques and their applications to several unified theories as well as to Norton's law for integrating a uniaxial stress-strain curve to a total strain of 1-2% is shown in Table IV. As illustrated in Table IV, the explicit Euler is stable when the size of the strain increment is kept below 10^{-4}. The size of the strain increment can be increased by using an implicit method such as the NONSS or α-method with $\alpha = 1$ (implicit Euler). By restricting the comparison to the explicit methods only, it appears that there is no substantial difference between the integrability of Walker and Miller theories nor between these unified theories and the classical Norton law. The size of the strain increment is, however, somewhat sensitive to the values of model constants which describe material strain rate sensitivity.

PREDICTIVE AND SIMULATIVE CAPABILITIES OF UNIFIED CONSTITUTIVE THEORIES

Four of the unified models which have been successfully applied for simulating and/or predicting monotonic, cyclic, creep, and stress relaxation behavior are those of Robinson [8], Walker [2], Bodner-Partom [3,4], and Miller [5]. Robinson's model is based on a yield condition and utilizes loading and unloading criteria, while the latter three do not. The kinetic equations commonly used in unified theories without a yield surface or flow potential are based on the power-law, exponential, and hyperbolic sine functions; these kinetic equations are represented in Walker, Bodner-Partom and Miller theories, respectively. These four theories will be used to illustrate the simulative and predictive capabilities of the unified theories.

(1) Monotonic Stress-Strain Behavior

All unified theories are capable of reproducing the monotonic stress-strain curve. Figure 4 shows an experimental uniaxial tensile stress-strain curve of Hastelloy-X deformed at a strain rate of 1.3×10^{-4} sec^{-1} at 922 K and model simulation using Bodner-Partom theory. The computed curve includes contributions from both work hardening and thermal recovery.

(2) Cyclic Stress-Strain (Hysteresis) Behavior

Bauschinger Effect is represented in most unified theories by a kinematic or directional hardening internal variable. Cyclic hardening, however, can be represented by increases in the isotropic hardening variable, the directional hardening variable, or both. These different types of cyclic

hardening behavior are illustrated in Figure 5 for Bodner-Partom theory which does not use an equilibrium stress. The use of different evolutionary equations for the equilibrium stress in different regions of stress space allows Robinson's model to reproduce rounded hysteresis loops. Examples of cyclic saturated hysteresis loops calculated using Robinson's model are compared with experimental results of 2-1/2Cr-1Mo steel in Figure 6 [27].

(3) Creep Responses

Most of the unified models can predict primary and secondary creep responses of material subjected to constant load. Steady state creep rates are predicted by these unified models to occur when the evolutionary rates of the isotropic and/or directional hardening variable vanish as the hardening terms are balanced by the thermal recovery. Examples of calculated steady state creep rate under constant stress and comparison with experimental data are shown in Figure 7 for Bodner-Partom's model. According to the unified theories, the steady state creep rate is a function of stress and temperature only; it should not depend on the loading histories. This is demonstrated in both experimental data and predictions by Miller's model in Figure 8 [28].

(4) Stress Relaxation Response

The behavior of unified constitutive models under stress relaxation is analogous to the creep behavior. Under a constant strain condition, the relaxation rate would, again, depend on the current values of the internal variables and on the growth laws which describe their changes with time and inelastic deformation. Stress relaxation calculations based on Walker theory is compared with experimental data of Hastelloy-X [2] in Figure 9.

(5) Thermomechanical Response

The behavior of unified constitutive theories under thermomechanical cycling depends critically on the change of material constants with temperature. In particular, the shape of the predicted thermomechanical loop is sensitive to the growth of the kinematic hardening variable (the equilibrium stress) with temperature. Walker's model prediction of thermomechanical loop of Hastelloy-X is shown in Figure 10.

(6) Multiaxial Behavior

All the unified theories utilize single-valued kinetic equations formulated in terms of either $3J_2/K^2$ or $3J_2'/K^2$. For a constant value of the internal variable K and under proportional paths, these kinetic equations predict a locus of constant inelastic strain rate invariant in stress space; the shape of the predicted "yield surface" or "flow potential" is identical to von Mises yield function. For unified models formulated based on the equilibrium stress, the size of the "yield surface" is proportional to K, while the center of the "yield surface" is at Ω_{ij} and translates according to the evolution rate of Ω_{ij}.

Recent studies [22,29], indicate that materials exhibit considerably more cyclic hardening when tested under nonproportional paths of combined tension and torsion than under proportional paths of tension or torsion only. As a result, most if not all,of the constitutive models need to be modified to take into account the hardening behavior due to out-of-phase loading.

SUMMARY AND CONCLUSIONS

1. A review of more than ten time-temperature dependent elastic-viscoplastic constitutive theories indicates that these theories differ in the choice of flow law, kinetic equation, and evolutionary equation of the internal variables.

2. The unified approach treats all aspects of inelastic deformation including plasticity, creep, and stress relaxation using the same set of flow law, kinetic equation, and internal variables.

3. The unified constitutive theories satisfy the uniqueness and stability criteria imposed by Drucker's postulate for rate independent stable plastic flow and Ponter's inequalities for constitutive theories based on internal variables.

4. The unified theories can be formulated either with or without the use of a yield criterion. Three basic flow laws are identified in theories without a yield criterion. For theories with a yield criterion, the associated flow law is derived from the yield function or the flow potential.

5. Three different formulations of the kinetic equations are identified, and they include the exponential, power law, and hyperbolic sine functions. The exponential formulation gives a limiting inelastic strain rate and appears to give better results for high strain rate applications.

6. All three forms of kinetic equations are functions of $3J_2/K^2$ (or $3J_2'/K^2$) and result in "yield surfaces" and equi-creep rate surfaces which are described by the J_2-based von Mises criterion.

7. The number of internal variables varies among the unified theories. Most unified theories use two internal variables, one to represent isotropic hardening and one to present kinematic or directional hardening. The measure of hardening is either the inelaslastic strain rate or the inelastic work rate.

8. Directional (kinematic) hardening can be modeled with or without the use of an equilibrium stress. The directional index of kinematic hardening can be based on either the inelastic strain rate or the direct stress.

9. Material constants in the unified models are necessarily temperature-dependent and required to be evaluated at the temperatures of interest. There are indications that a temperature rate term is also required in the unified theories.

10. All of the unified theories which are reviewed do not automatically predict additional cyclic hardening under nonproportional loading paths. Additional terms are needed in the unified theories to include such hardening behavior.

11. The equilibrium-stress-based unified theories can describe reverse creep and/or reverse stress relaxation behavior without further modifications. Unified models which are not based on the equilibrium stress would require modification by adding an anelastic term in order to take into account these types of behavior.

12. The unified constitutive equations are stiff but can be integrated using either explicit or implicit methods.

ACKNOWLEDGEMENTS

The financial support of NASA through Contract No. NAS3-23925 is gratefully acknowledged.

REFERENCES

1. C. E. Pugh and D. N. Robinson, Nucl. Eng. and Design, 1978, Vol. 48, No. 1, p. 269.

2. K. P. Walker, NASA Contract Report NASA CR 165533, 1981.

3. S. R. Bodner and Y. Partom, ASME J. of Applied Mechanics, Vol. 42, 1975, p. 385.

4. S. R. Bodner, "Evolution Equations for Anisotropic Hardening and Damage of Elastic-Viscoplastic Materials," Pro. Conference on Plasticity Today, Udine, Italy, 1983.

5. A. K. Miller, ASME J. of Eng. Mat. & Tech., Vol. 96, 1976, p. 97.

6. R. D. Krieg, J. C. Swearengen, and R. W. Rohde, in "Elastic Behavior of Pressure Vessel and Piping Components," PVP-PB-028, 1978, p. 15.

7. J. L. Chaboche, Bulletin de L'Academie des Sciences, Serie des Science Techniques, Vol. XXV, No. 1, 1977, p. 33.

8. D. N. Robinson, ORNL Report/TM-5969, 1978.

9. E. W. Hart, ASME J. of Eng. Mat. and Tech., Vol. 98, 1976, p. 193.

10. S. R. Bodner and D. C. Stouffer, Int. J. Engng. Sci., Vol. 21, 1983, pp. 211-215.

11. D. Lee and F. Zaverl, Jr., Acta Met., Vol. 26, No. 11, 1975, p. 385.

12. A. K. Ghosh, Acta Metallurgica, Vol. 28, 1980, p. 1443.

13. H. Kagawa and Y. Asada, Proceedings of the ASME Int. Conf. on Advances in Life Prediction Methods, Albany, New York, 1983, p. 33.

14. E. H. Lee, Int. J. Solids Structures, Vol. 17, 1981, pp. 859-872.

15. P. Perzyna, Advances in Applied Mechanics, Vol. 9, 1966, pp. 243-377.

16. W. Prager, Proc. Inst. Mech. Engrs., Vol. 169, 1955, p. 41.

17. U. S. Lindholm and S. R. Bodner, unpublished research, 1983.

18. R. W. Bailey, J. of Institute of Metals, Vol. 35, 1926, p. 27.

19. E. Orowan, J. West. Scot. Iron & Steel Inst., Vol. 54, 1946, p. 45.

20. J. Friedel, "Dislocations," Addison Wesley Pub. Co., 1967, pp. 277-279.

21. H. Ziegler, Quart. Appl. Math., Vol. 17, 1959, p. 55.

22. U. S. Lindholm, K. S. Chan, S. R. Bodner, and K. P. Walker, unpublished research, 1983.

23. A.R.S. Ponter, Int. J. Solids Structure, Vol. 16, 1980, p. 793.

24. D. C. Drucker, J. de Mechanique, Vol. 3, 1964, p. 235.

25. V. Kumar, M. Morjaria and S. Mukerjee, ASME J. of Eng. Mat. and Tech., 1980, Vol. 102, p. 92.

26. T. G. Tanaka, "Deformation of Metals and Alloys," Ph.D. Thesis, Stanford University, 1983.

27. D. N. Robinson and R. W. Swindeman, ORNL Report TM-8444, 1982.

28. O. D. Sherby and A. K. Miller, ASME J. of Eng. Mat. and Tech., 1979, Vol. 101, p. 387.

29. H. S. Lamba and O. M. Sidebotton, ASME J. of Eng. Mats. and Technology, 1978, Vol. 100, p. 96.

30. B. N. Cassenti, Proceedings of AIAA/SAE/ASME 19th Joint Propulsion Conference, Seattle, WA, 1983.

31. D. Lee, C. F. Shih, F. Zaverl, Jr., and M. D. German, EPRI NP-500 RP 452-2, Final Report, May 1977.

TABLE I

FIVE FORMS OF TEMPERATURE-DEPENDENT KINETIC EQUATIONS WITH THE CORRESPONDING ACTIVATION ENERGY FUNCTION

Activation Energy	Temperature-Dependent Kinetic Equations
$\Delta H = C\ell n\left(\frac{K^2}{3J_2}\right)$	$D_2^p = D_0\left[\frac{3J_2}{K^2}\right]^{C/kT}$
$\Delta H = H_0 - Vg(J_2)$	$D_2^p = D_0 exp\left[-\frac{H_0 - Vg(J_2)}{kT}\right]$
$\Delta H = \frac{H^* K^2}{3J_2}$	$D_2^p = D_0 exp\left[-\frac{H^*}{kT}\left(\frac{K^2}{3J_2}\right)\right]$
$\Delta H = kT\left[\frac{K^2}{3J_2}\right]^{C/kT}$	$D_2^p = D_0 exp\left[-\left(\frac{K^2}{3J_2}\right)^{C/kT}\right]$
$\Delta H = Q$	$D_2^p = D_0 exp\left[-\frac{Q}{kT}\right]\left[sinh\left(\frac{3J_2}{K^2}\right)^m\right]^n$

where C, D_0, H*, H_0, Q, m, and n are constants; V is the activation volume; and k is the Boltzmann's constant.

TABLE II

THE SPECIFIC FORMS OF ISOTROPIC HARDENING AND STATIC THERMAL RECOVERY FUNCTIONS USED IN THE SELECTED UNIFIED CONSTITUTIVE THEORIES

$$\dot{K} = h_1(K)\dot{M}_1 - r_1(T,K)$$

where $\dot{M}_1 = \dot{\bar{\varepsilon}}$; $\dot{\bar{\varepsilon}} = \sqrt{\frac{2}{3}\dot{\varepsilon}_{ij}^{p}\dot{\varepsilon}_{ij}^{p}}$

or $\dot{M}_1 = \dot{W}_p$ (Bodner-Partom's Theory)

Model	Hardening Function, $h_1(K)$	Static Thermal Recovery Function, $r_1(T,K)$
Bodner-Partom	$C_1(K_1 - K)$	$C_2(K - K_o)^p$
Walker	$C_1(K_1 - K)$	-
Krieg et al	C_1	$C_2(K - K_o)^p$
Robinson	C_1	-
Chaboche	$C_1(K_1 - K) + f_1(\bar{\varepsilon}, \dot{\bar{\varepsilon}}, \Omega_{ij})$	-
Lee and Zaverl	$C_1(K_1^* - K)/\sqrt{J_2}$	-
Hart	C_1	-
Ghosh	$C_1 K^{-q}$	$C_2(K - K_o)^p$
Miller	$C_1[K_1 - C_4(\sinh^{-1} C_3\lvert\dot{\bar{\varepsilon}}\rvert)^q K^m]$	$C_2[\sinh C_3 K^m]^p$

where C_1, C_2, C_3, C_4, C_5, m, p, q, K_o, and K_1 are material constants; K_1^* is the saturated value of K; K_1^* is governed by an evolutionary equation which is function of $\dot{\bar{\varepsilon}}$ and J_2.

TABLE III

THE SPECIFIC FUNCTIONS OF ANISOTROPIC HARDENING, DYNAMIC RECOVERY, STATIC THERMAL RECOVERY, AND THE TEMPERATURE RATE TERM IN SELECTED UNIFIED CONSTITUTIVE THEORIES

$$\overset{\nabla}{\alpha}_{ij} = h_2(\alpha_{ij}, T)\dot{\alpha}_{ij} - d(\alpha_{ij}, T)\dot{\alpha}_{ij} - r_2(\alpha_{ij}, T)v_{ij} + \dot{\alpha}(\alpha_{ij}, T)\dot{T}\omega_{ij}$$

where: $v_{ij} = \alpha_{ij}/(T_2)^{1/2}$, $T_2 = \beta/2\ \alpha_{kl}\alpha_{kl}$ (except Walker, $v_{ij} = g_{ij}$)

$$g_{ij} = \Omega_{ij} - \overset{\circ}{\Omega}_{ij} - n_1\dot{\varepsilon}_{ij}$$

Model	Hardening Function, h_2	$\dot{h}_{ij}$	Dynamic Recovery Function, d	$\dot{d}_{ij}$	Static Thermal Recovery function, r_2	Temperature Rate function, $\dot{\theta}$	ω_{ij}
Bodner-Partom	$n_1 n_2$	$\dot{W}_p v_{ij}$	$n_1(T_2)^{1/2}$	$\dot{W}_p v_{ij}$	$n_3 T_2^s$	-	-
Walker	$n_1 + n_2$	$\dot{\varepsilon}_{ij}$	f_1	$\dot{\varepsilon} g_{ij}$	$n_6 T_2^s$	$\frac{\partial n_1}{\partial T} + \frac{1}{n_2}\frac{\partial n_2}{\partial T}$	ε_{ij}, g_{ij}
Krieg et al	$n_1 + n_2 \exp[-f_0/n_2]$	$\dot{\varepsilon}_{ij}$	-	-	$n_3 T_2^s$	-	-
Robinson	$n_1 T_2^{-s}$	$\dot{\varepsilon}_{ij}$	-	-	$n_2 T_2^b$	-	-
Chaboche	$n_1 n_2 f_2$	$\dot{\varepsilon}_{ij}$	$n_2 f_2$	$\dot{\varepsilon}\Omega_{ij}$	$n_3 n_2 T_2^s$	f_3	ω_{ij}
Lee and Zaverl	$1.5n_1[J_2']^{-1/2}$	$\dot{\varepsilon}\alpha^{\circ}_{ij}$	$1.5n_1[J_2']^{-1/2}$	$\dot{\varepsilon}\Omega_{ij}$	-	-	-
Hart	n_1	$\dot{\varepsilon}_{ij}$	-	-	$n_2 n_3 \left(\frac{\sigma^{\circ}_{ij}}{\nu}\right)^b \left[\log\left(\frac{\sigma^{\circ}_{ij}}{\sqrt{J_2'}}\right)\right]^{-s}$	-	-
Ghosh	-	-	-	-	-	-	-
Miller	n_1	$\dot{\varepsilon}_{ij}$	n_2/f_4	$\dot{\varepsilon}\Omega_{ij}$	$n_3(\sinh n_4\sqrt{T_2})^s$	-	-

where: $f_0 = (\omega_{ij} - \Omega_{ij})\omega_{ij}$

$f_1 = n_3 + n_4\exp(-n_5\bar{\varepsilon})$

$f_2 = n_4 + (1 - n_4)\exp(-n_5\bar{\varepsilon})$

$f_3 = \frac{1}{n_2}\frac{\partial n_2}{\partial T} + \frac{1}{n_1}\frac{\partial n_1}{\partial T} + \frac{1}{f_2}\frac{\partial f_2}{\partial T}$

$f_4 = \sinh^{-1}(n_6\bar{\varepsilon})^b$

$\omega_{ij} = \omega_{ij}/(\omega_{kl}\omega_{kl})^{1/2}$

$J_2' = 1/2(s_{ij} - \alpha_{ij})(s_{ij} - \alpha_{ij})$

$\beta = 1$, 2, or 4/3, depending on the model

n_1, n_2, n_3, n_4, n_5, n_6, b, and s are material constants.

Ω°_{ij} are the saturated values of Ω_{ij}; Ω°_{ij} are governed by evolutionary equations which are functions of $\bar{\varepsilon}$ and J_2'.

TABLE IV

COMPARISONS OF THE INTEGRATABILITY OF VARIOUS CONSTITUTIVE MODELS

Comparison is based on the size of the average strain increment per step for integrating a uniaxial tensile stress-strain curve to a total strain of 1-2%

Constitutive Model	Integration Method	Strain Increment Per Step	Automatic Time or Strain Increment Control	Stability	Reference
Walker	Explicit Euler	10^{-5} to 10^{-4}	No	Stable	Walker [2]; Cassenti [30]
Bodner-Partom	NONSS (α-Method)				Present Investigation
	$\alpha = .1$	1×10^{-4}	No	Stable	
	$\alpha = .5$	1×10^{-4}		Stable	
	$\alpha = 1$	1×10^{-3}		Stable	
Miller	Explicit Euler	4×10^{-4}	No	Unstable	Lee et al [31]
	Tayler Series Modified Euler	4×10^{-4}	No	Stable	Lee et al
	NONSS (α-Method, $\alpha = 1$)	3×10^{-3}*	Yes	Stable	Tanaka [26]
Hart	Explicit Euler	2×10^{-5}*	Yes	Stable	Kumar et al [25]
	Predictor-Corrector	3×10^{-5}*	Yes	Stable	Kumar et al
	High Order Predictor-Corrector	3×10^{-5}*	Yes	Stable	Kumar et al
	Two-Step Adam	2×10^{-5}*	Yes	Stable	Kumar et al
Norton	Explicit Euler	1×10^{-3}	No	Unstable	Lee et al [31]
		5×10^{-4}	No	Stable	Lee et al
	Taylor Series Modified Euler	1×10^{-3}	No	Stable	Lee et al

* Average strain increment per step = total strain/number of time steps.

DEVIATORIC STRESS SPACE

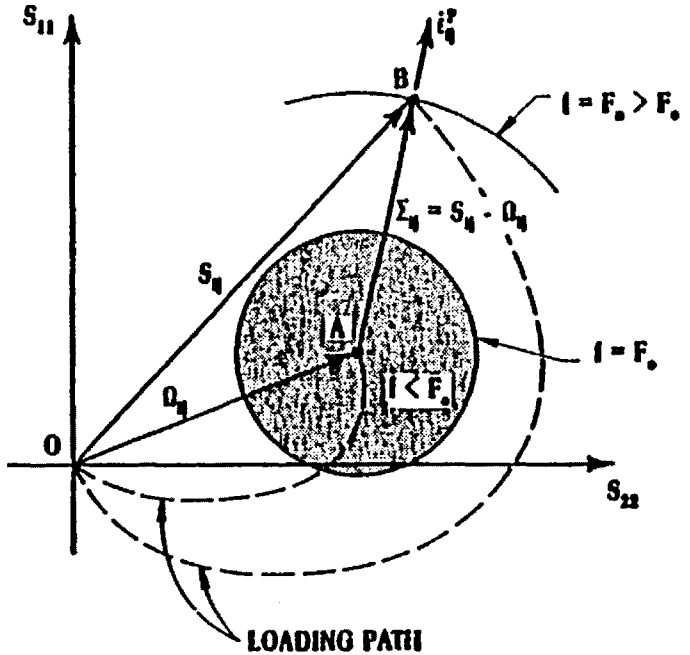

Figure 1. Graphical representation of the basic flow laws used in the unified constitutive theories. For theories based on an equilibrium stress, the inelastic strain rate vector $\dot{\varepsilon}^p_{ij}$ is coaxial with the effective stress Σ_{ij} and normal to the flow potential f if such a concept is used. For theories which do not include an equilibrium stress, $\dot{\varepsilon}^p_{ij}$ is coaxial with the deviatoric stress S_{ij} for both isotropic and incrementally isotropic cases but is noncoaxial with S_{ij} for generalized anisotropic cases.

KINETIC RELATIONS

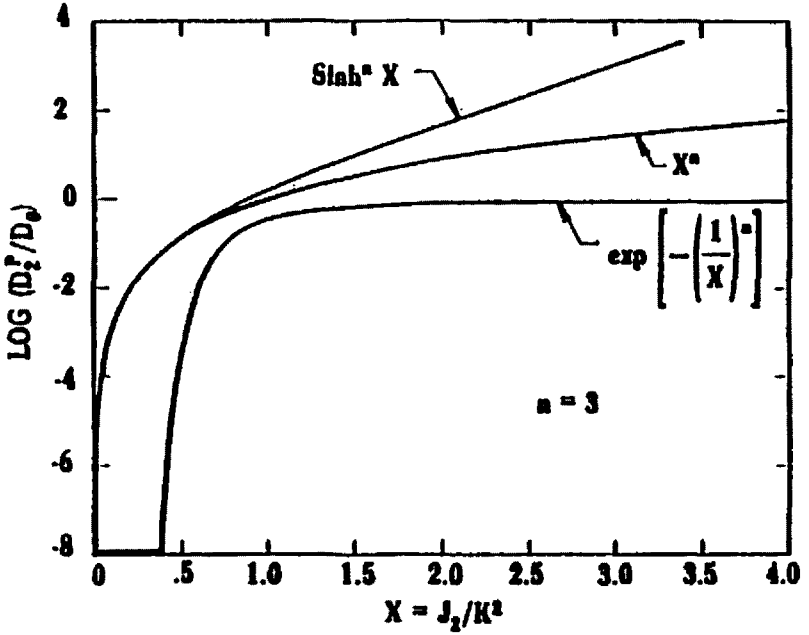

Figure 2. Functional behavior of the kinetic equations used in the unified constitutive theories. The exponential formulation in Bodner-Partom's theory is seen to give a limiting inelastic strain rate of D_0.

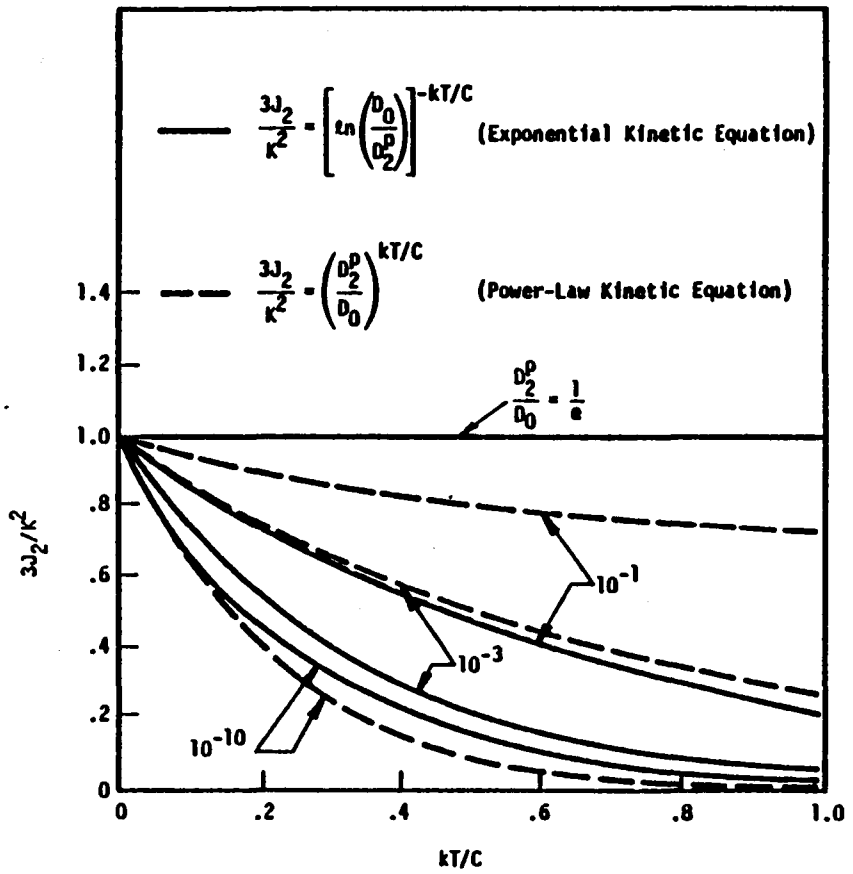

Figure 3. Functional behavior of temperature-dependent kinetic equations utilized in Bodner-Partom and Walker theories.

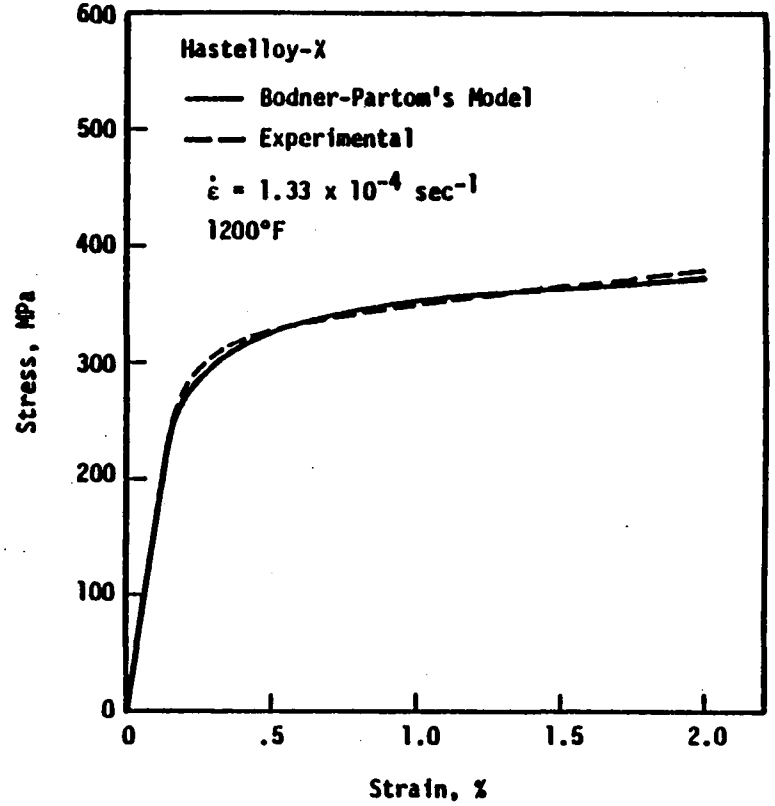

Figure 4. A monotonic stress-strain curve simulated by Bodner-Partom's Model for Hastelloy-X at 1200°F.

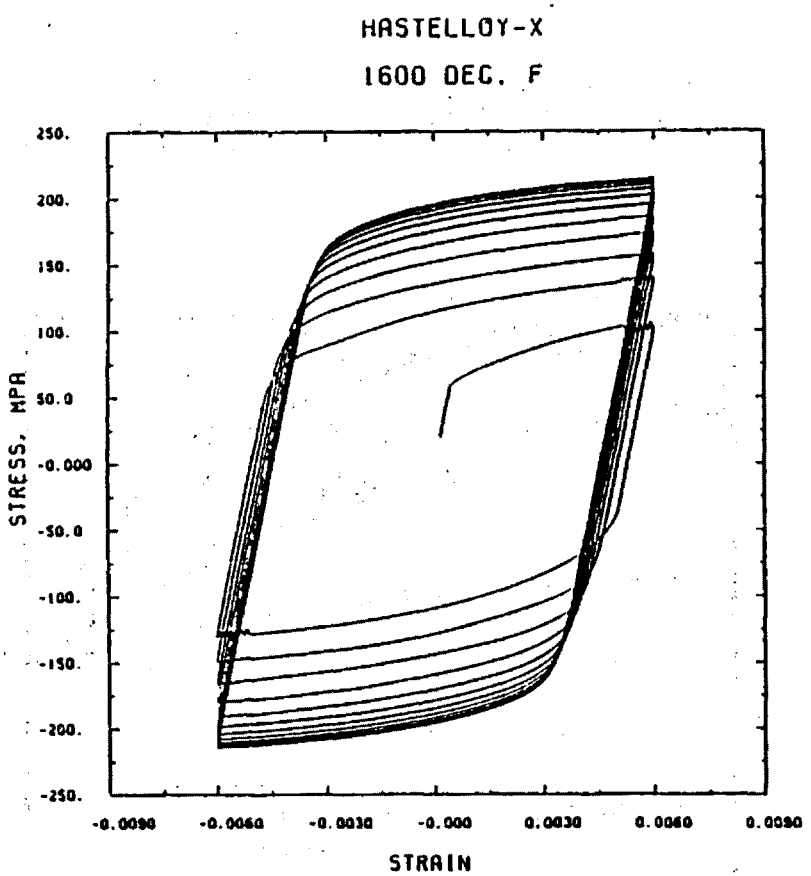

Figure 5. Cyclic stress-strain hysteresis loop simulated by Bodner-Partom's Model for Hastelloy-X at 1600°F.

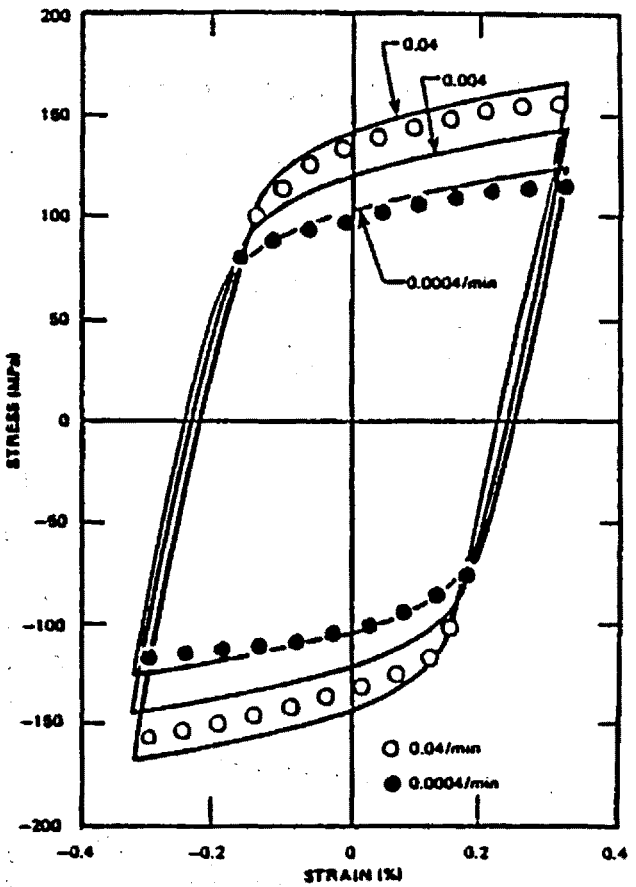

Figure 6. Stable hysteresis loops of 2-1/4Cr-1Mo steel for $\Delta\epsilon \approx \pm .32\%$ at various strain rates at 538°C. The calculated curves (solid lines) are generated with Robinson's Model, from [27].

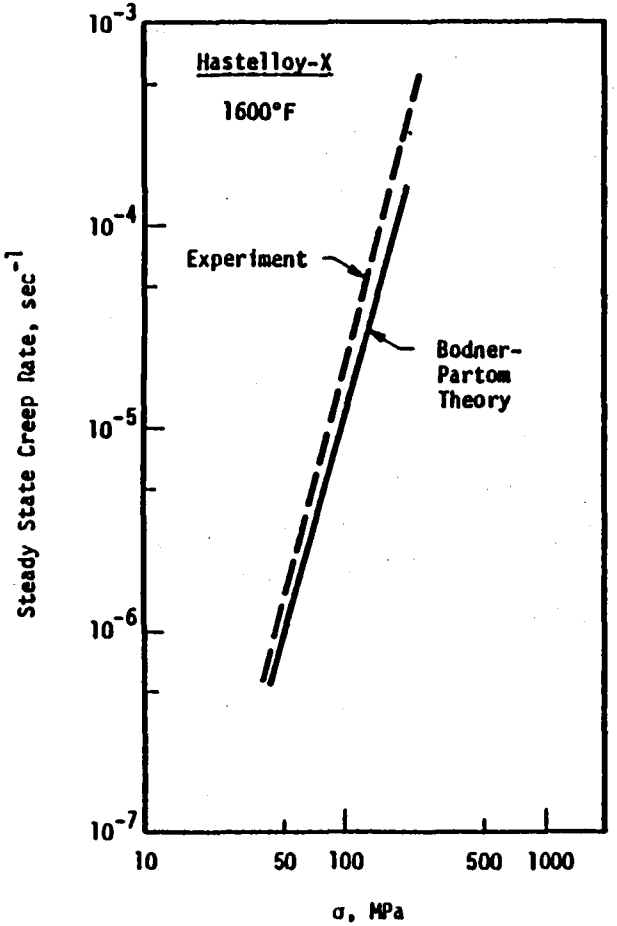

Figure 7. Steady creep rates as a function of stress simulated by Bodner-Partom's Model.

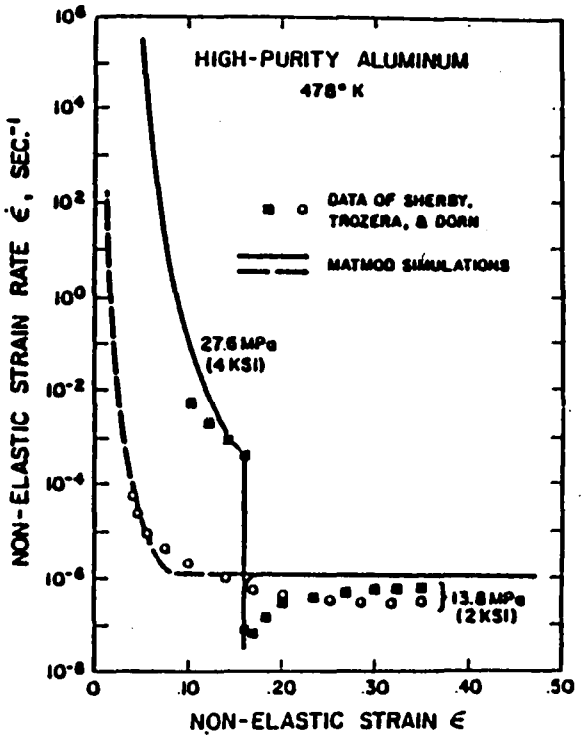

Figure 8. Miller's Model prediction compared with experimental data for a creep test with a sudden decrease in applied stress, from [28].

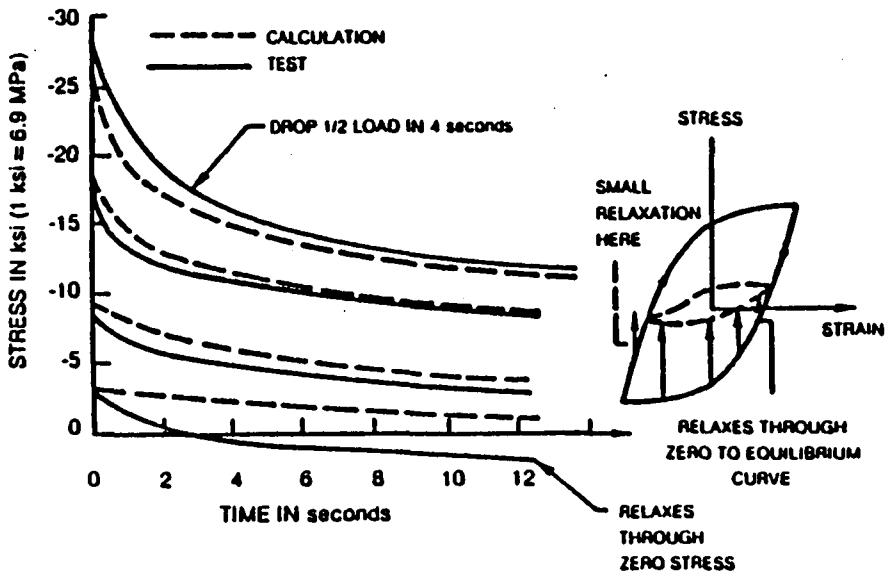

Figure 9. Negative stress relaxation response of Hastelloy-X at 871°C (1600°F) initiated from a steady state hysteresis loop executed at a constant strain rate of $\pm$ 1.35 x 10^{-3} sec^{-1} with a strain amplitude of $\pm$ .4%. The calculated curves are based on Walker's theory, from [2].

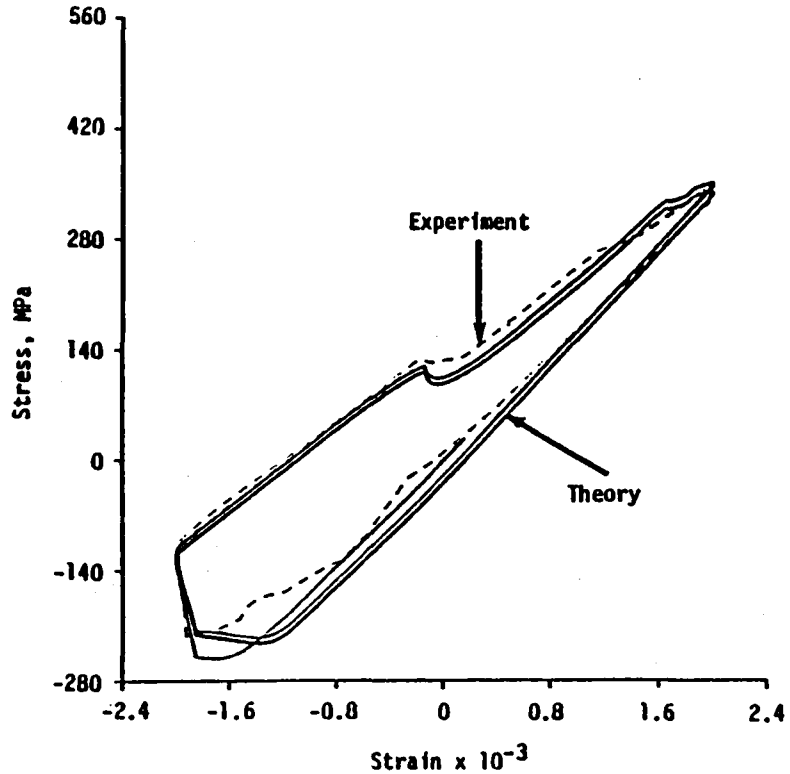

Figure 10. Thermomechanical stress-strain prediction by Walker's theory.

Page intentionally left blank

VISCOPLASTICITY BASED ON OVERSTRESS WITH A DIFFERENTIAL GROWTH LAW FOR THE EQUILIBRIUM STRESS

E. Krempl, J.J. McMahon[1], D. Yao
Department of Mechanical Engineering
Aeronautical Engineering & Mechanics
Rensselaer Polytechnic Institute
Troy, New York 12181

Two coupled, nonlinear differential equations are proposed for the modeling of the elastic and rate (time)-dependent inelastic behavior of structural metals in the absence of recovery and aging. The structure of the model is close to the unified theories but contains essential differences. The properties of the model are delineated by analytical means and numerical experiments.

It is shown that the model reproduces almost elastic regions upon initial loading and in the unloading regions of the hysteresis loop. Under loading, unloading and reloading in strain control the model simulated the experimentally observed sharp transition from nearly elastic to inelastic behavior. These properties are essential for modeling mean stress effects in tension-tension strain cycling. When a formulation akin to existing unified theories is adopted the almost elastic regions reduce to points and the transition upon reloading is very gradual.

For different formulations the behavior under sudden in(de)creases of the strain rate by two orders of magnitude is simulated by numerical experiments and differences are noted.

The model presently represents cyclically neutral behavior and contains three constants and two positive, decreasing functions. It is described how these constants and functions can be determined from tests involving monotonic loading with strain rate changes and relaxation periods.

---

[1] Now at NASA, Houston, Texas.

INTRODUCTION

Within the last decade the modeling of inelastic deformation through unified constitutive equations has made considerable progress [1-6]. With the exception of [5], yield surfaces are not used in these approaches and creep and time independent plasticity are not considered separately. It is shown in [6] that these constitutive equations have similar mathematical structure but that they differ with regard to the specific choices of material functions.

The models make the inelastic strain rate a function of the effective stress defined as stress minus some quantity referred to as kinematic stress, rest stress or back stress. In examining the mathematical properties of a first-order nonlinear differential constitutive equation it was shown [7] that making the inelastic strain rate solely dependent on the overstress gives qualitative solution properties of the differential equations found in corresponding experiments. The overstress is the difference between the stress and the equilibrium stress and is equivalent to the effective stress mentioned above.

This approach has been verified for monotonic loading of Type 304 SS [8] and of a Ti alloy [9]. The purpose of the present paper is to present a further development of the theory of viscoplasticity based on overstress for cyclic loading. It will be shown that this development is similar to the unified theories but contains essential modifications which are necessary for reproducing regions of nearly elastic behavior and realistic reloading behavior. These properties are basic for the modeling of mean stress effects in zero to maximum strain strain controlled cycling.

THE MAIN PROPOSED MODEL

Differential Formulation

For the uniaxial state of stress with σ and ϵ denoting the engineering stress and infinitesimal strain, respectively, the model is given by the two coupled nonlinear differential equations

$$\dot{\epsilon} = \dot{\epsilon}^{e\ell} + \dot{\epsilon}^{in} = \dot{\sigma}/E + \frac{\sigma - g}{Ek[\sigma - g]} \tag{1}$$

$$\dot{g} = \psi[\ ]\dot{\epsilon} - \frac{g - f[\ ]}{b[\ ]} |\dot{\epsilon}^{in}| \ . \tag{2}$$

In the above E is the elastic modulus and square brackets following a symbol denote "function of." The positive, bounded, decreasing function k is called the viscosity function, it has the dimension of time and controls the rate dependence. In the growth law for the equilibrium stress g there are three positive bounded functions, ψ, f and b, the argument of which will be determined in the sequel. For this

reason their arguments are not specified presently. A superposed dot denotes differentiation with respect to time and the absolute value of a quantity is denoted by placing it between vertical bars.

At the present this constitutive equation does not have any provisions for modeling recovery and/or aging. It is therefore only applicable in regions where these two phenomena are not pronounced.

By using the chain rule (1) and (2) can be rewritten as

$$\frac{d\sigma}{d\epsilon} = E - \frac{\sigma - g}{k[\sigma - g]\dot{\epsilon}} \tag{3}$$

$$\frac{dg}{d\epsilon} = \psi - \frac{g - f}{b}\left|1 - \frac{1}{E}\frac{d\sigma}{d\epsilon}\right| \operatorname{sign} \dot{\epsilon} \ . \tag{4}$$

The basic equations (1) - (4) will now be reformulated so as to identify the as yet unspecified functions with physical properties and to obtain mathematical properties of this system of nonlinear differential equations.

Integral Formulation

Following the procedures of [7], (1) and (2) can be transformed to the integral relations

$$\sigma - g = (\sigma_o - g_o)\exp - \int_{t_o}^{t} \frac{d\tau}{k} + \int_{t_o}^{t} (E\dot{\epsilon} - \dot{g})\left(\exp - \int_{\tau}^{t} \frac{ds}{k}\right)d\tau \tag{5}$$

and

$$g - f = (g_o - f_o)\exp - \int_{t_o}^{t} \frac{|\dot{\epsilon}_{in}|}{b}\,d\tau + \int_{t_o}^{t} (\psi\dot{\epsilon} - \dot{f})\left(\exp - \int_{\tau}^{t} \frac{|\dot{\epsilon}_{in}|}{b}\,ds\right)d\tau \tag{6}$$

respectively. A subscript zero indicates the value of the subscripted quantity at the initial time $t = t_o$.

Since the integrand of each first term on the right-hand side of (5) and (6) is positive its value will tend to zero for large times, provided that in (6) $|\dot{\epsilon}^{in}|$ will be different from zero as time increases.

The second terms tend to a limiting value for infinite time [7] so that

$$\{\sigma - g\} = \left\{E - \frac{dg}{d\epsilon}\right\} \dot{\epsilon} k\left[\{\sigma - g\}\right] \tag{7}$$

and

$$\{g - f\} = \left\{\psi - \frac{df}{d\epsilon}\right\} \left\{\frac{b}{|\dot{\epsilon}^{in}|}\right\} \dot{\epsilon} \tag{8}$$

where braces denote asymptotic values. By differentiation of (5) and (6) and taking the limit for $t \to \infty$ [7]

$$\{\dot{\sigma}\} = \{\dot{g}\} \tag{9}$$

and

$$\{\dot{g}\} = \{\dot{f}\} \tag{10}$$

are, respectively, obtained.

It is evident that (1) and (2) require σ, g and f to grow ultimately at the same rate, provided the functions have the properties stated initially and that $|\dot{\varepsilon}^{in}|$ does not become zero for large times. Also from (7) and (8) it is required that $\dot{\varepsilon}$ be bounded and constant for large times.

Behavior Under Instantaneous Changes in Stress or Strain Rate

The behavior of (1) under an instantaneous change in stress or strain rate has been determined in [10-12].

A superposed +(-) designates the value of a quantity immediately after (before) the jump. Then applying (3) and (4) before and after the jump yields ($\dot{\varepsilon}^{in}$ is continuous under a jump)

$$\left(\frac{d\sigma^+}{d\varepsilon} - E\right)\dot{\varepsilon}^+ = \left(\frac{d\sigma^-}{d\varepsilon} - E\right)\dot{\varepsilon}^- \tag{11}$$

and

$$\frac{dg^+}{d\varepsilon} = \frac{dg^-}{d\varepsilon}\frac{\dot{\varepsilon}^-}{\dot{\varepsilon}^+} + \psi\left(1 - \frac{\dot{\varepsilon}^-}{\dot{\varepsilon}^+}\right) \quad \text{for strain control} \tag{12a}$$

$$\frac{dg^+}{d\varepsilon} = \frac{dg^-}{d\varepsilon}\frac{\dot{\sigma}^-}{\dot{\sigma}^+}\alpha + \psi\left(1 - \alpha\frac{\dot{\sigma}^-}{\dot{\sigma}^+}\right) \quad \text{for stress control} \tag{12b}$$

where $\alpha = \dfrac{d\sigma^+/d\varepsilon}{d\sigma^-/d\varepsilon}$. It is seen that the slope of g is related to that of σ but the slope of σ is not influenced by g at all. As a consequence the properties of $d\sigma/d\varepsilon$ as determined in [10-12] remain unaltered.

If it is now assumed that the asymptotic properties (7) - (10) and $d\sigma^-/d\varepsilon \approx E_t \ll E$ with $E_t \geq 0$ the tangent modulus[1] in the inelastic range hold, then the slopes of σ and g can be calculated for increase, decrease, reversal, reversal with increase and reversal with decrease of the stress or strain rate. Under the above assumptions (12) simplifies to

---

[1] This designates the slope at the limit of the region of interest.

$$\frac{dg^+}{d\epsilon} = \psi + \frac{\dot{\epsilon}^-}{\dot{\epsilon}^+}(E_t - \psi) \quad \text{for strain control} \tag{13a}$$

and

$$\frac{dg^+}{d\epsilon} = \psi + \frac{\dot{\sigma}^-}{\dot{\sigma}^+}(E_t - \psi)\,\frac{d\sigma^+/d\epsilon}{E_t} \quad \text{for stress control} \tag{13b}$$

It can be observed that no changes in the slope of g are realized when the asymptotic value of ψ is equal to E_t.

Values obtained from (11) and (13a), (13b) are given in Table 1 where it is assumed that rate changes involve at least one order of magnitude.

Creep and Relaxation Behavior

During relaxation $\dot{\epsilon} = 0$ and from (1) and (2)

$$\dot{\sigma} = -\frac{\sigma - g}{k[\sigma - g]} \tag{14}$$

and

$$\dot{g} = -\frac{g - f}{b}\,|\dot{\epsilon}^{in}| \tag{15}$$

respectively. It is seen that both $\dot{\sigma} < 0$ and $\dot{g} < 0$, if $\sigma - g > 0$ and $g - f > 0$. From (5) and (6) it can be deduced that these conditions are met at any point during a prior tensile test provided $\dot{\epsilon} > 0$ and $E - \frac{dg}{d\epsilon} > 0$ and $\psi - \frac{df}{d\epsilon} > 0$. (If $\dot{\epsilon} < 0$ the sign of $\sigma - g$ and $g - f$ reverses and $\dot{\sigma}$ and $\dot{g}$ are positive.) Therefore σ and g always decrease in magnitude but not uniformly. Indeed from (14) and (15)

$$\frac{\dot{\sigma}}{\dot{g}} = \frac{bE}{g - f} \tag{16}$$

Unless $(g - f)/b < E$ the quantity on the right-hand side exceeds one and $\dot{\sigma} > \dot{g}$, so that σ relaxes faster than g.

Stress relaxation stops at $\sigma = g$ but since $\dot{g}$ is zero at both $\sigma = g$ and at $g - f$ it is not clear whether equilibrium is reached at $g = f$, or at $g > f$ when $\sigma = g$. If the right-hand side of (16) is greater than one it is expected that $\dot{\sigma} = 0$ at $g > f$.

In creep (1) and (2) specialize to (σ_c is the constant stress in the creep test)

$$\dot{\epsilon} = \frac{\sigma_o - g}{Ek[\sigma_o - g]} \tag{17}$$

and

$$\dot{g} = \psi\dot{\epsilon} - \frac{g - f}{b} |\dot{\epsilon}| , \qquad (18)$$

respectively. It is seen by comparing (18) and (2) that the growth of g in creep is slightly modified compared to constant strain rate loading since in creep $\dot{\epsilon} = \dot{\epsilon}^{in}$. Differentiation of (17) yields

$$\ddot{\epsilon} = - \frac{\dot{g}}{k^2 E} (k - (\sigma_o - g)k') \qquad (19)$$

where $k' = \frac{dk[x]}{dx} < 0$ by initial stipulation. Secondary creep will be obtained when $\dot{g} = 0$ and this is accomplished when $\dot{f} = \frac{df}{d\epsilon} \dot{\epsilon} = 0$, i.e., when the tangent of f is ultimately horizontal, see (10). Primary creep results if $\dot{g} > 0$. In this case creep terminates at $\sigma_o = g$. If $\sigma_o > g$ for all values of g creep will never terminate.

REQUIREMENTS ON A REALISTIC MODEL

The following requirements are put on the model:

1) There is an initial nearly linear elastic region starting from zero to some finite stress. In this region there is not only $d\sigma/d\epsilon = E$ but there is also no creep and relaxation.

2) After unloading there is again an elastic region with the same properties as 1) which starts below the stress at which reversal begins and can end at zero stress but usually ends at a stress magnitude larger than zero.

3) When a creep test is performed at zero stress after prior inelastic deformation the strain magnitude will either stay constant or will decrease. However, equilibrium will be reached very close to the inelastic strain at which the creep test started. In no way should the strain magnitude increase nor should zero strain be reached at equilibrium if the strain magnitude decreases. (Aftereffect, recovery test.)

4) After the initial linear elastic region inelastic deformation sets in characterized by a tangent modulus much less than the elastic modulus. The material exhibits normal rate sensitivity (an increase in rate increases the stress level), creep and relaxation. (The region of creep and relaxation may already begin upon loading before $d\sigma/d\epsilon$ decreases appreciably.)

5) Primary and secondary creep may be experienced together with possible "anomolous" creep behavior. (Creep rate may not necessarily increase with stress increase, at the same stress level creep rate is higher on loading than on unloading, see [6,8,13,14].)

6) When relaxation behavior is considered it is not uniform everywhere on the hysteresis loop. It is most pronounced where the tangent modulus is low. It is minimal when the tangent modulus is close to the elastic modulus below the stress at which unloading started and above zero stress. At zero stress relaxation, if it occurs, is small and such that the stress magnitude increases [14,15]; see also 2).

7) After unloading to zero stress and subsequent reloading in strain control the transition to inelastic deformation is very sharp. A small hysteresis loop may develop in the quasielastic region.

8) In cyclic loading cyclic hardening, softening or cyclic neutral behavior should be reproduced.

9) The behaviors listed in 3) - 8) should not be peculiar to a certain stress or strain value or region. Rather they are inelastic properties found in the nonelastic regions.

SELECTION OF FUNCTIONS ψ, f AND b

In the following the simplest choice for these functions will be made such that the requirements listed above will be met as far as possible. The choices have been arrived at after numerous numerical experiments [16,17] which included other possibilities than those allowed by (1) and (2).

In view of (9) and (10)

$$f = E_t \epsilon \ . \tag{20}$$

This selection permits the final slope of the stress-strain diagram to be selected by the usual choice $E_t \geq 0$. (The model permits the use of a negative E_t. This will be explored in the future.)

The choice

$$\psi = \psi[\sigma - g] > 0 \tag{21}$$

with

$$\psi' < 0 \ , \ \psi[0] = \bar{E} < E$$

and $\psi[-x] = \psi[x]$ helps to satisfy conditions 1) - 3), 6), 7) and 9). (It is not possible to have ψ depend on $\sigma - g$ and to have $\psi[0] = E$. In this case (1) and (2) produce only linear elastic behavior. For this reason $\bar{E} = 0.99\ E$ is usually chosen.)

This choice makes g rate dependent, see (8). In this case k and g would both be responsible for rate dependence and inverse rate-sensitivity could be modeled (the stress decreases upon an increase in stress (strain) rate). However, for the present purposes it was decided to make the

asymptotic value of g - f and therefore of g independent of rate by selecting

$$b = \frac{A}{\psi[\sigma - g] - E_t} \tag{22}$$

where $A > 0$ is the asymptotic value of $\{g - f\}$. With this choice g will be rate dependent after the initial elastic region and before the asymptotic solution is reached. However, the initial and final properties of g are independent of loading rates.

Using (22), (1) and (2) reduce to

$$\dot{\epsilon} = \frac{\dot{\sigma}}{E} + \frac{\sigma - g}{Ek[\sigma - g]} \tag{23}$$

$$\dot{g} = \psi[\sigma - g]\dot{\epsilon} - \frac{(g - E_t\epsilon)(\psi[\sigma - g] - E_t)}{A} |\dot{\epsilon}^{in}| \ . \tag{24}$$

In this version the model has two free functions k and ψ and three positive constants with dimensions of stress E, E_t and A which permit fitting to experimental data of a given material. The functions k (dimension time) and ψ (dimension stress) are restricted to be positive and to decrease with increasing argument. Appropriate mathematical forms must be found and their choice will influence rate dependence (k) and the shape of the stress-strain diagram especially the transition from elastic behavior to inelastic behavior (ψ). A procedure for curve fitting is given in the Appendix.

With this choice of functions the model represents symmetry with regard to the origin and a generalized Masing hypothesis. To illustrate this consider a test starting from the origin loaded with constant $\dot{\epsilon}$ in compression. Another test is first loaded to some positive value of stress and strain, so that $\sigma_o - g_o > 0$ and $g_o - f_o > 0$, before loading with the same $\dot{\epsilon}$ in compression as the first test. From (5) and (6) we see that ultimately both tests produce the same g - f and σ - g. Since $f = E_t\epsilon$ the same g and therefore the same σ will be finally obtained, see also (7) and (8).

Because of these properties the model does not reproduce cyclic hardening or softening. These properties require that one or more constants be made dependent on an accumulating measure of history such as the inelastic strain path length. Another possibility is to postulate an extra growth law for A which controls the stress level and/or to make E_t depend on, say, the inelastic strain-path length. These additions are under development.

Whether or not these ultimate values are obtained at strain levels of interest depends on how fast the first terms on the right-hand side of (5) and (6) become negligible. Experience with numerical experiments

has shown that these asymptotic values can be obtained with reasonable accuracy at strains of one percent.

Aside from these general properties the details must be evaluated through numerical experiments, i.e., the automatic integration of (23) and (24) subject to various stress or strain histories. This will be done presently by selecting the constants and functions. Numerical integration was performed using the IMSL program DGEAR on an IBM 3033 or 3081D computer.

DISCUSSION AND NUMERICAL EXPERIMENTS

Relation to Other Models

The present model falls in the general category of the unified models which do not separately consider the actions of creep and plasticity. According to [6] the unified models can be written as

$$\dot{\epsilon} = \dot{\epsilon}^{el} + \dot{\epsilon}^{in} \tag{25}$$

$$\dot{\epsilon}^{in} = F\left[\frac{\sigma - \Omega}{K}\right]; \quad F[0] = 0; \quad F[-x] = -F[x] \tag{26}$$

$$\dot{\Omega} = f_1 \dot{\epsilon}^{in} - f_2 \Omega |\dot{\epsilon}^{in}| - f_3 |\Omega| \tag{27}$$

$$\dot{K} = f_4 \dot{\epsilon}^{in} - f_5 K |\dot{\epsilon}^{in}| - f_6 K \tag{28}$$

where $f_1 - f_6$ are either positive constants or positive functions of one, two or three of the variables σ, Ω and K.

Comparison of (23) through (28) with (1) and (2) reveals the following:

i) The functions f_3 and f_6 are absent

ii) The variable K is not represented

iii) ψ assumes the role of f_1 but it is multiplied by $\dot{\epsilon}$ instead of $\dot{\epsilon}^{in}$.

The reasons for these choices are:

i) Since the model is intended for regions where recovery of hardening (annealing) are considered to be insignificant the recovery terms f_3 and f_6 are omitted.

ii) The isotropic drag stress term is not included since it implies that rate sensitivity changes significantly with deformation behavior. Inversion of (26) yields

$$\sigma - \Omega = KF^{-1}(\dot{\epsilon}^{in}) . \tag{29}$$

It demonstrates that the overstress (effective stress) $\sigma - \Omega$ is proportional to K. Comparing two specimens at the same inelastic strain rate, but different histories leading to different values of K would also lead to different effective stresses (overstresses) and therefore different rate sensitivities.

Elevated temperature experiments aimed at determining whether hardening is due to growth in Ω or to a growth in K or both are not known to the authors. Indeed a recent review does not address this question [18]. However, in [30] a change in K was inferred from a change in the stress drop with cycling during constant strain hold-time tests on 316 stainless steel at 600°C. Experiments at room temperature on the strongly hardening annealed Type 304 SS [19,20] showed that essentially all hardening was due to an increase in Ω. For cyclically neutral Ti-alloy no changes in Ω and K due to prior deformation were found [21].

Judging from a review of elevated temperature data [22,23] one might infer hardening primarily due to changes in Ω but this is not clear.

Because of these uncertainties it was decided to stay with the cyclically neutral model, see (23), (24). Moreover, even the room temperature experiments have shown results [20,21] which demonstrate that strong cyclic hardening cannot be adequately modeled with the present approaches, see also [24].

iii) The use of $\dot{\epsilon}$ instead of $\dot{\epsilon}^{in}$ to multiply the initial term in (24) will be disturbing to materials scientists who will argue that g is a state variable which should grow only when inelastic deformation occurs. Therefore the approach presented in (24) is not "physical." From (25), (26) and (27), and the chain rule

$$\left.\begin{aligned} \frac{d\sigma}{d\epsilon} &= E \\ \text{and} \\ \frac{d\Omega}{d\epsilon} &= 0 \end{aligned}\right\} \qquad (30)$$

are obtained, respectively, at the origin ($\sigma = 0$; $\Omega = 0$). On the other hand from (23) and (24)

$$\left.\begin{aligned} \frac{d\sigma}{d\epsilon} &= E \\ \text{and} \\ \frac{dg}{d\epsilon} &= \psi[0] \ , \end{aligned}\right\} \qquad (31)$$

so that the slope of g at the origin can be controlled by ψ. By a proper choice of $\psi[0]$ nearly linear elastic regions can be reproduced.

The difference between the two approaches is demonstrated in Figures 1 and 2. In both figures the evolution of σ and g under a strain controlled loading, unloading and reloading experiment are plotted. The material functions used are listed in Table 2 (they

are not intended to represent a specific alloy and the difference between Figure 1 and Figure 2 is only that $\dot{\varepsilon}^{in}$ is used to multiply ψ in (2) or (24) in the former whereas $\dot{\varepsilon}$ is employed in the latter.

Regarding the evolution of σ both figures show the same initial slope. From then on the σ curve in Figure 1 is more gradual than in Figure 2. Upon reloading a sizeable hysteresis loop develops and the transition is gradual in Figure 1 whereas almost no hysteresis and a very sharp transition is observed in Figure 2. This sharp transition corresponds to that observed in strain controlled experiments [25].

Figure 1 also demonstrates the zero slope of the g (back stress) curve at the origin. Since the inelastic strain rate depends on $(\sigma - g)$ and since in strain control the same time is represented by the same strain it can be seen that only the origin and two other points in Figure 1 where σ and g intersect have zero inelastic strain rate. Elasticity is reduced to three isolated points in Figure 1. In all other regions creep and relaxation can be found. This fact is of course not noticeable if the figure does not contain the evolution of g.

In contrast, in Figure 2 there are regions where σ and g essentially overlap. In these regions nearly linear elastic behavior without noticeable creep and relaxation is reproduced.

This behavior is closer to reality than the one depicted in Figure 1 and partly for this reason we have chosen to use $\dot{\varepsilon}$ instead of $\dot{\varepsilon}^{in}$ in the growth law for g.

Aside from the existence of elastic regions the use of $\dot{\varepsilon}$ instead of $\dot{\varepsilon}^{in}$ makes quite a difference in the evolution of mean stress with cycles in a strain controlled test with positive mean strain. Figures 3 and 4 again depict results of numerical experiments under such loading. The only difference in the two graphs is the use $\dot{\varepsilon}^{in}$ in Figure 3 and of $\dot{\varepsilon}$ in Figure 4.

Qualitatively the results on Figure 4 are more realistic than those in Figure 3, see [12]. Because of this behavior the formulation with $\dot{\varepsilon}$ is preferred.

Figure 5 shows the results of numerical simulations such as depicted in Figures 3 and 4 for two strain ranges and two strain rates. The decay of mean stress is plotted vs cycles. It is evident that at the slow strain rate the decay is less rapid for the $\dot{\varepsilon}$ than for the $\dot{\varepsilon}^{in}$ formulation. However, when a fast strain rate (10^{-2} s^{-1}) is used the difference is less pronounced and the $\dot{\varepsilon}$ formulation predicts the smaller mean stress of the two.

The cycles depicted in Figures 3 and 4 occur in turbine disks and buckets. For their life prediction the remaining mean stress must be known from analysis. Figure 5 clearly demonstrates that the two formulations predict considerably different mean stresses.

The Material Functions of the Theory

In the absence of recovery and of cyclic hardening the present model has three constants and two material functions that must be identified. The method of identification which requires considerable expertise and uses the asymptotic solution properties (7) - (10) is described in the Appendix.

In contrast to other approaches [1-6] the specific forms of the functions are not given rather general properties are stated, see (21). Within these properties specific functions must be found to suit the specific application. It was demonstrated in [8,26] how k affects rate sensitivity and a selection of specific k-functions was given in [8].

The function ψ affects the knee of the stress strain diagram and the behavior upon rate changes, see Table 1. For the purposes of demonstrating its influence two forms of ψ are given in Table 2. One leads to an almost elastic viscoplastic behavior, see Figure 6, the other to a gradual transition from elastic to inelastic deformation, Figure 7.

Corresponding hysteresis loops are shown in Figures 8 and 9. It is seen that Masing behavior is represented in either case and that cyclic hardening is absent. The regions of nearly elastic behavior are clearly identified as those where σ and g coincide.

Note that the constants of the functions given in Table 2 are selected to give the same E_t and the same stress level, only the transition behavior is different.

Once the material functions have been set the behavior of the model is completely determined. As an example, the behavior at different strain rates and under strain rate changes shown in Figures 6 and 7 is cited.

Both figures show an effect of loading rate on g in the transition region which disappears after some strain has accumulated. The influence of rate on g is smaller but seems to disappear slower in Figure 6 than in Figure 7.

The transition from elastic to viscoplastic behavior for σ is sharp in Figure 6 but gradual in Figure 7. As the strain rate increases the sharpness of transition increases.

At point A in Figures 6 and 7 the strain rate is increased (reduced) by two orders of magnitude. Whereas little overshoot (undershoot) is observed in Figure 6 it is considerable for both the σ and g curves in Figure 7. After some transient period the original curves are traced over again. Again the transition period is longer in Figure 6 than in Figure 7.

The difference in behavior is solely attributable to the change in the function ψ. The question arises whether these overshoots could lead to instabilities. A separate stability analysis [27] shows that the critical points which are the asymptotic values of (23), (24) are stable. Even if there are overshoots (undershoots), they will be transient in nature, see also (5), (6).

Although overshoots (undershoots) are experienced in testing, see Figure 9 of [19], and [28], and are similar to those shown in Figure 7 the size of these transients is somewhat large.

If ψ in (24) is multiplied by $\dot{\epsilon}^{in}$ a simple analysis corresponding to (12) and (13) shows that

$$\frac{dg^+}{d\epsilon} = \frac{dg^-}{d\epsilon}\frac{\dot{\epsilon}^-}{\dot{\epsilon}^+} = E_t\frac{\dot{\epsilon}^-}{\dot{\epsilon}^+} \tag{32}$$

and

$$\frac{dg^+}{d\epsilon} = \frac{dg^-}{d\epsilon}\alpha\frac{\dot{\sigma}^-}{\dot{\sigma}^+} = \frac{d\sigma^+}{d\epsilon}\frac{\dot{\sigma}^-}{\dot{\sigma}^+} \tag{33}$$

for strain and stress control, respectively. It is clear that (32) and (33) lead to less variations of $dg^+/d\epsilon$ than experienced with the $\psi\dot{\epsilon}$ formulation, see Table 1. This is demonstrated in Figure 10 where the conditions are identical to those used in Figure 7, except for the multiplication of ψ by $\dot{\epsilon}^{in}$. Very little overshoot is observed in this case.

The second term in (2) or (24) is multiplied by $|\dot{\epsilon}^{in}|$ and has so far not been varied. If this term is replaced by $|\dot{\epsilon}|$ the reloading behavior is similar to that shown in Figure 1. (See also [16], Figures 5.21 and 5.22.) It can be seen from (4) that $\frac{dg}{d\epsilon} \approx \psi$ as long as $\frac{d\sigma}{d\epsilon} \approx E$. Since under this condition $\sigma - g \approx 0$ and since $\psi[0] \approx E$ the slope of g remains very close to E as long as $\frac{d\sigma}{d\epsilon} = E$ and the behavior results in the sharp transition upon reloading shown in Figure 2. If $|\dot{\epsilon}^{in}|$ is replaced by $|\dot{\epsilon}|$ in (2), (4) shows that the second term on the right-hand side is not negligible from the beginning and $\frac{dg}{d\epsilon}$ decreases faster than in the previous case. (See [16] for a further discussion of the subject.)

A comparison of the hysteresis loops in Figures 8, 9 and 11 shows clearly the linear elastic regions for the $\psi\dot{\epsilon}$-formulation which are absent in Figure 11. (Elastic regions are those where $\sigma = g$.) It is not possible to model regions of no creep and no relaxation in Figure 11 but Figures 8 and 9 display such regions.

CONCLUSIONS

Mathematical methods permit the establishment of some properties of the proposed constitutive equation, but numerical experiments are very necessary to investigate the detailed properties.

The proposed system which uses total strain rate in the growth law for the equilibrium stress (or back stress or kinematic stress) is able to reproduce regions of almost linear elastic behavior. If inelastic strain rate is used instead, these regions were shown to be absent.

Loading, unloading and reloading under strain control are reproduced in a realistic manner using the present approach. A much too gradual transition is exhibited when inelastic strain rate is employed instead.

These properties have an influence on the decay of mean stress under tension-tension strain controlled cycling. It appears that the present approach represents a realistic decay of mean stress. This quantity is important for fatigue life prediction of turbine components.

All comparisons were made by changing one parameter at a time. Although it is strongly suggested that presently available state variable theories share the qualitative properties of the present model with using the inelastic strain rate instead of the total strain rate a proof is outstanding. Such a proof requires numerical integration of the respective theories under the loading histories used in this paper.

ACKNOWLEDGEMENT

The financial support of NASA-Lewis Research Center and of the National Science Foundation made this research possible. Early on Dr. E.P. Cernocky suggested the structure for the growth law of the equilibrium stress.

APPENDIX

Determination of Material Functions

The model is given by (23) and (24) and contains three material constants (E, E_t, A)* and two material functions (k, ψ). Both functions must be continuous positive and decreasing functions. They are otherwise not specified. In applications specific forms must be chosen.

The elastic modulus E and the tangent modulus E_t are easily identified as the slopes of the stress-strain diagram at the origin and at the maximum strain of interest, respectively.

In determining k, ψ and A the asymptotic solutions (7) - (10) are needed and used. Points of g and the viscosity function k are determined as shown in [8] or [26]. The strain rate change tests proposed in [8] are preferred. The relaxation tests [26] are also useful provided the solution properties of (14) and (15) are accounted for (in [26] $g = g[\epsilon]$ only). Candidate functions for k are also given in [8, 26] but new ones may be easily proposed. In this step extrapolation, trial and error with judgement are required.

Once a point of g is known, the asymptotic value of $\{g - f\} = A$ can be determined from the corresponding value of σ and $f = E_t\epsilon$.

With $\psi[0] = \frac{dg}{d\epsilon}[0] = \bar{E}$, $\frac{dg}{d\epsilon}[\epsilon_{max}] = E_t$ and at least one point of g known, g can be approximated by the functions provided in [29] or by other representations (i.e., Ramberg Osgood relation). A similar procedure is used to approximate the stress-strain diagram. These two functions are now used as inputs to

$$\frac{dg}{d\epsilon} = \psi[\sigma - g;\ B,C,D] - \frac{g - E_t\epsilon}{b[\sigma - g]}\left|1 - \frac{1}{E}\frac{d\sigma}{d\epsilon}\right| \qquad (A.1)$$

which is obtained from (24) and where b is given by (22). The arguments B, C, D of ψ are the free constants in the assumed representation of

$$\psi = B + \frac{C}{f(x/D)} \qquad (A.2)$$

where $f\left(\frac{x}{D}\right)$ is an increasing function. Examples of such functions are given in Table 2. Since $\psi[0] = \bar{E} = B + C/f[0]$ only two constants need

---

* $\bar{E} = \psi[0]$ is selected to be slightly less than E.

be determined in the subsequent nonlinear least square analysis* which employs (A.1), (A.2) and the fitted analytical expressions for σ and g (since the derivatives are needed in (A.1), analytical expressions are preferred). This analysis then yields the constants for (A.2).

With all the constants determined the model can now be integrated numerically and should reproduce the experimental results used to determine the constants. Due to the nonlinearity of the problem some iterations are probably necessary. These iterations may employ different forms of ψ and k consistent with the general requirements.

---

* The IMSL subroutine ZXSSQ is an example of possible algorithm

REFERENCES

1. S.R. Bodner and Y. Partom, "Constitutive Equations for Elastic-Viscoplastic Strain-Hardening Materials," Trans. ASME, J. Appl. Mech., 42, 385-389 (1975).

2. A.K. Miller, "An Inelastic Constitutive Model for Monotonic, Cyclic and Creep Deformation, Parts I and II," Trans. ASME, J. Eng. Matls. and Tech., 98, 97-113 (1976).

3. E.W. Hart, "Constitutive Relations for the Nonelastic Deformation of Metals," Trans. ASME, J. Eng. Matls. and Tech., 98, 193-201 (1976).

4. R.W. Rhode and J.C. Swearengen, "Deformation Modeling Applied to Stress Relaxation of Four Solder Alloys," Trans. ASME, J. Eng. Matls. and Tech., 102, 207-214 (1980).

5. J.L. Chaboche, "Viscoplastic Constitutive Equations for the Description of Cyclic and Anisotropic Behavior of Metals," Bull. de l'Acad. Polonaise des Sciences, Série Sc. et Techn., 25, 33-42 (1977).

6. K.P. Walker, "Research and Development Program for Nonlinear Structural Modeling with Advanced Time-Temperature Dependent Constitutive Relationships," NASA Report CR-165533, November 1981.

7. E.P. Cernocky and E. Krempl, "A Nonlinear Uniaxial Integral Constitutive Equation Incorporating Rate Effects, Creep, and Relaxation," Int'l. J. of Nonlinear Mechanics, 14, 183-203 (1979).

8. E. Krempl, "The Role of Servocontrolled Testing in the Development of the Theory of Viscoplasticity Based on Total Strain and Overstress," Amer. Society for Testing and Materials, STP 765, 5-28 (March 1982).

9. D. Kujawski and E. Krempl, "The Rate(Time)-Dependent Behavior of Ti-7Aℓ-2Cb-1Ta Titanium Alloy at Room Temperature under Quasi-Static Monotonic and Cyclic Loading," Trans. ASME, J. Appl. Mech., 48, 55-63 (1981).

10. E.P. Cernocky and E. Krempl, "A Coupled Theory of Thermoviscoplasticity Based on Total Strain and Overstress and its Predictions in Monotonic Torsional Loading," Journal of Thermal Stresses, 4, 69-82 (1981).

11. E.P. Cernocky and E. Krempl, "A Nonlinear Uniaxial Integral Constitutive Equation Incorporating Rate Effects, Creep, and Relaxation," Int'l. J. of Nonlinear Mechanics, 14, 183-203 (1979).

12. E. Krempl and V.V. Kallianpur, forthcoming.

13. E. Krempl and V.V. Kallianpur, "Some Critical Uniaxial Experiments for Viscoplasticity at Room Temperature," to appear J. Mech. Phys. Solids.

14. D. Kujawski, V.V. Kallianpur and E. Krempl, "An Experimental Study of Uniaxial Creep, Cyclic Creep and Relaxation of AISI Type 304 Stainless Steel at Room Temperature," J. Mechanics and Physics of Solids, 28, 129-148 (1980).

15. Y. Asada and S. Mitsuhashi, "Creep-Fatigue Interaction of Types 304 and 316 Stainless Steel in Air and Vacuum," Proc. 4th Int. Conf. on Pressure Vessel Technology, I. Mech. Eng., London, C48/80, 321-327, 1980.

16. J.J. McMahon, M.S. Thesis, Rensselaer Polytechnic Institute, Troy, New York, December 1983.

17. G. Wang, D. Yao and E. Krempl, "Viscoplasticity Based on Overstress with an Integral Growth Law for the Equilibrium Stress, RPI Report MML-83-2, October 1983; submitted for publication.

18. J.C. Swearengen and J.H. Holbrook, "Internal Variable Models for Rate-Dependent Plasticity: Analysis of Theory and Experiment," Sandia Report Sand. 83-8607, February 1984, to appear in Res. Mechanica.

19. E. Krempl, "An Experimental Study of Room-Temperature Rate Sensitivity, Creep and Relaxation of Type 304 Stainless Steel," J. Mechanics and Physics of Solids, 27, 363-375 (1979).

20. E. Krempl and H. Lu, "The Hardening and Rate-Dependent Behavior of Fully Annealed Type 304 Stainless Steel Under Biaxial In-Phase and Out-of-Phase Strain Cycling at Room Temperature," submitted to ASME 1984 WAM Symposium on Constitutive Equations. Micro and Macro Aspects.

21. H. Lu, forthcoming.

22. J.B. Conway, "An Analysis of the Relaxation Behavior of AISI 304 and 316 Stainless Steel at Elevated Temperatures," GEMP-730, General Electric Nuclear Systems Programs, Cincinnati, Ohio, December 1969.

23. E. Krempl, "Cyclic Creep. An Interpretive Literature Survey," WRC Bulletin No.195, Welding Research Council, New York, June 1974.

24. J.L. Chaboche, K. Dang Van and G. Cordier, "Modelization of the Strain Memory Effect on the Cyclic Hardening of 316 Stainless Steel," Paper L11/3, Proc. SmiRT V, Commission of the European Communities, 1979.

25. E. Krempl, "On the Interaction of Rate- and History-Dependence in Structural Metals," Acta Mechanica, 22, 53-90 (1975).

26. M.C.M. Liu and E. Krempl, "A Uniaxial Viscoplastic Model Based on Total Strain and Overstress," J. Mechanics and Physics of Solids, 27, 377-391 (1979).

27. M. Sutcu and E. Krempl, "Viscoplasticity Based on Overstress with a Differential Growth Law for the Equilibrium Stress," to be presented at 2nd Army Conference on Appl. Math. and Computing, May 1984, RPI, Troy, New York.

28. Unpublished Results, Mechanics of Materials Laboratory, Rensselaer Polytechnic Institute.

29. E.P. Cernocky and E. Krempl, "Construction of Nonlinear Monotonic Functions with Selectable Intervals of Almost Constant or Linear Behavior," Trans. ASME, J. Applied Mech., 45, 780-784 (1978).

30. J.L. Chaboche and G. Rousselier, "On Plastic and Viscoplastic Constitutive Equations - Part II: Application of Internal Variable Concepts to the 316 Stainless Steel," J. of Pressure Vessel Technology, 105, 159-164 (1983).

TABLE 1

SLOPES AFTER A JUMP IN STRESS OR STRAIN RATE

Change	Condition[1)]	$d\sigma^+/d\epsilon$		$dg^+/d\epsilon$	
		Strain Control	Stress Control	Strain Control	Stress Control
Increase	$0 < \delta \ll 1$	E	$\frac{E}{1+\delta E/E_t}$	ψ	$\frac{E\delta+\psi}{1+\delta E/E_t}$
Decrease	$\delta \gg 1$	$-\delta E$	E_t/δ	$\delta(E_t-\psi)$	E_t
Reversal	$\delta = -1$	$2E$	$-E_t$	$2\psi - E_t$	E_t
Reversal increase	$-1 \ll \delta < 0$	E	$\frac{E}{1+\delta E/E_t}$	ψ	$\frac{E\delta+\psi}{1+\delta E/E_t}$
Reversal decrease	$\delta \ll -1$	$-\delta E$	E_t/δ	$\delta(E_t-\psi)$	E_t

1) $\delta = \dot{\epsilon}^-/\dot{\epsilon}^+$ or $\dot{\sigma}^-/\dot{\sigma}^+$.

TABLE 2

MATERIAL CONSTANTS AND FUNCTIONS USED

E = Modulus of elasticity = 120,000 MPa E_t = Asymptotic tangent modulus = 1200 MPa A = 120 MPa
† $k[x] = 2.296 \times 10^{-4} \exp\left(21.275 \exp - \frac{\lvert x\rvert}{58.28}\right)$ s
$\psi_1[x] = 48{,}000 + 70{,}800 \exp(-0.12 \lvert x\rvert)$ MPa Used in all figures except in Figures 6 and 8
$\psi_2[x] = 12{,}000 + 106{,}800 \cosh(-0.2 \lvert x\rvert)$ MPa Used in Figures 6 and 8

† All x used here are measured in units of MPa.

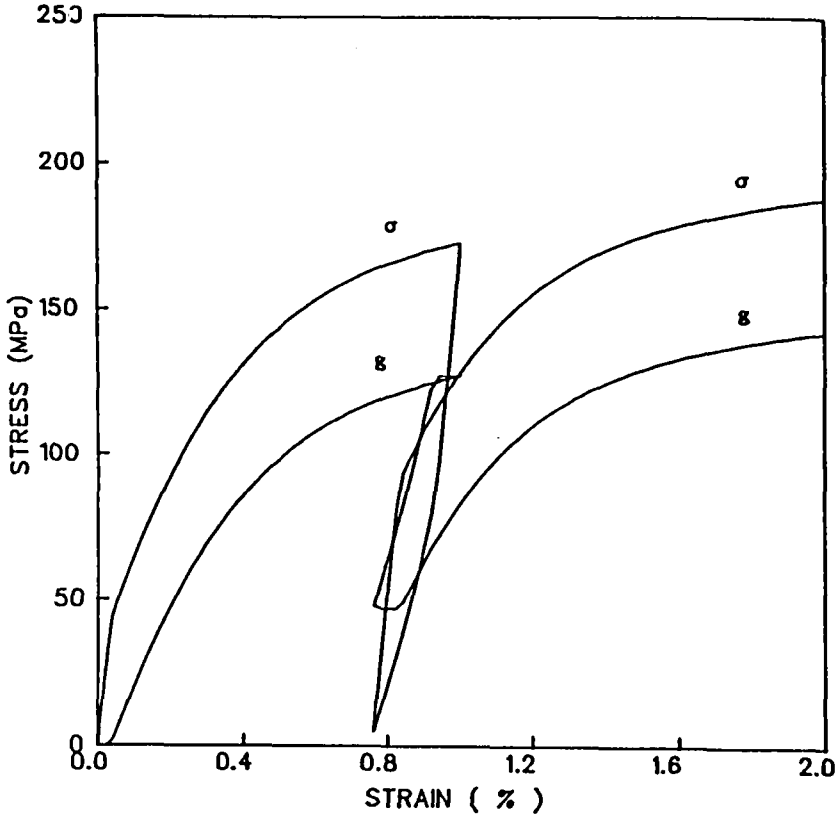

Figure 1 The Evolution of σ and g During Loading, Unloading and Reloading Under Strain Control. The function ψ_1 is multiplied by $\dot{\epsilon}^{in}$. Material functions used are given in Table 2. $|\dot{\epsilon}| = 10^{-4}\ s^{-1}$.

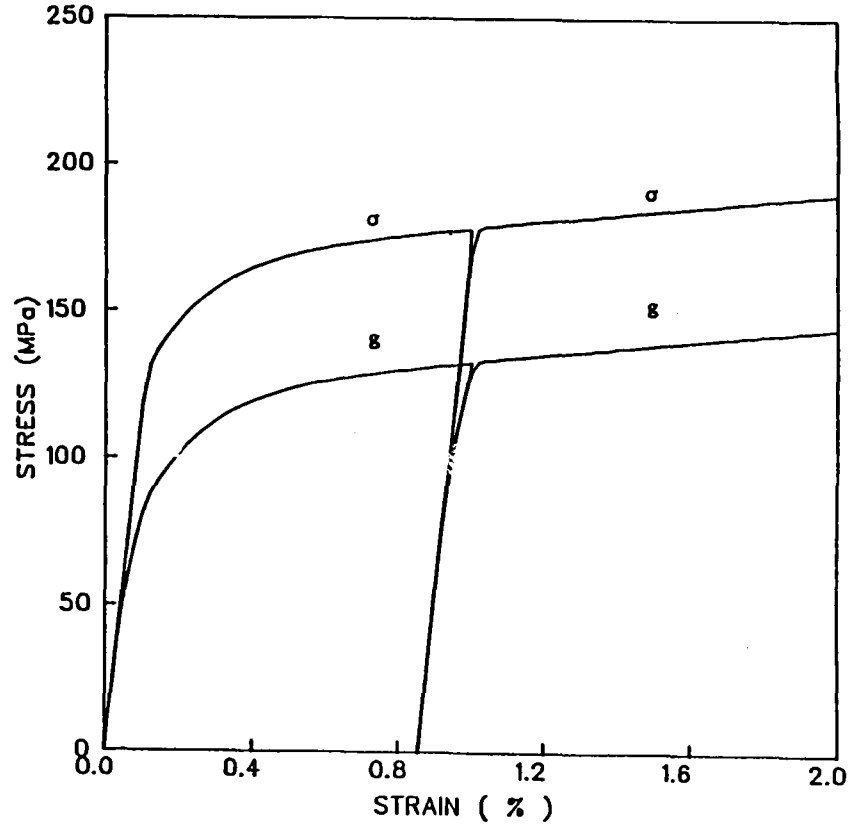

Figure 2 Same as Figure 1 Except that ψ_1 is Multiplied by $\dot{\epsilon}$. Regions of almost linear elastic behavior are those where σ = g.

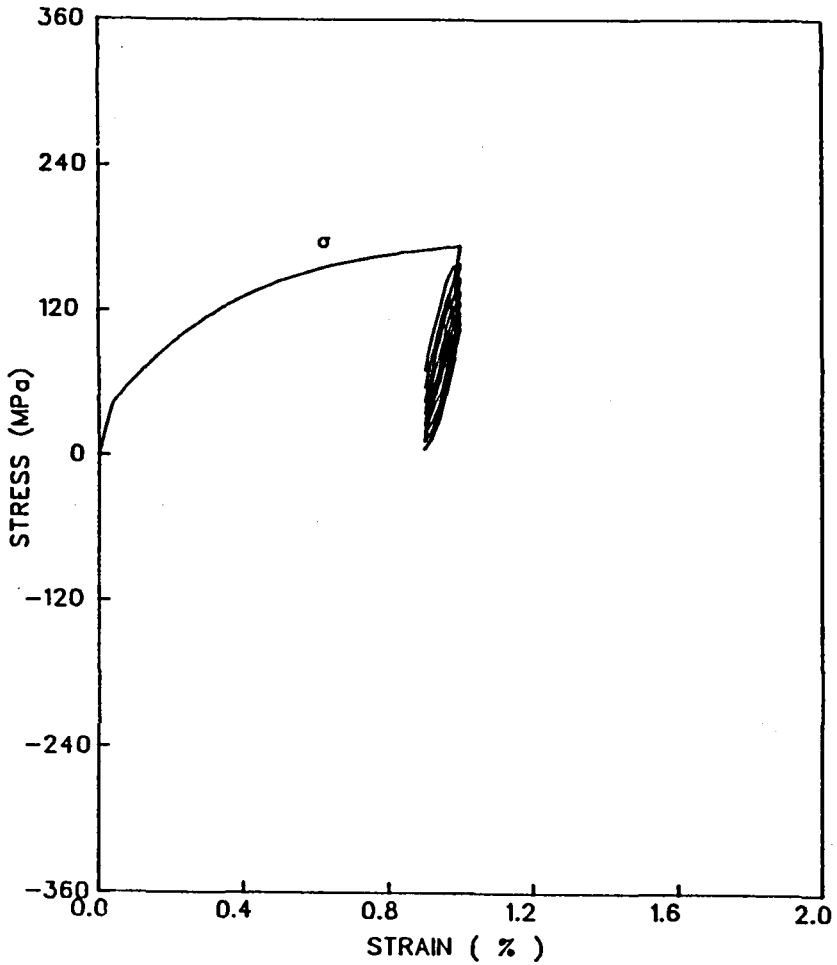

Figure 3 Strain Controlled Loading with Positive Mean Strain. $\epsilon_{max} = 1.0\%$, $\epsilon_{min} = 0.9\%$, $|\dot{\epsilon}| = 10^{-4}\ s^{-1}$. The function ψ_1 is multiplied by $\dot{\epsilon}^{in}$. Material functions are given in Table 2. The equilibrium curve g is not plotted.

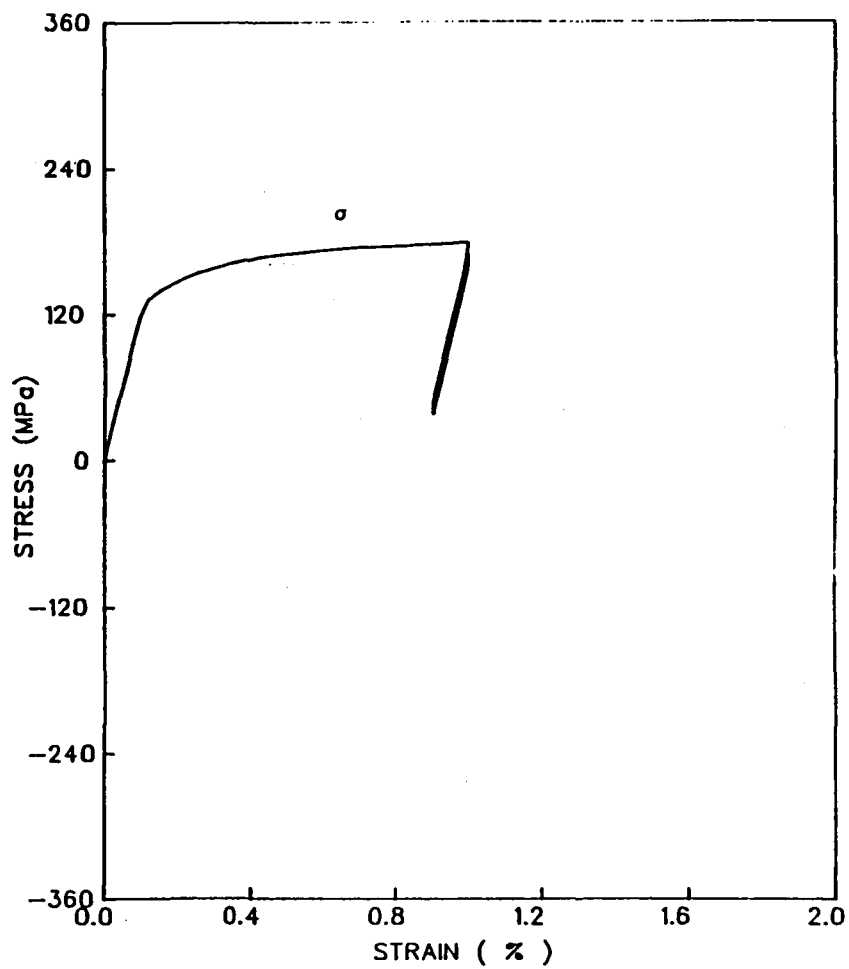

Figure 4 Same as Figure 3 Except that ψ_1 is Multiplied by $\dot{\epsilon}$

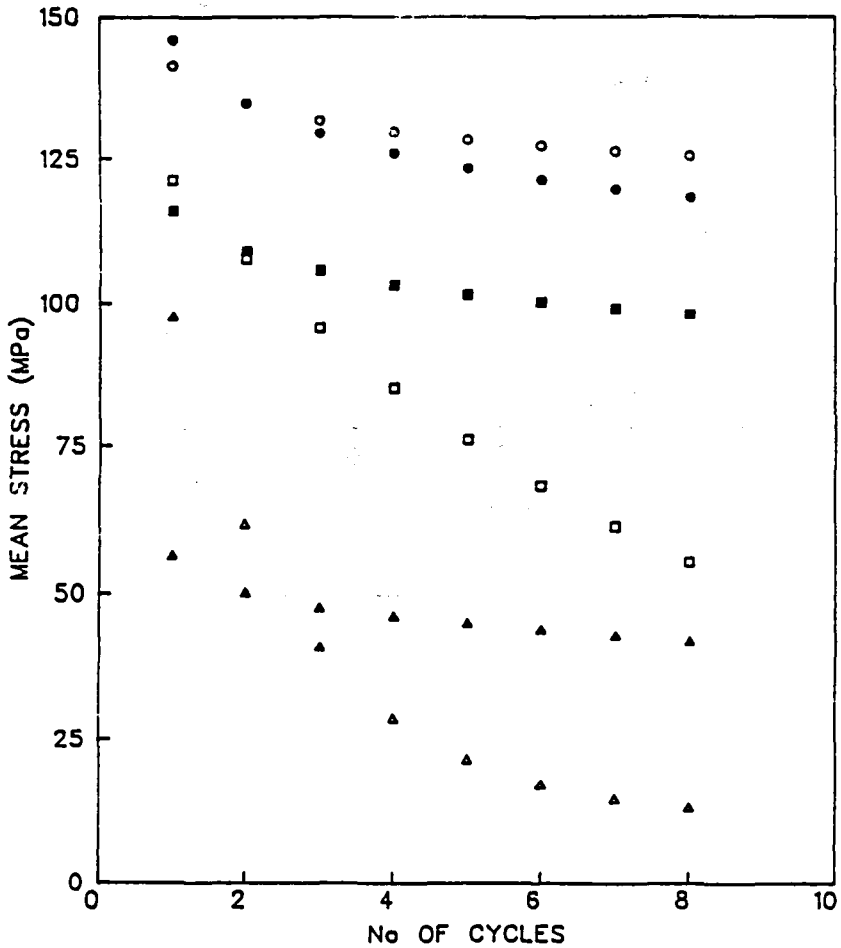

Figure 5 Evolution of Mean Stress with Cycles for the Conditions of Figures 3 and 4. Open symbols $\dot{\epsilon}^{in}$ multiplies ψ_1. Filled symbols $\dot{\epsilon}$ multiplies ψ_1.

○ $\epsilon_{max} = 1.0\%$ $\epsilon_{min} = 0.9\%$ $|\dot{\epsilon}| = 10^{-2}\ s^{-1}$

□ $\epsilon_{max} = 1.0\%$ $\epsilon_{min} = 0.9\%$ $|\dot{\epsilon}| = 10^{-4}\ s^{-1}$

△ $\epsilon_{max} = 1.0\%$ $\epsilon_{min} = 0.8\%$ $|\dot{\epsilon}| = 10^{-4}\ s^{-1}$

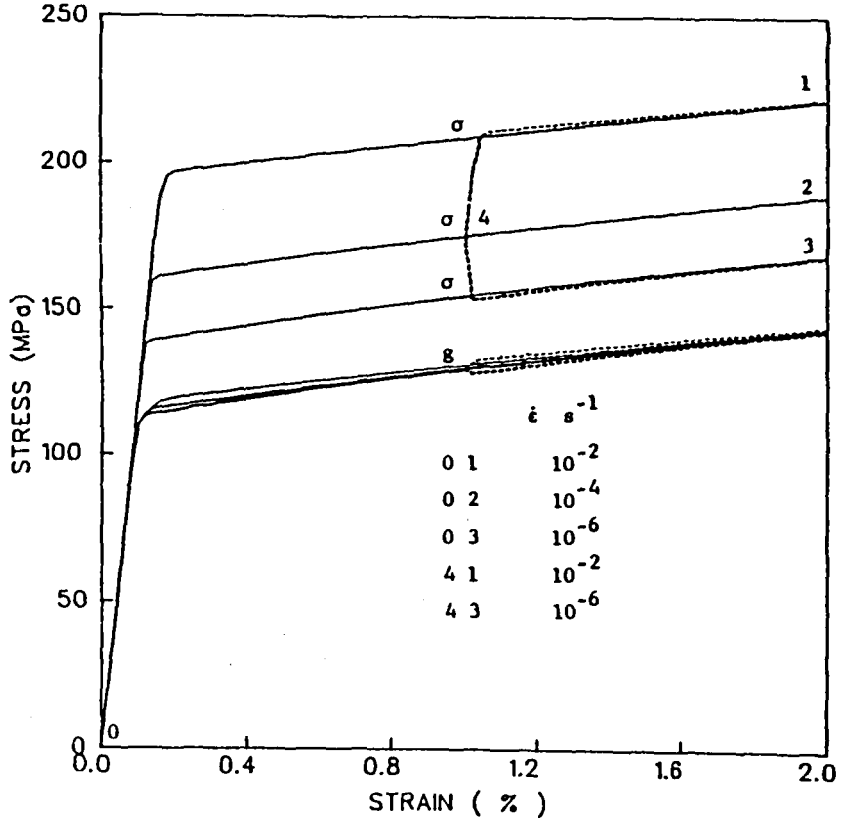

Figure 6 Evolution of σ and g During Constant Strain Rate Loading and During Sudden Changes in Strain Rate. The function ψ_2 of Table 2 is used.

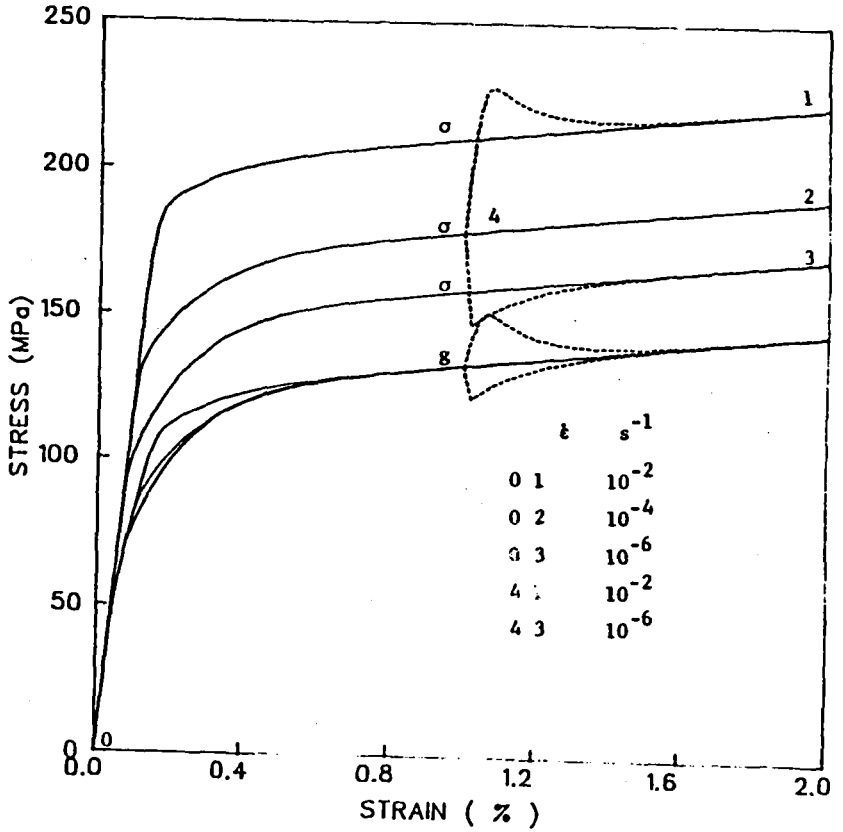

Figure 7 Same as Figure 6 Except that ψ_1 of Table 2 is Used

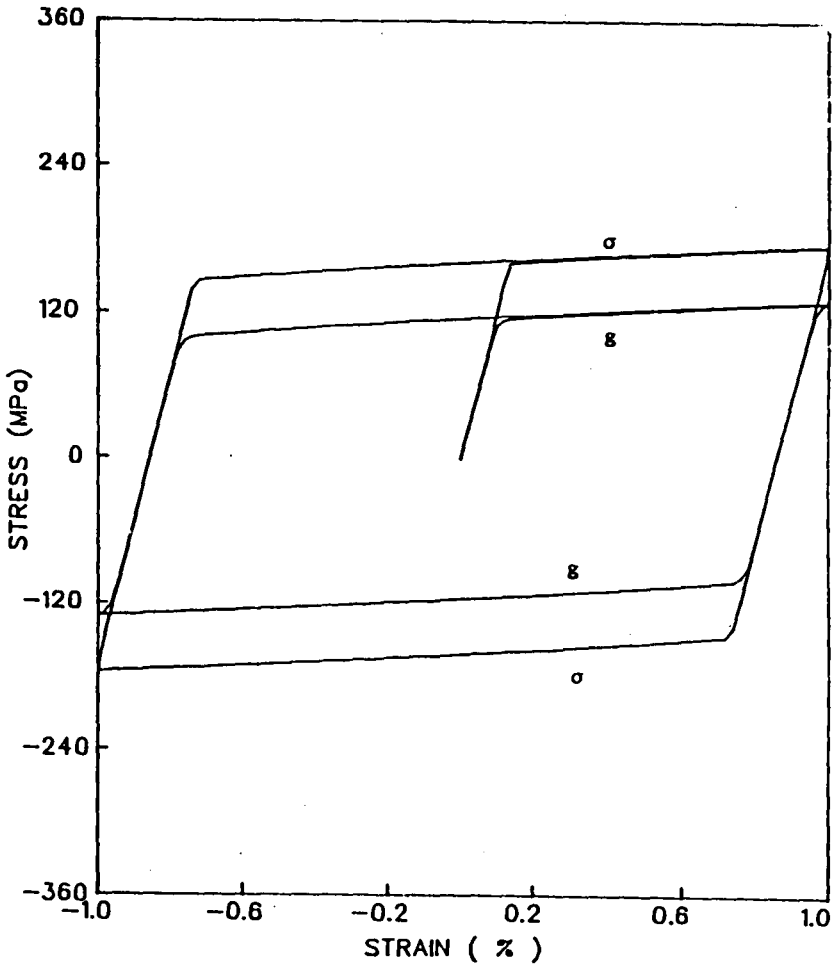

Figure 8 One Hysteresis Loop Represented by the Functions Used in Figure 6

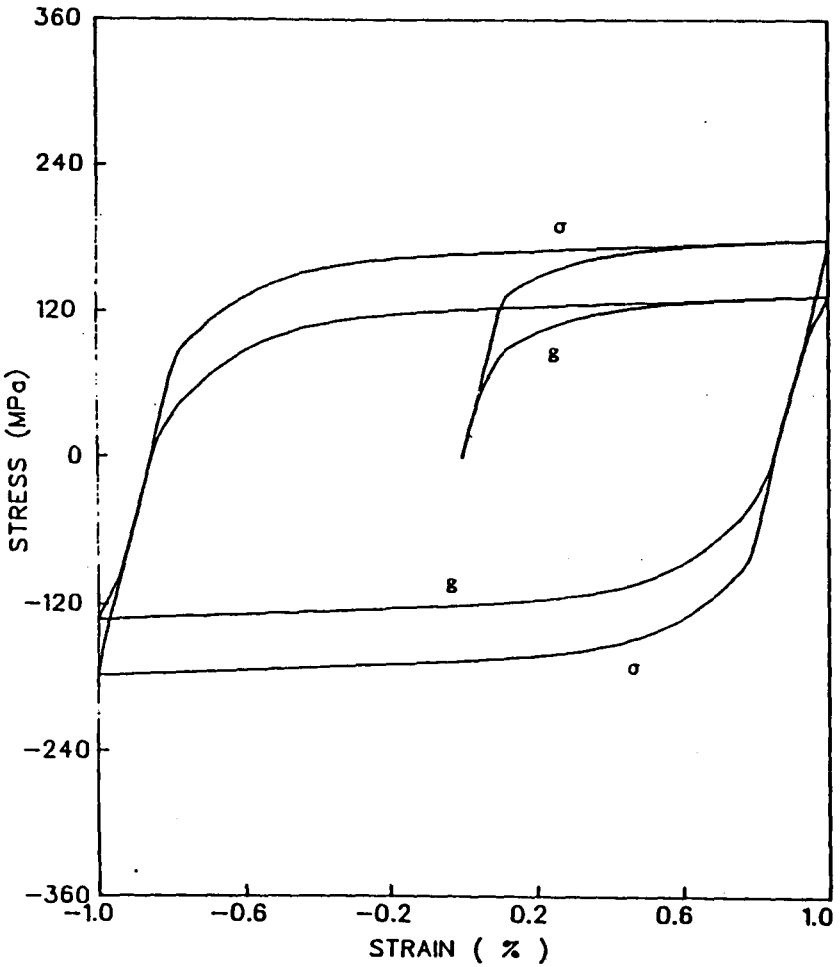

Figure 9 One Hysteresis Loop Represented by the Functions Used in Figure 7

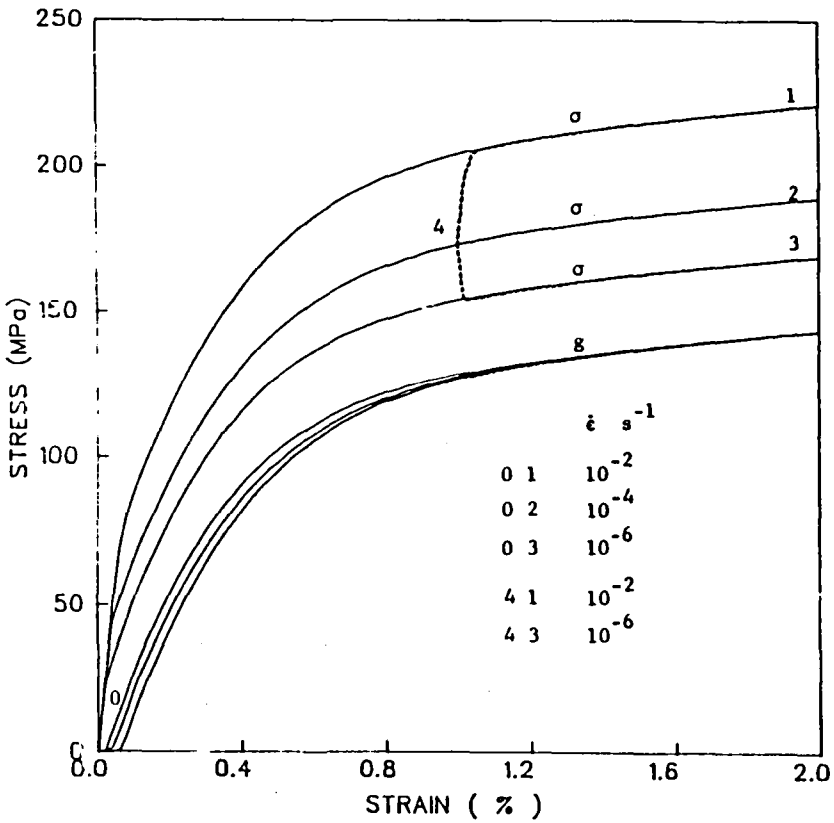

Figure 10 Same as Figure 7 Except $\dot{\epsilon}^{in}$ is Used to Multiply Ψ_1

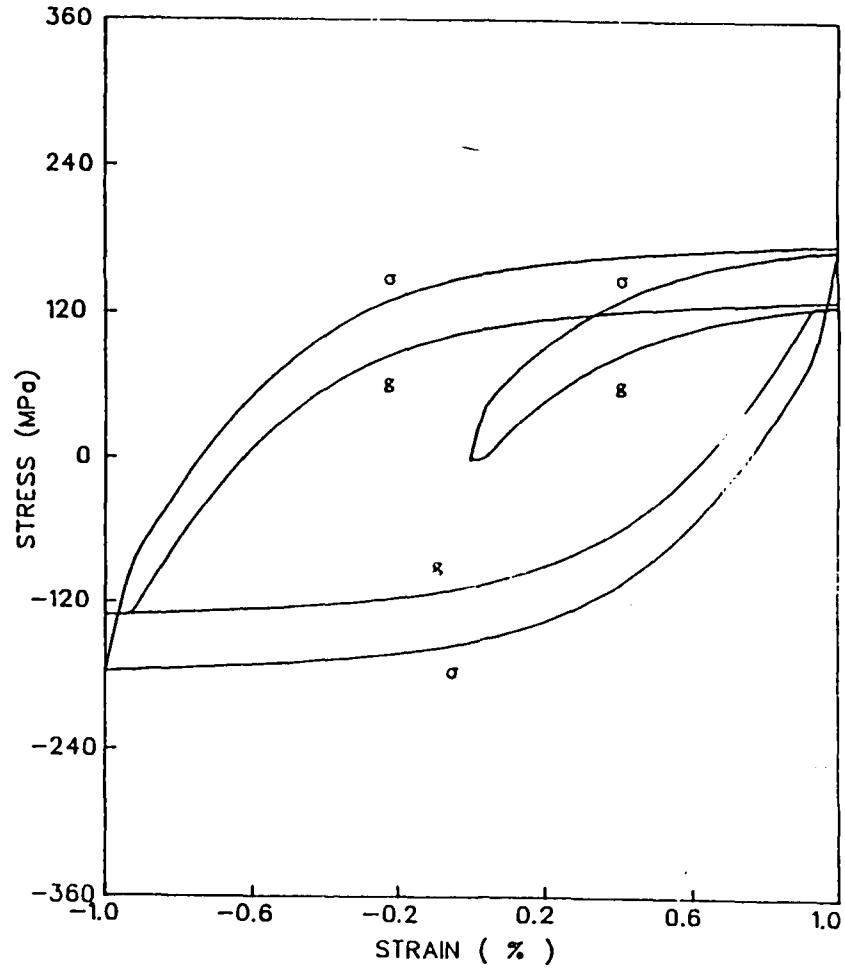

Figure 11 Same as Figure 9 Except that $\dot{\epsilon}^{in}$ is Used to Multiply Ψ_1

THERMOMECHANICAL DEFORMATION IN THE PRESENCE OF METALLURGICAL CHANGES*

D.N. Robinson
University of Akron
Akron, Ohio 44325

Cyclic hardening of some common structural alloys within their temperature range of interest is believed to be influenced by the phenomenon of dynamic strain aging.[1] Strain aging occurs in solid solutions where solute atoms (e.g., carbon, nitrogen, etc.) are particularly free to diffuse through the parent lattice. It is energetically preferable for these solute atoms to occupy sites in the neighborhood of mobile dislocations where their presence immobilizes the dislocations or at least makes their movement difficult, thus causing strengthening.

Isothermal cycling at temperatures where such metallurgical changes occur might therefor be expected to show abnormal hardening, i.e., higher hardening rates and greater saturation strengths than at temperatures both lower and higher. Macroscopic evidence of strain aging in three common alloys (i.e., Hastelloy X and types 304 and 316 stainless steel) is shown in Figures 1 through 3. In each case the hardening rate and the stress range at "saturation" are maximal at an intermediate temperature in the range. This hardening peak is interpreted as a manifestation of dynamic strain aging. At lower temperatures the mobility of solute atoms is far less and strain aging cannot occur; at higher temperatures normal recovery precesses, e.g., climb of edge dislocations, take over.

In the aging process described dislocations can, under some circumstances, break away from their Cottrell solute atmospheres becoming mobile again. Although temporarily freed, dislocations can again be immobilized as solute atoms gradually diffuse back to them. As the thermally activated process of diffusion is involved

*This work was performed under NASA Grant NAG-3-379.

and solute atoms are migrating to dislocations which themselves are moving under the applied stress, it is expected that the ensuing inelastic deformation (cyclic hardening in particular) has a complex dependence on thermomechanical history.

Phenomenological evidence of themomechanical path dependence under cyclic conditions is seen in the results of the simple nonisothermal tests reported in Figures 1 and 2 (dotted curves). In these tests cycling is initiated at one temperature and after some cycling the temperature is changed and cycling resumed.

Figure 1 shows the results of two nonisothermal tests on Hastelloy X cycled over a strain range at constant strain rate. In one, the specimen is cycled at 800F for five cycles; the temperature is them changed to 1000F and cycling is continued to virtual saturation, at about one hundred cycles. In the second, this history is repeated up to thirty cycles where the specimen is then brought back to 800F and cycling continued. Results of a similar test on type 304 stainless steel are shown in Figure 2 (dotted line).

The features of these test results that reflect thermomechanical history dependence are: 1) The change in strength (stress range) with temperature at a fixed number of cycles is always negative, i.e., an increase in temperature always produces a decrease in strength and vice versa, contrary to the implication of the isothemal data; 2) The current strength, in particular the "saturation" strength, depends on the temperature-strain history. Evidently, the information contained in the isothermal data is not sufficient for a complete nonisothermal description of the cyclic deformation in the temperature range of interest. In fact, the data suggests that, with accompanying metallurgical changes, the materials retain a full memory of their themomechanical history to cyclic saturation.

In the present work a discussion is given of nonisothermal testing that can be used as a basis of a nonisothermal representation. Related tests were discussed in Ref. 2 with regard to metallurgical changes that occur in other high temperature

structural alloys.

In spite of the sparseness of nonisothermal data, a viscoplastic constitutive model capable of qualitatively representing the behavioral features observed in Figures 1 through 3 has been formulated. This model is used here to begin to assess the differences in ultimate life prediction in some typical nonisothermal structural problems when the constitutive model does or does not account for metallurgically induced thermomechanical history dependence.

REFERENCES

1. J.D. Baird, "Dynamic Strain Aging", The Inhomogeneity of Plastic Deformation, ASM, Metals Park, Ohio (1973).

2. G. Cailletaud and J.-L. Chaboche, Macroscopic Description of The Microstructural Changes Induced by Varying Temperature: Example of IN 100 Cyclic Behavior, ICM, 3, Vol. 2 (1979)

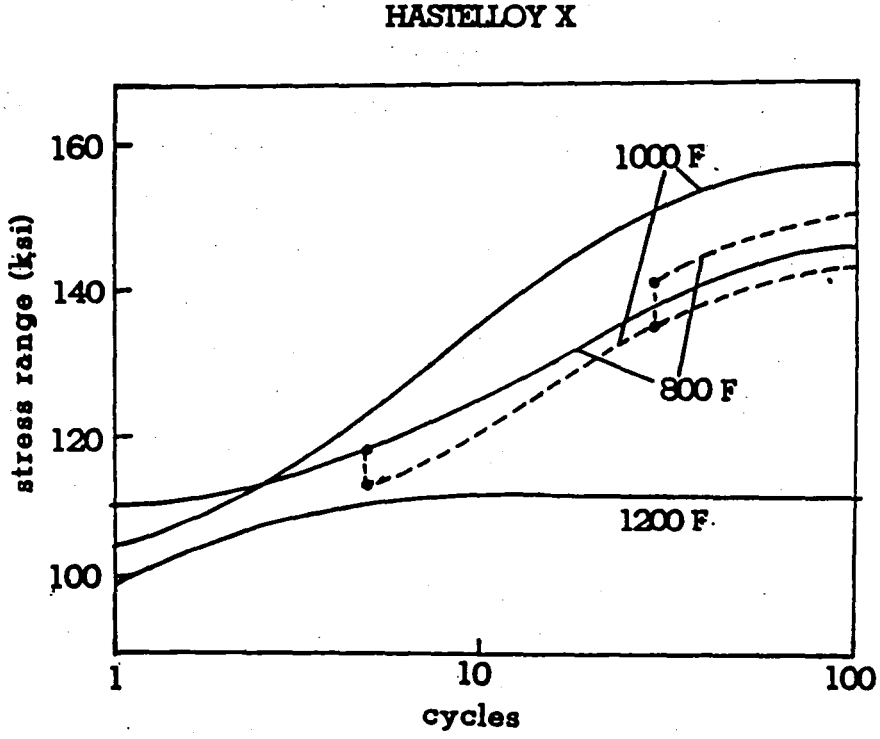

Fig.1 Isothermal (solid) and nonisothermal (dotted) cyclic hardening curves for Hastelloy X.

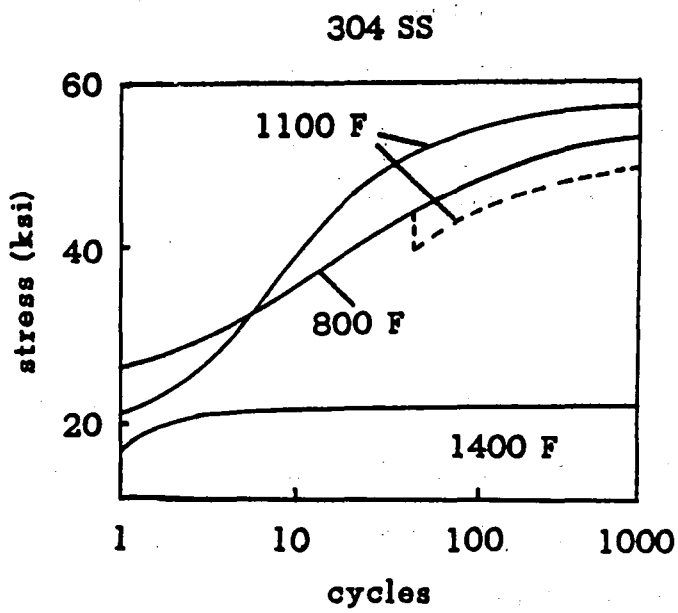

Fig.2 Isothermal (solid) and nonisothermal (dotted) cyclic hardening curves for type 304 stainless steel.

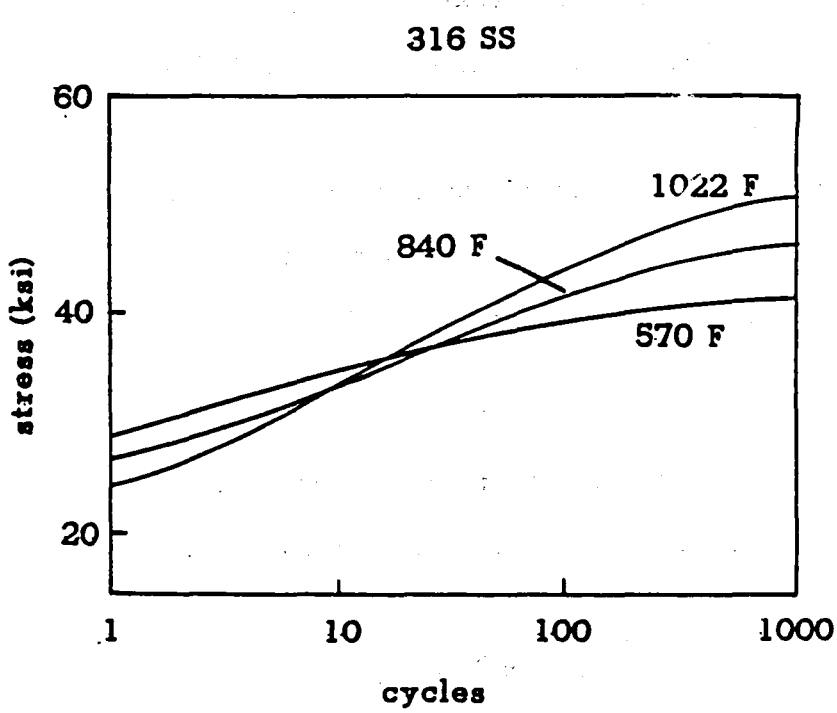

Fig.3 Isothermal cyclic hardening curves for type 316 stainless steel.

MICROMECHANICS OF HIGH TEMPERATURE DEFORMATION AND FAILURE

S. Nemat-Nasser and J.R. Weertman
Northwestern University
Evanston, Illinois 60201

The aim of the current research sponsored by NASA-Lewis Research Center at Northwestern University has been to examine the micromechanics of the constitutive behavior of elasto-plastic materials at high temperatures. This research involves theoretical and experimental effort.

The experimental work has focused on the development of microscopic defects in superalloys (Waspaloy), especially the formation of voids at grain boundary carbides, and slip-induced surface cracks within grains upon cyclic loading at high temperatures. The influence of these defects on the life-expectancy of the material is being examined.

The theoretical work consists of two parts: (1) Analytical description of the mechanisms that lead to defects observed experimentally; and (2) development of macroscopic elasto-plastic nonlinear constitutive relations on the basis of micromechanical modeling.

1. PROGRESS TO DATE

A list of articles completed under the current grant is given in Section 2. Progress in experimental and theoretical efforts is briefly discussed in Subsections 1.1 and 1.2.

1.1 Experimental Effort

A study is under way of the effect of prior deformation, carried out at room temperature, on the subsequent high temperature fatigue behavior of Waspaloy.

At room temperature Waspaloy deforms by coarse, planar slip whereas by 650°C slip has become fine and homogeneous. Pineau and coworkers, Refs. [1,2], have shown that the planar low temperature behavior can be extended to higher temperatures if the material is deformed at room temperature prior to high temperature fatigue.

In the series of experiments now in progress the effect of monotonic prestrain and of prefatiguing at room temperature on samples fatigued at 650-750°C is being investigated. Samples of Waspaloy were pulled at room temperature to a strain of about 4% or were fatigued with a plastic strain amplitude of 0.3% or 0.6% at a frequency of 0.05 Hz. The specimens then were fatigued at 0.05 Hz at 650°C with a stress amplitude of 810 MPa or at 750°C with an amplitude of 770 MPa. All high temperature fatiguing was carried out in a vacuum of about 10^{-6} torr. Several samples were subjected to high temperature fatiguing which had undergone no prior deformation, in order to observe the effect of prior deformation on high temperature fatigue behavior.

Both monotonic straining and fatiguing produce coarse slip at room temperature. While some slip lines appear straight, many detour around the larger γ' particles. Shearing of γ' particles is not universal during room temperature deformation. (The distribution of sizes of the γ' particles is bimodal. The larger are about 200 nm in diameter.) An appreciable amount of microcracking was seen along coarse slip lines in the fatigued samples (Fig. 1) but no grain boundary cracking. A small number of grain boundary microcracks were found in the pulled material but no slip line cracks (Fig. 2). Waspaloy which was prestrained either in tension or fatigue and then fatigued at 650° or 750° also showed coarse slip bands, an appreciable number of which had turned into cracks. Prefatiguing seems to favor microcracking along the slip lines, while prior deformation by pulling produces more grain boundary voids and cracked boundaries

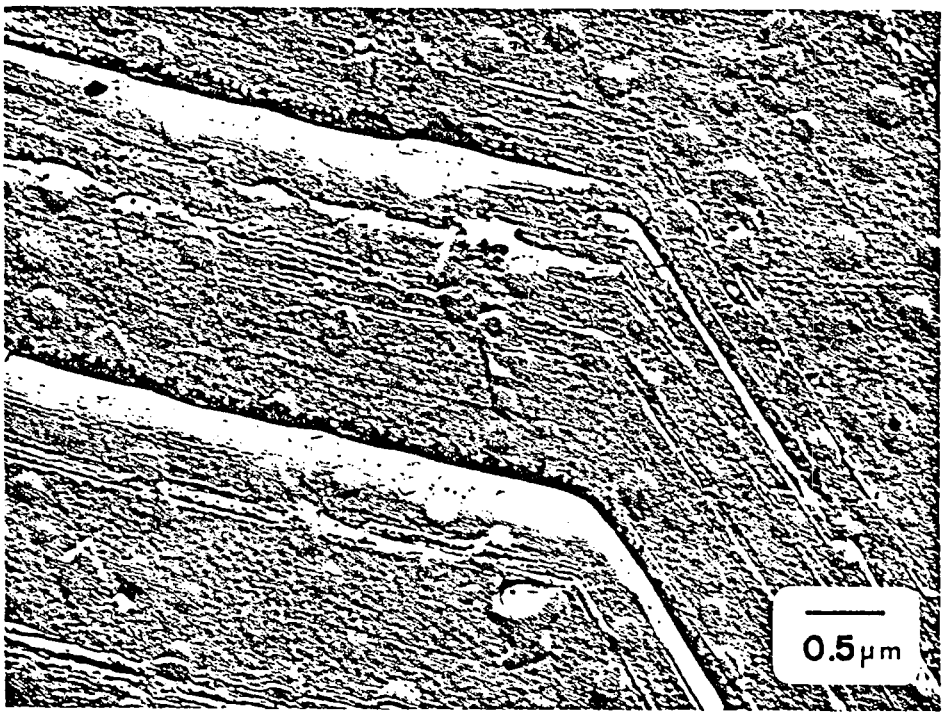

Fig. 1: TEM micrograph of a shadowed 2-stage replica of Waspaloy fatigued at room temperature for 100 cycles (0.1 N_f) at a plastic strain amplitude of 0.6% at a frequency of 0.05 Hz. Several microcracks along coarse slip lines are seen on either side of the twin boundary.

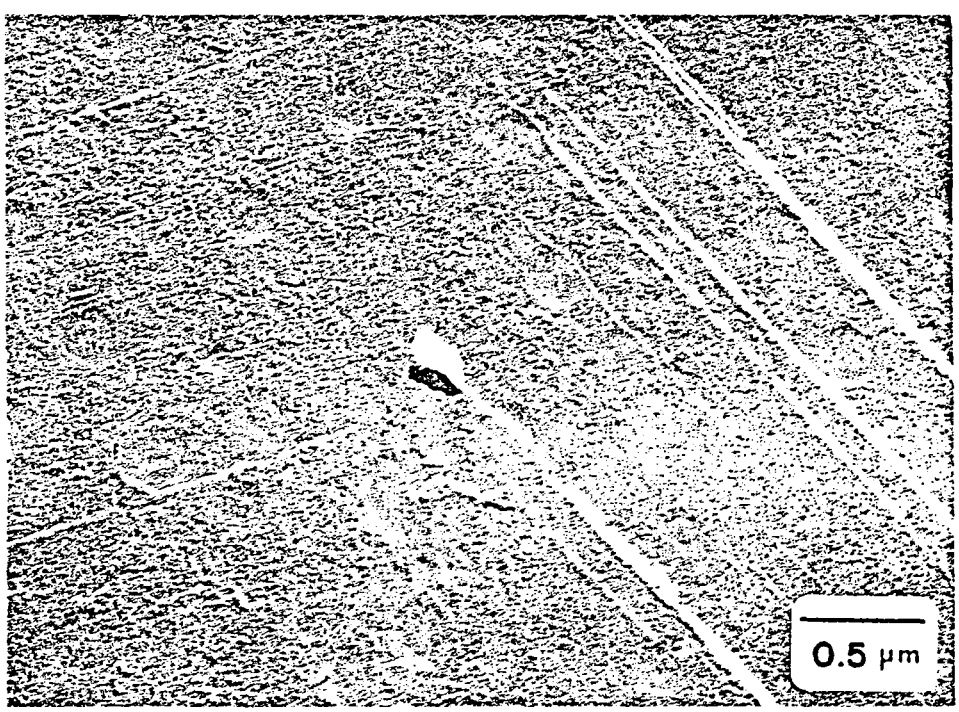

Fig. 2: Shadowed 2-stage replica of Waspaloy pulled to a 4% strain at room temperature. Note coarse slip lines, one of which ends in a microcrack at the grain boundary.

(Figs. 3 and 4). The slip generally is finer in specimens fatigued at high temperature which had not undergone prior deformation (Fig. 5). Slip line and grain boundary cracking appear only after 500 cycles in these specimens, whereas such features appear by 200 cycles in the prestrained samples.

1.2 Theoretical Effort

A complete formulation of the overall macroscopic elasto-plastic response of polycrystalline solids at finite strains and rotations has been made; Ref. [3]. A number of illustrative examples have been worked out. A number of interesting new results have been obtained. In particular, the influence of residual stresses (backstress) at the micro-level on the overall mechanical response has been thoroughly examined. In addition, based on a micromechanical modeling, the macroscopic Bauschinger effect and kinematic hardening are exemplified.

In Refs. [4,5] dynamic crack growth in elasto-plastic materials is given a complete asymptotic solution. These results shed new light on this difficult problem area and bring out a number of technically important questions pertaining to criteria for ductile fracture.

Other articles listed in Section 3 respresent various other micromechanical aspects of the research which has been completed.

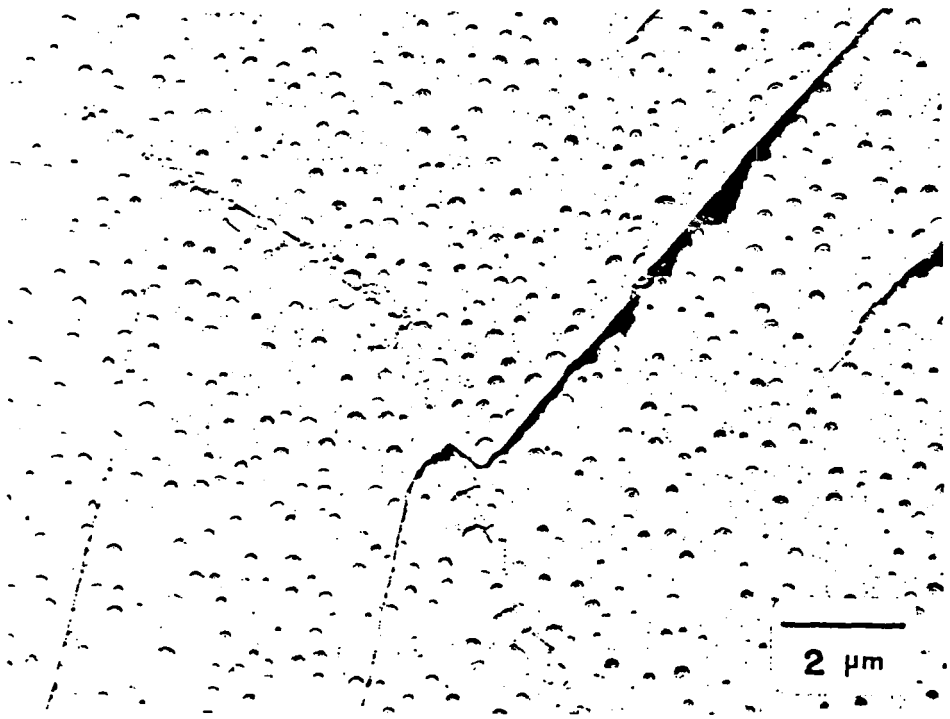

Fig. 3: Replica of a slip line crack which has jumped the grain boundary and continued on another slip system. Specimen of Waspaloy prefatigued at room temperature for 200 cycles (0.1 N_f) at a plastic strain amplitude of 0.3%, then fatigued for 160 cycles at 650°C with a stress amplitude of 810 MPa. All fatiguing done at a frequency of 0.05 Hz, and in a vacuum of $\sim 10^{-6}$ torr.

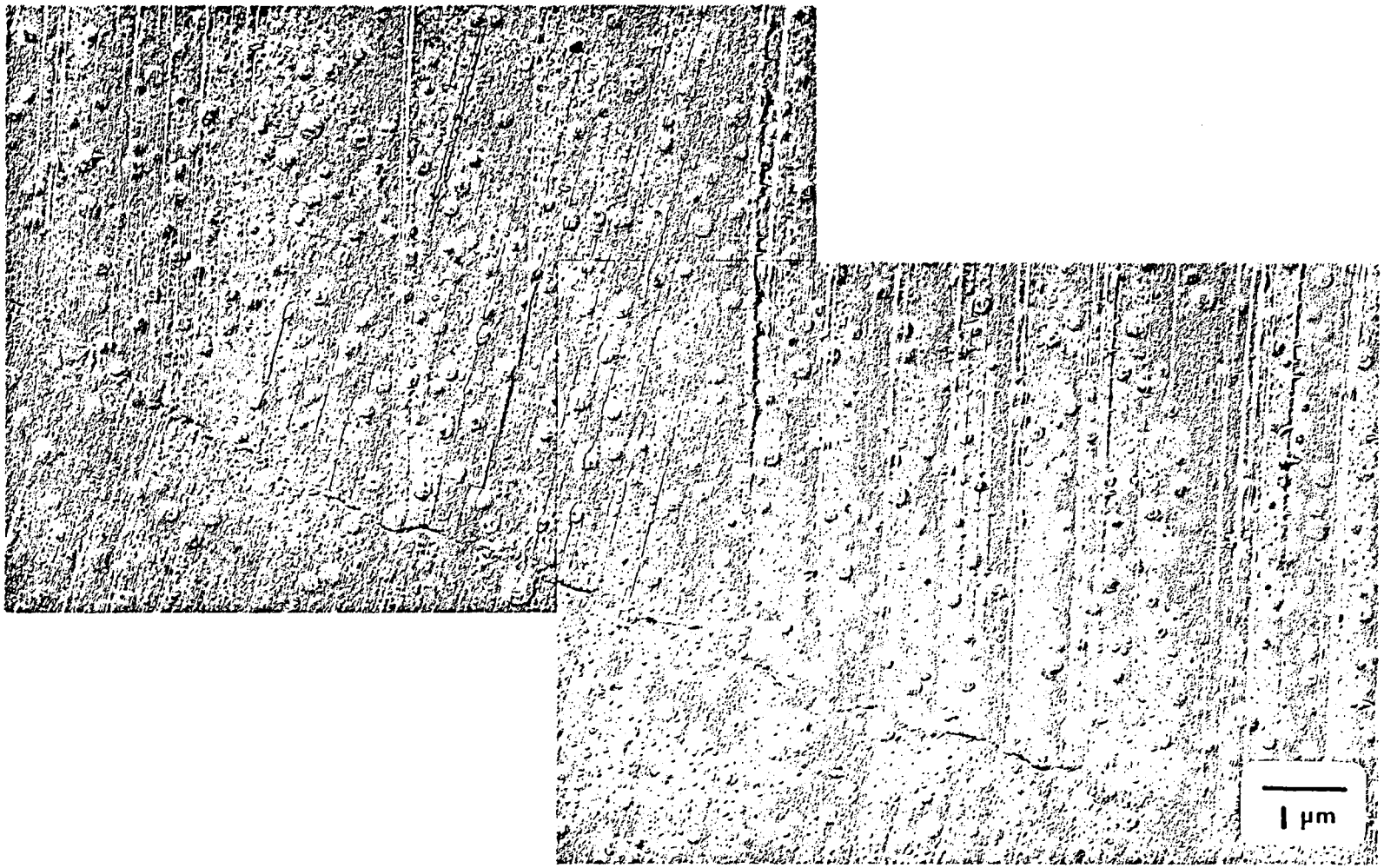

Fig. 4: Micrograph of replica of Waspaloy specimen pulled at room temperature to a 4.1% strain, then fatigued at 750°C at a frequency of 0.05 Hz with a stress amplitude of 770 MPa for 150 cycles. Note the coarse slip and the numerous microcracks along the grain boundary. A slip line crack also can be seen.

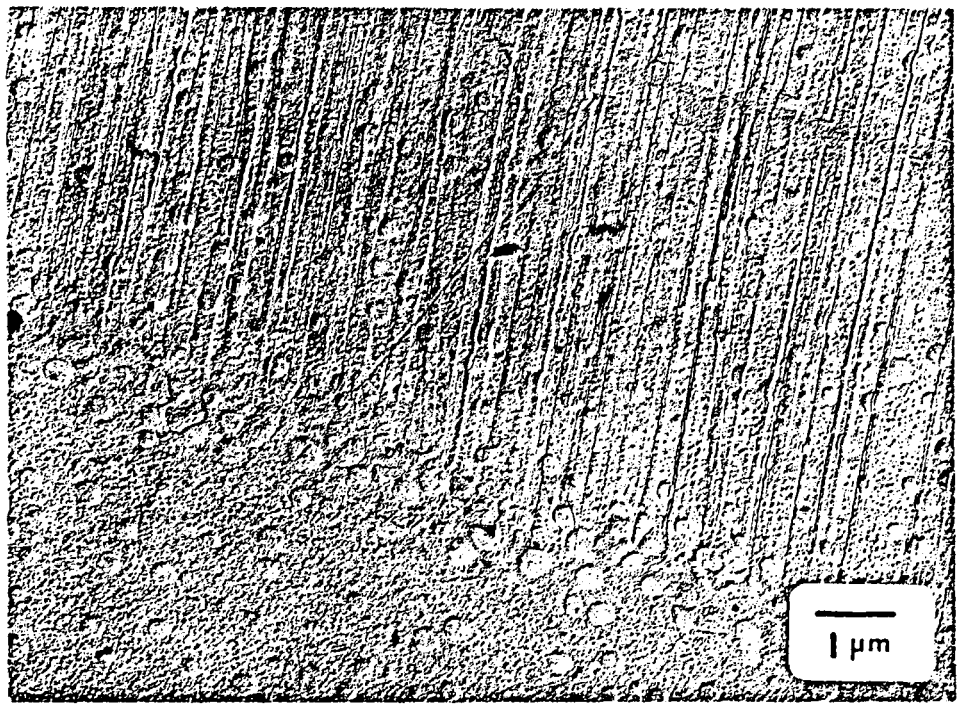

Fig. 5: Slip on a finer scale in Waspaloy fatigued for 160 cycles, 0.05 Hz, 650°C with a stress amplitude of 810 MPa. No prior deformation. Note the tendency of the slip lines to go around the large γ' particles.

2. PUBLICATIONS

1. S. Nemat-Nasser, T. Iwakuma, and M. Hejazi, "On Composites with Periodic Structure," Mechanics of Materials, Vol. 1 (1982), pp. 239-267.

2. S. Nemat-Nasser, "On Finite Deformation Elasto-Plasticity," International Journal of Solids and Structures, Vol. 18 (1982), pp. 857-872.

3. Y. Murakami and S. Nemat-Nasser, "Growth and Stability of Interacting Surface Flaws of Arbitrary Shape," Engineering Fracture Mechanics, Vol. 17 (1983), pp. 193-210.

4. T. Iwakuma and S. Nemat-Nasser, "Composites with Periodic Microstructure," Advances and Trends in Structural and Solid Mechanics, Proc. Symp., Washington, D.C., Oct. 4-7, 1982, A. K. Noor and J. M. Housner (eds.), Pergamon Press (1983), pp. 13-19; also in Computers and Structures, Vol. 16 (1983), pp. 13-19.

5. Y. C. Gao and S. Nemat-Nasser, "Dynamic Fields Near a Crack Tip Growing in an Elastic-Perfectly-Plastic Solid," Mechanics of Materials, Vol. 2, (1983), pp. 47-60.

6. K. Motoie, M. Sakane, and J. Schmidt, "An Extensometer for Axial Strain Measurement at High Temperature," Mechanics of Materials, Vol. 2 (1983), pp. 179-182.

7. S. Nemat-Nasser, "Recent Progress in the Description of Inelastic Behavior of Materials with Microdefects," (Invited Lecture), Transactions of the 7th International Conference on Structural Mechanics in Reactor Technology, North-Holland (1983), Vol.L, Paper L/1*, pp. 69-77.

8. T. Iwakuma and S. Nemat-Nasser, "Finite Elastic-Plastic Deformation of Polycrystalline Metals," to appear in Proc. Roy. Soc. London (1984).

REFERENCES

[1] M. Clavel and A. Pineau, Scripta Metall. 16 (1982), 361.

[2] M. Clavel, C. Levaillant, and A. Pineau, in: Creep-Fatigue-Environment Interactions, R. M. Pelloux and N. S. Stoloff (eds.), TMS-AIME (1980).

[3] T. Iwakuma and S. Nemat-Nasser, "Finite Elastic-Plastic Deformation of Polycrystalline Metals, to appear in Proc. R. Soc. London (1984).

[4] Y. C. Gao and S. Nemat-Nasser, "Dynamic Fields Near a Crack Tip Growing in an Elastic-Perfectly-Plastic Solid," Mechanics of Materials 2 (1983), 47-60.

[5] Y. C. Gao and S. Nemat-Nasser, "Mode II Dynamic Fields Near a Crack Tip Growing in an Elastic-Perfectly-Plastic Solid," J. Mech. Phys. Solids 32 (1984), 1-19.

Page intentionally left blank

CONSTITUTIVE MODELING OF SUPERALLOY SINGLE CRYSTALS AND DIRECTIONALLY SOLIDIFIED MATERIALS

Kevin P. Walker
Engineering Science Software, Inc.
Smithfield, Rhode Island 02906

Eric H. Jordan
University of Connecticut
Storrs, Connecticut 06268

A unified viscoplastic constitutive relation based on crystallographic slip theory is developed for the deformation analysis of nickel-base face-centered cubic superalloy single crystals at elevated temperature. The single crystal theory is then embedded in a self-consistent method to derive a constitutive relation for a directionally solidified material comprised of a polycrystalline aggregate of columnar cylindrical grains. One of the crystallographic axes of the cylindrical crystals points in the columnar direction whilst the remaining crystallographic axes are oriented at random in the basal plane perpendicular to the columnar direction. These constitutive formulations are currently being coded in FORTRAN for use in nonlinear finite element and boundary element programs. An experimental program to determine the biaxial tension-torsion behavior of PWA 1480 single crystal tubular specimens at 1600°F is also underway.

INTRODUCTION

This paper represents a first quarterly progress report on a program to develop anisotropic constitutive equations for use in modeling the multiaxial viscoplastic stress-strain response of single crystal and directionally solidified gas turbine alloys at elevated temperature. Two approaches are being pursued. The first approach consists of modeling the anisotropic response from a macroscopic continuum point of view, whilst the second approach consists of taking a micromechanics viewpoint using crystal plasticity concepts. Tubular specimens of the single crystal superalloy PWA 1480 are currently being machined. Tension-torsion experiments on tubular specimens of PWA 1480 will be conducted at 1600°F to provide a data base for exercising the theoretical formulations. The anisotropic viscoplastic theories will be incorporated into a nonlinear finite element code since the non-uniform stress distribution in the tubular specimens will require the solution of a boundary value problem for data reduction purposes.

SINGLE CRYSTAL ANALYSIS

An analysis of single crystal superalloys undergoing steady state creep deformation was presented by Paslay, Wells and Leverant [1] in 1970 using a theoretical formulation based on crystallographic slip theory of face-centered cubic materials. In 1971 the theory was applied by Paslay, Wells, Leverant and Burck [2] to describe the creep behavior of single crystal nickel-base superalloy tubes under biaxial tension. Steady state creep formulations suitable for the analysis of single crystals were used by Brown [3] in 1970 and by Hutchinson [4] in 1976 to predict the behavior of polycrystalline materials whose aggregate consists of randomly oriented single crystal grains. Recently, Weng [5] has developed a single crystal creep formulation which accounts for transient (primary) as well as steady state (secondary) creep. However, in order to describe the combined plastic and creep behavior of polycrystalline materials, Weng combines the rate-independent and rate-dependent components of crystal behavior in such a way that each component is governed by a separate constitutive relation. The averaging of the single crystal creep relations to obtain the overall macroscopic creep response of the polycrystalline aggregate is easily accomplished by using Kroner's self-consistent method [6]. In a general analysis the constitutive relations for the overall macroscopic plastic response of the polycrystalline aggregate must be obtained using Hill's self-consistent method [7]. Kroner's method for calculating the macroscopic creep properties of a polycrystalline aggregate of single crystals is explicit in nature; but Hill's method for calculating the macroscopic plastic properties is implicit in nature and requires lengthy iterative computations.

In the decade of the seventies the creep and plastic responses of materials were combined into unified viscoplastic formulations [8]. These formulations differ from steady state creep theories by introducing history dependent state variables to account for primary creep and plasticity. Most of these unified theories exhibit an elastic response under instantaneous deformation. This instantaneous elastic response occurs because the inelastic strain rate is assumed to depend only on stress, state variables and temperature and not on the rates of these variables. These unified theories may, therefore, be integrated in time by means of an explicit Euler forward difference method. Macroscopic properties of a polycrystalline aggregate, comprised of single crystal grains which are assumed to deform according to a unified viscoplastic slip process, can therefore be obtained by means of Kroner's explicit self-consistent method.

In the unit cell of the face-centered cubic crystal shown in Figure 1 we denote by $\underset{\sim}{m}_i$ a unit vector in the i^{th} slip direction (say of type $\langle 110 \rangle$), whilst $\underset{\sim}{n}_i$ is a unit vector in the normal direction to the slip plane (of type $\{111\}$) of which $\underset{\sim}{m}_i$ constitutes a slip direction. The four octahedral $\{111\}$ planes and the twelve corresponding $\langle 110 \rangle$ slip directions (three on each plane) are shown in Figure 1.

From the geometry of the unit cubic cell in Figure 1 the unit vectors are given by

$$\underset{\sim}{m}_1 = (\underset{\sim}{i} - \underset{\sim}{k})/\sqrt{2} \ , \quad \underset{\sim}{m}_2 = (-\underset{\sim}{j} + \underset{\sim}{k})/\sqrt{2} \ , \quad \underset{\sim}{m}_3 = (\underset{\sim}{i} - \underset{\sim}{j})/\sqrt{2} \ , \quad \underset{\sim}{m}_4 = (\underset{\sim}{i} - \underset{\sim}{k})/\sqrt{2} \ ,$$

$\underset{\sim}{m}_5 = (\underset{\sim}{i}+\underset{\sim}{j})/\sqrt{2}$, $\underset{\sim}{m}_6 = (\underset{\sim}{j}+\underset{\sim}{k})/\sqrt{2}$, $\underset{\sim}{m}_7 = (\underset{\sim}{i}+\underset{\sim}{j})/\sqrt{2}$, $\underset{\sim}{m}_8 = (-\underset{\sim}{j}+\underset{\sim}{k})/\sqrt{2}$,

$\underset{\sim}{m}_9 = (\underset{\sim}{i}+\underset{\sim}{k})/\sqrt{2}$, $\underset{\sim}{m}_{10} = (\underset{\sim}{j}+\underset{\sim}{k})/\sqrt{2}$, $\underset{\sim}{m}_{11} = (\underset{\sim}{i}-\underset{\sim}{j})/\sqrt{2}$, $\underset{\sim}{m}_{12} = (\underset{\sim}{i}+\underset{\sim}{k})/\sqrt{2}$,

with

$$\underset{\sim}{n}_1 = \underset{\sim}{n}_2 = \underset{\sim}{n}_3 = (\underset{\sim}{i}+\underset{\sim}{j}+\underset{\sim}{k})/\sqrt{3} \ , \ \underset{\sim}{n}_4 = \underset{\sim}{n}_5 = \underset{\sim}{n}_6 = (\underset{\sim}{i}+\underset{\sim}{j}-\underset{\sim}{k})/\sqrt{3} ,$$

$$\underset{\sim}{n}_7 = \underset{\sim}{n}_8 = \underset{\sim}{n}_9 = (\underset{\sim}{i}-\underset{\sim}{j}-\underset{\sim}{k})/\sqrt{3} \ , \ \underset{\sim}{n}_{10} = \underset{\sim}{n}_{11} = \underset{\sim}{n}_{12} = (-\underset{\sim}{i}-\underset{\sim}{j}+\underset{\sim}{k})/\sqrt{3} ,$$

where $\underset{\sim}{i}$, $\underset{\sim}{j}$, $\underset{\sim}{k}$ are unit vectors along the x,y,z crystallographic axes.

Figure 2 shows a single crystal whose global axes are denoted by x^*, y^*, z^* and whose crystallographic axes are denoted by x,y,z. If Q denotes the orthogonal tensor which rotates the crystallographic (unstarred) axes into the global (starred) axes, viz., $x_i^* = Q_{ij} x_j$, then the stress tensor $\underset{\sim}{\sigma}$ and the strain rate tensor $\underset{\sim}{\dot{\varepsilon}}$ in the crystallographic axes may be obtained from the stress tensor $\underset{\sim}{\sigma}^*$ and the strain rate tensor $\underset{\sim}{\dot{\varepsilon}}^*$ in the global system from the usual transformation relations,

$$\underset{\sim}{\sigma} = \underset{\sim}{Q} \cdot \underset{\sim}{\sigma}^* \cdot \underset{\sim}{Q}^T \quad \text{and} \quad \underset{\sim}{\dot{\varepsilon}} = \underset{\sim}{Q} \cdot \underset{\sim}{\dot{\varepsilon}}^* \cdot \underset{\sim}{Q}^T . \tag{1}$$

The assumption is now made that any of the unified viscoplastic theories discussed in Reference [8], when specialized to the case of shear deformation, is a valid constitutive relation in each of the twelve crystallographic slip directions. In the r^{th} slip direction the resolved shear stress, π^r_{mn} , is obtained from the relation

$$\pi^r_{mn} = \underset{\sim}{m}_r \cdot \underset{\sim}{\sigma} \cdot \underset{\sim}{n}_r \quad \text{for } r = 1, 2, \cdots, 12 . \tag{2}$$

It is further assumed, in a manner analogous to the unified isotropic viscoplastic models, that the applicable relation governing the inelastic shear strain rate in the r^{th} slip direction is

$$\begin{aligned} \dot{\gamma}_r = K_r^{-p} \Big\{ & (\pi^r_{mn} - \omega^r_{mn}) |\pi^r_{mn} - \omega^r_{mn}|^{p-1} + \alpha_{mm} (\pi^r_{mm} - \omega^r_{mm}) |\pi^r_{mm} - \omega^r_{mm}|^{p-1} \\ & + \alpha_{nn} (\pi^r_{nn} - \omega^r_{nn}) |\pi^r_{nn} - \omega^r_{nn}|^{p-1} + \alpha_{zz} (\pi^r_{zz} - \omega^r_{zz}) |\pi^r_{zz} - \omega^r_{zz}|^{p-1} \\ & + 2\alpha_{mz} (\pi^r_{mz} - \omega^r_{mz}) |\pi^r_{mz} - \omega^r_{mz}|^{p-1} + 2\alpha_{nz} (\pi^r_{nz} - \omega^r_{nz}) |\pi^r_{nz} - \omega^r_{nz}|^{p-1} \Big\} , \end{aligned} \tag{3}$$

where K_r and ω^r_{pq} (with p and q = m,n,z) denote the drag stress and equilibrium (rest or back) stress in the r^{th} slip direction. The expression for π^r_{mn} is defined in equation (2). Terms such as π^r_{mz} denote, by analogy, expressions of the type

$$\pi^r_{mz} = \underset{\sim}{m}_r \cdot \underset{\sim}{\sigma} \cdot \underset{\sim}{z}_r , \tag{4}$$

where $\underset{\sim}{z}_r$ denotes a unit vector perpendicular to the unit vectors $\underset{\sim}{m}_r$ and $\underset{\sim}{n}_r$. The vector $\underset{\sim}{z}_r$ is in the slip plane containing the vector $\underset{\sim}{m}_r$ and the vectors $\underset{\sim}{m}_r$, $\underset{\sim}{n}_r$, $\underset{\sim}{z}_r$ form an orthogonal triad for the r^{th} slip system. In equation (3) the tensor α_{pq} represents the effect of the non-Schmid factors [9] upon the inelastic strain rate in the r^{th} slip direction.

For example, the term containing α_{mn} represents the effect of the resolved stress, normal to the slip plane containing the r^{th} slip direction, on the inelastic strain rate in the r^{th} slip direction. Such terms can represent the effect of a pressure dependent inelastic strain rate. The dominant term in equation (3) is the Schmid type term containing the expression π^r_{mn} ; estimates of the magnitude of the non-Schmid type terms containing the tensor α_{pq} have been given by Asaro and Rice in Reference [10].

To complete the constitutive formulation it is necessary to specify the growth relations for the equilibrium and drag stress state variables. The equilibrium stress in the r^{th} slip system may be assumed to evolve according to the evolution equation

$$\dot{\omega}^r_{pq} = \rho^1_{pq}\dot{\gamma}_r - \rho^2_{pq}|\dot{\gamma}_r|\omega^r_{pq} - \rho^3_{pq}|\omega^r_{pq}|^{m-1}\omega^r_{pq}\,, \tag{5}$$

where ρ^1_{pq}, ρ^2_{pq}, ρ^3_{pq} and m are temperature dependent material constants. A simplifying assumption is to take

$$\lim_{\substack{R_r\to\infty \\ \dot{\gamma}_r\to\infty}} \frac{\omega^r_{pq}}{\pi^r_{pq}} = \lim_{\substack{R_r\to\infty \\ \dot{\gamma}_r\to\infty}} \frac{\omega^r_{mn}}{\pi^r_{mn}} \quad \text{for } p,q = m,n,z\,, \tag{6}$$

where the cumulative inelastic strain is defined by

$$R_r = \int_0^t \left|\frac{\partial \gamma_r}{\partial \xi}\right| d\xi\,. \tag{7}$$

Equation (6) states that the ratio of the saturated equilibrium (back) stress, i.e. the equilibrium stress for continued inelastic straining ($R_r\to\infty$) under fast straining conditions ($\dot{\gamma}_r\to\infty$), to the resolved shear stress in the same direction, is equal for all the non-Schmid systems. Moreover, the ratio is equal to the ratio of the saturated equilibrium stress to the resolved shear stress for the Schmid-type components, ω^r_{mn} and π^r_{mn} . Under continued inelastic straining the equilibrium stress saturates and $\dot{\omega}^r_{pq}\to 0$. Under fast straining conditions ($\dot{\gamma}_r\to\infty$) equation (5) shows that the saturated equilibrium stress is given by the relation

$$\lim_{\substack{R_r\to\infty \\ \dot{\gamma}_r\to\infty}} \omega^r_{pq} = \frac{\rho^1_{pq}}{\rho^2_{pq}}\,, \tag{8}$$

since the thermal recovery term containing the material constant ρ^3_{pq} can be neglected for $\dot{\gamma}_r\to\infty$. The material constants ρ^ℓ_{pq} must therefore satisfy the relation

$$\frac{\rho^1_{pq}}{\rho^2_{pq}\,\pi^r_{pq}(R_r\to\infty)} = \frac{\rho^1_{mn}}{\rho^2_{mn}\,\pi^r_{mn}(R_r\to\infty)}\,. \tag{9}$$

Assuming the constants ρ^1_{mn} and ρ^2_{mn} and the limiting saturated value of the resolved shear stress π^r_{mn} are known for the Schmid-type terms, equation (9) determines the ratio of ρ^1_{pq} to ρ^2_{pq} for the non-Schmid terms. If it is further assumed that the initial hardening rate for the non-Schmid equilibrium stresses are all equal to the Schmid equilibrium stress hardening rate, then $\rho^\ell_{pq} = \rho^\ell_{mn}$ for $\ell = 1,2$ and $p,q = m,n,z$.

The drag stress may be assumed to grow according to the evolution equation

$$\dot{K}_r = \sum_{k=1}^{12} h_{rk} |\dot{\gamma}_k| \ , \tag{10}$$

in which the hardening moduli are given by

$$h_{rk} = \left[q + (1-q)\delta_{rk} \right] e^{-h \sum_{i=1}^{12} \int_0^t \left| \frac{\partial \gamma_i}{\partial \xi} \right| d\xi} \ . \tag{11}$$

The hardening moduli h_{rk} defined in equation (10) account for the latent hardening effects observed in single crystal materials, and equation (11) is similar in form to that proposed by Hutchinson [11], Asaro [12] and Peirce, Asaro and Needleman [13]. Numerous forms for the hardening moduli h_{rk} have been proposed in the literature and a review of hardening moduli may be found by consulting Havner's papers (cf. Reference [14]). The drag stress evolution equation does not contain thermal recovery terms, but these terms can easily be included in the formulation.

The shear slip strain rates may now be resolved into the crystallographic system and summed for each slip system to obtain the inelastic strain rate tensor with respect to the crystallographic axes in the form

$$\dot{\underset{\sim}{\varepsilon}} = \sum_{k=1}^{12} \tfrac{1}{2} \dot{\gamma}_k \left(\underset{\sim}{n}_k \underset{\sim}{m}_k + \underset{\sim}{m}_k \underset{\sim}{n}_k \right) . \tag{12}$$

Finally, the stress rate tensor with respect to the crystallographic axes is determined from the relation

$$\dot{\underset{\sim}{\sigma}} = \underset{\sim}{D}^c : \left(\dot{\underset{\sim}{\varepsilon}} - \dot{\underset{\sim}{\varepsilon}} \right) , \tag{13}$$

where $\underset{\sim}{D}^c$ is the anisotropic elasticity tensor for the face-centered cubic crystal referred to the crystallographic axes.

The variables can now be updated in the Euler forward difference form:

$$\underset{\sim}{\sigma} = \underset{\sim}{\sigma} + \dot{\underset{\sim}{\sigma}} \Delta t \ , \quad \underset{\sim}{\varepsilon} = \underset{\sim}{\varepsilon} + \dot{\underset{\sim}{\varepsilon}} \Delta t \ , \quad \omega^r_{pq} = \omega^r_{pq} + \dot{\omega}^r_{pq} \Delta t \ ,$$

$$\gamma_r = \gamma_r + \dot{\gamma}_r \Delta t \ , \quad \underset{\sim}{\sigma}^* = \underset{\sim}{Q}^T \cdot \underset{\sim}{\sigma} \cdot \underset{\sim}{Q} \ , \quad \underset{\sim}{\varepsilon}^* = \underset{\sim}{Q}^T \cdot \underset{\sim}{\varepsilon} \cdot \underset{\sim}{Q} \ , \tag{14}$$

where Δt is the current time increment. The process may then be repeated by integrating equations (1), (2), (3), (4), (5), (10), (11) for each time increment.

The preceding discussion has focussed on slip which occurs on the {111} octahedral planes in the <110> type directions of face-centered cubic nickel-base superalloys. Paslay, Wells, Leverant and Burck [1,2] also found that slip occurs under creep conditions on the {111} planes in the <112> type directions. Cube slip on the crystallographic faces was also found to occur. For each different slip system the foregoing theory

is altered only by virtue of having different slip and normal vectors defining the triad $\underset{\sim}{m}$, $\underset{\sim}{n}$ and $\underset{\sim}{z}$. In general, the total inelastic strain rate may be written as the sum,

$$\dot{\underset{\sim}{\varepsilon}} = \sum_{i=1}^{N} \lambda_i \dot{\underset{\sim}{\varepsilon}}_i \ , \tag{15}$$

where $\dot{\underset{\sim}{\varepsilon}}_1$ is due to {111} ⟨110⟩ type slip, $\dot{\underset{\sim}{\varepsilon}}_2$ is due to {111} ⟨112⟩ type slip, $\dot{\underset{\sim}{\varepsilon}}_3$ is due to cube slip, etc. Such a combination was stated to be required to model primary creep behavior in Reference [1] by Paslay, Wells and Leverant. It is possible that {111} ⟨112⟩ type primary creep may evolve into {111} ⟨110⟩ type secondary creep as described by Leverant, Kear and Oblak in Reference [15]. In this instance it may be necessary to modify the theory so that the λ_i evolve with deformation, inelastic strain rate and temperature according to evolution growth equations similar to that employed for the equilibrium and drag stress state variables. This mixing of different slip systems to model the anisotropy of nickel-base superalloys was also stated by Ezz, Pope and Paidar [16] to be necessary in order to model tension-compression flow stress asymmetry observed in nickel-base superalloys.

DIRECTIONALLY SOLIDIFIED ANALYSIS

A model for directionally solidified alloys can be constructed by making use of a suitable self-consistent method to average the results of the single crystal viscoplastic constitutive theory. The directionally solidified material consists of aligned columnar single crystal grains which are oriented at random in the basal plane perpendicular to the cylindrical growth direction. This random orientation of the grains produces a material with transversely isotropic properties.

The directionally solidified material comprised of an aggregate of single crystal columnar grains may therefore be modeled in the following manner. We first choose a particular single crystal columnar grain and replace the aggregate of single crystal grains surrounding the chosen grain by a transversely isotropic material. The properties of this surrounding transversely isotropic material are found by averaging the properties of the chosen single crystal grain about its cylindrical growth axis. It is then possible to relate the stress and strain increments in the single crystal grain to those in the surrounding transversely isotropic matrix by means of the method proposed by Eshelby [17] in 1957.

Viscoplastic formulations which exhibit an instantaneous elastic response can be integrated by means of an Euler forward difference method. In physical terms this integration process consists of letting the material creep at constant stress at the level $\underset{\sim}{\sigma}$ appropriate to the beginning of the increment for a time interval Δt. After the creep increment is completed the material is subjected to an instantaneous strain increment $\Delta\underset{\sim}{\varepsilon} - \Delta\underset{\sim}{c}$, where $\Delta\underset{\sim}{\varepsilon}$ is the total strain increment during the time increment Δt and $\Delta\underset{\sim}{c}$ is the completed creep strain increment. The instantaneous application of the strain increment $\Delta\underset{\sim}{\varepsilon} - \Delta\underset{\sim}{c}$ induces an elastic stress increment given by Hooke's law in the form $\Delta\underset{\sim}{\sigma} = \underset{\sim}{D}:(\Delta\underset{\sim}{\varepsilon}-\Delta\underset{\sim}{c})$ where $\underset{\sim}{D}$ is the elasticity tensor for the material.

Let $\mathcal{L}^c$ and $\mathcal{L}^m$ denote the fourth rank cubic and transversely isotropic elasticity tensors for the single crystal and the surrounding matrix, respectively. In the cylindrical single crystal grain the inelastic strain increment is denoted by $\Delta\underset{\sim}{c}$ and the corresponding quantity in the matrix is denoted by $\langle\Delta\underset{\sim}{c}\rangle$. The quantity $\langle\Delta\underset{\sim}{c}\rangle$ is obtained from $\Delta\underset{\sim}{c}$ by averaging $\Delta\underset{\sim}{c}$ over all angular orientations (viz. from 0 to 2π) in the basal plane perpendicular to the cylindrical growth axis. In the single crystal grain the constitutive relation has the form

$$\Delta\sigma_{ij} = D^c_{ijkl}\left(\Delta\varepsilon_{kl} - \Delta c_{kl}\right), \tag{16}$$

whilst in the directionally solidified matrix the constitutive form is

$$\langle\Delta\sigma_{ij}\rangle = D^m_{ijkl}\left(\langle\Delta\varepsilon_{kl}\rangle - \langle\Delta c_{kl}\rangle\right). \tag{17}$$

Given a known strain increment $\langle\Delta\varepsilon_{kl}\rangle$ in the directionally solidified matrix, the object is to determine the corresponding inelastic strain increment Δc_{kl} in the single crystal cylinder and then average this quantity by means of the relation

$$\langle\Delta c_{kl}\rangle = \frac{1}{2\pi}\int_0^{2\pi}\Delta c_{kl}(\theta)\,d\theta\,, \tag{18}$$

where θ is the angle between the crystallographic axes x,y in the specimen and the global axes x^*,y^* in the matrix, with the z,z^* axes aligned in the cylindrical crystal's growth direction. The stress increment in the directionally solidified matrix is then determined by equation (17).

The first step consists of determining the state of stress and strain in the cylindrical crystal grain when the matrix and crystal undergo creep for a time increment Δt . A preliminary step in this analysis consists of replacing the single crystal grain by a fictitious material which has elastic and inelastic properties which differ from those of the single crystal but in which the elastic properties are the same as that of the transversely isotropic matrix with elasticity tensor $\mathcal{L}^m$. Eshelby's cutting, straining and welding operations [17] are now applied to the fictitious crystal grain.

The fictitious cylindrical grain is now cut out of the matrix and the instantaneous shapes of the grain and resulting cylindrical hole in the matrix are maintained by appropriate equal and opposite surface tractions applied to the respective cylindrical surfaces of the grain and hole. The stress in the matrix is denoted by $\langle\underset{\sim}{\sigma}\rangle$ and that in the fictitious grain by $\underset{\sim}{\sigma}$, where $\underset{\sim}{\sigma}$ is the stress state in the actual single crystal grain. From Eshelby's results, if the strain history in the matrix is homogeneous, the resulting stress in the actual and fictitious cylindrical grains will be constant throughout the cylindrical volume. This will be demonstrated subsequently. The fictitious cylindrical grain and the surrounding matrix are now assumed to undergo creep responses for a time increment Δt at their respective stress levels of $\underset{\sim}{\sigma}$ and $\langle\underset{\sim}{\sigma}\rangle$. In the grain the resulting creep strain increment is denoted by $\Delta\underset{\sim}{\varepsilon}^T$ and the corres-

ponding creep strain increment in the matrix is $\langle \Delta \underset{\sim}{\varepsilon} \rangle$. If incremental surface tractions are instantaneously applied to the cylindrical surface of the fictitious grain so that it is elastically strained by an amount $-\Delta \underset{\sim}{\varepsilon}^T$, it will regain the original size and shape which it had upon removal from the matrix prior to the creep response. If it is subsequently elastically strained by an amount $\langle \Delta \underset{\sim}{\varepsilon} \rangle$ through the application of a further set of incremental tractions applied instantaneously to the cylindrical surface of the grain, it will fit back into the matrix from which it was removed. The fictitious grain and matrix now fit compatibly together, and the strain increment experienced by the grain is $-\Delta \underset{\sim}{\beta}$ where

$$\Delta \beta_{kl} = \Delta \varepsilon^T_{kl} - \langle \Delta c_{kl} \rangle \cdot \tag{19}$$

However, a layer of surface traction exists on the cylindrical surface boundary between the grain and the matrix. This layer of surface traction is given in magnitude by the relation

$$\Delta t_i = n_j \Delta \sigma_{ij} = n_j D^m_{ijkl} \left(\langle \Delta c_{kl} \rangle - \Delta \varepsilon^T_{kl} \right) = -n_j D^m_{ijkl} \Delta \beta_{kl} \, ,$$

and can be removed by the application of an equal and opposite layer of surface body force of magnitude

$$\Delta f_i = n_j D^m_{ijkl} \Delta \beta_{kl} \, . \tag{20}$$

The displacement increment Δu^c_i induced in the fictitious grain due to the application of surface tractions Δf_i over its cylindrical surface is given by

$$\Delta u^c_i = \iint_S \Delta f_j \, G_{ij} (\underset{\sim}{r} - \underset{\sim}{r}') \, dS(\underset{\sim}{r}') \tag{21}$$

where $G_{ij}(\underset{\sim}{r} - \underset{\sim}{r}')$ is the elastic Green's function for the transversely isotropic matrix and the fictitious grain. Application of Gauss' divergence theorem to the surface integral produces the result

$$\begin{aligned} \Delta u^c_p &= \iint_S n_i D^m_{jikl} \Delta \beta_{kl} G_{pj} (\underset{\sim}{r} - \underset{\sim}{r}') \, dS(\underset{\sim}{r}') \\ &= D^m_{ijkl} \Delta \beta_{kl} \iiint_V \frac{\partial G_{pj} (\underset{\sim}{r} - \underset{\sim}{r}')}{\partial x'_i} \, dV(\underset{\sim}{r}') \\ &= -D^m_{ijkl} \Delta \beta_{kl} \frac{\partial}{\partial x_i} \iiint_V G_{pj} (\underset{\sim}{r} - \underset{\sim}{r}') \, dV(\underset{\sim}{r}') \, . \end{aligned} \tag{22}$$

The resulting strain increment $\Delta \varepsilon^c_{ip}$ in the fictitious grain due to this annihilation of the incremental surface traction built up during the creep response of the fictitious grain and the matrix is

$$\Delta \varepsilon^c_{ip} = \frac{1}{2} \left(\frac{\partial (\Delta u^c_i)}{\partial x_p} + \frac{\partial (\Delta u^c_p)}{\partial x_i} \right) = S_{iplm} \Delta \beta_{lm} \, , \tag{23}$$

where the Eshelby tensor $\underset{\sim}{S}$ is defined by the relation

$$S_{iplm} = -\frac{1}{2} D^m_{kjlm} \left\{ \frac{\partial^2}{\partial x_i \partial x_k} \iiint_V G_{pj} (\underset{\sim}{r} - \underset{\sim}{r}') \, dV(\underset{\sim}{r}') + \frac{\partial^2}{\partial x_p \partial x_k} \iiint_V G_{ij} (\underset{\sim}{r} - \underset{\sim}{r}') \, dV(\underset{\sim}{r}') \right\} . \tag{24}$$

The strain increment induced in the fictitious grain in order to make it fit compatibly in the matrix is given by $-\Delta \beta_{ij}$, whilst the additional

strain induced in the grain by removing the unwanted surface traction increment Δt_i is given by $\Delta \varepsilon^c_{ij}$. At the end of the creep increment the total strain increment induced in the fictitious grain is given by $\Delta \varepsilon^c_{ij} - \Delta \beta_{ij}$, or from equation (23), by $S_{ijkl}\,\Delta\beta_{kl} - \Delta\beta_{ij}$. The stress increment in the grain is therefore

$$\Delta\sigma_{ij} = D^m_{ijkl}\left(S_{klmn} - I_{klmn}\right)\Delta\beta_{mn} \,, \tag{25}$$

where $\underset{\sim}{I}$ is the fourth rank identity tensor. Note that the strain increment responsible for changing the size of the cylindrical grain from the size it had when it was placed back into the matrix is $\Delta \varepsilon^c_{ij} = S_{ijkl}\,\Delta\beta_{kl}$, since the change in size is due to the annihilation of the surface traction increment Δt_i by the equal and opposite traction increment Δf_i .

Now consider the actual situation where the cylindrical grain has its own anisotropic elastic constant tensor with cubic symmetry, $\underset{\sim}{D}^c$. We remove the cylinder from the matrix, as before, and let the cylindrical grain undergo a creep strain increment $\Delta\underset{\sim}{\varepsilon}$ in time Δt and the matrix undergo a creep strain increment $\langle\Delta\underset{\sim}{\varepsilon}\rangle$. If we now apply surface traction increments instantaneously to the cylindrical boundary so that the cylinder is elastically strained by an amount $\langle\Delta\underset{\sim}{\varepsilon}\rangle - \Delta\underset{\sim}{\varepsilon}$, it will fit back into the matrix from which it was removed. Moreover, since the matrix creep strain increment $\langle\Delta\underset{\sim}{\varepsilon}\rangle$ is the same as that in the problem with the fictitious cylinder, the cylindrical grain will have the same size and shape as the fictitious cylinder had when it was put back into the matrix. The strain increment responsible for changing the size of the cylindrical grain from the size it had when it was placed back into the matrix to the size in its final configuration is $S_{klmn}\,\Delta\beta_{mn}$. Hence, if the actual cylindrical grain is strained by the increment $S_{klmn}\,\Delta\beta_{mn} + \langle\Delta c_{kl}\rangle - \Delta c_{kl}$, it will have the same final size as the previously considered fictitious cylindrical grain with transversely isotropic elastic properties. The stress increment in the actual cylinder due to the strain increment $S_{klmn}\,\Delta\beta_{mn} + \langle\Delta c_{kl}\rangle - \Delta c_{kl}$ is

$$\Delta\sigma_{ij} = D^c_{ijkl}\left\{S_{klmn}\,\Delta\beta_{mn} + \langle\Delta c_{kl}\rangle - \Delta c_{kl}\right\} . \tag{26}$$

If the stress increments in equations (25) and (26) are equal, the actual cylindrical grain which has the elasticity tensor $\underset{\sim}{D}^c$ appropriate to cubic symmetry and which undergoes an increment of transformation strain $\Delta\underset{\sim}{\beta}$, may be replaced with the fictitious cylindrical grain with elasticity tensor $\underset{\sim}{D}^m$ equal to that of the matrix without upsetting continuity of displacements and tractions across the cylinder-matrix interface. Equating (25) and (26) shows that

$$\Delta\beta_{ij} = \left[\left(D^c_{ijkl} - D^m_{ijkl}\right)S_{klmn} + D^m_{ijmn}\right]^{-1} D^c_{mnpq}\left\{\Delta c_{pq} - \langle\Delta c_{pq}\rangle\right\} . \tag{27}$$

If this transformation strain increment occurs in a cylinder with elasticity tensor $\underset{\sim}{D}^m$, the stress increment in the cylinder is equal to that which actually occurs in the single crystal cylinder with elasticity tensor $\underset{\sim}{D}^c$ undergoing a transformation strain increment $\Delta\underset{\sim}{\varepsilon} - \langle\Delta\underset{\sim}{\varepsilon}\rangle$. Substitution of the expression for $\Delta\underset{\sim}{\beta}$ into equation (25) [or (26)] gives the stress increment in the cylindrical single crystal grain at the end of the creep re-

sponse in the form

$$\Delta\sigma_{ij} = D^m_{ijkl}\left(S_{klmn} - I_{klmn}\right)\left[\left(D^c_{mnpq} - D^m_{mnpq}\right)S_{pqrs} + D^m_{mnrs}\right]^{-1} \times D^c_{rstu}\left\{\Delta c_{tu} - \langle \Delta c_{tu}\rangle\right\}. \tag{28}$$

According to the Euler foward difference integration method the crystal grain and matrix are now to be instantaneously loaded with the elastic strain increment $\langle\Delta\underset{\sim}{\varepsilon}\rangle - \langle\Delta\underset{\sim}{c}\rangle$. To this end we first consider the single crystal to be replaced by a fictitious cylinder having the same transversely isotropic properties as the surrounding matrix. If the fictitious cylinder undergoes a stress increment free uniform strain increment $\Delta\varepsilon^T$, the final strain increment inside the cylinder is $(S_{ijkl} - I_{ijkl})\,\Delta\tilde{\varepsilon}^T_{kl}$. A uniform strain increment $\langle\Delta\underset{\sim}{\varepsilon}\rangle - \langle\Delta\underset{\sim}{c}\rangle$ may now be applied to the matrix and fictitious cylinder to produce the final strain increment of $(S_{ijkl} - I_{ijkl})\,\Delta\varepsilon^T_{kl} + \langle\Delta\varepsilon_{ij}\rangle - \langle\Delta c_{ij}\rangle$. The resulting stress increment in the fictitious cylinder is

$$\Delta\sigma_{ij} = D^m_{ijkl}\left\{\left(S_{klmn} - I_{klmn}\right)\Delta\varepsilon^T_{mn} + \langle\Delta\varepsilon_{kl}\rangle - \langle\Delta c_{kl}\rangle\right\}. \tag{29}$$

Only the strain increment $\underset{\sim}{S}:\Delta\underset{\sim}{\varepsilon}^T + \langle\Delta\underset{\sim}{\varepsilon}\rangle - \langle\Delta\underset{\sim}{c}\rangle$ is responsible for changing the size of the cylindrical volume, since the strain increment $-\Delta\underset{\sim}{\varepsilon}^T$ is used to force the cylindrical volume back to its original size after removal from the matrix. If the actual cylindrical grain with elasticity tensor $\underset{\sim}{\mathcal{D}}^c$ is now subjected to the strain increment $\underset{\sim}{S}:\Delta\underset{\sim}{\varepsilon}^T + \langle\Delta\underset{\sim}{\varepsilon}\rangle - \langle\Delta\underset{\sim}{c}\rangle$ it will aquire the same shape and size as the fictitious cylinder which has elastic properties identical to the matrix. The stress increment in the actual single crystal is then given by

$$\Delta\sigma_{ij} = D^c_{ijkl}\left\{S_{klmn}\,\Delta\varepsilon^T_{mn} + \langle\Delta\varepsilon_{kl}\rangle - \langle\Delta c_{kl}\rangle\right\}. \tag{30}$$

The actual and fictitious cylinders now have the same final shape and size and if the stress increments in equations (29) and (30) are equal, the actual crystal cylinder can replace the transversely isotropic cylinder and still preserve continuity of displacements and tractions across the cylinder-matrix interface. Equating (29) and (30) gives

$$\Delta\varepsilon^T_{ij} = -\left[\left(D^c_{ijkl} - D^m_{ijkl}\right)S_{klmn} + D^m_{ijmn}\right]^{-1}\left(D^c_{mnpq} - D^m_{mnpq}\right)\left\{\langle\Delta\varepsilon_{pq}\rangle - \langle\Delta c_{pq}\rangle\right\}. \tag{31}$$

Substitution of this result into equation (29) [or (30)] produces the stress increment in the cylinder due to the instantaneous application of the strain increment $\langle\Delta\underset{\sim}{\varepsilon}\rangle - \langle\Delta\underset{\sim}{c}\rangle$ in the matrix in the form

$$\Delta\sigma_{ij} = D^m_{ijkl}\left(\langle\Delta\varepsilon_{kl}\rangle - \langle\Delta c_{kl}\rangle\right) - D^m_{ijkl}\left(S_{klmn} - I_{klmn}\right)\left[\left(D^c_{mnpq} - D^m_{mnpq}\right)S_{pqrs} + D^m_{mnrs}\right]^{-1} \times \left(D^c_{rstu} - D^m_{rstu}\right)\left\{\langle\Delta\varepsilon_{tu}\rangle - \langle\Delta c_{tu}\rangle\right\}. \tag{31}$$

At the end of the creep response during the time interval Δt the stress increment in the single crystal cylindrical grain is given by equation (28). When the matrix is further elastically strained by the instantaneous application of the strain increment $\langle\Delta\underset{\sim}{\varepsilon}\rangle - \langle\Delta\underset{\sim}{c}\rangle$ the additional stress

increment in the single crystal grain is given by equation (31). Accordingly, the total stress increment in the single crystal due to the application of the strain increment $\langle \Delta \underset{\sim}{\varepsilon} \rangle$ in the time interval Δt is given by the Euler forward difference method as the sum of the stress increments in equations (28) and (31), viz.

$$\Delta\sigma_{ij} = \langle \Delta\sigma_{ij} \rangle + D^m_{ijkl}\left(S_{klmn} - I_{klmn}\right)\left[\left(D^c_{mnpq} - D^m_{mnpq}\right)S_{pqrs} + D^m_{mnrs}\right]^{-1}$$

$$\times \left\{ D^c_{rstu}\left(\Delta c_{tu} - \langle \Delta c_{tu} \rangle\right) - \left(D^c_{rstu} - D^m_{rstu}\right)\left(\langle \Delta\varepsilon_{tu} \rangle - \langle \Delta c_{tu} \rangle\right) \right\}, \quad (32)$$

where the first term in equation (31) is the definition of the matrix stress increment given in equation (17).

Provided the stress level $\underset{\sim}{\sigma}$ is known in the single crystal at the beginning of the increment, the single crystal analysis in the preceding section furnishes the value of the inelastic strain increment $\Delta \underset{\sim}{\varepsilon}$. Averaging $\Delta \underset{\sim}{\varepsilon}$ over the basal plane for crystals of different orientation by means of equation (18) then furnishes the value of $\langle \Delta \underset{\sim}{\varepsilon} \rangle$. Assuming that the strain increment in the matrix is given, equation (17) furnishes the required stress increment in the matrix. The stress increment in the single crystal constrained by the transversely isotropic matrix is given by equation (32). All pertinent quantities can now be updated according to the Euler forward difference procedure and the process repeated for the next time increment. A procedure for evaluating the Eshelby tensor $\underset{\sim}{S}$ is given in the appendix.

WORK IN PROGRESS

The single crystal analysis has been coded into a FORTRAN subroutine and is currently undergoing numerical test experiments. Coding of the directionally solidified analysis is due to commence shortly. Single crystal tubular specimens of PWA 1480 are being machined and will be tested at 1600°F under biaxial tension-torsion loading conditions.

APPENDIX

The Eshelby tensor $\underset{\sim}{S}$ is defined by the relation

$$S_{iplm} = -\tfrac{1}{2} D^{m}_{kjlm} \left\{ \frac{\partial^2}{\partial x_i \partial x_k} \iiint_V G_{pj}(\underset{\sim}{r}-\underset{\sim}{r}')\,dV(\underset{\sim}{r}') + \frac{\partial^2}{\partial x_p \partial x_k} \iiint_V G_{ij}(\underset{\sim}{r}-\underset{\sim}{r}')\,dV(\underset{\sim}{r}') \right\}, \quad (1)$$

where $G_{ij}(\underset{\sim}{r}-\underset{\sim}{r}')$ is the elastic Green's function for the transversely isotropic matrix material. Although the Green's function for transversely isotropic materials is known [18], it is more convenient to work with the Fourier representation of the Green's function. The Fourier transform of $G_{ij}(\underset{\sim}{r}-\underset{\sim}{r}')$ is known [19,20] and it can be shown, by taking the Fourier transform of the defining equation, viz.

$$D^{m}_{jkmn} \frac{\partial^2 G_{im}(\underset{\sim}{r}-\underset{\sim}{r}')}{\partial x_k \partial x_n} + \delta_{ij}\,\delta(\underset{\sim}{r}-\underset{\sim}{r}') = 0, \quad (2)$$

and inverting the result, that

$$G_{ij}(\underset{\sim}{r}-\underset{\sim}{r}') = \frac{1}{8\pi^3} \iiint_{-\infty}^{\infty} d^3\underset{\sim}{K}\, \frac{M^{-1}_{ij}(\underset{\sim}{\xi})}{K^2} e^{-i\underset{\sim}{K}\cdot(\underset{\sim}{r}-\underset{\sim}{r}')}. \quad (3)$$

In this equation the real part of the Fourier integral corresponds to the Green's function, and the Christoffel tensor $\underset{\sim}{M}$ is defined by

$$M_{ij}(\underset{\sim}{\xi}) = \xi_p D^{m}_{pijq} \xi_q \quad (4)$$

with

$$\underset{\sim}{\xi} = \underset{\sim}{K}/\sqrt{K_i K_i} = \underset{\sim}{K}/K \quad (5)$$

being a unit wave vector in the direction of the Fourier wave vector $\underset{\sim}{K}$. Introduction of this result into one of the integral terms in the definition of $\underset{\sim}{S}$ gives, on reversing the order of the volume and wave vector integrations,

$$\begin{aligned} L_{kgij} &= \frac{\partial^2}{\partial x_k \partial x_g} \iiint_V G_{ij}(\underset{\sim}{r}-\underset{\sim}{r}')\,dV(\underset{\sim}{r}') \\ &= \frac{1}{8\pi^3} \frac{\partial^2}{\partial x_k \partial x_g} \iiint_{-\infty}^{\infty} d^3\underset{\sim}{K}\, \frac{M^{-1}_{ij}(\underset{\sim}{\xi})}{K^2} e^{-i\underset{\sim}{K}\cdot\underset{\sim}{r}} \iiint_V e^{i\underset{\sim}{K}\cdot\underset{\sim}{r}'} dV(\underset{\sim}{r}'). \end{aligned} \quad (6)$$

The volume integration extends over the cylindrical volume of the fictitious cylindrical grain and can be written as

$$I = \iiint_V e^{i\underset{\sim}{K}\cdot\underset{\sim}{r}'} dV(\underset{\sim}{r}') = \iiint_V e^{i(K_1 x_1 + K_2 x_2 + K_3 x_3)}\, dx_1 dx_2 dx_3. \quad (7)$$

Let $x_1 = \rho\cos\theta$, $x_2 = \rho\sin\theta$. Then in cylindrical coordinates

$$I = \int_{\theta=0}^{2\pi} \int_{\rho=0}^{a} \int_{x_3=-\infty}^{\infty} e^{iK_3 x_3}\, e^{i(K_1\rho\cos\theta + K_2\rho\sin\theta)}\, dx_3\, \rho\, d\rho\, d\theta, \quad (8)$$

where a is the cylindrical radius. Since

$$\int_{-\infty}^{\infty} e^{iK_3 x_3}\, dx_3 = 2\pi\,\delta(K_3), \quad (9)$$

where $\delta(K_3)$ is the Dirac delta function, the integral takes the form

$$I = 2\pi\delta(K_3)\int_{\theta=0}^{2\pi}\int_{\rho=0}^{a} e^{i(K_1\rho\cos\theta + K_2\rho\sin\theta)}\,\rho\,d\rho\,d\theta. \qquad (10)$$

Let $\rho = q/\sqrt{K_1^2+K_2^2}$, $d\rho = dq/\sqrt{K_1^2+K_2^2}$. Then

$$I = 2\pi\delta(K_3)\int_{\theta=0}^{2\pi}\int_{q=0}^{a\sqrt{K_1^2+K_2^2}} e^{i\left\{q\frac{K_1}{\sqrt{K_1^2+K_2^2}}\cos\theta + q\frac{K_2}{\sqrt{K_1^2+K_2^2}}\sin\theta\right\}}\,\frac{q\,dq\,d\theta}{\sqrt{K_1^2+K_2^2}}. \qquad (11)$$

If we now set $K_1/\sqrt{K_1^2+K_2^2} = \cos\theta'$, then $K_2/\sqrt{K_1^2+K_2^2} = \sin\theta'$, so that

$$I = \frac{2\pi\delta(K_3)}{K_1^2+K_2^2}\int_{q=0}^{a\sqrt{K_1^2+K_2^2}}\int_{\theta=0}^{2\pi} e^{iq\cos(\theta-\theta')}\,q\,dq\,d\theta. \qquad (12)$$

Since the integration extends over a whole circumference, it is immaterial where the origin of θ is placed. The integral may therefore be written as

$$I = \frac{2\pi\delta(K_3)}{K_1^2+K_2^2}\int_{q=0}^{a\sqrt{K_1^2+K_2^2}} q\,dq\int_{\theta=0}^{2\pi} e^{iq\cos\theta}\,d\theta$$

or

$$= \frac{2\pi\delta(K_3)}{K_1^2+K_2^2}\int_{q=0}^{a\sqrt{K_1^2+K_2^2}} q\,dq\cdot 2\pi J_0(q)$$

$$I = \frac{4\pi^2\delta(K_3)}{K_1^2+K_2^2}\,a\sqrt{K_1^2+K_2^2}\,J_1\left(a\sqrt{K_1^2+K_2^2}\right), \qquad (13)$$

where J_0 and J_1 denote the usual Bessel functions.

Equation (6) can now be written as

$$L_{kgij} = \frac{1}{8\pi^3}\iiint_{-\infty}^{\infty} d^3\underset{\sim}{K}\,\frac{M_{ij}^{-1}(\underset{\sim}{\xi})}{K^2}\cdot\frac{\partial^2 e^{-i\underset{\sim}{K}\cdot\underset{\sim}{r}}}{\partial x_k\partial x_g}\cdot\frac{4\pi^2\delta(K_3)}{K_1^2+K_2^2}\cdot a\sqrt{K_1^2+K_2^2}\,J_1\left(a\sqrt{K_1^2+K_2^2}\right) \qquad (14)$$

Now $\dfrac{\partial^2 e^{-i\underset{\sim}{K}\cdot\underset{\sim}{r}}}{\partial x_k\partial x_g} = -K_kK_g\,e^{-i\underset{\sim}{K}\cdot\underset{\sim}{r}}$, so that

$$L_{kgij} = -\frac{1}{2\pi}\iiint_{-\infty}^{\infty}\frac{dK_1\,dK_2\,dK_3\,M_{ij}^{-1}(\underset{\sim}{\xi})K_kK_g}{K_1^2+K_2^2+K_3^2}\,e^{-iK_3z_3}\,e^{-i(K_1z_1+K_2z_2)}\,\frac{\delta(K_3)}{K_1^2+K_2^2}\,a\sqrt{K_1^2+K_2^2}\,J_1\left(a\sqrt{K_1^2+K_2^2}\right). \qquad (15)$$

If k=3 or g=3, the Dirac delta function $\delta(K_3)$ gives zero values for the integral. Hence, the non-zero values of the Eshelby tensor $\underset{\sim}{S}$ are given by k=1,2 and g=1,2. This arises because there are no components of the body force layer of surface tractions in the x_3 direction at the cylindrical interface between the grain and the matrix. Invoking the properties of the Dirac delta function gives

$$L_{kgij} = -\frac{1}{2\pi}\int_{-\infty}^{\infty}\int dK_1 dK_2\, M_{ij}^{-1}(\zeta_1,\zeta_2,\zeta_3=0)\,\zeta_k\zeta_g\, e^{-i(K_1x_1+K_2x_2)}\,\frac{a}{\sqrt{K_1^2+K_2^2}}\,J_1\left(a\sqrt{K_1^2+K_2^2}\right). \qquad (16)$$

Now put

$$\zeta_1 = \frac{K_1}{\sqrt{K_1^2+K_2^2}} = \cos\theta\,, \quad \zeta_2 = \frac{K_2}{\sqrt{K_1^2+K_2^2}} = \sin\theta\,,$$

so that the Fourier wave vector components K_1 and K_2 correspond to the x_1 and x_2 axes, respectively. Then in cylindrical coordinates,

$$L_{kgij} = -\frac{1}{2\pi}\int_{\theta=0}^{2\pi}\int_{K=0}^{\infty} K\,dK\,d\theta\; M_{ij}^{-1}(\xi)\,\zeta_k\zeta_g\, e^{-iKr}\,\frac{a}{K}\,J_1(aK)$$

or

$$L_{kgij} = -\frac{1}{2\pi}\int_{\theta=0}^{2\pi} M_{ij}^{-1}(\xi)\,\zeta_k\zeta_g\,d\theta\int_{K=0}^{\infty} a e^{-iKr}\,J_1(aK)\,dK. \qquad (17)$$

Since $\underset{\sim}{S}$ is real, the real part of the preceding integral is

$$J = \int_{K=0}^{\infty} a\cos(Kr)\,J_1(aK)\,dK.$$

But, (cf. Gradstyn and Rizhik, p. 730, Eq. 6.671, No. 2)

$$J = \left[a\cos\{\sin^{-1}(r/a)\}\right]/\sqrt{a^2-r^2} \quad \text{for } 0\le r\le a.$$

If $\theta=\sin^{-1}(r/a)$, then $J = a\cos\theta/\sqrt{a^2-r^2} = \cos\theta/[\sqrt{a^2-r^2}/a] = \cos\theta/\cos\theta = 1$.

Thus

$$L_{kgij} = -\frac{1}{2\pi}\int_0^{2\pi} M_{ij}^{-1}(\xi)\,\zeta_k\zeta_g\,d\theta\,,$$

independent of position $\underset{\sim}{r}$ in the cylinder as expected from Eshelby's result. In this integral we have $\zeta_1=\cos\theta, \zeta_2=\sin\theta, \zeta_3=0$, $M_{ij}^{-1}(\xi) = (\zeta_m D^m_{ijn}\zeta_n)^{-1}$ and k and g are restricted to the values 1 and 2. The Eshelby tensor may now be written as

$$S_{ijlm} = D^m_{kjlm}\left\{\frac{1}{4\pi}\left(\int_0^{2\pi} M_{pj}^{-1}(\zeta_1,\zeta_2)\zeta_i\zeta_k\,d\theta + \int_0^{2\pi} M_{ij}^{-1}(\zeta_1,\zeta_2)\zeta_p\zeta_k\,d\theta\right)\right\}. \qquad (19)$$

For a transversely isotropic material the Chistoffel tensor $\underset{\sim}{M}$ has the component form

$$M_{ij}(\xi_1,\xi_2) = \begin{bmatrix} c_{11}\xi_1^2 + \frac{1}{2}(c_{11}-c_{12})\xi_2^2 & \frac{1}{2}(c_{11}+c_{12})\xi_1\xi_2 & 0 \\ \frac{1}{2}(c_{11}+c_{12})\xi_1\xi_2 & c_{11}\xi_2^2 + \frac{1}{2}(c_{11}-c_{12})\xi_1^2 & 0 \\ 0 & 0 & c_{44} \end{bmatrix}. \quad (20)$$

The Eshelby tensor can now be evaluated by inverting the matrix in equation (20) and integrating according to equation (19). Explicit results may be deduced, according to the calculations in Mura's book [21], for the resulting integrals. Checking of these integrals is currently in progress.

REFERENCES

1. P.R. Paslay, C.H. Wells and G.R. Leverant, "An Analysis of Primary Creep of Nickel-Base Superalloy Single Crystals", ASME Journal of Applied Mechanics, Vol. 37, pp. 759-764, 1970.

2. P.R. Paslay, C.H. Wells, G.R. Leverant and L.H. Burck, "Creep of Single Crystal Nickel-Base Superalloy Tubes under Biaxial Tension", Vol. 38, pp. 623-626, 1971.

3. G.M. Brown, "A Self-Consistent Polycrystalline Model for Creep under Combined Stress States", Journal of Mechanics and Physics of Solids, Vol. 18, pp. 367-381, 1970.

4. J.W. Hutchinson, "Bounds and Self-Consistent for Creep of Polycrystalline Materials", Proceedings of the Royal Society of London, Vol. A 348, pp. 101-127, 1976.

5. G.J. Weng, "The Influence of Fatigue Stress on the Creep Behaviour of Metals", Acta Metallurgica, Vol. 31, pp. 207-212, 1983.

6. E. Kroner, "Zur Plastischen Verformung des Vielkristalls", Acta Metallurgica, Vol. 9, pp. 155-161, 1961.

7. R. Hill, "Continuum Micro-Mechanics of Elastoplastic Polycrystals", Journal of Mechanics and Physics of Solids, Vol. 13, pp. 89-101, 1965.

8. K.S. Chan, S.R. Bodner, K.P. Walker and U.S. Lindholm, "A Survey of Unified Constitutive Theories", Proceedings of this Conference.

9. E. Schmid and W. Boas, "Plasticity of Crystals with Special Reference to Metals", Chapman and Hall Ltd., London, 1968.

10. R.J. Asaro and J.R. Rice, "Strain Localization in Ductile Single Crystals", Journal of Mechanics and Physics of Solids, Vol. 25, pp. 309-338, 1977.

11. J.R. Hutchinson, "Elastic-plastic Behaviour of Polycrystalline Metals and Composites", Proceedings of the Royal Society of London, Vol. A 319, pp. 247-272, 1970.

12. R.J. Asaro, "Geometrical Effects in the Inhomogeneous Deformation of Ductile Single Crystals", Acta Metallurgica, Vol. 27, pp. 445-453, 1979.

13. D. Peirce, R.J. Asaro and A. Needleman, "An Analysis of Nonuniform and Localized Deformation in Ductile Single Crystals", Acta Metallurgica, Vol. 30, pp. 1087-1119, 1982.

14. K.S. Havner and S.A. Salpekar, "Theoretical Latent Hardening of Crystals in Double-Slip-II. F.C.C. Crystals Slipping on Distinct Planes", Journal of Mechanics and Physics of Solids, Vol. 31, pp. 231-250, 1983.

15. G.R. Leverant, B.H. Kear and J.M. Oblak, "Creep of Precipitation-Hardened Nickel-Base Alloy Single Crystals at High Temperatures", Metallurgical Transactions, Vol. 4, pp. 355-362, 1973.

16. S.S. Ezz, D.P. Pope and V. Paidar, "The Tension/Compression Flow Stress Asymmetry in $Ni_3(Al,Nb)$ Single Crystals", Acta Metallurgica, Vol. 30, pp. 921-926, 1982.

17. J.D. Eshelby, "The Determination of the Elastic Field of an Ellipsoidal Inclusion, and Related Problems", Proceedings of the Royal Society of London, Vol. A 241, pp. 376-396, 1957.

18. J.R. Willis, "The Elastic Interaction Energy of Dislocation Loops in Anisotropic Media", Quarterly Journal of Mechanics and Applied Mathematics, Vol. 18, pp. 419-433, 1965.

19. R.J. Asaro, "Somigliana Dislocations and Internal Stresses; with Application to Second Phase Hardening", International Journal of Engineering Science, Vol. 13, pp. 271-286, 1975.

20. D.M. Barnett, "The Precise Evaluation of Derivatives of the Anisotropic Elastic Green's Function", Physica Status Solidi (b), Vol. 49, pp.741-748, 1972.

21. T. Mura, "Micromechanics of Defects in Solids", Martinus Nijohff Publishers, The Hague/Boston/London, 1982.

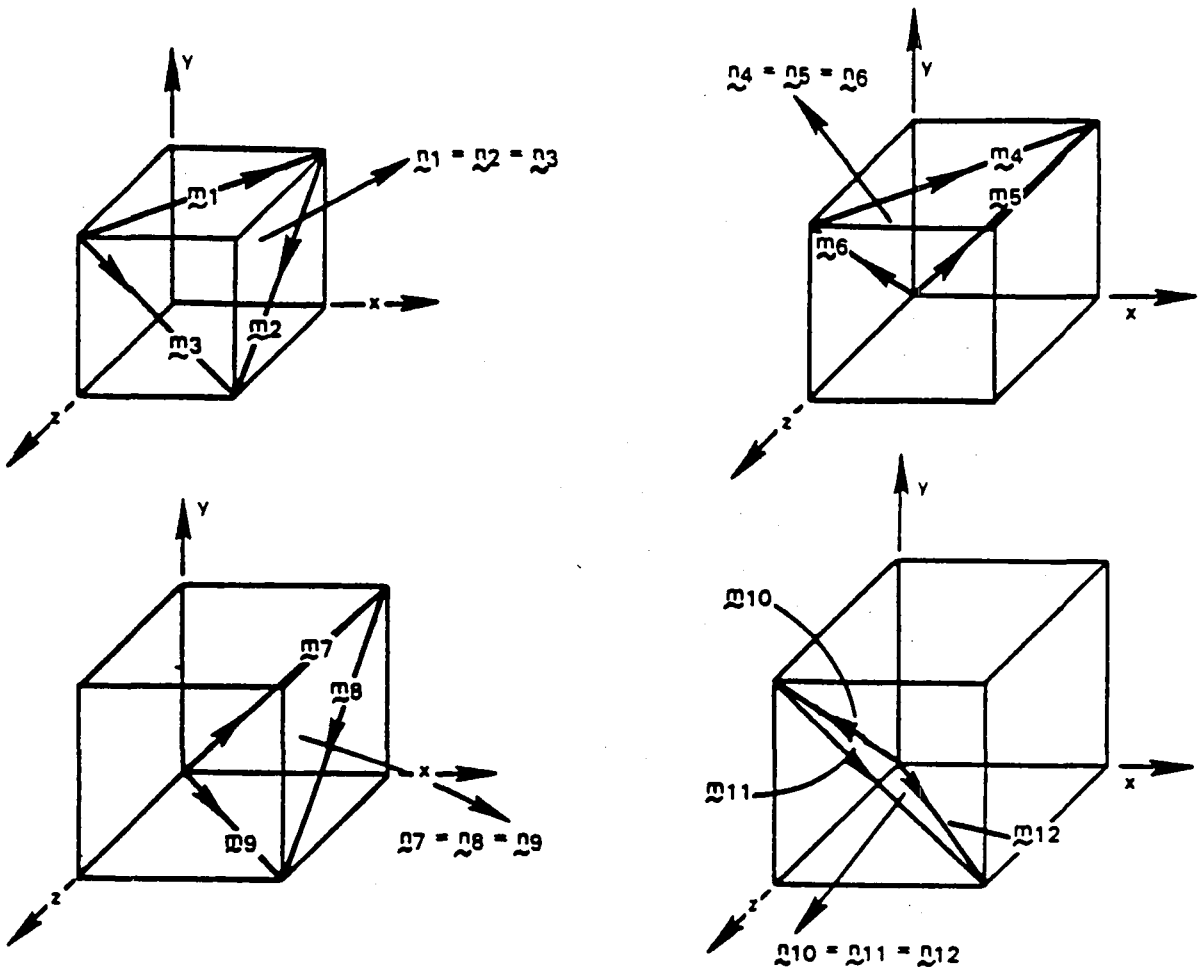

Fig. 1. The twelve ⟨110⟩ slip direction vectors on the four octahedral {111} planes.

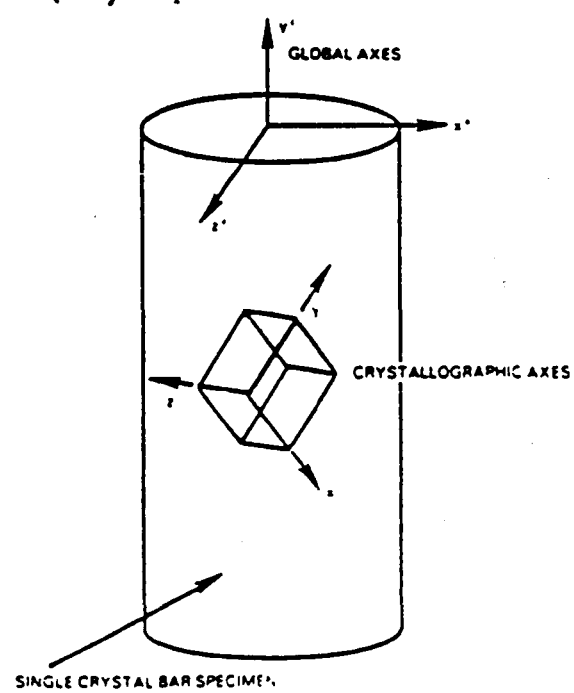

Fig. 2. Global and crystallographic axes of the specimen.

Page intentionally left blank

ON THE USE OF INTERNAL STATE VARIABLES IN THERMOVISCOPLASTIC CONSTITUTIVE EQUATIONS

D.H. Allen and J.M. Beek
Aerospace Engineering Department
Texas A&M University
College Station, Texas 77843

The use of internal state variables in modeling of inelastic solids is gaining widespread usage in current research. Therefore, it is useful to construct a well-defined framework for internal state variable models which is based in continuum mechanics. The objective of this paper is to review and clarify the general theory of internal state variables and to apply it to inelastic metals currently in use in high temperature environments. In this process, certain constraints and clarifications will be made regarding internal state variables.

It will be shown that the Helmholtz free energy can be utilized to construct constitutive equations which are appropriate for metallic superalloys. Furthermore, internal state variables will be shown to represent locally averaged measures of dislocation arrangement, dislocation density, and intergranular gracture. Finally, the internal state variable model will be demonstrated to be a suitable framework for comparison of several currently proposed models for metals and can therefore be used to exhibit history dependence, nonlinearity, and rate as well as temperature sensitivity.

INTRODUCTION

The prediction of inelastic behavior of structural materials at elevated temperature is a problem of great importance which has accordingly been given a great deal of interest by the research community in recent years. These materials exhibit substantial complexity in their thermomechanical constitution. In fact, so complex is their material response that it could be argued that without useful a priori information, experimental characterization is futile. The purpose of this paper is to show how the thermodynamics with internal state variables can be utilized to emplace certain constraints on the allowable form of thermomechanical constitutive equations, thus providing some limited insight regarding experimental requirements.

Historically, there have been two distinct approaches to the modelling of inelastic materials: 1) the functional theory [1], in which all dependent variables are assumed to depend on the entire history of independent variables; and 2) the internal state variable (ISV) approach [2], wherein history dependence is postulated to appear implicitly in a set of internal state variables. Lubliner [3] has shown that in most circumstances ISV models can be considered to be special cases of functional models. For experimental as well as analytic reasons numerous recently proposed models for the classes of materials

discussed herein have been proposed in ISV form. Therefore, in this paper the ISV method will be reviewed as well as clarified and it will be shown that this general framework is useful in modeling metals at elevated temperature.

The paper begins with a review of ISV theory, and this is supplemented with a section describing the procedure for constructing macroscopically averaged internal state variables. These concepts are then applied to metals at elevated temperatures. Finally, applications to boundary value problem solving techniques are discussed.

REVIEW OF THE INTERNAL STATE VARIABLE (ISV) APPROACH

The concept of internal state variables, sometimes called hidden variables, was apparently first utilized in thermodynamics by Onsager [4,5] and numerous applications are recorded since the second world war [2,6-14]. Although not originally described for application to solids, the approach which will be discussed herein is due to Coleman and Gurtin [2].

In the theory of internal state variables applied to solids the following state variables are required in order to fully characterize the state of the body at all points x_j and at all times t:*

1) the displacement field $u_i = u_i(x_k,t)$; (1)

2) the stress tensor $\sigma_{ij} = \sigma_{ij}(x_k,t)$; (2)

3) the body force per unit mass $f_i = f_i(x_k,t)$; (3)

4) the internal energy per unit mass $u = u(x_k,t)$; (4)

5) the heat supply per unit mass $r = r(x_k,t)$; (5)

6) the entropy per unit mass $s = s(x_k,t)$; (6)

7) the absolute temperature $T = T(x_k,t)$; (7)

8) the heat flux vector $q_i = q_i(x_k,t)$; (8)

and

9) $\alpha^k_{ij} = \alpha^k_{ij}(x_m,t)$, $k = 1, 2, \ldots, n$; (9)

where α^k_{ij} are a set of n internal state variables which are necessary to account for inelastic material behavior. Although they are listed here as second order tensors, they may be tensors of other rank as well [15].

---

* For convenience, only infinitesimal deformations will be considered here, although the general theory applies to finite deformations as well.

The method of Coleman and Noll [16] may be used to obtain the spatial and time distribution of the body force f_i and heat supply r from the conservation of linear momentum and energy, respectively, assuming the displacements u_i and the temperature T are specified independent variables. Subsequently, it is hypothesized that constitutive equations of state may be constructed for the state variables described in (1) through (8) in terms of u_i and T and their spatial derivatives:

$$\sigma_{ij}(x_k,t) = \sigma_{ij}(\varepsilon_{mn}(x_k,t),\ T(x_k,t),\ g_m(x_k,t),\ \alpha^p_{mn}(x_k,t)) \quad ; \quad (10)$$

$$u(x_k,t) = u(\varepsilon_{mn}(x_k,t),\ T(x_k,t),\ g_m(x_k,t),\ \alpha^p_{mn}(x_k,t)) \quad ; \quad (11)$$

$$s(x_k,t) = s(\varepsilon_{mn}(x_k,t),\ T(x_k,t),\ g_m(x_k,t),\ \alpha^p_{mn}(x_k,t)) \quad ; \quad (12) \text{ and}$$

$$q_i(x_k,t) = q_i(\varepsilon_{mn}(x_k,t),\ T(x_k,t),\ g_m(x_k,t),\ \alpha^p_{mn}(x_k,t)) \quad ; \quad (13)$$

where g_m is the spacial temperature gradient $T_{,m}$ and

$$\varepsilon_{ij} \equiv \tfrac{1}{2}(u_{i,j} + u_{j,i}) \quad (14)$$

The form of equations (11) through (13) implies that all constitutive equations are evaluated in the specified state (x_k,t). For this reason σ_{ij}, u, s, and q_i are termed observable state variables since they can be determined from equations of state even though there is implicit history dependence via the internal state variables α^p_{mn}, which are defined to be of the form:

$$\dot{\alpha}^k_{ij} \equiv \Omega^k_{ij}(\varepsilon_{mn},\ T,\ g_m,\ \alpha^\ell_{mn}) \quad ; \quad (15)$$

where time and spacial dependence have been dropped for notational convenience. If equations (15) are at all times integrable in time, then the following form is equivalent to (15):

$$\alpha^k_{ij}(x_m,t) = \int_{-\infty}^{t} \Omega^k_{ij}(x_m,t')dt' \quad ; \quad (16)$$

where t is the time of interest and t' is a dummy variable of integration. Therefore, it is apparent that α^k_{ij} are not directly observable at any time and must therefore be considered to be hidden or internal.

Although the above framework has been shown to be applicable to rate dependent crystalline solids [17,18], it is often misconstrued that the absence of explicit strain-rate dependence renders the model inappropriate for use in viscoplasticity theories. It is alternatively hypothesized that

$$\sigma_{ij} = \sigma_{ij}(\varepsilon_{mn},\ \dot{\varepsilon}_{mn},\ T,\ g_m,\ \alpha^\ell_{mn}) \quad (17)$$

is an appropriate form of thermomechanical constitutive equations (10). Although metals at elevated temperature certainly exhibit strain-rate dependence, there are several reasons why equations (17) are less desirable than equations (10). First, equations (17) are not actually equations of state since the inclusion of strain rate implies knowledge is required at some time other than the current time t. Secondly, as demonstrated in discussions of

materials similar to (17) but without internal state variables [19], very little useful information will come from thermodynamic constraints. Finally, explicit strain rate dependence is actually redundant for the materials discussed herein, as will be shown later. Therefore, although this is certainly a semantical issue, equations (10) through (13) and (15) are utilized as the constitutive model in the balance of this paper.

It should also be pointed out that internal state variable growth laws (15) could contain explicit strain-rate dependence:

$$\dot{\alpha}^{k}_{ij} = \Omega^{k}_{ij}(\varepsilon_{mn}, \dot{\varepsilon}_{mn}, T, g_m, \alpha^{\ell}_{mn}) \quad , \quad (18)$$

as in the example of a rate independent elastic-plastic material, in which equations of the above form are linear in strain rate:

$$\dot{\alpha}^{\ell}_{ij} = \Omega^{k}_{ijpq}(\varepsilon_{mn}, T, g_m, \alpha^{\ell}_{mn})\dot{\varepsilon}_{pq} \quad . \quad (19)$$

Such a form, although not excluded by the principle of equipresence [20], is only necessary in the circumstance wherein specific rate independence is required, as can be demonstrated by direct substitution of (19) into (16). Furthermore, although the thermodynamic constraints will vary somewhat when (19) are utilized [21,22], the results will be quite similar to those described below.

On the basis of the Coleman-Mizel procedure [23] it can be shown that satisfaction of the first and second laws of thermodynamics for the class of materials detailed above will lead to the following conclusions:

$$h \equiv u - Ts = h(\varepsilon_{mn}, T, \alpha^{k}_{mn}) \quad ; \quad (20)$$

where h is the specific Helmholtz free energy;

$$\sigma_{k\ell} = \rho \frac{\partial h}{\partial \varepsilon_{k\ell}} \quad ; \quad (21)$$

$$s = - \frac{\partial h}{\partial T} \quad ; \quad (22)$$

and

$$q_i = -k_{ij}\, g_j + 0(g_i) \quad . \quad (23)$$

Equations (21) should not be interpreted as defining as hyperelastic material since the Helmholtz free energy, described by (20), is dependent on the internal state and therefore path dependent.

Although not directly related to our problem, it is useful to note that the path dependence of the Helmholtz free energy precludes the usefulness of equations (21) in Rice's J-integral for fracture mechanics [24]. However, in the case wherein the loading path is radial:

$$\varepsilon_{ij} = k_{ij}\bar{\varepsilon} \; ; \; \alpha^{\ell}_{ij} = k^{\ell}_{ij}\bar{\varepsilon} \; ; \; \bar{\varepsilon} \equiv \sqrt{\varepsilon_{ij}\varepsilon_{ij}} \quad , \quad (24)$$

where k_{ij} and k^{ℓ}_{ij} are constant coefficients, then it is well known that equations (15) are directly integrable so that the free energy can be described by

$$h = h(\varepsilon_{mn}, T, \alpha^{i}_{pq}) = h(\varepsilon_{mn}, T, \alpha^{i}_{pq}(\varepsilon_{mn})) = h(\varepsilon_{mn}, T) \tag{25}$$

Thus, for the case of proportional loading only, the constitutive equations are derivable directly from a potential function and the J-integral method is applicable.

THE LOCAL AVERAGING PROCESS

Constitutive equations (10) through (13) and (15) are theoretically pointwise in nature; that is, they are applicable to fixed infinitesimal material points. However, practically speaking, there is no way to construct experiments on material points since at the microscopic level the continuum assumption becomes invalid. Rather, it is considered acceptable to construct constitutive equations by subjecting local specimens to surface deformations (or tractions) which lead to spacially homogeneous stresses and strains so that some local average of the pointwise observable state variables can be determined directly from the effects on the boundaries of the specimens.

As shown in Fig. 1, the scale of the smallest dimension of a local specimen is generally constructed so as to be at least an order of magnitude larger than the scale of the largest material inhomogeneity. This sizing helps preserve the continuum assumption while at the same time averaging out the effects of point defects such as crystal lattice dislocations. Conversely, the scale of the largest dimension of a typical specimen should be as small as possible compared to the scale of the global boundary value problem of interest. This constraint is necessary in order to preserve the notion that constitutive equations are indeed pointwise in nature, but it is pragmatic in that it is a simple matter of economy.

The local rather than pointwise constitutive equations that result from experimentation are assumed to be of the same form as pointwise equations (10) through (13) and (15). For example, in the uniaxial test described in Fig. 1 it is customary to define

$$\bar{\sigma}_{11} \equiv \frac{1}{A} \int_{B_1} \sigma_{11} dx_2 dx_3 \quad , \tag{26}$$

$$\bar{\varepsilon}_{11} \equiv \frac{1}{L} \int_{L} \varepsilon_{11} dx_1 \quad , \tag{27}$$

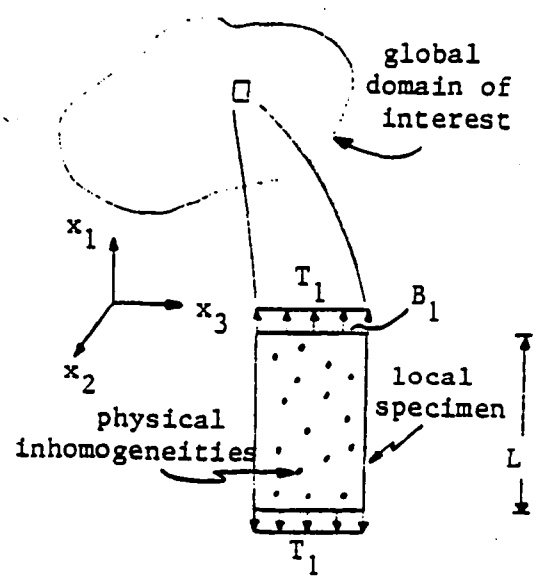

Figure 1

and

$$\bar{T} \equiv T(a_1, a_2, a_3) \quad , (28)$$

where L is the local specimen gage length, A is the cross-sectional area in the x_2-x_3 plane, and (a_1, a_2, a_3) is some arbitrary point on the surface of the specimen. Utilizing these quantities, it is then hypothesized that

$$\sigma_{11}(\varepsilon_{11}, T, \alpha^{\ell}_{mn}) \equiv \bar{\sigma}_{11}(\bar{\varepsilon}_{11}, \bar{T}, \bar{\alpha}^{\ell}_{mn}) \quad , (29)$$

where

$$\bar{\alpha}^{\ell}_{mn} \equiv \frac{1}{V} \int_V \alpha^{\ell}_{mn} \, dx_1 \, dx_2 \, dx_3 \quad , (30)$$

and all quantities with bars represent the locally measured state variables.

Although equations (29) represent an often used way of relating pointwise equations to experimental results, the local averaging process is nevertheless fraught with shortcomings since definitions (26) through (28) all represent nonunique relations between pointwise state variables σ_{ij}, ε_{ij}, T, α^{k}_{ij} and their locally defined counterparts $\bar{\sigma}_{ij}$, $\bar{\varepsilon}_{ij}$, $\bar{T}$, and $\bar{\alpha}^{k}_{ij}$. There are in fact an infinite number of distributions $\alpha^{\ell}_{mn}(x_1, x_2, x_3)$ which will result in identical values of $\bar{\alpha}^{\ell}_{mn}$. However, assuming that the scale of inhomogeneities is small and that the distribution of α^{ℓ}_{mn} is random the specimen will be statistically homogeneous and the relation between $\bar{\alpha}^{\ell}_{mn}$ and α^{ℓ}_{mn} will be reasonably one to one.

For example, suppose that during some monotonically increasing local strain history $\bar{\varepsilon}_{11}$ a particular internal state variable α^{1}_{11} such as a single dislocation arrangement is governed on a pointwise basis by the almost discontinuous behavior shown in Fig. 2. Suppose further that the time t at which the internal state begins to change is determined by the pointwise stress state. Then the number of dislocation rearrangements occurring in the local specimen as a function of time might be distributed as shown in Fig. 3. If the local specimen is large compared to the scale of the dislocation, and there are numerous dislocation rearrangements, as is usually the case in testing of metals, then the peak of the curve shown in Fig. 3 will be several orders of magnitude greater than unity. It follows from equations (30) that the locally averaged value of the internal state variable represented in Fig. 2 will be as qualitatively shown in Fig. 4.

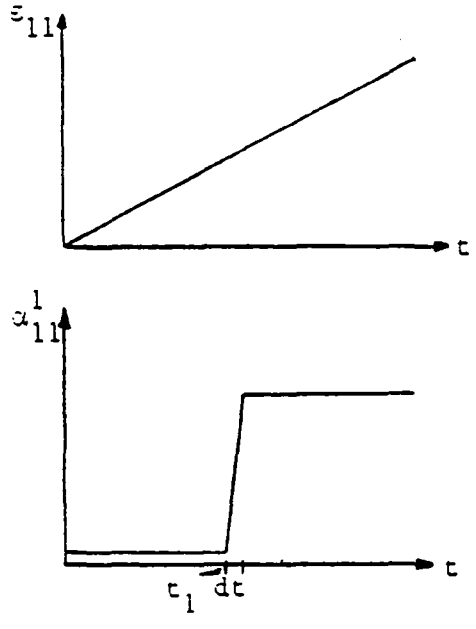

Figure 2

APPLICATION TO METAL CONSTITUTION

In order to describe the class of metals discussed herein, the free energy maybe expanded in terms of the elastic strain tensor ε^E_{kl} and the temperature T in a second order Taylor series expansion as follows:

$$\varepsilon^E_{ij} \equiv \varepsilon_{ij} - \varepsilon^I_{ij} - \varepsilon^T_{ij} \quad , (31)$$

where ε^T_{ij} is the thermal strain tensor and ε^I_{ij} is the inelastic strain tensor, considered to be an internal state variable [17,18,22,25], and

$$h = h_R + \frac{1}{2\rho}\varepsilon^E_{ij}D_{ijkl}\varepsilon^E_{kl} - \frac{C_v}{2T}(T - T_R) \quad , (32)$$

where the subscript R refers to quantities in the reference state, D_{ijkl} is the linear elastic modulus tensor, and $C_v \equiv -T\left(\frac{\partial^2 h}{\partial T^2}\right)$ is the specific heat at constant elastic strain. Substitution of equation (32) into (21) will result in

$$\sigma_{kl} = D_{klmn}(\varepsilon_{mn} - \varepsilon^I_{mn} - \varepsilon^T_{mn}) \quad . (33)$$

The above equations, together with internal state variable growth laws (15), will be shown to be a suitable framework for comparison of all of the models to be discussed herein.

Internal State Variables in Metals

It is now generally agreed in the literature that in single crystals there are two locally averages internal state variables: the back stress ($\alpha_{1_{ij}}$) representing dislocation arrangement; and the drag stress (α_2) representing dislocation density; where the bars have been dropped for convenience and the superscript has been converted to a subscript in order to avoid the confusion which would arise if a state variable were raised to some power. For obvious reasons the back stress is a second order tensor, whereas the drag stress is a scalar. In specimens composed of multiple crystals it is generally agreed that a third internal state variable loosely termed damage ($\alpha_{3_{ij}}$) is necessary in order to account for intergranular mechanisms such as grain boundary sliding and microvoid growth and coalescence that may occur at high temperature and/or large strain. Although damage is obviously a directionally related quantity and therefore tensorial in nature, it is difficult to distinguish phenomenologically between damage and drag stress since both are primarily stiffness reducing mechanisms.

Within the thermodynamic framework described earlier it is also possible to define the inelastic strain tensor to be an internal state variable. However, this interpretation is not generally utilized within the materials

literature. It is hypothesized that the rate of growth of the internal state variables does not depend on the inelastic strain tensor so that

$$\dot{\alpha}^k_{ij} = \Omega^k_{ij}(\varepsilon_{mn}, T, g_m, \alpha_{1_{mn}}, \alpha_2, \alpha_{3_{mn}}) \quad . \quad (34)$$

Due to the form of equations (34) it is said that since the inelastic strain tensor does not appear on the right hand side it is not an internal state variable. However, within the framework defined herein, it is still possible to construct an internal state variable growth law of the form

$$\dot{\varepsilon}^I_{ij} \equiv \Omega^I_{ij}(\varepsilon_{mn}, T, g_m, \alpha_{1_{mn}}, \alpha_2, \alpha_{3_{mn}}) \quad , \quad (35)$$

which is precisely in agreement with definitions (15).

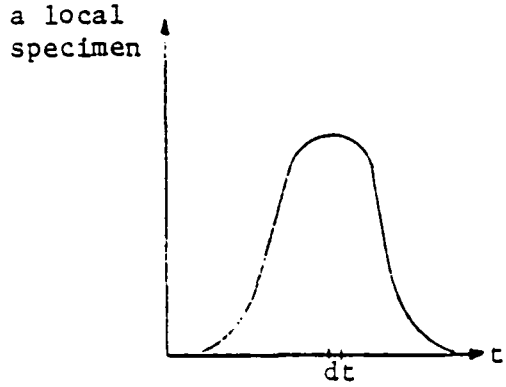

Figure 3

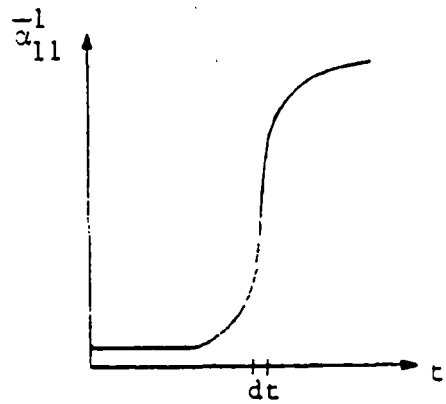

Figure 4

In order to qualitatively verify the supposition that the inelastic strain tensor can be regarded to be an ISV, consider the example of a uniaxial bar subjected to applied displacements such that the end tractions will be evenly distributed. It is customary to deduce the inelastic strain in an experiment of this type by utilizing the output from a load cell to determine the stress and then making use of equations (33) to determine the elastic strain. This result and the total strain measured by an extensometer are then substituted into equations (31) to determine the inelastic strain. Nevertheless, this does not imply that the inelastic strain tensor in an observable state variable. This result can be arrived at only in constitutive experiments such as uniaxial bar tests in which the stress and strain tensors are spacially homogeneous. In heterogeneous boundary value problems, only two state variables may be input (temperature and either stress or strain), and for this case equations (31) and (33) must be supplemented with an ISV growth law of the form of equations (35) in order to determine the inelastic strain tensor. Therefore, in the context of the current thermodynamic framework the inelastic strain tensor may be interpreted to be an ISV.

A Framework for Current Metals Models

In order to establish that current models can be constructed from equations (33), consider the standard solid shown in Fig. 5. The governing differential equation for this analog is

$$\sigma + \frac{\eta_M}{E_M}\dot{\sigma} = E_\infty \varepsilon + \eta_M \left[1 + \frac{E_\infty}{E_M}\right] \dot{\varepsilon} \quad , \quad (36)$$

where by convention the stress is denoted σ and the strain is ε. Equation (36) may be written in the following equivalent form

$$\dot{\varepsilon} = \frac{\dot{\sigma}}{[E_M+E_\infty]} + \frac{E_M}{\eta_M}\frac{[\sigma-E_\infty\varepsilon]}{[E_M+E_\infty]} \qquad (37)$$

In accordance with the instantaneous linear elastic behavior of metals, it is assumed that

$$E_M+E_\infty \equiv E = \text{Young's modulus} = \text{constant}, \qquad (38)$$

so that it is clear that equation (37) can be integrated in time to give the following stress formulation

$$\varepsilon(t_1) = \frac{\sigma(t_1)}{E} + \varepsilon^I(t_1) \qquad (39)$$

where ε^I is the inelastic strain, defined by

$$\varepsilon^I(t_1) = \int_{-\infty}^{t_1} \frac{E_M}{E}\,\frac{[\sigma-E_\infty\varepsilon]}{\eta_M}\,dt \qquad (40)$$

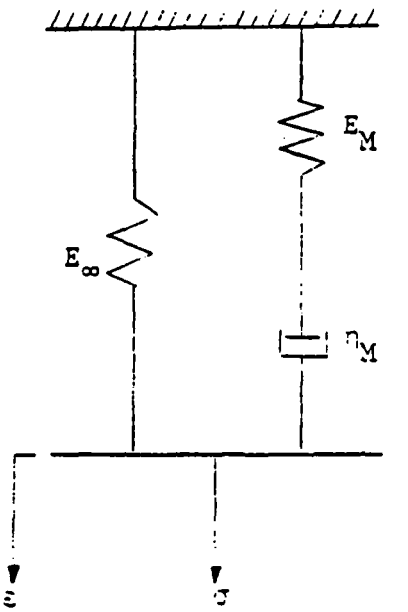

Figure 5

Equation (39) may be solved for the stress and substituted into equation (40) so that it is clear that equation (40) is in accordance with ISV growth laws (16). Further, it can be seen from the standard solid analog in Fig. 5 that since $\sigma-E_\infty\varepsilon$ represents the stress in the Maxwell element, ε^I is not observable, so that ε^I satisfies the two conditions required for it to be an internal state variable.

Equation (39) may be written equivalently in the following strain formulation:

$$\sigma(t_1) = E[\varepsilon(t_1) - \varepsilon^I(t_1)] \qquad , (41)$$

which is an equation of state compatible with constitutive equations (10) as well as equations (33). Since no other internal state variables are present in this equation, and also, no additional internal state variables are present in growth law (40) it is apparent that the standard solid analog with constant coefficients E_M, η_M and E_∞ is a single internal state variable model.

It has been noted by several researchers that the standard solid is an appropriate analog for thermoviscoplastic metals if the springs and dashpot are nonlinearized [26,27]. In order to demonstrate this feature, consider a multiaxial extension of equation (36):

$$\sigma_{pq} + K_{pqmn}\,\dot{\sigma}_{mn} = G_{pqmn}\,\varepsilon_{mn} + M_{pqmn}\,\dot{\varepsilon}_{mn} \quad , \quad (42)$$

where by convention the small strain tensor ε_{ij} is used in conjunction with the work conjugate stress tensor σ_{ij}. In order to model metals K_{pqmn}, G_{pqmn}, and M_{pqmn} are required to be nonlinear in some as yet undetermined way. In addition, in accordance with constraint equation (38), it is required that

$$K^{-1}_{ijmn}\,M_{mnkl} = D_{ijkl} \quad , \quad (43)$$

where D_{ijkl} is the linear elastic modulus tensor. Equations (42) may be rewritten in a strain formulation equation of state form as follows:

$$\sigma_{ij} = D_{ijkl}\,[\varepsilon_{kl} - \varepsilon^{I}_{kl}] \quad , \quad (44)$$

where ε^{I}_{kl} is the inelastic strain tensor, defined by

$$\varepsilon^{I}_{ij} \equiv \int_{-\infty}^{t_1} M^{-1}_{ijpq}\,[\sigma_{pq} - G_{pqmn}\varepsilon_{mn}]dt \quad . \quad (45)$$

Substituting equations (43) and (44) into equations (45) will result in

$$\varepsilon^{I}_{ij} = \int_{-\infty}^{t_1} \{K^{-1}_{ijmn}[\varepsilon_{mn} - \varepsilon^{I}_{mn}] - M^{-1}_{ijpq}\,G_{pqmn}\varepsilon_{mn}\}\,dt \quad , \quad (46)$$

so that equations (46) are in accordance with growth laws (16). The number of internal state variables contained in the model will depend on the degree of nonlinearity proposed in the nonlinear tensors K_{pqmn}, G_{pqmn}, and M_{pqmn}, and this will be discussed in the following section. However, before continuing, it should be pointed out that the constitutive equations developed in this section assume that the elastic and inelastic strain tensors may be linearly decoupled. It has been shown that this assumption is invalid for finite deformation [28]. However, even under finite deformation conditions the inelastic strain is decoupled from the elastic strain in such a way that the inelastic strain tensor may be considered to be an internal state variable.

Current Models for Metals

The framework for metals models discussed in the previous section can be used to describe numerous models currently under development [26,27,29-58]. For example, the microphysically based isothermal model proposed by Krieg, et al., [30] is of the form described by equations (33):

$$\sigma_{ij} = D_{ijkl}(\varepsilon_{kl} - \varepsilon^{I}_{kl}) \quad , \quad (47)$$

where

$$\dot{\varepsilon}^I_{ij} \equiv \dot{\varepsilon}_o \left\{ \frac{\left[\left(\sigma'_{kl} - \alpha'_{l_{kl}}\right)\left(\sigma'_{kl} - \alpha'_{i_{kl}}\right)\right]^{\frac{1}{2}}}{\alpha_2} \right\}^m \frac{\left(\sigma'_{ij} - \alpha'_{l_{ij}}\right)}{\left[\left(\sigma'_{pq} - \alpha'_{l_{pq}}\right)\left(\sigma'_{pq} - \alpha'_{l_{pq}}\right)\right]^{\frac{1}{2}}} \quad , \quad (48)$$

and $\dot{\varepsilon}_o$ and m are material constants, and σ'_{ij} is the deviatoric stress tensor and $\alpha'_{l_{ij}}$ is the deviatoric component of the back stress tensor. Since equations (48) contain the stress tensor, substituting equations (33) into (48) will result in equations consistent eith growth laws (15). In addition, Krieg, et al., give the back stress and drag stress to be, respectively,

$$\dot{\alpha}'_{l_{ij}} = A_\alpha \dot{\varepsilon}^I_{ij} - r_\alpha \frac{\alpha'_{l_{ij}}}{\left(\alpha'_{l_{pq}} \alpha'_{l_{pq}}\right)^{\frac{1}{2}}} \quad , \quad (49)$$

and

$$\dot{\alpha}_2 = A_R \left(\dot{\varepsilon}^I_{ij} \dot{\varepsilon}^I_{ij}\right)^{\frac{1}{2}} - r_R \quad , \quad (50)$$

where A_α and A_R are hardening constants, and r_α and r_R are recovery functions of temperature and internal state variables. It can be seen that since ISV growth laws (49) and (50) are consistent with equations (15), the model proposed by Krieg, et al., contains three internal state variables: the inelastic strain tensor, the back stress tensor, and the drag stress tensor.

Furthermore, classical plasticity theories can be described by the general form

$$\sigma_{ij} = D_{ijmn} \left(\varepsilon_{mn} - \varepsilon^I_{mn}\right) \quad , \quad (51)$$

where

$$\dot{\varepsilon}^I_{ij} = \dot{\lambda} \frac{\partial F}{\partial \sigma_{ij}} \quad . \quad (52)$$

$\dot{\lambda}$ is a scalar valued function of state, and F is a scalar valued state function for inelastic behaviour often taken to be the yield function. If F is described by the von Mises yield criterion [53], given by

$$F(\sigma_{ij} - \alpha_{l_{ij}}) = \tfrac{1}{2}(\sigma_{ij} - \alpha_{l_{ij}})(\sigma_{ij} - \alpha_{l_{ij}}) = k^2 \quad , \quad (53)$$

where $\alpha_{l_{ij}}$ is a tensor describing the yield surface center in stress space and k is a constant representing the yield surface size, then equations (52) can be written as

$$\dot{\varepsilon}_{ij} = \dot{\lambda}(\sigma_{ij} - \alpha_{1_{ij}}) \quad , (54)$$

resulting in a kinematic hardening model with constant yield surface size. Substitution of equations (51) into the above will yield a result consistent with rate independent ISV growth laws (19).

Furthermore, if the yield surface translation is derived from the Ziegler modification [60] of the Prager work hardening rule [61], it may be described by

$$\dot{\alpha}_{1_{ij}} = \dot{\mu}(\sigma_{ij} - \alpha_{1_{ij}}) \quad , (55)$$

where $\dot{\mu}$ is a scalar valued function of state. By use of equations (51), equations (55) can also be shown to be consistent with equations (19). Therefore, a classical plasticity-based kinematic hardening model contains two internal state variables: the inelastic strain tensor and the yield surface translation tensor representing the back stress.

In order to further illustrate the applicability of equations (33), (35) and (15) to current models for metals, ten of these models have been cast in uniaxial form in Table 1, wherein it is shown that although the framework for each model is identical (Valanis' model is in simplified form), the ISV growth laws vary widely both in number and form.

CONCLUSION

The main content of this paper has been to review and clarify the continuum and thermodynamics based internal state variable model for application to thermoviscoplastic metals. In this process the following points have been made:

1) the definition of an internal state variable utilized in this model has been clarified;

2) internal state variables in metals represent local averages of dislocation arrangement, dislocation density, and intergranular damage,

3) in the context of the ISV definition given here, inelastic strain may also be interpreted as an internal state variable;

4) the path dependent Helmholtz free energy may be expanded in a second order expansion in elastic strain and temperature in order to obtain a stress-strain equation of state;

5) rate dependence enters the constitutive equations implicitly via the inelastic strain, as demonstrated by the nonlinear standard solid analog; and

6) a three-dimensional generalization of the standard solid may be used as a means of comparison of the general form of several currently proposed models.

Further ramifications of the ISV model discussed are also of importance, although not detailed herein. For example, this model may be utilized to construct a coupled heat conduction equation which may be utilized to predict heat generation in thermoviscoplastic metals [62]. Furthermore, the concept of internal state variables may be utilized to construct models for the mechanical constitution of composites with damage [63,15,65,66].

ACKNOWLEDGEMENT

The authors gratefully acknowledge support for this research which was sponsored by NASA Lewis Research Center under grant no. NAG 3-491.

REFERENCES

1. Coleman, B.D.: Thermodynamics of Material with Memory. Archive for Rational Mechanics and Analysis, Vol. 17, pp. 1-46, 1964.

2. Coleman, B.D., and Gurtin, M.E.: Thermodynamics with Internal State Variables. Journal of Chemical Physics, Vol. 47, pp. 597-613, 1967.

3. Lubliner, J.: On Fading Memory in Materials of Evolutionary Type. Acta Mechanica, Vol. 8, pp. 75-81, 1969.

4. Onsager, L.: Reciprocal Relations in Irreversible Processes I. Physics Review, Vol. 37, pp. 405-426, 1931.

5. Onsager, L.: Reciprocal Relations in Irreversible Processes II. Physics Review, Vol. 38, pp. 2265-2279, 1931.

6. Eckart, C.: Thermodynamics of Irreversible Processes, I. The Simple Fluid. Physics Review, Vol. 58, p. 267, 1940.

7. Meixner, J.: Die thermodynamische Theorie der Relaxationserscheinungen und ihr Zusammenhang mit der Nachwirkungstheorie. Kolloid-Z., Vol. 134, p. 2, 1953.

8. Biot, M.A.: Theory of Stress-Strain Relations in Anisotropic Viscoelasticity and Relaxation Phenomena. Journal of Applied Physics, Vol. 25, p. 1385, 1954.

9. Biot, M.A.: Variational Principles in Irreversible Thermodynamics with Application to Viscoelasticity. Physics Review, Vol. 97, p. 1463, 1955.

10. Ziegler, H.: An Attempt to Generalize Onsager's Principle, and Its Significance for Rheological Problems. Z. angew. Math. Phys., Vol. 9, p. 748, 1958.

11. Valanis, K.C.: Unified Theory of Thermomechanical Behavior of Viscoelastic Materials. Mechanical Behavior of Materials Under Dynamic Loads, p. 343, Springer,1968.

12. Kestin, J., and Rice, J.R.: Paradoxes in the Application of Thermodynamics to Strained Rods. A Critical Review of Thermodynamics, p. 275, Mono Book Corp., 1970.

13. Schapery, R.A.: Application of Thermodynamics to Thermomechanical, Fracture and Birefringent Phenomena in Viscoelastic Media. Journal of Applied Physics, Vol. 35, p. 1941, 1964.

14. Schapery, R.A.: A Theory of Non-Linear Thermoviscoelasticity Based on Irreversible Thermodynamics. Proceedings 5th U.S. National Congress of Applied Mechanics, ASME, pp. 511-530, 1966.

15. Krajcinovic, D., and Fonseka, G.U.: The Continuous Damage Theory of Brittle Materials - Part I - General Theory. Journal of Applied Mechanics, Vol. 48, pp. 809-815, 1981.

16. Coleman, B.D., and Noll, W.: The Thermodynamics of Elastic Materials with Heat Conduction and Viscosity. Archive for Rational Mechanics and Analysis, Vol. 13, p. 167, 1963.

17. Kratochvil, J., and Dillon, O.W., Jr.: Thermodynamics of Crystalline Elastic-Visco-Plastic Materials. Journal of Applied Physics, Vol. 41, pp. 1470-1479, 1970.

18. Kratochvil, J., and Dillon, O.W., Jr.: Thermodynamics of Elastic-Plastic Materials as a Theory with Internal State Variables. Journal of Applied Physics, Vol. 40, pp. 3207-3218, 1969.

19. Day, W.A.: The Thermodynamics of Simple Materials with Fading Memory. Springer, New York, 1972.

20. Truesdell, C., and Noll, W.: The Nonlinear Field Theories of Mechanics. Handbuck der Physik, Vol. III/3, Springer, Berlin, 1965.

21. Lubliner, J.: On the Thermodynamic Foundations of Non-Linear Solid Mechanics. International Journal of Non-Linear Mechanics, Vol. 7, pp. 237-254, 1972.

22. Green, A.E., and Naghdi, P.M.: A General Theory of an Elastic-Plastic Continuum. Archive for Rational Mechanics and Analysis, Vol. 18, pp. 251-281, 1965.

23. Coleman, B.D., and Mizel, V.J.: Thermodynamics and Departures from Fourier's Law of Heat Conduction. Archive for Rational Mechanics and Analysis, Vol. 13, pp. 245-261, 1963.

24. Rice, J.R.: A Pathe Independent Integral and the Approximate Analysis of Strain Concentration by Notches and Cracks. Journal of Applied Mechanics, Vol. 35, pp. 379-386, 1968.

25. Allen, D.H.: Some Comments on Inelastic Strain in Thermoviscoplastic Metals. Texas A&M University Report No. MM NAG 3-31-83-8, June 1983.

26. Cernocky, E.P., and Krempl, E.: A Theory of Thermoviscoplasticity Based on Infinitesimal Total Strain. International Journal of Solids and Structures, Vol. 16, pp. 723-741, 1980.

27. Walker, K.P.: Representation of Hastelloy X Behavior at Elevated Temperature with a Functional Theory of Viscoplasticity. Presented at ASME Pressure Vessels Conference, San Francisco, Aug. 12, 1980.

28. Lee, E.H., and McMeeking, R.M.: Concerning Elastic and Plastic Components of Deformation. International Journal of Solids and Structures, Vol. 16, pp. 715-721, 1980.

29. Hart, E.W.: Constitutive Relations for the Nonelastic Deformation of Metals. ASME J. Eng. Mater. Tech., Vol. 98-H, p. 193, 1976.

30. Krieg, R.D., Swearengen, J.C., and Rohde, R.W.: A Physcially-based Internal Variable Model for Rate-Dependent Plasticity. Proceedings ASME/CSME PVP Conference, pp. 15-27, 1978.

31. Bodner, S.R., and Partom, Y.: Constitutive Equations for Elastic-Viscoplastic Strain-Hardening Materials. Journal of Applied Mechanics, Vol. 42, No. 2, pp. 305-389, 1975.

32. Bodner, S.R.: Representation of Time Dependnet Mechanical Behaviour of Rene 95 by Consitutive Equations. Air Force Materials Laboratory, AFML-TX-79-4116, 1979.

33. Stouffer, D.C., and Bodner, S.R.: A Relationship Between Theory and Experiment for a State Variable Constitutive Equation. Air Force Materials Laboratory, AFWAL-TR-80-4194, 1981.

34. Bodner, S.R., Partom, I., and Partom, Y.: Uniaxial Cyclic Loading of Elastic-Viscoplastic Materials. J. App. Mech., 1979.

35. Cescotto, S., and Leckie, F.: Determination of Unified Constitutive Equations for Metals at High Temperature. Proc. Int. Conf. on Constitutive Laws for Eng. Mater., pp. 105-111, 1983.

36. Robinson, D.N.: A Unified Creep-Plasticity Model for Structural Metals at High Temperatures. ORNL-TM-5969, October 1978.

37. Miller, A.K.: An Inelastic Constitutive Model for Monotonic, Cyclic, and Creep Deformation: Part I - Equations Development and Analytical Procedures and Part II - Application to Type 304 Stainless Steel. ASME J. Eng. Mater. Tech., Vol. 98-H, p. 97, 1976.

38. Krempl, E.: On the Interaction of Rate and History Dependence in Structural Materials. Acta Mechanica, Vol. 22, pp. 53-90, 1975.

39. Liu, M.C.M., and Krempl, E.: A Uniaxial Viscoplastic Model Based on Total Strain and Overstress. J. Mech. Phys. Solids, Vol. 27, pp. 377-391, 1979.

40. Cernocky, E.P., and Krempl, E.: A Theory of Viscoplasticity Based on Infinitesimal Total Strain. Acta Mechanica, Vol. 36, pp. 263-289, 1980.

41. Cernocky, E.P., and Krempl, E.: A Nonlinear Uniaxial Integral Constitutive Equation Incorporating Rate Effects, Creep and Relaxation. Int. J. Nonlinear Mechanics, Vol. 14, pp. 183-203, 1979.

42. Valanis, K.C.: A Theory of Viscoplasticity Without a Yield Surface Part I. General Theory. Archives of Mechanics, Vol. 23, pp. 517-533, 1971.

43. Valanis, K.C.: A Theory of Viscoplasticity Without a Yield Surface Part II. Application to Mechanical Behaviour of Metals. Archives of Mechanics, Vol. 23, pp. 535-551, 1971.

44. Valanis, K.C.: On the Foundations of the Endochronic Theory of Viscoplasticity. Arch. Mech., Vol. 27, pp. 857-868, 1975.

45. Allen, D.H., and Haisler, W.E.: A Theory for Analysis of Thermoplastic Materials. Computers and Structures, Vol. 13, pp. 124-135, 1981.

46. Allen, D.H.: Computational Aspects of the Nonisothermal Classical Plasticity Theory. Accepted for publication in Computers and Structures, 1982.

47. Kocks, U.F.: Laws for Work-hardening and Low-Temperature Creep. Journal of Engineering Materials and Technology, Vol. 98-H, pp. 76-85, 1976.

48. Cailletaud, G., and Chaboche, J.L.: Macroscopic Description of the Microstructural Changes Induced by Varying Temperature: Example of IN100 Cyclic Behaviour. Third International Conference of Mechanical Behaviour of Materials, Vol. 2, pp. 23-32, ICM3, Cambridge, England, August 1979.

49. Lee, D., and Zaverl, F., Jr.: A Generalized Strain Rate Dependent Constitutive Equation for Anisotropic Metals. Acta Metallica Vol. 26, No. 11, p. 1771, 1978.

50. Laflen, J.H., and Stouffer, D.C.: An Analysis of High Temperature Metal Creep: Part I - Experimental Definition of an Alloy and Part II - A Constitutive Formulation and Verification. ASME J. Eng. Mat. & Tech., Vol. 100, p. 363, 1978.

51. Zienkiewicz, O.C., and Cormeau, I.C.: Visco-Plasticity -- Plasticity and Creep in Elastic Solids -- A Unified Numerical Approach. Int. Journal for Numerical Methods in Engineering, Vol. 8, pp. 821-845, 1974.

52. Perzyna, P.: Fundamental Problems in Viscoplasticity. Advan. Appl. Mech., Vol. 9, pp. 243-377, 1966.

53. Perzyna, P., and Wojno, W.: Thermodynamics of Rate Sensitive Plastic Materials. Arch. Mech. Stos., Vol. 20, p. 5, 1968.

54. Perzyna, P.: The Constitutive Equations for Work-Hardening and Rate-Sensitive Plastic Materials. Proc. Vibr. Probl., Vol. 4, pp. 281-290, 1963; Bull. Acad. Polon. Sci., Ser. Sci. Tech., Vol. 12, pp. 199-206,

55. Perzyna, P.: On the Thermodynamic Foundations of Viscoplasticity. Symposium on the Mechanical Behavior of Materials Under Dynamic Loads., San Antonio, Texas, 1967.

56. Yamada, Y., and Sakurai, T.: Basic Formulation and a Computer Program for Large Deformation Analysis. Pressure Vessel Technology, Part I, ASME, pp. 341-352, 1977.

57. Yamada, Y.: Constitutive Modelling of Inelastic Behaviour and Numerical Solution of Nonlinear Problems by the Finite Element Method. Computers and Structures, Vol. 8, pp. 533-543, 1978.

58. Snyder, M.D., and Bathe, K.J.: Formulation and Numerical Solution of Thermo-Elastic-Plastic and Creep Problems. National Technical Information Service, No. 82448-3, June 1977.

59. von Mises, R.: Mechanik der Festen Koerper im Plastich Deformablen Zustand. Goettinger Nachr., Math.-Phys. Kl., pp. 582-592, 1913.

60. Ziegler, H.: A Modification of Prager's Hardening Rule. Quarterly of Applied Mathematics, Vol. XVIII, pp. 55-65, 1959.

61. Prager, W.: The Theory of Plasticity: A Survey of Recent Achivements. Proceedings of the Institution of Mechanical Engineers, London, Vol. 169, pp. 41-57, 1955.

62. Allen, D.H.: A Prediction of Heat Generation in a Thermoviscoplastic Uniaxial Bar. Texas A&M Mechanics and Materials Center, Report no. MM 4875-83-10, July, 1983 (to be published in International Journal of Solids and Structures).

63. Schapery, R.A.: On Viscoelastic Deformation and Failure Behavior of Composite Materials with Distributed Flaws. Advances in Aerospace Structures and Materials, ASME AD-01, pp. 5-20, 1981.

64. Talreja, R.: A Continuum Mechanics Characterization of Damage in Composite Materials. The Technical University of Denmark, Lyngby, to be published.

65. Allen, D.H., Groves, S.E., and Schapery, R.A.: A Damage Model for Continuous Fiber Composites. In preparation.

TABLE 1. COMPARISON OF UNIAXIAL MODELS

Theory	Stress-Strain Relaxation	Internal State Variable Growth Laws	Comments	Material Parameters
Cernocky and Krempl	(T1) $\sigma=E[\varepsilon-\varepsilon^I-\varepsilon^T]$	(T2) $\dot{\varepsilon}^I=\frac{\sigma-G}{Ek}$	1. $G=G(\varepsilon,T)$ is obtained from extrapolation of relaxation data. 2. k is curve-fit to $k=R_0 e^{R_1 e^{-\left[\frlvert\sigma-G\rvert}{R_2}\right]^{R_3}}$	E, R_0, R_1, R_2, R_3
Krieg, Swearengen, and Rohde	(T3) $\sigma=E[\varepsilon-\varepsilon^I]$	(T4)[1] $\dot{\varepsilon}^I=c_1\left[\frac{\lvert\sigma-a_1\rvert}{a_2}\right]^{c_2}\operatorname{sgn}(\sigma-a_1)$ (T5)[1,2] $\dot{a}_1=c_3\dot{\varepsilon}^I-c_4 a_1^2[e^{c_5 a_1^2}-1]\operatorname{sgn}(a_1)$ (T6)[2] $\dot{a}_2=c_6\lvert\dot{\varepsilon}^I\rvert-c_7[a_2-a_{2_0}]^n$		$E, c_1, c_2, c_3, c_4, c_5, c_6, c_7, a_{2_0}, n$
Bodner <u>et al.</u>	(T7) $\sigma=E[\varepsilon-\varepsilon^I]$	(T8)[1] $\dot{\varepsilon}^I=\frac{2}{\sqrt{3}}D_0 e^{-\left[\frac{n+1}{2n}\right]\left[\frac{\sigma}{a_2}\right]^{-2n}}\operatorname{sgn}(\sigma)$ (T9) $\dot{a}_2=[Z_1-a_2]\dot{W}_p-AZ_1\left[\frac{a_2-Z_I}{Z_1}\right]^r$	1. $\dot{W}_p=\sigma\dot{\varepsilon}^I$	$E, D_0, n, m, Z_1, Z_I, A, r$
Walker	(T10) $\sigma=E[\varepsilon-\varepsilon^I]$	(T11)[1] $\dot{\varepsilon}^I=\left[\frac{\lvert\sigma-a_1\rvert}{a_2}\right]^n\operatorname{sgn}(\sigma-a_2)$ (T12)[2] $\dot{a}_1=[n_1+n_2]\dot{\varepsilon}^I-[a_1-a_{1_0}-n_1\varepsilon^I][\lvert\dot{\varepsilon}^I\rvert\frac{\partial}{\partial R}([n_3+n_4 R][\ln(\frac{n_5 R}{1+n_6 R}+1)])+n_7\lvert a_1-a_{1_0}\rvert^{m-1}]$ (T13) $\dot{a}_2=n_8\lvert\dot{\varepsilon}^I\rvert-n_9\lvert\dot{\varepsilon}^I\rvert a_2-n_{10}[a_2-a_{2_0}]^q$	1. R is the cumulative inelastic strain: $R=\int^t\frac{\partial\varepsilon^I}{\partial\tau}d\tau$. 2. The growth law for a_2, eq.(T13), is not presently used in the model; a_2 is assumed to be a constant.	$E, n, n_1, n_2, n_3, n_4, n_5, n_6, n_7, n_8, n_9, n_{10}, m, q, a_{1_0}, a_{2_0}$
Miller	(T14) $\sigma=E[\varepsilon-\varepsilon^I-\varepsilon^T]$	(T15)[1] $\dot{\varepsilon}^I=B\theta'\left[\sinh(\frac{\lvert\sigma-a_1\rvert}{a_2})1.5\right]^n\operatorname{sgn}(\sigma-a_1)$ (T16)[1,2] $\dot{a}_1=H_1\dot{\varepsilon}^I-H_1 B\theta'[\sinh(A_1\lvert a_1\rvert)]^n\operatorname{sgn}(a_1)$ (T17)[2] $\dot{a}_2=H_2\lvert\dot{\varepsilon}^I\rvert[C_2+\lvert a_1\rvert-\frac{A_2}{A_1}a_2^3]-H_2C_2B\theta'[\sinh(A_2 a_2^3)]^n$	1. $\theta'=e^{-\frac{Q}{RT}}$ for $T>0.6\,T_m$ $\theta'=e^{-\left[\frac{Q}{0.6RT_m}\right]\left[\ln(\frac{0.6T_m}{T})+1\right]}$ for $T\leq 0.6\,T_m$ T_m is the melting temp. k is the gas constant.	$E, B, n, H_1, A_1, H_2, C_2, A_2, Q$

Cescotto and Leckie	(T18) $\sigma=E[\varepsilon-\varepsilon^I-\varepsilon^T]$	(T19)[1] $\dot{\varepsilon}^I=f\left(\left\|\frac{\sigma-a_1}{a_2}\right\|\right)\ \mathrm{sgn}(\sigma-a_1)$ (T20)[2] $\dot{a}_1=\frac{3}{2}h_\alpha\dot{\varepsilon}^I-r_\alpha a_1$ (T21) $\dot{a}_2=h_\kappa-r_\kappa$	1. f, h_α, r_α, h_κ, and r_κ are experimentally determined functions.	E
Hart	(T22) $\sigma=E[\varepsilon-\varepsilon^I-\varepsilon^T]$	(T23)[1] $\dot{\varepsilon}^I=\dot{a}^*\left[\frac{2}{3}\right]^{M/2}\left[\frac{\lvert\sigma-a_1\rvert}{\mu}\right]^M\mathrm{sgn}(\sigma-a_1)$ (T24)[2] $\dot{a}_1=\frac{3}{2}\mu\dot{\varepsilon}^I-\frac{\mu\left[\frac{a_2'}{G}\right]^m f_\alpha^{-\frac{Q}{RT}}}{\left[\ln\left(\frac{3a_2'}{2\lvert a_1\rvert}\right)\right]^{1/\lambda}}$ (T25) $\dot{a}_2'=c\left[\frac{2}{3}\right]^{k/2}f_\alpha^{-\frac{Q}{RT}}\left[\frac{\sigma}{a_2'}\right]^k\frac{a_2'}{\left[\ln\left(\frac{a_2'}{\sqrt{\frac{2}{3}}a_1}\right)\right]^{1/\lambda}}$	1. The drag stress is taken to be a constant, μ, hence there is no a_2 as in other models. There is, however, a third internal state variable, termed a_2'. 2. T is the absolute temp. R is the gas constant.	E, $\dot{a}^*$, M, μ, G, m, f, Q, k, λ, c
Robinson	(T26) $\sigma=E[\varepsilon-\varepsilon^I-\varepsilon^T]$	(T27) $\dot{\varepsilon}^I=\frac{1}{2\mu}\left[\frac{1}{\sqrt{3}}\left\|\frac{\sigma-a_1}{K}\right\|\right]^{n-1}[\sigma-a_1]$ (T28)[2] $\dot{a}_1=\frac{2\mu H}{\left[\frac{1}{\sqrt{3}}\left|\frac{a_1}{K}\right|\right]^\beta}\dot{\varepsilon}^I-R\left[\frac{1}{\sqrt{3}}\left|\frac{a_1}{K}\right|\right]^{n-\beta-1}a_1$	1. G_0 is the initial value of $\frac{a_1^2}{2K^2}$.	E, μ, K, n, β, H, R, G_0
Valanis	(T29) $\sigma=E[\varepsilon-\varepsilon^I-\varepsilon^T]$	(T30) $\dot{\varepsilon}^I=k_1f_1(\sigma,\varepsilon)\varepsilon+k_2f_2(\sigma,\varepsilon)$	1. Represents simplified form of Valanis' model.	E, k_1, k_2, f_1, f_2
Allen and Haisler	(T31) $\sigma=E[\varepsilon-\varepsilon^I-\varepsilon^T]$	(T32) $\dot{\varepsilon}^I=\dot{\lambda}[\sigma-a_1]+\dot{g}[\sigma-a_1]$ (T33) $\dot{a}_1=\dot{\mu}[\sigma-a_1]$ (T34) $\dot{a}_2=f(\dot{\varepsilon}^{I^2})$	1. Considerable curve-fitting and interpolation of stress-strain and creep data required to obtain material parameters $\dot{\lambda}$, $\dot{g}$, and $\dot{\mu}$.	E, $\dot{\lambda}$, $\dot{g}$, $\dot{\mu}$, f

Note: parentheses ( ) imply "function of", whereas brackets [ ] imply multiplication.

1 $\mathrm{sgn}(x)=\begin{cases}1 & x>0\\ 0 & x=0\\ -1 & x<0\end{cases}$

2 $\dot{\varepsilon}^I$ can be substituted directly into growth law for a_1 and a_2 to obtain a form consistent with internal state variable growth laws (14).

Page intentionally left blank

PHYSICAL CONCEPTS IN THE DEVELOPMENT OF CONSTITUTIVE EQUATIONS

Brice N. Cassenti
United Technologies Research Center
East Hartford, Connecticut 06108

The currently proposed viscoplastic material models include in their formulation observed material response but do not generally incorporate principles from thermodynamics, statistical mechanics, and quantum mechanics. In the existing literature, numerous hypotheses have been made for material response based on first principles. Many of these hypotheses have been tested experimentally. Not only must the currently proposed viscoplastic theories be checked against these hypotheses but the experimental basis of these hypotheses must also be checked. The physics of thermodynamics, statistical mechanics and quantum mechanics, including the effects of defects, will be reviewed for their application to the development of constitutive laws.

INTRODUCTION

The currently proposed viscoplastic material models include in their formulation observed material response but do not generally incorporate principles from thermodynamics, statistical mechanics, and quantum mechanics. In the existing literature, numerous hypotheses have been made for material response based on first principles. Many of these hypotheses have been tested experimentally. Not only must the currently proposed viscoplastic theories be checked against these hypotheses but the experimental basis of these hypotheses must also be checked.

As an example of hypotheses commonly accepted but not usually tested, consider the assumption that inelastic deformations in isotropic materials are volume preserving. This is primarily based on the intuitive belief that under large strains the volume must be preserved and on experiments that show the hydrostatic yield stress is much larger than the shear yield stress. Even though many tensile tests on round specimens are performed little attempt is made to check for a change in volume.

The response of engineering materials is generally described in terms of the macroscopic behavior of large numbers of atoms. Such descriptions are semi-empirical in nature and usually neglect the information available from more fundamental theories, such as thermodynamics, statistical mechanics and quantum mechanics. Actually the macroscopic response of materials depends intimately on the quantum mechanical interaction of electrons in neighboring atoms. To illustrate this dependence, the distribution of the outer (valence) electrons of an atom determines the binding energy of the atoms in a solid.

The distribution and motion of these electrons can be calculated using quantum mechanics principles. The response of atoms bound by their outer electrons can be "averaged" using statistical mechanics principles including the effects of defects. The statistical mechanics analysis will result in the thermodynamic mechanical response of the material.

Thermodynamic principles can be examined to determine constraints on the mechanical response of materials. Allen in Ref. 1 presents a clear and concise thermodynamic formulation. From thermodynamics, constraints on the isothermal and adiabatic elastic moduli variation with temperature and strain can be determined based solely on the definitions of the moduli. The second law of thermodynamics has been used to determine the constraints that should exist between state variables. Statistical mechanics can be applied to the determination of material response. This theory has not been extensively applied to solid materials but has been used to determine some relationships.

Quantum mechanics principles also have not generally been applied to the determination of material properties because of the difficulty in analyzing the interaction between electrons in many electron atoms. Recently a new quantum mechanics analysis method, the pseudopotential method, has been developed which examines only the outer valence electrons. The pseudopotential method has been applied not only to electronic proprties but also to mechanical and thermal properties.

The effects of defects on the response of materials can be described using topological and statistical concepts. For example, atomic vibration models near defects dictate that at moderate-to-high strain rates the yield stress should vary linearly with the logarithm of the strain rate. The yield stresses and slip directions in a crystal lattice can be estimated based on atomic configurations, forces, and the effects of defects. Defects themselves can be characterized based on topological considerations of atomic configurations. The topological specifications of many defects and defect types can be described statistically and the macroscopic response of the materials specified.

In the discussion that follows, the thermodynamics of materials will be discussed first including illustrations on the constraints it places on material behavior. The derivation of thermodynamic principles from statistical mechanics is then reviewed. The statistical mechanics results, though, are dependent on the energy levels derived from quantum mechanics principles. The analysis of the response of solid materials directly from quantum mechanics principles is illustrated in the next section. The following section discusses the effects of imperfections and the last section summarizes the conclusions.

THERMODYNAMIC CONSIDERATIONS

Reversible Process Large Strains

Thermodynamic restrictions for systems undergoing reversible processes (e.g., an elastic response) can be quite severe and the restrictions are not readily apparent. For a system of volume, V, the first law of thermodynamics requires the increase in internal energy, $\dot{U}$, to be equal to the heat added, $\dot{Q}$, plus the work done on the system, $\dot{W}$

$$\dot{U} = \dot{Q}+\dot{W} \tag{1}$$

The work done on the system is

$$\dot{W} = \int_V \sigma_{ij} v_{ij} dV \tag{2}$$

where $v_{ij} = 1/2(\dot{U}_{i,j}+\dot{U}_{j,i})$ is the symmetric part of the velocity gradient, and σ_{ij} is the Cauchy or current stress. For a reversible process, the rate of change of entropy is

$$\dot{S} = \frac{\dot{Q}}{T} \tag{3}$$

where T is the temperature.

Consider a uniform closed system; a system with a small volume would be nearly uniform. Refer all quantities to the original configuration. Then

$$\dot{W} = \sigma_{ij} v_{ij} V = \frac{\rho}{\rho_o} S_{ij} V \dot{E}_{ij} \tag{4}$$

where S_{ij} is the Kirchoff stress,

$\dot{E}_{ij}$ is the Lagrangian strain rate,

ρ is the current density, and

ρ_o is the initial density.

Consider the internal energy, u, and entropy, s, per unit mass of the system where

$$M = \rho V \tag{5}$$

is the total mass, then Eqs. (1) and (3) become

$$\dot{u} = T\dot{s} + \frac{1}{\rho_o} S_{ij}\dot{E}_{ij} \tag{6}$$

for a reversible process u and s are functions of the end points of the system and not dependent on the path taken. Using the temperature, and the strain as the state variables

$$u = u(T,\underset{\sim}{E}),\ s=s(T,\underset{\sim}{E}) \tag{7}$$

or

$$\dot{u} = \frac{\partial u}{\partial T}\dot{T} + \frac{\partial u}{\partial E_{ij}}\dot{E}_{ij} = T\dot{s} + \frac{1}{\rho_o} S_{ij}\dot{E}_{ij} \tag{8}$$

$$\dot{s} = \frac{\partial s}{\partial T}\dot{T} + \frac{\partial s}{\partial E_{ij}}\dot{E}_{ij} \tag{9}$$

From Eq. (8)

$$\left.\frac{\partial u}{\partial E_{ij}}\right|_{s=\text{const}} = \frac{1}{\rho_o} S_{ij} \tag{10}$$

This is not convenient if temperature is used as a state variable since entropy will be a function of temperature and strain. Instead defining the Hemholtz free energy as

$$a = u - Ts = a(T,\underset{\sim}{E}) \tag{11}$$

then

$$\dot{a} = -s\dot{T} + \frac{1}{\rho_o} S_{ij}\dot{E}_{ij} = \frac{\partial a}{\partial T}\dot{T} + \frac{\partial a}{\partial E_{ij}}\dot{E}_{ij} \tag{12}$$

or

$$\frac{\partial a}{\partial T} = -s, \quad \frac{\partial a}{\partial E_{ij}} = \frac{1}{\rho_o} S_{ij} \tag{13}$$

From the mixed partials of Eq. (13)

$$\frac{1}{\rho_o} \frac{\partial S_{ij}}{\partial T} + \frac{\partial s}{\partial E_{ij}} = 0 \tag{14}$$

and

$$\frac{\partial S_{ij}}{\partial E_{kl}} = \frac{\partial S_{kl}}{\partial E_{ij}} \tag{15}$$

Consider a linear elastic material

$$S_{ij} = D_{ijkl}[E_{kl} - \alpha_{kl}(T-T_o)] \tag{16}$$

where D_{ijkl}, α_{kl} and T_o are constants. Then from Eq. (15)

$$D_{ijkl} = D_{klij} \tag{17}$$

The symmetry of the stress (if there are no body moments) and strain tensors yields

$$D_{ijkl} = D_{jikl} \tag{18}$$

and

$$D_{ijkl} = D_{ijlk} \tag{19}$$

These results imply that there can be at most 21 elastic constants for a generally anisotropic material. In addition, if the material is assumed to have a specific heat at constant volume (strain), C_v, that is not a function of strain or temperature, then

$$C_v = \frac{1}{M} \frac{\dot{Q}}{\dot{T}} = T \frac{\partial s}{\partial T} = \text{const} \tag{20}$$

All of the thermodynamic functions can now be found for a linear elastic material

$$s = \frac{1}{\rho_o} D_{ijkl} E_{ijkl} \alpha_{kl} + C_v \ln\left(\frac{T}{T_R}\right) \tag{21}$$

$$u = u_o + C_v T + \frac{1}{2\rho_o} D_{ijkl} E_{ij} E_{kl} + \frac{T_o}{\rho_o} D_{ijkl} E_{ij} \alpha_{kl} \tag{22}$$

$$a = u_o + C_v\left[1 - \ln\left(\frac{T}{T_R}\right)\right] + \frac{1}{2\rho_o} D_{ijkl} E_{ij} E_{kl} - \frac{1}{\rho_o} D_{ijkl} E_{ij} \alpha_{kl} (T - T_o) \tag{23}$$

where u_o and T_R are arbitrary constants.

The thermodynamics of reversible processes places restrictions on the manner in which the elastic constants can be defined for nonisothermal loadings. Researchers have sometimes introduced the elastic constants as instantaneous constants, see Ref. 2, where

$$\dot{S}_{ij} = D_{ijkl}\left[\dot{E}_{kl} - \alpha_{kl} \dot{T}\right] \tag{24}$$

From Eq. (13)

$$S_{ij} = \rho_o \frac{\partial a}{\partial E_{ij}} = \rho_o \, a,_{E_{ij}} \tag{25}$$

and

$$\dot{S}_{ij} = \rho_o \left\{\frac{\partial a,_{E_{ij}}}{\partial T} \dot{T} + \frac{\partial a,_{E_{ij}}}{\partial E_{kl}} \dot{E}_{kl}\right\} \tag{26}$$

Comparing Eqs. (26) and (24)

$$\frac{\partial a,_{E_{ij}}}{\partial T} = -\frac{1}{\rho_o} D_{ijkl} \alpha_{kl}, \quad \frac{\partial a,_{E_{ij}}}{\partial E_{kl}} = \frac{D_{ijkl}}{\rho_o} \tag{27}$$

But the mixed partials are equal, therefore

$$\frac{\partial^2 a, E_{ij}}{\partial T \, \partial E_{kl}} = -\frac{1}{\rho_o} \frac{\partial (D_{ijmn}\alpha_{mn})}{\partial E_{kl}} = \frac{1}{\rho_o} \frac{\partial D_{ijkl}}{\partial T}$$

or

$$\frac{\partial D_{ijkl}}{\partial T} + \frac{\partial (D_{ijmn}\alpha_{mn})}{\partial E_{kl}} = 0 \tag{28}$$

Equation (28) implies variations in the elastic moduli with temperature as defined in Eq. (24), will produce variations with strain of the sum $D_{ijmn}\alpha_{mn}$. For an isotropic material

$$D_{ijkl} = 2\mu\delta_{ik}\delta_{jl} + \lambda\delta_{ij}\delta_{kl} \tag{29}$$

and Eq. (28) becomes

$$2\frac{\partial \mu}{\partial T}\delta_{ik}\delta_{jl} + \frac{\partial \lambda}{\partial T}\delta_{ij}\delta_{kl} \frac{\partial [\alpha(2\mu+3\lambda)]}{\partial E_{kl}}\delta_{ij} = 0 \tag{30}$$

If $i \neq j$ in Eq. (30)

$$\frac{\partial \mu}{\partial T} = 0 \tag{31}$$

Hence, the shear modulus cannot vary with temperature! Contracting on i,j in Eq. (30)

$$2\frac{\partial \mu}{\partial T}\delta_{kl} + 2\frac{\partial \lambda}{\partial T}\delta_{kl} + 3\frac{\partial [\alpha(2\mu+3\lambda)]}{\partial E_{kl}} = 0 \tag{32}$$

If $k \neq 1$

$$\frac{\partial[\alpha(2\mu+3\lambda)]}{\partial E_{kl}} = 0 \tag{33}$$

the product $\alpha(2\mu+3\lambda)$ is not a function of shear strain. Contracting Eq. (32) again

$$3\frac{\partial K}{\partial T} + \frac{\partial(\alpha K)}{\partial E_{kk}} = 0 \tag{34}$$

where $K = 1/3\ (2\mu+3\lambda)$ is the bulk modulus.

The restrictions in Eqs. (31), (33) and (34) are mathematically quite severe for elastic (or reversible) processes. Equations equivalent to Eq. (28) are cited in Ref. 3 but the conditions of Eq. (24), are not stated leaving the result confused. If instead of Eq. (24) the stress is given by

$$S_{ij} = D_{ijkl}(T,\underset{\sim}{E})\left[E_{kl} - \alpha_{kl}(T,\underset{\sim}{E})(T-T_o)\right] + S^o_{ij} \tag{35}$$

Then $S_{ij} = S_{ij}(T,\underset{\sim}{E})$ and Eq. (27) are automatically satisfied.

Irreversible Process Small Strains

For irreversible processes thermodynamics is not as clearly defined. Two additional assumptions are made (Ref. 4): (1) the entropy is a function of state, this will hold for sufficiently slow processes, and (2) the second law is extended to the local level. Then for some volume V

$$\frac{D}{Dt}\int_v \rho s dV = -\int_A \phi_i n_i dA + \frac{D}{Dt}\int \rho \mathcal{S} dV \tag{36}$$

where ϕ_i = entropy flow vector,

$\mathcal{S}$ = internal entropy source, and

n_i = is the normal to the surface element dA.

Transforming the surface integral to a volume integral and using the conservation of mass

$$\rho \frac{DS}{Dt} = -\phi_{i,i} + \rho \frac{D\mathcal{S}}{Dt} \tag{37}$$

where the second law now requires

$$\frac{D\mathcal{S}}{Dt} \geq 0 \tag{38}$$

The heat being added to the volume V is

$$\frac{DQ}{Dt} = \int_v [-h_{i,i} + \sigma_{ij} v^D_{ij}] dV = \int \rho \frac{Dq}{Dt} dV \tag{39}$$

where q is the heat added per unit mass in the volume dV

v^D_{ij} is the symmetric part of the velocity gradient which is converted to heat (the dissipative part). The total velocity gradient is

$$v_{ij} = v^c_{ij} + v^D_{ij} \tag{40}$$

and v^c_{ij} represents the part of the velocity gradient that is converted to recoverable internal energy, the conservative part. The internal energy is then governed by

$$\frac{Du}{Dt} = \frac{Dq}{Dt} + \frac{1}{2} \sigma_{ij} v^c_{ij} \tag{41}$$

The change in entropy can be found by proceeding along a reversible path, or

$$\frac{Ds}{Dt} = \frac{1}{T} \frac{Dq}{Dt} = - \frac{h_{i,i}}{\rho T} + \frac{\sigma_{ij} v^D_{ij}}{\rho T} \tag{42}$$

Equivalently

$$\rho \frac{Ds}{Dt} = -\left(\frac{h_i}{T}\right)_{,ii} - \frac{h_i T_{,i}}{T^2} + \frac{\sigma_{ij} v^D_{ij}}{T} \tag{43}$$

Comparing this with Eq. (37)

$$\phi_i = \frac{h_i}{T} \tag{44}$$

and

$$\rho \frac{D\mathcal{S}}{Dt} = -\frac{h_i T_{,i}}{T^2} + \frac{\sigma_{ij} v^D_{ij}}{T} \geq 0 \tag{45}$$

For <u>small</u> strains take

$$v^D_{ij} = \dot{c}_{ij} \qquad v_{ij} = \dot{\varepsilon}_{ij} \tag{46}$$

where $\dot{c}_{ij}$ is the inelastic strain, and

$\dot{\varepsilon}_{ij}$ is the total strain.

For uniform temperature distributions and small strains, Eq. (45) becomes

$$\sigma_{ij} \dot{c}_{ij} \geq 0 \tag{47}$$

Equation (47) is related to Drucker's postulate but in Ref. 5 there is no mention to isothermal conditions. Equation (47) can be extended to states with an initial stress and infinitesimal stress changes, Ref. 3. Note that the condition in Eq. (47) holds only for systems with uniform temperature distributions. Other assumptions in addition to the second law of thermodynamics must be made for Eq. (47) to apply more generally. For example, if linear phenomenological laws are assumed and Gibb's condition for a reversible process is applied, then the internal entropy production must be a positive definite function of the state variables. Consider the functional theory, described in Ref. 6, where

$$\dot{c}_{ij} = \dot{\lambda} \left(\frac{3}{2} S_{ij} - \Omega_{ij}\right) \tag{48}$$

where $S_{ij} = \sigma_{ij} - 1/3\ \sigma_{kk}\delta_{ij}$ on the deviatoric stress, and Ω_{ij} is the equilibrium stress.

Equation (46) requires

$$\frac{3}{2} S_{ij}S_{ij} = 3J_2 \geq S_{ij}\Omega_{ij} \tag{49}$$

For uniaxial loading, Eq. (49) becomes

$$\sigma^2 \geq \sigma\Omega \tag{50}$$

which means if the equilibrium stress and the stress have the same sign then the stress must be larger in absolute value than the equilibrium stress. Experimental evidence shows that Eq. (49) is violated. The reason for the disagreement arises from the fact that all of the inelastic strain is not dissipated initially, which is assumed in Eq. (39). Initially some of the inelastic strain can raise the recoverable internal energy of the material. This rise in recoverable internal energy can be pictured as an atomic arrangement that is at a higher state, as shown in Fig. 1. This higher energy state can be relatively stable, represented by the higher of the two relative minimums. Thermal diffusion of the atoms to a lower state will gradually dissipate some or all of the inelastic strain energy as heat. The quantity, Ω, can now be viewed as representing structural changes in the atomic arrangement of a material.

If Eq. (39) is replaced by

$$\frac{DQ}{Dt} = \int_v \left[-h_{i,i} + \left(\sigma_{ij} - \frac{2}{3}\Omega_{ij}\right)v^D_{ij}\right]dV \tag{39'}$$

Then Eq. (49) will be converted to

$$\frac{2}{3}\dot{\lambda}\left(\frac{3}{2} S_{ij} - \Omega_{ij}\right)\left(\frac{3}{2} S_{ij} - \Omega_{ij}\right) \geq 0 \tag{49'}$$

This is always satisfied since $\dot{\lambda}$ is positive.

STATISTICAL MECHANICS CONSIDERATIONS

From statistical mechanics, which characterize the overall response of large numbers of atoms, many of the postulates and results of thermodynamics can be found. For example, the Onsager reciprocal relation, Ref. 7, for materials with linear phenomenological laws, can be derived from statistical mechanics considerations. Statistical mechanics is based on the assumption that "all microstates of a system that have the same energy are assumed to be equally likely" Ref. 8. By considering two large systems of atoms, A and B, in equilibrium, the probability that the total system, A and B, is at energy E_A+E_B is

$$P_{A+B}(E_A+E_B) = P_A(E_A)P_B(E_B) \tag{51}$$

This follows from the fact that the energy of atoms in system A (or B) where system A and B are each in contact with a thermal reservoir will be independent of the energy of the atoms in system B (or A). From Eq. (51) it can be shown that the probability that a system is at energy, E_K is given by

$$P(E_k) = \frac{1}{Z} e^{-\beta E_k} \tag{52}$$

where $Z = \sum_k e^{-\beta E_k}$ is the partition function, and (53)

β is a parameter to be determined.

To determine this parameter, consider the internal energy which is now defined as the average energy of the system, then

$$U = \bar{E} = \sum_k E_k P(E_k) = \frac{1}{Z} \sum_k E_k e^{-\beta E_k} \tag{54}$$

From Eq. (53)

$$U = -\frac{\partial(\ln Z)}{\partial \beta} \tag{55}$$

For a perfect monitonic gas, Ref. 8, the partition function is

$$Z = V^N \left(\frac{2\pi}{\beta m}\right)^{3N/2} \tag{56}$$

where N is the number of atoms of mass, m, in volume V. From Eq. (55)

$$U = \frac{3N}{2\beta} \tag{57}$$

but the internal energy is also

$$U = \frac{3}{2} NkT \tag{58}$$

where k is Boltzmann's constant. Therefore comparing Eqs. (57) and (58)

$$\beta = \frac{1}{kT} \tag{59}$$

The result in Eq. (59) is general and applies to all systems.

One thermodynamic function, the internal energy, is now determined from the statistical response of the individual atoms. A second function needs to be determined to specify the system. To accomplish this, consider

$$d(\ln Z) = \frac{\partial \ln Z}{\partial \beta} d\beta + \frac{\partial \ln Z}{\partial \varepsilon_{ij}} d\varepsilon_{ij} \tag{60}$$

Substituting for the first partial derivative using Eq. (55) and using

$$U d\beta = d(\beta U) - \beta dU \tag{61}$$

$$d(\ln Z + \beta U) = \beta dU + \frac{\partial \ln Z}{\partial \varepsilon_{ij}} d\varepsilon_{ij} \tag{62}$$

From the first law of thermodynamics (i.e., the conservation of energy) for reversible reactions,

$$dU = TdS + \sigma_{ij} V d\varepsilon_{ij} \tag{63}$$

Substituting Eq. (62) with (63)

$$d(\ln Z + \beta U) = \frac{1}{k} dS + \left[\beta V \sigma_{ij} + \frac{\partial \ln Z}{\partial \varepsilon_{ij}}\right] d\varepsilon_{ij} \tag{64}$$

Equation (64) must hold for arbitrary changes in strain and entropy therefore

$$dS = k d(\ln Z + \beta U) \tag{65}$$

and

$$\sigma_{ij} = -\frac{1}{\beta V} \frac{\partial \ln Z}{\partial \varepsilon_{ij}} = -\frac{kT}{V} \frac{\partial \ln Z}{\partial \varepsilon_{ij}} \tag{66}$$

Statistical mechanics has been applied to the response of solids, (e.g., Refs. 9 and 10). For example, consider a solid to be a collection of N atoms each of which can vibrate in three orthogonal directions. Then if the atoms are assumed to be linear harmonic oscillations, quantum mechanics can be used to determine the possible energy levels in Eqs. (52) and (53). These energy levels are from Ref. 10 or the Appendix.

$$E_i = \left(n_i + \frac{1}{2}\right) h \nu_i \qquad \begin{matrix} n_i = 0, 1, 2, \ldots, \infty \\ i = 1, 2, 3, \ldots, 3N \end{matrix} \tag{67}$$

where $\nu_i = \frac{1}{2\pi} \sqrt{\frac{k_i}{m_i}}$ is the natural frequency of atom i. The total energy for a state is

$$E = \sum_{i=1}^{3N} E_i$$

and the partition function is

$$Z = \sum_{\text{states}} e^{-\beta E} = \sum_{n_1=0}^{\infty} \sum_{n_2=0}^{\infty} \cdots \sum_{n_{3N}=0}^{\infty} e^{-\beta(E_1+E_2+\ldots+E_{3N})} \tag{68}$$

Substituting Eq. (67) into Eq. (68) and summing over each N_i

$$Z = \sum_{i=1}^{3N} \frac{e^{-\beta h\nu_i/2}}{1-e^{-\beta h\nu_i}} \tag{69}$$

or

$$\ln Z = \sum_{i=1}^{3N} \left\{ -\frac{\beta h\nu_i}{2} - \ln\left(1-e^{-\beta h\nu_i}\right) \right\} \tag{70}$$

From Eq. (55)

$$U = \sum_{i=1}^{3N} \left(\frac{h\nu_i}{2} + \frac{1}{\beta} \left[\frac{\beta h\nu_i e^{-\beta h\nu_i}}{1-e^{-\beta h\nu_i}} \right] \right) \tag{71}$$

and, at high temperatures β approaches zero ($\beta = 1/kT$)

$$U = \sum_{i=1}^{3N} \left(\frac{h\nu_i}{2} + \frac{1}{\beta} \right) = 3NkT + \sum_{i=1}^{3N} \frac{h\nu_i}{2} \tag{72}$$

the specific heat at constant volume is then

$$C_v = \frac{\partial V}{\partial T} = 3Nk \tag{73}$$

which is the classical thermodynamic result and from experimental data is accurate at high temperatures. For a complete discussion of this result, see Refs. 9 or 10.

The above result does not include the stress strain response. To accomplish this, consider the atoms to be stretched to a new position a distance x_o from their relative equilibrium positions by an external applied force. The energy levels will now increase approximately by

$$\frac{1}{2} k_i x_o^2$$

or

$$E_i = \frac{1}{2} h\nu_i + \frac{1}{2} k_i x_o^2 + n_i h\nu_i \tag{74}$$

is the approximate energy of atom i.

Using $k_i = 4\pi^2 m_i \nu_i^2$ and $x_o = 2a\varepsilon$ where 2a is the distance between atomic centers and ε is the strain. Equation (68) can now be rewritten as

$$E_i = \frac{1}{2} h\nu_i + 8\pi^2 a^2 m_i \nu_i^2 \varepsilon^2 + n_i h\nu_i \tag{75}$$

Assuming the frequencies of each atom in each direction are the same, the Einstein approximation, the partition function becomes

$$\ln Z = 3N \left[-\frac{\beta}{2} h\nu - 8\pi^2 a^2 m \beta \nu^2 \varepsilon^2 - \ln\left(1 - e^{-\beta h\nu}\right) \right] \tag{76}$$

and the stress is from Eq. (66)

$$\sigma = \frac{48N\pi^2 a^2 m\nu^2 \varepsilon}{V} = 48\pi^2 \rho a^2 \nu^2 \varepsilon \tag{77}$$

where $\rho = nm/V$ is the density, then the elastic modulus

$$E = 48\pi^2 \rho a^2 \nu^2 \tag{78}$$

It should be possible to test Eq. (78) against available data.

QUANTUM MECHANICAL APPLICATIONS TO THE RESPONSE OF MATERIALS

In considering the statistical mechanics aspects of material response, quantum mechanics provided the means for determining the energy states of a system. Only the potential energy between neighboring atoms was considered, but actually this potential energy is determined by the chemical bonding between adjacent atoms, which in turn is determined by the outer electrons. Summarizing the mechanical properties of a solid are ultimately tied to the binding energy present in the outer electrons. In the analyses discussed in the section on statistical mechanics, the contribution to the energy of the system from the electrons was neglected; an assumption that generally produces accurate results, as quantum mechanics principles are considerably more important for low mass particles such as electrons than for higher mass particles like atomic nuclei.

Nevertheless the pseudopotential method for describing these outer electrons is being developed,Refs. (12, 13),and shows promise for describing elementary mechanical properties. The pseudopotential method is based on assuming a potential which is approximately correct in the regions where the outer electrons are likely to be. For example, in Ref. (13), the potential energy, V, is assumed to be

$$V(r) = \begin{cases} 0 & r \leq R_e \\ -\frac{e^2}{r} & r > R_e \end{cases} \tag{79}$$

where

r is the distance from an atomic nucleus
e is the charge on an electron, and
R_e is a semi-empirical constant.

The approximation in Eq. (79) is referred to as the empty core model, and is relatively accurate compared with numerical solutions. The approximation is based on the assumption that when a valence electron enters the region of an atom's core electrons that it moves as if there is little change in potential energy.

In Ref. (14), several somewhat more complex approximations to the potential are compared for their accuracy in predicting the bulk moduli of solids and liquids at temperatures from absolute zero to over 1000 deg F. For

example, one theory predicts a bulk modulus for aluminum at room temperature that is within twenty percent of the experimental value and these results are predicted using initially rough analytical calculations. Certainly the pseudopotential method deserves careful examination.

Quantum mechanics has, since the early stages of its development, been applied to the prediction of the interatomic potentials for diatomic hydrogen. Using these results, it has been possible to determine higher order terms in the energy eigenvalues, Ref. (15), as

$$E_n = \left(n + \frac{1}{2}\right) \hbar\nu - \left(\frac{\hbar^2\nu^2}{4D}\right)\left(n + \frac{1}{2}\right)^2 \tag{80}$$

The first term is the same as Eq. (67) used in the discussion on statistical mechanics, the second term is a correction. The constant D is the dissociation energy for the molecule, and the maximum energy level cannot exceed the dissociation energy, or

$$E_{n_{max}} \leq D < E_{n_{max}+1} \tag{81}$$

The second term in Eq. (80) is quite small and has only a small effect on the partition function, Eq. (68). A correction for the angular momentum can also be included in Eq. (80) but again the effect on the partition function is small. Better approximations to the energy levels lead to extremely accurate results for the thermodynamic properties, for example, see Ref. 10.

EFFECTS OF IMPERFECTIONS

In principle it is possible to derive the properties of solids by considering the energy levels of the atoms (and electrons). The discussion on statistical mechanics has been applied to essentially perfect crystals. Imperfections, or defects, have a profound effect on the response of solid materials. These imperfections will generally lower the oscillation frequencies of the atoms to such an extent that they will control the inelastic deformation of the material.

For example, in Ref. (3), it is shown from a consideration of activation energies and dislocation geometry that

$$\sigma(\varepsilon) = f\left[T\left(1-\alpha \ln \frac{\dot{\varepsilon}}{\dot{\varepsilon}_o}\right)\right] \tag{82}$$

where

$\dot{\varepsilon}_o$ and α are constants determined by the dislocation geometries
T is the absolute temperature
$\dot{\varepsilon}$ is the strain rate
σ is the stress, and
f is an arbitrary function

The quantity

$$T_m = T\left(1-\alpha \ln \frac{\dot{\varepsilon}}{\dot{\varepsilon}_o}\right) \tag{83}$$

is referred to as the velocity modified temperature, and has been shown to have some experimental validity.

An important concept employed in the derivation of Eq. (82) is Burgers vector. The Burgers vector is found by comparing a path about a line imperfection (e.g., a screw dislocation) and a closed path in a perfect crystal. The path about the imperfection follows the same atomic path as the path in the perfect crystal. The path about the imperfection then will not close. The vector required to close this path is the Burgers vector.

In a similar manner, it should be possible to represent plane and point imperfections in addition to line imperfections by similar integrations. For example, the line imperfection is described by performing a one dimensional integration. A point imperfection can be described by performing an integration on a surface that surrounds the point and a surface imperfection can be described by taking a difference between two points on each side of the surface. In other words: (1) a zero dimensional (point) imperfection is described by performing a two dimensional (surface) integration, (2) a one dimensional (line) imperfection is described by performing one dimensional integration and (3) a two dimensional imperfection is described by a zero dimensional integration. The sum of the dimension of the imperfection and the dimension of integration required to describe it is always the same number, or

$$n + m = 2 \tag{84}$$

where

n is the dimension of the imperfection
m is the dimension of the integration

Topological descriptions like those resulting in Eq. (84) have been applied to material description (e.g. see Refs. 16-17).

Defects can be classified quantatively by performing the proper integration. Not all defects will be identical and there will be some probabilistic distribution in the quantities used to classify the distributions. These probability distributions will ultimately determine the inelastic response of the material.

CONCLUSIONS

The effects of a defect on the stress-strain law can, in principle, be found by using quantum mechanics to determine the energies from the potential energy of the neighboring atoms. The energies in turn, determine the results from a statistical mechanics analysis. Furthermore, the results of the statistical mechanics analysis determine the thermodynamic response of the material.

Although such a procedure is possible in principle, it is not practical because the results would be overly complex for engineering applications. However, such an approach should produce important results which place constraints on the form of any newly proposed constitutive relations.

REFERENCES

1. Allen, D. H.: A Thermodynamic Framework for Comparison of Current Thermoviscoplastic Constitutive Models for Metals at Elevated Temperature. Constitutive Laws Conference, Tucson, Arizona, January 10-14, 1983.

2. Walker, K. P.: Research and Development Program for Nonlinear Structural Modeling with Advanced Time-Temperature Dependent Constitutive Relationships CR-165533 National Aeronautics and Space Administration, Contract NAS3-22055, 1981.

3. Fung, Y. C.: Foundations of Solid Mechanics, Prentice-Hall, Englewood Cliffs, N.J. 1965.

4. McClintock, F. A. and A. S. Argon (editors): Mechanical Behavior of Materials. Addison-Wesley Publishing Company, Inc., Reading, Mass., 1966.

5. Naghdi, P. M.: Some Constitutive Restrictions in Plasticity, from Constitutive Equations in Viscoplasticity. Computational and Engineering Aspects, AMD-Vol. 20. ASME, New York, 1976.

6. Cassenti, B. N.: Research and Development Program for the Development of Advanced Time-Temperature Dependent Constitutive Relationships. NASA CR-168191 National Aeronautics and Space Administration, Contract NAS3-23273, 1983.

7. Onsager, L.: Reciprocal Relations in Irreversible Process II. Phys. Rev. Vol. 38, 1931, pp. 2265-2279.

8. Jackson, E. A.: Equilibrium Statistical Mechanics, Prentice Hall, Inc., Englewood Cliffs, N.J. 1968.

9. Tollman, R. C.: The Principles of Statistical Mechanics, Dover Publications, Inc., New York republished 1979, original publication, 1938.

10. Sears, F. W.: An Introduction to Thermodynamics, The Kinetic Theory of Gases, and Statistical Mechanics. Addison-Wesley Publishing Company, Inc., Reading, Mass., 1953.

11. Schiff, L. I.: Quantum Mechanics. McGraw-Hill Book Company, New York, 3rd edition, 1968.

12. Austin, B. J., V. Heine and L. F. Sham: General Theory of Pseudopotentials. Physical Review, Vol. 127, 1962, pp. 276-282.

13. Kittel, C.: Introduction to Solid State Physics. John Wiley & Sons, Inc., New York, 1971.

14. Hangawa, M. and W. H. Young: Bulk Moduli of Solid and Liquid Metals, J. Phys. F (Metal Physics) pp. 977-994, 1981.

15. Slater, J. C.: Quantum Theory of Molecules and Solids. McGraw-Hill Book Company, Inc., New York, 1963.

16. Barrett, L. K. and C. S. Yust: Some Fundamental Ideas in Topology and their Application to Problems in Metallurgy. ORNL-4411 Oak Ridge National Laboratory, Contract No. W-7405-eng-23, 1969.

17. Trebin, H. R.: The Topology of Non-Uniform Media in Condensed Matter Physics. Advances in Physics, Vol. 31, No. 3, 1982, pp. 195-254.

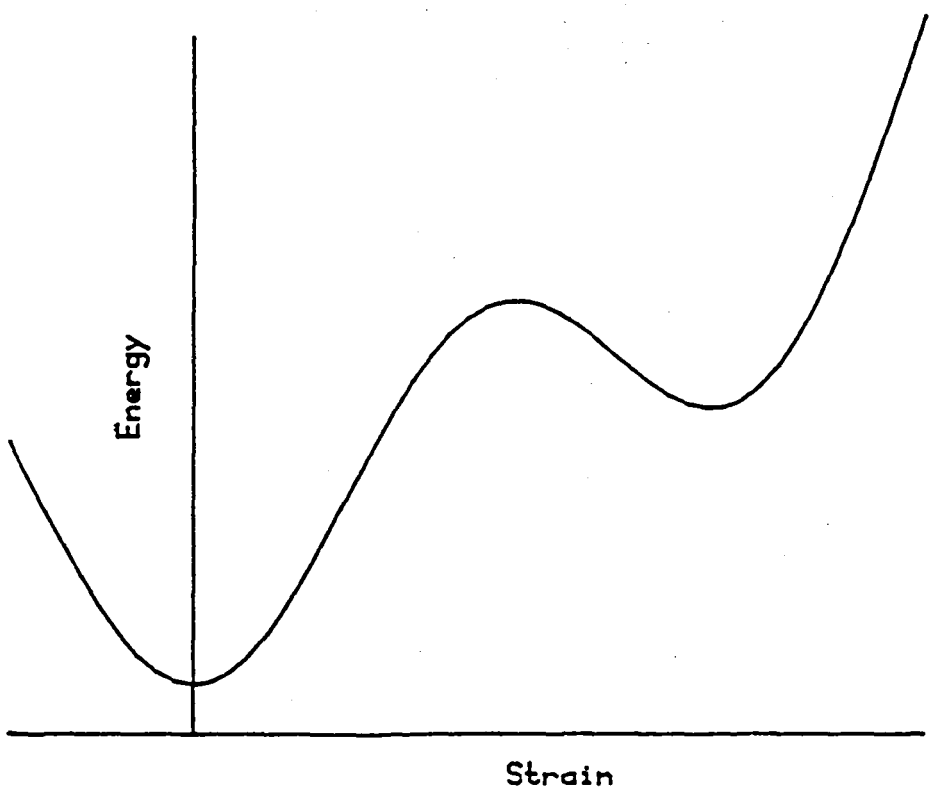

Fig. 1 Hypothetical Internal Energy Variation

A COMPARISON OF TWO CONTEMPORARY CREEP-FATIGUE LIFE PREDICTION METHODS

by

Michael A. McGaw
NASA Lewis Research Center
Cleveland, Ohio 44135

A comparison of two contemporary approaches to creep-fatigue life prediction, the Continuous Damage Mechanics as developed at ONERA, and Strain Range Partitioning, is presented. The general framework of each of these approaches, both being crack-initiation life prediction tools, are examined. The basis for, and implications of each predictive method are discussed, relative to the material class(es) for which each was developed, as well as to their general applicability. Evident is a need for critical experiments capable of discriminating among the models; to this end, the question of choice of experiment and material is addressed.

(Paper not available at time of printing.)

Page intentionally left blank

A NUMERICAL ALGORITHM FOR ENDOCHRONIC PLASTICITY AND COMPARISON WITH EXPERIMENT

K.C. Valanis and Jinghong Fan
University of Cincinnati
Cincinnati, Ohio 45221

A numerical algorithm based on the finite element method of analysis of the boundary value problem in a continuum is presented, in the case where the plastic response of the material is given in the context of endochronic plasticity. The relevant constitutive equation is expressed in incremental form and plastic effects are accounted for by the method of an induced pseudo-force in the matrix equations.

The results of the analysis are compared with observed values in the case of a plate with two symmetric notches and loaded longitudinally in its own plane. The agreement between theory and experiment is excellent.

INTRODUCTION

The greatest difficulty encountered in the application of the classical theory of plasticity is the lack of knowledge of the configuration of the subsequent yield surface for the particular material at hand, and the experimental difficulties encountered in finding it in the fully three dimensional case. More importantly, however,

it has been observed by many experimenters that the shape of the subsequent yield surface and its position in stress space depends very strongly on the definition of the yield point, particularly in situations following prior deformation [1-3].

The essential premise of the classical plasticity theory is the assumption of an a priori existence of a yield surface. This implies a finite elastic domain. From the mathematical standpoint, a finite domain is necessary because of the requirement that the increment in plastic strain be normal to the yield surface. Thus, the direction of the plastic strain increment is dictated by the yield surface configuration.

If plastic effects were to begin immediately upon loading, perforce, the domain of the yield surface would collapse to a point, thus making the direction of the plastic strain increment indeterminate since all directions are normal to a point. Thus, the classical plasticity theory cannot deal with materials that yield immediately upon loading. There are other difficulties associated with experimental attempts to describe and analyze a two-or three-dimensional response of a material [4]. For instance, investigations in the hardening rule are much discussed in the current literature, but definitive functional forms outside the Prager-Ziegler rule are very few, and lack firm experimental verification. This rule specifically can have only limited application, and is inappropriate for

complicated loading histories. Moreover, it gives rise to large discrepancies between calculated and experimental data in loading-unloading processes [1]. Other numerical difficulties arise from the fact that the loading increments cannot be assigned arbitrarily a priori. When the current loading increment makes the stress state of a particular element traverse the yield surface it is necessary to come back to the previous loading state and adjust the magnitude of the new increment of loading to ensure that the new stress state is located just on the yield surface. Certainly, this process increases the time of computation.

In 1971, Valanis proposed an alternative theory of viscoplasticity called "endochronic theory" [5,6], which is based on irreversible thermodynamics and the concept of intrinsic time. The theory provides a unified point of view to describe the elastic-plastic behavior of materials since it places no requirement for a yield surface and a "loading function" to distinguish between loading and unloading.

In a series of recent works, Valanis, Wu and others [7-10] demonstrated that the endochronic theory could apply more precisely to situations involving unloading and cyclic behavior of metals, as well as wave propagation in the plastic region.

However, in all of the works, involving more than one dimension, where the loading was quasi-static, the stress fields were homogeneous.

In the present paper a numerical algorithm is first implemented in a computer program, which can be used to analyze the material response in monotonic and cyclic loading in the case of plane stress or plane strain. The calculated results are then compared with the data obtained from a specially designed experiment on a notched plate cyclically loaded in its own plane. The validity of the endochronic analysis, using this numerical algorithm, is thereby demonstrated.

AN INCREMENTAL FORM OF THE ENDOCHRONIC ELASTOPLASTIC CONSTITUTIVE EQUATION IN TERMS OF {dσ} and {dε}

The following are the formulae concerning the endochronic constitutive equations for plastically incompressible isotropic materials and small deformation [7]

$$\underset{\sim}{s} = \int_0^z \rho(z-z') \frac{\partial \underset{\sim}{e}^p}{dz'} dz' \tag{2.1}$$

$$d\zeta = \|de^p\| \tag{2.1a}$$

$$dz = \frac{d\zeta}{f(\zeta)} \tag{2.1b}$$

where $\rho(z)$ and $f(\zeta)$ are two material functions namely the kernel function and hardening function respectively.

$$\sigma_{kk} = 3K\varepsilon_{kk} \tag{2.2}$$

$$d\underset{\sim}{e}^p = d\underset{\sim}{e} - \frac{1}{2\mu} d\underset{\sim}{s} \tag{2.3}$$

By definition

$$de_{ij} = d\varepsilon_{ij} - \frac{1}{3} d\varepsilon_{\alpha\alpha}\delta_{ij} \tag{2.4a}$$

$$ds_{ij} = d\sigma_{ij} - \frac{1}{3} d\sigma_{\alpha\alpha}\delta_{ij} \tag{2.4b}$$

In this paper the form of $\rho(z)$ given by equation (2.5) was used in equation (2.1)

$$\rho(z) = \sum_{r=1}^{\infty} c_r e^{-\alpha_r z} \tag{2.5}$$

with the conditions that β_r and R_r are positive for all r and

$$\sum_{r=1}^{\infty} c_r = \infty \ , \quad \sum_{r=1}^{\infty} \frac{c_r}{\alpha_r} < \infty \ . \tag{2.6a,b}$$

This form of $\rho(z)$ is continuous and differentiable in $(0,\infty)$ and therefore the incremental form of equation (2.1) specified below can be used in conjunction with a finite element code.

Specifically in the case where the infinitely large value of $\rho(0)$ is approximated by a suitably large value, as is done in this paper, one may differentiate equation (2.1) with respect to z to obtain the following differential form of the endochronic constitutive equation:

$$d\underset{\sim}{s} = \rho(0) d\underset{\sim}{e}^p + \underset{\sim}{h}(z)\,dz \tag{2.7}$$

where

$$\underset{\sim}{h}(z) = \int_0^z \hat{\rho}(z-z') \frac{\partial \underset{\sim}{e}^p}{\partial z'} dz' \tag{2.8}$$

and

$$\hat{\rho}(z) = \frac{d\rho}{dz} \tag{2.8a}$$

The elastoplastic constitutive equations (2.3) and (2.7), can then be combined and expressed in the differential form

$$ds_{ij} = 2\hat{\mu}\{de_{ij} + \frac{1}{\rho(0)} h_{ij}(z)dz\} \tag{2.9}$$

where

$$\hat{\mu} = \rho(0) \{1 + \frac{\rho(0)}{2\mu}\}^{-1} \tag{2.9a}$$

Alternately, for computational purposes the incremental form given by equation (2.10) may be used, i.e.,

$$\Delta s_{ij} = 2\hat{\mu} \{\Delta e_{ij} + \frac{1}{\rho(0)} h_{ij}(z) \Delta z\} \tag{2.10}$$

Substituting (2.4a,b) into (2.9) and using (2.2) one obtains the operational incremental form of the elastoplastic constitutive equation in matrix notation as follows:

$$\{d\sigma\} = \{D\} \{d\varepsilon\} + \{dH_p\} \tag{2.11}$$

where

$$\{D\} = \begin{bmatrix} c_1 & c_2 & 0 \\ c_2 & c_1 & 0 \\ 0 & 0 & \hat{\mu}_p \end{bmatrix}, \tag{2.12}$$

and

$$\{dH_p\} = \begin{Bmatrix} dH_{px} \\ dH_{py} \\ dH_{pxy} \end{Bmatrix} \tag{2.13}$$

In plane stress

$$c_1 = \frac{12K\hat{\mu} + 4\hat{\mu}^2}{3K + 4\mu} \tag{2.14}$$

$$c_2 = \frac{6K\hat{\mu} - 4\hat{\mu}^2}{3K + 4\mu} \tag{2.15}$$

$$D_1 = \frac{2\hat{\mu}(3k-2\hat{\mu})}{3k + 4\mu} \tag{2.16}$$

$$dH_{px} = \{2\hat{\mu}h_x(z) - D_1 h_z(z)\}\, dz/\rho(0) \tag{2.17}$$

$$dH_{py} = \{2\hat{\mu}h_y(z) - D_1 h_z(z)\}\, dz/\rho(0) \tag{2.18}$$

$$dH_{pxy} = 2\hat{\mu}h_{xy}(z)\, dz/\rho(0) \tag{2.19}$$

In plane strain

$$c_1 = \frac{3K + 4\hat{\mu}}{3} \tag{2.20}$$

$$c_2 = \frac{3K - 2\hat{\mu}}{3} \tag{2.21}$$

$$dH_{px} = 2\hat{\mu}\, h_x(z)\,dz/\rho(0) \tag{2.22}$$

$$dH_{py} = 2\hat{\mu}\, h_y(z)\,dz/\rho(0) \tag{2.23}$$

$$dH_{xy} = 2\hat{\mu}\, h_{xy}(z)\,dz/\rho(0) \tag{2.24}$$

We note that {D} is an adequate approximation to the elastic matrix {E}. It is evident from equation (2.9a) that when $\rho(0) \to \infty$, {D} becomes the elastic matrix {E}. Take plane stress as an example on the simple tension curve (Fig. 1) draw

$$\lim_{\rho(0)\to\infty} \{D\} = \{E\} = \frac{E}{2(1+\nu)(1-\nu)} \begin{Bmatrix} 2 & 2\nu & 0 \\ 2\nu & 2 & 0 \\ 0 & 0 & (1-\nu) \end{Bmatrix} \tag{2.25}$$

We use axial tension to show the geometric meaning of equation (2.11). From a point A on simple tension curve (Fig. 1) draw a straight line AB, the slope of which is Young's modulus E and its horizontal projection is $d\varepsilon$. For simple tension

$$\{D\}\{d\varepsilon\} = E\,d\varepsilon \tag{2.26}$$

and

$$BD = E\,d\varepsilon$$

so BD can be considered as the first term of right hand in (2.11). Since CD is equal to $d\sigma$, the geometric meaning of dH_p is represented by the segment BC the value of which is negative for simple tension.

Using (2.11) and the principle of virtual work [11], one may formulate an initial stress finite element computational algorithm of the endochronic theory. In fact, we have

$$\iiint_V \{\sigma\}^T \{\delta\varepsilon\} dv = \{p_{ex}\}^T \delta\{q\} \tag{3.1}$$

and $\{p_{ex}\}$ and $\{q\}$ are respectively the vectors of nodal external forces and displacements of the element. Substituting (2.11) into (3.1) one finds that

$$\{K\}\ \{\Delta q\} = \{\Delta p_{ex}\} + \{\Delta p_p\} \tag{3.2}$$

where $\{K\}$ is the stiffness matrix of the element and is the same as the stiffness matrix of an element in the usual elastic analysis but the constants C_1, C_2 are obtained from equations (2.14 - 2.16) or (2.20 - 2.21).

The quantity $\{\Delta P_p\}$ is the incremental plastic pseudo-force vector for a typical triangular element used in the analysis and has the form

$$(\Delta P_{px})_i = -\frac{t}{2}(\alpha_i \Delta H_{px} + \beta_i \Delta H_{pxy})$$

$$(\Delta P_{py})_i = -\frac{t}{2}(\beta_i \Delta H_{py} + \alpha_i \Delta H_{pxy}) \qquad i = 1,2,3 \tag{3.3}$$

Where the components of $\{\Delta H_p\}$ are given in equations (2.17 -19) or (2.22-24) by changing operator "d" to "Δ". α_i and β_i are related to the differences of nodal coordinates, i.e.,

$$\alpha_i = \frac{1}{2} e_{ijk}\Delta y_{jk} \quad , \quad \beta_i = -\frac{1}{2} e_{ijk}\Delta x_{jk} \qquad (i = 1,2,3) \tag{3.4}$$

where $\Delta y_{jk} = y_j - y_k$, $\Delta x_{jk} = x_j - x_k$ and e_{ijk} is the permutation symbol.

From equations (3.2) and (3.3) one obtains the total stiffness matrix $\{k\}$, total plastic pseudo force matrix $\sum\{\Delta P_p\}$ and the linear simultaneous equations for the structure.

THE CALCULATION OF h(z)

Equations (2.17) through (2.19) show that $\underset{\sim}{h}(z)$ plays a central role in the calculation of $\{\Delta H_p\}$ and plastic pseudo-force $\{\Delta P_p\}$. To calculate h(z) numerically, we divide the domain of integration (0,z) in equation (2.8) into n subregions whereupon

$$h(z_m) = \int_0^{z_1} \hat{\rho}(z_m - z') \frac{\partial \underset{\sim}{e}^p}{\partial z'} dz' \ldots\ldots + \int_{z_{i-1}}^{z_i} \hat{\rho}(z_m - z') \frac{\partial \underset{\sim}{e}^p}{\partial z'} dz' \ldots\ldots$$

$$\ldots + \int_{z_{m-1}}^{z_m} \hat{\rho}(z_m - z') \frac{\partial \underset{\sim}{e}^p}{\partial z'} dz' \tag{4.1}$$

where z_{i-1}, z_i are the intial and end values, respectively, of the intrinsic time scale of ith interval, which corresponds

to the ith incremental loading process, and z_m is the current value of the intrinsic time scale.

The mean value theorem, and the smoothness of $\underset{\sim}{e}^p$ allows the approximation

$$\int_{z_{i-1}}^{z_i} \hat{\rho}(z_m - z')\, \frac{\partial \underset{\sim}{e}^p}{\partial z'}\, dz' \approx \left.\frac{\partial \underset{\sim}{e}^p}{\partial z}\right|_{z=z_i} \int_{z_{i-1}}^{z_i} \hat{\rho}(z_m - z')\, dz' \tag{4.2}$$

provided that there is no strain reversal in the interval considered. In the present work we approximate the series on the right hand side of equation (2.5) by three terms, i.e.,

$$\rho(z) = \sum_{r=1}^{3} C_r e^{-\alpha_r z} \tag{4.3}$$

Substituting equation (4.3) into equation (4.1) and using equation (4.2) we obtain the result

$$\underset{\sim}{h}(z_m) = \sum_{r=1}^{3} \sum_{i=1}^{m} C_r \left.\frac{\partial \underset{\sim}{e}^p}{\partial z}\right|_{z=z_i} e^{-\alpha_r (z_m - z_{i-1})} \left[1 - e^{\alpha_r (z_i - z_{i-1})}\right] \tag{4.4}$$

This form of $\underset{\sim}{h}$ is unsuitable for numerical compulation. The term $\alpha_r(z_m - z_{i-1})$ may in the course of calculation become very large of ther order of 5×10^4. Consequently, the value of the function $\exp\{-\alpha_r(z_m - z_{i-1})\}$ becomes a very small number leading to serious truncation errors. To avoid this difficulty we proceed as follows. By mathematical induction the following formula can be shown:

$$\underset{\sim}{h}(z_i) = \sum_{r=1}^{3} h(z_{i-1})e^{-\alpha_r \Delta z_i} + \sum_{r=1}^{3} c_r(e^{-\alpha_r \Delta z_i} - 1) \left.\frac{\partial \underset{\sim}{e}^p}{\partial z}\right|_{z=z_i} \quad (i = 1,..m \tag{4.5}$$

where $\underset{\sim}{h}(0) = 0$ and $\Delta z_i = z_i - z_{i-1}$.

This is an important result to the effect that the history dependence of the material response (through $\underset{\sim}{h}(z_i)$) at the intrinsic time z_i will be determined by $\underset{\sim}{h}(z_{i-1})$ and the new incremental step (through $\left.\frac{\partial \underset{\sim}{e}^p}{\partial z}\right|_{z=z_i}$ and z_i). This formula is also of value in the computer program, because (a) one need only store the information at z_{i-1} to obtain results at z_i, and (b) when using (4.5) instead of equation (4.4), the value of the term $\exp(\alpha_r \Delta z_i)$ is no longer small thus avoiding truncation errors present in the previous formulation (equation 4.4).

THE ITERATIVE PROCESS

For every increment of loading or unloading an initial value Δz^o is assigned to the increment of intrinsic time. The linear simultaneous equations are then solved and the displacement increments are obtained, from which the total deviatoric strain $\Delta \underset{\sim}{e}$ is calculated. Also $\Delta \underset{\sim}{s}$ and $\Delta \underset{\sim}{e}^p$ are calculated using equations (2.10) and (2.3) respectively. Upon use of equations (2.1a), (2.1b) and (4.5) Δz, $\frac{\partial \underset{\sim}{e}^p}{\partial z}$ and $\underset{\sim}{h}$ are obtained. Also, from equations (2.17)-(2.19) or (2.22)-

(2.24) ΔH_{px}, ΔH_{py}, ΔH_{pxy} and finally (ΔP_p) are obtained. Substituting $\{\Delta P_p\}$ into the simultaneous equations (4.2) we then obtain a new solution for the displacement increments as well as the other variables, including Δz. The iteration process is continued until the difference in two consecutive values of Δz, corresponding to two consecutive iterations, is less than some defined tolerance. Results are stored for the next step. The new loading process is then repeated.

In this initial stress method of classical plasticity one [12] usually stops the iteration process if the difference in the magnitudes of the plastic pseudo-force vector corresponding to two consecutive iterations is sufficiently small. We use the scale Δz as a criterion of convergence instead of the pseudo-force vector, not only because of its simplicity but because of its crucial role in endochronic plasticity.

CONVERGENCE AND TOLERANCE

The rate of convergence is very important because it relates to consumption of computer time, truncation error and other related considerations. The key of accelerating the convergence rate is how to choose the initial Δz in order to begin the iteration process of a new incremental loading (unloading) step. An accelerator K_a was used to determine the starting value of the increment of intrinsic time Δz_I^o by the relation

$$\Delta z_I^o = K_a^I \Delta z_{I-1}^L \qquad (6.1)$$

where the subscript I denotes the current incremental loading step and I-1 denotes the preceding step. The superscript o denotes the initial value, L denotes the last value and K_a^I is called the accelerator for the I'th increment. Equation (6.1) is not suitable for reversal points, at which Δz_I^o is taken equal to zero, because at the onset of unloading the response is elastic. The value of the accelerator was determined by the ratio of the final value of Δz in the two previous steps, i.e.,

$$K_a^I = \frac{\Delta z_{I-1}^L}{\Delta z_{I-2}^L} \tag{6.2}$$

With the exception of the first few (three) increments the value of K_a^I was substantially constant. To illustrate its utility and average value of 1.24 was used and the number of iterations needed for convergence was compared in cases where $K_a^I = 1$ and $K_a^I = 0$. See Fig. 2 where n pertains to the fifteenth increment and ε^{yp} is the plastic strain near the tip of the notch. Curve 1 ($K_a = 0$) shosws that the convergent process is very slow. The reason is that at the first iteration $\Delta z_I^o = 0$ since $K_a = 0$ and therefore $\{\Delta P\}^P = 0$, i.e., the loading process so initiated is elastic and is far away from the real case. Curve 2($K_a = 1$) shows the convergent rate is much better than in curve 1, because it takes the final value of Δz in the previous incremental loading step as the initial value of Δz in the current step. However, in this procedure the plastic pseudo-load is underestimated. A value of K_a greater than

unity does increase the rate of convergence as shown in curve 3 ($K_a = 1.24$). Figure 3 shows the effect of accelerator factor K_a on the average iteration number N_{ave} per incremental loading step.

By definition the relative error ERR is defined as

$$ERR = \frac{\Delta z_n - \Delta z_{n-1}}{\Delta z_n} \qquad (4.41)$$

where n is the number of iteration steps. Tolerance is defined as the maximum acceptable value of ERR. Figures 4 and 5 show the effect of tolerance on the accuracy and rate of convergence. In the example shown the smaller the tolerance the higher the accuracy (Fig. 4), but the number of iterations increases (Fig. 5). One however must guard against an excessively small tolerance, which may lie outside the inherent accuracy of the numerical computation and computer capability, leading to accumulation of truncation errors. In the present work the tolerance was 1%.

COMPARISON BETWEEN EXPERIMENTAL DATA AND CALCULATED RESULTS

To verify the validity of the endochronic analysis, using the present numerical algorithm, the distribution of strain of a notched specimen (made of OFHC copper) cyclicly loaded in its own plane was calculated and measured. One quarter of the specimen is shown in Fig. 6. The material functions $\rho(z)$ and $f(\zeta)$ were determined by means of an experiment on a round

specimen of precisely the same material as the notched specimen, in terms of purity, grain size and treatment. The method of determination of these functions will not be given here but may be found in Ref. 13. Suffice it to say that they are of the following form:

$$\rho(z) = \sum_{r=1}^{3} A_r e^{-\alpha_r z} \qquad \text{(GPA)}$$

where $A_{1,2,3} = (592, 220, 46)$ and $\alpha_{1,2,3} = (27.5, 11.5, 7.67) \times 10^3$ and

$$f(\zeta) = 1 + 0.53\zeta^{0.72}$$

The calculations were conducted on an electronic computer (AMDAHL 470 V/7A, close to IBM 370) in the computer center of the University of Cincinnati. There are 413 elements and 230 nodes in one quarter of the specimen (Fig. 6). The side of the smallest element is 0.25 mm. By "varying band storage" the amount of storage for the total stiffness matrix is 17698. The incremental loading for each step is 4% of the maximum load. The average number of iterations for each incremental loading was about 10, varying from 3 to 20. The computer time for each iteration was about 3.36 sec., most of which is used to solve the 460 simultaneous equations. The experiments were conducted in Metcut Research Associates Corporation. The strain distribution was measured using strain gauges, the smallest nominal length of which was 0.2 mm. Since the locations of the elements and the strain gauges did not coincide exactly, we compared the calculated results with experimental data in terms of plotted curves. Comparisons were made over a wide

range of magnitude of applied maximum stress, location and type of histories.

Measured and Calculated Strain Distributions ε_y Along the Notch Center Line oo' are Shown, for Applied Stress Amplitude 3.7×10^7 PA

(i) at first tensile peak A. Fig. 7

(ii) at first unloading point C. Fig. 8

(iii) at first compressive loading peak B. Fig. 9

Letter designations as shown in those Figures.

Measured and Calculated Strain Distributions ε_y Along the Vertical Line ob are Shown for Applied Stress Amplitude 2.3×10^7 PA

(i) at first tensile peak E. Fig. 10

(ii) at first compressive peak L. Fig. 11

(iii) at second loading peak H. Fig. 12

Letter designations as shown in above figures.

Despite the complexity of the boundary value problem and the inherent experimental difficulties the agreement between experimental and calculated results is excellent both from the aspect of tendency and magnitude.

REFERENCES

1. Lamba, H.S. and Sidebottom, O.M., "Biaxial Cyclic Hardening of Anealed Copper Cylinders Evaluated by Deformation Plasticity Theories," T. & A.M. Report No. 406 (1976), The University of Illinois, Urbana-Champaign.

2. Hunsaker, B. Jr., Vanghan, D.K. and Stricklin, J.A., "A Comparison of the Capacity of Four Hardening Rules to Predict a Material's Plastic Behavior," TEES-RPT-2926-73-3, Oct. 1973. Aerospace Engineering Department, Texas A. & M. University, College Station, Texas.

3. Tanaka, M., "Large Deflection Analysis of Elastic-Plastic Circular Plates with Combined Isotropic and Kinematic Hardening," Ingenicur-Archiv 41, 1972, pp. 342-356.

4. Haythronthwaite, R.M., "A More Rational Approach to Strain Hardening Data," Engnr. Plasticity, J. Heymon & F.A. Leckie, (ed.), Cambridge Press, 201 (1968).

5. Valanis, K.C., "A Theory of Viscoplasticity Without a Yield Surface, Part I. General Theory," Archives of Mechanics, 1971, pp. 517-533.

6. Valanis, K.C., "A Theory of Viscoplasticity without a Yield Surface. Part II. Application to Mechanical Behavior of Metals," Archives of Mechanics, 1971, pp. 535-551.

7. Valanis, K.C., "Endochronic Theory with Proper Hysteresis Loop Closure Properties," Systems, Science and Software Report SSS-R-80-4182, 1979.

8. Valanis, K.C. and Read, H., "New Endochronic Plasticity Model for Soils," Soil Mechanics - Transient and Cyclic Loads. Ed. G.N. Pande and O.C. Zienkiewicz, John Wiley and Sons, 1982.

9. Valanis, K.C. and Lee, C.F., "Some Recent Developments of the Endochronic Theory with Applications," Nuclear Eng. and Design, 69, 1983, pp. 327-343.

10. Lin, H.C. and Wu, H.C., "On the Improved Endochronic Theory of Viscoplasticity and It's Application to Plastic-Wave Propagation," to be published in Int. J. Solids Structures.

11. Argyris, J.H., "Energy Theorems and Structural Analysis," Butterworth, 1960. (Reprinted from Aircraft Eng., 1954-1955).

12. Zienkiewicz, O.C., Valliappan, S. and King, I.P., "Elasto-plastic Solutions of Engineering Problems 'Initial Stress', Finite Element Approach," International Journal for Numerical Methods in Engineering. Vol. 1, 1969, pp. 75-100.

13. Fan, Jinghong, "A Comprehensive Numerical Study and Experimental Verification of Endochronic Plasticity," Ph.D. Dissertation, Department of Aerospace Engineering and Applied Mechanics, University of Cincinnati, 1983.

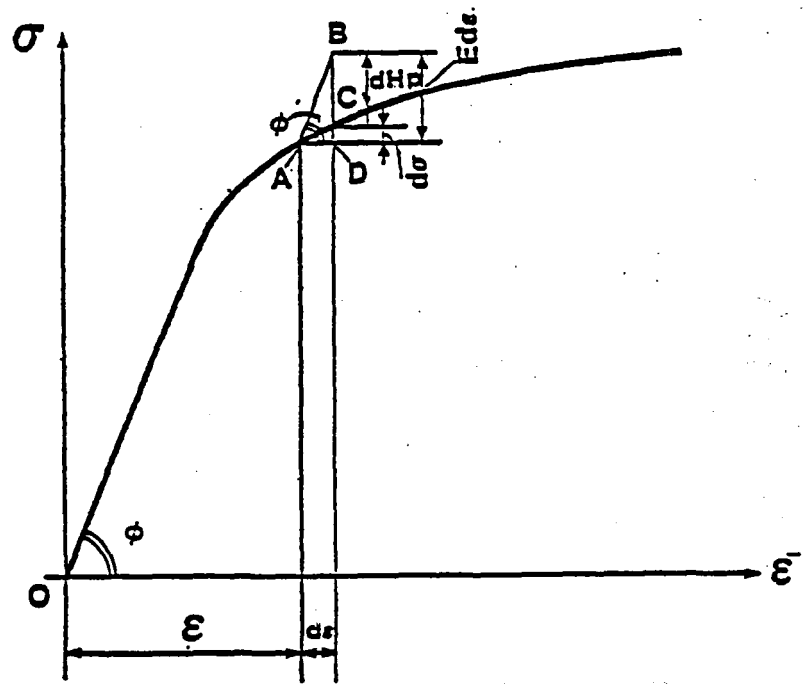

Figure 1. - The Geometric Meaning of The Incremental Endochronic Elastoplastic Constitutive Equation

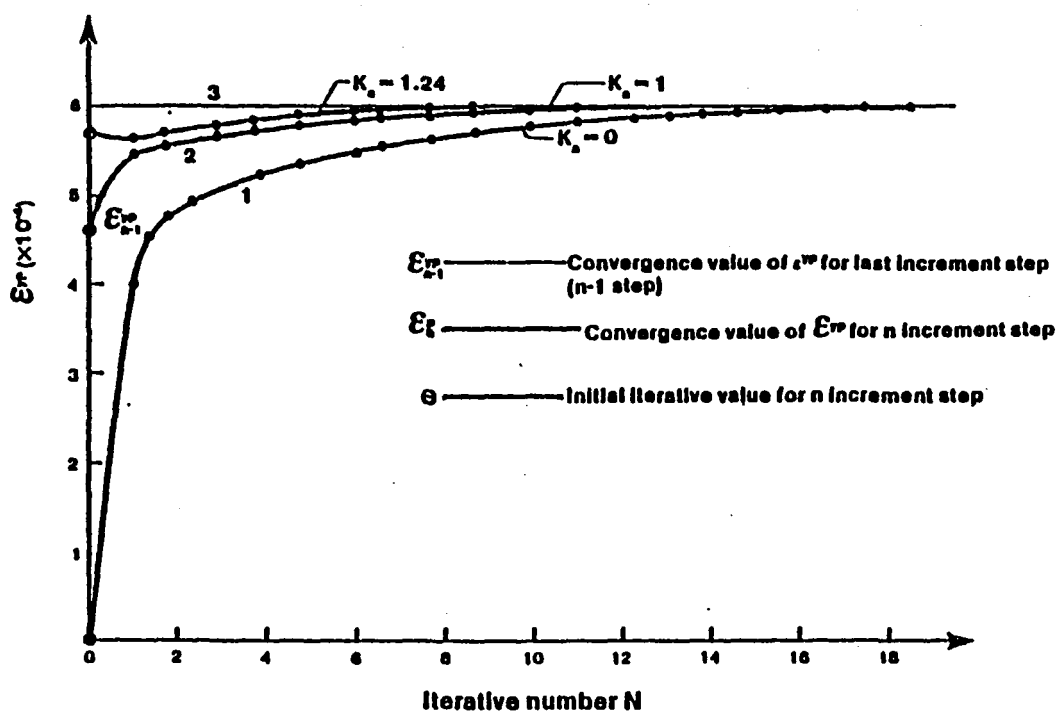

Figure 2. - The Effect of Acceleration Factor K_a on the Convergence of $\varepsilon_{y_{max}}$

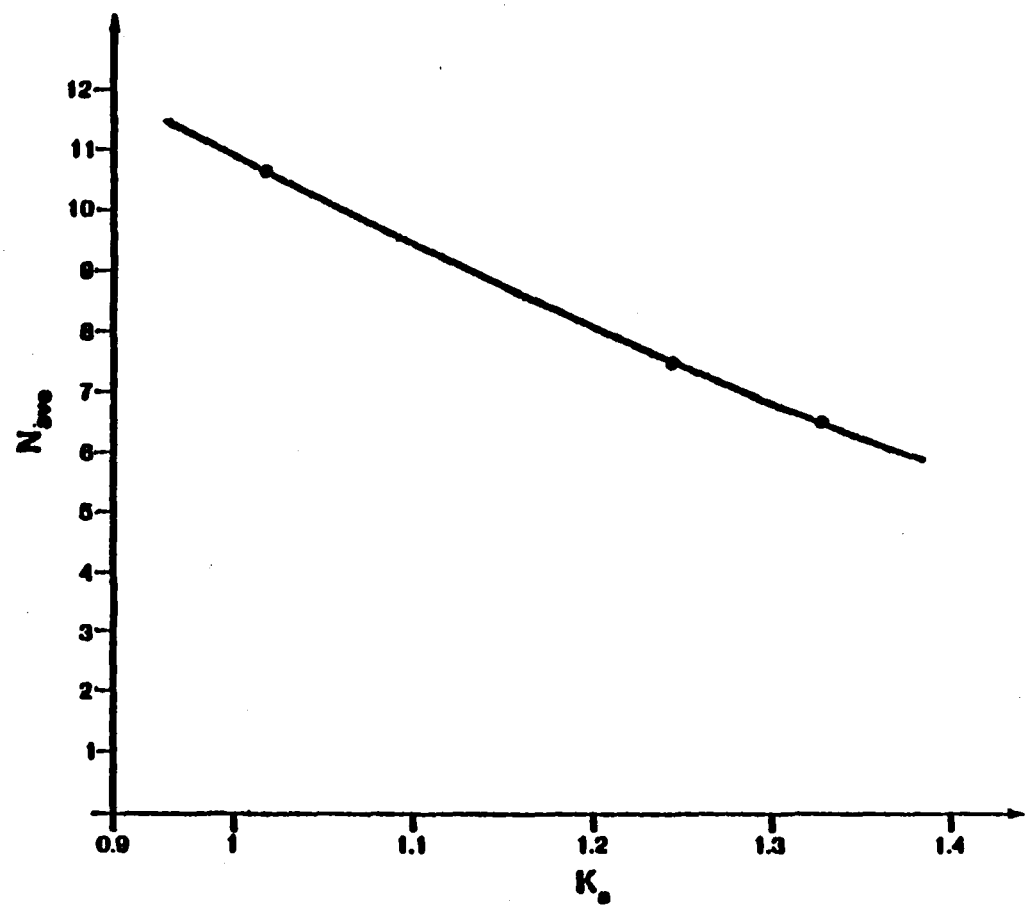

Figure 3. - The Effect of Acceleration Factor K_a on the Average Iteration Numbers per Incremental Loading Step

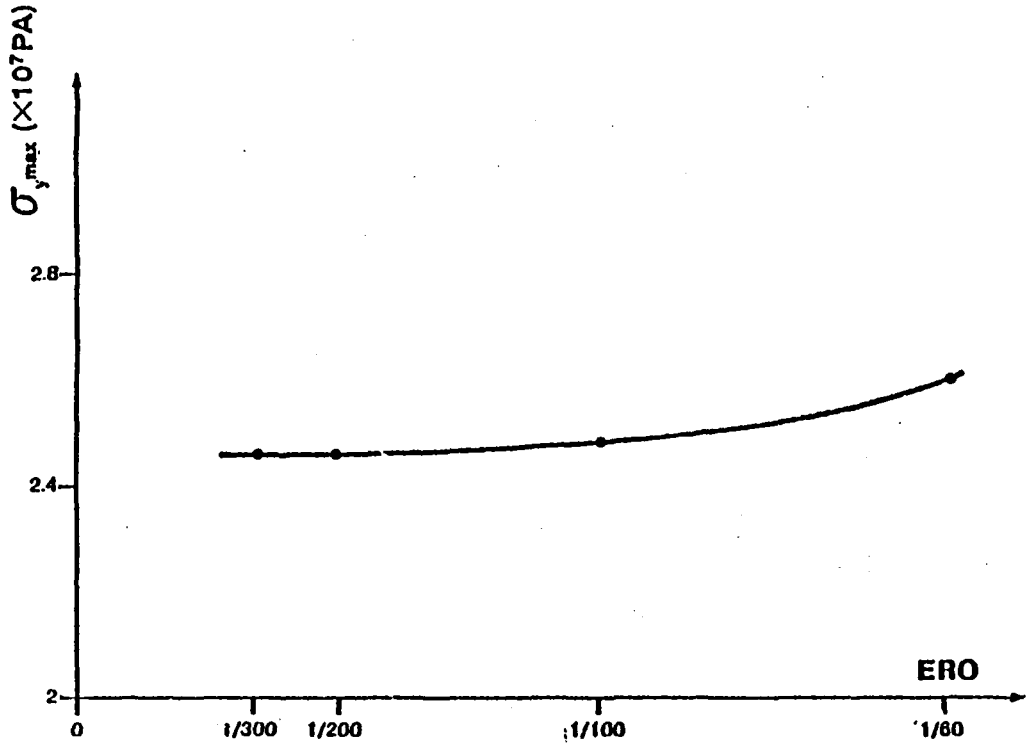

Figure 4. - The Effect of Tolerance on the Magnitude of $\sigma_{y_{max}}$

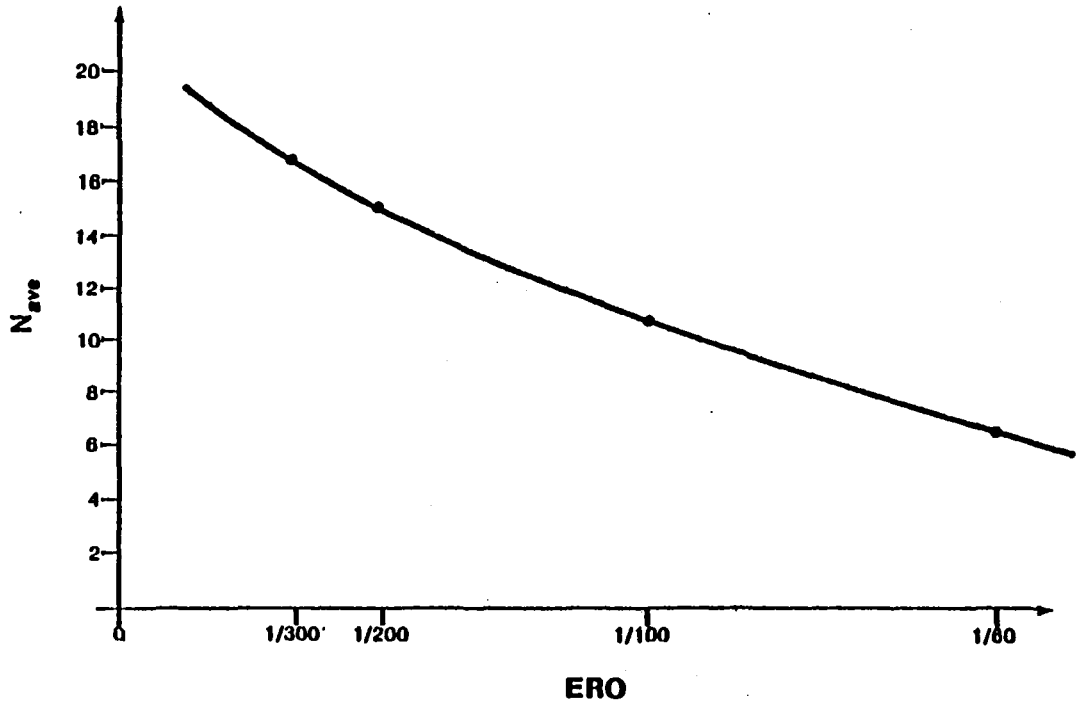

Figure 5. - The Effect of the Tolerance on the Average Iteration Number per Incremental Loading Step

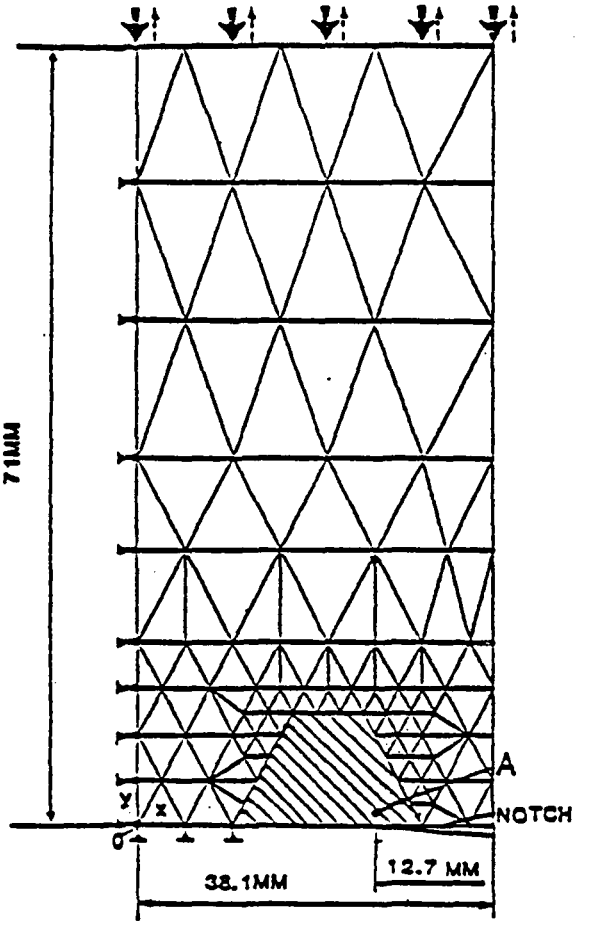

(a) Coarse Mesh

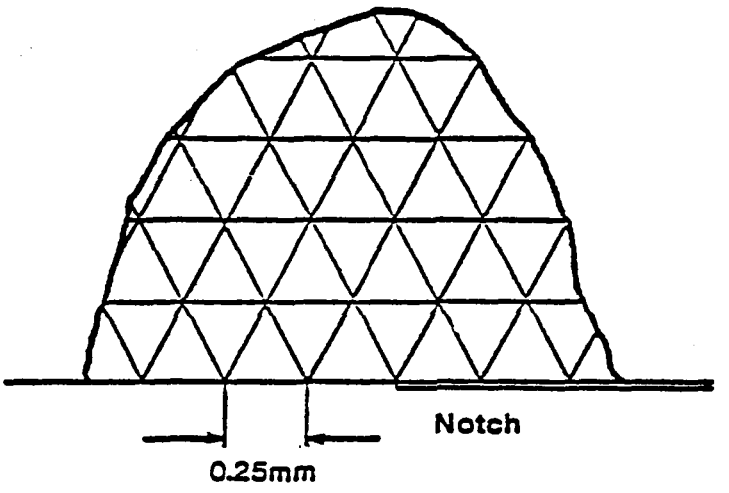

(b) Fine Mesh Near the Notch Tip

Figure 6. - Plate Geometry and Grid Arrangement (one quarter)

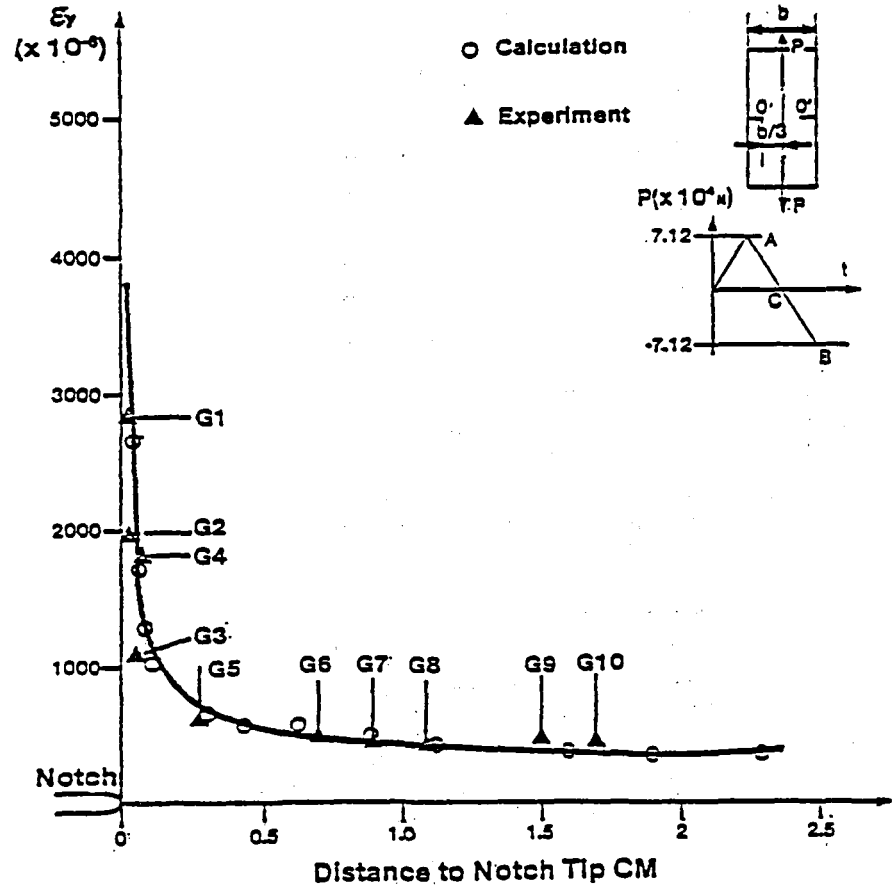

Figure 7. - Comparison Between Experimental and Calculated Distribution of Strain ε_y Along Notch Line OO' at Positive Peak A

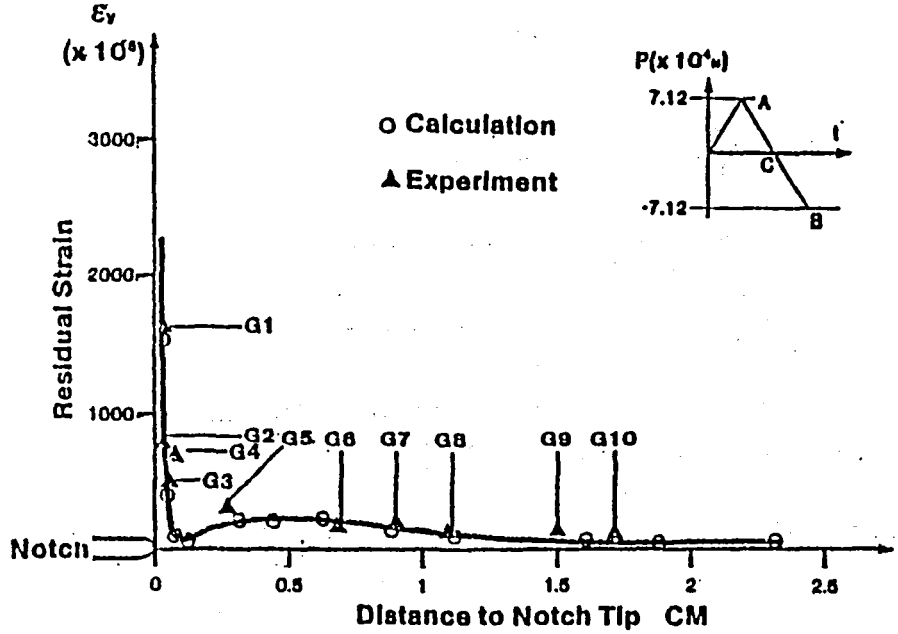

Figure 8. - Comparison Between Experimental and Calculated Residual Strain Distribution ε_y Along Notch Line OO' at Point C

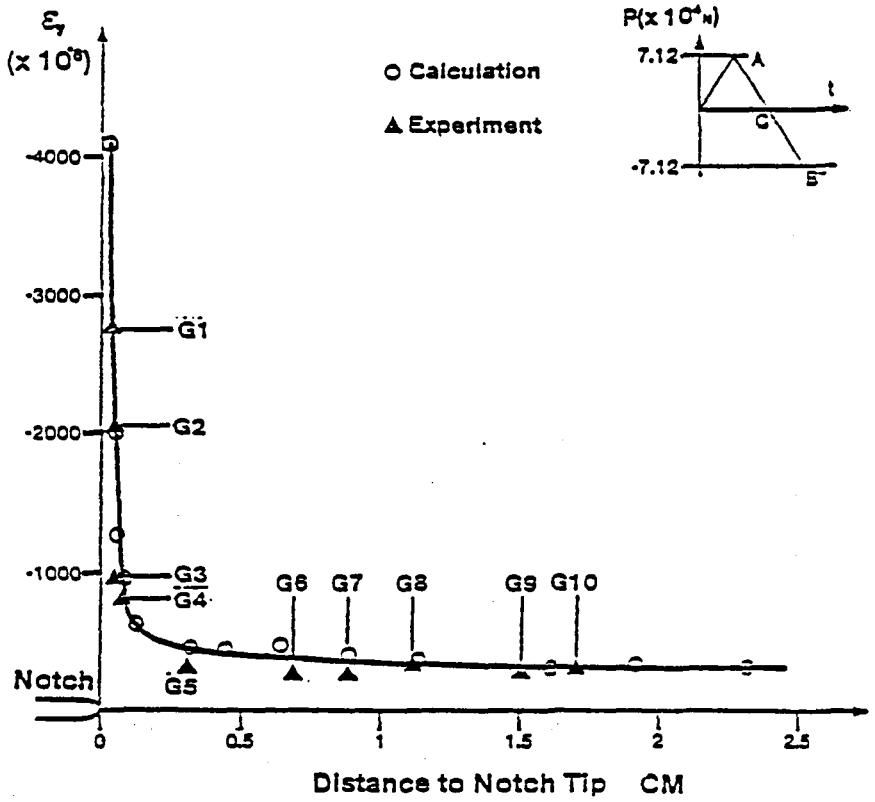

Figure 9. - Comparison Between Experimental and Calculated Strain Distribution ε_y Along Notch Line OO' at Negative Peak B

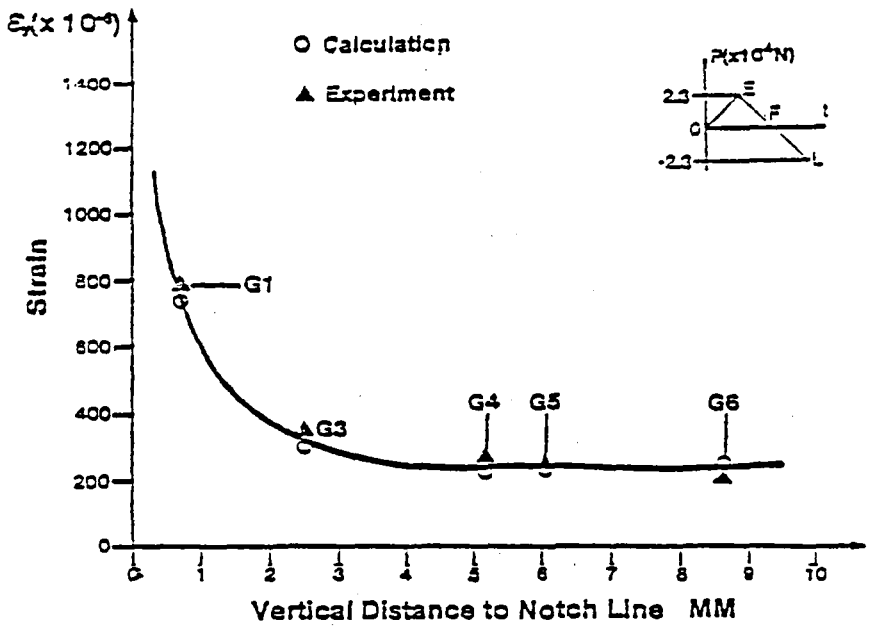

Figure 10. - Comparison Between Experimental and Calculated Strain Distribution ε_y at the Positive Peak E Along the Vertical Line ob at the Top of Notch Tip

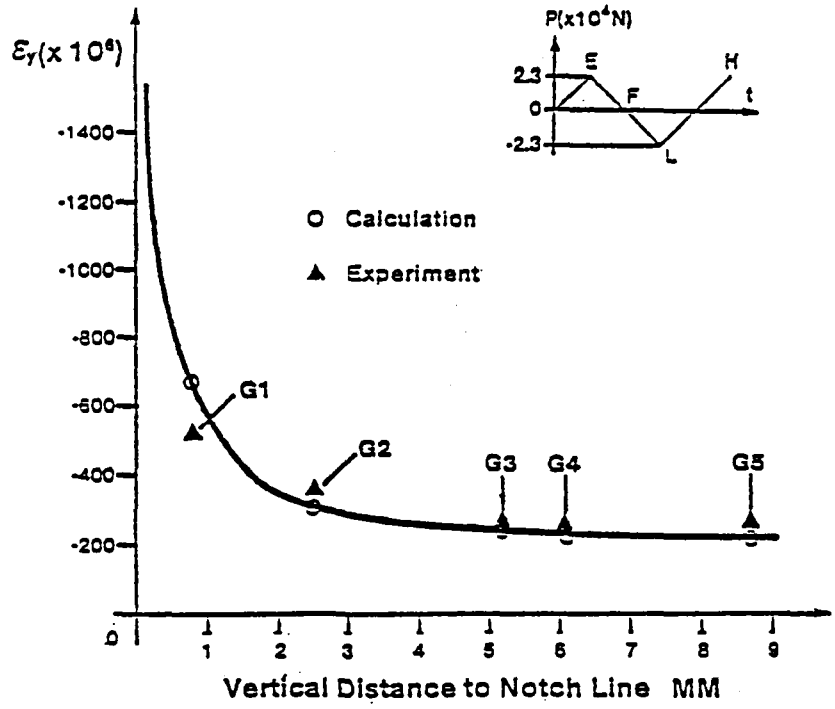

Figure 11. - Comparison Between Experimental and Calculated Strain Distribution ε_y at the Negative Peak L Along the Vertical Line ob at the Top of Notch Tip

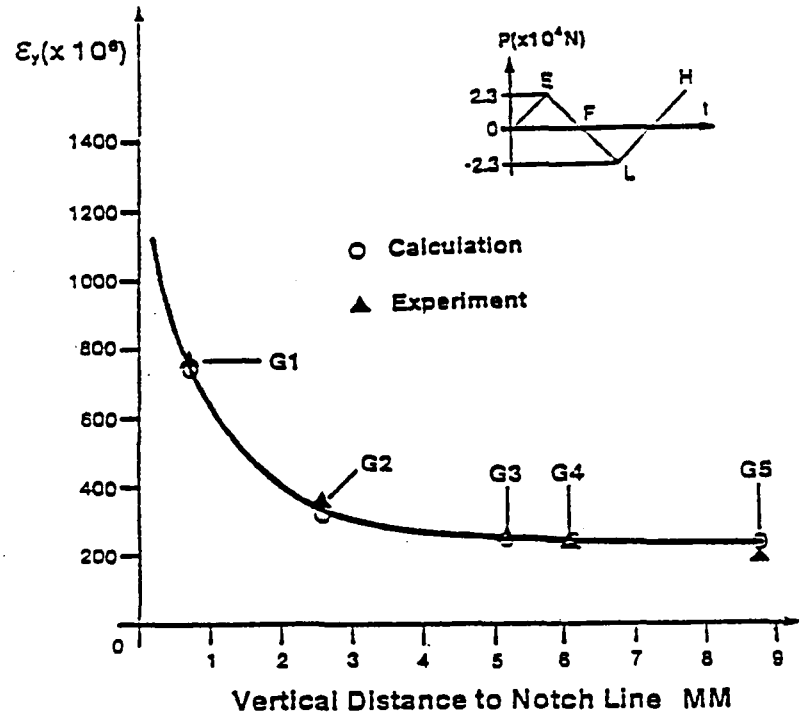

Figure 12. - Comparison Between Experimental and Calculated Strain Distribution ε_y at the Positive Peak E Along the Vertical Line ob at the Top Notch Tip

Page intentionally left blank

THERMOMECHANICALLY INDUCED PRE AND POSTBUCKLING OF GENERAL STRUCTURE

Joseph Padovan
The University of Akron
Akron, Ohio 44325

This paper develops an algorithmic solution strategy which enables handling the positive/indefinite stiffness characteristics associated with the pre and postbuckling of structures subject to complex thermomechanical loading fields. The flexibility of the procedure is such that it can be applied to both finite difference and element type simulations. Due to the generality of the algorithmic approach developed, both kinematic and thermal/mechanical type material nonlinearity including inelastic effects can be treated. This includes the possibility of handling completely general thermomechanical boundary conditions. To demonstrate the scheme, the results of several benchmark problems is presented.

INTRODUCTION

Literally a multitude of studies have been reported on the isothermal simulation of problems wherein kinematic and/or material nonlinearity is excited. In recent years, most typically such work involved the use of the powerful finite element (FE) scheme [1]. In contrast, much less work is available for nonisothermal versions of such problems. This is an outgrowth of several main factors namely:

i) Unlike mechanical type loads which are generally applied at specific points around a given structure, transient thermally induced loads occur at every body point causing complex distributed loading and unloading fields which typically induce difficulties in simulating proper inelastic type behavior;

ii) Since thermal loads are internally induced, for nonlinear situations, it is typically quite difficult to adequately forecast the level of incrementation necessary for nonlinear equation solvers to yield converged solutions without involving an expensive time consuming trial and error procedure;

iii) For problems with highly nonlinear kinematic behavior, little is understood of the process of thermomechanical interaction; and lastly,

iv) Thermomechanically induced pre and postbuckling behavior exhibits indefinite stiffness characteristics [2]; such behavior precludes the use of the classical form of the incremental Newton Raphson (INR) scheme which is restricted to problems with a given definiteness [2,3].

Since numerous thermomechanical problems fall into the foregoing categories, this paper will consider the development of a solution strategy which

bypasses the difficulties denoted by items i) - iv) noted earlier. Specifically, a constrained type strategy [4-7] will be developed for use with either the finite element [1] or difference methodologies. The generality of the procedure is such that both pre and postbuckling behavior can be handled along with arbitrary kinematic and material nonlinearity. In this context, problems exhibiting indefinite stiffness characteristics can be handled.

GOVERNING EQUATIONS: MECHANICAL

Assuming the possibility of large deformations, the equations of motion complementing the thermal formulation are given by the expression

$$\frac{\partial}{\partial a_j}\left(S_{jk}\left(\delta_{ik} + \frac{\partial u_i}{\partial a_k}\right)\right) + g_{oi} = \rho_o \frac{\partial^2 u_i}{\partial t} \tag{2.1}$$

where g_{oi} designates the body force vector, δ_{ik} is the Kronecker delta, S_{ji} the second Piola Kirchhoff stress tensor, u_i the deflection vector and a_j the Lagrangian coordinates. For the current purposes, the Lagrangian strain measure L_{ij} is employed in conjunction with S_{ij} namely

$$L_{ij} = \frac{1}{2}\left(\frac{\partial u_i}{\partial a_j} + \frac{\partial u_j}{\partial a_i} + \frac{\partial u_\ell}{\partial a_i}\frac{\partial u_\ell}{\partial a_j}\right. \tag{2.2}$$

In terms of the S_{ij} and L_{ij} measures, the thermoelastic-plastic behavior is handled in terms of the usual yield surface flow rule assumption. The creep effects will be treated in terms of strain hardening concepts wherein variations in creep rate depend on the existing strain rate. From a computational point of view, the overall thermoelastic-plastic-creep behavior is solved via incremental type flow rules. Under the condition of large deformation moderate strain behavior and the usual flow rule assumption, the following incremental type constitutive relation is adopted, that is [8]

$$\Delta \underset{\sim}{S} = [D_{ep}](\Delta \underset{\sim}{L} - \Delta \underset{\sim}{L}_C - \Delta \underset{\sim}{L}_T) \tag{2.3}$$

where $[D_{ep}]$ is the elastic-plastic material stiffness and $\Delta \underset{\sim}{L}$, $\Delta \underset{\sim}{L}_C$ and $\Delta \underset{\sim}{L}_T$ are increments in Lagrangian creep and thermal strain. For the current work, $\Delta \underset{\sim}{L}_C$ is expressed in terms of mechanical equations of state. In particular, it takes the form

$$\Delta \underset{\sim}{L}_C = \Delta t\ \gamma\ \underset{\sim}{S}_d \tag{2.4}$$

where S_d is the deviatoric stress and

$$\gamma = \frac{1}{\sigma_d}\frac{\partial \varepsilon_c}{\partial t} \tag{2.5}$$

such that σ_d and $\frac{\partial \varepsilon_c}{\partial t}$ are respectively the equivalent stress and creep strain rates. Lastly, the increment in thermal strain appearing in (2.3) is defined by

$$\Delta \underset{\sim}{L}_T = \underset{\sim}{\alpha} \Delta T \tag{2.6}$$

where $\underset{\sim}{\alpha}$ is the thermal expansion coefficient matrix and ΔT is the temperature increment. Note, based on the thermal fields generated earlier, it follows that the various coefficients are temperature dependent.

In the context of (2.3) it follows that depending on the load step, the current stress state is given by the expression

$$\underset{\sim}{S} = \Sigma \Delta \underset{\sim}{S} \tag{2.7}$$

where the matrix S takes the form

$$\underset{\sim}{S}' = (\underset{\sim}{S}_{11}, \underset{\sim}{S}_{22}, \underset{\sim}{S}_{33}, \underset{\sim}{S}_{12}, \underset{\sim}{S}_{23}, \underset{\sim}{S}_{31}) \tag{2.8}$$

Noting the linear structure of $\Delta \underset{\sim}{S}$, we see that the incremental scheme enables the following segregation of contributing components namely

$$\underset{\sim}{S} = \underset{\sim}{S}_{ep} + \underset{\sim}{S}_{epc} + \underset{\sim}{S}_{epT} \tag{2.9}$$

where

$$\underset{\sim}{S}_{ep} = \Sigma \Delta \underset{\sim}{S}_{ep} \tag{2.10}$$

$$\underset{\sim}{S}_{epc} = \Sigma \Delta \underset{\sim}{S}_{epc} \tag{2.11}$$

$$\underset{\sim}{S}_{epT} = \Sigma \Delta \underset{\sim}{S}_{epT} \tag{2.12}$$

such that

$$\Delta \underset{\sim}{S}_{ep} = [D_{ep}] \, \Delta \underset{\sim}{L} \tag{2.13}$$

$$\Delta \underset{\sim}{S}_{epc} = - [D_{ep}] \, \Delta \underset{\sim}{L}_C \tag{2.14}$$

$$\Delta \underset{\sim}{S}_{epT} = - [D_{ep}] \, \Delta \underset{\sim}{L}_T \tag{2.15}$$

As will be seen later, such a partitioning of the stress state will enable the establishment of an improved control of successive iterates during the incrementation process.

FE FORMULATION/SOLUTION ALGORITHM: MECHANICAL

Following the thermal formulation, we shall employ a displacement type procedure to develop the requisite mechanical FE expressions. In this context, the deflection field is approximated by

$$\underset{\sim}{U} = [N_U] \underset{\sim}{Y} \tag{3.1}$$

where

$$\underset{\sim}{U}' = (u_1, u_2, u_3) \tag{3.2}$$

such that $[N_U]$ is the displacement type shape function while Y is the nodal deflection vector. For consistencies sake, the same order polynomial is used for both the thermal and mechanical phases. Based on (3.1) and the virtual work principle, the following FE expression can be developed [1]

$$[M_U]\ddot{\underset{\sim}{Y}} + \int_{V_o} [B_U^*]' \underset{\sim}{S}\, dv = \underset{\sim}{F}_{ext} \tag{3.3}$$

where

$$[B_U^*] = [B_U] + [B_n][G] \tag{3.4}$$

$$[M_U] = \int_{V_o} \rho_o\, [N_U]'[N_U]\, dv \tag{3.5}$$

$$\underset{\sim}{F}_{ext} = \underset{\sim}{F}_{nodal} + \int_{V_o} [N_U]'\, \underset{\sim}{g}_{ext}\, dv \tag{3.6}$$

such that

$$\underset{\sim}{g}_{ext} = (g_1, g_2, g_3) \tag{3.7}$$

Note $\underset{\sim}{F}_{nodal}$ represents the externally applied nodal loads.

Since dynamic postbuckling problems will be the subject of another paper, for the current purposes, we shall consider quasi-static thermo-mechanical problems. In this context, (3.3) reduces to the form

$$\int_{V_o} [B_U^*]'\, \underset{\sim}{S}\, dv = \underset{\sim}{F}_{ext} \tag{3.8}$$

To simplify the development of the requisite solution algorithm, the partitioned form of $\underset{\sim}{S}$ will be used to recast (3.8) into a more tractable form. Before doing so, we note that due to their analytical form, the creep and thermal partitions of $\underset{\sim}{S}$ can be lumped with $\underset{\sim}{F}_{ext}$ to yield a pseudo applied force field namely

$$\underset{\sim}{F} = \underset{\sim}{F}_{ext} - \int_{V_o} [B_U^*]'\, (\underset{\sim}{S}_{epc} + \underset{\sim}{S}_{epT})\, dv \tag{3.9}$$

Hence (3.8) reduces to the form

$$\underset{\sim}{F} = \int_{V_o} [B_U^*]'\, \underset{\sim}{S}_{ep}\, dv \tag{3.10}$$

Since $\underset{\sim}{S}_{epc}$ and $\underset{\sim}{S}_{epT}$ are time dependent terms, the solution to (3.10) requires the introduction of a time stepping algorithm to generate the requisite solution. This is achieved by expanding (3.10) in truncated Taylor series. To start, $\underset{\sim}{Y}(t+\Delta t)$ is expanded to yield

$$\underset{\sim}{Y}(t+\Delta t) = \underset{\sim}{Y}(t) + \Delta\underset{\sim}{Y} \tag{3.11}$$

Substituting (3.11) into (3.10) and truncating higher order terms yields the expression

$$\int_{V_o} [B_U^*]' \, \underset{\sim}{S}_{ep} \, dv \Big|_{t+\Delta t} = \int_{V_o} [B_U^*]' \, \underset{\sim}{S}_{ep} \, dv \Big|_{t} + [K_U] \Big|_{t} \, \underset{\sim}{\Delta Y} \tag{3.12}$$

where

$$[K_U] \Big|_{t} = \int_{V_o} ([G]'[S][G] + [B_U^*]'[D_{ep}][B_U^*]) \Big|_{t} \, dv \tag{3.13}$$

such that [S(t)] is the prestress matrix at time t. Based on the definition of pseudo force, Eq. (3.9), it follows that

$$\underset{\sim}{F} \Big|_{t+\Delta t} = \underset{\sim}{F}_{ext} \Big|_{t+\Delta t} - \int_{V_o} [B_U^*]' \Big|_{t} \, (\underset{\sim}{S}_{epC} + \underset{\sim}{S}_{epT}) \Big|_{t+\Delta t} \, dv \tag{3.14}$$

Now in terms of (3.10), (3.12) and (3.14), we obtain the following time stepping Newton Raphson type algorithm, that is

$$\underset{\sim}{F}_{ext} \Big|_{t+\Delta t} - \int_{V_o} [B_U^*]' \Big|_{t} \, (\underset{\sim}{S}_{epC} + \underset{\sim}{S}_{epT}) \Big|_{t+\Delta t} \, dv =$$

$$\int_{V_o} [B_U^*]' \, \underset{\sim}{S}_{ep} \Big|_{t} \, dv + [K_U] \Big|_{t} \, \underset{\sim}{\Delta Y} \tag{3.15}$$

Based on the use of such a relation, successive time steps lead to the following thermomechanical history namely

t	T(t)	$\underset{\sim}{S}$(t)	$\underset{\sim}{L}$(t)	...
0	T(0)	$\underset{\sim}{S}$(0)	$\underset{\sim}{L}$(0)	...
Δt	T(Δt)	$\underset{\sim}{S}$(Δt)	$\underset{\sim}{L}$(Δt)	...
$2\Delta t$	T($2\Delta t$)	$\underset{\sim}{S}$($2\Delta t$)	$\underset{\sim}{L}$($2\Delta t$)	...
$3\Delta t$	T($3\Delta t$)	$\underset{\sim}{S}$($3\Delta t$)	$\underset{\sim}{L}$($3\Delta t$)	...
$4\Delta t$	T($4\Delta t$)	$\underset{\sim}{S}$($4\Delta t$)	$\underset{\sim}{L}$($4\Delta t$)	...
⋮	⋮	⋮	⋮	
$i\Delta t$	T($i\Delta t$)	$\underset{\sim}{S}$($i\Delta t$)	$\underset{\sim}{L}$($i\Delta t$)	...

As noted earlier, the NR base of (3.15) suffers from several shortcomings. The more important of these are:

1. Cannot handle turning points (buckling);
2. No direct control on successive iterations; and,
3. Difficult to ascertain zones of convergence as solution proceeds.

Such drawbacks will be circumvented through the use of constraints in the manner of Padovan and Arechaga [6]. Specifically the load increments

associated with successive time steps will be constrained. Such a process leads to nonuniform time stepping. From the nature of (3.15) it follows that constraints must be imposed on increments in the pseudo load F. For the current purposes the hyper-elliptic constraint surface (HECS) of Padovan, Tovichakchaikul and Arechaga [7] will be employed to control successive iterations of a given time step. Such a process is illustrated in Fig. 1. The development of the requisite constraint algorithm for the given problem requires several main steps, namely:

i) Establish form of INR extrapolation for a given iteration;
ii) Establish shape and size of HECS;
iii) Determine intersection of HECS and INR extrapolation;
iv) Establish iterative/time stepping aspects of solution algorithm; and,
v) Establish information required for next time step.

To start the development, it follows from Fig. 1 that the hyperline defining the INR extrapolation takes the form

$$[K_{UB}](\underset{\sim}{y}-\underset{\sim}{y}_B) = (\underset{\sim}{f}-\underset{\sim}{f}_B) \tag{3.16}$$

On solving for y we obtain

$$\underset{\sim}{y} = \underset{\sim}{y}_B + [K_{UB}]^{-1}(\underset{\sim}{f}-\underset{\sim}{f}_B) \tag{3.17}$$

such that

$$\underset{\sim}{f}_B = \underset{\sim}{F}_B - \underset{\sim}{F}_A \tag{3.18}$$

$$\underset{\sim}{y}_B = \underset{\sim}{Y}_B - \underset{\sim}{Y}_A \tag{3.19}$$

The HECS appearing in Fig. 1 is given by the following normed polynomial expression

$$||\underset{\sim}{f}||^2 + \mu_A||\underset{\sim}{y}||^2 = ||\underset{\sim}{f}_C||^2 \tag{3.20}$$

such that

$$\underset{\sim}{f}_C = \underset{\sim}{F}_C - \underset{\sim}{F}_A \tag{3.21}$$

The parameter μ_A appearing in (3.21) regulates the aspect ratio (abscissa/ordinate) of the HECS.

The intersection of the HECS and INR extrapolation occurs at point I as defined in Fig. 1. Specifically the coordinates of position I are given by

$$\underset{\sim}{y}_I = \underset{\sim}{Y}_I - \underset{\sim}{Y}_A \tag{3.22}$$

$$\underset{\sim}{f}_I = \lambda^I (\underset{\sim}{F}_C - \underset{\sim}{F}_A) \tag{3.23}$$

such that λ^I is a single parameter constraint on the allowable load step size and hence the interval in time utilized. Based on (3.22) and (3.23),

it follows that (3.17) and (3.20) yield the expressions

$$\underset{\sim}{y}_I = \underset{\sim}{y}_B + [K_{UB}]^{-1}(\underset{\sim}{f}_I - \underset{\sim}{f}_B) = \underset{\sim}{y}_B + [K_{UB}]^{-1}(\lambda^I \underset{\sim}{f}_C - \underset{\sim}{f}_B) \tag{3.24}$$

$$||\underset{\sim}{f}_I||^2 + \mu_A||\underset{\sim}{y}_I||^2 = ||\underset{\sim}{f}_C||^2 \tag{3.25}$$

In terms of (3.24), (3.25) takes the form

$$||\lambda^I \underset{\sim}{f}_C||^2 + \mu_A||\underset{\sim}{y}_B + [K_{UB}]^{-1}(\lambda^I \underset{\sim}{f}_C - \underset{\sim}{f}_B)||^2 = ||\underset{\sim}{f}_C||^2 \tag{3.26}$$

Expanding (3.26) and collecting like terms in λ^I yields the following polynomial identity namely

$$(\lambda^I)^2\alpha_{1I} + 2\lambda^I\alpha_{2I} + \alpha_{3I} = 0 \tag{3.27}$$

where

$$\alpha_{1I} = ||\underset{\sim}{F}_C||^2 + \mu_A||[K_{UB}]^{-1}\underset{\sim}{F}_C||^2 \tag{3.28}$$

$$\alpha_{2I} = \mu_A(\underset{\sim}{y}_B)'[K_{UB}]'\underset{\sim}{f}_B \tag{3.29}$$

$$\alpha_{3I} = ||\underset{\sim}{y}_B - [K_{UB}]^{-1}\underset{\sim}{f}_B||^2 - ||\underset{\sim}{f}_C||^2 \tag{3.30}$$

Solving (3.27) for λ^I, we obtain

$$\lambda^I = \frac{1}{\alpha_{1I}}\{-\alpha_{2I} \pm \sqrt{(\alpha_{2I})^2 - \alpha_{1I}\alpha_{3I}}\} \tag{3.31}$$

Based on (3.22), (3.24) and (3.31), $\underset{\sim}{Y}I$ the nodal deflection associated with the I^{th} intersection of the INR extrapolation and the HECS takes the form

$$\underset{\sim}{Y}_I = \underset{\sim}{Y}_A + \underset{\sim}{y}_B + [K_{UB}]^{-1}\{\frac{1}{\alpha_{1I}}(-\alpha_{2I} \pm \sqrt{(\alpha_{2I})^2 - \alpha_{1I}\alpha_{3I}})\ \underset{\sim}{f}_C - \underset{\sim}{f}_B\} \tag{3.32}$$

To establish the requisite time stepping aspects of the solution algorithm, the following variables must be redefined in terms of incrementation namely $\underset{\sim}{Y}_A$, $\underset{\sim}{Y}_B$, $\underset{\sim}{Y}_I - \underset{\sim}{Y}_B$, $\underset{\sim}{F}_A$, $\underset{\sim}{F}_B$, $\underset{\sim}{F}_C$ and $[K_{UB}]$. Letting ℓ denote the time step number and i the iteration count, it follows that positions A, B and I in Fig. 1 designate the location of the 0^{th}, i^{th} and $(i+1)^{th}$ iterations. In this context, it follows that

$$\underset{\sim}{Y}_A = \underset{\sim}{Y}^0_{\ell+1} \tag{3.33}$$

$$\underset{\sim}{Y}_B = \underset{\sim}{Y}^i_{\ell+1} = \underset{\sim}{Y}^0_{\ell+1} + \sum_{k=1}^{i} \Delta\underset{\sim}{Y}^i_{\ell+1} \tag{3.34}$$

$$\underset{\sim}{y}_I - \underset{\sim}{y}_B = \Delta\underset{\sim}{Y}^{i+1}_{\ell+1} \tag{3.35}$$

The time associated with point A is the summation of the ℓ preceeding constrained time steps. Hence, since the interval utilized over a given load step is $\lambda_k^{\nabla}\Delta t$, it follows that the time at the end of the ℓ^{th} step is given by

$$t_\ell^\lambda = \sum_{k=1}^{\ell} \lambda_k^{\nabla}\Delta t \tag{3.36}$$

such that λ_k^{∇} is the finally converged value of the constraint for the k^{th} step.

Employing the foregoing nomenclature, it follows that

$$\underset{\sim}{F}_A = \int_{V_o} [B_U^*(\underset{\sim}{Y}^o_{\ell+1})]^{\prime}\underset{\sim}{S}_{ep}(\underset{\sim}{Y}^o_{\ell+1})\, dv \tag{3.37}$$

$$\underset{\sim}{F}_B = \int_{V_o} [B_U^*(\underset{\sim}{Y}^i_{\ell+1})]^{\prime}\underset{\sim}{S}_{ep}(\underset{\sim}{Y}^i_{\ell+1})\, dv \tag{3.38}$$

$$\underset{\sim}{F}_C = \underset{\sim}{f}_{ext}\Big|_{t_\ell^\lambda+\Delta t_{\ell+1}} - \int_{V_o} [B_U^*(\underset{\sim}{Y}^i_{\ell+1})]\,(\underset{\sim}{S}^i_{epC} + \underset{\sim}{S}^i_{epT})\Big|_{t_\ell^\lambda+\Delta t_{\ell+1}} dv \tag{3.39}$$

The various stress components appearing in (3.37) - (3.39) take the form

$$\underset{\sim}{S}_{ep}(\underset{\sim}{Y}^o_{\ell+1}) = \sum_{k=1}^{\ell} \Delta\underset{\sim}{S}_{ep}(\underset{\sim}{Y}^o_k) \tag{3.40}$$

$$\underset{\sim}{S}_{ep}(\underset{\sim}{Y}^i_{\ell+1}) = \underset{\sim}{S}_{ep}(\underset{\sim}{Y}^o_{\ell+1}) + \Delta\underset{\sim}{S}_{ep}(\underset{\sim}{Y}^i_{\ell+1}) \tag{3.41}$$

$$\underset{\sim}{S}_{epC}(t_\ell^\lambda) = \sum_{k=1}^{\ell} \Delta\underset{\sim}{S}_{ep_C}(t_{k-1}^\lambda + \lambda_k^{\nabla}\Delta t_k) \tag{3.42}$$

$$\underset{\sim}{S}^i_{epC}(t_\ell^\lambda + \Delta t) = \underset{\sim}{S}_{epC}(t_\ell^\lambda) + \Delta\underset{\sim}{S}^i_{epC}(t_\ell^\lambda+\Delta t) \tag{3.43}$$

$$\underset{\sim}{S}_{epT}(t_\ell^\lambda) = \sum_{k=1}^{\ell} \Delta\underset{\sim}{S}_{epT}(t_{k-1}^\lambda+\lambda_k^{\nabla}\Delta t_k) \tag{3.44}$$

$$\underset{\sim}{S}^i_{epT}(t_\ell^\lambda+\Delta t) = \underset{\sim}{S}_{epT}(t_\ell^\lambda) + \Delta\underset{\sim}{S}^i_{epT}(t_\ell^\lambda+\Delta t) \tag{3.45}$$

such that the various increments are given by

$$\Delta\underset{\sim}{S}_{ep}(\underset{\sim}{Y}^i_{\ell+1}) = [D_{ep}(\underset{\sim}{Y}^i_{\ell+1})]\Delta\underset{\sim}{L}(\underset{\sim}{Y}^i_{\ell+1}) \tag{3.46}$$

$$\Delta\underset{\sim}{L}(\underset{\sim}{Y}^i_{\ell+1}) = [B_U^*(\underset{\sim}{Y}^i_{\ell+1})](\underset{\sim}{Y}^i_{\ell+1} - \underset{\sim}{Y}^o_{\ell+1}) \tag{3.47}$$

$$\Delta\underset{\sim}{S}_{epC}(t_{k-1}^\lambda + \lambda_k^{\nabla}\Delta t) = -[D_{ep}(\underset{\sim}{Y}_k)]\Delta\underset{\sim}{L}_C(t_{k-1}^\lambda, \lambda_k^{\nabla}\Delta t) \tag{3.48}$$

$$\Delta \underset{\sim}{S}_{ept}(t^{\lambda}_{k-1} + \lambda^{\nabla}_{k}\Delta t) = - [D_{ep}(\underset{\sim}{Y}_{k})]\alpha(T(t^{\lambda}_{\ell}))(T(t^{\lambda}_{\ell}+\lambda^{\nabla}_{k}\Delta t) - T(t^{\lambda}_{\ell})) \quad (3.49)$$

$$\Delta \underset{\sim}{S}^{i}_{epC}(t^{\lambda}_{\ell}+\Delta t) = - [D_{ep}(\underset{\sim}{Y}^{i}_{\ell+1})]\Delta \underset{\sim}{L}_{C}(t^{\lambda}_{\ell},\Delta t) \quad (3.50)$$

$$\Delta \underset{\sim}{S}^{i}_{ept}(t^{\lambda}_{\ell}+\Delta t_{\ell+1}) = - [D_{ep}(\underset{\sim}{Y}^{i}_{\ell+1})]\alpha(T(t^{\lambda}_{\ell}))(T(t^{\lambda}_{\ell}+\Delta t) - T(t^{\lambda}_{\ell})) \quad (3.51)$$

To check the convergence of the foregoing algorithm, several tests are employed. These include:

i) Definiteness check:

$$(\alpha_{2I})^2 - \alpha_{1I}\alpha_{3I} > 0 \quad (3.52)$$

ii) Pseudo force norm check:

$$\frac{||\underset{\sim}{F}(t^{\lambda}_{\ell}+\lambda^{i+1}_{\ell+1}\Delta t) - \underset{\sim}{F}(t^{\lambda}_{\ell}+\lambda^{i}_{\ell+1}\Delta t)||}{||\underset{\sim}{F}(t^{\lambda}_{\ell}+\lambda^{i+1}_{\ell+1}\Delta t)||} < \varepsilon_{F} \quad (3.53)$$

iii) Displacement norm check:

$$\frac{||\underset{\sim}{Y}^{i+1}_{\ell+1} - \underset{\sim}{Y}^{i}_{\ell+1}||}{||\underset{\sim}{Y}^{i+1}_{\ell+1}||} < \varepsilon_{Y} \quad (3.54)$$

iv) Constraint check:

$$\frac{\lambda^{i+1}_{\ell+1} - \lambda^{i}_{\ell+1}}{\lambda^{i+1}_{\ell+1}} < \varepsilon_{\lambda} \quad (3.55)$$

The preceeding tests are applied at different phases of the iteration process. Test i) is used to resize the HECS by self-adaptively readjusting μ_A the aspect ratio so as to guarantee an intersection with the INR extrapolation and thus ensure a convergent solution [6]. Test ii) is employed to monitor the monotonicity of successive load excursions. Lastly tests iii) and iv) are used to quantify when adequate convergence has been achieved.

Once convergence is obtained for a given time step, the overall solution algorithm must be prepared for the next interval. This requires that the various field variables are properly updated. Specifically this includes such terms as $\underset{\sim}{Y}$, $\underset{\sim}{S}_{ep}$, $\underset{\sim}{S}_{epC}$, $\underset{\sim}{S}_{epT}$ and t. In this context, if we let $I_{\ell+1}$ designate the number of iterations required to yield convergence of the $(\ell+1)^{th}$ time step, then $\underset{\sim}{Y}$ at the outset of the $(\ell+2)^{th}$ is given by the expression

$$\underset{\sim}{Y}^{0}_{\ell+2} = \underset{\sim}{Y}^{0}_{\ell+1} + \sum_{k=1}^{I_{\ell+1}} \Delta \underset{\sim}{Y}^{k}_{\ell+1} \quad (3.56)$$

Note as the iteration process converges, the constraints $\lambda^{i}_{\ell+1}$ represent a sequence which approaches the limit (cluster) point $\lambda^{\nabla}_{\ell+1}$ namely

$$\lambda^{1}_{\ell+1},\ \lambda^{2}_{\ell+1},\ \lambda^{3}_{\ell+1},\ldots,\ \lambda^{i}_{\ell+1},\ldots,\ \lambda^{\nabla}_{\ell+1} \tag{3.57}$$

In this context, the time at the start of the $(\ell+1)^{th}$ step is given by

$$t^{\lambda}_{\ell+1} = t^{\lambda}_{\ell} + \lambda^{\nabla}_{\ell+1}\,\Delta t \tag{3.58}$$

Now, based on (3.56) and (3.58), it follows that the various stress partitions take the form

$$\underset{\sim}{S}_{ep}(\underset{\sim}{Y}^{o}_{\ell+2}) = \underset{\sim}{S}_{ep}(\underset{\sim}{Y}^{o}_{\ell+1}) + \Delta\underset{\sim}{S}_{ep}(\underset{\sim}{Y}^{o}_{\ell+2}) \tag{3.59}$$

$$\underset{\sim}{S}^{o}_{epc}\Big|_{t^{\lambda}_{\ell+1}+\Delta t} = \underset{\sim}{S}_{epC}(t^{\lambda}_{\ell+1}) + \Delta\underset{\sim}{S}^{o}_{epC}(t^{\lambda}_{\ell+1}+\Delta t) \tag{3.60}$$

$$\underset{\sim}{S}^{o}_{epT}\Big|_{t^{\lambda}_{\ell+1}+\Delta t} = \underset{\sim}{S}_{epT}(t^{\lambda}_{\ell+1}) + \Delta\underset{\sim}{S}^{o}_{epT}(t^{\lambda}_{\ell+1}+\Delta t) \tag{3.61}$$

such that the various increments are defined by the expressions:

$$\Delta\underset{\sim}{S}_{ep}(\underset{\sim}{Y}^{o}_{\ell+2}) = [D_{ep}(\underset{\sim}{Y}^{o}_{\ell+2})]\Delta\underset{\sim}{L}(t^{\lambda}_{\ell+1}) \tag{3.62}$$

$$\Delta\underset{\sim}{L}(t^{\lambda}_{\ell+1}) = [B^{*}_{U}(\underset{\sim}{Y}^{o}_{\ell+2})](\underset{\sim}{Y}^{o}_{\ell+2} - \underset{\sim}{Y}^{o}_{\ell+1}) \tag{3.63}$$

$$\underset{\sim}{S}_{epC}(t^{\lambda}_{\ell+1}) = \sum_{k=1}^{\ell+1} \Delta\underset{\sim}{S}_{epC}(t^{\lambda}_{k-1} + \lambda^{\nabla}_{k}\Delta t) \tag{3.64}$$

$$\underset{\sim}{S}_{epT}(t^{\lambda}_{\ell+1}) = \sum_{k=1}^{\ell+1} \Delta\underset{\sim}{S}_{epT}(t^{\lambda}_{k-1} + \lambda^{\nabla}_{k}\Delta t) \tag{3.65}$$

$$\Delta\underset{\sim}{S}^{o}_{epC}(t^{\lambda}_{\ell+1} + \Delta t) = -[D_{ep}(\underset{\sim}{Y}^{o}_{\ell+2})]\Delta\underset{\sim}{L}_{C}(t^{\lambda}_{\ell+1},\ \Delta t) \tag{3.66}$$

$$\Delta\underset{\sim}{S}^{o}_{epT}(t^{\lambda}_{\ell+1} + \Delta t) = -[D_{ep}(\underset{\sim}{Y}^{o}_{\ell+2})]\alpha(T(t^{\lambda}_{\ell+1}))(T(t^{\lambda}_{\ell+1} + \Delta t) - T(t^{\lambda}_{\ell+1})) \tag{3.67}$$

Note for the present purposes, to enhance the speed of calculation of the stiffness inverse, the BFGS [3,7] scheme is employed. This approach was chosen over the straight updating scheme which is particularly expensive when several iterations are involved. Such situations typically occur in the vicinity of buckling points.

As was noted earlier, if the INR type scheme is employed to solve the thermomechanical problem, uniform time stepping in the thermal phase of calculations also leads to equal time intervals for the mechanical stage. In contrast, the use of constraints in the INR methodology yields

unequal time stepping requirements for the mechanical phase. Namely, the following type thermomechanical history is obtained, that is

t	$T(t)$	$\underset{\sim}{S}(t)$	...
0	$T(0)$	$\underset{\sim}{S}(0)$	...
$\lambda_1^{\nabla}\Delta t$	$T(\lambda_1^{\nabla}\Delta t)$	$\underset{\sim}{S}(\lambda_1^{\nabla}\Delta t)$	...
$t_1^{\lambda} + \lambda_2^{\nabla}\Delta t$	$T(t_1^{\lambda} + \lambda_2^{\nabla}\Delta t)$	$\underset{\sim}{S}(t_1^{\lambda} + \lambda_2^{\nabla}\Delta t)$	...
$\vdots$	$\vdots$	$\vdots$	
$t_\ell^{\lambda} + \lambda_{\ell+1}^{\nabla}\Delta t$	$T(t_\ell^{\lambda} + \lambda_{\ell+1}^{\nabla}\Delta t)$	$\underset{\sim}{S}(t_\ell^{\lambda} + \lambda_{\ell+1}^{\nabla}\Delta t)$	...

where here the sequence $0, \lambda_1^{\nabla}\Delta t, \ldots t_\ell^{\lambda} + \lambda_{\ell+1}^{\nabla}\Delta t$ is typically nonuniform. Because of this, the temperature data required to generate the thermal strains and material properties are interpolated from the uniformly generated data.

BENCHMARKING

In the preceeding sections, a specialized HECS constrained BFGS updated INR time stepping strategy has been developed. The methodology enables the static solution of pre and postbuckling thermomechanical problems. In order to thoroughly evaluate the procedure, several highly nonlinear benchmark problems were undertaken. The main thrust of this work was to ascertain the capability of the constraint methodology to deal with thermomechanical problems involving:

a) Large deformation kinematics including the possibility of pre and postbuckling behavior;
b) Thermoelastic-plastic-creep material behavior;
c) Temperature dependent thermomechanical material properties; as well as,
d) Time dependent thermomechanical loads with varying combinations/ interactions between the thermal and mechanical components.

This was achieved by programming the solution scheme into ADINA [9] and its complementing thermal code ADINAT [10]. Such an approach enabled benchmarking over a wide variety of geometric configurations, material types and boundary conditions. For the present purposes, the demonstrational benchmarking consists of calculating the pre and postbuckling response of an arch to various types of thermomechanical loading fields.

For demonstration purposes, Fig. 2 illustrates the geometry of the centrally loaded arch used for the benchmarking. The creep law employed is given by the expression

$$\varepsilon_c = A_0 \sigma^{A_1} t^{A_2}$$

As seen from Fig. 2, eight noded plane stress isoparametric elements are used to generate the FE simulation.

To demonstrate the numerical efficiency and stability of the improved constrained MINR time stepping scheme, the thermoelastic-plastic-creep pre-postbuckling problem depicted in Fig. 3 is considered. As can be seen from this figure, the problem is driven into the postbuckling range of behavior by the time dependent growth of creep. Overall, the creep generated reshaping initiates a redistribution in the internal loads hence causing a change in load carrying capacity. Due to the nature of redistribution, plasticity is initiated in the later stages of postbuckling. Noting Fig. 3, $t_{critical}$ marks the time at which the pre to postbuckling transition occurs. This time zone is marked by changes in the definiteness of the structural stiffness. Table 1 illustrates the numerical efficiency/stability of the BFGS updated constrained scheme in capturing such behavior. In the case of Δt = .8 hours, Table 1, the improved algorithm yielded 210% reduction in computer time over the constrained MINR scheme. Note the classical unconstrained INR scheme completely fails in such zones of behavior for any choice of Δt. As the time step is increased further, unless some intermediate updating is employed, even the constrained MINR approach fails. This is in contrast to the BFGS updated scheme which shows significantly enhanced convergence, efficiency and stability characteristics.

As a more severe test of the scheme, we shall consider the case of cyclical creep loading problems wherein buckling occurs after several cycles. Figure 4 illustrates the load deflection behavior of the arch under a cyclically applied external load. As can be seen, as the load is cycled the accumulated creep over the various cycles progressively reduces the buckling limit of the arch. In essence, after several cycles the arch behaves as a structure with shape imperfections. Such reductions in load carrying capacity are illustrated in Fig. 5. Specifically, this figure depicts successive families of load-deflection curves which illustrate the decrease of buckling strength with time. Note, due to the efficiency and stability of the improved constrained MINR time stepping scheme, problems involving variable/cyclic loading environments can be handled more effectively.

The last example considered consists of the thermally induced buckling of the bimetallic arch depicted in Fig. 6. Noting Fig. 7, as the arches temperature is raised, a critical value is reached wherein excessive deflections occur with no essential raise in T. Such behavior constitutes the thermal equivalent of buckling. This follows from the fact that the structural stiffness is indefinite during the event.

SUMMARY

As noted earlier, the main thrust of this work has been to develop an improved solution procedure for elastic-plastic creep pre-postbuckling problems. Also of major importance is the maintenance of maximum algorithmic compatibility with currently available general purpose codes such as ADINA, ANSYS, MARC, NASTRAN, etc. As can be seen from the proceeding benchmarking, the improved constrained scheme developed herein significantly enhances the numerical operating characteristics of MINR type algorithms. It should be further noted that due to the manner of formulation, the overall procedure can be encoded into most general purpose codes with little rearchitecturing of the programming.

ACKNOWLEDGEMENT

The first author is grateful to Dr. C. Chamis of NASA-Lewis for the stimulating discussions and encouragements during the course of this work.

REFERENCES

1. Bathe, K.J.: FINITE ELEMENT PROCEDURES IN ENGINEERING ANALYSIS. Prentice Hall Inc., Englewood Cliffs, New Jersey, 1982.

2. Padovan, J.: Self Adaptive Incremental Newton-Raphson Algorithms. Symposium on Computer Methods in Nonlinear Structures and Solid Mechanics, Washington D.C., also NASACP-2147, 1980.

3. Bathe, K. J. and Cimento, A. P.: Some Practical Problems for the Solution of Nonlinear Finite Element Equations. Comp. Meth. Appl. Mech. Engrg., 22, 59, 1980.

4. Riks, E.: An Incremental Approach to the Solution of Snapping and Buckling Problems. Int. J. Solids Structures, 15, 529 (1979).

5. Crisfield, M. A.: A Fast Incremental/Iterative Procedure that Handles Snapthrough. Computers and Structures, 13, 55-62 (1981).

6. Padovan, J. and Arechaga, T.: Formal Convergence Characteristics of Elliptically Constrained Incremental Newton-Raphson Algorithms. Int. J. Engrg. Sci., 20, 1077, 1982.

7. Padovan, J., Tovichakchaikul, S., Arechaga, T.: Operating Characteristics of Hyperbolically and Elliptically Constrained Self-Adaptive Incremental Newton-Raphson Algorithms. Jr. Franklin Inst.

8. Mendelson, A.: PLASTICITY: THEORY AND APPLICATION. MacMillan, New York, 1968.

9. Bathe, K. C.: ADINA: A Finite Element Program for Automatic Dynamic Incremental Nonlinear Analysis. Rept. No. 8244-1, MIT, Cambridge, MA, 1978.

10. Bathe, K. C.: ADINAT: A Finite Program for Automatic Dynamic Incremental Nonlinear Analysis of Temperatures. MIT, Cambridge, MA, Rept. No. 82448-5, 1978.

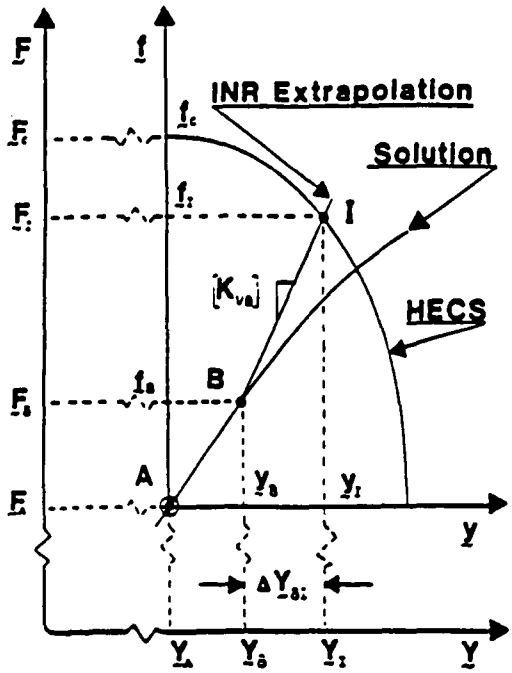

Fig.1 HECS constrained INR iterations

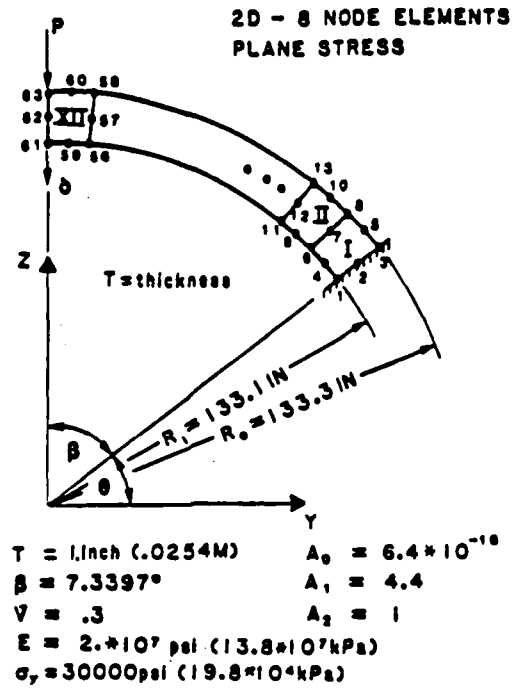

Fig.2 Centrally loaded arch

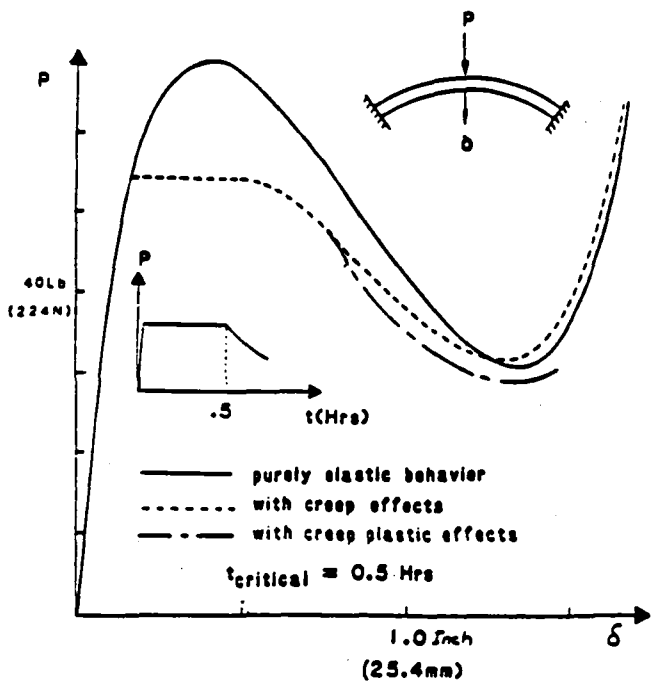

Fig.3 Single cycle arch response

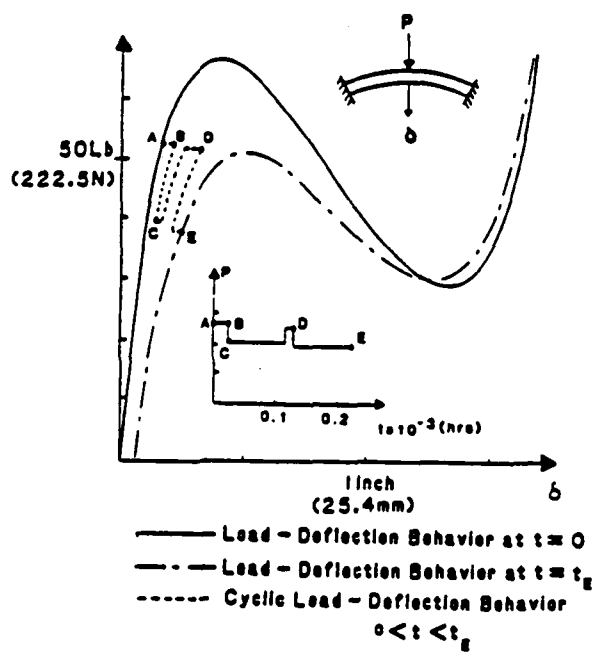

Fig.4 Multi-cycle arch response

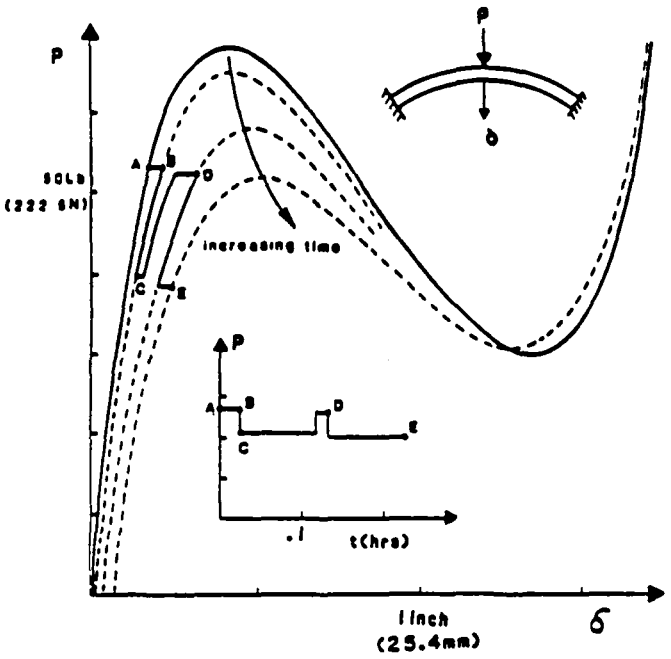

Fig.5 Cyclical degradation of arch stability

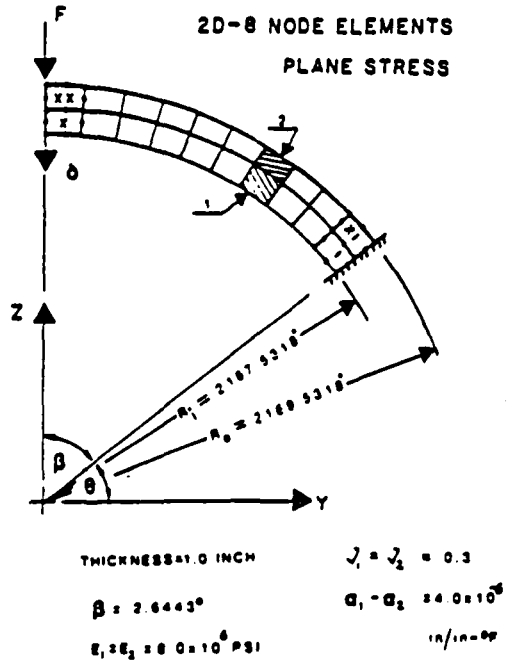

Fig.6 Bimetallic arch

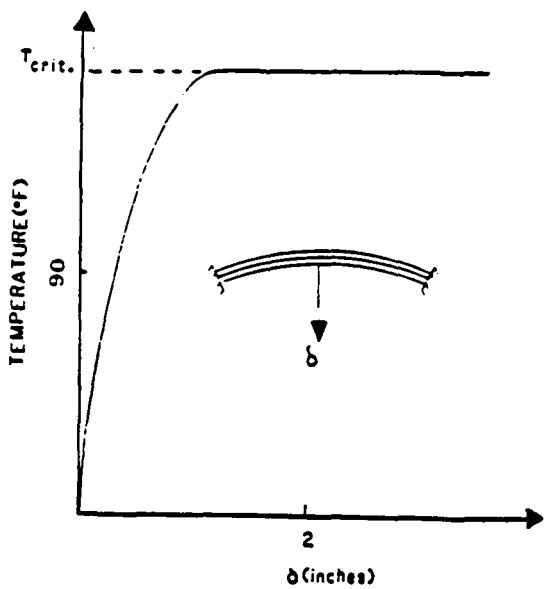

Fig.7 Response of bimetallic arch to uniform temperature

	No. of Iteration Δt = .8 Hrs.		
Step	Classical MINR	Constrained MINR	Improved Constrained MINR
1-17	SOLUTION FAILED OUT OF BALANCE LOADS	.	.
18		3	3
19		4	3
20		5	4
21		7	4
22		12	5
23		32	5
24		40	5
25		9	4
26		4	3
27		3	3
28		3	2
29		2	1
30		1	1
		.	.
		.	.
		.	.

Table 1 Numerical comparisons

Page intentionally left blank

NUMERICAL CONSIDERATIONS IN THE DEVELOPMENT AND IMPLEMENTATION OF CONSTITUTIVE MODELS

W.E. Haisler and P.K. Imbrie
Aerospace Engineering Department
Texas A&M University
College Station, Texas 77843

Several unified constitutive models were tested in uniaxial form by specifying input strain histories and comparing output stress histories. The purpose of the tests was to evaluate several time integration methods with regard to accuracy, stability, and computational economy. The sensitivity of the models to slight changes in input constants was also investigated. Results are presented for IN100 at 1350°F and Hastelloy-X at 1800°F.

INTRODUCTION

The characterization of the constitutive behaviour of metals has its roots in the early work of Tresca, Levy, vonMises, Hencky, Prandtl, Reuss, Prager, and Ziegler (Refs. 1-8). These early models are incremental in nature, assume that plasticity and creep can be separated, and they incorporate a yield function, flow rule, and hardening rule to define the plastic strain increment. These original incremental theories have been expanded and modified by many researchers so that they provide adequate, and often very good predictions of rate-independent plastic flow (see for example Refs. 9-10). However, they are sometimes criticized as having no formal micromechanical basis upon which to make the assumption of an uncoupling of the inelastic strain into rate-independent (plastic) and rate-dependent (creep) strain components. Nevertheless, the classical incremental theories are widely used.

During the last ten years, a number of unified constiutive models have been proposed which retain the inelastic strain as a unified quantity without aritifical separation into plasticity and creep components. These include the models developed by Bodner (Refs. 11-13), Stouffer (Refs. 14-15), Krieg (Ref. 16), Miller (Ref. 17), Walker (Refs. 18-19), Valanis (Refs. 20-21), Krempl (Ref. 22), Cernocky (Ref. 23-24), Hart (Ref. 25), Chaboche (Ref. 26), Robinson (Ref. 27), Kocks (Ref. 28), and Cescotto and Leckie (Ref. 29). The applicability of these viscoplastic constitutive theories (mostly to high temperature applications) has been investigated by several researchers. Walker (Ref. 19) compared the predictive capability of several models (Walker, Miller and Krieg) for Hastelloy-X at 1800°F. More recently, Milly and Allen

(Ref. 30) provided a qualitative as well as quantitative comparison of the models developed by Bodner, Krieg, Walker and Krempl for IN100. Both Refs. 19 and 30 conclude that these models generally provide adequate results for elevated isothermal conditions, they provide poor and overly-square results at low temperature, the material constants are often difficult to obtain experimentally, the resulting rate equations are "stiff" and sensitive to numerical integration, and the models do not provide any satisfactory transient temperature capability. Beek, Allen, and Milly (Ref. 31) have shown that all the unified viscoplastic models mentioned above can be cast in a functionally similar form (in terms of internal state variables).

None of the published literature provides a thorough evaluation of current viscoplastic constitutive models with comparison to experimental response for complex input histories. Such an evaluation is difficult at present for many reasons, namely: 1) Material constants for most models are usually available only for a single material and often for a single temperature; 2) The experimental procedures given by model developers for determining material constants from experimental data are often sketchy at best; 3) Material constants for some models are often obtained by trial-and-error and are not based on experiments; and 4) There is a lack of good experimental data against which the models can be evaluated (that is, test data which is significantly different from that used to generate the material constants).

The purpose of the present paper is to report some preliminary evaluations of several of the unified viscoplastic models (Bodner, Krieg, Miller, and Walker). These four models are evaluated with regard to 1) their sensitivity to numerical integration and 2) their sensitivity to slight changes in input material constants.

CONSTITUTIVE MODELS CONSIDERED

The constitutive theories which have been studied to date include Bodner's (Refs. 11-15), Krieg's (Ref. 16), Miller's (Ref. 17), and Walker's (Refs. 18-19). These particular models were selected for this initial study because material constants for Hastelloy-X were available for three of the models. Other models are currently being considered as material constants become available. Each model is listed below in uniaxial form using a consistent notation as presented by Beek, Allen and Milly (Ref. 31). In Ref. 31, it is shown that all of the current viscoplastic models considered may be written in uniaxial form as

$$\sigma = E(\varepsilon - \alpha_1 - \varepsilon^T) \tag{1}$$

where σ is stress, E is Young's modulus, ε is strain, α_1 is the inelastic strain (internal state variable), and ε^T is the thermal strain. Each viscoplastic theory postulates a particular growth law for the internal state variable(s) and the inelastic strain is obtained by time integration of the growth law for α_1, i.e.

$$\alpha_1 = \int_{-\infty}^{t} \dot{\alpha}_1(t')dt' \tag{2}$$

where

$$\dot{\alpha}_1 = \frac{d\alpha_1}{dt} = \dot{\alpha}_i(\varepsilon, T, \alpha_2, \alpha_3, \ldots, \alpha_m) \tag{3}$$

In equations (2) and (3), t is time, T is temperature, α_2 is the back stress (related to the dislocation arrangement and produces kinematic hardening or the Bauschinger effect), and α_3 is the drag stress (which represents the dislocation density and produces isotropic hardening).

Bodner's Theory

The growth law for the inelastic strain in Bodner's model may be written in uniaxial form as

$$\dot{\alpha}_1 = \frac{2}{\sqrt{3}} D_o \exp\left[-\left(\frac{n+1}{2n}\right)\left(\frac{\sigma}{\alpha_3}\right)^{-2n}\right] \operatorname{sgn}(\sigma) \tag{4}$$

where

$$\dot{\alpha}_3 = m(Z_1 - \alpha_3)\dot{W}_p - AZ_1\left(\frac{\alpha_3 - Z_I}{Z_1}\right)^r \tag{5}$$

$$\dot{W}_p = \sigma\,\dot{\alpha}_i \tag{6}$$

The quantities E, D_o, n, m, Z_I, A, Z_1 and r are material constants. As noted before, the variable α_3 is similar to the drag stress used in many models (a measure of isotropic hardening or dislocation density). It is noted that the model contains no parameter representing the back stress and cannot account for the Bauschinger effect in kinematic hardening materials. The material constants are tabulated for IN100 at 1350°F (732°C) in Table 1 (taken from Ref. 14).

Krieg's Theory

The inelastic strain growth law for the model developed by Krieg and coworkers may be written in terms of state variables representing back stress and drag stress:

$$\dot{\alpha}_1 = C_1 \left(\frac{|\sigma - \alpha_2|}{\alpha_3} \right)^{C_2} \operatorname{sgn}(\sigma - \alpha_2) \tag{7}$$

$$\dot{\alpha}_2 = C_3 \dot{\alpha}_1 - C_4 \alpha_2^2 [\exp(C_5 \alpha_2^2) - 1] \operatorname{sgn}(\alpha_2) \tag{8}$$

$$\dot{\alpha}_3 = C_6 |\dot{\alpha}_1| - C_7 (\alpha_3 - \alpha_{3_o})^n \tag{9}$$

The model contains ten constants (C_1, C_2 . . . , C_7, E, α_{3_o}, and n). These have been evaluated by Walker (Ref. 19) for Hastelloy-X at 1800°F (982°C) and are tabulated in Table 2. It should be noted that equations (7), (8) and (9) form a coupled set of ordinary differential equations.

Miller's Theory

The growth laws for Miller's model may be written in uniaxial form as

$$\dot{\alpha}_1 = B\theta' \left[\sinh \left(\frac{|\sigma - \alpha_2|}{\alpha_3} \right)^{1.5} \right]^n \operatorname{sgn}(\sigma - \alpha_2) \tag{10}$$

$$\dot{\alpha}_2 = H_1 \dot{\alpha}_1 - H_1 B\theta' [\sinh (A_1 |\alpha_2|)]^n \operatorname{sgn}(\alpha_2) \tag{11}$$

$$\dot{\alpha}_3 = H_2 |\dot{\alpha}_1| \left(C_2 + |\alpha_2| - \frac{A_2}{A_1} \alpha_3^3 \right) - H_2 C_2 B\theta' \left[\sinh \left(A_2 \alpha_3^3 \right) \right]^n \tag{12}$$

Miller's theory contains nine constants which are tabulated for Hastelloy-X at 1800°F (982°C) in Table 3 (see Ref. 19).

Walker's Theory

Walker's nonlinear viscoplastic theory can be cast in the following uniaxial form

$$\dot{\alpha}_1 = \left(\frac{|\sigma - \alpha_2|}{\alpha_3}\right)^n \operatorname{sgn}(\sigma - \alpha_2) \tag{13}$$

$$\dot{\alpha}_2 = (n_1 + n_2)\dot{\alpha}_1 - (\alpha_2 - \alpha_{2_o} - n_1\alpha_1)\left\{|\dot{\alpha}_1|\frac{\partial}{\partial R}\left[(n_3 + n_4 R)\ln\left(\frac{n_5 R}{1+n_6 R} + 1\right)\right]\right.$$

$$\left. + n_7 |\alpha_2 - \alpha_{2_o}|^{m-1}\right\} \tag{14}$$

$$\dot{\alpha}_3 = n_8 |\dot{\alpha}_1| - n_9 |\dot{\alpha}_1|\alpha_3 - n_{10}(\alpha_3 - \alpha_{3_o})^q \tag{15}$$

where R is the cumulative inelastic strain

$$R = \int_o^t \left|\frac{\partial \alpha_1}{\partial t'}\right| dt' \tag{16}$$

The general model requires sixteen constants (E, n, m, q, n_1, n_2, . . . , n_{10}, α_{2_o} and $\alpha_3(t=0)$. In determining the constants for Hastelloy-X at 1800°F (982°C), Walker made several simplifying assumptions [including α_3 = constant = $\alpha_3(t=0)$] which reduces the number of parameters to those shown in Table 4 (see Ref. 19). Further, the constants reported in Ref. 19 were developed from tests using strain rates in the range 10^{-3} to 10^{-6} sec^{-1} and strain ranges of ±0.6%.

NUMERICAL TIME INTEGRATION STUDY

The integration of the constitutive relationship given by equations (1), (2) and (3) forms an integral and extremely important part in any numerical solution of a nonlinear field problem. It has been observed by many researchers that the coupled system of ordinary differential equations defining the state variables may be locally "stiff" and thus are sensitive to the time step size and numerical algorithm. The accurate integration of these stiff equations can be accomplished by various means: use of small time steps, higher-order or multi-point integration schemes, subincrementation

procedures (Refs. 33-35), "smart" algorithms which attempt to select appropriate time steps in order to achieve accuracy and stability (Refs. 36,37), algorithms tailored for individual constitutive theories (Refs. 32,37), or combinations of these approaches. In general, the computation time required for the accurate solution of materially nonlinear problems is directly related to the numerical integration scheme used.

Regarding the constitutive models reviewed herein, Walker (Ref. 32) uses a stable, iterative implicit scheme which takes advantage of the functional form of the integrand in the development of the reccurence relation. Miller originally used Gear's method (Ref. 36) to integrate the stiff equations in his theory but later concluded in Ref. 37 that an implicit backward difference method was more economical and preferable to either Gear's method or the explicit Euler forward integration method. The type of numerical integration scheme used by Bodner and Krieg is not known.

The selection of an appropriate time integration scheme to be used in a computer code is very important but is often based on the answers to such questions as: "What is available in the present code?", "What will work most of the time?", "What can we use that most users will understand?", "What is the cheapest and easiest to use?", and the like. The usual response given is "it depends on the problem being solved!"

In general, equation (3) may be integrated between time t and t + Δt by writing

$$\int_{t}^{t+\Delta t} d\alpha_1 = \int_{t}^{t+\Delta t} \dot{\alpha}_1 \, dt \tag{17}$$

or

$$\Delta\alpha_1 = \alpha_1(t + \Delta t) - \alpha_1(t) = \int_{t}^{t+\Delta t} \dot{\alpha}_1 \, dt \tag{18}$$

where $\dot{\alpha}_1$ is defined by the particular constitutive theory being used. The present investigation considers four integration schemes: explicit Euler forward integration, implicit trapezoidal method, trapezoidal predictor-corrector (iterative) method, and Runge-Kutta 4th order method. The approximations for each of these methods is given in Table 5.

Each of the integration schemes in Table 5 were used to obtain stress-time and stress-strain responses for the four constitutive models considered herein when subjected to the uniaxial, alternating square-wave strain-rate history shown in Fig. 1. Figure 1 shows the 35 second response obtained

by Krieg's theory for Hastelloy-X at 1800°F using a time step of 0.1 seconds. For this time step, the Euler and trapezoidal predictor-corrector methods provide essentially the same results and are virtually identical to that obtained for all methods using a time step of 0.005 seconds. The 4th order Runge-Kutta method generally overestimates the peak response while the trapezoidal method underestimates the response. Figure 2 presents results for three integration methods such that the total computation time for a 35 second response solution is approximately the same. For equivalent computation times, the Euler method provides the most accurate results although smaller time steps are required. Similar results are observed for Miller's model.

Figures 3 and 4 illustrate that various constitutive models may behave appreciably different using the same integration method (in this case the Euler method). In Fig. 3, Miller's theory (for Hastelloy-X at 1800°F) gives considerable oscillatory response for a time step of 0.005 seconds while Walker's theory shown in Fig. 4 gives a much smoother response for the same time step. Comparing Figs. 3 and 4, it is seen that a smaller time step is required (with Euler integration) in Miller's theory than in Walker's theory.

Figure 5 presents results for IN100 at 1350°F using Bodner's model. Time steps were chosen for each integration scheme to obtain solutions which required approximately equal computation times. These results, when compared to solutions with much smaller time steps, indicate that the Euler method provides the most accurate results. Again, the time step used is smaller than that for the other methods but the computation time is the same (for integrating the constitutive equations).

SENSITIVITY STUDY FOR MATERIAL CONSTANTS

In the previous section, results were presented which showed how the numerical integration method used to integrate the constitutive equations could affect the accuracy and computation times of predicted results for stress-time and stress-strain responses. In this section, we consider another important parameter in the application of any constitutive theory. Namely, "how does the accuracy to which material constants are determined from experimental test data affect the predicted response?"

Figures 6 and 7 present results for Walker's model (Hastelloy-X at 1800°F subjected to an alternating square-wave strain-rate history as shown) wherein specified input material constants have been adjusted by 5%. Figure 6 shows the effect of a -5% change (error) in the stress exponent n (the most sensitive parameter). Figure 7 shows that a +5% error in all test data required to compute material constants results in significant predicted response errors, up to 30% over-prediction in the stress at a time of 35 seconds (during the relaxation period).

Figures 8 and 9 present similar results for Krieg's model (Hastelloy-X at 1800°F) and Bodner's model (IN100 at 1350°F), respectively. Both results indicate that the most sensitive parameter is the stress exponent "n" and

that a 5% error in specifying n may produce significant errors in the predicted response. Miller's model appears to be much less sensitive to errors in input material parameters.

Figure 10 provides a comparison of the Miller, Krieg, and Walker models for the Hastelloy-X test at 1800°F (using constants obtained by Walker for all models). The Euler method was used with a time step of 0.0005 seconds which provides a solution with no significant truncation error. The results obtained here show approximately 10-15% differences in peak stress amplitudes between the three constitutive models. Since no experimental results are available at this time, no conclusions can be drawn as to which model more accurately represents observed test data. However, the results do point out that significant differences (greater than 15%) can be obtained for stress peaks and stress relation values through the use of different constitutive models.

CONCLUSIONS AND FUTURE WORK

The results of this study are not complete since only a portion of the available constitutive models and numerical integration schemes have been considered. However, some tentative conclusions can be reached. First, it appears clear from the present investigation, and the work of others, that simple integration schemes (like the Euler forward defference method) are often preferable to more complex schemes from the standpoint of accuracy, computation time, and ease of implementation. Although not reported herein, our work in progress indicates that Euler's method used with a simple subincrementation strategy provides the most accurate and economical solution for most constitutive models.

The sensitivity study on material constants indicates that most viscoplastic constitutive models are significantly sensitive to one or more material constants derived from laboratory tests. It has been shown that a 5% "error" in laboratory measurements may lead to errors of 25%, or greater, in predicted stress responses. Although most model developers have fine-tuned their models and input material constants for specific material/temperature/strain-rate combinations, it is not clear that end-users will be able to do so when called upon to develop material constants for a new situation. The problem can be negated to some extent by defining more explicit testing procedures for obtaining material constants and by guidelines defining which constants are most sensitive to experimental error.

Our current and future work concerns the application of several integration schemes to the other constitutive theories, investigation of subincremental strategies, and consideration of "smart" integration methods which detect local "stiffness" and adjust time steps but without significant computational expense. The material parameter sensitivity study will be continued by considering other constitutive theories, and more importantly, by comparison with laboratory tests which involve complex thermomechanical loadings including transient temperature inputs.

ACKNOWLEDGEMENT

The authors gratefully acknowledge the financial support for this research by NASA Lewis Research Center under Grant no. NAG3-491.

REFERENCES

1. Tresca, H., "Notes on Yield of Solid Bodies Under Strong Pressures," Comptes Rendus del' Academie des Sciences, Vol. 59, p. 754, 1864.
2. Levy, M., "Memoire sur les equations generales des mouvements interieurs des corps solides ductiles au dela des limites ou l'elasticite pourrait les ramener a leur premier eata.," C.R. Acad. Sci. (Paris), Vol. 70, pp. 1323-1325, 1870.
3. von Mises, R., "Mechanik der Festen Koerper im plastisch deformablen Zustant," Goettinger Nachr., Math.-Phys., Kl, pp. 582-592, 1913.
4. Hencky, H., "Zur Theorie Plastischer Deformationen und die Hierduch im Material Hervorgerufenen Nach-Spannungen," Z. ang. Math. Mech., Vol. 4, pp. 323-334, 1924.
5. Prandtl, L., "Spannungsverteilurg in Plastischen Koerpen," Proceedings of the First International Congress on Applied Mechanics, Delft, Technische Boekhandel en Druckerin, Jr. Waltman, Jr., pp. 43-45, 1925.
6. Reuss, E., "Bereuchkisichtigung der Elastischen Formaenderungen in der Plastizitaetstheorie," Zeitschrift fuer Angewandte Mathematic und Mechanik, Vol. 10, pp. 266-274, 1930.
7. Prager, W., "The Theory of Plasticity: A Survey of Recent Achievements," Proceedings of the Institution of Mechanical Engineers, London, Vol. 169, pp. 41-57, 1955.
8. Ziegler, H., "A Modification of Prager's Hardening Rule," Quarterly of Applied Mathematics, Vol. XVIII, pp. 55-65, 1959.
9. Allen, D.H. and Haisler, W.E., "A Theory for Analysis of Thermoplastic Materials," Computers and Structures, Vol. 13, pp. 125-135, 1981.
10. Haisler, W.E. and Cronenworth, J., "An Uncoupled Viscoplastic Constitutive Model for Metlas at Elevated Temperature," Proceedings of the 24th AIAA Structures, Structural Dynamics and Materials Conference, Lake Tahoe, Nevada, May 2-4, 1983.
11. Bodner, S.R. and Partom, Y., "Constitutive Equations for Elastic-Viscoplastic Strain-Hardening Materials," Journal of Applied Mechanics, Vol. 42, No. 2, pp. 385-389, 1975.
12. Merzer, A. and Bodner, S.R., "Analytical Formulation of a Rate and Temperature Dependent Stress-Strain Relation," Journal of Engineering Materials and Technology, Vol. 101, pp. 254-257, 1979.
13. Bodner, S.R., "Representation of Time Dependent Mechanical Behaviour of Rene 95 by Constitutive Equations," Air Force Materials Laboratory, AFML-TR-4116, 1979.
14. Stouffer, D.C., "A Constitutive Representation for IN100," AFWAL-TR-81-4039, Air Force Materials Laboratory, June 1981.
15. Stouffer, D.C. and Bodner, S.R., "A Relationship Between Theory and Experiment for a State Variable Constitutive Equation," ASTM Special Technical Publication 785, 1982 (also AFWAL-TR-80-4194, 1981).

16. Krieg, R.D., Swearengen, J.C., and Rohde, R.W., "A Physically-Based Internal Variable Model for Rate-Dependent Plasticity," Proceedings ASME/CSME/PVP Conference, pp. 15-27, 1978.
17. Miller, A.K., "An Inelastic Constitutive Model for Monotonic, Cyclic, and Creep Deformation: Part I--Equations Development and Analytical Procedures" and "Part II--Application to Type 304 Stainless Steel," ASME Journal of Engineering Materials and Technology, pp. 97-113, April 1976.
18. Walker, K.P., "Representation of Hastelloy-X Behavior at Elevated Temperature with a Functional Theory of Viscoplasticity," Presented at the ASME Pressure Vessels Conference, San Francisco, 1980, also ASME Journal of Engineering Materials and Technology, 1981.
19. Walker, K.P., "Research and Development Program for Nonlinear Structural Modeling with Advanced Time-Temperature Dependent Constitutive Relationships," PWA-5700-50, United Technologies Research Center, (also NASA CR-165533), 1981.
20. Valanis, K.C., "A Theory of Viscoplasticity Without a Yield Surface - Part I. General Theory," and "Part II. Application to Mechanical Behavior of Metlas," Archives of Mechanics, Vol. 23, pp. 517-533, 1971.
21. Valanis, K.D., "On the Foundations of the Endochronic Theory of Viscoplasticity," Archives of Mechanics, Vol. 27, pp. 857-868.
22. Krempl, E., "On the Interaction of Rate and History Dependence in Structural Materials," Acta Mechanica, Vol. 22, pp. 53-90, 1975.
23. Cernocky, E.P. and Krempl, E., "A Nonlinear Uniaxial Integral Constitutive Equation Incorporating Rate Effects, Creep and Relaxation," International Journal of Nonlinear Mechanics, Vol. 14, pp. 183-205, 1979.
24. Cernocky, E.P. and Krempl, E., "A Theory of Thermoviscoplasticity Based on Infinitesimal Total Strain," International Journal for Solids and Structures, Vol. 16, pp. 723-741, 1980.
25. Hart, E.W., "Constitutive Relations for the Nonelastic Deformation of Metals," ASME Journal of Engineering Materials and Technology, Vol. 98-H, p. 193, 1976.
26. Cailletaud, G. and Chaboche, J.L., "Macroscopic Description of the Microstructural Changes Induced by Varying Temperature: Example of IN100 Cyclic Behaviour," Third International Conference on Mechanical Behaviour of Materials, Vol. 2, pp. 22-32, ICM3, Cambridge, England, August 1979.
27. Robinson, E.N., "A Unified Creep-Plasticity Model for Structural Metals at High Temperatures," ORNL-TM-5969, October 1978.
28. Kocks, U.F., "Laws for Work-Hardening and Low-Temperature Creep," Journal of Engineering Materials and Technology, Vol. 98-H, pp. 76-85, 1976.
29. Cescotto, S. and Leckie, F., "Determination of Unified Constitutive Equations for Metals at High Temperature," Proceedings of the International Conference on Constitutive Laws for Engineering Materials, pp. 105-111, 1983.
30. Milly, T.M. and Allen, D.H., "A Comparative Study of Nonlinear Rate-Dependent Mechanical Constitutive Theories for Crystalline Solids at Elevated Temperature," VPI-E-82-5, Virginia Polytechnic Institute and State University, March 1982.

31. Beek, J.M., Allen, D.H., and Milly, T.M., "A Qualitative Comparison of Current Models for Nonlinear Rate-Dependent Material Behaviour of Crystalline Solids," MM 4246T-83-14, Mechanics and Materials Research Center, Texas A&M University, November 1983.
32. Walker, K.P., "Research and Development Program for Nonlinear Structural Modeling with Advanced Time-Temperature Dependent Constitutive Relations," First Quarterly Technical Narrative, NAS3-22055, January 1980.
33. Bushnell, D., "A Subincremental Strategy for Solving Proglems Involving Large Deflections, Plasticity and Creep," in Constitutive Equations in Viscoplasticity: Computational and Engineering Aspects, AMD Vol. 20 (ASME), p. 171, 1976.
34. Krieg, R.D. and Key, S.W., "Implementation of a Time Independent Plasticity Theory into Structural Computer Programs," in Constitutive Equations in Viscoplasticity: Computational and Engineering Aspects, AMD Vol. 20 (ASME), p. 125, 1976.
35. Zaphir, Z. and Bodner, S.R., "Implementation of Elastic-Viscoplastic Constitutive Equations into NDNSAP with Applications to Fracture Mechanics," presented at the MIT Conference on ADINA, 1979.
36. Gear, C.W., "The Automatic Integration of Ordinary Differential Equations," Communications of ACM, Vol. 14, p. 176, 1971.
37. Miller, A.K. and Shih, C.F., "An Improved Method for Numerical Integration of Constitutive Equations of the Work Hardening-Recovery Type," ASME Journal of Engineering Materials and Technology, Vol. 99-H, p. 275, 1977.

Table 1. Material Constants Used in Bodner's Model for IN100 at 1350°F (732°C)

Bodners notation	Beek and Allen's notation	Numerical Value
E	E	21.3×10^6 psi
n	n	0.7
Z_1	Z_1	1.105×10^6 psi
m	m	2.57×10^3 psi^{-1}
D_o	D_o	10^4 sec^{-1}
A	A	1.9×10^{-3} sec^{-1}
r	r	2.66
Z_1	Z_I	0.6×10^6 psi
ε^p (t=0)	α_1 (t=0)	0.0
Z_o	α_3 (t=0)	0.915×10^6 psi

Table 2. Material Constants Used in Krieg's Model for Hastelloy-X at 1800°F (982°C)

Walker's notation for Krieg's constants	Beek and Allen's notation	Numerical Value
	C_1	1.0
n	C_2	4.49
A_1	C_3	1.0×10^{6} psi
A_2	C_4	6.21×10^{-6} psi^{-1} sec^{-1}
A_3	C_5	4.027×10^{-7} psi^{-2}
A_4	C_6	100 psi $sec^{1/n}$
A_5	C_7	4.365 psi^{1-n} $sec^{1/n-2}$
E	E	13.2×10^{6} psi
K_o	α_{3_o}	59,292 psi $sec^{1/n}$
n	n	4.49
c(t=0)	α_1(t=0)	0.0
Ω(t=0)	α_2(t=0)	0.0
K(t=0)	α_3(t=0)	59,292 psi

Table 3. Material Constants Used in Miller's Model for Hastelloy-X at 1800°F (982°C)

Miller's notation	Beek and Allen's notation	Numerical Value
n	n	2.363
$B\theta'$	$B\theta'$	2.616×10^{-5} sec^{-1}
H_1	H_1	1×10^{6} psi
A_1	A_1	1.4053×10^{-3} psi^{-1}
H_2	H_2	100 psi $sec^{1/n}$
C_2	C_2	5,000 psi
A_2	A_2	4.355×10^{-12} psi^{-3}
E	E	13.2×10^{6} psi
ε(t=0)	α_1(t=0)	0.0
R(t=0)	α_2(t=0)	0.0
D_o	α_3(t=0)	8,642 psi

Table 4. Material Constants Used in Walker's Model for Hastelloy-X at 1800°F (982°C)

Walker's notation	Beek and Allen's notation	Numerical Value
$\overset{\circ}{\Omega}$	α_2	-1,200 psi
n_1	n_1	0 psi (not used)
n_2	n_2	1×10^6 psi
n_9	*	312.5
n_7	n_7	2.73×10^{-3} psi^{1-m} sec^{-1}
n	n	4.49
m	m	1.16
E	E	13.2×10^6 psi
c(t=0)	$\alpha_1(t=0)$	0.0
$\Omega(t=0)$	$\alpha_2(t=0)$	0.0
K(t=0)	$\alpha_3(t=0)$	59,292 psi
	n_8, n_9, n_{10}, q	0 (not used)

$$* = \frac{\partial}{\partial R}\left[(n_3 + n_4 R)\ \ell n\left(\frac{n_5 R}{1+n_6 R} + 1\right)\right]$$

Table 5. Numerical Integration Approximation for $\Delta\alpha_1 = \int_t^{t+\Delta t} \dot{\alpha}_1\, dt$

Method	Approximation
Euler Forward Difference	$\Delta\alpha_1 = \Delta t\ \dot{\alpha}_1(t)$
Trapezoidal Rule	$\Delta\alpha_1 = \frac{\Delta t}{2}[\dot{\alpha}_1(t) + \dot{\alpha}_1(t+\Delta t)]$
Trapezoidal Predictor-Corrector	Same as trapezoidal except iterate
Runge-Kutta 4th Order	$\Delta\alpha_1 = \frac{1}{6}(K_1 + 2K_2 + 2K_3 + K_4)$
	$K_1 = \Delta t\ \dot{\alpha}_1(t, \alpha_1(t))$
	$K_2 = \Delta t\ \dot{\alpha}_1(t+\Delta t/2, \alpha_1(t)+K_1/2)$
	$K_3 = \Delta t\ \dot{\alpha}_1(t+\Delta t/2, \alpha_1(t)+K_2/2)$
	$K_4 = \Delta t\ \dot{\alpha}_1(t+\Delta t, \alpha_1(t)+K_3)$

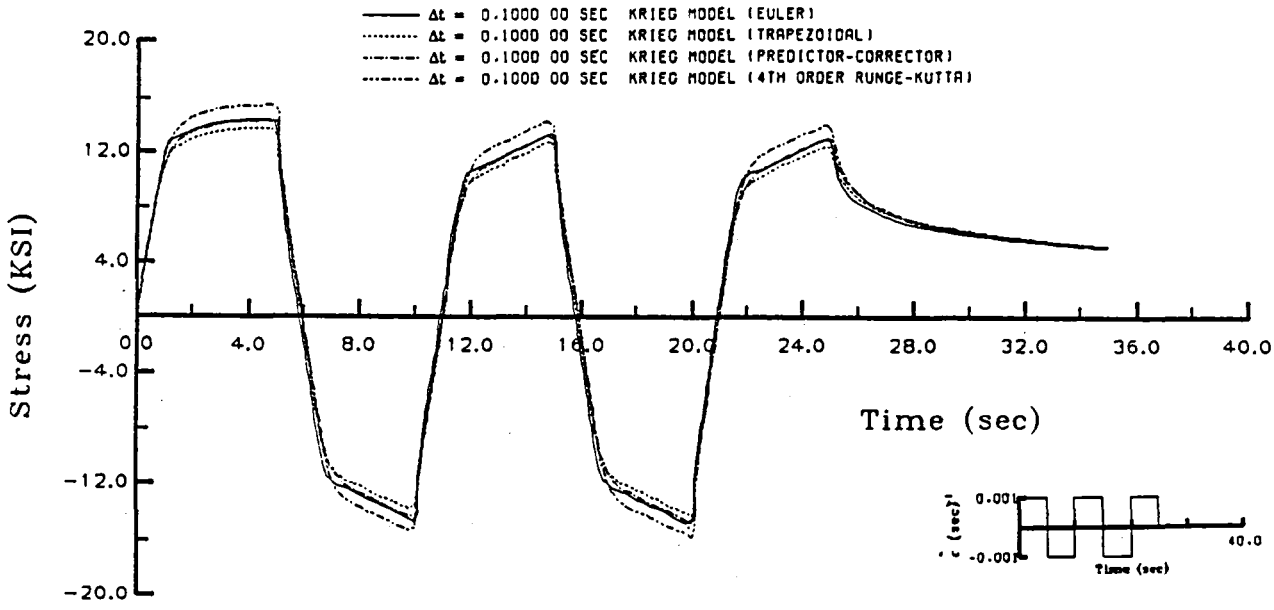

Fig. 1 Comparison of integration methods for Krieg's theory (Hastelloy-X at 1800°F)

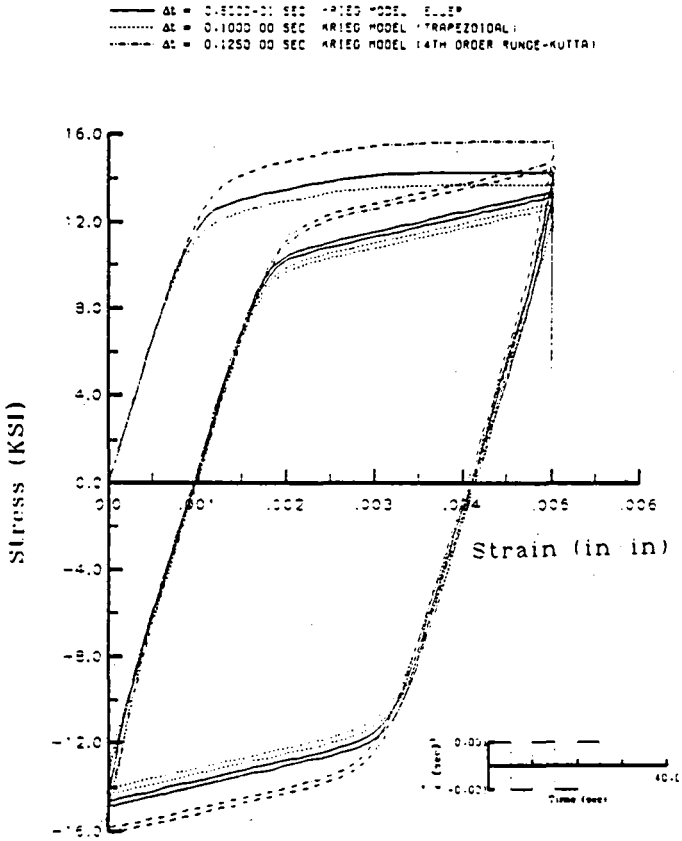

Fig. 2 Comparison of integration methods for Kreig's thoery with equal computation time allowed for each method (Hastelloy-X at 1800°F)

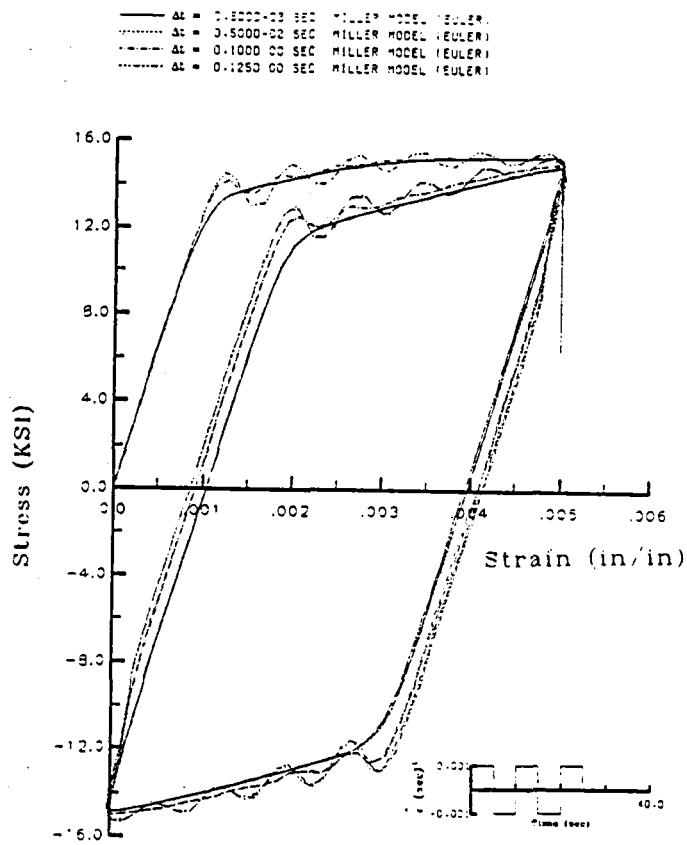

Fig. 3 Stability and accuracy of Euler's method for Miller's theory (Hastelloy-X at 1800°F)

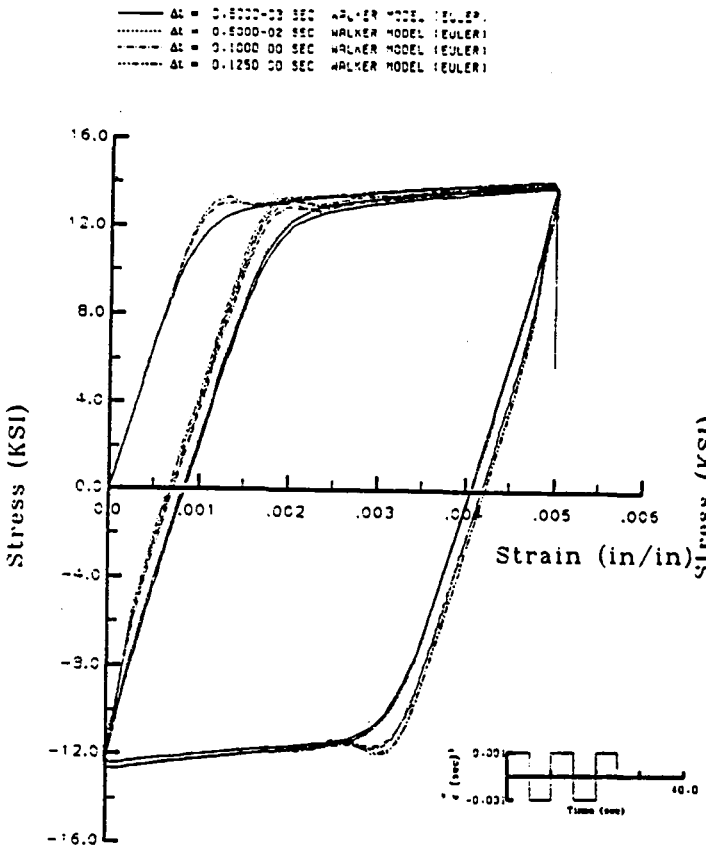

Fig. 4 Stability and accuracy of Euler's method for Walker's theory (Hastelloy-X at 1800°F)

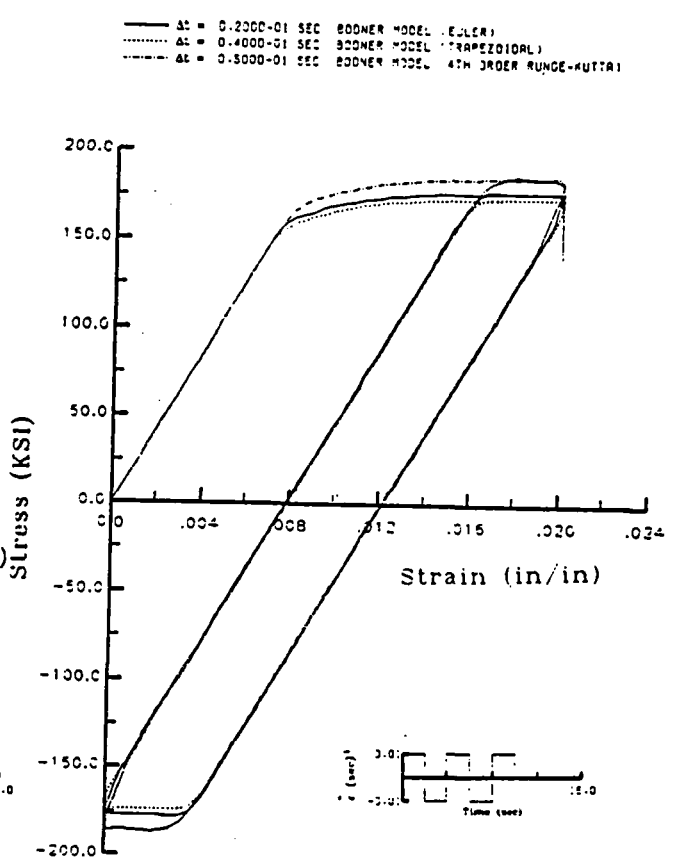

Fig. 5 Comparison of integration methods for Bodner's theory with equal computation time allowed for each method (IN100 at 1350°F)

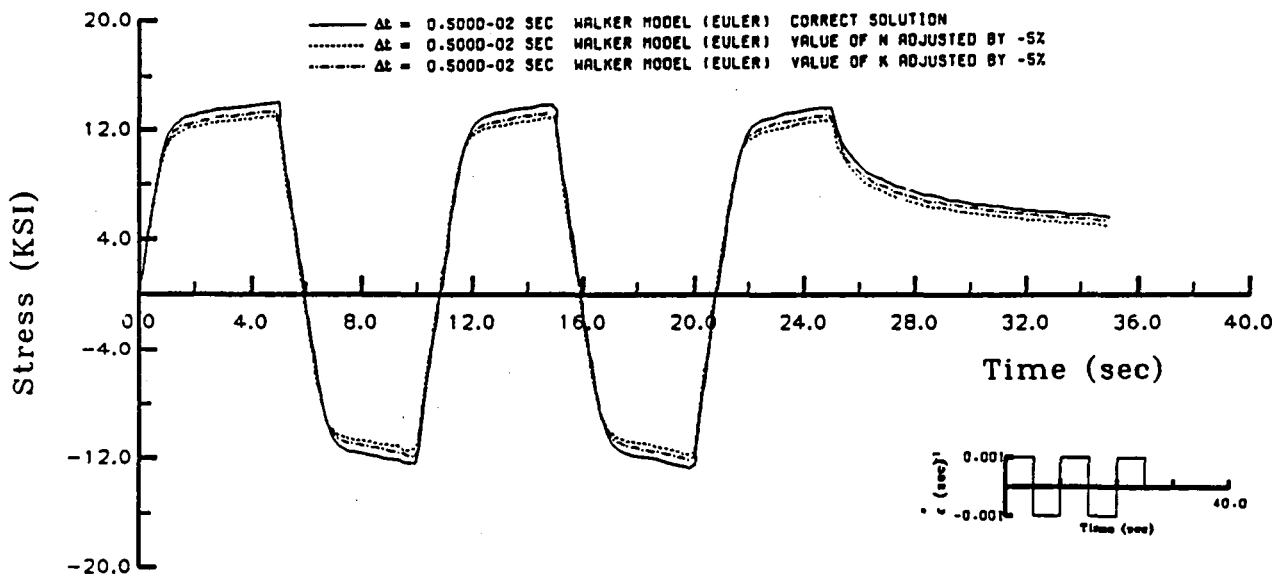

Fig. 6 Sensitivity of Walker's theory to -5% change in input constants (Hastelloy-X at 1800°F)

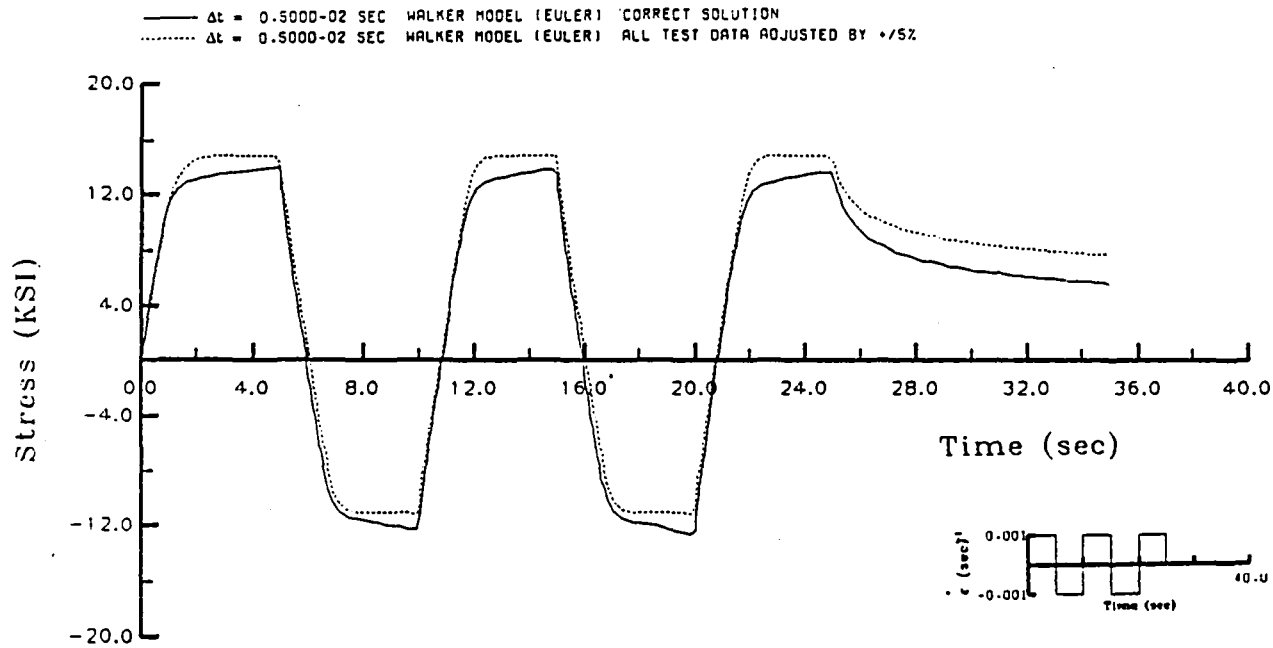

Fig. 7 Sensitivity of Walker's theory to 5% change in experimental test data used to generate constants (Hastelloy-X at 1800°F)

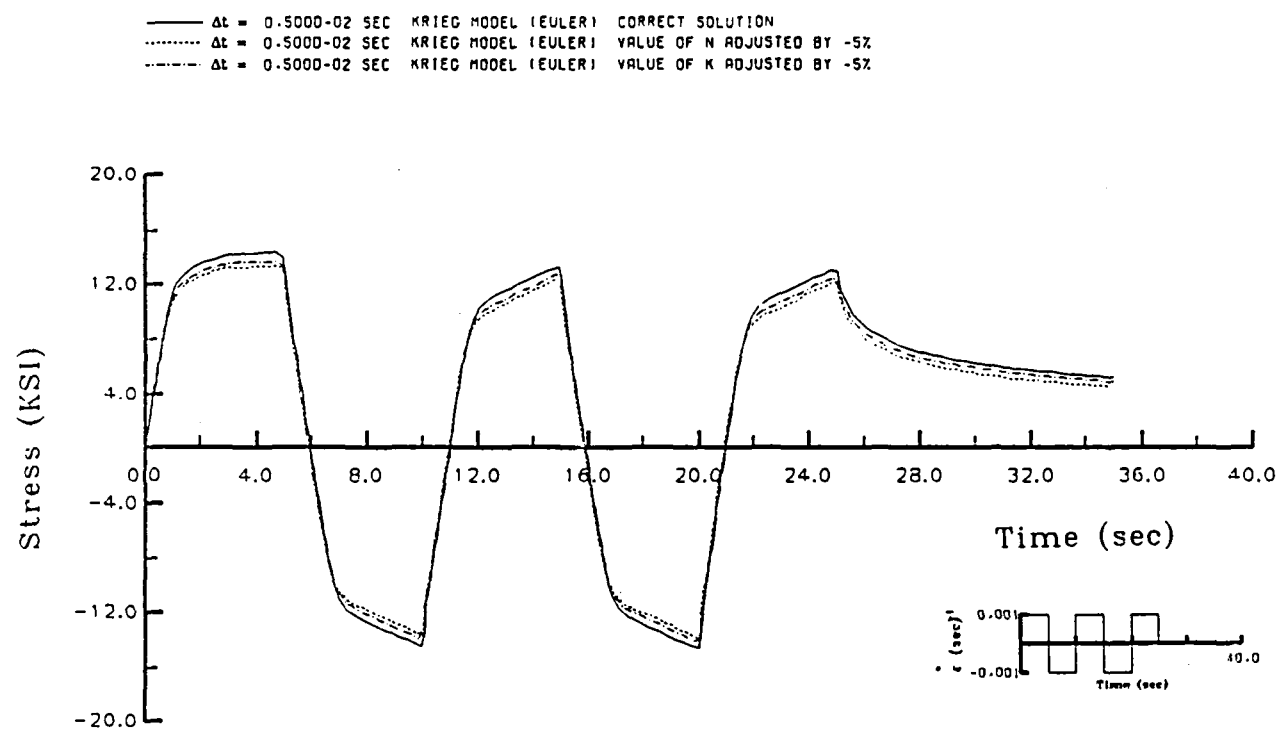

Fig. 8 Sensitivity of Krieg's theory to -5% change in input constants (Hastelloy-X at 1800°F)

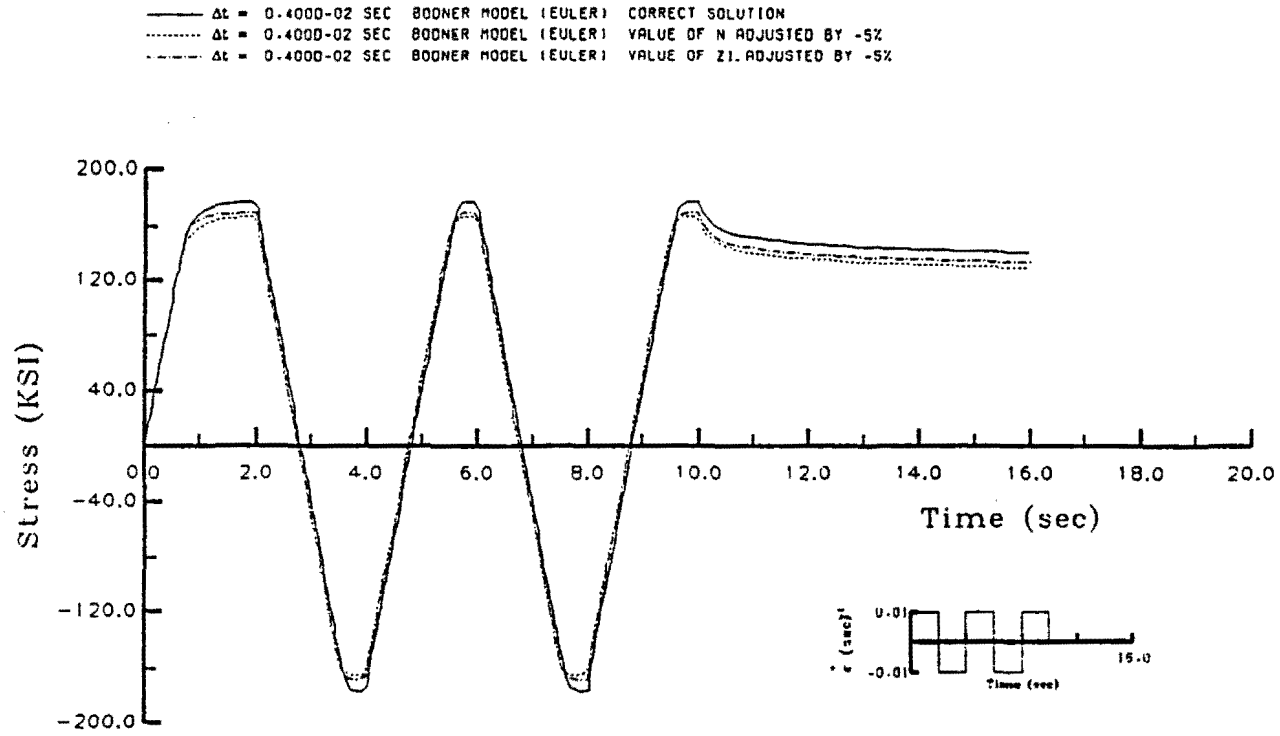

Fig. 9 Sensitivity of Bodner's theory to -5% change in input constants (IN100 at 1350°F)

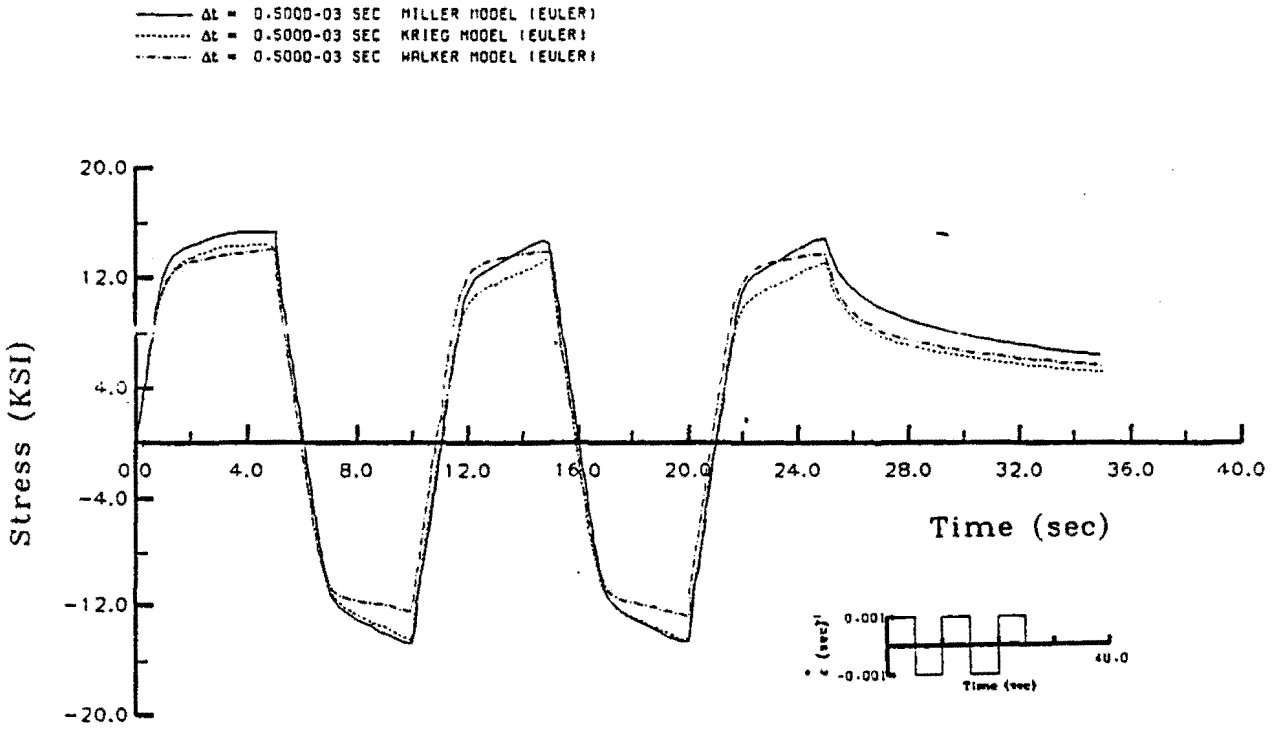

Fig. 10 Comparison of stress-time predictions for Miller, Krieg and Walker theories (Hastelloy-X at 1800°F)

Page intentionally left blank

ON NUMERICAL INTEGRATION AND COMPUTER IMPLEMENTATION OF VISCOPLASTIC MODELS

T.Y. Chang and J.P. Chang
Department of Civil Engineering
University of Akron
Akron, Ohio 44325

R.L. Thompson
NASA Lewis Research Center
Cleveland, Ohio 44135

Due to the stringent design requirement for aerospace or nuclear structural components, considerable research interests have been generated on the development of constitutive models for representing the inelastic behavior of metals at elevated temperatures. In particular, a class of unified theories (or viscoplastic constitutive models) have been proposed [1-10] to simulate material responses such as cyclic plasticity, rate sensitivity, creep deformations, strain hardening or softening, etc. This approach differs from the conventional creep and plasticity theory in that both the creep and plastic deformations are treated as unified time-dependent quantities. Although most of viscoplastic models give better material behavior representation, the associated constitutive differential equations have stiff regimes which present numerical difficulties in time-dependent analysis. In this connection, appropriate solution algorithm must be developed for viscoplastic analysis via finite element method.

In the past, inelastic finite element structural analyses were performed largely based on the classical concept of creep and plasticity [11-14]. Recently, some attempts have been made to incorporate a specific type of viscoplastic theories into finite element codes [15-20] for structural analysis. In this paper, three integration schemes are implemented into a nonlinear finite element program [21] to study their numerical efficiency pertaining to finite element analysis. Moreover, four viscoplastic models, namely, those due to Walker, Miller, Krieg-Swearingen-Rohde, and Robinson, were implemented into a finite element program for nonlinear analysis. A general implementation procedure is outlined in the paper.

VISCOPLASTIC THEORIES

The basic assumption embodied in viscoplastic theories is the unified treatment of inelastic strain; i.e. no distinction is given to creep and plastic deformations. In addition, both elastic and inelastic strains are considered to be present at all stages of loading and unloading processes. The unique feature of such treatment, as compared to classical theories, is that the yield condition is not explicitly involved. Consequently, the computational algorithm for complex loading history can be much simplified. In the context of small deformation, viscoplastic models may be written in the following general form

$$\dot{\underset{\sim}{\sigma}} = \underset{\approx}{D}^{E}\dot{\underset{\sim}{\varepsilon}} - (2G\dot{\underset{\sim}{\varepsilon}}^{I} + \underset{\sim}{\delta}\,(\lambda + 3G)\gamma\dot{T}) \tag{1}$$

$$\dot{\underset{\sim}{\varepsilon}}^{I} = f(\underset{\sim}{\sigma}\ \underset{\sim}{\alpha}\ K\ T)\ (\underset{\sim}{\sigma} - \underset{\sim}{\alpha}) \tag{2}$$

$$\dot{\underset{\sim}{\alpha}} = h_{\alpha}\dot{\underset{\sim}{\varepsilon}}^{2} - r_{\alpha} \tag{3}$$

$$\dot{k} = h_{k}|\dot{\varepsilon}^{1}| - r_{k} \tag{4}$$

where $\dot{(\ )}$ = Time devative; T = Temperature;

$\underset{\sim}{\varepsilon}$ = Total strain vector; $\underset{\sim}{\sigma}$ = Stress vector;

$\underset{\sim}{\alpha}$ = Back stress vector; K = Drag stress;

$\underset{\approx}{D}^{E}$ = Elasticity matrix; λ, G = Lame contant;

$\underset{\sim}{\varepsilon}^{I}$ = Inelastic strain vector;

γ = Linear thermal expansion coefficient;

f = Inelastic strain rate function;

h_α, h_k = Hardening functions for back and drag stresses, respectively;

r_α, r_k = Recovery functions for back and drag stresses, respectively.

Eqs. (1-4) represent a complete set of viscoplastic constitutive equations wherein the following assumptions are invoked in the extention from uniaxial case to the three-dimensional case, namely, i) isotropic material, ii) incompressible inelastic strain, and iii) linear bulk behavior. Eq. (1) defines stress rate to be proportional to elastic strain rate while Eq. (2) states the functional dependence of inelastic strain rate on applied stress, temperature, and state variables. Furthermore, Eqs. (3-4), so-called evolutional equations, are generally constructed in hardening/recovery form such that the net effect of two antagonistic mechanisms uniquely determines the growth rate of state variables α and k.

Although the mathematical expressions of viscoplastic models proposed by various researchers differ in their detailed descriptions, they do however portray several common phenomena: i) Initial linear elastic behavior wherein the inelastic effect is negligible and then nonlinear response afterwards, ii) strain-rate sensitivity, iii) time-dependent creep and relaxation, iv) cyclic hardening or softening, v) creep recovery, vi) creep plasticity interactions, and vii) Bauschinger's effect.

NUMERICAL INTEGRATION SCHEMES

For finite element applications, it is useful to choose an appropriate integration scheme for handling the nonlinear viscoplastic equations concerned. Krieg (22) pointed out the existance of numerical stiff regions in viscoplastic formulation together with a discussion of potential difficulties. The stiffness of the equations originates from the nonlinear relationship assumed in Eq. (1) and the hardening/recovery form in evolutional equations. Formal definition of the stiffness of a set of differential equations can be found in Ref.(23) where the measure of "stiffness" is given in terms of the spectra of eigenvalues obtained from the Jacobian matrix of associated equation system.

Numerical approaches intended for integrating stiff differential equations have been developed by a number of researchers. Among them

Gear's method is the most famous one. Although Gear's package has been used quite effectively in solving one-dimensional constitutive equations, (1) it is not suitable for large scale finite element analysis simply because its solution procedure is of a multistep nature. When employed in finite element analysis, this method usually requires a large amount of storage in order to follow the deformation history of the material. For this reason, one-step method is much preferable.

For the purpose of discussion, the constitutive equations are re-written as follows

$$\dot{\underset{\sim}{y}} = \underset{\sim}{f}(\underset{\sim}{y}, t) \tag{5}$$

where y represents stress, inelastic strain and state variables while f denotes nonlinear functions. One-step method for solving inelastic rate problems in the field of finite element has been investigated by several researchers (24-26). In a broad sense, it can be written in terms of one-parameter (θ) family of implicit algorithm (the - method) as follows.

$$\underset{\sim}{y}_{n+1} = \underset{\sim}{y}_n + \Delta t_n \left[(1-\theta)\, \underset{\sim}{f}_n + \theta\, \underset{\sim}{f}_{n+1} \right] \tag{6}$$

where $\Delta t_n = t_{n+1} - t_n$ is the n-th time step size and θ is an integration parameter which has the range of (0,1). In Eq. (6) it is assumed that a numerical solution at the beginning of time step n is known, the solution at the end of the step is to be sought.

The simplest integration scheme is the explicit forward Euler scheme corresponding to $\theta = 0$. It is an explicit scheme since the solution at time t_{n+1} is completely determined from conditions existing at time t_n. Therefore, in the forward Euler method, the solution at time t_{n+1} is approximated by

$$\underset{\sim}{y}_{n+1} = \underset{\sim}{y}_n + \Delta t_n \underset{\sim}{f}_n \tag{7}$$

When this method is employed in solving stiff equations, very small step size must be used in order to obtain stable and accurate solutions.

On the other hand, the case $\theta = 1/2$ results in the so-called implicit trapezoidal scheme which is also widely known as Crank-Nicholson rule in the context of linear differential equations. Then

$$\underset{\sim}{y}_{n+1} = \underset{\sim}{y}_n + \frac{\Delta t_n}{\gamma} (\underset{\sim}{f}_n + \underset{\sim}{f}_{n+1}) \tag{8}$$

Note that $\underset{\sim}{f}_{n+1} = \underset{\sim}{f}(y_{n+1}, t_{n+1})$ is unknown. Nonlinear implicit equation is best solved by the Newton-Raphson iteration. To this end, Eq. (8) is rewritten in the form

$$\underset{\sim}{F}^{i}_{n+1} = \underset{\sim}{y}^{i}_{n+1} - \underset{\sim}{y}_n - \Delta t_n(\underset{\sim}{f}^{i}_{n+1} + \underset{\sim}{f}_n)/2 = 0 \tag{9}$$

The right superscript "i" denotes iteration number. Since y_n and f_n are known, Newton-Raphson iteration gives

$$\underset{\sim}{y}^{i+1}_{n+1} = \underset{\sim}{y}^{i}_{n+1} - \frac{\underset{\sim}{F}^{i}_{n+1}}{\partial \underset{\sim}{F}^{i}_{n+1} / \partial \underset{\sim}{y}^{i}_{n+1}} \tag{10}$$

Rearranging Eq. (10) yields

$$\frac{\partial \underset{\sim}{F}^{i}_{n+1}}{\partial \underset{\sim}{y}^{i}_{n+1}} = \underset{\approx}{I} - \frac{\Delta t_n \partial \underset{\sim}{f}^{i}_{n+1}}{2\, \partial \underset{\sim}{y}^{i}_{n+1}} \tag{11}$$

Defining

$$\Delta \underset{\sim}{y}^{i+1}_{n+1} = \underset{\sim}{y}^{(i+1)}_{n+1} - \underset{\sim}{y}^{i}_{n+1} \tag{12}$$

and performing differentiation, one obtains

$$[\underset{\approx}{I} - \frac{\Delta t_n}{2} \frac{\partial \underset{\sim}{f}^{i}_{n+1}}{\partial \underset{\sim}{y}^{i}_{n+1}}] \Delta \underset{\sim}{y}^{i+1}_{n+1} = \underset{\sim}{y}_n - \underset{\sim}{y}^{i}_{n+1} + \frac{\Delta t}{2} (\underset{\sim}{f}_n + \underset{\sim}{f}^{i}_{n+1}) \tag{13}$$

where the initial value of $\underset{\sim}{y}^{1}_{n+1}$ may be obtained by an explicit scheme.

Eq. (13) stands for a linear system of equations for implicit trapezoidal method. The system is readily solved by Gaussian elimination and backward substitution. If this method is employed in an analysis, the immediate question is: how one can determine whether the solution has

converged or not? In fact, several convergence criteria could be used for this purpose. One convenient way is to check the iterative value of y such that

$$e = \left|\left|\frac{\Delta y^{(i)}}{y}\right|\right| < Tol \tag{14}$$

where $||\ ||$ = Euclidean norm

Tol = A tolerance ratio

Presently, the above criterion is employed to determine the convergence of a solution.

Comparing Eqs. (7) & (13), it is apparent that the implicit trapezoidal method requires not only much more functional evaluations but also solving a system of linear equations. As an alternative, the implicitness of $\underset{\sim}{f}_{n+1}$ in Eq. (8) may be removed by using Talor series expansion, namely,

$$\underset{\sim}{f}_{n+1} = \underset{\sim}{f}_n + \underset{\approx}{J}_n \Delta \underset{\sim}{y}_{n+1} \tag{15}$$

where

$$J_n = \partial \underset{\sim}{f}_n / \partial \underset{\sim}{y}_n \tag{16}$$

Thus, Eq. (13) becomes

$$[\underset{\approx}{I} - \underset{\approx}{J}_n \Delta t/2]\Delta \underset{\sim}{y}_n = \Delta t\ \underset{\sim}{f}_n \tag{17}$$

The above equation is referred as the explicit trapezoidal scheme since the solution is completely determined from the initial conditions.

At this point, it is instructive to make some qualitative comparisons among the aforementioned numerical schemes. Comparing explicit trapezoidal scheme with forward Euler scheme reveals that they differ only in the expression $J_n \Delta t/2$, i.e. the product of Jacobian matrix and half of step size. The addition of such matrix necessitates the solution be obtained by solving a system of simultaneous equations. Like implicit trapezoidal scheme, it also requires the evaluations of Jacobian matrix. Apparently, by including the extra term, the numerical behavior of the constitutive equations have become stabilized. In this context, $J_n \Delta t/2$ essentially plays the role of a correcting factor. On the other hand, since no itera-

tion is involved in the explicit trapezoidal scheme, it can be viewed as a starter of implicit trapezoidal scheme.

We consider another extreme case, i.e. $\theta = 1$, which is called implicit Euler scheme,

$$\underset{\sim}{y}_{n+1} = \underset{\sim}{y}_n + \Delta t_n \underset{\sim}{\dot{f}}_{n+1} \tag{18}$$

Hughes et al (24) demonstrated that for viscoplastic finite element analysis one-parameter family of implicit algorithm is unconditionally stable when $\theta > 1/2$ while only conditionally stable otherwise. In recent years, various numerical schemes have been applied to viscoplastic problems (15-20,24-26). Some of the authors have discarded the explicit Euler method due to its numerical instability. However, the validity of this conclusion needs to be further explored. In Ref. (27), present investigators evaluated three numerical techniques for integrating the viscoplastic constitutive equations for a uniaxial state of stress. The schemes evaluated were: i) forward Euler method, ii) explicit trapezoidal method, and iii) implicit trapezoidal method with Newton-Raphson iteration method. Although implicit trapezoidal method with iteration appears to be more stable and accurate than the other methods even when the step size is considerable large, its suitability for finite element analysis must be re-assessed.

In principle, inelastic analysis using finite element method consists of a sequence of incremental process. Two most widely used approaches are the initial strain and tangent stiffness methods. In consideration of the formulation presented in Eqs. (1-4), one finds that the initial strain method is the most natural way to handle viscoplastic models. The reason behind this will be elaborated below.

In Eq. (1), we invoke an assumption that the strain increment is decomposed into elastic and inelastic components. Then, the inelastic part, which is governed entirely by Eqs. (1-4) at constitutive level, is converted into an equivalent load in the finite element formulation. Thus, we have

$$\underset{\approx}{K^E} \underset{\sim}{\Delta u} = (\underset{\sim}{\Delta p_0}) + (\underset{\sim}{\Delta p_\varepsilon}) \tag{19}$$

where

K^E = Elastic structural stiffness matrix, which may vary with the temperature

Δu = Incremental nodal displacement vector

Δp_o = Incremental vector of applied load

Δp_ε = Incremental vector due to inelastic and thermal strains.

In addition to the incremental procedure used for solving the global stiffness equations, a subincrementing technique is employed to calculate the constitutive material matrix. That is, let Δt be the time increment for solving the global stiffness equations. Then Δt is sub-divided into smaller increments with a constant step size, $\Delta\tau = \Delta t/m$. Moreover, the number of subincrements can be determined by an automatic stepping procedure for which an error measure is compared with a specified tolerance. Further discussion of this is given in [27].

COMPUTER IMPLEMENTATION

With the constitutive relations and numerical integration schemes outlined in the previous sections, the next step is to implement these relationships into a typical (general purpose) finite element program for intended analysis. For this purpose, the related computer subroutines are written in the form of an independent material module so that it can be easily interfaced with a finite element code.

The calculation steps for a viscoplastic model can be summarized as follows:

Step 1. Preset the strains, stresses, back stresses, inelastic strains, nodal temperatures, etc. transferred from the main program.

Step 2. For non-isothermal condition, interpolate temperature at Gauss points from nodal temperatures.

Step 3. Compute strain rate and temperature rate, and select step size of subincrements.

Step 4. Interpolate temperature dependent material constants based on the average temperature at the mid-point of a time step.

Step 5. Solve for the state variables from the constitutive equations using a subincrementing method with a selected integration technique.

Step 6. Check for solution convergence and determine whether cut-back of step size is necessary.

Step 7. Update the stresses, strains, inelastic strains and other state variables, then return to the main program.

EXAMPLE

To demonstrate the utility of the finite element procedures, Robinson's unified theory was applied to the analysis of a pressurized thick-walled cylinder which is restrained in its axial direction. Finite element mesh, its dimension and boundary condition are shown in Fig.1. The loading history consists of a 0.0028 hour ramp up to an internal pressure of 3.65 ksi followed by a hold period at that temperature for 200 hours. Explicit trapezoidal method was employed for this example.

Figs. 2 to 3 show the predicted redistribution of hoop and axial stress at several selected time following rapid pressurization, wherein zero time denotes the end of the loading ramp. As can be seen, while the internal pressure is held constant, these stresses undergo variation exhibiting rapid redistribution followed by a steady-steady response. The tendency of approaching to a saturated state is apparent.

Figs. 4 and 5 show the creep displacement at the outside wall of thick-walled cylinder using both Euler and explicit trapezoidal scheme with different time step sizes as well as number of subincrements. Solid line indicates the base-line solution using the explicit trapezoidal scheme. From the numerical experiments, it was found that the forward Euler integration scheme with an automatic stepping and error control is far more efficient in computation as compared to the explicit and implicit trapezoidal schemes.

REFERENCES

1. Miller, A.K., "An Inelastic Constitutive Model for Monotonic, Cyclic, and Creep Deformation" ASME Journal of Engineering Materials and Technology, Vol. 98, 1976, pp. 97-113.

2. Kreig, R.D., Swearingen, J.C., and Rohde, R.W., "A Physically-based Internal Variable Model for Rate-Dependent Plasticity", Inelastic Behavior of Pressure Vessel and Piping Components, T.Y. Chang and E. Krempl Eds., ASME PVP-PB-028, 1978, pp. 15-28.

3. Walker, K.P., "Representation of Hastelloy-X Behavior at Elevated Temperature with a Functional Theory of Viscoplaticity", Paper presented at ASME/PVP Century 2 Energy Technology Conference, San Francisco, CA., Aug. 1980.

4. Hart, E.W., "Constitutive Relations for the Nonelastic Deformation of Metals", ASME Journal of Engineering Material and Technology, Vol. 98, 1976, pp. 193-202.

5. Robinson, D.N., "A Unified Creep-Plasticity Model for Structural Metals at High Temperature" ORNL/TM-5969, Oak Ridge National Laboratory, Oct. 1978.

6. Cernocky, E.P., and Krempl, E., "A Theory of Theromo-Viscoplasticity Based on Infinitesimal Total Strain", International Jouranl of Solid and Structures, Vol. 16, 1980, pp. 723-741.

7. Cernocky, E.P., and Krempl, E., "A Nonlinear Uniaxial Integral Constitutive Equation Incorporating Rate Effects, Creep, and Relaxation" International Journal of Nonlinear Mechanics, Vol. 14, 1979, pp. 183-389.

8. Bodner, S.R., and PArtom, Y., "Constitutive Equations for Elastic-Viscoplastic Strain-Hardening Materials", ASME Journal of Applied Mechanics, Vol. 42, 1975, pp. 385-389.

9. Chaboche, J.L., and Rousselier, G., "On the Plastic and Viscoplastic Constitutive Equations", Inelastic Analysis and Life Prediction in Elevated Temperature Design, Edited by G. Baylac, ASME PVP-Vol. 59, 1982, pp. 33-35.

10. Larsson, B., and Storakers, B., "A State Variable Interpretation of Some Rate-Dependent Inelastic Properties of Steel", ASME Journal of Engineering Materials and Technology, Vol. 100, 1978, pp. 395-401.

11. Snyder, M.D., and Bathe, K.J., "A Solution Procedure for Thermo-Elastic-Plastic and Creep Problems", Journal of Nuclear Engineering and Design, Vol. 64, 1981, pp. 49-80.

12. Haisler, W.E., and Sander, D.R., "Elastic-Plastic-Creep-Large Strain Analysis at Elevated Temperature by the Finite Element Method", Computer and Structures, Vol. 10, 1979, pp. 375-382.

13. Cyr, N.A., and Teter, R.D., "Finite Element Elastic-Plastic-Creep Analysis of Two-Dimensional Continuum with Temperature Dependence Material Properties", Computer and Structures, Vol. 3, 1973, pp. 849-863.

14. Levy, A., and Pifko, A.B., "On Computational Strategies for Problems Involving Plasticity and Creep", International Journal for Numerical Methods in Engineering, Vol.17, 1981, pp. 747-771.

15. Morjaria, M., and Mukherjee, S., "Finite Element Analysis of Time-Dependent Inelastic Deformation in the Presence of Transient Thermal Stresses", International Journal of Numerical Methods in Engineering Vol. 17, 1981, pp. 909-921.

16. Robinson, D.N., and Swinderman, R.W., "Unified Creep-Plasticity Constitutive Equations for 2-1/4 Cr - 1 Mo Steel at Elevated Temperature", ORNL/TM-8444, Oak Ridge National Laboratory, 1983.

17. Zirin, R.M., and Krempl, E., " A Finite Element Integration Method for the Theory of Viscoplasticity Based on Infinitesimal Total Strain", ASME Journal of Pressure Technology, Vol. 104, May 1982, pp. 130-136.

18. Newman, M., Zaphir, Z., and Bodner, S.R., "Finite Element Analysis for Time Dependent Inelastic Material Behavior", Computer and Structures, Vol. 6, 1976, pp. 157-162.

19. Walker, K.P., "Research and Development Program for Nonlinear Structure Modeling with Advanced Time-Dependent Constitutive Relationships", Report to NASA Lewis Research Center, NAS3-22055.

20. Chang, T.Y., NFAP - A Nonlinear Finite Element Analysis Program, Vol. 1 and 2, Dept. of Civil Engineering, The University of Akron, Akron, Ohio, Oct. 1980.

21. Krieg, R.D., "Numerical Integration of Some New Unified Plasticity-Creep Formulation", Transactions of the 4-th SMIRT Conference, San Francisco, CA., Vol. M, 1977, Paper M 6/4.

22. van der Houwen, P.J., Construction of Integration Formular for Initial Value Problem, North-Holland Publishing Company, Amsterdam, 1977.

23. Hughes, T.J.R., "Unconditionally Stable Algorithms for Quasi-Static Elasto/Visco-plastic Analysis", Computer and Structures, Vol. 8, 1978, pp. 169-173.

24. Willam, K.J., "Numerical Solution of Inelastic Rate Processes", Computer and Structures, Vol. 8, 1978, pp. 511-531.

25. Cormeau, I., " Numerical Stability in Quasi-Static Elasto/Visco-Plasticity", International Journal for Numerical Methods in Engineering, Vol. 9, 1975, pp. 109-127.

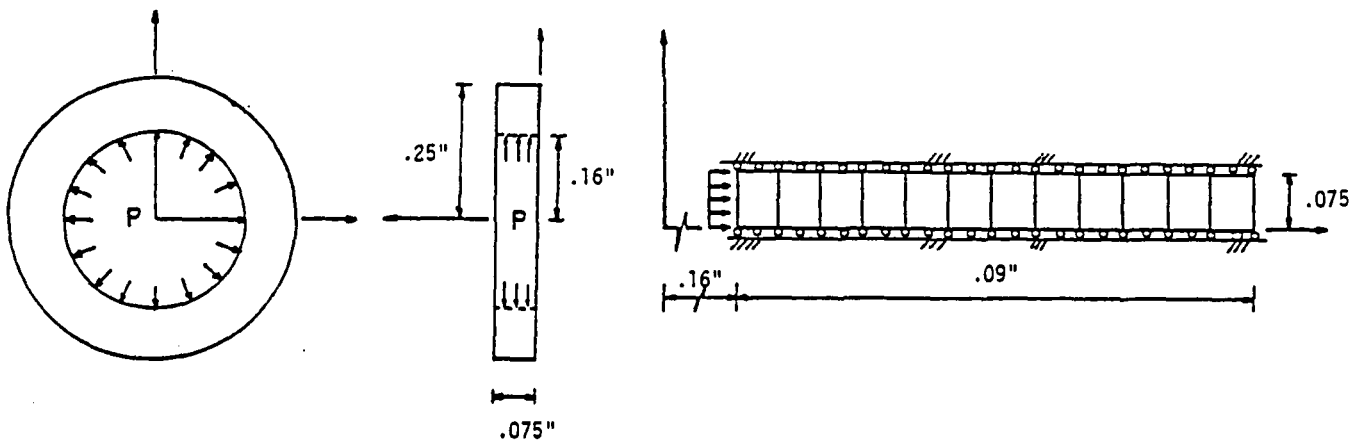

Fig. 1 - A Thick Wall Cylinder Under Internal Pressure

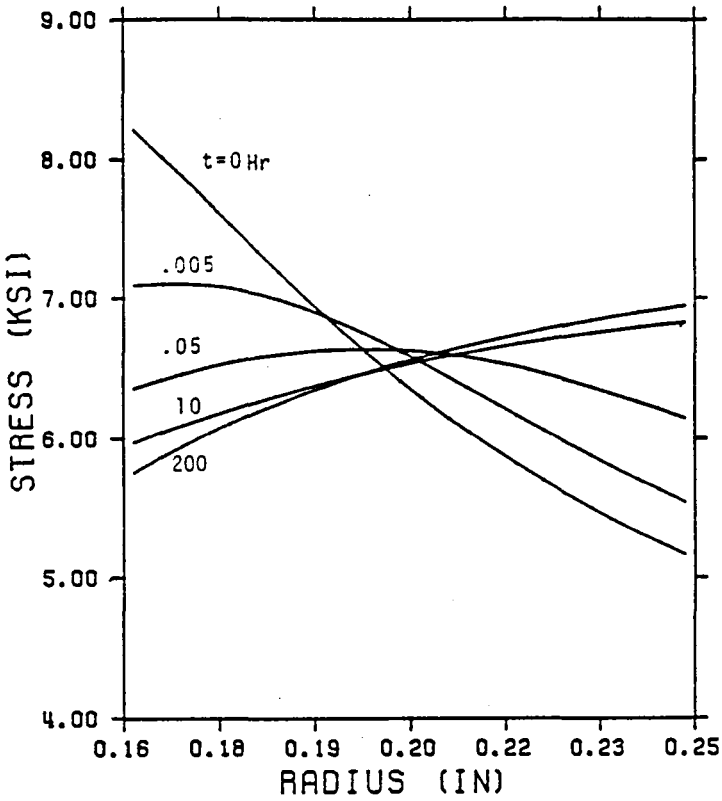

Fig. 2 - Hoop Stress Distribution

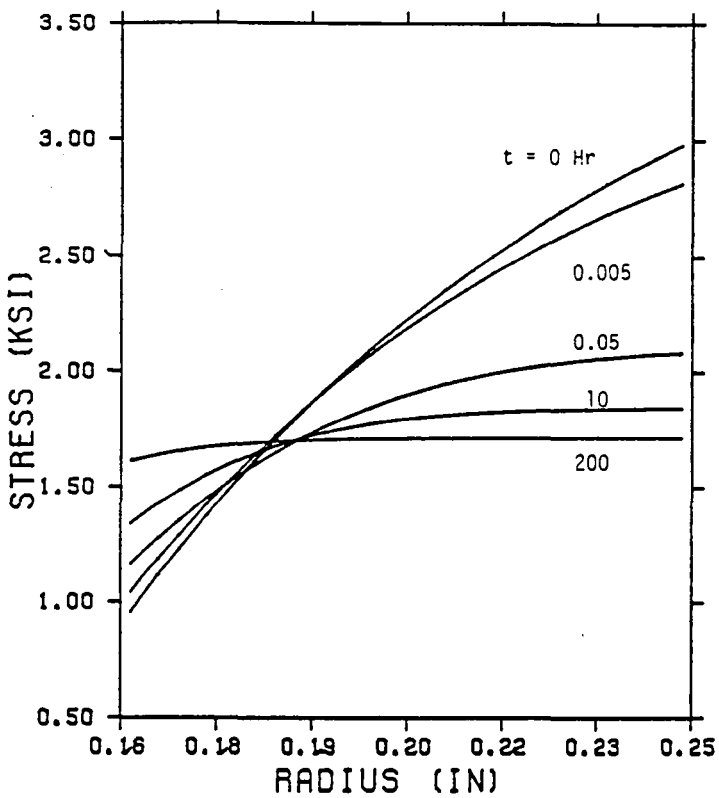

Fig. 3 - Axial Stress Distribution

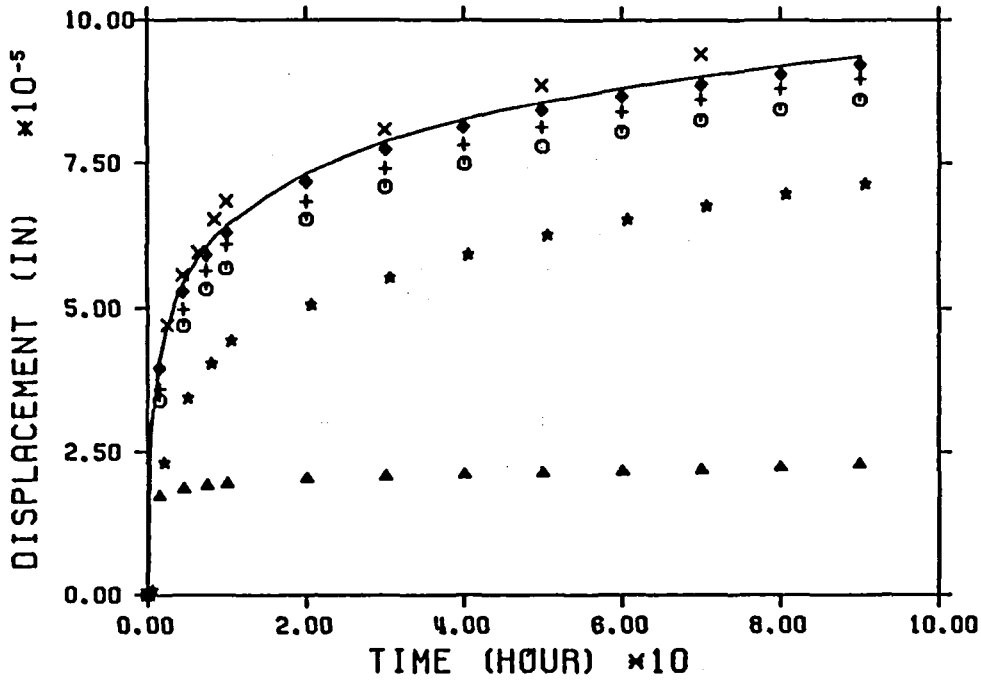

Fig. 4 - Creep Displacement at Outside Wall of the Cylinder by Various Integration Steps.

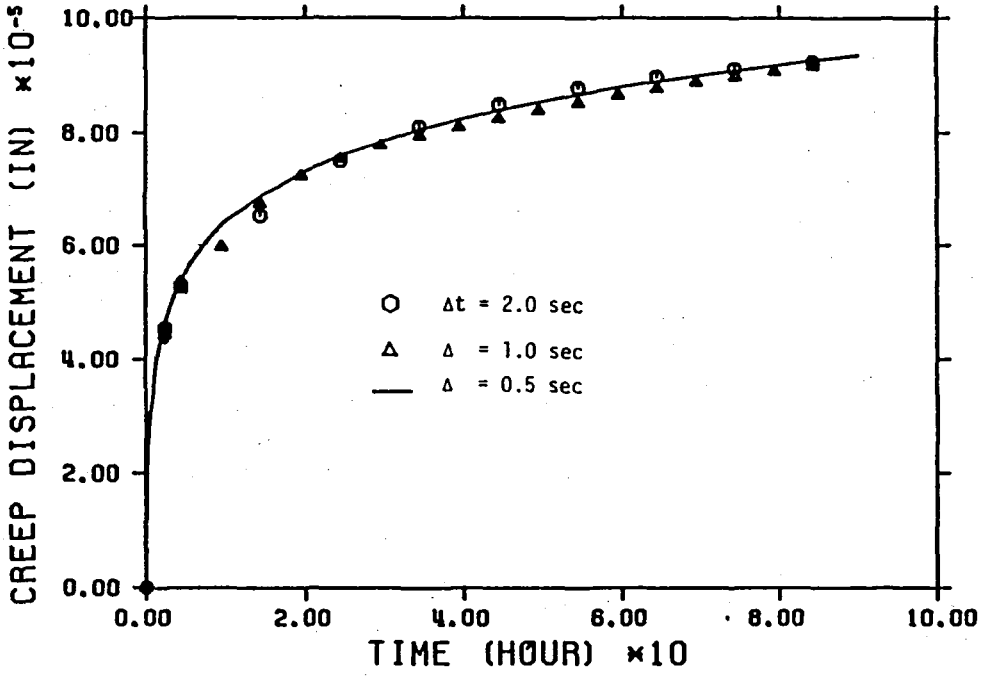

Fig. 5 - Creep Displacement Predicted by Euler Method with Automatic Stepping

TWO SIMPLIFIED PROCEDURES FOR PREDICTING CYCLIC MATERIAL RESPONSE FROM A STRAIN HISTORY

Albert Kaufman
NASA Lewis Research Center
Cleveland, Ohio 44135

Vito Moreno
Pratt & Whitney Aircraft
East Hartford, Connecticut 06108

Simplified inelastic analysis procedures were developed at NASA Lewis and Pratt & Whitney Aircraft for predicting the stress-strain response at the critical location of a thermomechanically cycled structure. These procedures are intended primarily for use as economical structural analysis tools in the early design stages of aircraft engine hot section components where nonlinear finite-element analyses would be prohibitively expensive. Both simplified methods use as input the total strain history calculated from a linear elastic analysis. The elastic results are modified to approximate the characteristics of the inelastic cycle by incremental solution techniques. A von Mises yield criterion is used to determine the onset of active plasticity. The fundamental assumption of these methods is that the inelastic strain is local and constrained from redistribution by the surrounding elastic material.

In the procedure developed by PWA, a power law creep expression is combined with the elastic response to define the stress change over an increment of time. A Taylor series expansion is used to calculate the stress at the end of an increment from the stress at the beginning and the appropriate derivatives.

In the NASA Lewis procedure, a computer program (ANSYMP) was developed to predict the stress history at the critical location using the total strain-temperature history as input. Material cyclic stress-strain and creep properties and appropriate constitutive models are coded into user subroutines in the program. Plastic strains are computed iteratively for each increment of loading. Creep effects can be calculated on the basis of stress relaxation at constant strain, creep at constant stress or a combination of stress relaxation and creep accumulation.

The two simplified procedures were exercised on a combustor liner louver lip cycle and two thermomechanical fatigue test cycles. Both methods were able to capture the overall shapes of the hysteresis loops and to predict the stress levels to a degree of accuracy sufficient for most life prediction models.

INTRODUCTION

Requirements for better performance and fuel economy in aircraft gas turbine engines have adversely affected the durability of the hot section components. Structures such as combustor liners, turbine blades and vanes, and support structures experience severe gas temperature environments and operating conditions which often result in significant cyclic plastic and creep strains. Structural analysis under these conditions becomes a formidable undertaking. Improvements in the durability of hot section structures depend on accurate definition of the cyclic stress-strain response at the critical fatigue location.

Finite-element computer programs have been used with increasing frequency for the structural analysis of gas turbine engine components. In lower temperature components, design stress levels are maintained below the material yield strength. Linear finite-element analysis is sufficient for this type of component and the elastic solutions can be obtained rapidly and economically over the range of loading conditions constituting the flight cycle. However, for structures in the hot part of the engine, local stresses can exceed the material yield strength and can induce time-dependent creep deformation. Accurate prediction of the local inelastic stress-strain response under these conditions requires nonlinear structural analysis.

An example of a nonlinear structural analysis of a hot section component is described in Reference 1 for a half-scale louver-type combustor liner. This liner specimen was constructed in an identical configuration with current combustor liners in service and was tested in an induction heated experimental rig. The three-dimensional finite element model of a segment of the half-scale combustor liner (Figure 1) was subjected to the thermal loading cycle shown in Figure 2 (a). Both linear elastic and nonlinear stress-strain solutions for the critical fatigue location at the end of the louver lip are shown in Figures 2 (b) and (c) with letter designations corresponding to the time points shown in Figure 2(a). The linear thermoelastic analysis was conducted at a number of specific points throughout the thermal loading cycle. The results show compressive stresses beyond the material yield strength and a closed cyclic reponse. An incremental nonlinear analysis predicts a more realistic stress-strain response that includes cyclic plasticity and strain ratchetting. These analyses were performed using the MARC nonlinear finite-element code (Ref. 2). This and similar general purpose nonlinear codes use uncoupled classical time-independent plasticity and time-dependent creep models and sophisticated computational algorithms. With these features, a nonlinear finite element analysis represents a labor intensive, time-consuming and costly effort which is generally incompatible with the iterative nature of the design process.

This paper presents two simplified procedures for more economically estimating the local hysteretic response produced by cyclic thermal loading by using as input the total strain history calculated from an elastic analysis. The two procedures were exercised on two thermomechanical fatigue test cycles and a "faithful cycle" simulation of the strain-temperature history at the combustor liner louver lip. Both methods were able to capture the overall shapes of the hysteresis loops and to predict the stress levels to a degree of

accuracy sufficient for most life prediction models. Development of these simplified analyses should reduce the need for nonlinear finite-element analysis in the early design stages for hot section components.

SYMBOLS

A,n = temperature-dependent constants in creep power law, equation (8)
E = modulus of elasticity
E_ρ = strain hardening slope of stress-strain curve
K,m = temperature-dependent constants in stress-strain equation
t = time
T = temperature
w = work hardening slope at maximum plastic strain
$\Delta\epsilon$ = strain increment
$\Delta\sigma$ = yield stress shift due to load reversal
Δt = time increment
ϵ = strain
$\dot{\epsilon}$ = strain rate
equation (1)
σ = stress
α = backstress,
$\dot{\sigma}$ = $E\dot{\epsilon} - EA|\sigma|^{n-1}\sigma$
$\ddot{\sigma}$ = $-nEA|\sigma|^{n-2}\sigma\dot{\sigma}$
$\dddot{\sigma}$ = $-n(n-1)EA|\sigma|^{n-3}\sigma\dot{\sigma}^2 - nEA\sigma^{n-2}\sigma\ddot{\sigma}$
ν = Poisson's ratio

subscripts:

c = creep
e = elastic
i = beginning of increment
$i+1$ = end of increment
max = maximum value at start of unloading
p = plastic
t = total
y = yield

ANALYTICAL PROCEDURE

Within the gas turbine engine, certain hot section components experience a degree of inelastic or nonlinear stress-strain response. These components (combustor liners, turbine vanes, cases and other support structures) are subjected to cyclic thermomechanical loading where the predominant stress is produced by temperature differentials within the structure. In general, the resulting inelastic response is localized to the area of maximum temperature gradient while the remainder of the structure remains elastic. The stiffer elastic material acts as a constraining body and controls the cyclic strain range experienced by the inelastic region. A comparison of predicted results from nonlinear and linear elastic finite-element analyses in References 1,3 and 4 have shown that the cyclic total strain range and total strain history at the location of maximum inelastic response can be estimated from the linear thermoelastic analyses. Therefore, these simplified procedures assume, that the

local mechanical strain and temperature histories at a location in the structure are known from previous linear analysis. Basic material (Hastelloy X) properties, including yield stresses and creep parameters developed for these analyses, are shown in Table I.

Simplified Procedure 1

This procedure for predicting local stress-strain response was developed at Pratt & Whitney Aircraft under contract to NASA Lewis Research Center and is fully documented in Reference 5. Development of the procedure assumes that the strain-temperature histories produced by a loading cycle are known from previous analysis. An incremental description of the histories together with the procedure described below is used to calculate the resulting stress history. Each increment in strain is assumed to be composed of either time-independent plasticity or time-dependent elastic and creep response.

$$\Delta\epsilon = \Delta\epsilon_p \tag{1a}$$

or $$\Delta\epsilon = \Delta\epsilon_e + \Delta\epsilon_c \tag{1b}$$

Since the solution strategy is based on the prediction of stress increments, equations (1) are rewritten as

$$\Delta\sigma = \Delta\sigma_p \tag{2a}$$

or $$\Delta\sigma = \Delta\sigma_e + \Delta\sigma_c \tag{2b}$$

During a loading cycle, the onset of plastic action is determined by the conventional yield surface concept taken from the classical time-independent plasticity model. The yield surface is assumed to be temperature dependent and isotropic with no strain hardening (fixed size and equal in tension and compression). Justification for this definition of the yield surface is based on two observations: (1) that at higher temperatures, Hastelloy X displays little cycle hardening and (2) that the variable temperature experienced in a thermomechanical cycle, which is the primary application of this procedure, reduces the amount of cyclic hardening developed at the lower temperatures.

The stress increment associated with time-independent plastic action is then calculated as

$$\sigma_{i+1} - \sigma_i = \Delta\sigma_p = \sigma_{y,i+1} - \sigma_{y,i} \qquad \text{for } \sigma_i = \sigma_{y,i} \text{ and } T_{i+1} \geq T_i \tag{3}$$

or $$\Delta\sigma_{i+1} - \sigma_i = \Delta\sigma_p = (E_{p,i+1} + E_{p,i})\Delta\epsilon/2 \qquad \text{for } \sigma_i = \sigma_{y,i} \text{ and } T_{i+1} < T_i \tag{4}$$

For all other loading conditions the strain, or stress, is assumed to be time dependent elastic and creep response.

$$\Delta\epsilon_t = \Delta\epsilon_e + \Delta\epsilon_c \tag{5}$$

However, rather than consider a separate uncoupled creep model, an integrated or viscoplastic approach is used. This approach was pursued based on the observation that the cyclic material response is not purely elastic in

either the loading or unloading parts of the response curves. Instead the transient response represents a simultaneous elastic and creep action. Development of the model is as follows:

$$\dot{\epsilon}_t = \dot{\epsilon}_e + \dot{\epsilon}_c \tag{6}$$

where $$\dot{\epsilon}_e = \dot{\sigma}/E \tag{7}$$

with Young's modulus, E, assumed to be temperature dependent but constant over any increment of loading. For the creep rate term, use is made of the short time monotonic creep model developed in Reference 1. This expression is

$$\dot{\epsilon}_c = (\sigma/A)^n \tag{8}$$

Thus, equation can be written as

$$\dot{\epsilon}_c = \sigma/E + A\sigma^n \tag{9}$$

or $$\dot{\sigma} = E\dot{\epsilon}_c - EA\sigma^n \tag{10}$$

An incremental solution of this nonlinear equation was developed using a Taylor series expansion.

$$\sigma_{i+1} = \sigma_i + \dot{\sigma}_i \Delta t + \ddot{\sigma}_i \Delta t^2/2! + \dddot{\sigma}_i \Delta t^3/3! + \ldots \tag{11}$$

For cyclic analysis the stresses used in equation (11) are effective values modified by a backstress, i.e:

$$\sigma^* = \sigma - \Omega \tag{12}$$

In a physical sense, the backstress is an internal stress generated by plastic deformation that changes the reference point for measurement of global stress. The function used to estimate the value of the backstress in these calculations is:

$$\Omega = \sigma_{max} - \sigma_i \quad \text{for } \sigma_{max} \leq 2\sigma_y \tag{13}$$

or $$\Omega = \sigma_y \quad \text{for } \sigma_{max} > 2\sigma_y \tag{14}$$

This is equivalent to considering a series of temperature-dependent circular yield surfaces pinned at the maximum tensile stress in the cycle and the back stresses as the centers of the yield circles. The limiting condition occurs when the diameter of the yield circle equals the maximum stress; a smaller (hotter) yield circle would predict reverse plasticity at the same sign of stress as the maximum stress which would be positive in this case. This is generally considered not possible and therefore the back stress is limited to the value of the yield stress for these temperatures.

Simplified Procedure 2

This fully automated procedure was developed at NASA Lewis Research Center for calculating the stress-strain history at the critical fatigue location of a structure subjected to cyclic thermomechanical loading. It has been implemented in a computer program (ANSYMP) which is documented in Reference 6. The procedure has been exercised on a wide variety of problems including multiaxial loading, nonisothermal conditions, different materials and constitutive models, and dwell times at various points in the cycles. Comparisons of the results of the simplified analyses for these problems with MARC inelastic solutions are reported in Reference 6. The basic assumption is that the total strain ranges calculated from linear elastic and nonlinear analyses are approximately equal. Another assumption of the method is that the effective stress-equivalent total strain hysteresis loops constructed from an elastic-plastic analysis will be parallel to the elastic hysteresis loop. The validity of these assumptions is demonstrated in References 1,3 and 4.

The procedure was set up to calulate the material cyclic response using the total strain obtained from an elastic analysis or strain measurements. Classical plasticity methods are used to characterize the yield surface by a yield condition to describe yielding under multiaxial stress states and by a hardening model to establish the location of the yield surface during cycling. This procedure was set up to accommodate itself to any yield criterion or hardening model. The only requirements are that the elastic input data, whether calculated or measured, be in a form consistent with the yield criterion and that the appropriate material properties be used in conjunction with the hardening model.

Most nonlinear computer programs use the von Mises yield criterion and incremental plasticity theory. Implicit in the von Mises yield criterion is the conversion of the total strain from a uniaxial stress-strain curve to modified equivalent total strain. The modified elastic equivalent total strain corresponds to the uniaxial total elastic strain multiplied by $2(1+\nu)/3$. This relationship must be taken into account for multiaxial problems in applying strain results from elastic finite-element programs or strain measurements as input for the simplified procedure.

In this study, all of the analyses were performed with the Hastelloy stress-strain properties and combined isotropic-kinematic hardening model used for the MARC nonlinear analyses in Reference 1. Creep computations were conducted with the same monotonic creep properties developed in Reference 1. Creep characteristics of the material were incorporated into the program with the creep model expressed by equation (8) and the constants given in Table I.

The yield stress shift ($\Delta\sigma_y$) due to load reversal under kinematic hardening is

$$\Delta\sigma_y = 2(\sigma_y - w(\epsilon_{p,max})) \tag{15}$$

where σ_y represents the current, not the initial, yield stress.

The procedure permits any of three creep options to be selected; (1) stress relaxation at constant strain, (2) cumulative creep at constant stress, and (3) a combination of (1) and (2). Option 1 was used for the simplified analyses conducted for this study since the problems involved strain controlled tests.

The elastic input data are subdivided into a sufficient number of increments to define the stress-strain cycle. To simulate the effects of time-dependent plasticity, dwell times for creep analysis were specified for all increments. The input data for the analyses were supplied by Pratt & Whitney Aircraft. The increments are analyzed sequentially to obtain the cumulative plastic and creep strains and to track the yield surface. An iterative procedure is used to calculate the yield stresses for increments undergoing plastic straining. First, an estimated plastic strain is assumed for calculating an initial yield stress from the stress-strain properties and the simulated hardening model. Second, a new plastic strain is calculated as

$$\epsilon_p = \epsilon_t - \epsilon_e - \sigma_y / E \tag{16}$$

The yield stress is then recalculated using the new plastic strain. This iterative procedure is repeated until the new and previous plastic strains agree within a tolerance of 1 percent.

A FORTRAN IV computer program (ANSYMP) was created to automatically implement the simplified analytical procedure. The program consists of the main executive routine, ANSYMP, and four subroutines, ELAS, YIELD, CREEP, and SHIFT. The incremental elastic data and temperatures are read into subroutine ELAS. Material stress-strain properties as a function of temperature and a simulated hardening model are incorporated in subroutine YIELD and the creep characteristics are incorporated in subroutine CREEP. Subroutine SHIFT is required to update the temperature effects on the yield stress shift. SHIFT also serves the function of deciding the future direction of the yield surface under nonisothermal conditions by determining the relation of future to past thermal loading.

The ANSYMP program is available from the Computer Software Management Information Center (COSMIC), University of Georgia, Athens, Ga. 30602 under LEW 14011. A flow chart of the program and sample input and output data are presented in Reference 6.

The calculational scheme initially follows the effective stress-equivalent strain input data from subroutine ELAS until the occurrence of initial yielding. The stress-strain solution then proceeds along the yield surface as determined from the stress-strain properties in subroutine YIELD. At each increment during yielding the stress shift (difference between new yield stress and stress predicted from elastic analysis) from the original input data is calculated. Elastic load reversal is signaled when the input stress is less than the yield stress from the previous increment. During elastic unloading, the stresses are translated from the original elastic analysis solution by the amount of the calculated stress shift. Reverse yielding occurs when the stress reaches the reverse yield surface as determined from the hardening model incorporated in subroutine YIELD. Again, the solution follows the yield surface until another load reversal is indicated when the stress based on the shifted elastic solution is less than the yield stress. The elastic response during load reversal is obtained by translating the original elastic solution according to the new stress shift calculated during reversed yielding. The stress-strain response for subsequent cycles is computed by repeating this procedure of identifying load reversals, tracking reverse yield surfaces and translating the original elastic solution during elastic loading and unloading.

Creep computations are performed for increments involving dwell times using the creep characteristics incorporated in subroutine CREEP. Depending on the nature of the problem, the creep effects are determined on the basis of one of the three options provided in the subroutine.

PREDICTION OF THERMOMECHANICAL CYCLES

Two types of thermomechanical cycles were considered in the evaluation of the models; (1) a simple continuous thermomechanical cycle having the mechanical strain and temperature in phase (sinusoidal strain and temperature variation) resulting in a linear strain-temperature history and (2) and "a faithful cycle" that was representative of actual structural component response to thermal loading. Details of the faithful cycle are described in Reference 1 for the analysis of a gas turbine engine combustor liner. The thermomechanical tests were conducted on uniaxial tubular specimens which are also described in Reference 1. The hollow geometry, in combination with low frequency induction heating and internal air cooling, permitted testing with the prescribed mechanical strain and temperature histories. An axial extensometer attached to the internal ridges was used for strain control.

Linear Strain-Temperature Cycles

Two temperature histories were selected for the evaluation, 760°C to 982°C (1400°F to 1800°F) and 649°C to 982°C (1200°F to 1800°F). Each temperature cycle and a single mechanical strain cycle (approximately -0.001 to -0.0045 m/m) were imposed on a tubular test specimen with the resulting stress and strain response recorded from startup to stabilization. A description of the cycle parameters and loading sequence for the cycles is presented in Figure 3. Each test started at a constant 982°C (point A). The specimen was then compressed to a mechanical strain of -0.0045 (point B). A sinusoidal variation in temperature from 982°C to a minimum value of either 760°C or 649°C was then generated on the specimen in phase with a sinusoidal variation in mechanical strain from about -0.0045 to -0.0100. The period for both the temperature and strain histories was 1 minute. Cross plotting of these quantities resulted in the linear paths B-C and B-D in Figure 3. Predictions of the stress-strain responses for the 760°C to 982°C and 649°C to 982°C test cycles with the two simplified procedures are presented in Figures 4 and 5. Both methods essentially capture the overall shape, inelastic strain range and approximate stress levels of the experimental response curves. This would be considered as sufficient information for use as input to a life prediction model for a preliminary estimate of the base cyclic durability.

There is a tendency for the simplified analyses to overpredict the peak compressive stresses. This is especially true for the analytical cycles from the NASA procedure as shown in Figures 4 (b) and 5 (b). These discrepancies may be attributable to the use of monotonic stress-strain data for cyclic stress-strain problems.

Prediction of Faithful Cycle Response

Final evaluation of the models considered the combustor liner faithful cycle defined in Reference 1. The predicted strain-temperature response at the end of

the louver lip differs from the previously defined conditions in that the strain and temperature are not continually in phase and the heatup and cooldown parts of the cycle are not identical. The nominal temperature-time history for this cycle is that shown for the louver lip in Figure 2 (a) and the approximate strain-time history imposed on the specimen was that obtained for the sixth cycle of the MARC nonlinear solution. Application of these loading spectrums on the thermomechanical specimen produced a stress-strain response considered to be representative of the local louver response. Prediction of the combustor liner "faithful cycle" response by the two simplified procedures is shown in Figure 6. Again the analytical results agreed reasonably well with the experimental data.

SUMMARY OF RESULTS

Two simplified analytical procedures are presented for predicting the local inelastic stress-strain response of a structure subjected to cyclic thermomechanical loading using as input the total strain history calculated from a linear elastic analysis. The first of these procedures was developed at Pratt & Whitney Aircraft under contract to NASA. The second procedure, which was developed at the NASA Lewis Research Center, is fully automated in a computer program (ANSYMP). These procedures were evaluated on their ability to predict the cyclic structural responses for three thermomechanically loaded test specimens. Both methods were able to simulate the overall shapes of the stress-strain hysteresis loops and to calculate the stress-strain histories to a degree of accuracy sufficient for most life prediction methods. The analyses were based on use of monotonic stress-strain material properties. It is likely that better agreement with experimental results would have been obtained if cyclic stress-strain data had been available. These simplified procedures provide economical structural analysis tools which can be applied in the preliminary design of hot section components of gas turbine engines where nonlinear finite-element programs would be prohibitively expensive and time-consuming to use.

REFERENCES

1. Moreno, V.: Combustor Liner Durability Analysis. NASA CR-165250, 1981.
2. User Manual - MARC General Purpose Finite Element Analysis Program. Vols. A and B, MARC Analysis Research Corporation, 1979.
3. McKnight, R. L.; Laflen J. H.; and Spamer, G. T.: Turbine Blade Tip Durability Analysis NASA CR-165268, 1981.
4. Kaufman A.: Evaluation of Inelastic Constitutive Models for Nonlinear Structural Analysis. NASA CP-2271, 1983.
5. Moreno, V.: Development of a Simplified Analytical Method for Representing Material Cyclic Response. NASA CR-168100, 1983.
6. Kaufman A.: Development of a Simplified Procedure for Cyclic Structural Analysis. NASA TP-1855, 1983.

TABLE I. - TEMPERATURE DEPENDENT PARAMETERS FOR SIMPLIFIED RESPONSE PROCEDURES

Temperature °C, (°F)	Young's Modulus, MPa (ksi)	Yield Stress, MPa (ksi)	Creep Parameters* A	n
427 (800)	170 03 (24.6 03)	314 (45.6)	-------	----
538 (1000)	170 03 (24.6 03)	314 (45.6)	-------	----
649 (1200)	161 03 (23.3 03)	303 (44.0)	-------	----
760 (1400)	152 03 (22.05 03)	252 (38.0)	592.54 (85.94)	4.15
815 (1500)	146 03 (21.15 03)	207 (30.0)	277.44 (40.24)	4.75
871 (1600)	137 03 (19.8 03)	103 (15.0)	188.05 (27.27)	5.25
927 (1700)	130 03 (18.85 03)	76 (11.0)	176.95 (25.66)	3.35
982 (1800)	123 03 (17.9 03)	48 (7.0)	91.53 (13.28)	3.15

*Equation (8).

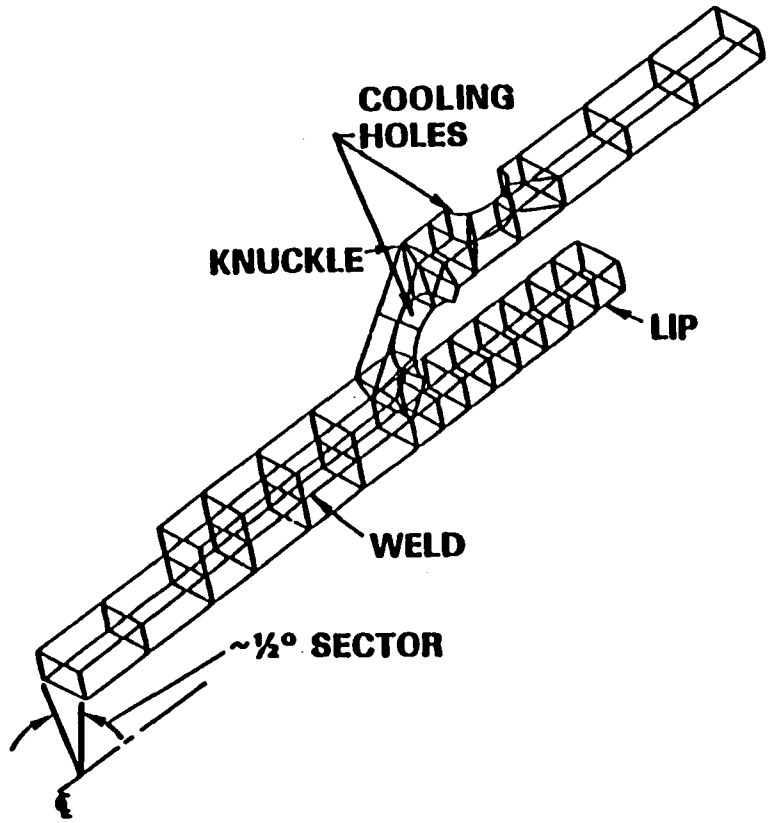

Figure 1. - Combustor liner finite element model.

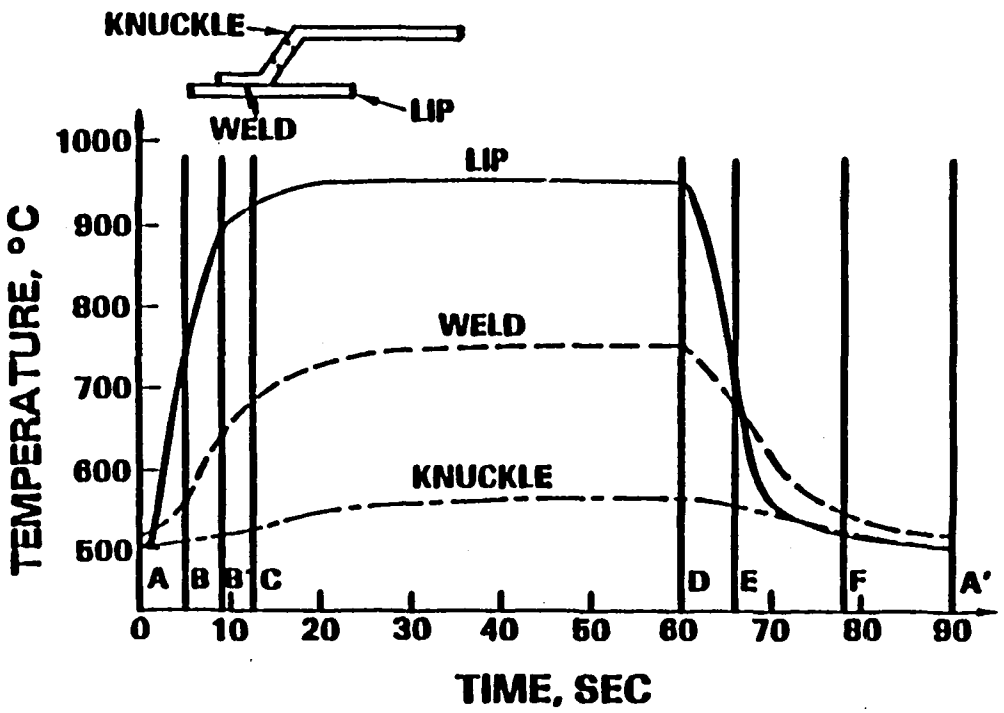

(a) - Louver temperature response.

Figure 2. - Combustor liner structural liner results.

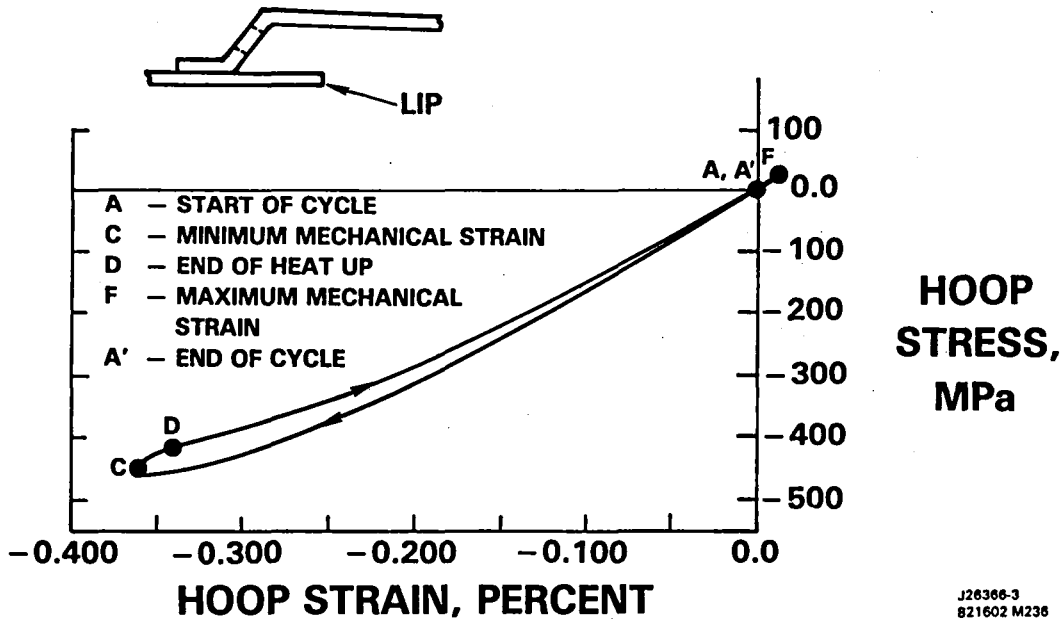

(b) - Elastic analysis stress-strain response at louver lip.

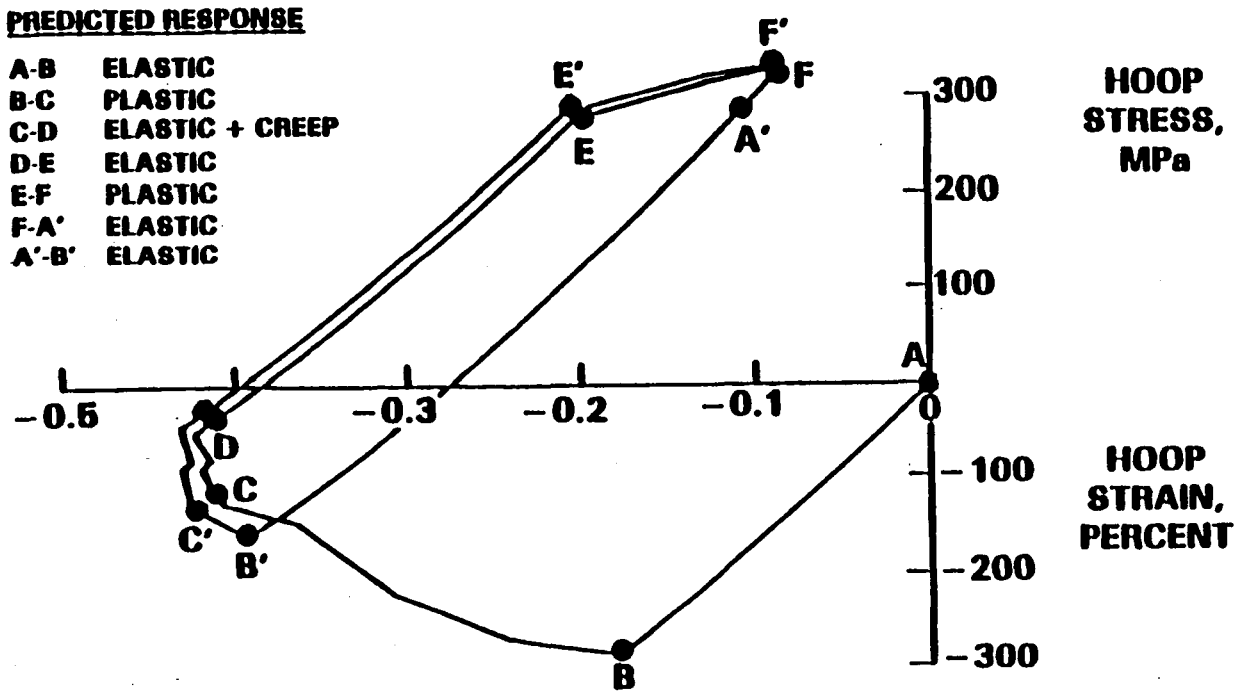

(c) - Nonlinear analysis stress-strain response at louver lip

Figure 2. - Concluded.

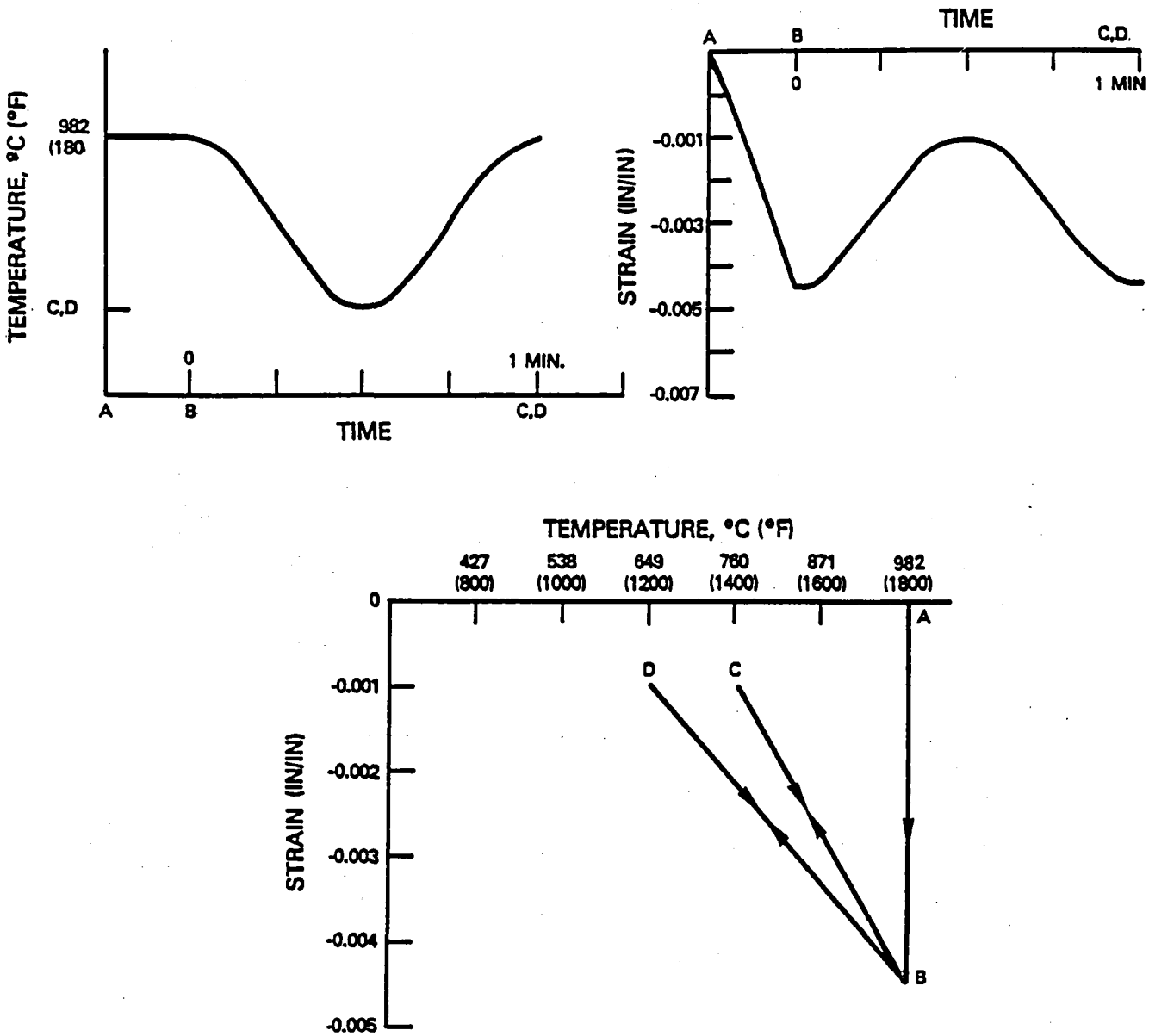

Figure 3. – Temperature and Strain Input Histories for Linear Thermomechanical Cycles.

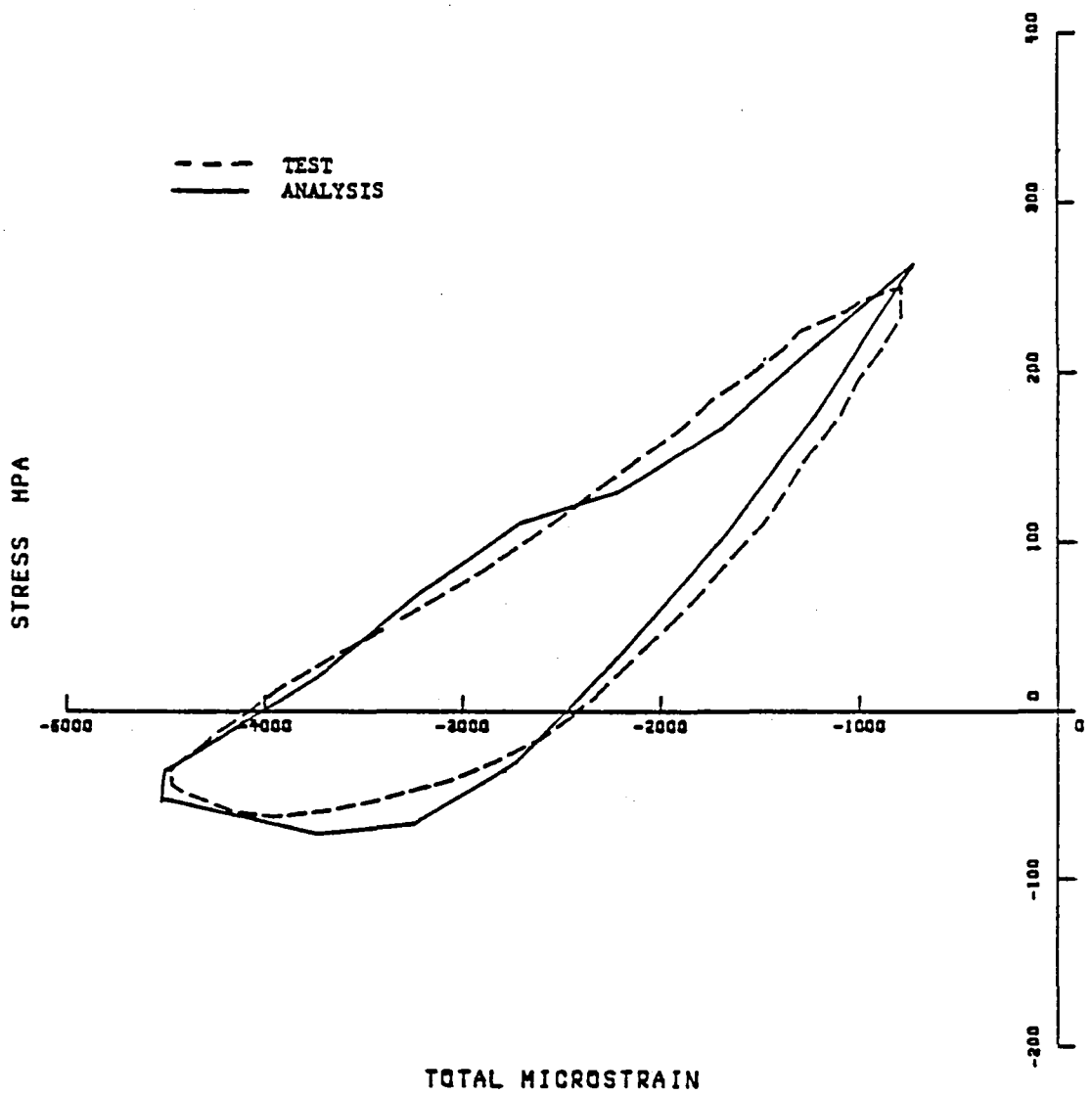

(a) Simplified Procedure 1.

Figure 4. - Simulation of 760 to 982°C thermomechanical test cycle.

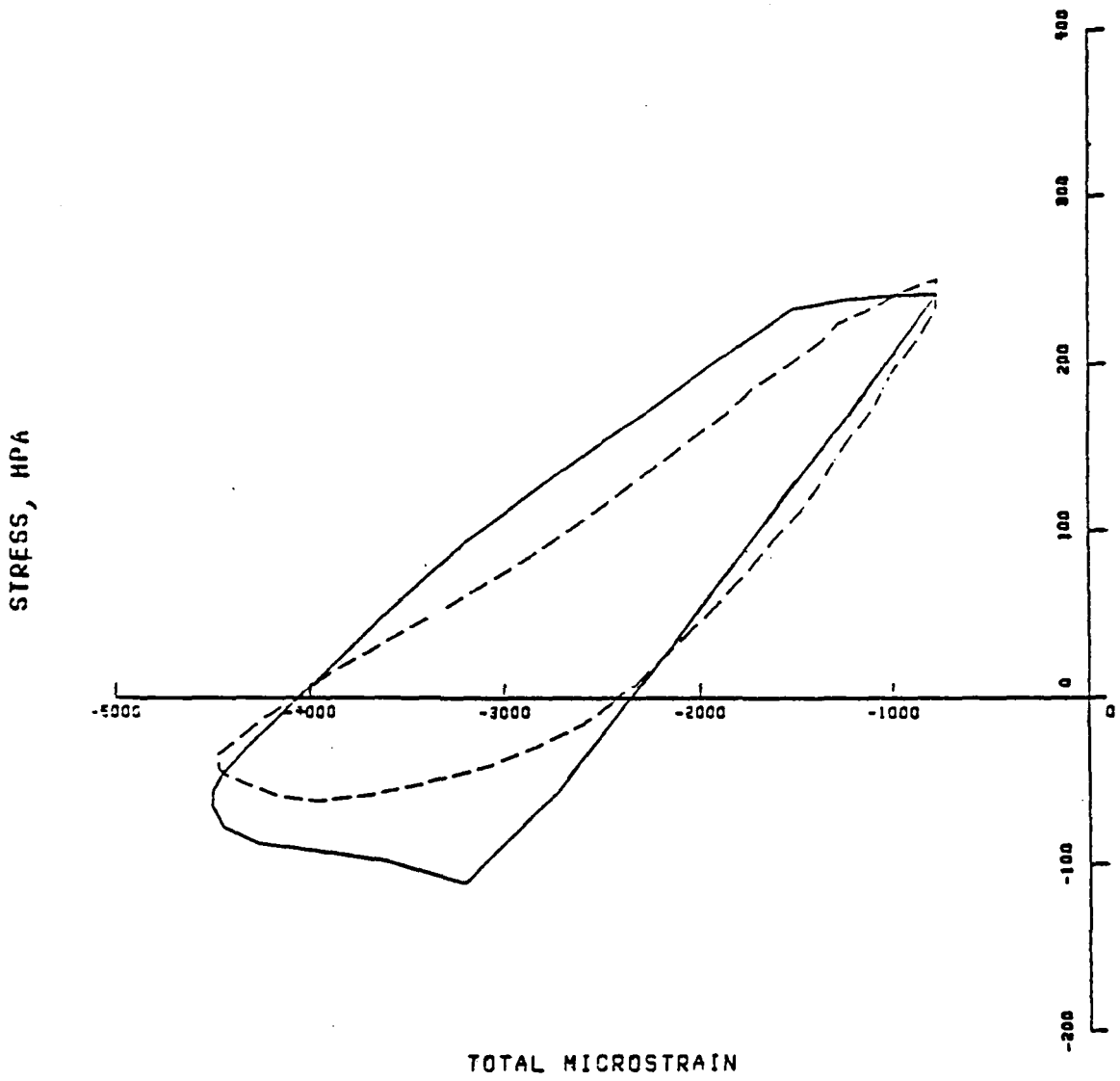

(b) Simplified Procedure 2

Figure 4. - Concluded.

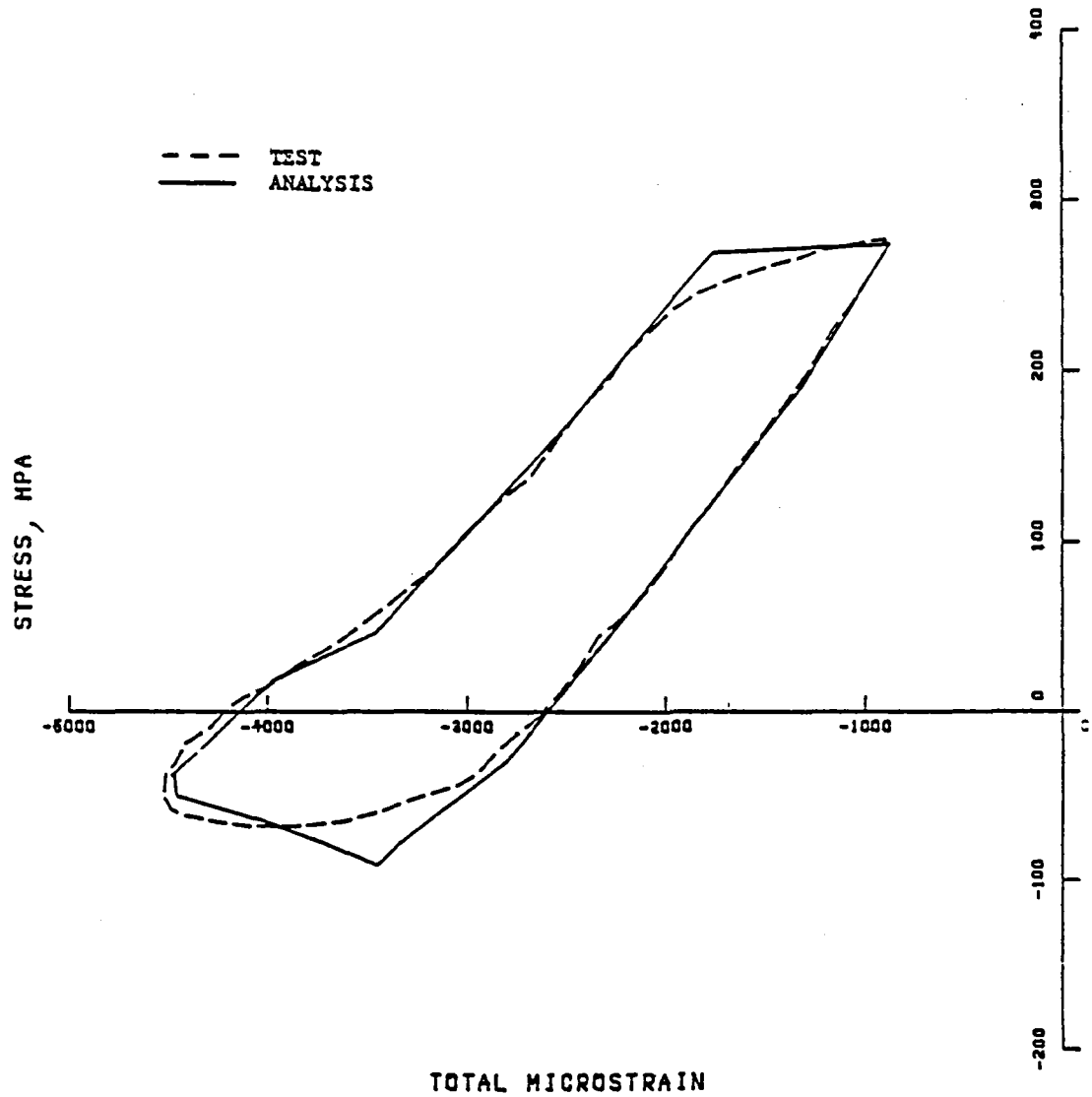

(a) Simplified Procedure 1

Figure 5. - Simulation of 649 to 982°C thermomechanical test cycle.

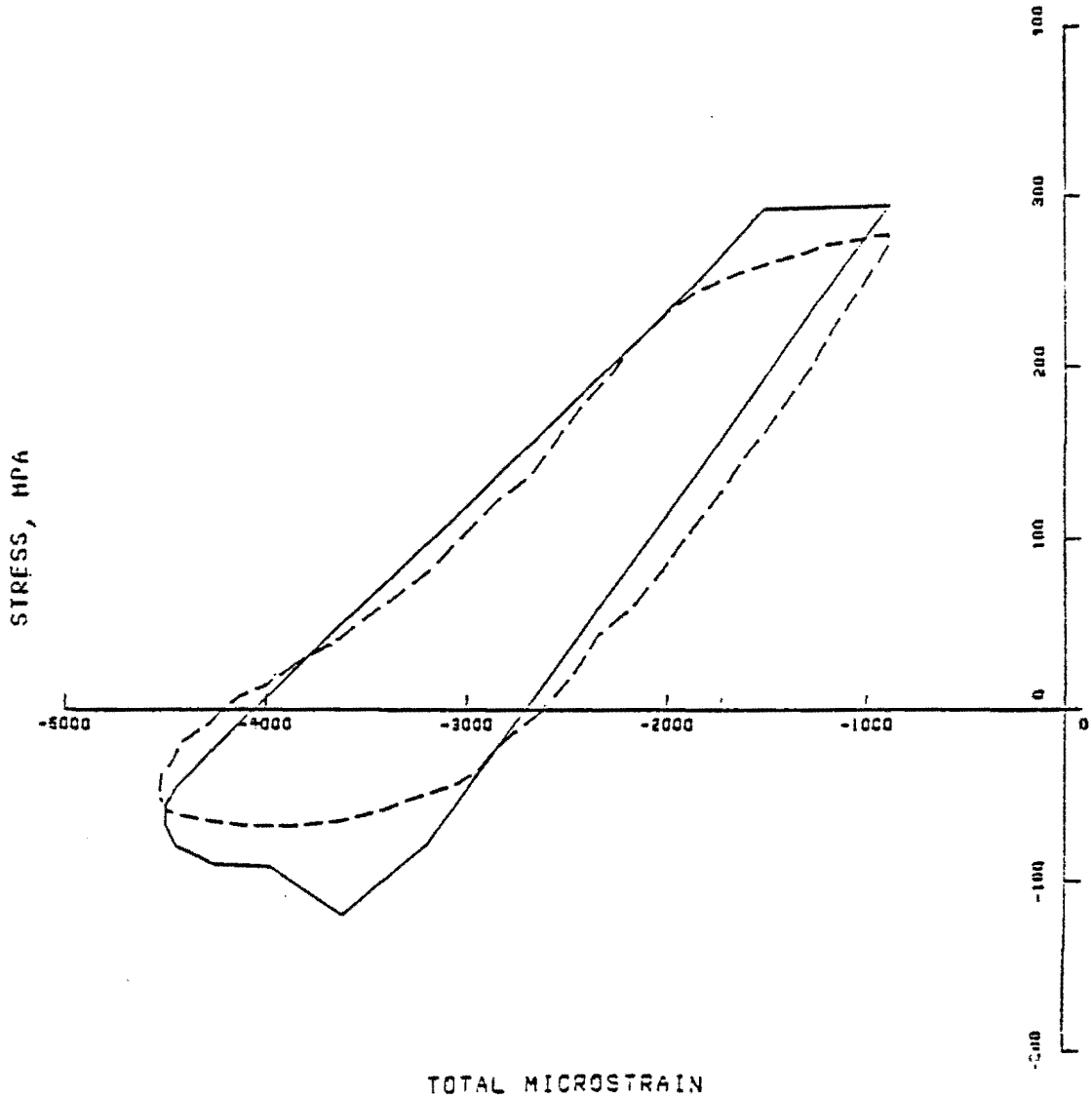

(b) Simplified Procedure 2

Figure 5. - Concluded.

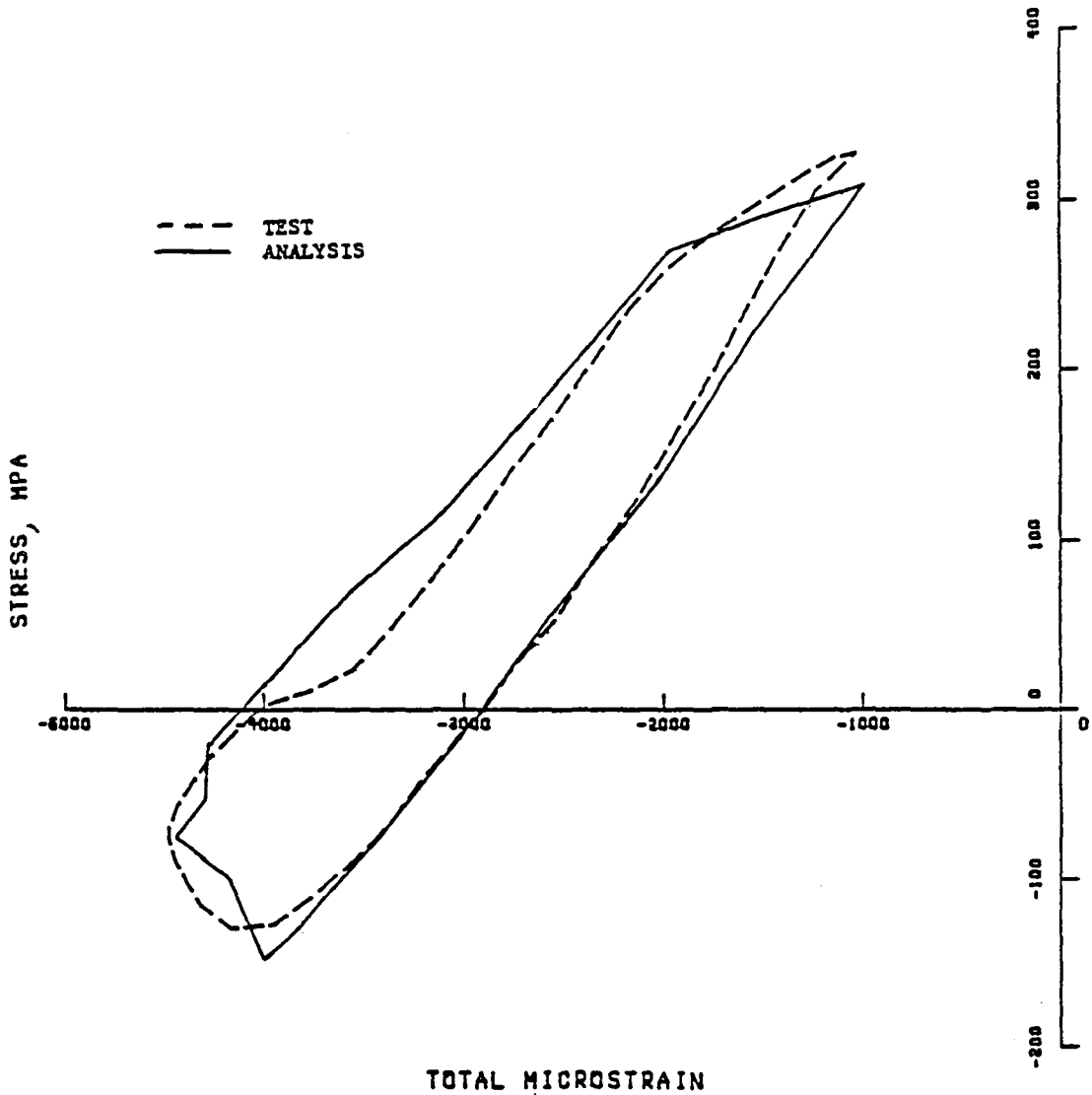

(a) Simplified Procedure 1

Figure 6. - Simulation of combustor liner "faithful cycle".

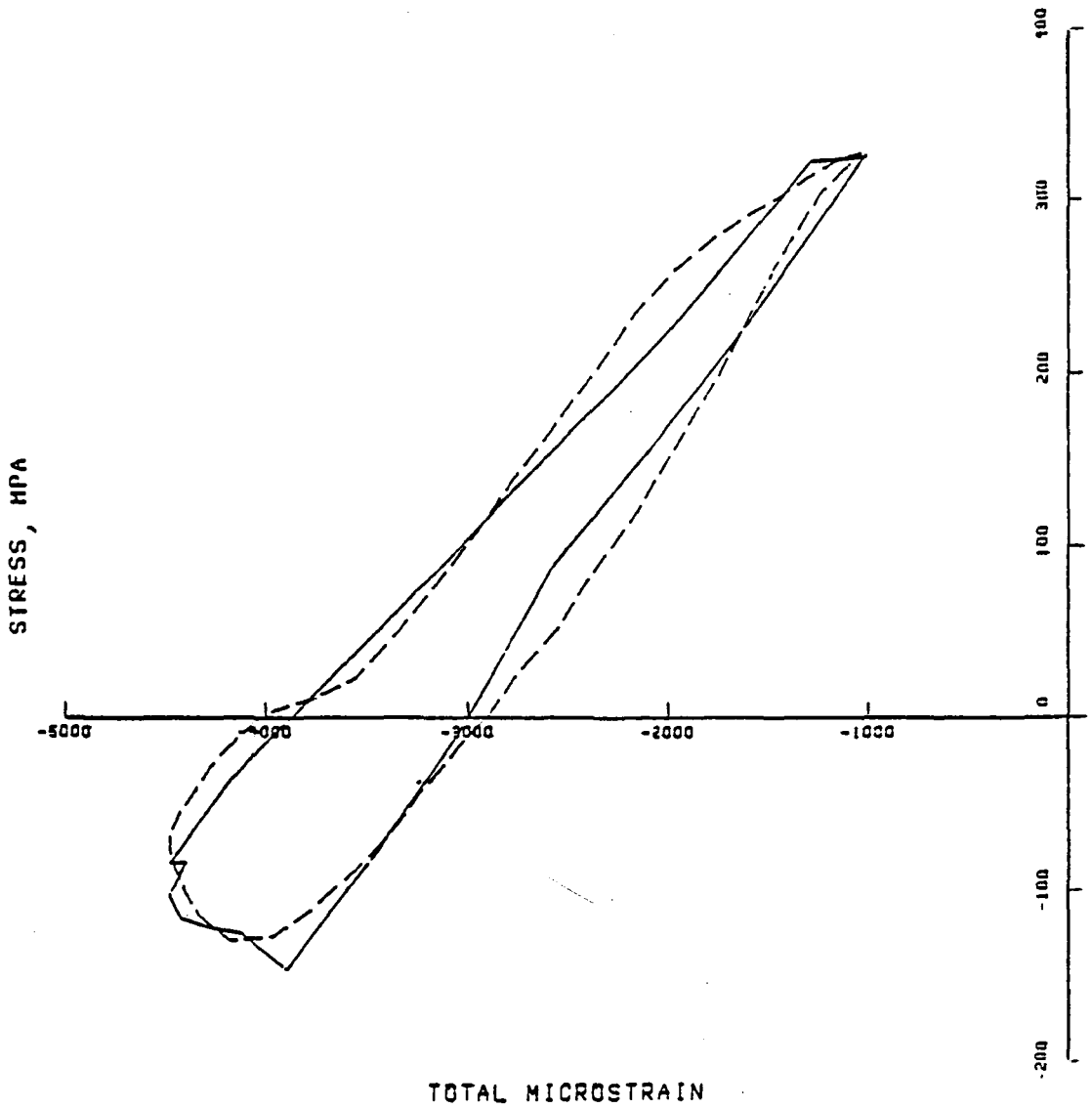

(b) Simplified Procedure 2

Figure 6. - Concluded.

Page intentionally left blank

MULTIAXIAL FATIGUE LOW CYCLE FATIGUE TESTING

S.Y. Zamrik
Engineering Science and Mechanics Department
The Pennsylvania State University
University Park, Pennsylvania 16802

Multiaxial testing methods are reviewed. Advantages and disadvantages of each type test is discussed. Significant multiaxial data available in the literature is analyzed. The yield theories are compared for multiaxial fatigue analysis.

INTRODUCTION

Multiaxial Fatigue Analysis is becoming an essential element in estimating the life of structural components. For example, at elevated temperature, most structural components experience a multiaxial stress condition either due to geometrical configuration, or to temperature variation or to both.

Generally, multiaxial fatigue analysis is based on some type of correlation that can be related to uniaxial data. The main reason for such an approach is the lack of sufficient multiaxial fatigue data and to the difficulty in producing such data.

In the early work of Manson-Coffin (1) it was recognized that, in low cycle fatigue, plastic strain and not stress can be well measured and related to life. Based on this observation, the static yield theories became the favorite approach to analyzing multiaxial fatigue. The most widely used criteria are the maximum shear strain (Tresca's) theory and

the maximum distortion energy theory (Von-Mises). These two static yield theories are identical for uniaxial and equi-biaxial stress states but differ at other biaxial conditions as shown in Figure (1).

The limited data that has been generated has not provided any definite conclusion to the applicability of either theory, particularly at high temperature environment, where creep is encountered. Also, these theories do not account for the influence of anisotropy or for the rotation of principal axes in the case of non-synchronous loading systems.

Multiaxial data at room or high temperature is greatly influenced by test conditions and in the manner in which the test is conducted. Numerous methods have been suggested for multiaxial fatigue testing, but a very limited number have been carried out successfully.

METHOD OF MULTIAXIAL FATIGUE TESTING

The complexity of multiaxial fatigue testing led researchers to simplify the test requirements due to the fact that fatigue failure is generally originated at a point on the surface of a structure. For example, in the case of pressure vessels the state of stress is considered to be biaxial and since the surface of the structure is free from discontinuities or surface tractions, several types of tests were devised to produce this biaxial state of stress. Among the favorites are:

a - cylindrical specimens subjected to internal pressure, open-and closed-end cylinders

b - rotating disks

c - plate-type specimens such as bulging plate, wide cantilever plate, cruciform plate and rhombic plate

d - torsional tests of cylindrical specimens

CYLINDRICAL-TYPE SPECIMENS

In the case of testing cylindrical-type specimens under internal pressure, the state of biaxial stress is 2:1. This biaxial stress ratio falls in the first quadrant of the yield envelope and it is possible to alter this ratio by introducing a bending or axial stress. To develop a state of stress in the 2nd and 4th quadrant of the yield envelope, compressive external load or torsional loads have to be added to produce a negative stress. It has been shown that the addition of such loads could easily produce a buckling situation or a stress gradient that cannot be controlled. Investigators such as Morrison, Crossland, and Parry (2) used only pressurized tubes and they controlled the biaxiality ratio by the radius to thickness ratio. Their data is not comparable nor consistent with present controlled fatigue testing techniques. Their objective was to relate the endurance limit of the material to the biaxial state of stress. Esztergar (3) indicated in his literature survey on fatigue under biaxial stress cycling that the data produced was qualitative since crack initiation could not be detected and the large amount of autofrettage affected the crack propagation through the wall thickness; thus, the data was greatly influenced by these two obstacles. In the case of a part-through crack presence, the circumferential stress is increased locally, which results in a reduced hoop restraint that causes a tendency for bulging.

McKenzie et. al. (4) compared uniaxial and biaxial (shear) data from tests on thin-walled cylinders. They correlated their results on the basis of hysteresis loop energy per cycle. A distinct difference in fatigue life becomes apparent if the comparison is based on the octahedral plastic shear strain as shown in Figure (2).

Biaxiality ratio can also be altered if torsional loading is added; however, a new problem arises in the generated data. Axial strain is accumulated in reversed torsion. Specimens develop axial compressive stresses which result in higher cycle life. This effect was shown independently by Yokobori et. al. (5) and by Zamrik (6) using torsional test data of Halford and Morrow. Additional data for cylindrical specimen tests can be obtained from references (7).

FLAT-PLATE SPECIMENS

There are three types of tests that can be conducted utilizing the flat plate specimens, namely:

(1) the cantilever plate

(2) the Rhombic plate

(3) the circular or elliptical plate (oval plates)

In the first type, the biaxial stress ratio was produced by considering the ratio of transverse stress σ_T to longitudinal stress σ_L. By successfully decreasing the width w, the biaxiality ratio decreases. This approach was taken by Weiss et. al. (8) and their results are shown in Figures (3) and (4). Figure (4) shows a comparison between push-pull type uniaxial tests and plate bending tests. They also demonstrated that the decrease in fatigue endurance is associated with the increase in biaxiality ratios. This decrease can be correlated with the proportional loss in the static fracture ductility, ε_f, as shown in Figure (5).

Wide-beam-type specimens of pressure vessel steel materials were tested at Lehigh University (9). The stress ratios of 1:1 results are shown in Figure (6) on the basis of effective Von-Mises strain. They

showed a slight reduction in the fatigue endurance of the lower-strength alloy and perhaps a greater effect on the high strength alloy (T-1). The data was reported on the basis of crack initiation.

Another type of plate specimen was developed by Zamrik et. al (10). The plate specimen known as the "rhombic" specimen showed a stress state in the second and fourth quadrants of the yield envelopes. The state of stress was produced by anticlastic bending as shown in Figure (7). Test data of three stress ratios from 0.1 to 1.0 were plotted on the basis of octahedral shear strain range and maximum strain range. The octahedral shear strain range shown in Figure (8) fitted the data well for all stress ratios. In the case of torsional data, the stress ratios exhibited a higher fatigue strength when compared to uniaxial fatigue data. The reason for this observation can be attributed to the degree of axial restraint imposed on the torsion specimen.

The rhombic plastic specimen is very attractive for biaxial testing since it affords simplicity in the loading system and provides a wide range of biaxial stress ratios.

Another type of plate specimen tested by Zamrik et. al (11) is the circular and elliptical specimen. For this type, shown in Figure (9a), pressure was applied to the specimen but the results showed a dependence on two variables: isotropy and Poisson's ratio as shown in Figure (9b). The method of analysis used in interpreting the flat plate specimen is described in appendix (A).

OUT-OF-PHASE STRAIN EFFECT

In some cases, particularly in temperature environment, the biaxial strain may become out-of-phase, e.g., non-synchronous loading as shown in

Figure (10); therefore, by applying the correlation used in analyzing the room temperature data, a large error may be produced in predicting the life of the material. A significant cause, in this case, is the distribution of the principal strain magnitudes and their directions, whereby a rotation of the principal strain axes takes place. The surface element of the material takes a new orientation and the maximum and minimum principal strains occur at different times as shown in Figure (11). The limited data available for phase angles of 0 to 90° was analyzed by Zamrik (12) on the basis of maximum total strain:

$$\varepsilon_T = \sqrt{[\varepsilon_1^2 + \varepsilon_2^2 + \varepsilon_3^2]}$$

A correlation, similar to that of Manson-Coffin relation, was obtained with the constants ($a \tilde{=} 0.3$, $c = \varepsilon_f \sqrt{1.5}$) as shown in Figure (12). The reasonable fit of the data for the entire range indicates that the damage mechanism in multiaxial fatigue may be similar to the uniaxial case even though the stress (strain) axis was rotated. This interpretation may be considered conclusive if and only when actual non-synchronous data at high temperature becomes available.

ENGINEERING CORRELATIONS

a - Maximum Shear Stress Theory (Tresca)

The theory predicts yield condition when the shear stress on any plane reaches the uniaxial yield stress. Therefore, the following condition exists for maximum and minimum principal stresses:

$$\tau = \frac{1}{2}(\sigma_1 - \sigma_3) = \frac{1}{2}\sigma_y$$

The equivalent stress and strain are defined as:

$$\bar{\sigma} = \sigma_1 - \sigma_3 = 2\tau$$

$$\bar{\varepsilon} = k\,(\varepsilon_1 - \varepsilon_3)$$

b - Distortion Energy Theory (Von-Mises)

$$\gamma_o = \frac{2}{3}\left[(\varepsilon_1 - \varepsilon_2)^2 + (\varepsilon_2 - \varepsilon_3)^2 + (\varepsilon_3 - \varepsilon_1)^2\right]^{\frac{1}{2}}$$

For low cycle fatigue condition, one assumes a constant volume and Poisson's ratio of $1/2$:

$$\varepsilon_1 + \varepsilon_2 + \varepsilon_3 = 0$$

For a biaxial case, a strain range ratio can be introduced in the form of:

$$\phi = \frac{\Delta\varepsilon_2}{\Delta\varepsilon_1}$$

and $$\Delta\gamma_o = \frac{2\sqrt{6}}{3}\,(\phi^2 + \phi + 1)^{\frac{1}{2}}\,\Delta\varepsilon_1$$

The effective strain range, $\Delta\varepsilon_e$, which is another form of the octahedral shear strain range, has a form:

$$\Delta\bar{\varepsilon}_e = \frac{2}{\sqrt{3}}\,(\phi^2 + \phi + 1)^{\frac{1}{2}}\,\Delta\varepsilon_1$$

or $$\Delta\bar{\varepsilon}_e = \frac{1}{\sqrt{2}}\,\Delta\gamma_o$$

on the basis of tests shown in Figure (8), a relation between unaxial and biaxial data can be derived in the following procedure:

$$(\Delta\gamma_o)_{uni} = \sqrt{2}\,\Delta\varepsilon$$

utilizing Manson's relation:

$$\Delta\epsilon N^z = C_1$$

then $$(\Delta\gamma_o)_{uni} = \frac{\sqrt{2}\, C_1}{N^z} = \frac{C}{N^z}$$

where $$C = \sqrt{2}\, C_1$$

if failure under multiaxial strain cycling can be defined to occur when:

$$(\Delta\gamma_o)_{multi} = (\Delta\gamma_o)_{uni}$$

then multiaxial strain cycling can be related to the number of cycles to failure N_f in a relation such as:

$$(\Delta\gamma_o)_{multi} N_f^z = C$$

CONCLUDING REMARKS

Multiaxial fatigue testing is a complex technique where the utmost care must be considered in analyzing the data. Variables such as anisotropy, Poisson's ratio, strain accumulation, crack initiation in cylindrical specimens, ..., must be monitored and accounted for. These variables have minimum influence on uniaxial fatigue data.

The static yield theories should be used conservatively since they are not designed for fatigue analysis, particularly in the presence of high temperature environment.

REFERENCES

1. S. S. Manson, "Behavior of Materials Under Conditions of Thermal Stress," NASA Technical Note 2933, 1954.

2. J. L. M. Morrison, B. Crossland, and J. S. Parry, "Strength of Thick Cylinders Subjected to Repeated Internal Pressures," J. Eng. Ind. 82, 143-53 (1960).

3. E. P. Esztergar, "Creep-Fatigue Interaction and Cumulative Damage Evaluations for Type 304 Stainless Steel," ORNL-4757, (1972).

4. C. T. MacKenzie, D. J. Burns, and P. P. Benham, "A Comparison of Uniaxial and Biaxial Low-Endurance Fatigue Behavior of Two Steels," Proc. Inst. Mech. Eng. 180, 414-23 (1966).

5. T. Yokobori, H. Yamanovchi, and S. Yamamoto, "Low-Cycle Fatigue of Thin-Walled Cylindrical Specimens of Mild Steel," Int. J. Fract. Mech. 1, 3-13 (1965).

6. S. Y. Zamrik and T. Goto, "The Use of Octahedral Shear Strain Theory in Biaxial Low Cycle Fatigue," pp. 551-62, Proc. of Inter-American Conference on Materials Technology," ASME 1968.

7. K. J. Pascoe and J. W. R. de Villiers, "Low-Cycle Fatigue Testing of Steel Under Biaxial Straining," J. Strain Anal. 2, 117-26 (1967). M. B. Reynolds, "Strain-Cycle Phenomena in Thin-Walled Tubing," GEAP-4462 (1964).

8. V. Weiss, J. Sessler, and P. Packman, "Low Cycle Fatigue of Pressure Vessels Material," TID-16455 (1962).

9. K. D. Ives and J. T. Tucker, "Equibiaxial Low-Cycle Fatigue Properties of Typical Pressure-Vessel Steels," ASME 65-MET-19, (1965).

10. S. Y. Zamrik, "Advances in Design For Elevated Temperature Environment," ASME, Sep. Publ. June 23-27, (1975).

11. J. Shewchuck, S. Zamrik, and J. Marin, "Low Cycle Fatigue of 7075-T651 Aluminum Alloy in Biaxial Bending," Exp. Mech. 8 504-12 (1968).

12. S. Y. Zamrik, and R. E. Frishmuth, "The Effects of Out-of-Phase Biaxial Strain Cycling on Low Cycle Fatigue," Exp. Mech. 13 (5): 204-208, (1973).

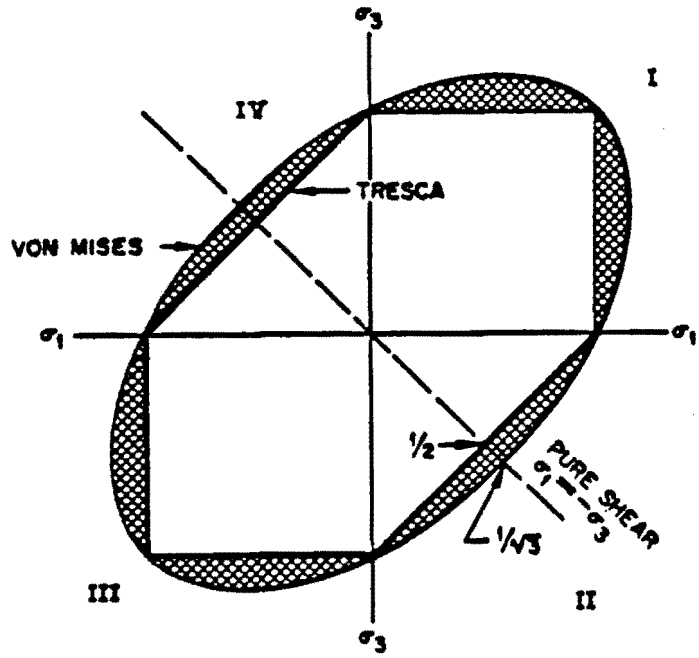

Fig. 1. Tresca and von Mises yield criteria.

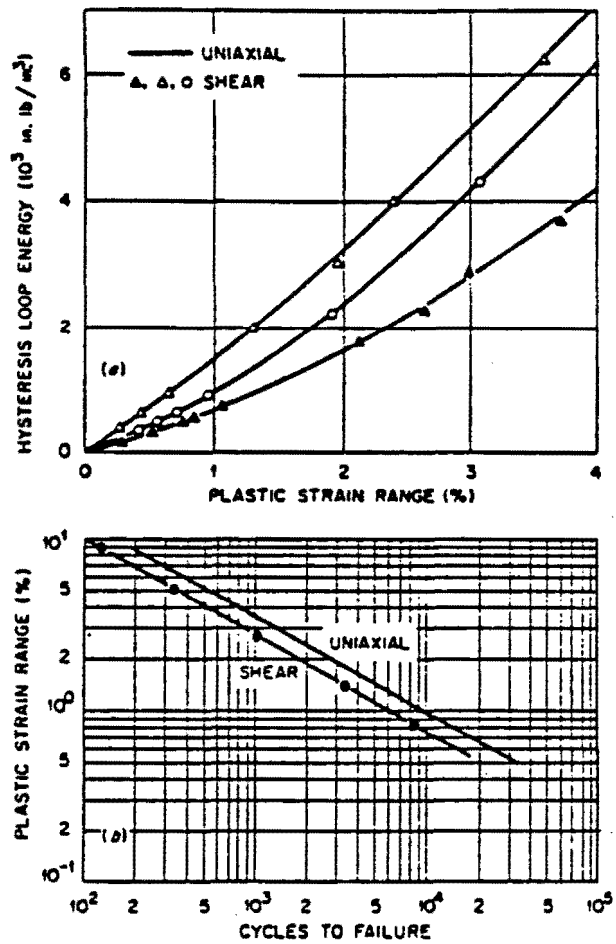

Fig. 2. Comparison of uniaxial and biaxial fatigue life of 2 1/2 Ni–Cr–Mo (Ref. 4).

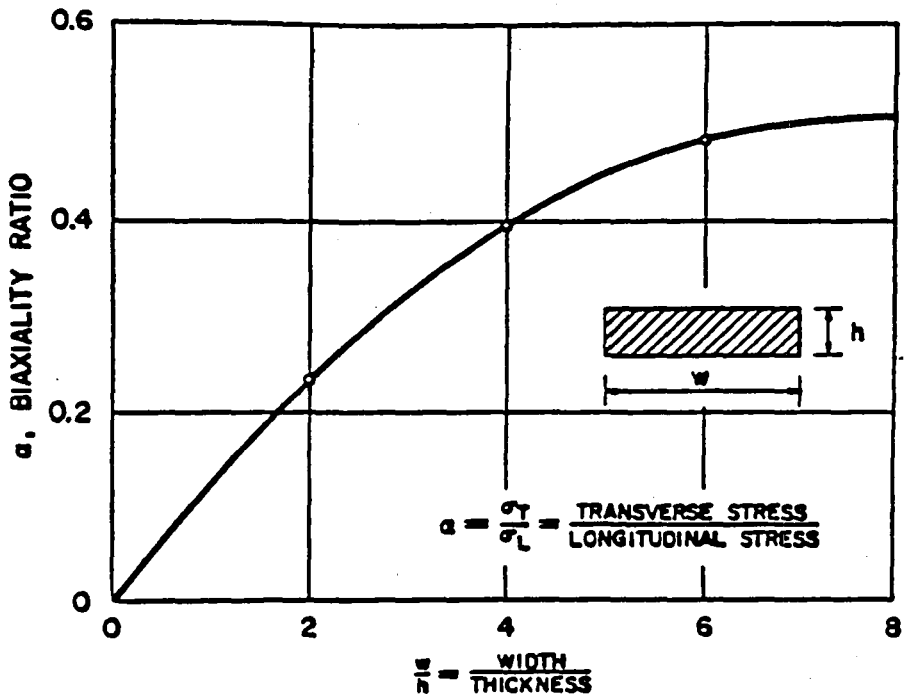

Fig. 3. Biaxiality of a bend plate (Ref. 8).

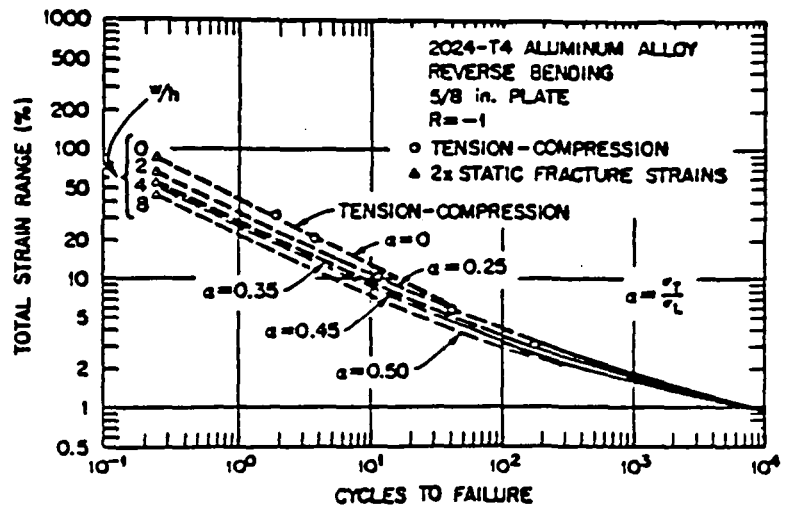

Fig. 4. Biaxial fatigue strength of aluminum (Ref. 8).

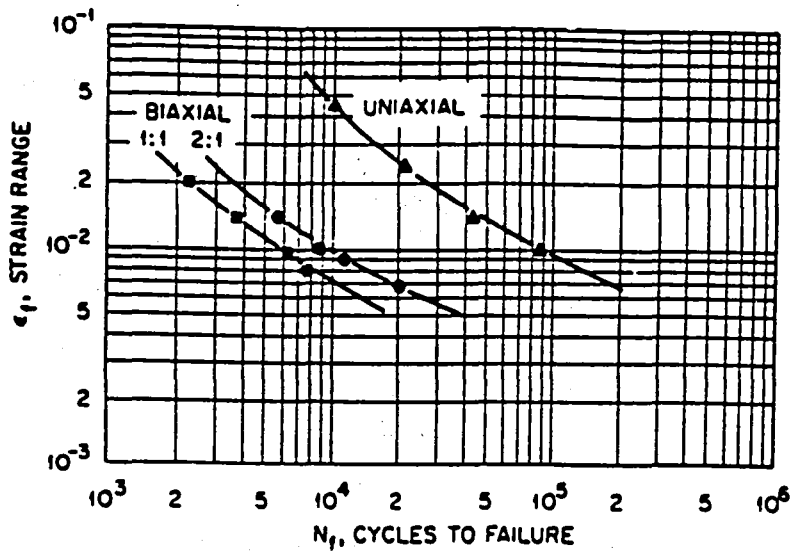

Fig 5. Biaxial fatigue endurance of 301 stainless steel (Ref. 3).

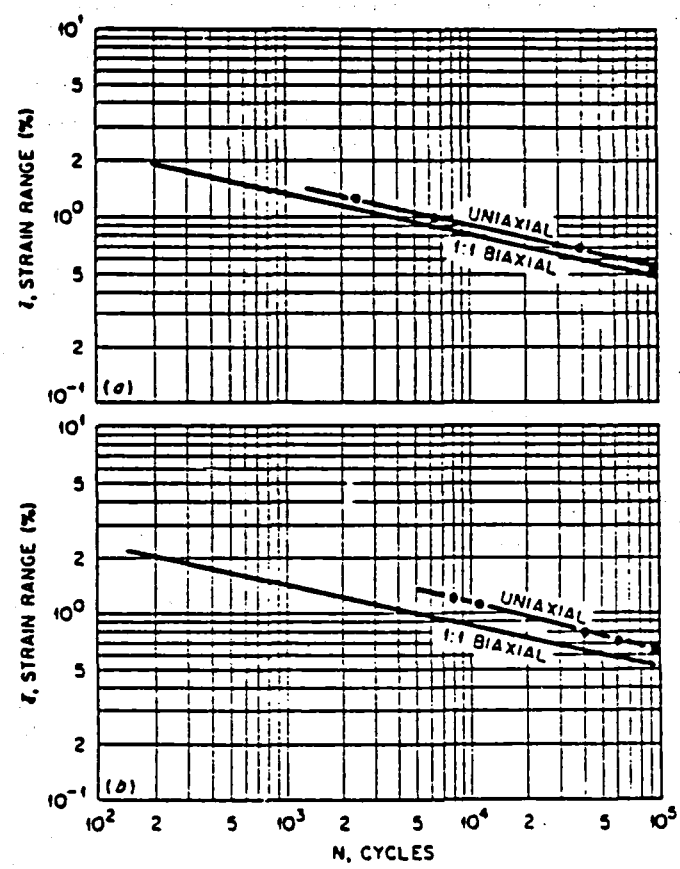

Fig. 6. Biaxial fatigue life of (a) A-302 carbon steel and (b) T-1 alloy (Ref. 9).

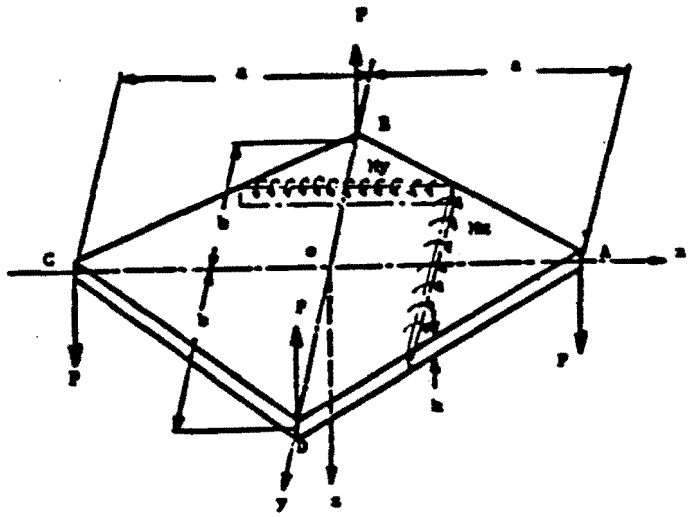

Fig. 7. A rhombic plate subjected to anticlastic bending

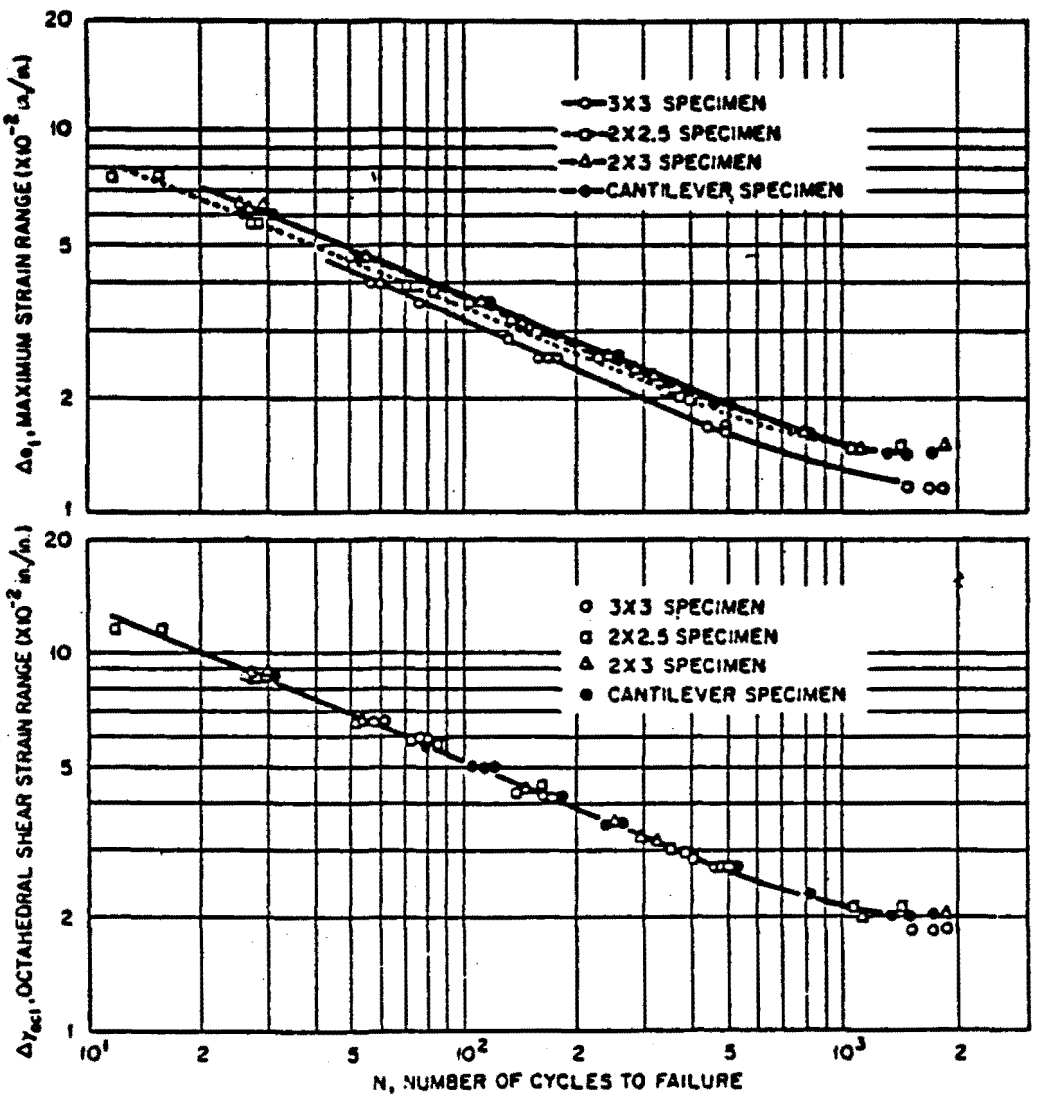

Fig. 8. Comparison of low-cycle fatigue data based on (a) maximum strain range and (b) octahedral shear strain range (Ref. 6).

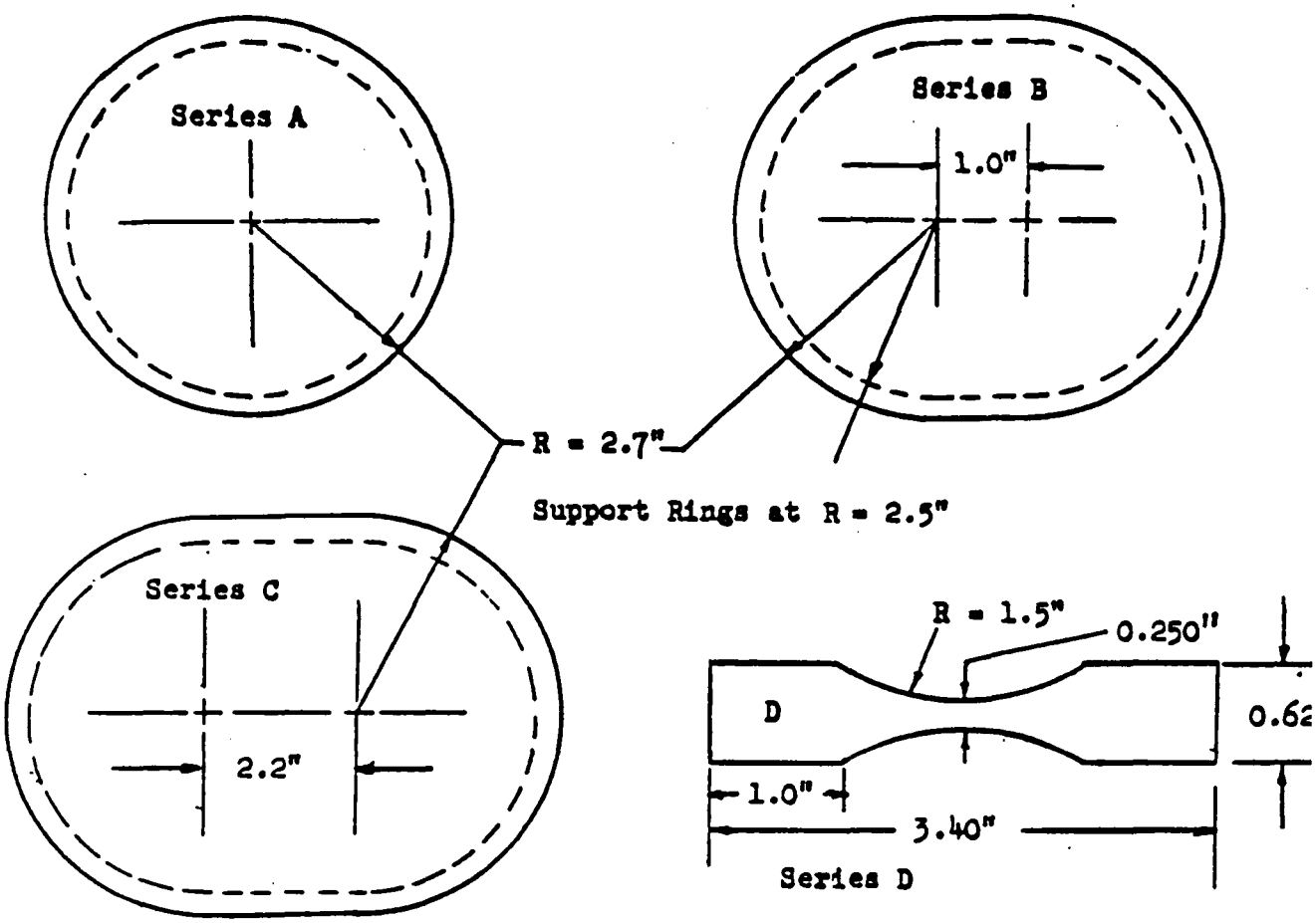

Figure 9a. Circular & Elliptical plate specimens.

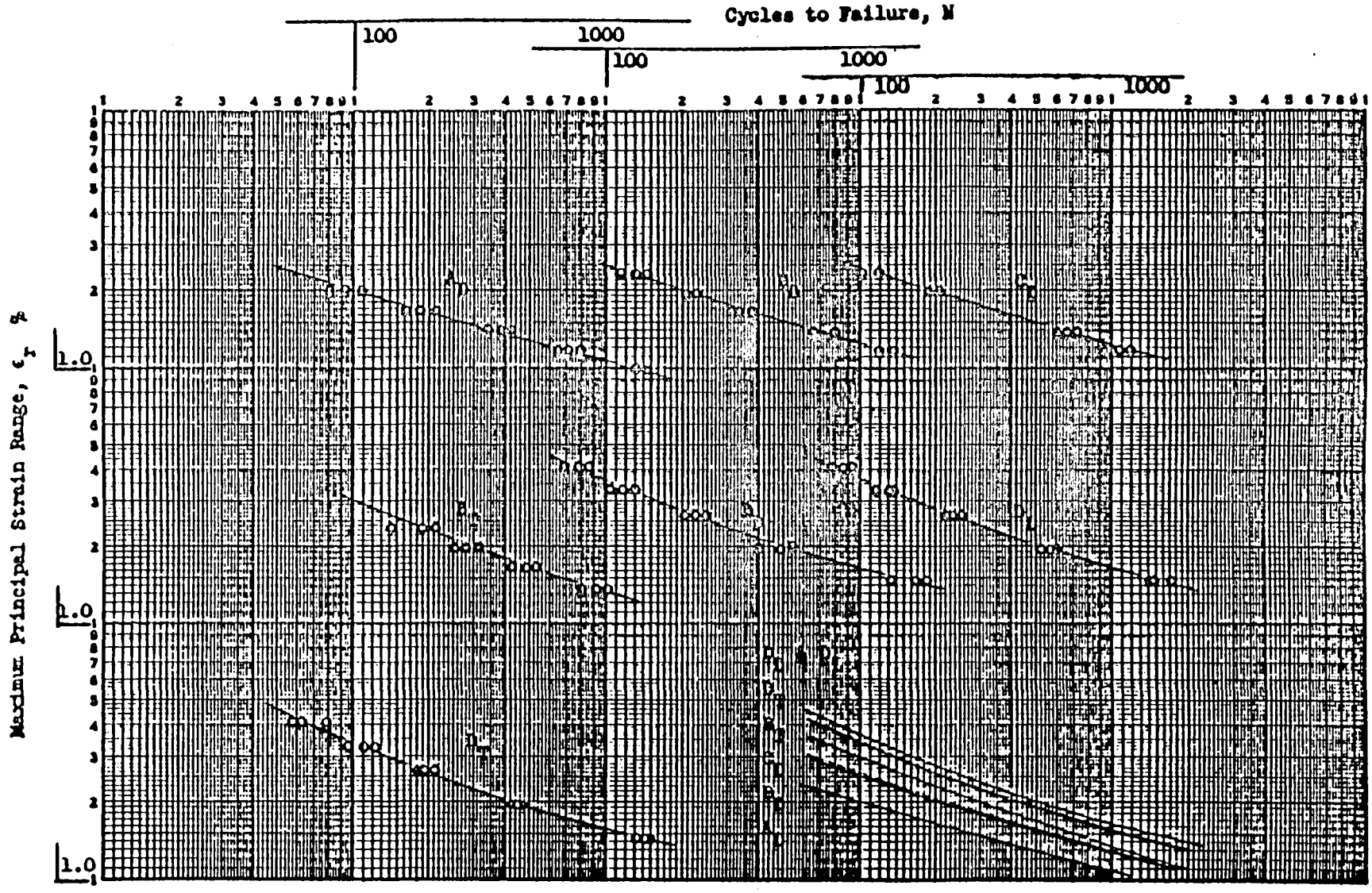

Figure 9b. Maximum Principal Strain Range vs. Cycles to Failure for 7075-T651 Aluminum Alloy in Bending (11).

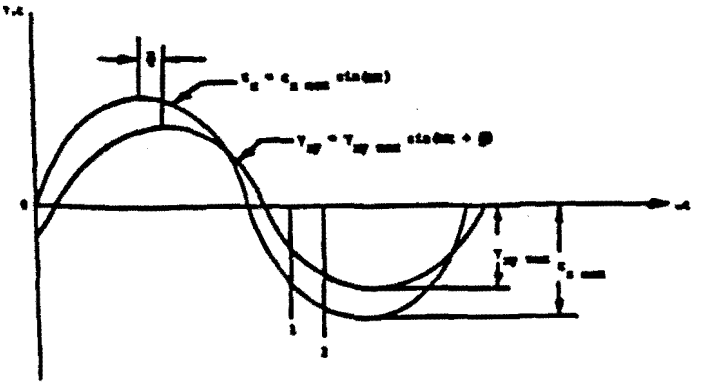

Fig. 10 Out-of-phase straining condition

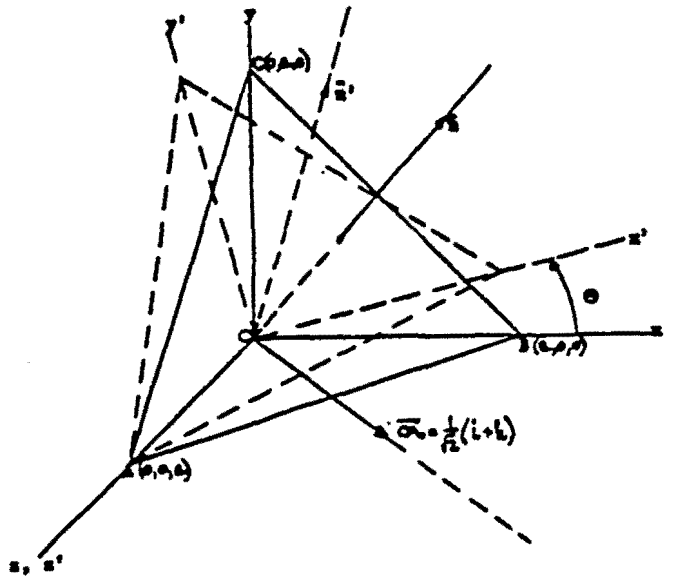

Fig. 11 Rotation of principal axes due to out-of-phase straining condition

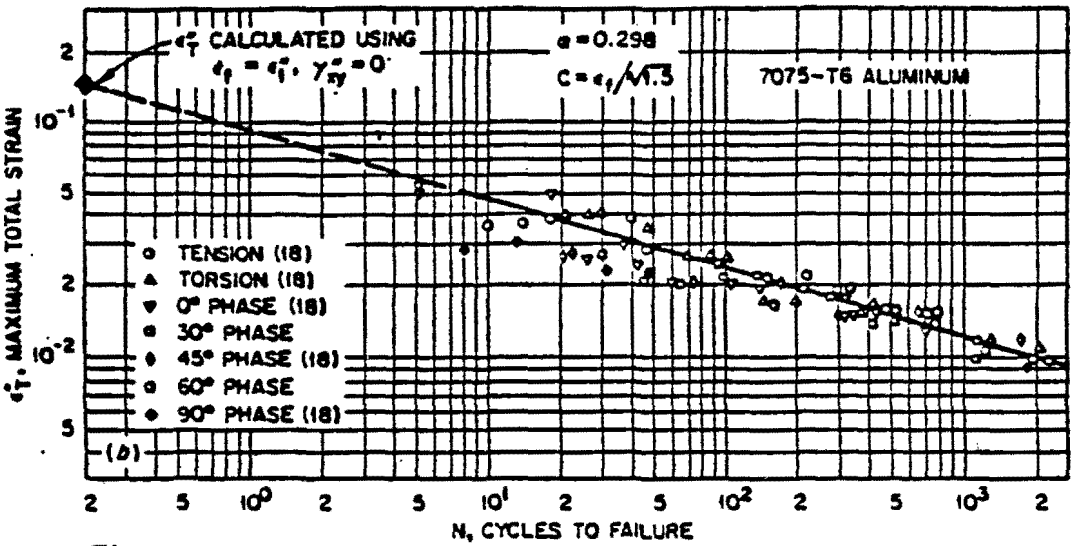

Fig. 12. Maximum total strain vs cycles to failure using experimental data from various phase angle tests. Both coordinates are logarithmic (Ref. 12).

SOME ADVANCES IN EXPERIMENTATION SUPPORTING DEVELOPMENT OF VISCOPLASTIC CONSTITUTIVE MODELS*

J.R. Ellis and D.N. Robinson†
University of Akron
Akron, Ohio 44325

The primary aim of this paper is to describe the design and development of a biaxial extensometer capable of measuring axial, torsion, and diametral strains to near-microstrain resolution at elevated temperatures. An instrument with this capability was needed to provide experimental support to the development of viscoplastic constitutive models. The operation of the instrument is described first in general terms. Attention is then concentrated on the method of torsional strain measurement. This emphasis is in keeping with the second aim of the paper which is to highlight the advantages gained when torsional loading is used to investigate inelastic material response at elevated temperatures.

The development of the biaxial extensometer was conducted in two stages. The first involved a series of bench calibration experiments performed at room temperature. These experiments investigated characteristics such as linearity and crosstalk over the maximum measurement ranges practicable with the instrument. The second stage of development involved a series of in-place calibration experiments conducted at room and elevated temperatures. The aim of these experiments was to investigate features such as signal stability and signal noise levels under actual test conditions. A review of the torsional calibration data indicated that all performance requirements regarding resolution, range, stability and crosstalk had been met by the subject instrument over the temperature range of interest, 20 to 650 °C.

On completing the instrument development work, the scope of the in-place calibration experiments was expanded to investigate the feasibility of generating stress relaxation data under torsional loading. This approach was found to be practicable and a number of exploratory tests were conducted. The data generated in these experiments were found to be in reasonable agreement with predictions made using the Robinson viscoplastic constitutive model. Also, the experimental data were used successfully to quantify the kinematic state variable in this model. The results of this study showed that the stress relaxation test conducted under torsional loading can be used to advantage in supporting the development of viscoplastic constitutive models.

*Research sponsored by the Office of Breeder Technology Projects, U.S. Department of Energy under Contract W-7405-ENG-26 with the Union Carbide Corporation and by NASA Lewis Research Center under Grant NAG 3-379.

†Resident Research Associates, NASA Lewis Research Center.

INTRODUCTION

One activity within the High Temperature Structural Design Program at the Oak Ridge National Laboratory (ORNL) is the development of constitutive equations for structural alloys intended for Advanced Reactor Systems. These equations were first developed using concepts borrowed from classical plasticity and classical creep (Ref. 1). Experiments conducted in support of this work included investigations of yield and hardening behavior under biaxial loading (Refs. 2 through 5). The type of loading used for this work was tension-torsion and the type of specimen was the thin-walled tube. It was possible, at temperatures in the range 20°C to 232°C, to use foil strain gage rosettes to measure the axial and torsional components of strain. The near-microstrain resolution of these gages allowed small-offset (10 με) yield behavior to be investigated without causing significant changes to the material's state.

More recently, a viscoplastic constitutive model was developed at ORNL which makes use of two internal state variables (Refs. 6 and 7). It was planned to conduct biaxial experiments at temperatures in the range 20°C to 538°C to verify the multiaxial form of this model and also to quantify the internal state variables. The lack of suitable high-temperature strain gages meant that the strain measurement technique used in the earlier experiments could not be used for this work. Since the specimen geometry and the type of loading were relatively simple, it appeared that this would be a suitable application for a biaxial extensometer. However, a detailed review of the literature revealed that existing instruments were not suited to high-precision, probing type experiments at elevated temperatures. This led to an effort being started at ORNL to design and develop such an instrument.

The design requirements for the instrument were based in part on the performance of foil strain gages at room temperature. It was required that the extensometer have near-microstrain resolution while allowing measurement of axial strains and shear strains (engineering) as high as ±20,000 με. An additional requirement was that the instrument should be capable of measuring diametral strains up to ±10,000 με. This was because it was planned to add internal pressure to the types of loading available for these experiments. It was required that this performance should be maintained up to 650° C.

The type of diametral extensometer developed by Slot et al for high temperature, low cycle fatigue testing was used as a starting point for the subject instrument. Two such diametral extensometers, termed sensors in the following, were used in conjuction with a system of levers to make the biaxial measurements. As might be expected, a lengthy period of development was needed to achieve the required level of performance.

The approach adopted was to first evaluate the instrument on the bench using a biaxial calibration fixture. Such experiments allowed the instrument's characteristics to be investigated at room temperature under closely controlled conditions. A series of in-place calibration experiments was then conducted with the extensometer positioned on strain gaged specimens. Initially, these experiments were conducted at room temperature so that direct comparisons could be drawn between the two strain measurement systems. Subsequently, the emphasis was shifted to investigating

performance at elevated temperatures. Characteristics of interest here were linearity, resolution, crosstalk, mechanical hysteresis, signal noise levels and signal stability.

Finally, exploratory tests were conducted to evaluate the instrument's performance in controlling experiments at elevated temperatures. One such series of tests was aimed at establishing whether the extensometer had sufficient resolution and stability to allow stress relaxation behavior to be investigated under purely torsional loading. This was of particular interest since interpretation of earlier stress relaxation data for 2-1/4 Cr-1 Mo steel, determined under uniaxial loading, had been complicated by coupling between specimen heating and specimen loading. It was anticipated that such coupling, discussed in detail later in the paper, would not be a factor in tests involving torsional loading.

This paper is written in three parts. The first describes the design and development of the ORNL biaxial extensometer, with particular emphasis being given to the method of torsional strain measurement. The second part describes a series of stress relaxation tests performed on 2-1/4 Cr-1 Mo steel under cyclic torsional loading. Finally, comparisons are drawn between the results of these experiments and theoretical predictions made using the Robinson viscoplastic model.

DESIGN AND DEVELOPMENT OF A HIGH-PRECISION BIAXIAL EXTENSOMETER

In designing high temperature extensometers, a number of advantages result if the body of the device is maintained at or near room temperature during elevated temperature tests. This situation can be achieved by using localized specimen heating, ceramic sensing probes, heat shields, and some form of cooling. Adopting these measures, room temperature transducers can be located on the body of the instrument and used in effect for high temperature strain measurement.

Another desirable feature of extensometers is that mechanisms can be incorporated to magnify specimen displacements before they are sensed by the transducers. Such magnification can be an important factor in achieving good resolution in tests involving small strains. One design which successfully incorporates these features in a relatively straightforward manner is the diametral extensometer developed for high temperature, low cycle fatigue testing (Ref. 8). With this simplicity and the need for diametral strain measurements in mind, it was decided to use this instrument as a starting point for the subject biaxial extensometer.

BASIC APPROACH

The basic approach is illustrated schematically in Fig.(1). Two sensors of the type shown in Fig (1a) are positioned on the specimen. These sensors incorporate ceramic probes which grip the specimen by means of friction. The assumption is that once installed, the point of contact of each probe remains fixed on the specimen. The probes serve, therefore, to transmit specimen displacements and rotations to the body of the instrument. A further assumption is that a suspension system

can be designed which constrains the sensors to planes parallel to the X-Y plane of Fig (1b). Two such planes are the DEFG and the HIJK planes shown in this figure.

The method of strain measurement is as follows. Under axial loading, the vertical distance between the sensors, BB in Fig (1b), changes and is used as a basis for axial strain measurement. This is achieved by positioning proximity transducers on the top sensor and a target on the bottom sensor. Regarding diametral strain measurement, loading in the radial sense resulting from internal pressure causes the specimen diameter to change. These changes are transmitted via the hinge to the mounting arms. Relative movement between the mounting arms, AA in Fig (1a), is used for diametral strain measurement. This is accomplished by positioning the core of a linear variable differential transformer (LVDT) on one mounting arm and the coil on the other. Under torsional loading, the sensors rotate different amounts about the Z axis within their respective reference planes. This difference in angular rotation, θ in Fig (1b), is used for torsional strain measurement. The various mechanisms and transducers used in making torsional measurements will be discussed in detail later in the paper.

Regarding the mechanical details, the instrument consists of three subassemblies; the sensors; the lever-arms; and the support structure. One of the extensometers two sensors is shown in Fig (2). The more important components of this subassembly are the ceramic probes, the elastic hinge, the mounting arms, and the preload spring. The function of the spring is to force the probes against the specimen to provide the frictional force necessary to prevent slippage. The strain gages mounted on the probes are monitored during this process to control the amount of preloading. The transducer mounting block is used to grip the coil of the LVDT used for diametral strain measurement. The core of this transducer is shown positioned on the null adjustment screw. Also shown in Fig (2) are the heat shields and water cooling arrangement used to prevent heat buildup in the instrument. Elimination of this effect was viewed as being desirable in isothermal tests and essential in the case of non-isothermal tests.

One of the instrument's four lever-arm assemblies is shown in Fig. (3). The primary function of these assemblies is, in conjunction with the sensors, to transmit specimen rotation to four rotary variable differential transformers (RVDTs) positioned on the support structure. These mechanisms can be thought of as consisting of two levers, BC and CD, which are free to rotate about the vertical axes designated B, C, and D. Such rotation is allowed by flexural pivots which act as bearings (Ref. 9). One end of the lever-arm is bolted to the sensor and the other to the support structure. This arrangement allows the sensors freedom to rotate and displace within planes perpendicular to the three axes. The larger of the two levers, BC, includes a parallel linkage which allows the sensors to displace vertically. At the same time, the parallel linkages ensure that the sensors are constrained to planes which are parallel to the original reference plane. Use is again made of flexural pivots in these linkages as they allow rotation with no associated friction.

The primary function of the instrument's support structure, Fig(4) is to provide a means of mounting the device on the test system or on a calibration fixture. This subassembly consists of a cross-arm which when suitably supported, facilitates positioning of the instrument prior

to testing or calibration. Two vertical posts are attached to the cross-arm and provide mounting locations for the lever-arm assemblies and the RVDTs. One further function of the support structure is to provide a means of supporting the sensors at their centers of gravity on soft vertical springs. This is accomplished using two support brackets which bolt directly to the cross-arm. In addition to housing the spring holders, the support brackets provide convenient mounting locations for the instrument's electrical connectors. This approach has the advantage of isolating the instrument from long lengths of cable.

The complete instrument is shown positioned on a calibration fixture in Fig (5). This figure serves to show the complexity of the assembled instrument. The method of suspending the sensors on springs is shown in this figure along with the method of mounting the electrical connectors.

DETAILS OF TORSIONAL STRAIN MEASUREMENT

The method of torsional strain measurement is shown in more detail in Figs (6) and (7). In the first of these figures, the sensors are considered to be two levers, AB and AE, which have a fixed angle between them and which are constrained to follow the rotation of the specimen. The lever-arms are idealized into three bearing/two lever systems which are supported at points D and G. This mechanism was analyzed to determine the relationship between specimen rotation, Θ, and the corresponding lever-arm rotations at the support points, α and α'. The results of this analysis are shown in Fig (7). Here, it can be seen that the relationships between specimen rotation and individual lever-arm rotation are highly nonlinear. However, the curve relating specimen rotation, Θ, with the sum of the rotations at the support points, $\alpha + \alpha'$, can be seen to be near-linear. Thus, by positioning RVDTs at the support points, D and G, and summing their outputs electronically, near-linear relationships are obtained between specimen rotation and summed transducer output. By summing in turn the outputs from the two sensors, a combined output is obtained which is proportional to torsional strain as defined in Fig (7).

One problem peculiar to biaxial and multiaxial extensometers is that interaction or crosstalk can occur between the various forms of straining. The mechanism by which specimen displacements in the axial sense can affect torsional strain measurements is shown in Fig. (8). Such displacements cause the parallel linkages incorporated in arms BC and EF to assume some angular position, δ, relative to the original reference plane. These rotations cause the projected lengths of arms BC and EF to shorten in this plane. This shortening in turn causes lever CD to rotate $-\alpha$ from its original position and lever FG to rotate $+\alpha$ from its original position. These rotations are sensed by the RVDTs positioned at locations D and G. However, since the outputs from these RVDTs are summed before being used for measurement purposes, it might be expected that the effect would be self-cancelling. In practice, this situation would only be realised if the lever-arms were manufactured and assembled so as to be identical. With this in mind, the four lever-arms were assembled with extreme care using a special purpose jig. Also, the support structure was designed to provide the linear and angular adjustments necessary during final assembly to achieve the self-cancelling condition.

EVALUATION OF THE BIAXIAL EXTENSOMETER'S PERFORMANCE IN MEASURING TORSIONAL STRAIN

The instrument's performance in measuring torsional strain was evaluated in two stages. The first involved a series of bench calibration experiments conducted at room temperature. A biaxial calibration fixture was designed and developed at ORNL specifically for this work. The aim of these experiments was to investigate linearity and crosstalk over the maximum measurement ranges practicable with instrument.

The second stage of the evaluation involved a series of in-place calibation experiments conducted on thin-walled tubular specimens instrumented with foil strain gage rosettes. The aim here was to investigate mechanical hysteresis, linearity and crosstalk over small strain ranges, say ±100με. This was accomplished by loading the specimen within its elastic range and drawing direct comparisons between strain measurements made using the extensometer with those made using the strain gages. This was the preferred evaluation technique in the case of small strains as it avoided placing unrealistic demands on the performance of the calibration fixture.

BENCH CALIBRATION EXPERIMENTS

The fixture used for the bench calibration experiments is shown in Fig.(9). The more important components of this fixture are the micrometer heads used for diametral and axial calibrations and the rotary table used for torsional calibrations. The fixturing shown attached to the diametral micrometer head is designed for diametral calibration work. That shown positioned on the rotary table in Fig. (5) allows axial and torsional calibration. In addition to routine calibration work, the fixture was used to establish ranges of linearity and also to investigate crosstalk between the various types of straining.

The approach adopted in determining torsional calibration data is shown in Fig (5). The extensometer's probes were positioned on the simulated specimen which in turn was positioned on the rotary table of the calibration fixture. The voltage outputs from the RVDTS associated with the top and bottom sensors were monitored after being summed in filter/amplifier modules. The procedure followed in these experiments was to rotate the simulated specimen through known angles and to note the corresponding RVDT output. The angular calibration data generated in this manner for the range ±60 arc-min. are shown in Fig (10). As indicated on this figure, the extensometer was removed from the calibration fixture and then reinstalled at total of six times in generating the data shown. This procedure was followed to determine the repeatability of the calibration data.

The multiaxial calibration fixture was also used to investigate crosstalk between axial and torsional straining. The approach adopted here was to set known angular rotations and then to note the change in RVDT output as axial displacements in the range ±1.27 mm were superimposed using the calibration fixture's axial micrometer head. This range of displacements corresponds to an axial strain range of ±50,000 με, assuming a 25.4 mm specimen gage length. Data generated for angular settings in the range 0 to +60 arc-min. are shown in Fig (11). These data

are typical for angular settings in the range 0 tO -60 arc-min. and also 0 to ±150 arc-min..

IN-PLACE CALIBRATION EXPERIMENTS

The second stage of the evaluation was performed with the extensometer positioned on strain gaged specimens which in turn were installed in a tension-torsion test system. This allowed direct comparisons to be drawn between strain gage output and extensometer output as the specimens were subjected to biaxial loading within the material's elastic range. These experiments showed that torsional measurements made using both systems exhibited minimum hysteresis and were well behaved on passing through zero. As indicated in Fig. (12a), the hysteresis exhibited by the extensometer was about 6με when the specimen was loaded over a torsional stress range of 32 mpa.

Crosstalk was further investigated by subjecting the specimen to axial loading and monitoring any resulting change in torsional strain output. These experiments confirmed the earlier results in that crosstalk was found to be small. It can be seen in Fig.(12b) that torsional strain output changed by about ±6με when the specimen was loaded axially over the range ±120mpa.

Finally, attention was directed at investigating the extensometer's performance at elevated temperatures. As already noted, a number of features had been incorporated into the design to ensure that the body of the device was at or near room temperature during elevated temperature tests. The effectiveness of these measures made it unlikely that the instrument's strain transfer characteristics at elevated temperatures would be significantly different from those at room temperature. Therefore, this stage of the evaluation was limited to investigating a number of electronic characteristics such as signal noise levels and signal stability.

After establishing base-line data at room temperature, signal noise levels were recorded under isothermal conditions at 232, 454, 538, and 650°C. It should be noted that specimen heating was by means of a 5kW radio frequency (RF) induction heater and that the heater incorporated a closed-loop temperature control system. This form of heating was found to cause drastic increases in signal noise levels. Thus, it was necessary to filter the signals from the extensometer to avoid problems with test system control. A variety of active and passive filtering systems were tried with mixed results. The best compromise was found to be obtained using passive filters with time constants of about 0.5 seconds. Typical strain signals recorded over 200 second time intervals after installing such filters are shown in Fig. (13). Behavior over this time interval was of particular interest as it approximates the time required for individual loading probes in multiaxial deformation experiments. Recordings of this type were also made over 24 hour periods to establish the influence of laboratory environment on signal stability.

EXPERIMENTS INVESTIGATING STRESS RELAXATION BEHAVIOR UNDER CYCLIC TORSIONAL LOADING

On completing the instrument development work, the scope of the in-place calibration experiments was expanded to investigate the feasibility of the generating stress relaxation data under torsional loading. By way of background, an attempt had been made to use stress relaxation data determined under uniaxial loading to quantify the kinematic state variable in the Robinson viscoplastic model (Refs. 10 and 11). However, interpretation of the data generated in these experiments was complicated by the extreme sensitivity of uniaxial strain measurements to thermal effects. In contrast, torsional strain measurements, as a result of being based on specimen rotations, are relatively unaffected by temperature changes and associated thermal expansion. For this reason, it was anticipated that less than ideal temperature control would not be a limiting factor in stress relaxation tests conducted under torsional loading.

TEST EQUIPMENT

Details of the test equipment are given in Table (1). In summary, the tests were performed on an MTS closed loop, electrohydraulic test system with provision for tension-torsion loading. The MTS system is controlled by a Digital Equipment Corporation PDP 8e computer and an Electronic Associates Inc. TR-10 Analog Computer. The type of specimen used is shown in Fig. (14). After fabrication, the specimen was solution annealed and postweld heat treated. Details of these heat treatments are given in Table (2) along with other information regarding the the particular heat of material tested.

Prior to installation in the test system, the specimen was instrumented with four rectangular strain gage rosettes and seven chromel/alumel thermocouples. The strain gages were used to minimize bending during specimen installation and also to check out the performance of the biaxial extensometer at room temperature. Specimen heating was by means of a 5kW RF induction heater. The geometry of the heater load coil was designed to give a temperature profile within ±5°C of the nominal test temperature over a 25 mm gage length. The outputs from six of the chromel/alumel thermocouples were used to achieve this condition while the seventh was used for temperature control. The test setup described above is shown in Fig.15. Not shown in this figure is the water cooled heat shield which is positioned between the specimen and the biaxial extensometer during tests. This heat shield, in conjunction with those mounted on the sensors, prevents heating of the instrument by radiation.

PRELIMINARY EXPERIMENTS

At the start of this investigation, well established procedures were followed to ensure that the loading system and the various measurement systems were functioning properly. This preliminary work was aimed at ensuring the following:

1. The specimen was installed in the test system such that bending strains were within ±5% of the average strain.
2. The foil strain gage measurement system was functioning properly.
3. The biaxial extensometer was installed and functioning properly.
4. The temperature profile over a 25mm gage length was within ±5°C of the nominal test temperature.

The various procedures adopted to achieve these conditions are summarized in Table (3) along with the results obtained in the present experiment. As indicated in this table, the required conditions were met with one exception. This was that the best temperature profile that could be obtained was 538±20°C.

EXPERIMENTAL PROCEDURES

The experimental procedures used to investigate stress relaxation behavior under cyclic torsional loading were based in part on those used earlier in uniaxial experiments (Ref. 10). First, the specimen was cycled over a tensorial shear strain range of 0.56% using a ramp waveform and a nominal strain rate of 600με/min. The required fully cyclically hardened condition was achieved after about ten cycles.

Stress relaxation experiments were then conducted from five starting locations on the stabalized hysteresis loops (Fig. 16). Details of the target values of stress and strain used for computer control are given in Table (4). Also shown in this table are the sequences of loading followed before and after individual stress relaxation experiments. The aim of these loadings was to return the material to the reference condition before starting the next experiment. Five stages of loading were required in stress relaxation tests conducted from the peak of the hysteresis loop while six stages of loading were required in tests conducted from other locations (Fig. 17).

TEST RESULTS

A typical stress-strain hysteresis loop for material in a fully cyclically hardened condition is shown in Fig. (18). Such loops were recorded directly using analog outputs from the test system's load cell and from the biaxial extensometer. One difficulty indicated in this figure is that strain rate was not controlled at the specified value, 600με/min., with any degree of precision during the various stages of loading. Post-test analysis of the results showed that strain rates during elastic straining were as high as 900με/min. while those during inelastic straining were as low as 300με/min.

The results of the stress relaxation tests are shown in Fig. (19). One feature of the raw data is that a ±1mpa amplitude cycle is superimposed on the overall stress relaxation response. It was established that this cycling resulted from less than ideal control of torsional strain during the 0.167hr hold-periods. More specifically, the problem was caused by a deadband incorporated in the computer software to allow for noise on the signal being controlled. The cycling apparent in Fig. (19) clearly indicates that the size of the deadband selected, ±5με,

was too wide for precise stress relaxation testing. However, as the trends in the raw data were well defined, it was possible to construct average curves without much difficulty (Fig. 20). These curves subsequently were used to establish relationships between initial stress rate and starting stress on the hysteresis loop. The results of this analysis are shown in Fig. (21).

THEORETICAL CONSIDERATIONS: COMPARISON OF EXPERIMENT AND THEORY

As the results of the exploratory tests were reasonable consistent, it was possible to proceed to the final stage of the investigation. This involved use of the ORNL viscoplastic constititutive model to predict material response under conditions approximating those of the experiments. Because of the lack of multiaxial test data for 2-1/4 Cr-1Mo steel at elevated temperatures, the constants in this model were determined through uniaxial testing only. Thus, it was of considerable interest to determine how closely the model would predict behavior under other forms of loading, in this case simple shear.

THE VISCOPLASTIC CONSTITUTIVE EQUATIONS

An isothermal statement of the ORNL viscoplastic constitutive model is as follows:

$$2\mu\dot{\varepsilon}_{ij} = \begin{cases} F^n \dfrac{\Sigma_{ij}}{\sqrt{J_2}} & ; \quad F > 0 \text{ and } S_{ij}\Sigma_{ij} > 0 \\ 0 & ; \quad \begin{array}{c} F \leq 0 \\ \text{or} \\ F > 0 \text{ and } S_{ij}\Sigma_{ij} \leq 0 \end{array} \end{cases} \tag{1}$$

$$\dot{a}_{ij} = \begin{cases} \dfrac{H}{G^\beta}\dot{\varepsilon}_{ij} - RG^{m-\beta}\dfrac{a_{ij}}{\sqrt{I_2}} & ; \quad G > G_o \text{ and } S_{ij}a_{ij} > 0 \\ \dfrac{H}{G_0^\beta}\dot{\varepsilon}_{ij} - RG_0^{m-\beta}\dfrac{a_{ij}}{\sqrt{I_2}} & ; \quad G \leq G_0 \text{ or } S_{ij}a_{ij} \leq 0 \end{cases} \tag{2}$$

in which,

$$\Sigma_{ij} = S_{ij} - a_{ij} \tag{3}$$

$$S_{ij} = \sigma_{ij} - \frac{1}{3}\sigma_{kk} S_{ij} \tag{4}$$

$$a_{ij} = \alpha_{ij} - \frac{1}{3}\alpha_{kk} S_{ij} \tag{5}$$

$$F = \frac{J_2}{K^2} - 1 \tag{6}$$

$$G = \frac{I_2}{K^2} \tag{7}$$

$$J_2 = \frac{1}{2}\Sigma_{ij}\Sigma_{ij} \tag{8}$$

$$I_2 = \frac{1}{2} a_{ij} a_{ij} \tag{9}$$

Here, ε_{ij} denotes the components of inelastic strain rate, K and α_{ij} are state variables and μ, n, m, β, R and H are material constants. Values of the constants for 2-1/4 Cr-1Mo steel at 538°C are as follows:

$$\mu = 3.6 \times 10^7$$

$$n = 4.0$$

$$\beta = 0.75$$

$$m = 3.87$$

$$R = 8.97 \times 10^{-8}$$

$$H = 9.92 \times 10^3$$

These values are consistent with the units of Ksi for stress, in/in for strain and time in hours. The scalar state variable, K, is taken to be constant for material in a fully cyclically hardened condition. The value of K used in the following analysis, 0.82, resulted from isothermal, uniaxial testing as did the other values listed above.

As indicated in equations (6) through (9), the stress dependence in this model enters through the second principal invariants of the applied stress and the internal stress. This infers that the material is initially isotropic and that it behaves independently of the third principal invariants. The validity of the latter assumption is examined later in the paper in light of the experimental results.

REDUCTION TO PURE SHEAR: COMPARISON OF PREDICTED AND EXPERIMENTAL RESULTS

In the case of simple shear, the equations (1) through (9) reduce to the following:

$$\dot{\varepsilon}_{12} = \begin{cases} 1.39 \times 10^{-8} F^{4} \operatorname{sgn}(\tau - s) & ; \quad F > 0 \text{ and } \tau(\tau - s) > 0 \\ 0 & ; \quad \begin{matrix} F<0 \\ \text{or} \\ F>0 \text{ and } \tau(\tau - s) < 0 \end{matrix} \end{cases} \tag{10}$$

$$\dot{s} = \begin{cases} \dfrac{7320}{|s|^{1.5}} \dot{\varepsilon}_{12} - 3.17 \times 10^{-7} |s|^{6.23} \operatorname{sgn}(s) & ; \quad s > s_0 \text{ and } \tau s > 0 \\ \dfrac{7320}{|s_0|^{1.5}} \dot{\varepsilon}_{12} - 3.17 \times 10^{-7} |s_0|^{6.23} \operatorname{sgn}(s) & ; \quad s < s_0 \text{ or } \tau s < 0 \end{cases} \tag{11}$$

in which

$$F = \frac{(\tau - s)^2}{0.67} - 1 \tag{12}$$

$$s_0 = 0.01 \tag{13}$$

Here, $\dot{\varepsilon}_{ij}$ is the tensorial component of inelastic shear strain rate, τ is the applied shear stress, and s is the shear component of the state variable α_{ij}.

The above equations were used to predict saturated stress-strain hysteresis loops under conditions approximating those of the experiments (Fig. 18). To avoid undue complication, the prediction shown in this figure was made assuming a single strain rate, 900με/min., applied for the entire cycle. These equations were also used to predict stress relaxation behavior from various starting points on the hysteresis loops (Fig. 20). It should be noted that the model has no provision for predicting the "reversed" stress relaxation observed from points 3, 4, and 5. The horizontal lines constructed through these points are shown to emphasize the reversal of the experimental data.

DISCUSSION

In discussing the results of theis investigation, consideration is given first to the performance of the biaxial extensometer. Of particular interest here are the characteristics important in high precision, probing type experiments. These include linearity, crosstalk, mechanical hysteresis, resolution and stability. This is followed by some general discussion on problems associated with traditional methods for investigating time dependent material behavior at elevated temperatures. Possible advantages resulting from the use of torsional loading are outlined and the results of some preliminary experiments are discussed in light of predictions made using the viscoplastic constitutive model. Finally, methods are discussed for quantifying the internal state variable and the constants in this model.

PERFORMANCE OF THE BIAXIAL EXTENSOMETER

One basic requirement for any strain measurement system is that its output should be linear over the full range of interest. As indicated in Fig. (7), the kinematic analysis performed during the preliminary design stage showed that this goal theoretically was attainable with the present design. This result subsequently was confirmed in bench calibration experiments conducted over angular ranges of ±60 and ±150 arc-min.. The data generated for the smaller range are shown for purpose of illustration in Fig. (10). The importance of this result is that the relationship between specimen strain and voltage output from the instrument is known with certainty even though conditions at the start of tests may not be well defined. This situation can arise, for example, as a result of less than ideal instrument installation or thermal expansion of the specimen. Provided the instrument's calibration is linear, voltages resulting from these effects can simply be nulled out prior to testing without compromising the accuracy of subsequent measurements.

Another important result shown in Fig. (10) is that the calibration data are repeatable for successive installations. This lent confidence to the assumption that calibrations performed on the bench would still apply when the instrument was installed on a specimen. Further confidence in this approach was obtained when strains measured using the biaxial extensometer were compared to those measured using foil strain gages. The results obtained using the two strain measurement systems were usually within 2% of each other.

As already noted, one problem peculiar to biaxial and multiaxial experiments is that interaction or crosstalk can occur between the various forms of loading and straining. This problem is particularly limiting in experiments involving small changes of inelastic strain or inelastic strain rate. The meaning of such experiments is lost if, for example, loading in the axial sense produces apparent torsional strains and vice versa. Also, crosstalk of this type clearly precludes any meaningful investigation of normality. This problem was approached in two ways during the design and development of the subject extensometer. First, crosstalk was recognized as being a problem from the outset and measures were taken to minimize its effect during the design stage. Second, in tests requiring extreme precision, techniques were developed to computer correct for crosstalk effects.

The effectiveness of the self-correcting feature designed into the instrument can be judged by the data shown in Fig. (11). Here, it can be seen that axial strains over the range ±50,000 με caused tensorial shear strain measurements to change by less than 30 με. A similar result is shown in Fig. (12b). In this case, loading a specimen over a ±125 MPa axial stress range caused measurements of shear strain to change by less than ±6 με. The linear relationship shown in this figure subsequently was used to computer correct for crosstalk effects in yield surface determinations conducted on 2-1/4 CR-1Mo steel at 20°C (Ref. 12). In these experiments, axial and torsional stresses and strains are sampled at 1 second intervals. Thus, for a known axial stress, the corresponding value of apparent torsional strain was computed using the expression $\Delta\varepsilon_{12} = 0.05\ \sigma_{11}$ and used to correct the measured value. A similar approach was used in these biaxial experiments to correct the measured values of axial strain. In this case, the analytical representation of crosstalk was $\Delta\varepsilon_{11} = 0.29\ \sigma_{12}$, where $\Delta\varepsilon_{11}$ and σ_{12} have units of microstrain and MPa. Such corrections were found to be a prerequisite for the successful definition of small offset (25 με) yield surfaces using the biaxial extensometer .

A further requirement in high-precision, probing type experiments is that the strain measurement system should not exhibit significant mechanical hysteresis. This is because differences in response between loading and unloading can provide a useful measure of change of material state. Clearly, any mechanical hysteresis in the instrumentation will complicate interpretations of this type. The need to minimize hysteresis influenced the design of the biaxial extensometer in two ways. First, flexural pivots were used in the lever-arms to act as bearings. These pivots, by utilizing sets of flat cross flexures, allow rotation between components without any associated rolling friction or backlash. Second, careful consideration was given to the method of mounting the instrument on specimens. The aim here was to avoid techniques which might lead to difficulties when the direction of loading is reversed or when loading passes through zero. The approach adopted was to use pairs of ceramic probes which grip the specimen by means of friction at three locations (Fig.2). The surfaces in contact with the specimen are flat resulting in line contact over 2.5mm lengths at each of the three locations. As indicated previously, preload springs are used to provide the frictional force necessary to prevent slippage.

The data shown in Fig. (12a) illustrate the effectiveness of these measures. These data were obtained by cycling a specimen over a 32 MPa

torsional stress range and recording the corresponding strain outputs from foil strain gages and the multiaxial extensometer. It was found that the extensometer exhibited only slightly more hysteresis than the strain gages the width of the hysteresis loop at zero load being about 6με. Also, the output from the extensometer was found to be well behaved when the direction of loading was reversed and when loading passed through zero.

High resolution is another important requirement for strain measurement systems supporting development of viscoplastic constitutive models. This characteristic plays a key role in experiments investigating behavior under multiaxial stress states. In these experiments, attempts are made to investigate inelastic response while maintaining the material in an unchanged state. This conflicting requirement can be approximated in probing type experiments in which very small changes in inelastic strain or inelastic strain rate are used as measures of inelastic response. Clearly, strain measurement systems used for this work must be capable of detecting these small changes which in practice requires near-microstrain resolution.

One feature of extensometers is that mechanical gain can be used to obtain high resolution. The kinematic analysis performed during the preliminary design stage showed that suitably designed lever-arm assemblies can provide significant mechanical magnification of specimen rotations. It was established that most magnification could be obtained by maximizing the length of lever BC and minimizing the length of lever CD (Fig. 3). Further gain was obtained by summing the rotations of the two lever-arm assemblies associated with a particular sensor. With the geometry used in the present experiments, one degree of specimen rotation produces a summed output of about 4 degrees at the attachment locations of the RVDTs. This meant that only modest amounts of electronic gain, x 100, were needed to calibrate the instrumentation such that ±3,000 με ≡ ±10 volts. Using this arrangement, the ability to detect voltage changes of the order of of 3mV would theoretically give the required microstrain resolution.

In practice, however, the resolution of strain measurment systems are usually limited by electrical noise. This is particularly the case in elevated temperature tests where the heating system and the temperature control system can add to the problem. As previously noted, passive filters were used to minimize this difficulty. It can be seen in Fig.(13) that even after filtering, noise levels at 650°C are a factor of at least five greater than those at room temperature. Based on these results, it appeared that the aim of developing an instrument with near-microstrain resolution had been achieved in the case of tests conducted at room temperature. In the case of elevated temperature tests, the resolution was about 5 με.

Regarding signal stability, considerable effort was needed to achieve the results shown in Fig.(13). First, it was found necessary to control the laboratory air temperature to within ±1°C. Further, in experiments requiring extreme precision, it was necessary to isolate the specimen, extensometer, and load frame from laboratory air currents. This was achieved by constructing an enclosure around the load frame and the ancillary equipment. Under these conditions, the strain signals from the extensometer exhibited negligible drift once thermal equilibrium had been established. It should be noted that the time periods investigated were relatively short, 24 hours and less. Such periods were consistent with early experiments which were short-term and exploratory in nature.

INVESTIGATION OF TIME DEPENDENT MATERIAL RESPONSE AT ELEVATED TEMPERATURES

Having developed instrumentation allowing precise biaxial strain measurement, the next problem addressed was how best to use this capability for investigating time dependent behavior at elevated temperatures. The two experimental approaches traditionally used for this purpose are the monotonic creep test and the stress relaxation test. Based on experience gained in previous uniaxial test programs, the preferred test method for the present experiments was the stress relaxation test and the preferred type of loading was pure torsion. Some background regarding these choices is given in the following.

One characteristic of creep data determined on test machines using dead weight loading is that the data usually exhibit considerable scatter (Ref. 13). Possible reasons for the variability include less than adequate control of conditions during initial loading and the test method's extreme sensitivity to errors in load and temperature. Also, difficulties arise as a result of the simple forms of extensometry used in the majority of these experiments. Poor dynamic response can result in unreliable strain measurements during the early stages of tests and less than adequate stability can result in errors in long term tests. Thus, although tests leading to steady state creep rates might appear advantageous from the modeling viewpoint, the associated experimental difficulties raise serious questions regarding the value of this test method in supporting constitutive equation development.

In contrast, the accuracy of stress relaxation data generated using closed-loop, electrohydraulic test systems appears less susceptable to experimental difficulties. Since these experiments are conducted under strain control, the magnitudes of both strain and strain rate are known with certainty during initial loading. Further, since total strain is simply held constant during the critical stage of the experiment, less demanding requirements are placed on the strain measurement system. One important advantage here is that the dynamic characteristics of load cell are limiting in detecting high inelastic strain rates rather than those of the extensometer. This is an advantage since load cells can detect dynamic events as rapid as 100in/in/sec. Also, since stress relaxation experiments are relatively short-term, unrealistic demands are not placed on the stability of the instrumentation. Another advantage of conducting these experiments on closed-loop, electrohydraulic test systems is that the material can be cycled over a known strain range between stress relaxation experiments and returned to a known reference condition. This approach allows a number of experiments to be conducted on a single specimen (Ref. 10).

Unfortunately, unless conducted with extreme care (Ref. 14), the stress relaxation test is not entirely free from experimental difficulties. One such difficulty is that the test method is extremely sensitive to temperature fluctuations when conducted under uniaxial loading. To illustrate, in tests conducted on 2-1/4CR-Mo steel at 538°C, a ±5°C or ±1% variation in specimen temperature causes stress to change by about ±10MPa. As can be seen in Fig. (19), stress variations of this magnitude will completely mask stress relaxation response in this material. It follows that both specimen temperature and laboratory temperature have to be controlled within very close limits if the production of misleading data is to be avoided.

A related difficulty arises in experiments in which radio frequency induction heaters are used to test ferritic steels. In these experiments, coupling can occur between specimen loading and specimen heating as a result of the magnetomechanical effect (Ref. 15). By way of explanation, the heat dissipated in inductively heated ferritic steels is a function of the material's ferromagnetic permeability. Also, it has been demonstrated that the permeability of these materials is a function of mechanical straining. Since specimen temperature typically is controlled by means of a single thermocouple located at a point on the specimen surface, straining an inductively heated specimen causes temperature to change at other locations in the specimen. The net result is that the temperature in the specimen gage length is not in a stabilized condition prior to conducting the stress relaxation test. As indicated above, the resulting temperature changes, occurring, say over a 25mm gage length, can invalidate the results of subsequent stress relaxation experiments.

One solution to these difficulties is to use an alternative form of loading. As noted earlier, torsional strain measurements are based on specimen rotations which theoretically are unaffected by temperature changes and associated thermal expansion of the specimen. This can be seen by inspection of the expression for torsional strain shown in Fig. (7). Also, the design of the biaxial extensometer is such that torsional measurements are insensitive to changes in laboratory temperature. This is because the symmetry of the instrument causes thermal effects to be self cancelling. In summary, therefore, it appeared that many of the difficulties experienced in previous uniaxial test programs would not be a factor in stress relaxation tests conducted under purely torsional loading. The exploratory tests described in the following were conducted to examine the feasibility of this approach.

The success of these experiments can be judged by the data shown in Figs. (18) through (21). Considering first the data shown in Fig. (18), no difficulty was experienced with the biaxial extensometer in cycling the specimen over a shear strain range of 0.56%. As in earlier experiments conducted at room temperature, no problems were experienced when the direction of loading was reversed or when loading passed through zero. Also, the extensometer exhibited no tendency to "walk" on the specimen with repeated cycling. The one difficulty which did occur during this stage of the experiment was that the nominal value of strain rate, 600με/min., was not maintained constant within reasonable limits. This resulted from a problem with the computer control and was not related to the instrumentation being used.

The data shown in Figs. (19) and (20) demonstrated that the biaxial extensometer had sufficient stability and resolution to allow stress relaxation behavior to be investigated under purely torsional loading. Perhaps the most striking feature of the data shown in these figures is that the sense of the relaxation process reverses at a stress value of about 45 MPa. To illustrate, in the experiments conducted from starting stresses of 87 and 69 MPa, stress dropped by 21 and 9 MPa during the 600 second hold-periods. In contrast, stress increased during the hold-period in the other three experiments. For example, in the experiment conducted from a starting stress of 0 MPa, stress increased by about 7 MPa. This result confirms trends observed in earlier programs conducted on 2-1/4CR-Mo steel under uniaxial loading (Ref.10). As will be

discussed later, use will be made of this characteristic of the data to quantify the kinematic state variable in the viscoplastic constitutive model under consideration.

One apparent disadvantage of the experimental approach described above is that the magnitude of the stress changes occurring during the relaxation process are relatively small. If, however, consideration is given to the rate of change of stress, then the relaxation data shown in Figs. (19) and (20) can be shown to vary over several orders of magnitude. This is illustrated in Fig. (21) for the case of the initial stress relaxation rate. Whereas the stress changes occurring during relaxation fall within a ±20MPa range, the initial stress rates for the same data can be seen to cover a ±1000 MPa/h range on average. It is reemphasized that these rates were measured using the test system's load cell. Bearing in mind the reliability of load cells, it was possible to place a high degree of confidence on the accuracy of these data.

Regarding the temperature insensitivity of the torsional strain measurements, no direct evidence has been presented thus far supporting this claim. Such evidence was obtained on completing the series of stress relaxation tests when the specimen was cooled from 538°C to room temperature. It was established that torsional strain output changed by less than 40με during this process. In comparison, the thermal contraction associated with this cooling would have resulted in apparent axial strains of the order of 8000με. Based on these values, use of torsional loading reduced temperature sensitivity by at least two orders of magnitude.

In related activity, the magnetomechanical effect was shown not to be a factor in these experiments. In a series of exploratory tests conducted at 538°C, the specimen was loaded within its elastic range to a torsional stress of 45 MPa and held constant at this value for about 600 seconds. Both torsional stress and torsional strain were monitored during this period to investigate the stability of the signals. It was found that both signals remained constant within the limits of accuracy of the measurement system during the hold-period. Thus, if any thermal readjustments were occurring in the specimen as a result of the loading, the torsional strain measurement was totally unaffected by them. As stated earlier, this insensitivity to thermal effects is viewed as being an important advantage of torsional loading since it eliminates a major source of uncertainty.

COMPARISON OF PREDICTIONS WITH EXPERIMENTAL RESULTS AND DETERMINATION OF THE INTERNAL STATE VARIABLE

As noted earlier, it was of considerable interest to compare the data generated in the cyclic relaxation experiments to predictions made using the viscoplastic constitutive model. This was because this model was developed before the present results were available and also because the formulation of the model was based entirely on uniaxial test data. Thus, the results of the present experiments provided a totally independent check of the predictive capability of the model for a more fundamental form of loading, pure shear.

First, equations (10) through (13) were used to predict the stabalized hysteresis loop for conditions approximating those of the experiments. As indicated in Fig. (18), the theoretical and experimental results were found to be in reasonable agreement considering that the experimental values of temperature and strain rate varied from the nominal test values. Although falling short of a proof of the adequacy of the "J_2" asssumption made in the theory, this comparison does provide some measure of its validity under the present conditions.

Equations (10) through (13) were also used to predict stress relaxation response from two of the starting locations on the stabilized hysteresis loop. These locations correspond to stress values of 87 MPa and 69 MPa. As indicated in Fig. (20), the predicted and the experimental data agree reasonably well. One feature of these data is that the viscoplastic model somewhat underpredicts the relaxation occurring in 600 seconds. It was not possible to make predictions of the curves from the other three starting locations as there is no provision in the model for predicting reversed stress relaxation.

One basic requirement for viscoplastic constitutive models incorporating internal state variables is that it should be possible to determine the current value of the state variable through simple phenomenological testing. The type of experiment described earlier, the stress-dip-test, can be used for this purpose. The particular value of starting stress, $\sigma_{12} = \tau^*$ at which the initial stress relaxation rate is zero can be obtained from equation (12) as follows:

$$F = \frac{(\tau^* - s)^2}{0.67} - 1 = 0 \tag{14}$$

giving in SI units

$$\tau^* - s = 5.6 \text{ MPa} \tag{15}$$

An experimental value of τ^* was determined from Fig. (21) to be 45 MPa. By substituting this value into equation (15) and solving for s, the value of the internal state variable was found to be 39.4 MPa. This value applies along the unloading side of the hysteresis loop, i.e., for the points 1 through 6 in Fig. (16), for material in a fully cyclically hardened condition at a temperature of 538°C.

It is of interest to note that the data generated in the stress-dip-test can also be used to determine the constants in the flow law. As indicated above, the internal state variable, s, is constant along the unloaded portion of the hysteresis loop. It follows that both σ_{12} and s are known at the start of each of the relaxation experiments. Further, the inelastic strain rates can be obtained for the start of the experiments using the expression,

$$\dot{\varepsilon}_{12} = - \frac{\dot{\sigma}_{12}}{G} \tag{16}$$

where $\dot{\sigma}_{12}$ is measured directly and G is the shear modulus.

In the case where the material constants are unknown, the flow law is written,

$$\dot{\varepsilon}_{12} = A\left[\frac{(\tau-s)^2}{0.67} - 1\right]^n \qquad (17)$$

The unknown constants, A and n, can be determined since τ, s and $\dot{\varepsilon}_{12}$ are known for a number of points. Optimized values of the constants can be determined by conducting a series of these experiments.

CONCLUSIONS

The following conclusions were drawn regarding the performance of the instrumentation, the practicality of the experimental approach proposed in this study, and the predictive capability of the Robinson viscoplastic constitutive model.

1. The ORNL biaxial extensometer gave excellent results when used to measure torsional strains at room and elevated temperatures. The instrument's output was linear over the strain range of interest, $\Delta\varepsilon_{12} = 0.56\%$, and exhibited minimum crosstalk and hysteresis.
2. The torsional strain output of the biaxial extensometer was found to be insensitive to temperature changes in the specimen. This indicated that torsional loading can be used to advantage in generating stress relaxation data.
3. Theoretical predictions made using the Robinson viscoplastic constitutive model were in reasonable agreement with the experimental results obtained in this study.
4. The experiments conducted under torsional loading confirmed that kinematic state variables can be quantified by investigating stress relaxation behavior at various locations around stabalized stress-strain hysteresis loops.

REFERENCES

1. Robinson, D.N., Pugh, C.E., and Corum, J.M., "Constitutive Equations for Describing High-Temperature Inelastic Behavior of Structural Alloys," Proc. of Specialists Meeting on High-temperature Structural Design Technology of LMFBRS, IAEA Report IWGFR/11, pp. 44-57 (April 1976).

2. Liu, K.C., "Room Temperature Elastic-Plastic Response of Thin-Walled Tubes Subjected to Nonradial Combinations of Axial and Torsional Loadings," Pressure Vessels and Piping: Verification and Qualification of Inelastic Analysis Computer Programs, ASME Publication G00088, pp. 1-12, (1975).

3. Liu, K.C., and Greenstreet, W.L., "Experimental Studies to Examine Elastic-Plastic Behavior of Metal Alloys Used in Nuclear Structures," Constitutive Equations in Viscoplasticity: Computational and Engineering Aspects, ASME Publication AMD-Vol. 20, pp. 25-56 (December 1976).

4. Ellis, J.R., Robinson, D.N., and Pugh, C.E., "Behavior of Annealed Type 316 Stainless Steel Under Monotonic and Cyclic Biaxial Loading at Room Temperature," Nuclear Engineering and Design 47, pp. 115-123 (1978).

5. Ellis, J.R., Robinson, D.N., and Pugh, C.E., "Time Dependence in Biaxial Yield at Room Temperature," Journal of Engineering Materials and Technology, Vol. 105, pp. 250-256 (October 1983).

6. Robinson, D.N., "A Unified Creep-Plasticity Model for Structural Metals at High Temperature," ORNL/TM 5969, Nov. 1978.

7. Robinson, D.N., and Swindeman, R.W., "Unified Creep-Plasticity Constitutive Equations for 2-1/4 CR-1 Mo Steel at Elevated Temperature," ORNL/TM-8444, October 1982.

8. Slot, T., Stentz, R.H., and Berling, J.T., "Controlled-Strain Test Procedures," Manual on Low-Cycle Fatigue Testing, ASTM STP 465, American Society for Testing and Materials, pp. 100-128 (1969).

9. Troeger, H., "Considerations in the Application of Flexural Pivots," Automatic Control, Vol. 17, No. 4, pp. 41-46 (November 1962).

10. Swindeman, R.W., Robinson, D.N., "Experimental Methods to Determine the Kinematic State Variable in 2 1/4 CR-1 Mo Steel at High Temperature," ORNL-5776 (July 1981).

11. Swindeman, R.W., Williams, B.C., and Robinson, D.N., "Evaluation of the Mechanical Behavior of Vacuum Arc Remelted 2 1/4 CR-1 Mo Steel in Support of Constitutive Equation Development," Oak Ridge National Laboratory Report, ORNL/TM-8402 (December 1982).

12. Ellis, J.R., "Multiaxial Exploratory Testing," High-Temperature Structural Design Progress Report, Oak Ridge National Laboratory Report, ORNL-5930, pp. 7-23 (June 1982).

13. McAffee, W.J., and Sartory, W.K., "Materials Heat-to-Heat Variability Study: Part 1 - Compilation and Analysis of Data," Oak Ridge National Laboratory Report, ORNL-5604 (November 1980).

14. Hart, E.W., et al., "Phenomenological Theory: A Guide to Constitutive Relations and Fundamental Deformation Properties," Constitutitve Equations in Plasticity, Edited by A.S. Argon, MIT Press (1975).

15. Jones, W.B., "Influence of the Magnetomechanical Effect in Testing Inductively Heated Ferritic Steel," Sandia Laboratories Report, Sand 82-0752 (May 1982).

Table (1) DETAILS OF TEST EQUIPMENT

Loading System	MTS Tension-Torsion Test System with ±200kN axial capacity and ±2000N - m torsional capacity.
Computer Control	Digital Equipment Corporation PDP 8e Computer in conjunction with an Electronics Associates Inc. TR-10 Analog Computer.
Software	ORNL enhanced version of FOCAL.
Specimen Type	Thin walled tubular design, the parallel section being 64mm long and the inside and outside diameters being 23.5mm and 26.04mm, respectively.
Specimen Heating	5kW radio frequency induction heater with closed loop temperature control. Details of the work coil are as follows: 84mm overall length; 48mm ID; 32mm spacing between the 4 turn windings; and manufactured from 5mm OD copper tubing.
Specimen Instrumentation	4 foil rectangular strain gage rosettes in full bridge circuit for torsional measurement and half-bridge circuit for axial measurements. The two bridge circuits were set up using shunt calibration procedures so that 3000$\mu\varepsilon$ = 10 V. 7 intrinsic chromel/alumel thermocouples located over the 25mm gage length.

Table (2) DETAILS OF THE MATERIAL TESTING

Materials Details	Vacuum arc remelted 2.25Cr-1Mo Steel, Cameron Iron Works Heat 56448, 50 mm-o.d. Bar Form
Heat Treatment Details	Solution anneal Heat to 927℃, hold for 60 min; cool at rate not exceeding 1°C/min. to 316°C; and air cool to room temperature. Postweld heat treatment Heat to 727°C, hold for 40 hr.; cool to 427°C at 1°C/min; and air cool to room temperature. Note: These heat treatments were performed under vacuum on fininsh-machined specimens.
Microstructural Characteristics	Equiaxed with grain size in the range 5-6 ASTM units Microhardness values in the range 110-125 (DPH) Microstructure consists of ferrite with globular $M_{23}C_6$ carbides and η carbide.

Table (3) RESULTS OF THE PRELIMINARY EXPERIMENTS

Experimental Stage	Method Adopted	Results	
		Target Value	Value Obtained
1. Specimen Installation	Special purpose fixturing was used to get the specimen parallel and concentric with the acutator rod	0.05 mm TIR[a]	0.05 mm TIR
	Bending was minimized by successively shimming the load train, loading the specimen in compression, and measuring the resulting strain distribution.	within ±5% of average	±3% of average
2. Checkout of the strain gage measurement system.	Measurements of torsional stress and strain were made while the specimen was loaded within its elastic range. A value of shear modulus was then determined and compared to a handbook value.[b]	G=11.72 x 10^6psi	G=11.67 x 10^6psi
3. Checkout of the biaxialextensometer at room temperature	Measurements of torsional stress and torsional strain were made while the specimen was loaded within its elastic range. A value of shear modulus was then determined and compared to the value obtained using foil strain gages.	G=11.67 x 10^6psi	G=11.79 x 10^6psi
4. Tuning the heating system	Adjustments were made to the load coil of the induction heater until the required profile was obtained over the 25mm gage length. The outputs from six chromel/alumel termocouples were used to achieve this condition.	538±5°C	538±20°C

a. Total indicator reading b. Nuclear Systems Material Handbook, Vol. (1)

TABLE (4) LOADING SEQUENCES USED TO INVESTIGATE STRESS RELAXATION BEHAVIOR UNDER CYCLIC TORSIONAL LOADING

EXPERIMENT NUMBER	LOADING SEQUENCE	LOADING TARGET		HOLD-PERIOD (h)
		TENSORIAL SHEAR STRAIN ($\mu\varepsilon$)	TORSIONAL STRESS (MP_a)	
1 and 2	1	2800		0
	2	-2800		0
	3	2800		0.167
	4	- 500		0
	5		0	0
3	1	2800		0
	2	-2800		0
	3	2800		0
	4		0	0.167
	5	- 500		0
	6		0	0
4	1	2800		0
	2	-2800		0
	3	2800		0
	4		41.37	0.167
	5	- 500		0
	6		0	0
5	1	2800		0
	2	-2800		0
	3	2800		0
	4		20.69	0.167
	5	- 500		0
	6		0	0
6	1	2800		0
	2	-2800		0
	3	2800		0
	4		68.95	0.167
	5	- 500		0
	6		0	0

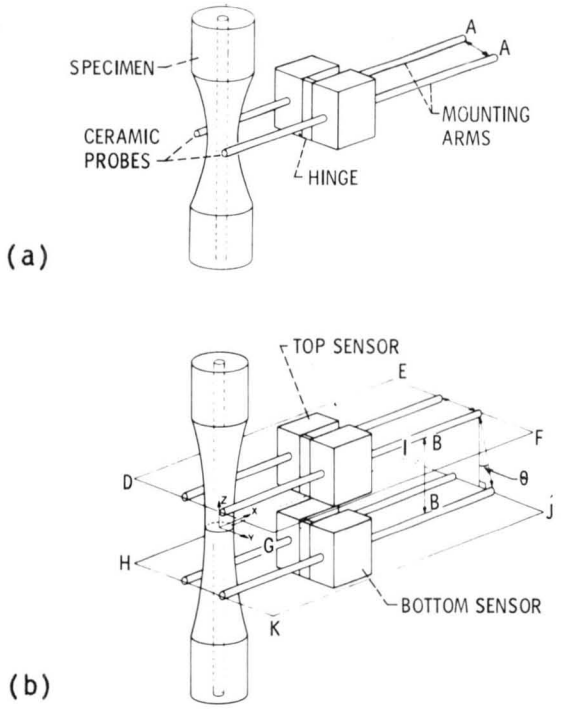

(a) Sensor positioned on specimen.
(b) Use of two sensors for multiaxial measurements.

Figure 1. - Basic approach.

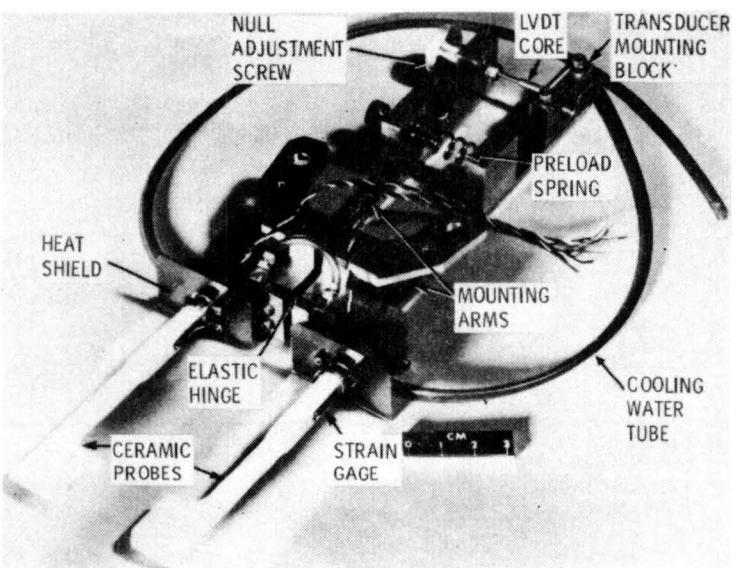

Figure 2. - Sensor assembly.

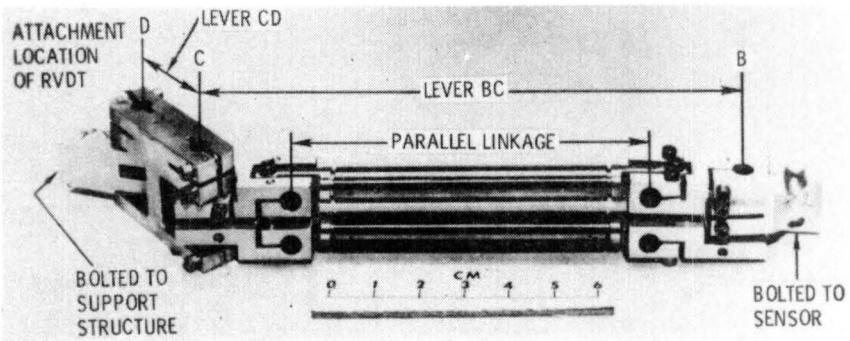

Figure 3. - Lever-arm assembly.

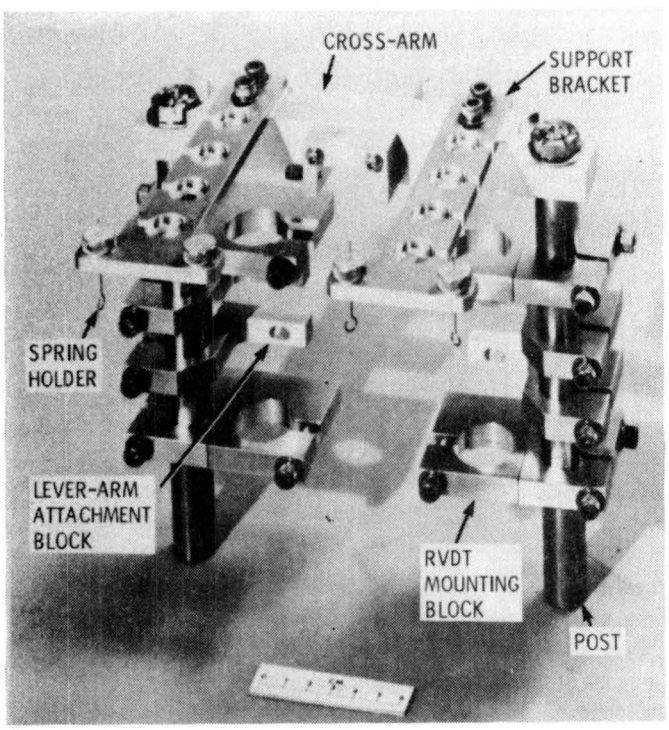

Figure 4. - Support structure.

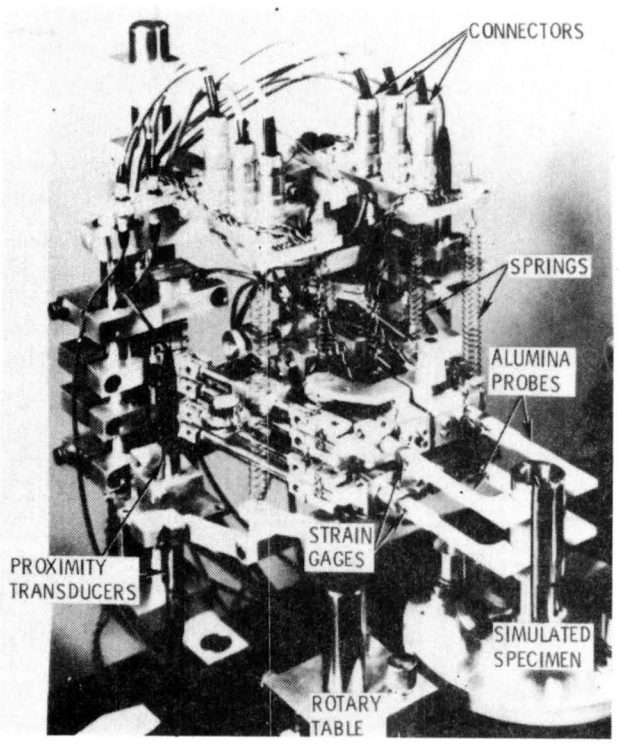

Figure 5. - Biaxial extensometer positioned on calibration fixture.

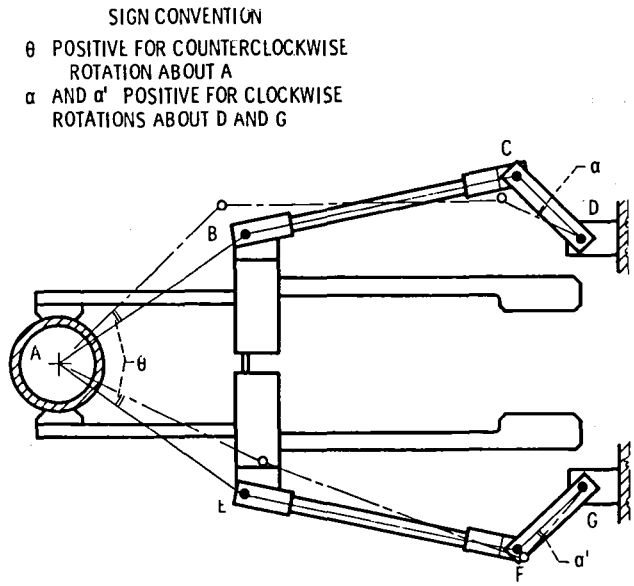

Figure 6. - Method of transmitting specimen rotation to fixed points on the support structure.

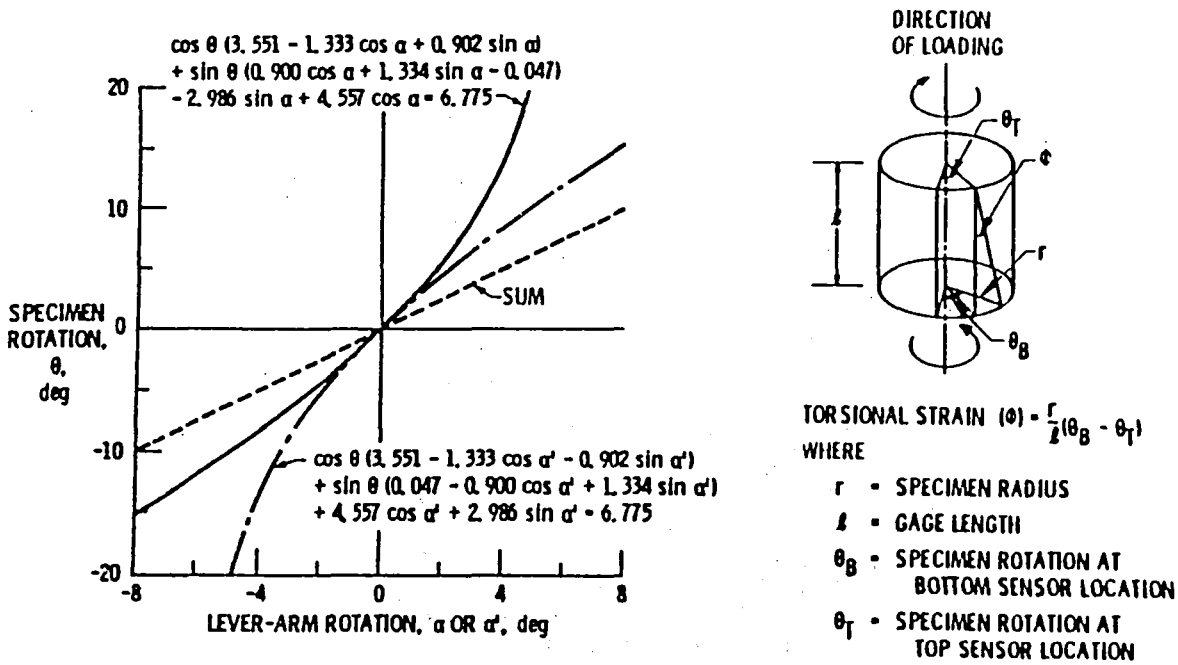

Figure 7. - Results of a kinematic analysis of the lever-arm assemblies.

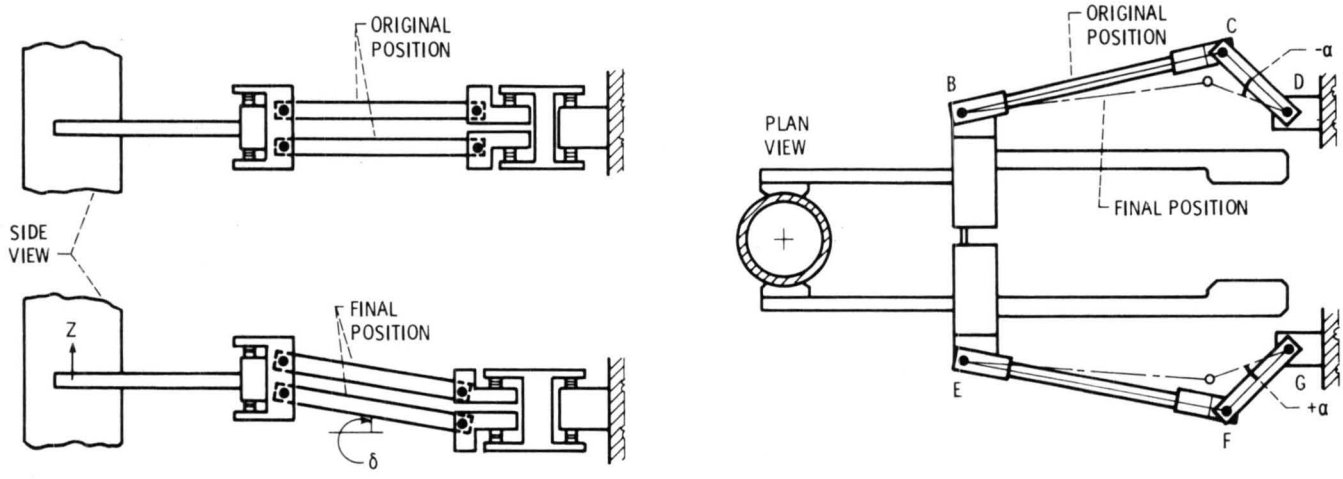

Figure 8. - Method of accommodating axial displacement.

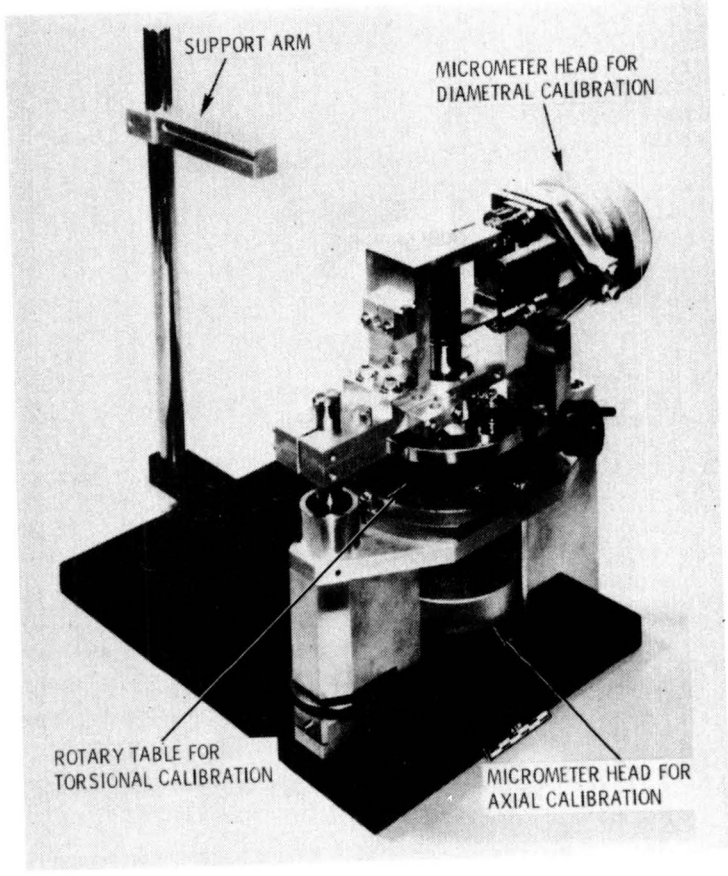

Figure 9. - Biaxial calibration fixture.

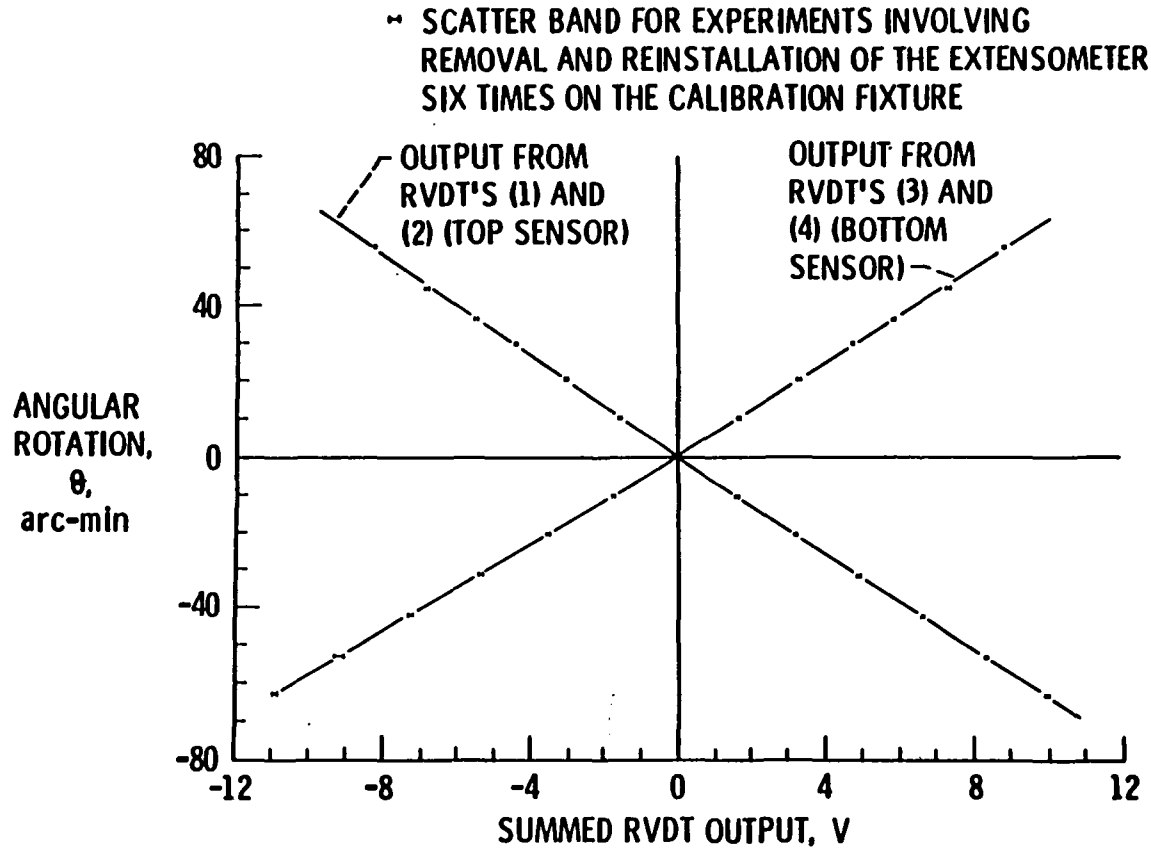

Figure 10. - Torsional calibration data for top and bottom sensors. (For a 25 mm-o.d. specimen and a 25 mm gage length, a relative rotation of ±60 arc min between top and bottom sensors is equivalent to a tensorial shear strain of ±4472 με.)

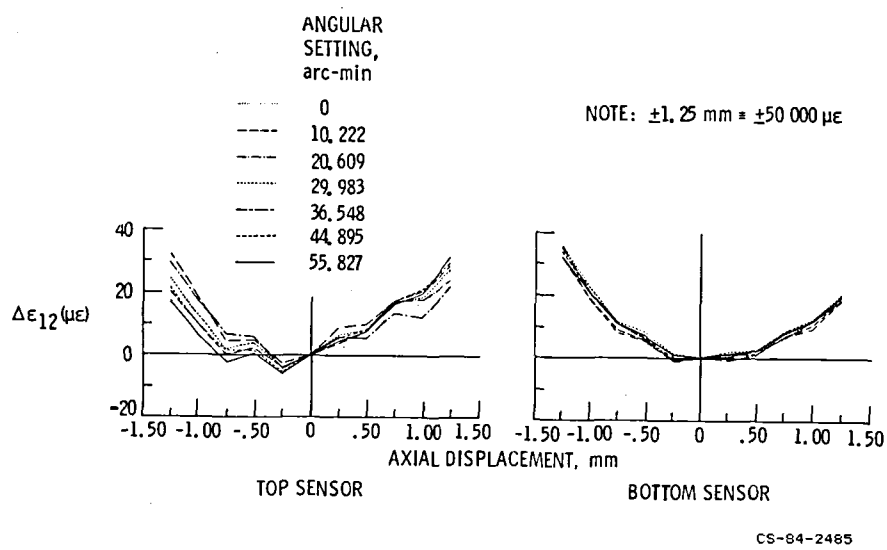

Figure 11. - Change in tensorial shear strain resulting from superimposition of axial displacement.

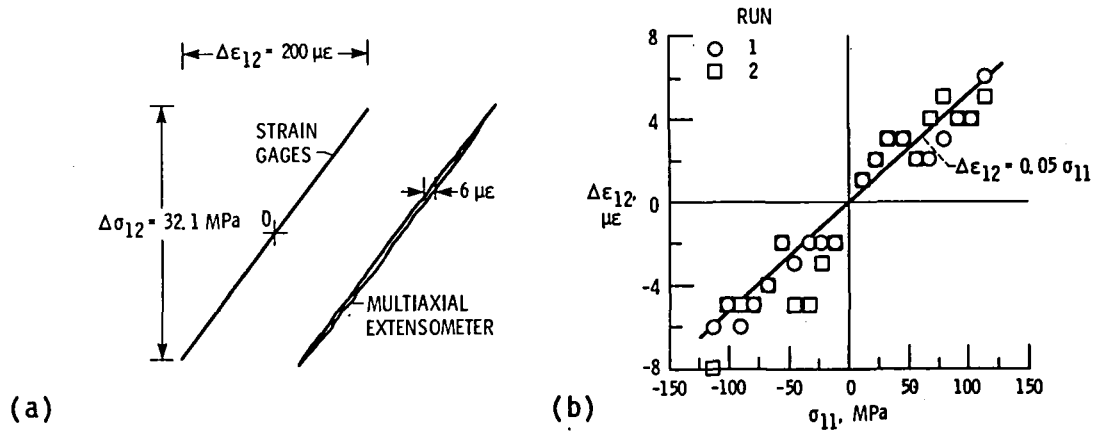

(a) Comparison of outputs from foil strain gages and the multiaxial extensometer.

(b) Effect of axial loading on torsional strain measurement.

Figure 12. - Results of in-place torsional calibration experiments performed at 20 °C. (The nominal calibration for all strain measurement systems was 3000 με ≡ 10 V.)

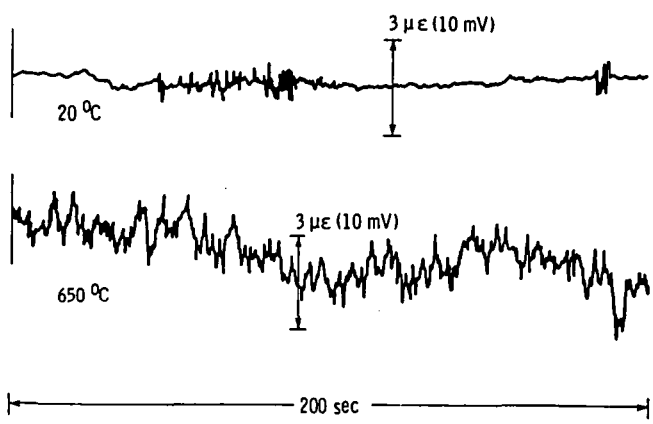

Figure 13. - Stability of torsional strain signals at 20 and 250 °C. (A passive filtering system with a 0.5 second time constant was used in obtaining the signals shown.)

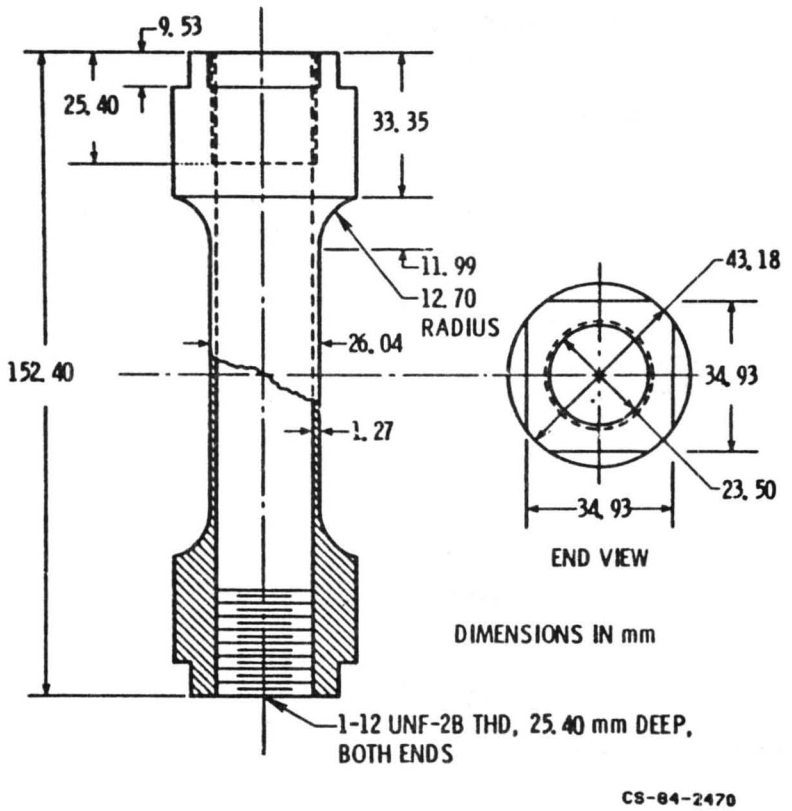

Figure 14. - ORNL tubular specimen design.

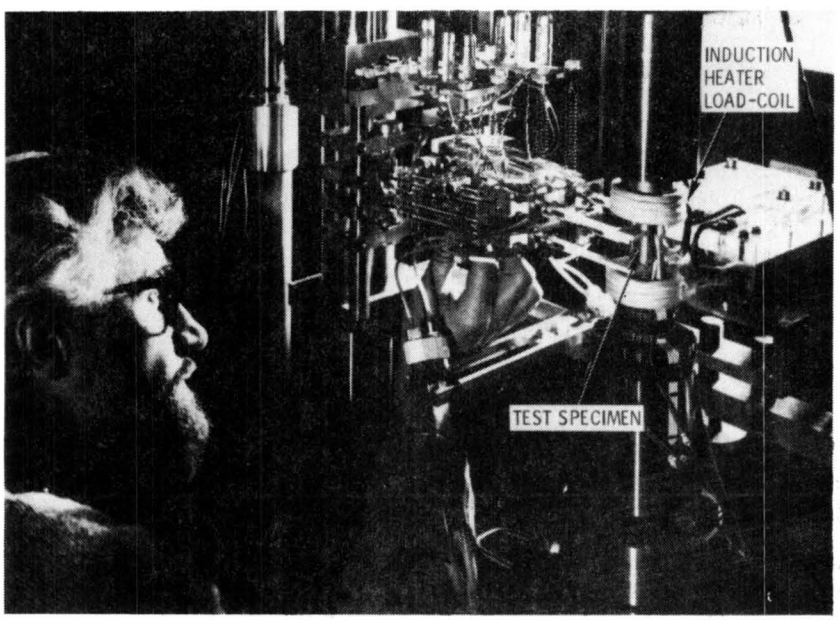

Figure 15. - Biaxial extensometer positioned on a tubular test specimen.

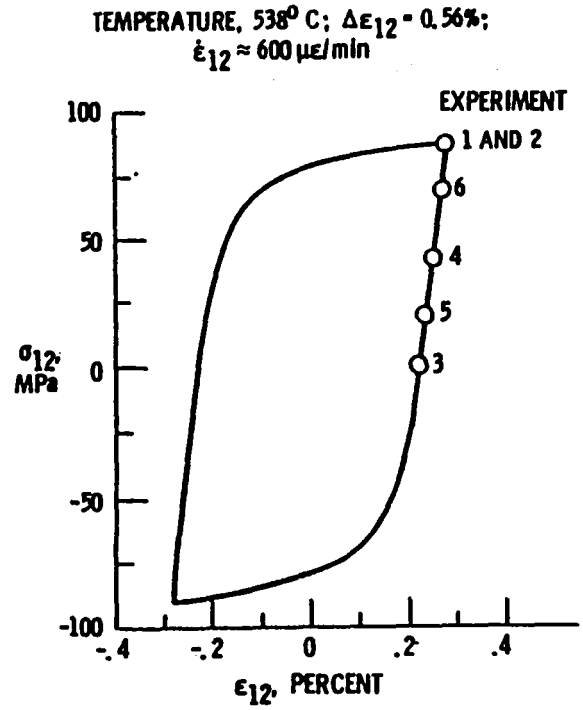

Figure 16. - Nominal stress-strain conditions at start of stress relaxation experiments.

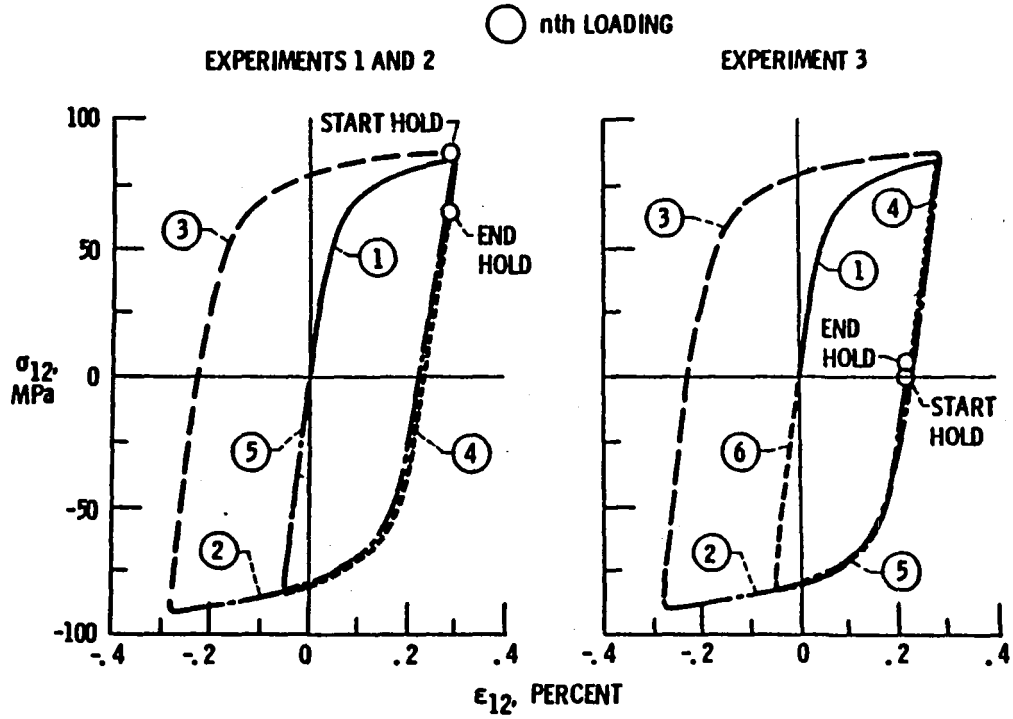

Figure 17. - Typical loading sequences.

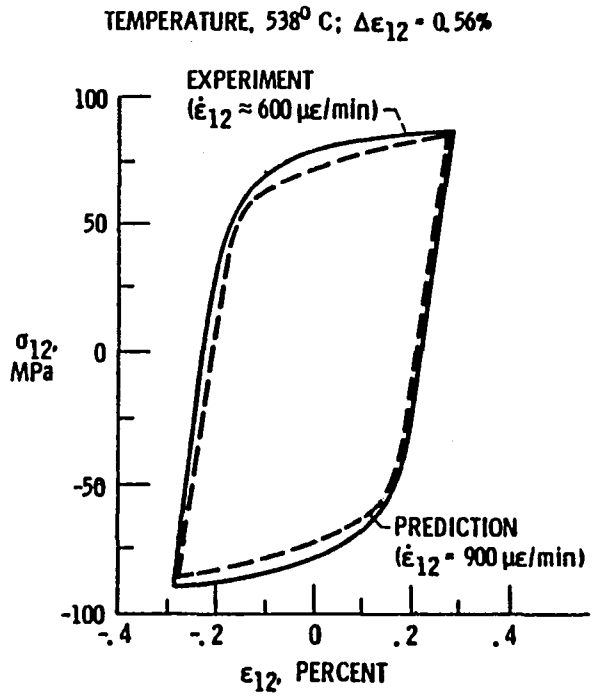

Figure 18. - Comparison of experimental and predicted stress-strain response.

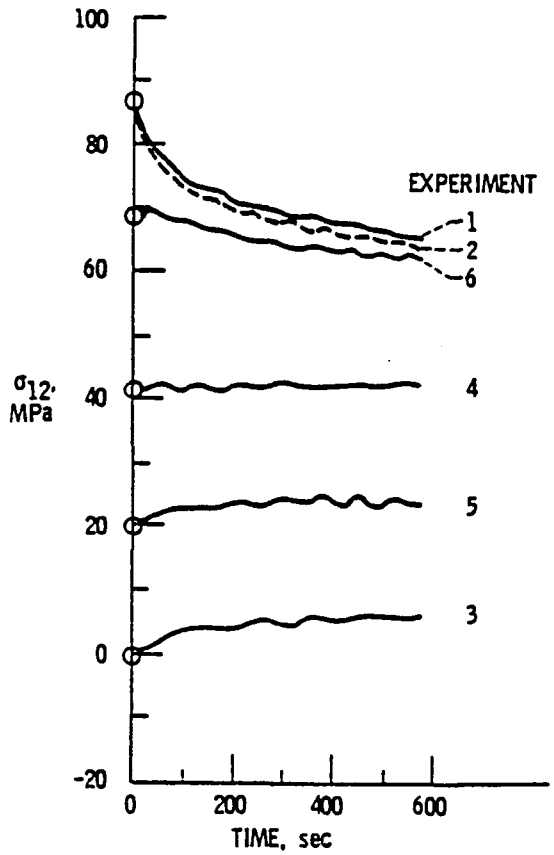

Figure 19. - Stress relaxation behavior from different starting stresses.

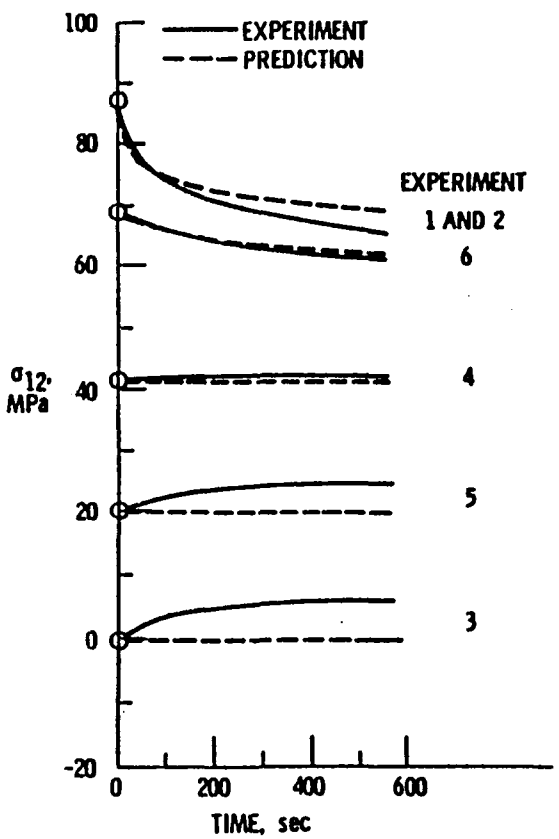

Figure 20. - Comparison of experimental and predicted stress relaxation behavior.

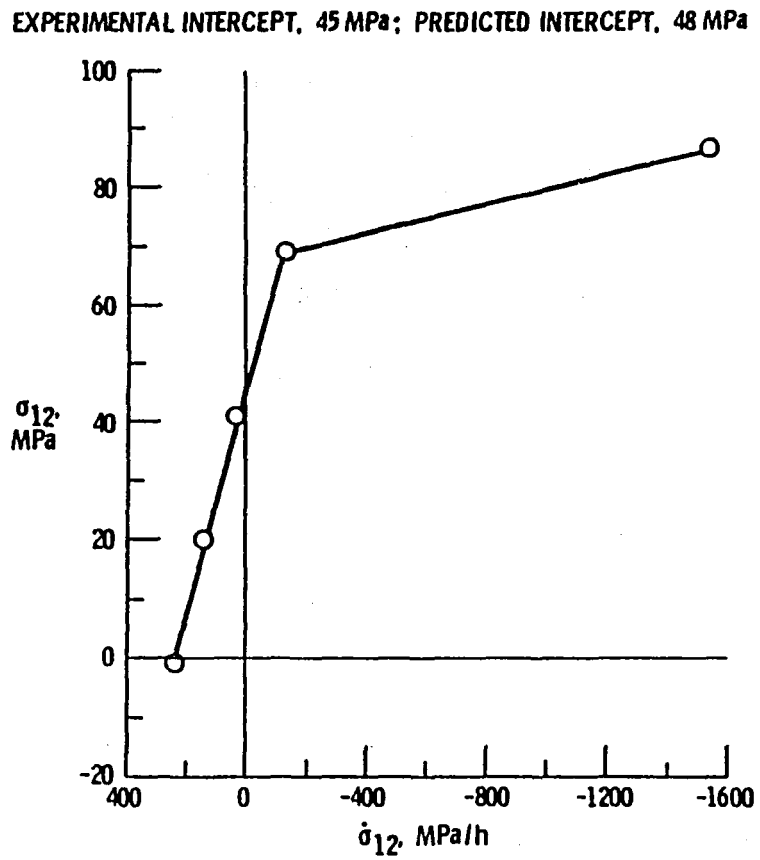

Figure 21. - Variation of initial stress relaxation rate with starting stress.

Page intentionally left blank

A COMPARISON OF SMOOTH SPECIMEN AND ANALYTICAL SIMULATION TECHNIQUES FOR NOTCHED MEMBERS AT ELEVATED TEMPERATURES

John F. Martin
Department of Metallurgy, Mechanics, and Materials Science
Michigan State University
East Lansing, Michigan 48824-1226

Experimental strain measurements have been made at the highly strained regions on notched plate specimens that were made of Hastelloy X. Tests were performed at temperatures up to 1,600°F. Variable load patterns were chosen so as to produce plastic and creep strains. Were appropriate, notch root stresses were experimentally estimated by subjecting a smooth specimen to the measured notch root strains. The results of three analysis techniques are presented and compared to the experimental data. The most accurate results were obtained from an analysis procedure that used a smooth specimen and the Neuber relation to simulate the notch root stress-strain response. When a generalized constitutive relation was used with the Neuber relation, good results were also obtained, however, these results were not as accurate as those obtained when the smooth specimen was used directly. Finally, a general finite element program, ANYSIS, was used which resulted in acceptable solutions, but, these were the least accurate predictions.

INTRODUCTION

A variety of methods are available for the analysis of structures and components that are subjected to variable loads that result in inelastic strains. These analysis techniques usually can accommodate inelastic strains produced by both time-dependent creep and time-independent plastic strain. The finite element method is perhaps the most popular technique for these problems. However, other methods exist that show potential for much more economical analyses.

Regardless of the analysis procedure employed, an accurate set of constitutive relationships are required. If the uniaxial stress-strain response of the material is not adequately described, an analysis of any notch geomtry will not be successful. Also, with all the possible variables associated with elevated temperature cyclic behavior, it is necessary to experimentally verify any analysis technique on simple notched laboratory specimens before attempting to analyze a complicated component such as a gas turbine engine.

Experimental data on smooth specimens and center notched plates have been generated. Smooth specimen data were generated at 70°, 1,200° and 1,600°F. Notched specimen data include temperatures of 70°, 1,200° and 1,550°F. All of

these data were generated for the purpose of establishing experimental evaluation criteria for constitutive models of time-dependent cyclic plasticity.

For comparison purposes, three analysis techniques were compared to some of these data. References 1-3 describe the analysis techniques and experimental procedures in detail. This paper presents a short summary of the three techniques and several examples of experimental versus analysis predictions.

MATERIAL, SPECIMENS AND EXPERIMENTAL TECHNIQUE

All tests were performed on specimens machined from Hastelloy X, a nickel-based superalloy used in components requiring oxidation resistance. Smooth specimens used for room temperature testing were machined with straight gage sections; specimens tested at elevated temperatures contained hour glass shaped gaged sections. For these high temperatures tests, diametral strain and axial stress were converted to axial strain. Elevated temperatures were produced with an induction furnace.

Notch specimen data that are presented in this paper were produced on thin plates with a notch located at the center of the plate. This notch was a circular hole with a theoretical stress concentration factor of 2.37 based on net section nominal stress. Notch root strains were determined with an interferometric technique that is described in Ref. 1 and 4. With this technique, normal strains were measured over very short gage lengths. The physical part of the gage consisted of indentations on the flat surface of the specimen. These indentations were pyramidal in shape with inclined sides tilted 45° to a normal of the surface. The indentations used for this experiment were placed 100 microns apart and were 25 microns square. They were placed 50 microns from the edge of the notch.

A He-Ne laser was used to simultaneously illuminate both indentations. Due to the coherent and monochromatic nature of this light, two interference fringe patterns resulted that were 90° relative to each other and 45° relative to the laser light. Movement of the indentations resulted in proportional movement of the fringe patterns. Averaging the movement of both fringe patterns eliminated rigid body motion. By monitoring the motion of these fringe patterns, strain could be determined. The fringe patterns were electronically sensed and the analog signal of relative light intensity was relayed to a minicomputer system. Final output of this system was an analog equivalent of strain that ranged from 0 to 10 volts.

SMOOTH SPECIMEN SIMULATION

The most direct approach to determine uniaxial constitutive behavior, is to directly control a smooth specimen so as to produce the required stress-strain combination that is dictated by a mechanics analysis of the notch geometry. The Neuber relation is the result of such an analysis that has been extensively used for room temperature fatigue life predictions. For cyclic loading this relation is written as:

$$(\Delta\sigma)(\Delta\varepsilon) = (K'_t)^2(\Delta S)(\Delta e) \qquad (1)$$

where: $\Delta\sigma$ and $\Delta\varepsilon$ are the notch root stress and strain ranges, respectively; ΔS and Δe are the remote stress and strain ranges, respectively; and K_t' is the experimentally determined elastic stress concentration factor (the $'$ indicates an experimental value as opposed to a calculated value, K_t).

Equation (1) by itself is indeterminate. Knowing the remote stress or strain range leaves three unknowns. For this study it was assumed that smooth specimens could be used to supply the needed stress-strain (constitutive behavior) at both remote and local regions. Notched specimens were subjected to controlled loading rates and peaks. Remote strains were measured with the ISG. Smooth specimens were subjected to the same strain patterns that were recorded from the ISG (the same strain rate was also maintained). The remote stress and strain versus time plots were multiplied by $(k_t)^2$ so that $(K_t)^2(\Delta S)(\Delta e)$, which is the right side of Eqn. (1) can be determined as a function of time. A smooth specimen was then controlled so that the product of stress and strain, $(\Delta\sigma)(\Delta\varepsilon)$, would follow the pattern predicted by the Neuber relation, Eqn. 1. Figures 1 and 2 show the stress-strain behavior as predicted by the Neuber relation versus the experimentally determined notch root stress-strain simulation. Notch root stresses were simulated by subjecting a smooth specimen to the same strains as measured with the ISG.

Room temperature results are shown in Fig. 1. Four load levels were used for this part of the program.

Level #	Load (KN)
1	±14.0
2	±14.5
3	±15.5
4	±16.0

All these data were generated with the material in the stable condition. As can be seen, the agreement is excellent. Similar elevated temperatue data at 1,200°F are shown in Fig. 2. Two load levels are shown.

Level #	Load (KN)
1	±10.5
2	±11.3

A 100 sec. hold time in both tension and compression was used for the elevated temperature tests. At both load levels the direct ISG-stress simulation data did not show stress relaxation from the hold periods, whereas the Neuber prediction showed a pronounced effect. The actual difference in the general trend of the stress-strain response would result in significant errors in the peak values, which are often used for damage analyses.

MODEL OF UNIAXIAL BEHAVIOR

The direct use of smooth specimens for determining constitutive behavior is not practical for most design applications. An accurate mathematical model of a materials behavior that can be used with mechanics analyses would be beneficial. In an attempt to satisfy this need, a new constitutive modeling technique was developed that is capable of predicting typical uniaxial materials behavior at room and elevated temperatures. Simulation of the time-independent phenomena of cyclic hardening or softening, cyclic relaxation of mean stress and history dependent memory, and the time-dependent behavior of creep and stress relaxation was accomplished. This constitutive model is based on a generalized analysis of any configuration of classical rheological model elements and special purpose elements that were developed specifically for this constitutive modeling technique.

The modeling technique provides for the use of classical elements such as elastic springs, viscous dampers and frictional sliders. Special elements to simulate cyclic hardening and relaxation of mean stress were also added. All these elements could be readily arranged in any manner to predict the stress-strain response of materials under complex loading. The theory supporting this technique is based on the ability to formulate matrix representations of the model parameters so as to provide a set of equations that may be solved numerically to determine the model response. For the analysis of notched members, a numerical technique was created to expand the Neuber relation with the constitutive model to include time-dependent phenomena. This technique was used to form a specific constitutive model that was constructed from the material properties of Hastelloy X.

For comparison purposes this model was used to predict the response of a uniaxial specimen that was subjected to a complicated strain history at 1,600°F. Figure 3 shows this comparison. The maximum discrepancy between the two responses is about 5 ksi or 9% of the total stress range experienced. The major differences occur during the times of stress relaxation.

This constitutive model was combined with the Neuber relation to predict the notch root strain response of a circular notched specimen tested at 1,200°F. This specimen was subjected to completely reversed constant rate, cyclic loads with hold times at both the tension and compression peaks. Comparisons of the experimental and model prediction for this test is shown in Fig. 4. The results of the comparison are relatively good. The general form of the response was very close to the measured output. The model strain values were within 18% of the experimental values at all times.

FINITE ELEMENT ANALYSIS

The previous two analysis techniques employed the Neuber relation to relate remote and local behavior. Although these analysis techniques are relatively economical, their ability to deal with complicated geometries, without any experimental data on the stress concentrations, is limited. The most popular and versatile method of stress analysis is the finite element method. This method was used in a straight forward manner to calculate the notch root strains for two notch geometries.

The finite element analysis of the experimental data that were generated in this study used a large scale general purpose program, ANSYS. This program was utilized on a Prime 750 computer system that is linked to Tektronix interactive graphics terminals.

For this study, 2-D models were created for elliptical and circular notched specimens. Because of symmetry, the models were reduced to quarter sections. These models consisted of approximately 100 elements.

ANSYS uses the initial stress method for plasticity effects. Yielding is governed by the von Mises yield criterion and multiaxial effects are based on Prandtl-Reuss flow equations. Plactic solutions are restricted to isotropic behavior. Bilinear kinematic hardening was found to best fit the available experimental data.

All materials behavior that were required for this program were obtained from uniaxial data. Only cyclic stable behavior was simulated under isothermal conditions. For the creep portion of the program, only secondary creep was accounted for even though ANSYS does allow for primary creep.

For notched members made of Hastelloy X, good correlation was obtained between the analysis and experimental data at room temperature. Figure 5 shows the notch root strains on an elliptical center notched plate as predicted by ANASYS and as measured by the ISG. This plate was subjected to a completely reversed, symmetric load pattern. This agreement is extremely good considering that the stress-strain behavior is simulated by only two straight line segments.

Figure 6 shows experimental data and predictions for a circular notch. This test was performed at 1,200°F. The load pattern was symmetric with hold times in both tension and compression. Correlation of experimental ISG results and analytical predictions are very poor compared to the room temperature results. At least a portion of this inaccuracy can be attributed to not including primary creep in the program.

CONCLUSIONS

The results presented in this paper represent only a small fraction of the experimental data that are available and of the analyses that were performed. In general, all three analysis techniques produced reasonably accurate predictions for both smooth specimen stress-strain behavior and notch root response for center notched plates made of Hastelloy X. The easiest experimental data to simulate were those generated at both temperature extremes, 70° and 1,600°F, where creep either dominated the strain response or had relatively little effect.

REFERENCES

1. Lucas, L.J. "Experimental Verification of the Neuber Relation at Room and Elevated Temperature," NASA CR-167967, NASA Lewis Research Center, June 1982.

2. Spletzer, B.L., "A Constitutive Modeling Technique Based on A Generalized Rheological Model to Predict the Responses of Materials," Ph.D. Thesis, Michigan State University, 1984.

3. Melis, M.E., "Finite Element Analysis of Notched Specimens with Experimental Verification at Room and Elevated Temperatures," M.S. Thesis, Michigan State University, 1983.

4. Sharpe, W.N., Jr., "Interferometric Surface Strain Measurement," International Journal of Nondestructive Testing, Vol. 3, 1981, pp. 59-76.

ACKNOWLEDGEMENTS

Support for this research was from the National Aeronautics and Space Administration, Lewis Research Center under Grant NAG 3-51.

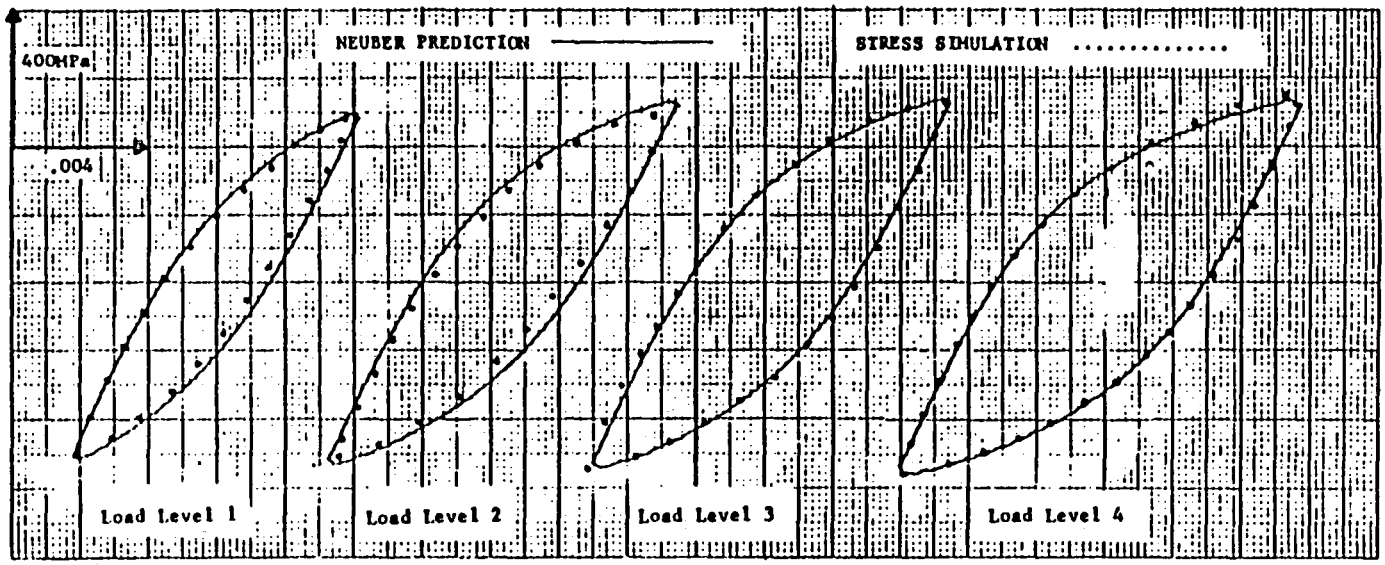

Figure 1. - Neuber prediction and stress simulation of stabilized local behavior.

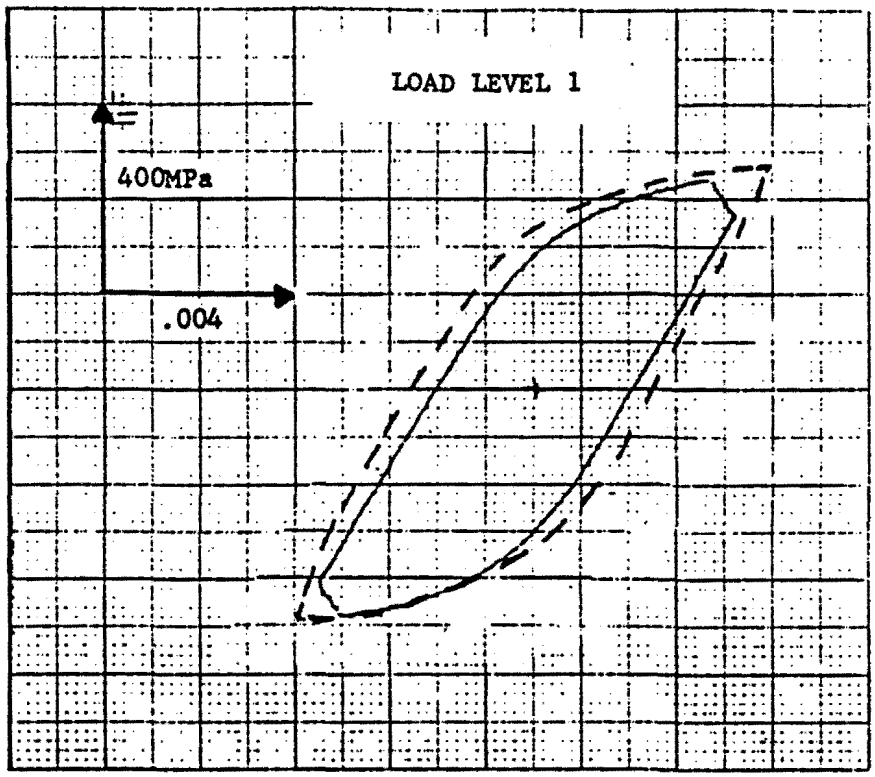

NEUBER PREDICTION ————————

STRESS SIMULATION ----------

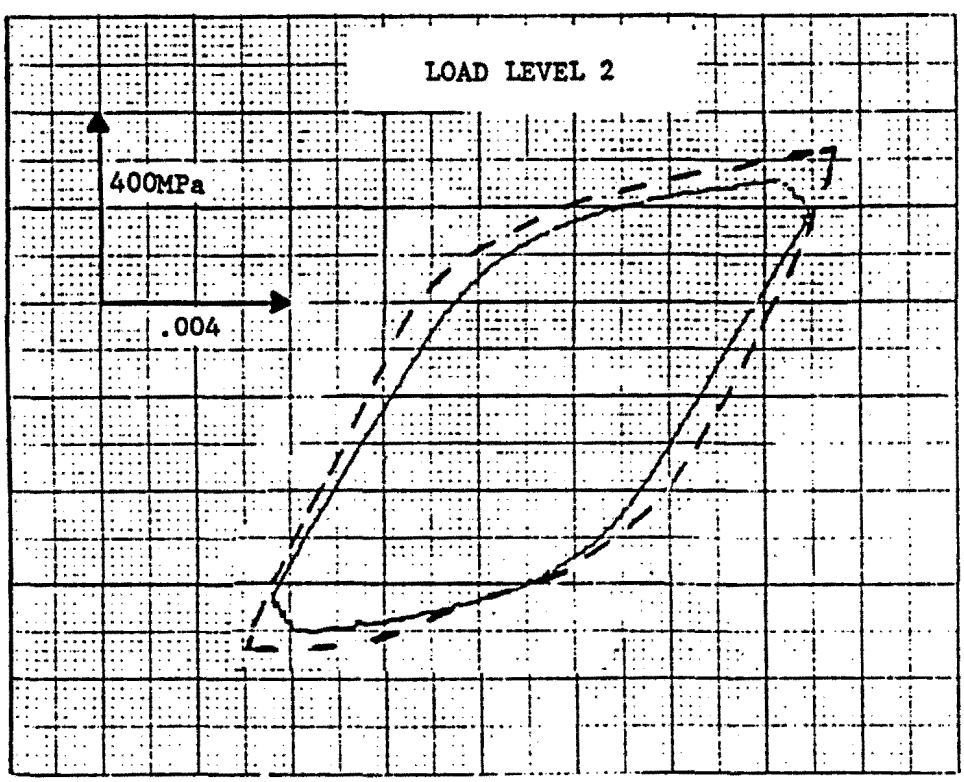

Figure 2. - Neuber prediction and stress simulation at 1200 °F.

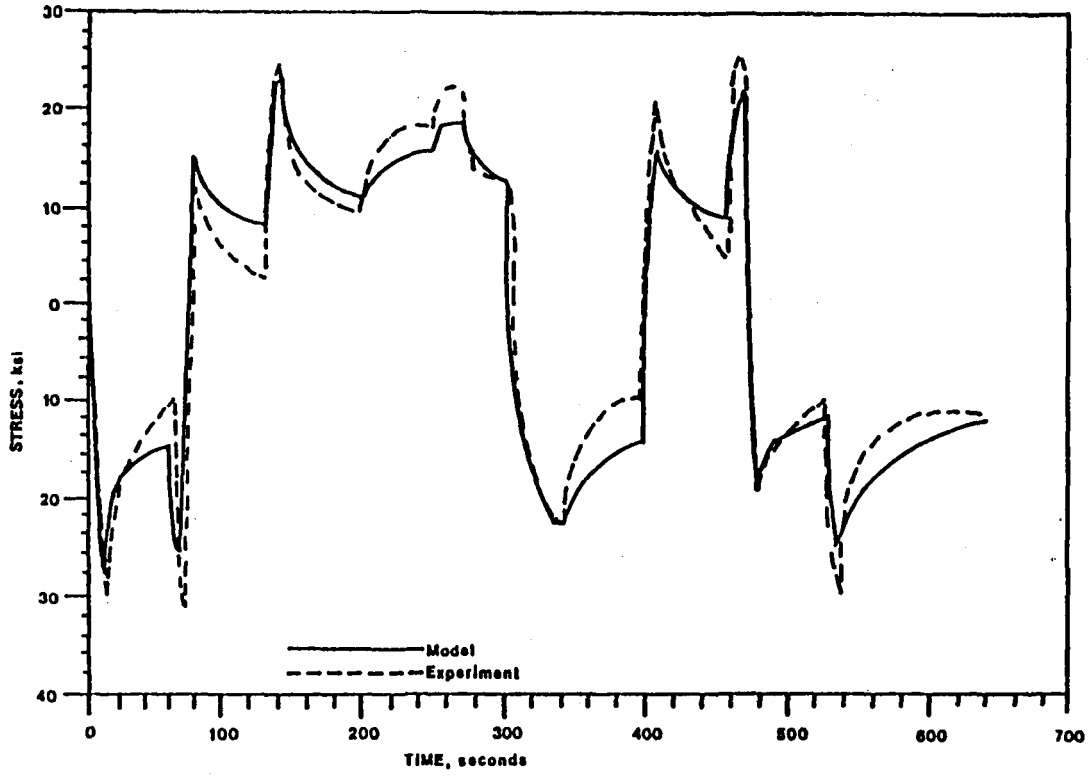

Figure 3. - Comparison of model and experimental response for 1600 °F test.

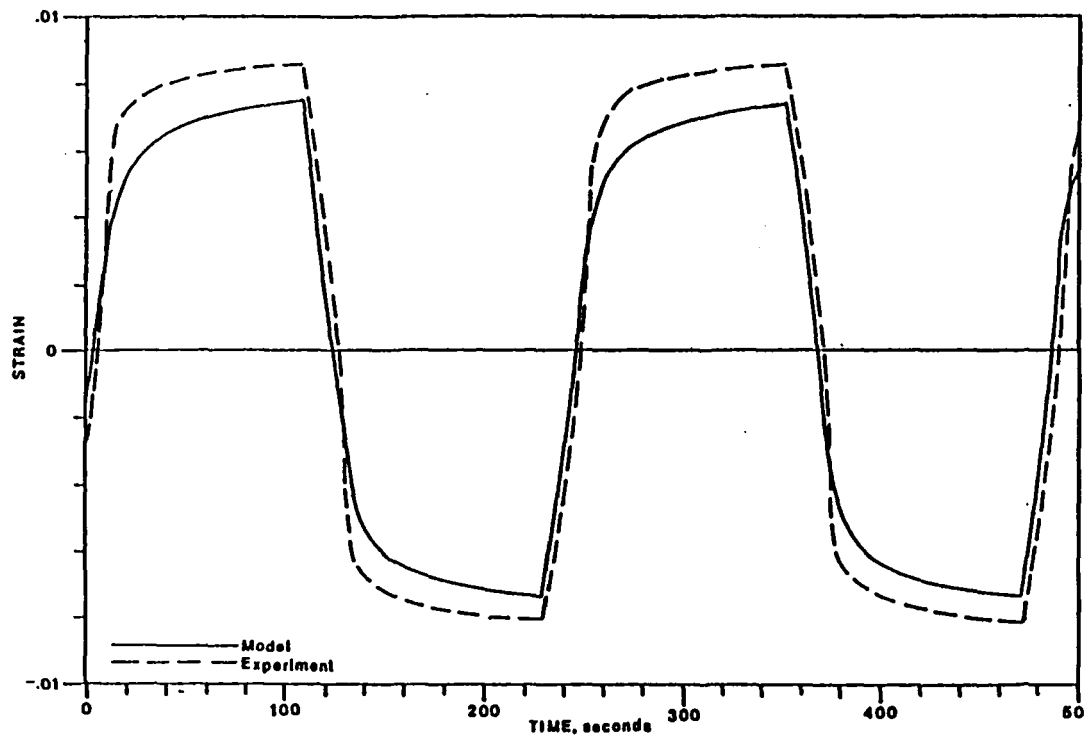

Figure 4. - Comparison of model and experimental notch root response for 1200 °F test.

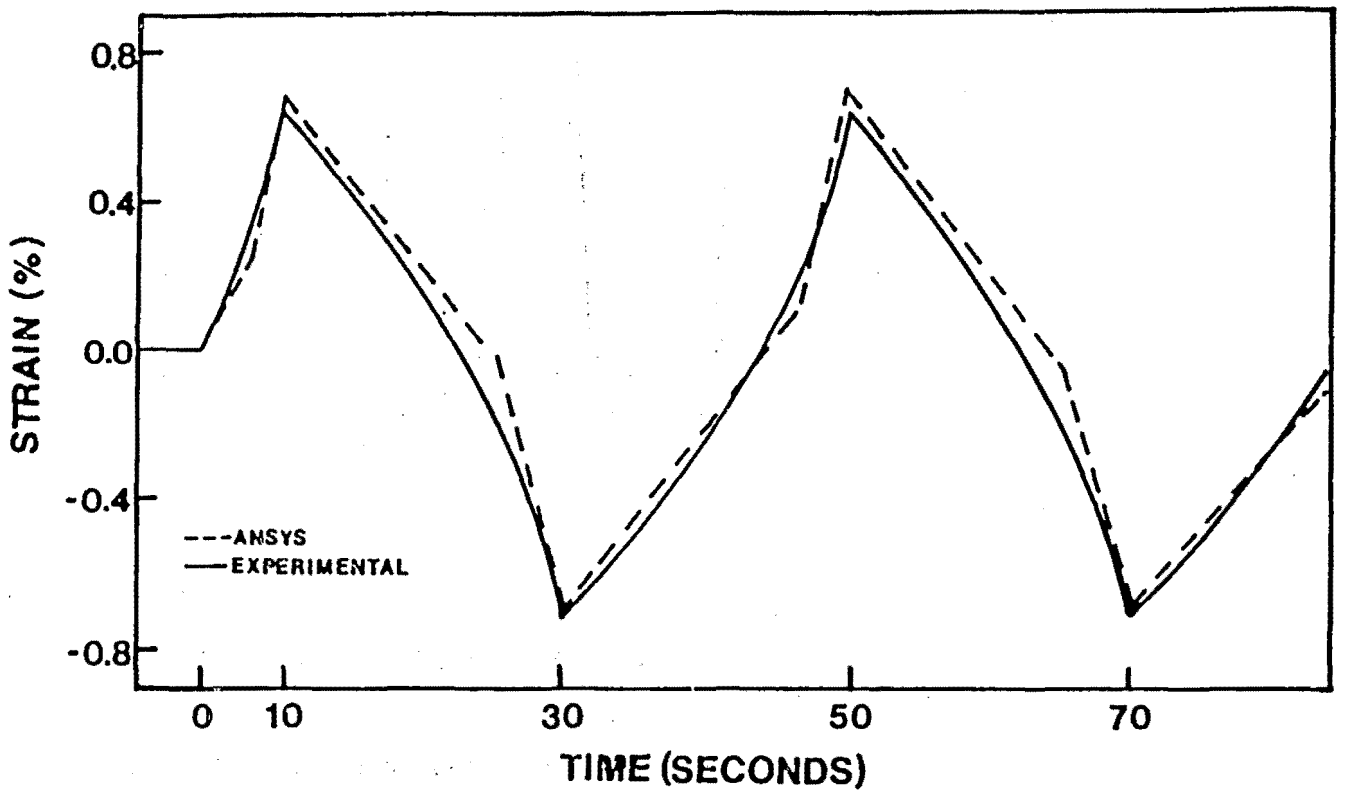

Figure 5. - Elliptical notch strain versus time at room temperature.

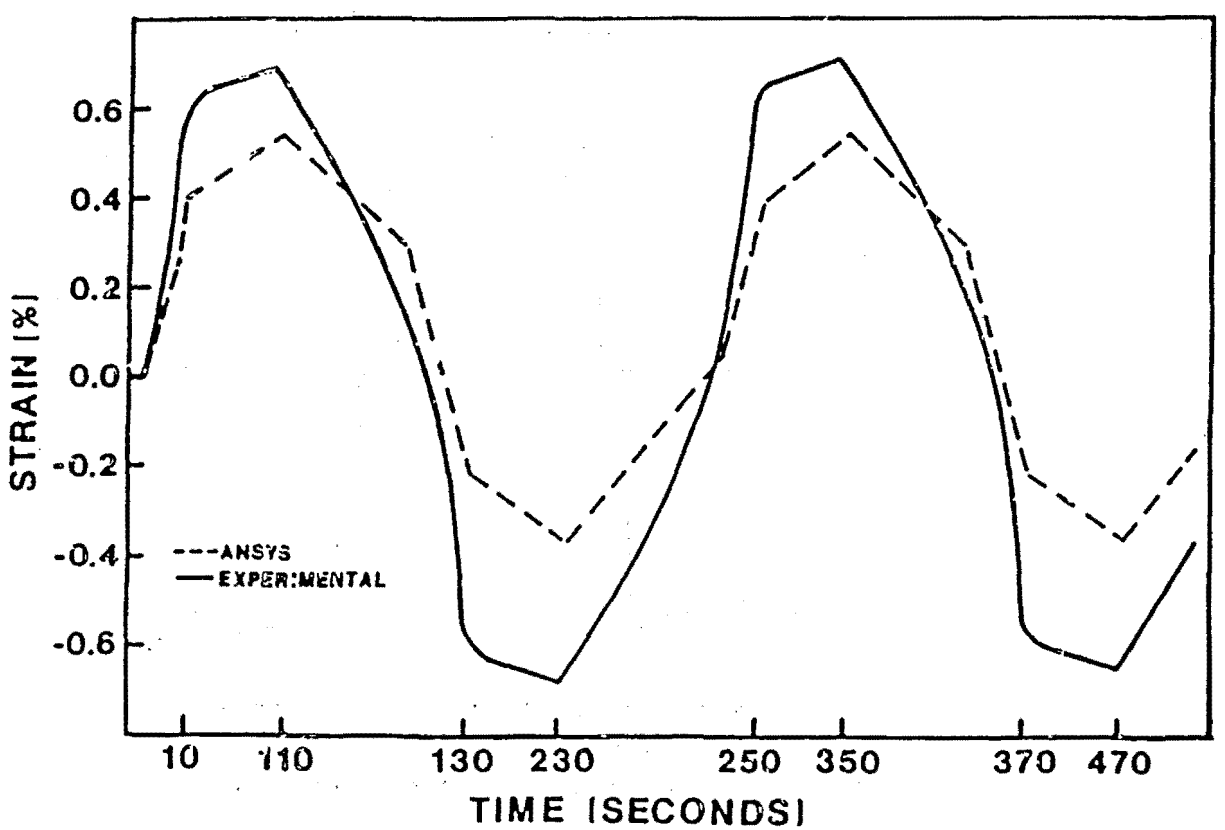

Figure 6. - Strain versus time of circular notched specimen at 1200 °F.

Page intentionally left blank

FINITE ELEMENT MODELING OF CRACKED BODIES

USING THE BODNER-PARTOM FLOW LAW

T. Nicholas and M. Bohun
Air Force Wright Aeronautical Laboratories
Wright Patterson Air Force Base, Ohio 45433

The Bodner-Partom flow law which models viscoplastic material behavior has been used to represent two nickel-base superalloys, Gatorized IN100 and Inconel 718 at elevated temperature. Procedures for the determination of the material parameters are presented along with a discussion of the physical significance of each parameter. The material model is then used in finite element computations to evaluate the response of cracked bodies to monotonic, sustained, or cyclic loading. Geometries investigated include the center cracked panel, the compact tension specimen, and the single cracked ring under tension. A Hybrid Experimental Numerical (HEN) procedure has been used to deduce crack growth rates from experimental displacement measurements which are input into finite element computations. The results of several studies conducted over the last several years are summarized.

INTRODUCTION

Sustained load crack growth data are often difficult to obtain at elevated temperatures for several reasons. Optical measurements of surface crack length produce large amounts of scatter when the oxidized surface reduces the visibility at high temperatures. Localized inelastic deformation in the vicinity of the crack tip makes the exact determination of surface crack length ambiguous and usually leads to variability in observations from one observer to another. Tunneling, where the interior of the specimen grows at a faster rate than on the surface, leads to erroneous crack length data when surface measurements are used. Very low crack growth rates, leading to small amounts of crack extension, can compound the difficulties associated with determining crack growth rates. For long-term tests, around the clock and weekend observations are required which are often impractical. As alternatives to optical measurements, automated data acquisition systems provide desirable features. Electric potential drop measurements, although requiring sophisticated equipment and calibration, can provide continuous data on crack length. Compliance measurements from periodic unloading and reloading can provide discrete crack length values in the absence of an observer. The simplest measurement, however, is a continuous displacement measurement across two suitably chosen points under constant load. If these displacement values can be related to crack extension, crack length data can be obtained easily and continuously.

A procedure has been developed for determining crack length from displacement measurements during sustained load crack growth tests. This procedure, labeled the Hybrid Experimental Numerical (HEN) method, utilizes experimental displacement data in finite element method computations where a realistic constitutive model describing the material behavior is incorporated. The model describes time-dependent viscoplastic flow in an incremental strain rate equation with a single state variable which includes the materials history of loading. The constants for the model are obtained from constant strain rate tests and creep data. The model has been incorporated into a constant strain triangle finite element program which is used in the HEN procedure. This procedure has been applied to several cracked specimen geometries using different displacement measurement techniques and locations. In addition, the finite element program has been used to evaluate the stress and strain states in cracked bodies under cyclic loading. This paper presents a review of these applications of the finite element method to cracked geometries.

BODNER-PARTOM FLOW LAW

The constitutive equations used to describe the elevated temperature viscoplastic material behavior in this investigation are those of Bodner and Partom.(ref. 1) The equations represent time-dependent viscoplastic flow over a wide range of strain rates using a state variable and are of the incremental type which does not require a yield surface. Total strain rate is decomposed into nonzero elastic and inelastic portions. The elastic portion is given by the time derivative of Hookes law while the inelastic portion takes the form

$$\dot{\epsilon}_{ij}^{p} = D_o \exp\left[\frac{-(n+1)}{2n}\left(\frac{Z^2}{3J_2}\right)^n\right] J_2^{-\frac{1}{2}} s_{ij} \qquad (1)$$

where D_o and n are material constants, J_2 and s_{ij} represent the second invariant and the components of the deviatoric stress tensor, respectively, and Z is a history dependent state variable representing the materials resistance to plastic flow. The evolution equation for Z is given in rate form

$$\dot{Z} = m(Z_1 - Z)W_p - AZ_1\left(\frac{Z-Z_2}{Z_1}\right)^r \qquad (2)$$

where m, Z_1, Z_2, A, and r are material constants and W_p is plastic work. In total, there are 7 constants to be determined from experimental data. A procedure has been developed by Stouffer (ref. 2) to determine the constants from constant strain rate stress-strain data and creep curves. This procedure was applied to Gatorized IN100 at 732°C. The constants used in the computations described here were obtained from that investigation. Further refinements to the procedure and a parametric study of the effects of each constant on material behavior were presented by Beaman (ref. 3) who obtained the constants for Inconel 718 at 649°C.

Determination of Constants

The constant D_o represents the limiting plastic strain rate or the rate at which applied stresses tend to infinity to sustain that strain rate. It can be chosen as 10^6/second for most metals and has been used as 10^4 in previous investigations. Unless high strain rate behavior is being evaluated, any value above the range of strain rates being computed is adequate. We recommend fixing the value at 10^6. The next pair of constants to be evaluated are n and Z_1. The strain rate sensitivity at conventional testing rates is determined by n. The value of Z_1 represents the maximum value or saturation value of Z. For the Bodner-Partom model, stress-strain curves at conventional constant strain rates asymptote towards a constant value of stress. At this stress, the material is fully saturated, ie $Z=Z_1$. At conventional strain rates, furthermore, the second term in eq. (2) can be neglected. The procedure for determining n and Z_1 is to obtain values of saturation stress for several (at least two) constant strain rate tests over several decades in strain rate. The uniaxial version of the flow law is written as

$$\dot{\varepsilon}^p = \frac{2}{\sqrt{3}} D_o \frac{\sigma}{|\sigma|} \exp\left[-\tfrac{1}{2}\left(\frac{Z}{\sigma}\right)^{2n}\left(\frac{n+1}{n}\right)\right] \tag{3}$$

Setting $Z=Z_1$ in eq. (3) and rearranging term leads to

$$\ln\left[-\ln\frac{\sqrt{3}}{2D_o}\dot{\varepsilon}^p\right] = -2n\ln\sigma + \left[2n\ln Z_1 + \ln\left(\frac{n+1}{2n}\right)\right] \tag{4}$$

The first term, which involves $\dot{\varepsilon}^p$, is linearly related to $\ln\sigma$. Plotting the experimental data and fitting the best straight line will provide a value -2n for the slope. From n, a value of Z_1 can be determined from eq. (3) from any pair of values of $\dot{\varepsilon}^p$ and σ along the straight line. Considering again the high strain rate regime where the recovery term in eq. (2) can be neglected, eq. (2) can be written in differential form and integrated to yield

$$\ln(Z_1 - Z) = \ln(Z_1 - Z_o) - mW_p \tag{5}$$

where Z_o is the initial hardness when no plastic work has been expended. From a stress-strain curve at a constant (high) rate, values of Z can be computed for corresponding values of W_p allows the determination of Z_o as the extrapolated value for $W_p = 0$ which are obtained by integrating the area under the stress-plastic strain curve. Plotting $\ln(Z_1-Z)$ against plastic work W_p allows the determination of Z_o as the extrapolated value for $W_p = 0$ from a best linear fit to the data. The slope of this line will define the value for m which controls the shape of the stress-strain curve.

If material behavior at very low strain rates, in the creep regime, is to be modeled, the second term in eq. (2) has to be used. Determination of the constants A, r, and Z_2 requires creep or very low rate stress-strain data. Note that the saturation

stress in a stress-strain test at very low constant strain rate is equivalent to an applied stress in a creep test causing a steady second stage creep rate. The constants can be determined by matching the experimental data on a plot of ln strain rate against stress as shown in Fig. 1a. For steady state values, ie constant strain rate under constant stress or vice versa, Z must achieve a steady state value from eq. (3) and, thus, $\dot{Z}$ must be zero in eq. (2). These two equations, when combined, provide a functional relation between the non-dimensional quantities $\dot{\varepsilon}^p/D_o$ and σ/Z_1. Figure 1a shows the overall behavior of the curve and the regions affected by the several constants. Figures 1b, c, and d show the effects of varying each of the constants, A r, and Z_2 individually. These curves also show the insensitivity to these constants at the higher strain rates. An interactive computer program with graphical display of the equations has been found useful in determining the constants A, r, and Z_2 by trial and error manipulation. Basically, each constant controls one aspect of the curve, ie either slope or location of an inflection point. Following the procedure outlined above in the correct order makes it relatively easy to arrive at the Bodner-Partom constants from uniaxial data.

THE HEN PROCEDURE

The hybrid experimental numerical procedure (HEN) was developed by Hinnerichs (ref. 4) to determine creep crack growth rates from expermental displacement measurements. The procedure uses a finite element computer program called VISCO (ref. 4) and utilizes the Bodner-Partom equations to describe the inelastic material behavior. These equations are incorporated into the VISCO computer code which uses constant strain triangular elements. The code computations utilize experimental displacement data as input in the HEN procedure. Essentially, the HEN procedure compares experimental displacements at a fixed point on a specimen to finite element model displacements at the same fixed experimental point. If the finite element displacement values (including creep and plasticity) are below the experimental ones, the crack is allowed to extend by popping a node. In this manner, increments of crack extension occur by node popping in the finite element scheme. Figure 1 shows a schematic of a center cracked specimen which was utilized by Hinnerichs et al (ref. 5) in the first application of the HEN procedure to determine creep crack growth rates in IN100. The experimental displacements were determined by Sharpe (ref. 6) using a laser interferometric technique which has a measurement precision of approximately 0.01 micron. The center cracked panel specimen was 25 mm wide by 7.6 mm thick. Displacements were obtained across two closely spaced microhardness indents on either side of the initial crack at distances of approximately 0.1 mm behind the crack tip as shown schematically in figure 2.

The computational scheme provides displacements at the measurement location from creep strains in the cracked specimen under sustained load. Figure 3a shows the computed displacements (NO CRACK GROWTH) compared to the experimental values. It is seen that the computed values are much less than those measured. The reason

is that the crack is extending in the experiment which increases the compliance of the specimen. To match the experimental displacement measurements, the HEN procedure provides for node popping to simulate crack growth. Nodes are popped whenever additional displacements are required to match the experimental values. In figure 3a, the points labeled RUN S2 show the displacements matched to the experimental data through the appropriate node popping. The node popping simulates the crack growth as seen in figure 3b. From the slope of the crack extension versus time plots for each of the experiments, a series of crack growth rates were obtained. These values are plotted against stress intensity factor in figure 4 and show very good correlation with creep crack growth data obtained by Donath et al (ref. 7) at higher K values. Additionally, the total amounts of crack extension computed for each numerically simulated experiment agreed very closely with those measured on the fracture surface of the specimen. In most of these cases, very small amounts of crack growth were obtained (see fig. 3b, for example).

Computational Procedure

The finite element analysis uses the residual force method to incorporate nonlinear viscoplastic material behavior into VISCO. This method increments time directly, but load, strain and stress are incremented indirectly through a time integration procedure. To implement the residual force method, the plastic strain rate of the material is determined from the Bodner-Partom constitutive eqns. (1) and (2) described in the previous section. Using the current time increment dt^i and the plastic strain rate, $\dot{\varepsilon}_{ij}^{p}$, the incremental plastic strain vector is

$$\left\{d\varepsilon_{ij}^{p}\right\}^{i} = \left\{\dot{\varepsilon}_{ij}^{p}\right\} dt^{i} \tag{6}$$

where the superscript "i" represents the current time increment. The total plastic strain is then computed from the incremental plastic strain from eqn. (6) as

$$\left\{\varepsilon_{ij}^{p}\right\}^{i} = \left\{\varepsilon_{ij}^{p}\right\}^{i-1} + \left\{d\varepsilon_{ij}^{p}\right\}^{i} \tag{7}$$

where $\left\{\varepsilon_{ij}^{p}\right\}^{i}$ is the total plastic strain at the current time increment. Next, the plastic load vector $\{Q\}$, representing the nodal forces generated by viscoplasticity is formulated as

$$\{Q\}^{i-1} = \int_{Vol} [B]^{T} [D] \left\{\varepsilon_{ij}^{p}\right\}^{i} dVol \tag{8}$$

where $[B]^T$ is the transposed strain-displacement matrix and [D] is the stress-strain matrix. The plastic load vector is then added to the current nodal loads $\{P\}^i$ to determine the current nodal displacements, computed by

$$\{U\}^{i} = [K]^{-1} \left(\{P\}^{i} + \{Q\}^{i-1}\right) \tag{9}$$

where $[K]^{-1}$, is the inverse elastic stiffness matrix and $\{U\}^i$ is the nodal displacement vector. The total strain vector is then computed by

$$\{\epsilon_{ij}\}^i = [B]\{U\}^i \tag{10}$$

Finally, the stress is updated using eqns. (7) and (10),

$$\{\sigma_{ij}\}^i = [D]\left(\{\epsilon_{ij}\}^i - \{\epsilon_{ij}^p\}^i\right) \tag{11}$$

where $\{\sigma_{ij}\}^i$ is the current updated stress. This becomes the new stress value to be entered into the constitutive model to generate a new viscoplastic strain rate. This procedure continues for each time increment until the desired simulation time for the problem is reached.

Application to CT Geometry

The Hen procedure was subsequently applied to the compact tension (CT) specimen geometry (ref. 8) using experimental displacement data of Donath et al (ref. 7). Displacements were obtained off E-shaped plates fixed to the top and bottom of the specimen along the load line using LVDT's. These specimens were 5.4 mm thick and were tested using initial K values ranging from 33.0 to 49.5 $MPa \cdot m^{\frac{1}{2}}$. Figure 5a shows the finite element mesh used in these computations. Figure 5b shows displacement data for one of the specimens for the early part of the test. The crack extensions computed from these data using the HEN procedure are shown in figure 5c. The data for the entire test which involved a considerable amount of crack extension are presented in figure 5d. It can be seen that the computed values follow those labeled "effective length" fairly well. The effective lengths were obtained from unloading compliance measurements taken periodically during the sustained load test. There was fairly severe tunneling in all of the tests after the crack had extended several millimeters. The final crack lengths, as determined from the numerical computations using the HEN procedure, agreed with these from the fracture surface better than those determined from compliance measurements!

Application to a Ring Geometry

The third type of specimen was a 6 mm thick circular ring having an outside diameter of 76 mm and an inner diameter of 38 mm. The ring is loaded in tension using a pin and clevise arrangement and is cracked from the inner diameter at a location 90° from the two loading pins as shown in figure 6 which also shows the finite element mesh details. The stress intensity solution for this geometry shows a region of nearly constant K over half the thickness of the ring. Displacements were obtained across the two loading pins using LVDT's. Since load is constant and the tests are under isothermal conditions, the differential displacements are not affected by deflection of the load train or pins after the

initial load is applied. The numerical solution in the HEN procedure is, however, very sensitive to the manner in which the load is applied to the finite element grid.

The displacement measurements along with experimental data on crack length from compliance measurements were obtained by Donath et al (ref. 7). There was considerable scatter in the experimentally determined crack lengths and difficulty in correlating total crack extension with that measured on the fracture surfaces. The displacement data, on the other hand, appeared to be smoother and more consistent. For this reason, the HEN procedure was applied to obtain a somewhat independent determination of crack extension in the same specimens. Results of a typical case are presented in figure 7. Crack extension versus time from the HEN procedure are compared to the experimental data. The final crack lengths from the HEN procedure agreed closely with those obtained experimentally. In figure 8, the stress in the "y" direction is plotted versus horizontal distance ahead of the crack tip after various crack extensions. These stresses are determined at the centroid of each triangular element ahead of the crack tip which has the same dimensions, therefore, element size effects are eliminated. Notice that the peak stress at a crack length of 8.26 mm (.325 in) is 955 MPa (138.5 KSI) but drops to 782 MPa (113.4 KSI) after 3.18 mm (.125 in) of crack growth. This peak stress reduces slightly with each subsequent crack advance. As the crack advances, the stress distribution becomes sharper indicating that as the crack propagates to the edge of the ring, stresses ahead of the crack are greatly reduced as the other side of the ring carries the major load.

CRACKED BODIES UNDER CYCLIC LOADING

The Bodner-Partom constitutive equations have been used in finite element computations to determine the stress and strain fields in a compact tension specimen in the vicinity of the crack tip when the specimen is subjected to cyclic loading. The VISCO computer code was used in these investigations. In the application of the Bodner-Partom equations, no modifications were made to account for kinematic versus isotropic hardening behavior of the material. The material was assumed to undergo isotropic hardening during cyclic loading. The first problem investigated was that of a CT specimen under cyclic loading at various frequencies at a stress ratio (ratio of minimum to maximum applied load) of 0.1. The uniaxial response of the constitutive model to an applied cyclic load of load ratio 0.1 was also computed for comparison. Figure 9a shows the uniaxial response to a maximum stress of 1241 MPa at a frequency of 0.167 Hz. Figure 9b shows the effective stress versus strain in an element directly ahead of the crack tip. It was observed in both the uniaxial model and the CT specimen at the crack tip that strain continued to accumulate under cyclic loading. In the CT specimen, the element ahead of the crack tip appears to cycle under more or less fixed stress limits. The finite element computations were able to provide additional details of the stress and strain fields around the crack tip. Figure 10

shows the stress profile ahead of the crack tip after 2½ cycles and then after a 15 min hold at maximum load. It can be seen that there is a slight change in the stress field during the hold time. Experimentally, sustained load crack growth occurs at this K value of 38.5 $MPa \cdot m^{\frac{1}{2}}$. To simulate this crack extension, a node was released. The results, shown in figure 10, indicate that the stress field with respect to the position of the crack tip has not changed. This is in contrast to the results in the ring tests where there was a change with crack extension (see fig. 8).

A similar study was carried out to evaluate the stress and strain field under fully reversed cyclic loading in a CT geometry (ref. 10). Figure 11 shows the displacement profile behind the crack tip at various load levels. It can be seen that residual displacements due to inelastic deformation have occured. At zero load, there is crack opening a small distance behind the crack tip. In these numerical exercises, no account was taken of any plastic wake which formed behind the crack due to prior cycling.

CONCLUSIONS

The Bodner-Partom flow law is a realistic representation of material behavior in nickel base superalloys at elevated temperatures. The use of this model in finite element computations of stress fields in cracked bodies provides valuable insight into elevated temperature creep and fatigue phenomenology. These tools are also very valuable in predicting sustained load crack growth rates from experimental displacement data using a hybrid-experimental-numerical procedure.

REFERENCES

1. Bodner, S.R. and Partom, Y., "Constitutive Equations for Elastic-Viscoplastic Strain Hardening Materials", Journal of Applied Mechanics, Transactions ASME, Vol. 42, 1975, pp. 385-389.

2. Stouffer, D.C., "A Constitutive Representation for IN100," AFWAL-TR-81-4039, 1981

3. Beaman, R.L., "The Determination of the Bodner Material Coefficients for IN718 and Their Effects on Cyclic Loading," M.S. Dissertation, Air Force Institute of Technology, Mar. 1984

4. Hinnerichs, T.D., "Viscoplastic and Creep Crack Growth Analysis by the Finite Element Method," AFWAL-TR-80-4140, 1981

5. Hinnerichs, T., Nicholas, T. and Palazotto, A.N., "A Hybrid Experimental Numerical Procedure for Determining Creep Crack Growth Rates, "Eng. Fract. Mech., Vol. 16, No. 2, 1982, pp. 265-277.

6. Sharpe, W.N. Jr., "A Technique for High Temperature Creep Displacement Measurement", Fracture Mechanics:Fourteenth Symposium - Volume II: Testing and Applications, ASTM STP 791, J.C. Lewis and G. Sines, Eds., American Society for Testing and Materials, 1983, pp. II-157-II-165.

7. Donath, R.C., Nicholas, T. and Fu, L.S., "An Experimental Investigation of Creep Crack Growth in IN100", Fracture Mechanics:Thirteenth Symposium, ASTM STP 743, Richard Roberts, Ed., American Society for Testing and Materials, 1981, pp. 186-206.

8. Smail, J. and Palazotto, A.N., "The Viscoplastic Crack Growth Behavior of a Compact Tension Specimen Using the Bodner-Partom Flow Law," Eng. Fract. Mech., Vol. 19, No. 1, 1984, pp. 137-158.

9. Keck, J.E., Nicholas, T. and Palazotto, A.N., "High Temperature Viscoplastic Fatigue Behavior of a Compact Tension Specimen," Eng. Fract. Mech. (in press).

10. Wilson, R.E., "The High Temperature Viscoplastic Fatigue Behavior of IN100 Using the Bodner-Partom Flow Law," M.S. Dissertation, Air Force Institute of Technlogy, Sept. 1983

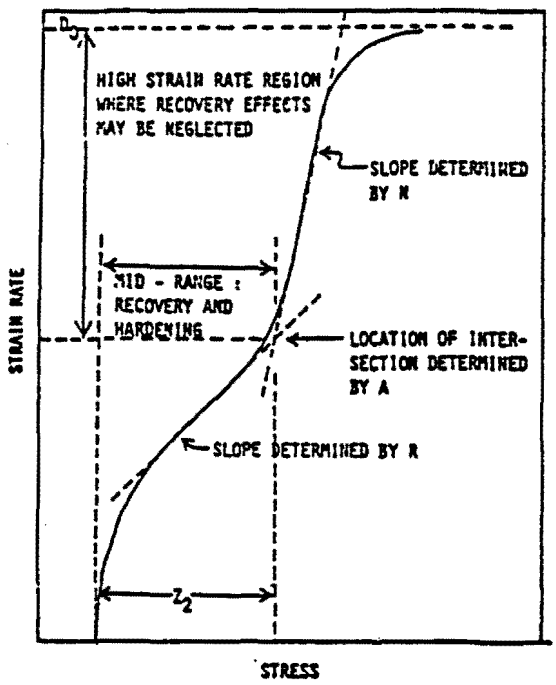

a) Overall behavior

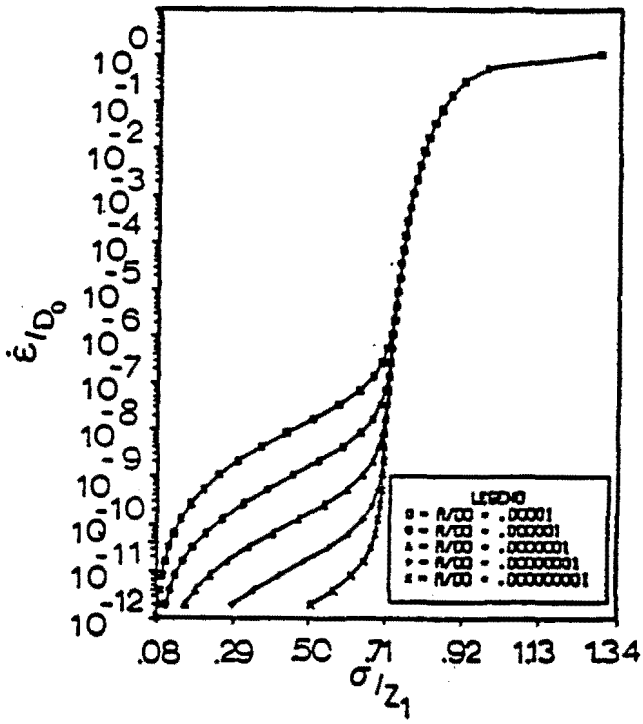

b) Variation with A.

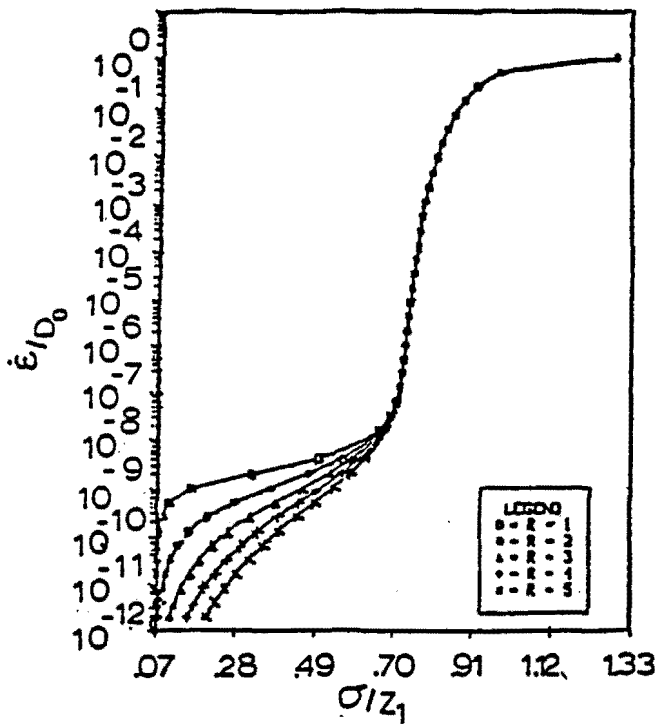

c) Variation with r.

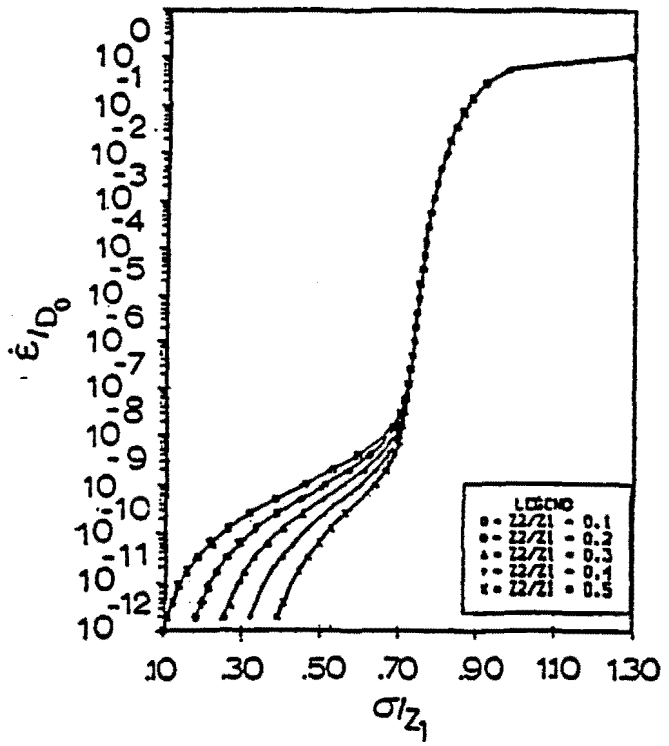

d) Variation with Z_2.

Fig. 1 Stress-strain rate response of Bodner-Partom model. (Ref. 3)

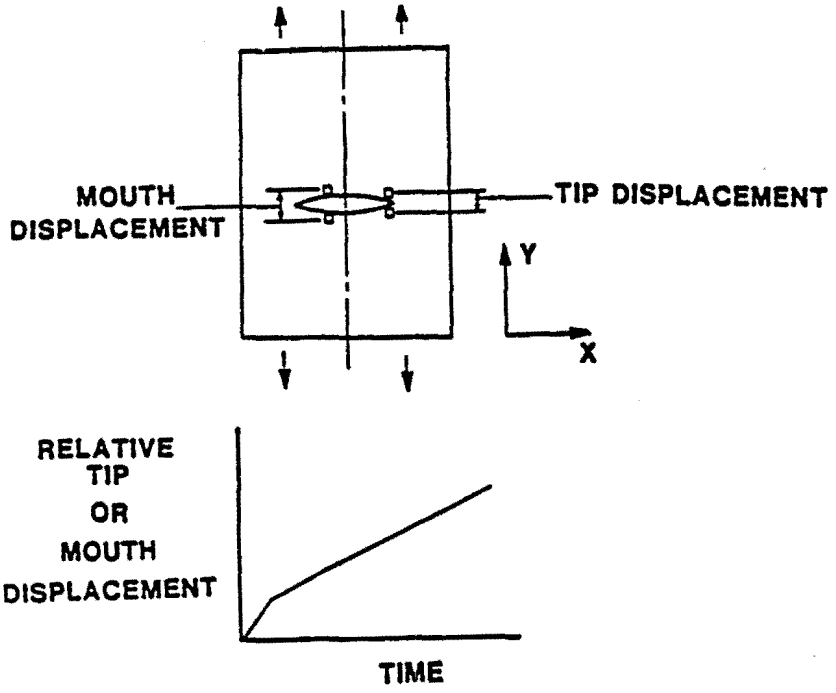

Fig. 2 Schematic of center cracked geometry showing indent locations and data.

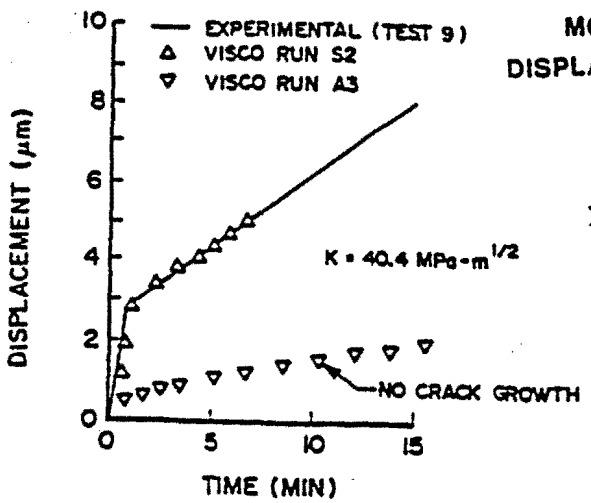

a) Displacements

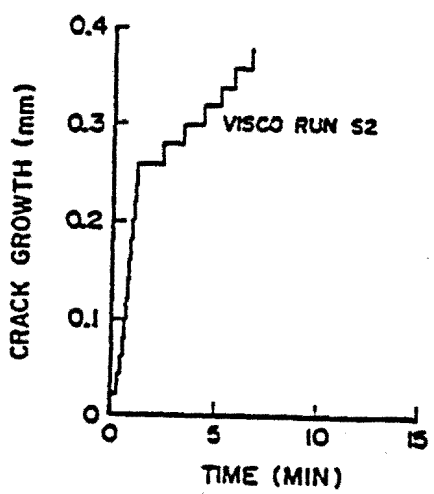

b) Crack extension

Fig. 3 Typical results from HEN procedure. (Ref. 5)

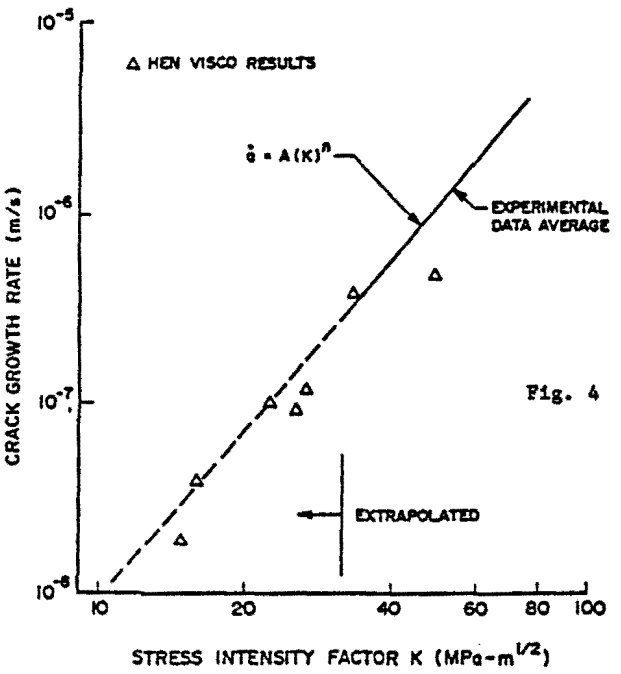

Fig. 4

Fig. 4 Sustained load crack growth rates from HEN calculations.

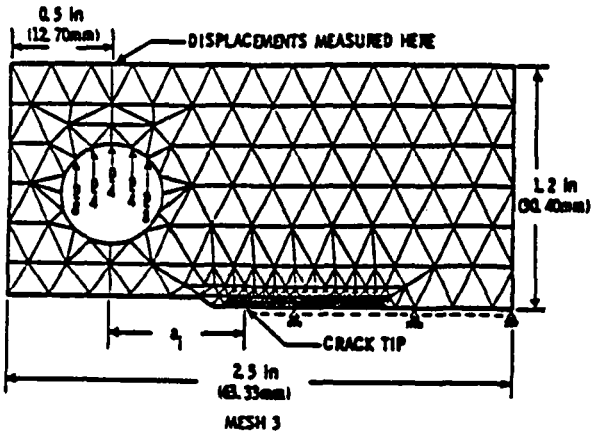

a) Finite element mesh

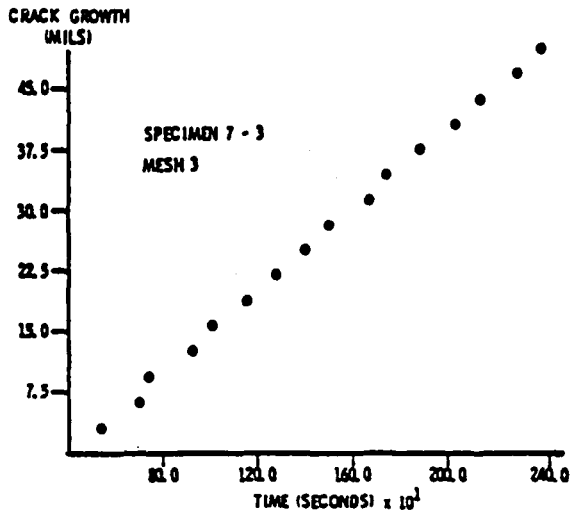

c) Computed crack extension

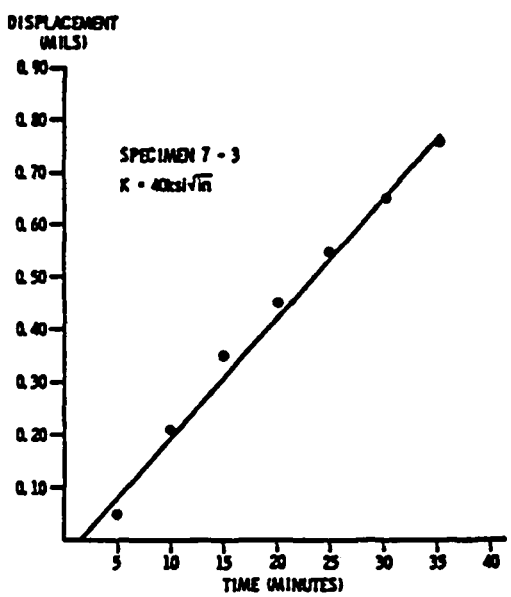

b) Computed displacements

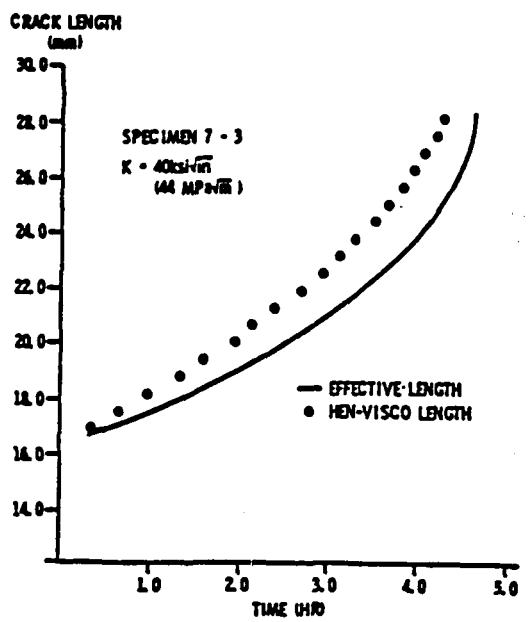

d) Comparison with experiment

Fig. 5 Typical results from application of HEN to CT geometry.(Ref. 8)

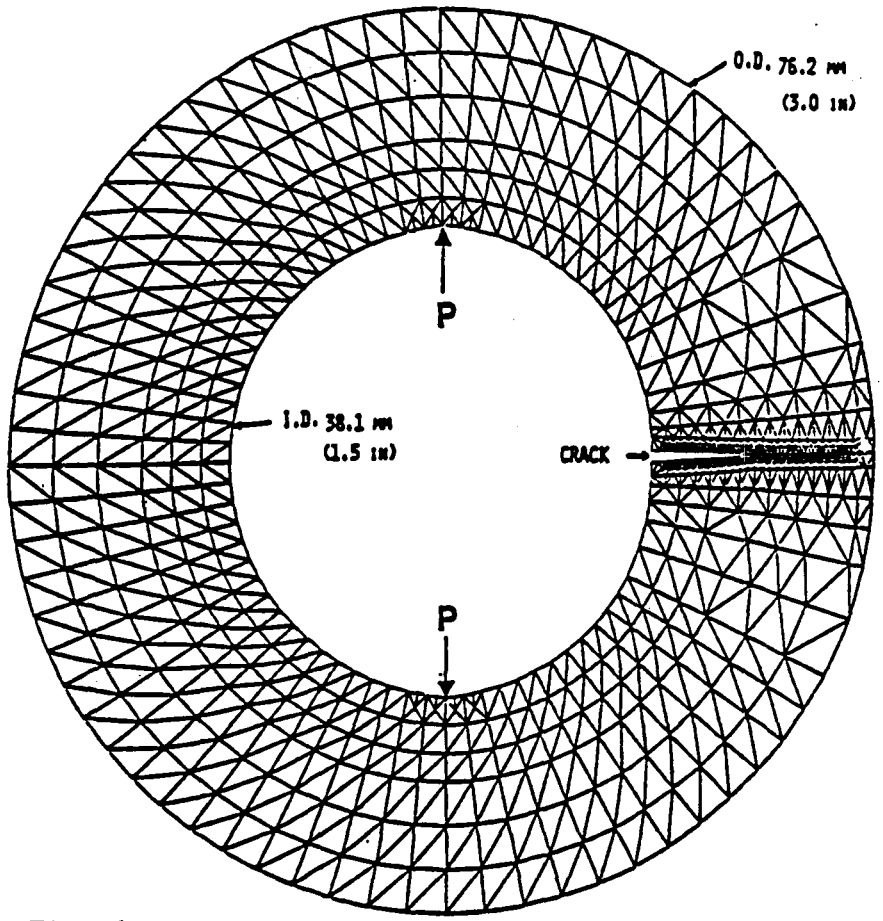

Fig. 6 Geometry and finite element mesh for cracked ring geometry.

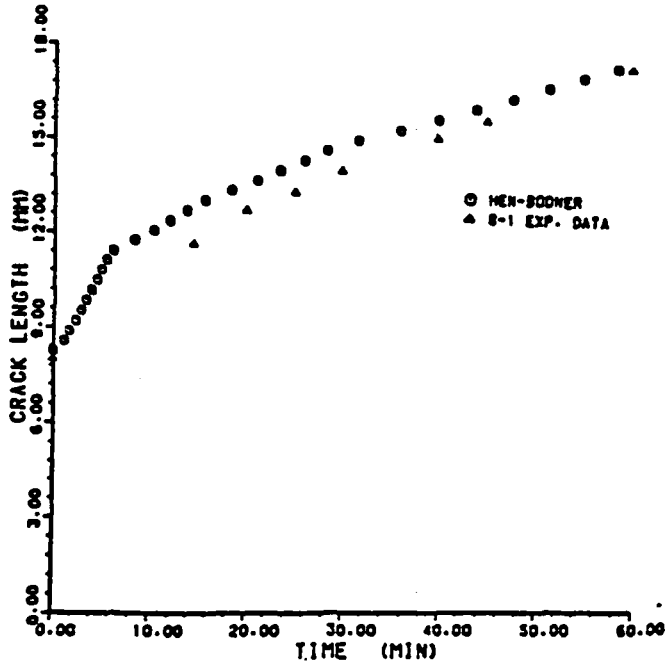

Fig. 7 Comparison of HEN crack length with experimental data for ring.

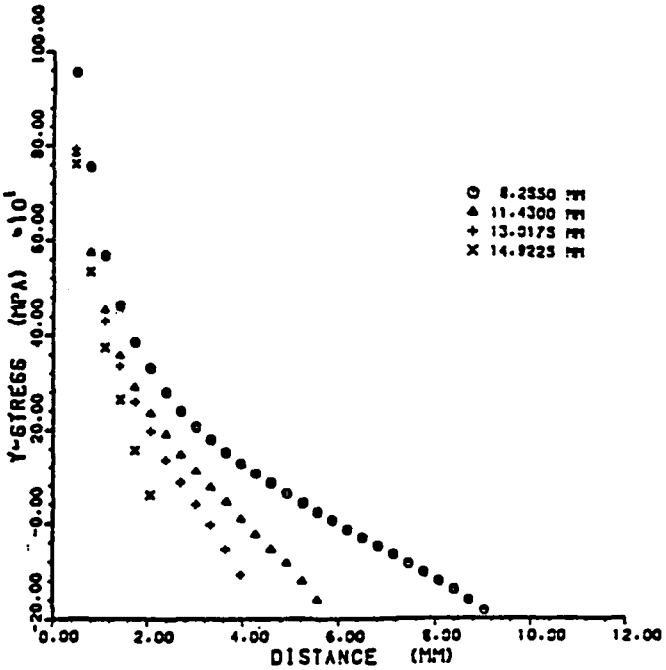

Fig. 8 Stress profile ahead of crack tip in ring.

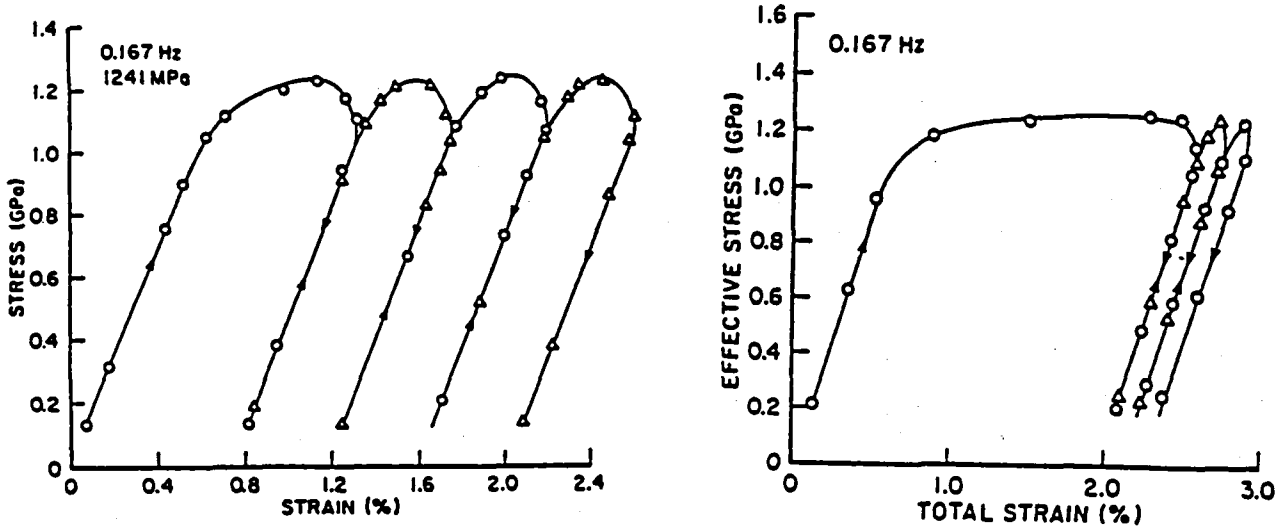

a) Uniaxial specimen

b) Ahead of crack tip in CT specimen

Fig. 9 Cyclic stress-strain response under load control at R=0.1. (Ref. 9)

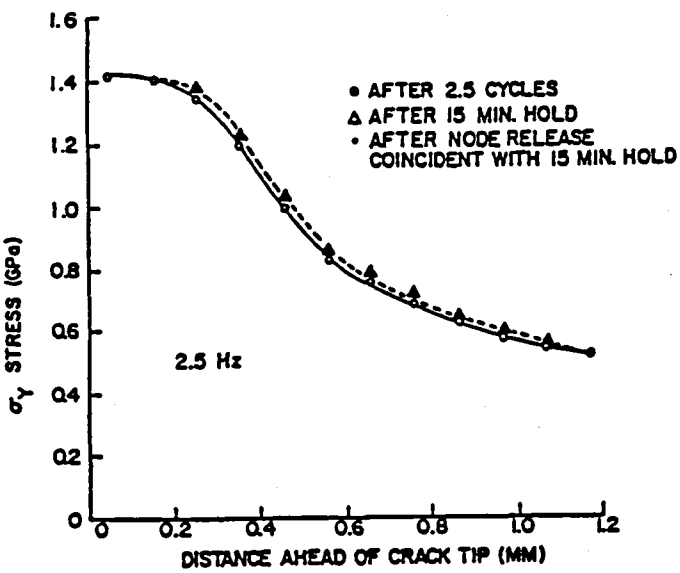

Fig. 10 Stress profiles ahead of crack tip in CT specimen, R=0.1 (Ref. 9)

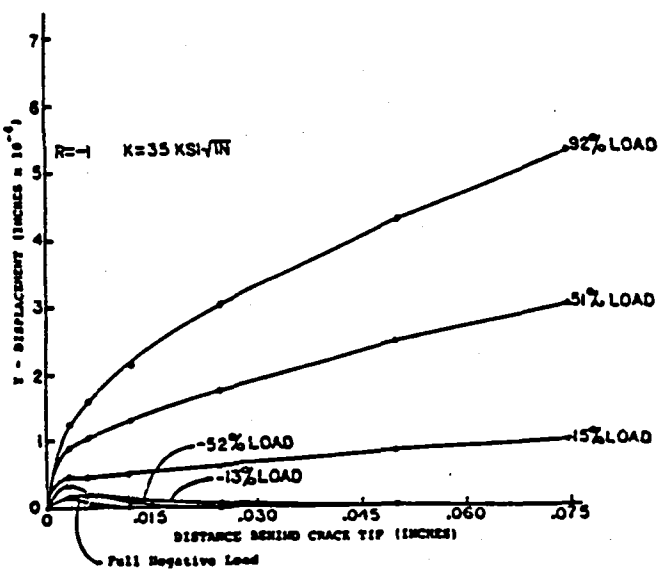

Fig. 11 Displacement profiles behind crack tip in CT specimen, R=-1 (Ref. 10)

FINITE ELEMENT ANALYSIS OF NOTCH BEHAVIOR USING A STATE VARIABLE CONSTITUTIVE EQUATION

L.T. Dame, D.C. Stouffer and N. Abuelfoutouh
Department of Aerospace Engineering and Applied Mechanics
University of Cincinnati, Cincinnati, Ohio 45221

The state variable constitutive equation of Bodner and Partom was used to calculate the load-strain response of Inconel 718 at 649°C in the root of a notch. The constitutive equation was used with the Bodner-Partom evolution equation and with a second evolution equation that was derived from a potential function of the stress and state variable. Data used in determining constants for the constitutive models was from one-dimensional smooth bar tests. The response was calculated for a plane stress condition at the root of the notch with a finite element code using constant strain triangular elements. Results from both evolution equations compared favorably with the observed experimental response. The accuracy and efficiency of the finite element calculations also compared favorably to existing methods.

INTRODUCTION

The purpose of this work is to explore the development, efficiency and accuracy of a finite element computer code for hot section gas turbine components that is based on a state variable constitutive equation. The Bodner-Partom constitutive equation [1,2,3] used for this study, does not require the use of a yield surface or separate representations for loading and unloading in the elastic and inelastic domains. The model contains a single state variable to define the resistance to inelastic flow or hardness. This variable is determined from the deformation history in this study using two different evolution equations. The results from the evolution equation developed by Bodner and Partom and proposed with the flow equation are compared to the results computed from an evolution equation that is derived from the inelastic flow equation itself, [4,5]. The second formulation is established using a potential function that can be derived from the first law of thermodynamics.

One of the important aspects of this study is to test the tensorial or multidimensional characteristics of the Bodner-Partom flow equation. The material parameters for the study are determined from one dimensional tests (tensile, creep and fatigue) on Inconel 718 at 649°C. The equations are used to compute the response of a notched specimen using a plane stress finite element computer analysis. The calculated results for the strain in the root of the notch are compared to measured values reported by Domas et al in [6] for the same material. This provides a test of the model to predict the response in a general state of loading from data obtained in uniaxial experiments. A comparison that is usually difficult to achieve.

Another important aspect of this work is the development of the finite element computer code as a design tool and utilizes the state variable constitutive model. The code is based on two-dimensional constant strain triangles, an initial strain iterative procedure, piecewise linear load histories in a steady state thermal environment and a dynamic time stepping algorithm.

THE BODNER-PARTOM EQUATIONS

These equations were motivated by the concepts of dislocation dynamics and formulated in the context of mechanics. For small strains, the strain rates are considered to be decomposable into elastic, $\dot{\varepsilon}^e_{ij}$, inelastic, $\dot{\varepsilon}^I_{ij}$, and thermal, $\dot{\varepsilon}^T_{ij}$, components; that is

$$\dot{\varepsilon}_{ij} = \dot{\varepsilon}^e_{ij} + \dot{\varepsilon}^I_{ij} + \dot{\varepsilon}^T_{ij} \tag{1}$$

where $\dot{\varepsilon}^e_{ij}$ are given in terms of the stress rates determined from the time derivative of Hooke's Law and ε^T_{ij} is proportional to the change in temperature from a reference state. All components of Equations (1) are always nonzero for all nonzero values of stress and stress rate. However, the values of the inelastic strain rate term are negligible for small values of stress; thus, a yield criteria and separate loading and unloading representations are not required.

The inelastic strain rate is written in a form similar to the Prandtl-Reuss flow law; i.e.

$$\dot{\varepsilon}^I_{ij} = D_0 \exp\{-\frac{n+1}{2n}[\frac{Z^2}{3J_2}]^n\} \frac{S_{ij}}{J_2} \tag{2}$$

where D_0 is the limiting strain rate in shear. The material constant n controls the strain rate sensitivity and also influences the overall level of the stress-strain curves and J_2 is the second invariant of the deviatoric stress tensor, S_{ij}. The internal state variable, Z, governs the resistance to inelastic flow such that an increase in Z corresponds to work hardening and would require an increase in stress to maintain a constant inelastic strain rate.

The hardening law proposed by Bodner and Partom for application with several materials is

$$\dot{Z} = m(Z_1 - Z)\dot{W}^I - AZ_1(\frac{Z-Z_2}{Z_1})^R \tag{3}$$

where $Z = Z_0$ initially. The first term defines the rate strain hardening and $\dot{W} = S_{ij}\dot{\varepsilon}^I_{ij}$ is the inelastic rate of working. The second term in Equation (3) characterizes the thermal recovery and is important for

predicting creep. The representation is only for primary and secondary creep, and the secondary creep rate is obtained when $\dot{Z} = 0$. The constant Z_1 defines the maximum value of Z and Z_2 is the minimum value of Z obtained in thermal recovery. Frequently Z_2 is taken equal to Z_0; that is, the initial hardness and minimum recoverable value of Z are equal. Methods to determine the constants are presented in References [7] and [8], and the constants for Inconel 718 at 649°C are given in Table 1.

The model presented above, in addition to neglecting tertrary creep, is limited to an isothermal environment and isotropic hardening. An extension to time varying temperature histories is based on making n temperature dependent as reported in [3]. Extension to a hardening rate similar to kinematic hardening for uniaxial histories is given Reference [9]; but a full three dimensional anisotropic hardening law still needs to be verified for a variety of loading conditions.

A POTENTIAL FUNCTION DERIVATION

Recently it has been shown [4,5] that a system of equations to predict the inelastic strain rate and evolution of the state variables are derivable from a potential function. The essential structure of the theory is based on the balance law of thermodynamics and the concept of work hardening. For isothermal histories, the reduced form of the potential relationship is

$$\dot{\varepsilon}^I_{ij} = \frac{\partial \phi}{\partial \sigma_{ij}} \quad \text{and} \quad \dot{\mu} = \frac{\partial \phi}{\partial Z} \tag{4}$$

where ϕ is a function the stress and stress state variable, Z. The quantity μ is a strain on the microscopic scale such that $Zd\mu$ is the stored energy of cold work. The relationship between μ and Z on the microscopic scale is taken in the form of the Prandtl-Reuss equation on the macroscopic scale; i.e.

$$\dot{\mu} = g\dot{Z} + hZ \tag{5}$$

where g and h are generally assumed to be functions of σ_{ij} and Z but are taken as constants in this study. Combining Equations (4) and (5) and redefining the constants as α and β gives

$$\dot{Z} = -\alpha(Z-\xi) + \alpha\beta I \tag{6}$$

where ξ is a material parameter. The quantity I is the integral

$$I = \frac{1}{|\dot{\underline{\varepsilon}}^I|} \int_0^t \frac{\partial \dot{\varepsilon}^I_{ij}}{\partial Z} \, d\sigma_{ij} \tag{7}$$

where $|\dot{\underline{\varepsilon}}^I| = (\dot{\varepsilon}^I_{ij}\dot{\varepsilon}^I_{ij})^{1/2}$ and $\dot{\varepsilon}^I_{ij}$ is evaluated using the Bodner Partom Equation in this example.

The parameter α characterizes the initial rate of hardening, $\dot{Z}_0$, which arises from the integration. This term contributes to the strain rate sensitivity of the model and includes the initial loading such as in a creep

test [4]. For this exercise α is taken as $125|\dot{\bar{\varepsilon}}_0|$. The remaining parameters ξ and β can be calculated directly from creep or tensile data during steady state conditions; that is, when both the strain rate and stress are approximately constant. In this case $\dot{Z} = 0$ and Z obtains a steady value, Z_s, that depends on the test conditions. A plot of Z_s vs I for Inconel 718 at 649°C shows that this response is nearly trilinear and can be represented by the parameters shown in Table 1.

FINITE ELEMENT IMPLEMENTATION

The finite element code utilizes two dimensional constant strain triangles and an initial strain iteration technique. To facilitate the simulation of arbitrary load histories, the load history is partitioned into piecewise linear segments. In order to simplify input, reduce stability problems and minimize cost a dynamic time stepping procedure is also incorporated.

The incremental equilibrium equation for the initial strain method with steady state thermal conditions is

$$[K]\{\Delta d^T\} = \{\Delta F\} + \{\Delta F^I\} \tag{8}$$

where [K] is the elastic stiffness matrix, $\{\Delta d^T\}$ is the increment in the total displacement vector, $\{\Delta F\}$ is the increment in the applied force vector and $\{\Delta F^I\}$ is a pseudo force vector due to the increment in a vector of the inelastic strains components. The vector $\{\Delta F^I\}$ is calculated by

$$\{\Delta F^I\} = \sum_1^N \left(\int_v [B]^T[E]\{\Delta \varepsilon^I\}dv\right) \tag{9}$$

where N is the number of elements. In Equation (9), [B] is the strain displacement matrix and [E] is the elastic constitutive matrix.

At the beginning and end of a linear load case the elastic solutions are obtained using

$$\{d^E\}_0 = [K]^{-1}\{F\}_0$$

and

$$\{d^E\}_F = [K]^{-1}\{F\}_F \; . \tag{10}$$

The vectors $\{d^E\}_{0,F}$ are the initial and final elastic displacements due to initial and final applied thermomechanical loads. The elastic displacements at any time t_i in the load case are given by

$$\{d^E\}_i = \{d^E\}_0 + \frac{t_i - t_0}{t_F - t_0}\left[\{d^E\}_F - \{d^E\}_0\right]. \tag{11}$$

The total displacement vector at time t_i is written as

$$\{d^T\}_i = \{d^E\}_i + \{d^I\}_{i-1} + \{\Delta d^I\} \tag{12}$$

where the increment in the inelastic displacement vector is

$$\{\bar{\Delta d}^I\} = [K]^{-1}\{\Delta F^I\} \tag{13}$$

and the increment in the inelastic pseudo force vector is given by Equation (9). Thus, it is necessary to integrate the constitutive model from time t_{i-1} to t_i. Although any number of integration schemes could be used, a second order Adams-Moulton method was employed. Since the flow equation and the state variable evolution equation are coupled an iterative procedure is required to compute $\{\dot{\varepsilon}^I\}$ and $\dot{Z}$ at the end of a time step. The integration of the constitutive equation is within the overall equilibrium iteration loop as shown in Figure 1.

A significant improvement in the iteration scheme was achieved by making an initial estimate of the incremental inelastic pseudo force vector $\{\Delta F^I\}$ in the first iteration of a new time step. If $\{\Delta F^I\}$ is set equal to zero on the first iteration of a new time step (as is usually done) the first estimate of the solution may be very poor. An initial estimate of the inelastic strain increment for each element can be made using $\{\Delta \varepsilon^I\} = \{\dot{\varepsilon}^I\}_{i-1}\Delta t$, where $\{\dot{\varepsilon}^I\}_{i-1}$ is the inelastic strain rate at the beginning of the time increment. If this is then used in Equation (9) to make an initial estimate of the incremental inelastic force vector the stability and rate of convergence of the method is improved. By including this logic, the number of equilibrium iterations was reduced by about 60%.

In a finite element code that allows a linear variation of applied loads, large excursions in stress and inelastic strain rate are to be expected. To be economical and easy to use, dynamic time incrementing is a necessity. There are two important considerations in developing such an algorithm; first the stability of the iteration scheme and second the accuracy of the integration procedure. The stability of the system of equations depends on the constitutive model, geometry, loading history and material parameters. An approximate but simple and effective approach is to base the time step on the maximum inelastic strain increment to occur in all of the elements. In order not to overshoot the point where inelastic strain rates become significant it is also necessary to limit the maximum stress increment. A final consideration is controlling the local integration error when computing inelastic strain increments. For components in which fatigue life is a major consideration the accurate calculation of local stresses and strains is crucial. In order to control the error the time step should be chosen such that the local integration error does not exceed some allowable value.

CALCULATED AND EXPERIMENTAL RESULTS

A recent comprehensive study, [6], of the strain in the root of a notch was conducted for a variety of local patterns in Inconel 718 notch specimens at 649°C (1200°F). A laser interferometric strain displacement gage was used with reasonable certainty to evaluate the displacement of a gage 100 microns in length at the root of the notch at temperature. The

measurements were made for six load histories including continuous cycling and cycling with hold time periods in tension, tension and compression, and compression. The specimen was a thin flat double notch bar, as shown in Figure 2, with an elastic stress concentration factor of 1.9. The geometry in the test section is approximately plane stress and is modeled by the constant strain triangular element mesh also shown in Figure 2.

The above study included a limited number of smooth bar tests in tension, creep and cycling for use with a Neuber analysis. These data and other published tensile, [10], and creep, [11], data were used to evaluate the material parameters in the flow and evolution equations. The constants were evaluated using the methods reported in [4], [7] and [8]. The major difficulty encountered was not having two complete tensile curves at different strain rates to evaluate the parameter n in the inelastic flow equation. Thus an estimate was used based on one curve and the other constants, as shown in the Table 1, were evaluated based on this value. Increases in n would change the values of the other parameters, but the combined effect would produce essentially the same predictions with less strain rate sensitivity in the tensile response. Decreases in n would cause the equations to overpredict the tensile strain rate sensitivity.

The calculated response to a smooth bar tensile test at a strain rate of one percent per minute is shown in Figure 3a for the two evolution equations. The potential function representation overpredicts the observed stress in the transition from elastic to plastic response; however the asymptotic behavior of both representations match the data very well. The calculated smooth bar creep response is shown in Figure 3b for three values of stress. The results of the calculations are mixed with the potential function representation better at the high value of stress, the Bodner-Partom representation better at the intermediate value of stress and both models underpredicting the creep strain at lower values of stress. In general, representations could be improved by adjusting the material parameters; however, with only five curves in the smooth bar data base there is no guarantee that this would improve the predicted response of the notch strain. The flow law is also limited to primary and secondary creep, so no correlation with the tertiary creep is included.

The strain response at the root of the notch for three tests is shown in Figures 4, 5 and 6. The total specimen load is held constant for two minutes in compression, tension and compression, and tension as shown in Figures 4, 5 and 6, respectively. The finite element and experimental results are for the first cycle. In general, both evolution equations match the measured data rather well. The largest error is the over prediction of the tensile creep in Figure 6 by both equations; however, the measured tensile creep in Figure 6 is much less than the measured tensile creep in Figure 5 where the predictions are satisfactory. The assumption of isotropic hardening appears reasonable for the first cycle and the correlation with compressive creep is shown in Figures 4 and 5.

DISCUSSION

The state variable constitutive models used in this study have several advantages and limitations. The formulation is convenient for finite

element methods, because it admits a forward time marching integration procedure and does not require separate loading and unloading representations. The flow law and evolution equation can predict many inelastic effects; however, for Inconel 718 there still are some areas that need improvement. Inconel 718 general exhibits a combination of "kinematic and isotropic" hardening and softening in uniaxial cycling which is not included in the current formulation. Further, the constitutive models have not been fully developed and verified for nonisothermal loading conditions. For extension to multiple cycle analysis it would also be advantageous to use the cyclic stress-strain curve rather than the monotonic response curve to determine the material parameters.

There is a correlation in the errors observed in the calculated finite element response at the root of notch and the smooth bar calculated response. When using the Bodner-Partom evolution equation, (3), the creep strain at 827MPa(120KSI) was over predicted. The calculated tensile creep response in the root of the notch is largest for the Bodner-Partom equations as shown in Figures 5 and 6. This observation indicates that the finite element predictions could be refined by improving the smooth bar calculated response. Recalling that the constitutive parameters were obtained from five curves, one tensile and four creep published [6,10,11] between 1971 and 1982, the calculations are reasonable and could be improved by improving the smooth bar data base.

The computational exercises were limited to initial cycle of three load patterns for reasons of cost and lack of cyclic data to develop the model. The computational efficiency proved to be very good. On a Honeywell 6000 computer, the run times varied from 1.5 to 3.5 CPU hours for a model with over 1000 elements. This is very competitive with similar finite element calculations based on classical plasticity and creep formulations. Further, the longest time could have been reduced by incorporating all the time saving features used in the later runs.

ACKNOWLEDGEMENT

The authors thank the National Aeronautics and Space Administration for their support under grant NAG 3-511 to the University of Cincinnati, Cincinnati Ohio and Contracts NAS3-23698 and NAS3-23927 to the Aircraft Engine Business Group, General Electric Co., Evendale Ohio.

REFERENCES

[1] Bodner S.R. and Partom Y., "A Large Deformation Elastic Viscoplastic Analysis of Thickwalled Spherical Shells," Journal of Applied Mechanics V39, pp 751-757 (1972).

[2] Bodner S.R. and Partom Y., "Constitutive Equations for Elastic Viscoplastic Strain Hardening Materials," Journal of Applied Mechanics V42, pp 385-389 (1975).

[3] Bodner S.R., Partom I and Partom Y., Journal of Applied Mechanics, V46, pp 805-810 (1979).

[4] Abuelfoutouh N.M. "A Thermodynamically Consistent Constitutive Model for Inelastic Flow of Materials," Ph.D. Dissertation, University of Cincinnati 1983.

[5] Stouffer D.C. and Abuelfoutouh N.M., "A Potential Function Constitutive Equation for Inelastic Material Response," NASA Conference Publication 2271, pp 153-177 (1982).
[6] Domas P.A., Sharpe W.N., Ward N. and Yau J., "Benchmark Notch Test for Life Prediction," NASA CR-165571, 1982.
[7] Stouffer D.C. and Bodner S.R., "A Relationship Between Theory and Experiment for a State Variable Constitutive Equation," American Society for Testing and Materials, ASTM-STP765, pp 239-250 (1982).
[8] Nicholas T., "Finite Element Analysis of Cracked Bodies Using the Bodner-Partom Flow Law," 2nd Symposium of Nonlinear Constitutive Relations for High Temperature Application, NASA Lewis Research Center, June 1984.
[9] Stouffer D.C. and Bodner S.R., "A Constitutive Model for Deformation Induced Anisotropic Plastic Flow of Metals," International Journal of Engineering Science, V17, pp 757-764 (1979).
[10] Brinkman C.R. and Korth G.E., "Strain Fatigue and Tensile Behavior of Inconel 718 at Room Temperature to 650°C," Journal Testing and Evaluation, 2.4, pp 249-259, July 1974.
[11] NIR (Kushnir) N, Eylon D. and Rosen A., "The Effect of Rapid Thermal Fluctuations on the Creep Rate in Inconel 718," Metallurgical Transactions, 2, pp 2237-2241, Aug. 1971.

Table 1. Constitutive Parameters

Flow Equation:

$D_0 = 10^4 SEC^{-1}$ $\quad n = 1.954$

Bodner Partom Evolution Equation:

$Z_0 = 1805MPa$ (262 KSI) $\quad A = 5.6 \times 10^{-5} SEC^{-1}$

$Z_1 = 2253MPa$ (327 KSI) $\quad M = 0.160MPa^{-1}$

$Z_2 = 1805MPa$ (262 KSI) $\quad R = 1.37$

Potential Function Evaluation Equation:

$Z_0 = 1860MPa$ (270 KSI) $\quad \alpha = 125|\dot{\varepsilon}_0|$

$|\dot{\varepsilon}^I| \leq 3.2 \times 10^{-10} SEC^{-1}$ $\quad \zeta = 0$

$\beta = 4.01 \times 10^7 MPa/SEC (5.82 \times 10^6 KSI/SEC)$

$|\dot{\varepsilon}^I| > 3.2 \times 10^{-10} SEC^{-1}$ and $\quad \zeta = -4033MPa(-585$ KSI)

$|\dot{\varepsilon}^I| \leq 7 \times 10^{-6} SEC^{-1}$ $\quad \beta = 1.60 \times 10^8 MPa/SEC (2.33 \times 10^7 KSI/SEC)$

$|\dot{\varepsilon}^I| > 7 \times 10^{-6} SEC^{-1}$ $\quad \zeta = 1102MPa(160$ KSI)

$\beta = 2.94 \times 10^7 MPa/SEC (4.27 \times 10^6 KSI/SEC)$

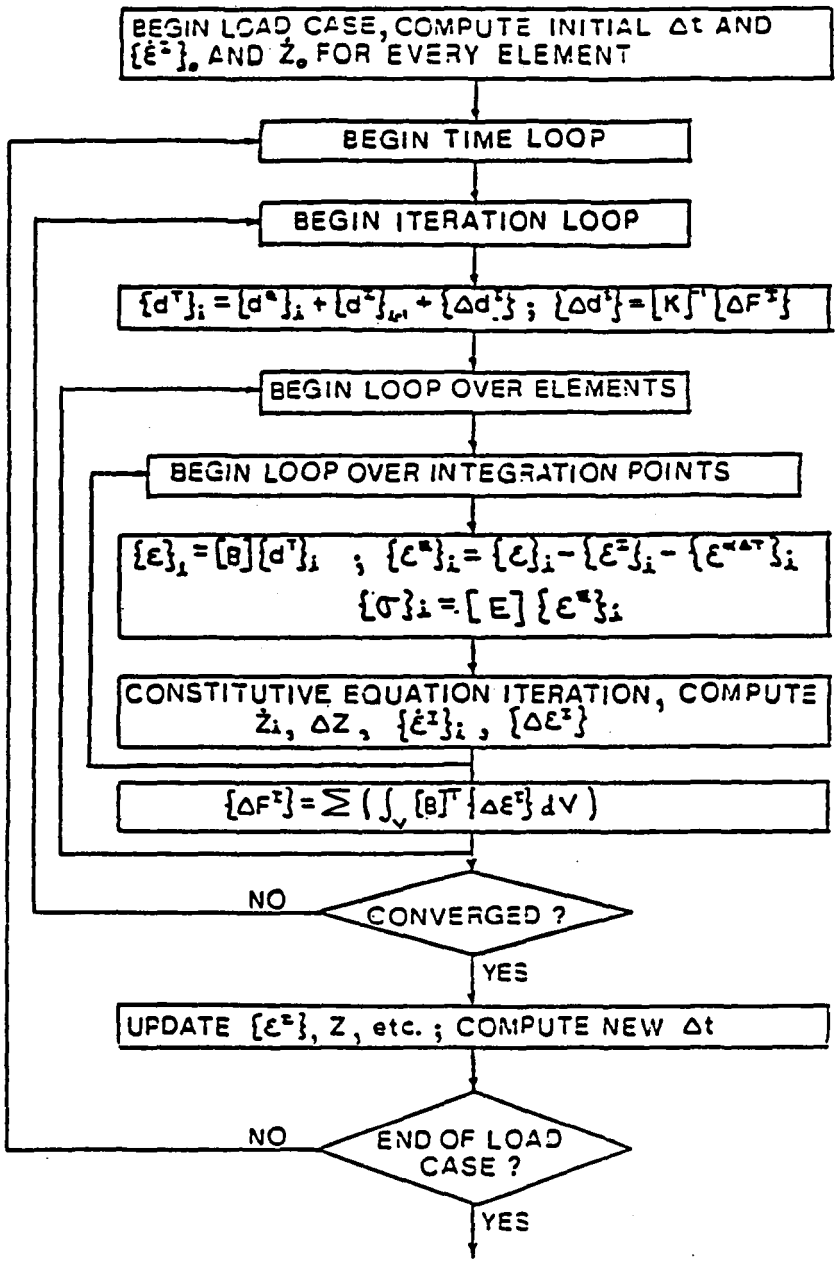

Figure 1. Schematic diagram of the iteration procedure for the finite element program.

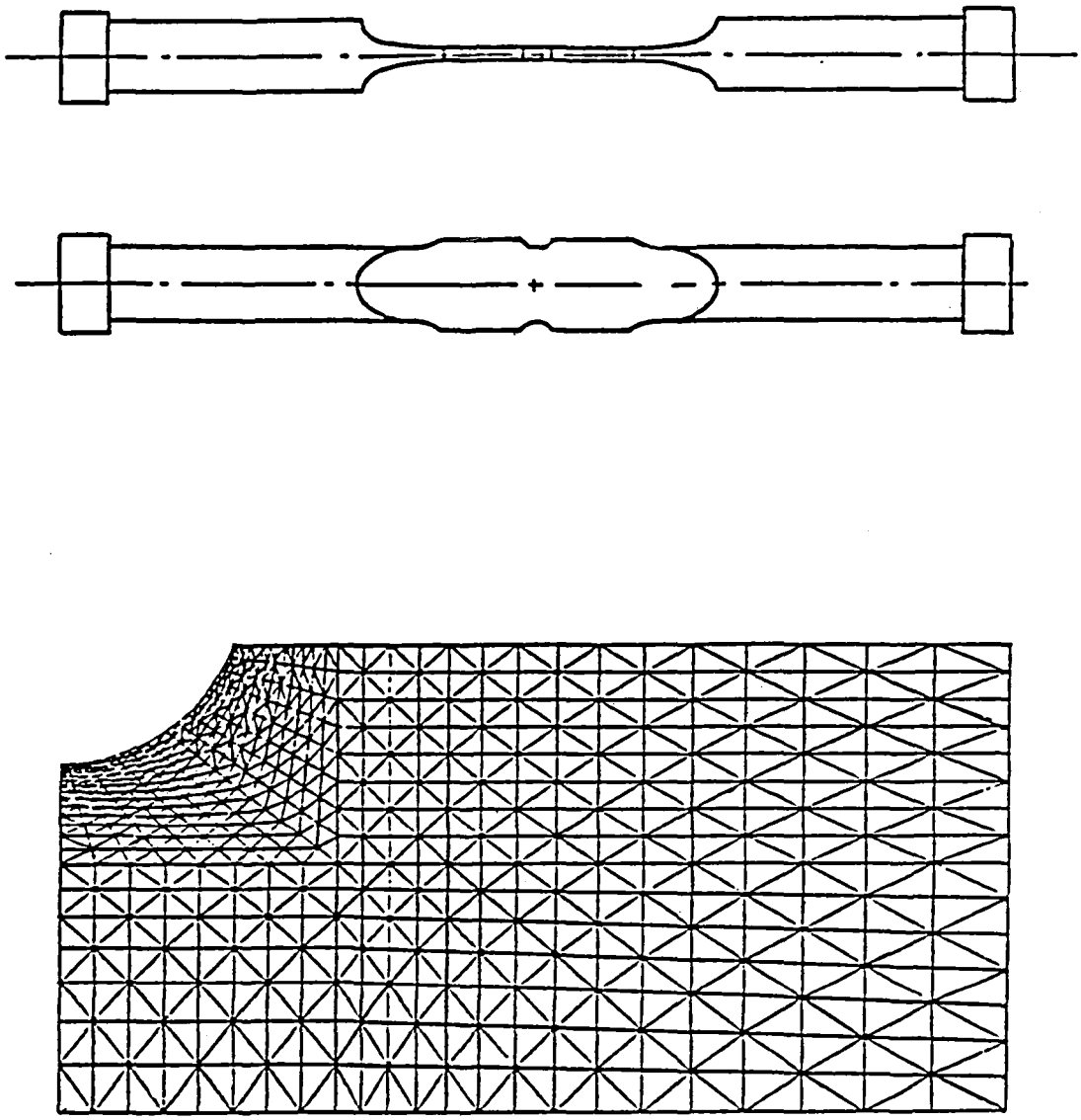

Figure 2. Description of the benchmark notch specimen and the finite element mesh at the root of the notch.

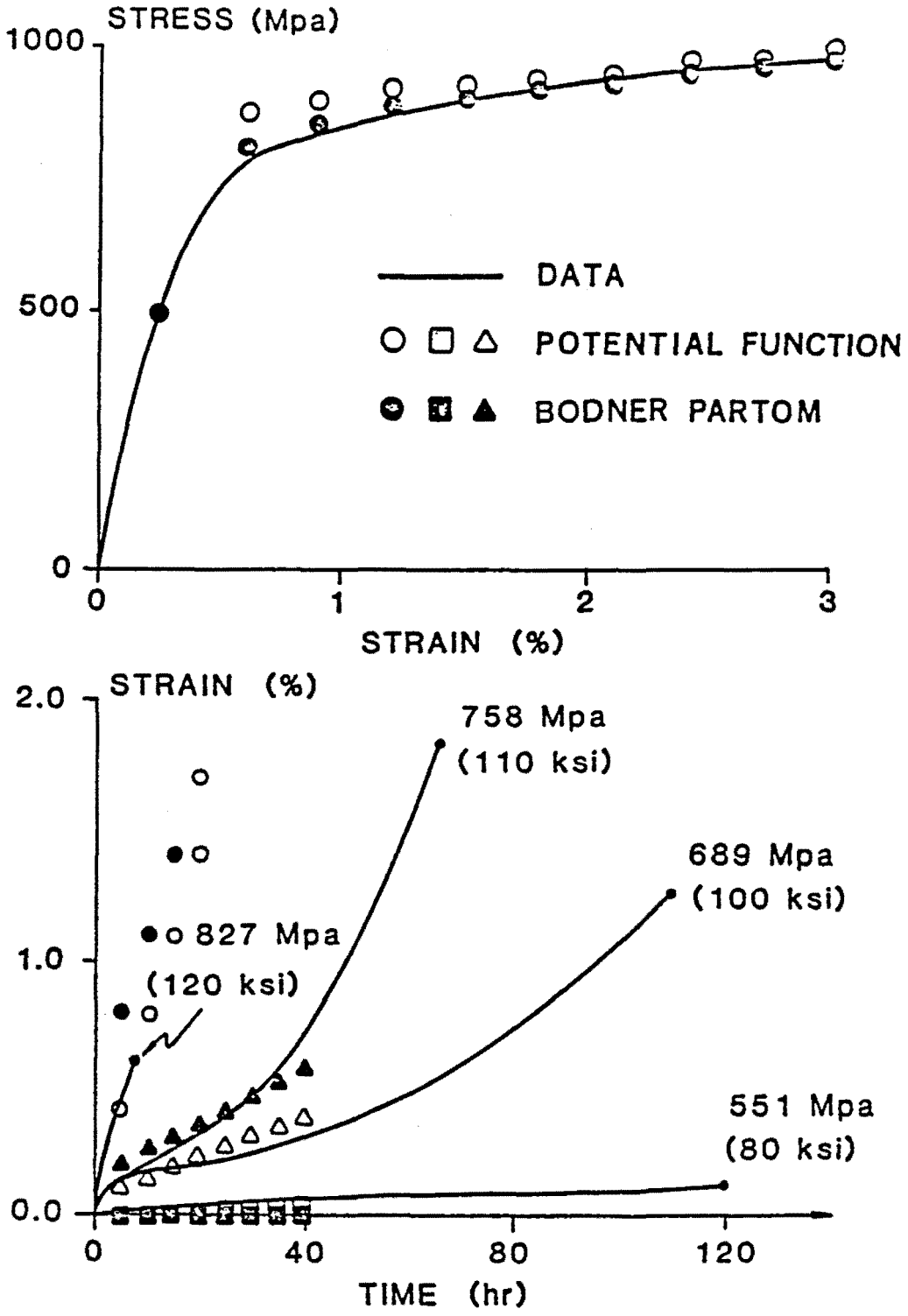

Figure 3. Comparison of experimental and calculated response of Inconel 718 at 649°C using the Bodner-Partom and potential function evolution equations: (A) tensile response at 1% per minute and (b) comparison of creep response at 689MPa(100KSI), 758MPa(110KSI) and 827MPa(120KSI).

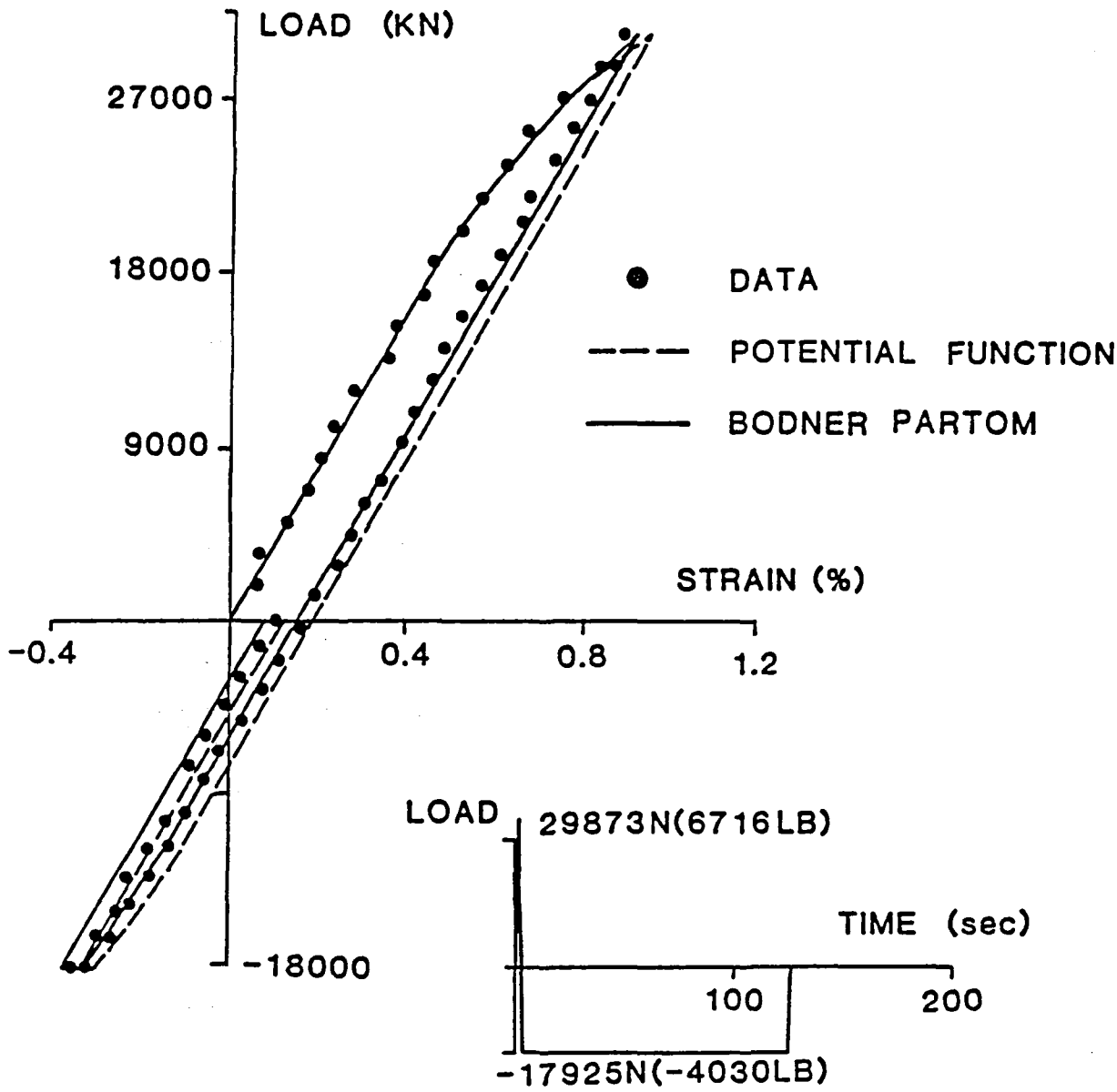

Figure 4. Comparison of experimental and calculated load-strain response at the root of the notch for Benchmark Notch Test 8 with a hold in compression.

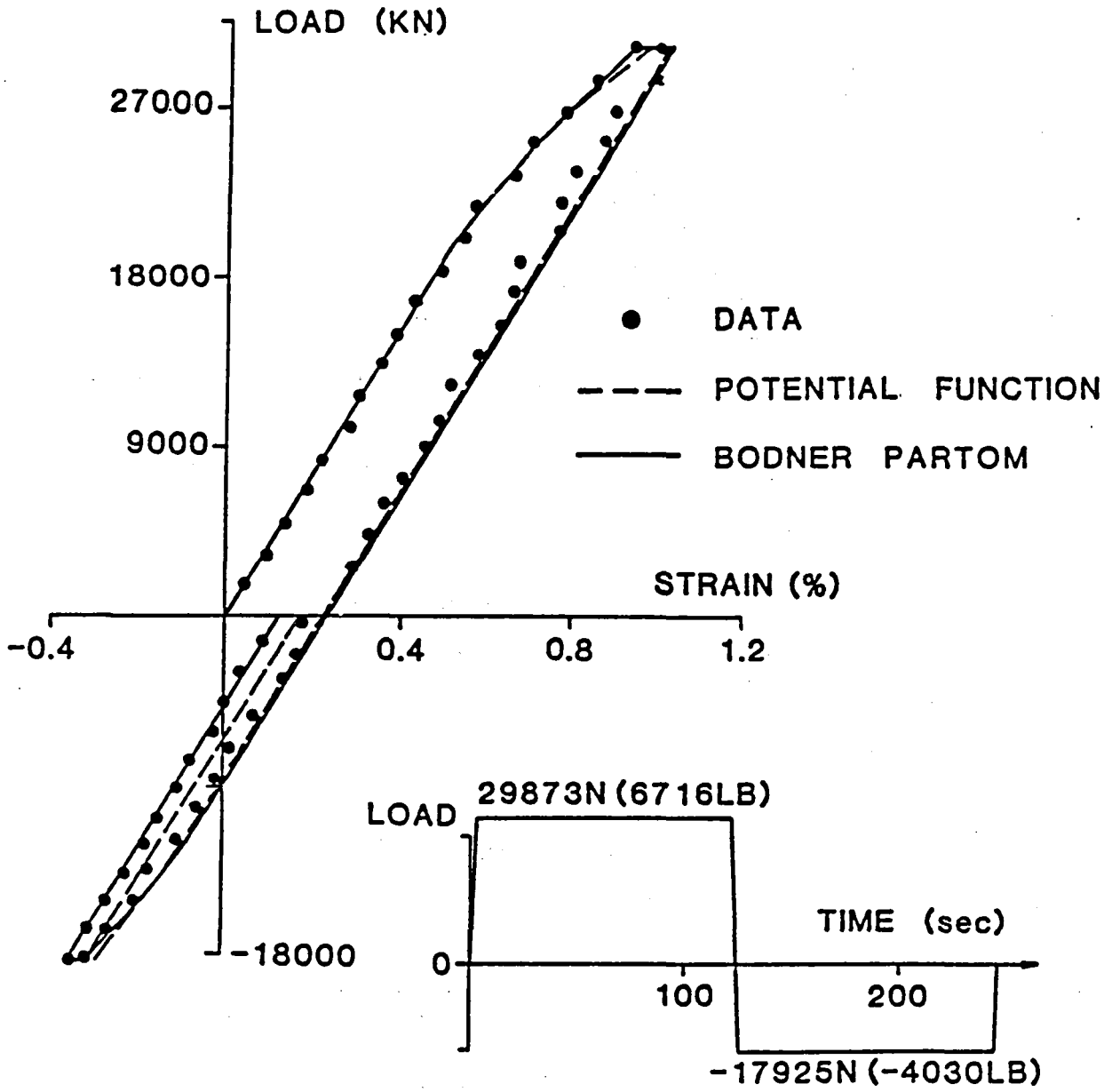

Figure 5. Comparison of experimental and calculated load-strain response at the root of the notch for Benchmark Notch Test 9 with hold in tension and compression.

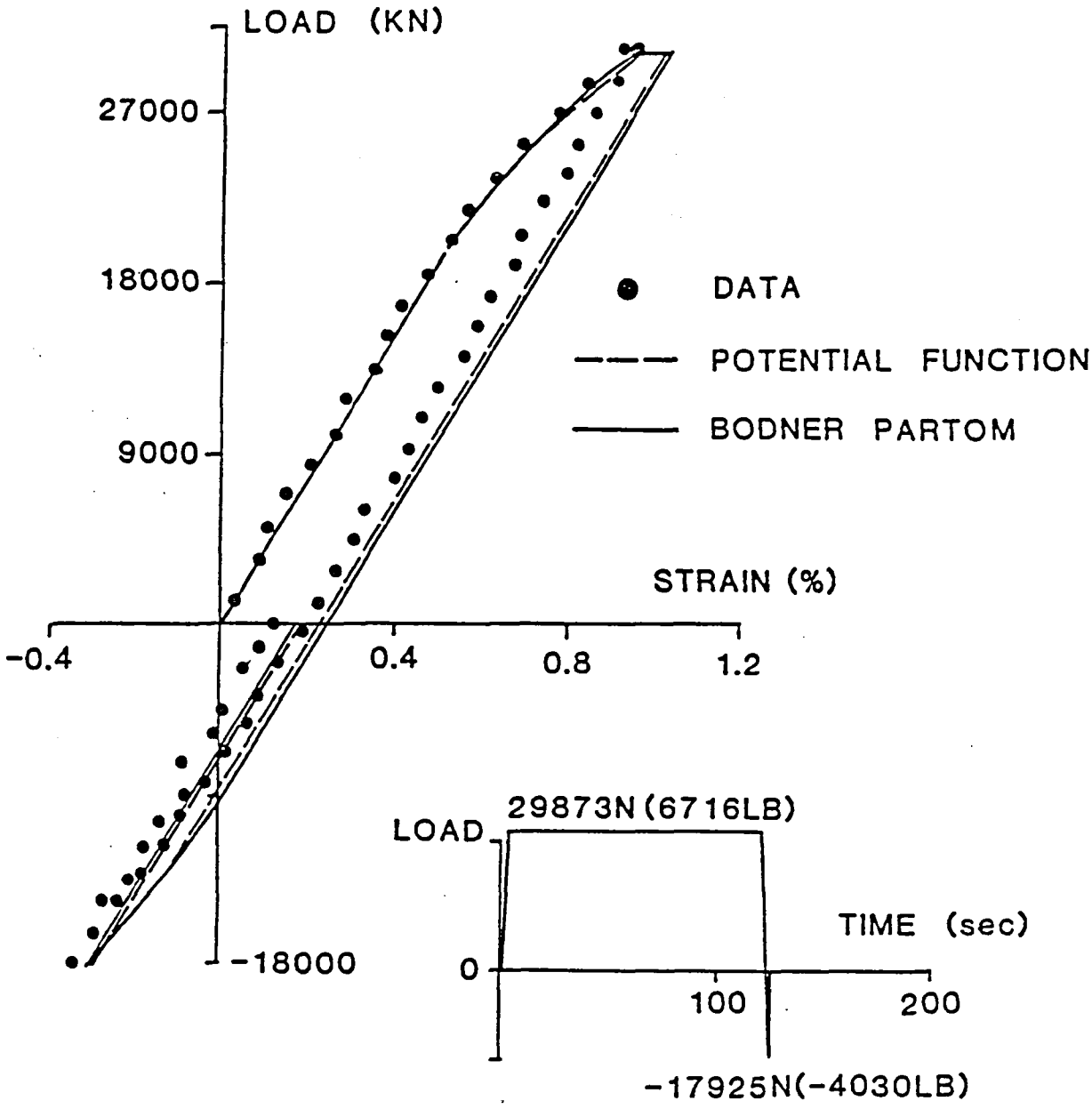

Figure 6. Comparison of experimental and calculated load-strain response at the root of the notch for Benchmark Notch Test 10 with hold in compression.

NONLINEAR ANALYSIS OF AN AXISYMMETRIC STRUCTURE SUBJECTED TO NON-AXISYMMETRIC LOADINGS

P.C. Chen and R.L. McKnight
General Electric Company
Cincinnati, Ohio 45215

The development of the SHELPC finite element computer program is detailed. This program is specialized to simulate the nonlinear material behavior which results from combustor liner "hot streaks". This problem produces a nonlinear Fourier Series type loading on an axisymmetric structure. Example cases are presented.

One problem which is unique to Aircraft Gas Turbine Engines (AGTE's) is the thermal hot streak problem experienced by certain combustor liners. These liners are thin axisymmetric pressure shells whose function is to contain and promote the combustion process. Because of the high temperatures involved in this combustion process, the functioning of these liners depends on their being "cooled" by lower temperature air from the compressor. To complicate this problem further, the temperatures generated by the combustion process are not uniform in either the axial or circumferential directions of the combustor liner.

The temperature variation in the axial direction is the variation normally shown in textbooks and calculated from the thermodynamic laws based on pressure/volume considerations. The circumferential variation is a more complex, three dimensional mixing problem. It is a function of the number of fuel nozzles employed and the geometry and thermodynamics of the combustor. The result is a circumferential variation in the metal temperature of these liners which can be approximated with Fourier Series.

The functional lives of these liners are primarily dictated by the resulting material response to these temperature variations, which produce thermal stresses. The stresses produced by the differential pressures across the liner walls are limited to small values and are secondary contributors to the problem. Because of the high temperatures and large temperature variations involved, the material response problem is nonlinear and time dependent. AEBG has been active in developing internal computer tools for attacking these types of unique AGTE problems. Our capabilities include both two-dimensional and three-dimensional nonlinear finite element computer programs.

The thermal stress problem generated by the axial variation in metal temperatures can be handled quite readily by a two-dimensional (axisymmetric) analysis. However, the thermal stresses generated by the circumferential variation in metal temperatures is truly a three-dimensional problem. As such, one method of attack would be to develop a simulation using three-dimensional finite elements, such as our 8, 16 or 20 noded isoparametric elements.

This method of attack has drawbacks in economy, accuracy, and utility. The number of hot streaks can be quite large (in the 60's) and the hot to cold temperature variations can be in the hundreds of degrees Fahrenheit. This would require a large number of 3D elements to produce an acceptable simulation. This could also produce bad element aspect ratios, resulting in solution accuracy problems. Varying these models in an iterative design process would be manpower and computer intensive. For these reasons we sought other methods of attacking this problem.

Since the circumferential temperature variations can be represented as Fourier Series expansions, this suggests attacking the structural problem by means of Fourier Series. This method of attack for linear elastic problems in a finite element format was presented by E.L. Wilson in Reference (1). For linear elastic problems the method of superposition of Fourier Series loading is mathematically exact and precise. However the problem in question is nonlinear.

In Reference (2), E.A. Witmer and J.J. Kotanchik presented a nonlinear solution procedure for axisymmetric shells under asymmetrical loading. In their approach, they utilized an initial strain method with Besseling's isothermal constitutive model in a sublayer format. This then presented a method of attacking nonlinear Fourier Series loading problems but with one tremendous deficiency; our problem under consideration is totally nonisothermal in nature.

Subsequently, one of the present authors, R.L. McKnight, developed a variable temperature version of Besseling's constitutive model in a subvolume format as presented in References (3) and (4). This has been the primary basis of AEBG's internal nonlinear computer tools since 1975. To this time-independent plasticity formulation, we added classical creep capability with time-hardening, strain-hardening, and life-fraction rules for attacking quasi-static time-dependent nonlinear problems. Over the years, through large amounts of production usage, these tools have been provided with much verification, validation, and operational experience for both 2D and 3D problems. With this background, we decided to reattack the combustor liner hot streak problem:

SHELPC

The following is a synopsis of the theoretical development of the combustor liner program, SHELPC. A complete development will be found in the Ph.D. Dissertation of P.C. Chen, to be published later.

As in Reference (1), the finite element employed is the triangular ring element shown in Figure 1. This is an extension of that element commonly used for plane stress, plane strain, and axisymmetric analysis. In those cases, there are two degrees of freedom, or displacements at each node. To allow for

the circumferential variation in load a third degree of freedom, the circumferential or hoop displacement, is introduced. These three displacement components are assumed to be linear functions of position in the R-Z plane. This is expressed mathematically as follows

$$\begin{aligned} U_R &= b_1 + b_2R + b_3Z \\ U_Z &= b_4 + b_5R + b_6Z \\ U_S &= b_7 + b_8R + b_9Z \end{aligned} \tag{1}$$

The strain components in terms of these displacements are (for small displacement theory).

$$\begin{aligned} \varepsilon_R &= \frac{\partial U_R}{\partial R} \\ \varepsilon_Z &= \frac{\partial U_Z}{\partial Z} \\ \varepsilon_\theta &= \frac{1}{R}\frac{\partial U_\theta}{\partial \theta} + \frac{U_R}{R} \\ \varepsilon_{RZ} &= \frac{\partial U_R}{\partial Z} + \frac{\partial U_Z}{\partial R} \\ \varepsilon_{Z\theta} &= \frac{\partial U_\theta}{\partial Z} + \frac{1}{R}\frac{\partial U_Z}{\partial \theta} \\ \varepsilon_{\theta R} &= \frac{1}{R}\frac{\partial U_R}{\partial \theta} + \frac{\partial U_\theta}{\partial R} - \frac{U_\theta}{R} \end{aligned} \tag{2}$$

The loading is now allowed to varying in the circumferential direction in a sine or cosine fashion as defined in Table 1.

Equations (1), then become

$$\begin{aligned} U_R &= (b_{1n} + b_{2n}R + b_{3n}Z)\cos N\theta \\ U_Z &= (b_{4n} + b_{5n}R + b_{6n}Z)\cos N\theta \\ U_\theta &= (b_{7n} + b_{8n}R + b_{9n}Z)\,\mathrm{Sin}\, N\theta \end{aligned} \tag{3}$$

or

$$\begin{aligned} U_R &= (b_{1n} + b_{2n}R + b_{3n}Z)\,\mathrm{Sin}\, N\theta \\ U_Z &= (b_{4n} + b_{5n}R + b_{6n}Z)\,\mathrm{Sin}\, N\theta \\ U_\theta &= (b_{7n} + b_{8n}R + b_{9n}Z)\,\mathrm{Cos}\, N\theta \end{aligned} \tag{4}$$

TABLE 1

FOURIER SERIES LOADING AND DISPLACEMENT DESCRIPTION

Symmetric about a plane containing the axis of revolution	Anti-symmetric about a plane containing the axis of revolution
$T = \Sigma T_n(r,z) \cos n\theta$	$T = \Sigma T_n(r,z) \sin n\theta$
$S_r = \Sigma S_{rn}(r,z) \cos n\theta$	$S_r = \Sigma S_{rn}(r,z) \sin n\theta$
$S_z = \Sigma S_{zn}(r,z) \cos n\theta$	$S_z = \Sigma S_{zn}(r,z) \sin n\theta$
$S_\theta = \Sigma S_{\theta n}(r,z) \sin n\theta$	$S_\theta = \Sigma S_{\theta n}(r,z) \cos n\theta$
$U_r = \Sigma U_{rn}(r,z) \cos n\theta$	$U_r = \Sigma U_{rn}(r,z) \sin n\theta$
$U_z = \Sigma U_{zn}(r,z) \cos n\theta$	$U_z = \Sigma U_{zn}(r,z) \sin n\theta$
$U_\theta = \Sigma U_{\theta n}(r,z) \sin n\theta$	$U_t = \Sigma U_{tn}(r,z) \cos n\theta$

n is the harmonic number.

T is the temperature.

S's are the loads.

U's are the displacements.

To introduce nonlinear material behavior, we make the classical assumption that the total strains consist of a summation of elastic, plastic, creep, and thermal components

$$\varepsilon = \varepsilon^e + \varepsilon^P + \varepsilon^C + \varepsilon^T \tag{5}$$

We also assume that stress is linearly related to the elastic strain only

$$\sigma = C\,\varepsilon^e \tag{6}$$

$$\sigma = C(\varepsilon - \varepsilon^P - \varepsilon^C - \varepsilon^T) \tag{7}$$

Where C is the elastic Hook's Law matrix.

The sum of the plastic, creep, and thermal strains are considered as initial strains.

$$\varepsilon^I = \varepsilon P + \varepsilon C + \varepsilon T \tag{8}$$

or

$$\sigma = C(\varepsilon - \varepsilon^I) \tag{9}$$

Applying the precepts of Reference (2), we make use of the Principle of Stationary Total Potential Energy.

The strain energy density is expressed as

$$\bar{U} = \tfrac{1}{2}\,\sigma^T\,\varepsilon^e \tag{10}$$

or

$$\bar{U} = \tfrac{1}{2}[C(\varepsilon - \varepsilon^I)^T]\,(\varepsilon - \varepsilon^I) \tag{11}$$

$$\bar{U} = \tfrac{1}{2}\,(\varepsilon - \varepsilon^I)^T\,C(\varepsilon - \varepsilon^I) \tag{12}$$

The total potential energy of one ring element is

$$PE = \int_V \tfrac{1}{2}(\varepsilon - \varepsilon^I)^T\,C\,(\varepsilon - \varepsilon^I)dV - \delta^T F \tag{13}$$

where δ is the generalized displacements and F is the generalized external forces.

For a system of ring elements, this development leads to

$$K\delta = F + F^I \tag{14}$$

where

K = elastic stiffness matrix for discretized system

δ = generalized displacements of the discretized system

F = applied generalized forces

F^I = generalized forces due to initial strains

Now, to introduce the Fourier Series loading into this system of equations. Our assumption is that the total strain can be considered to be made up of the sum of a certain number of A-series and B-series Fourier components. The A-series components are those symmetrical about a plane containing the axis of rotation. The B-series components are those antisymmetrical about a plane containing the axis of rotation (see Table 1). Thus we assume

$$U(R,Z,\theta) = \Sigma\, U_N^A\,(R,Z)\cos N\theta + \Sigma\, U_N^B\,(R,Z)\,\mathrm{Sin}\,N\theta \tag{15}$$

and therefore

$$\varepsilon(R,Z,\theta) = \Sigma\, \varepsilon_N^A\,(R,Z)\cos N\theta + \Sigma\, \varepsilon_N^B\,(R,Z)\,\mathrm{Sin}\,N\theta \tag{16}$$

or

$$\varepsilon(R,Z,\theta) = \varepsilon^A(R,Z,\theta) + \varepsilon^B(R,Z,\theta) \tag{17}$$

and, using Equation (5)

$$\begin{aligned}\varepsilon(R,Z,\theta) = {} & \varepsilon^{eA}(R,Z,\theta) + \varepsilon^{PA}(R,Z,\theta) + \varepsilon^{CA}(R,Z,\theta) \\ & + \varepsilon^{TA}(R,Z,\theta) + \varepsilon^{eB}(R,Z,\theta) \\ & + \varepsilon^{PB}(R,Z,\theta) + \varepsilon^{CB}(R,Z,\theta) \\ & + \varepsilon^{TB}(R,Z,\theta)\end{aligned} \tag{18}$$

For a discretized model, the system of equations are set up and solved a harmonic and a series at a time

$$[K_N^A]\,\delta_N^A = F_N^A + F_N^{IA} \tag{19}$$

$$[K_N^B]\,{}_N^B = F_N^B + F_N^{IB} \tag{20}$$

The nodal displacements are then given by

$$\delta(R,Z,\theta) = \Sigma\, \delta_N^A \cos N\theta + \Sigma\, \delta_N^B \text{ Sin } N\theta \tag{21}$$

NONLINEAR SOLUTION SCHEME

A given axisymmetric geometry with thermal and mechanical loadings which can be simulated by Fourier Series is first discretized by triangular rings. The pertinent system of equations, (19) and (20), are set up and solved, first assuming elastic behavior. This gives a first approximation for the nodal point displacements. With these results, which are the amplitudes of Fourier Series displacement components, we can now determine the displacements at any circumferential location.

A minimum period is selected based on the lowest order harmonic other than 0 (for the combustor liner this is determined by the number of fuel nozzles). This minimum period is then approximated by 10 points in the 0-direction. At each of these 10 points, each rings nodal point displacements can be determined. From this the total strain can be determined for each location. Then using the constitutive models as covered in References (3) and (4), an initial estimate is made for the inelastic strains and from these inelastic pseudo-forces, F^P and F^C. These inelastic pseudo-forces are then approximated by the Fourier Series harmonics.

$$F^P(R,Z,\theta) = \Sigma F_N^{PA}(R,Z) \text{ Cos } N\theta + \Sigma F_N^{PB}(R,Z) \text{ Sin } N\theta$$

$$F^C(R,Z,\theta) = \Sigma F_N^{CA}(R,Z) \text{ Cos } N\theta + \Sigma F_N^{CB}(R,Z) \text{ Sin } N\theta \tag{22}$$

The amplitudes of these harmonic pseudo-forces are then added to the initial force vector.

$$\begin{aligned} F_N^I(R,Z,\theta) = {} & F_N^{TA}(R,Z) \text{ Cos } N\theta + F_N^{TB}(R,Z) \text{ Sin } N\theta \\ & + F_N^{PA}(R,Z) \text{ Cos } N\theta + F_N^{PB}(R,Z) \text{ Sin } N\theta \\ & + F_N^{CA}(R,Z) \text{ Cos } N\theta + F_N^{CB}(R,Z) \text{ Sin } N\theta \end{aligned} \tag{23}$$

This new value for the initial force vector is used to obtain a new series of solutions. From these, new inelastic strains are predicted and from these a third initial force vector. This process is continued until convergence occurs.

EXAMPLE CASES

In order to verify the correctness of the solution scheme as outlined, several comparisons with finite element methods were made. Two problems analyzed are presented, one representing combined thermoplasticity and creep under cyclic loading, and the other a verification of the elastic Fourier series analysis capability. These cases represent a check on the two basic aspects of the combined elastic/plastic technique for harmonic loading.

In the first case, which verifies the cyclic plasticity and creep capability, a thick-walled cylinder is subjected to a time-varying pressure and temperature loading history (Figure 2). These loadings are the predominant types experienced by combustors. Plane strain conditions were assumed, the finite element model being composed of triangular ring elements as shown in Figure 3. The model was also run using the CYANIDE 2-D computer code, subjected to the same temperature and pressure history as shown in Figure 2. The comparison between SHELPC and CYANIDE 2-D under these axisymmetric loadings was then made, the results being presented in Figures 2 and 4. Figure 2 shows a comparison of radial displacement versus time for the two methods. Figure 5 shows the residual stress distribution through the wall at t = 10 hours when the pressure was equal to zero. As can be seen from these results, correlation was very good.

A second test case was used to check the Fourier series method under a thermal loading represented by the combination of temperature harmonics of the form:

$$T(\theta) = 70 + 30 \cos (4\theta)$$

In an actual component, such as a combustor, the harmonics used would be a function of the number of "hot streaks" around the circumference. The model used was again a thick-walled cylinder as shown in Figure 3. To verify the response of the structure to this type of loading, the same model was run using the CLASS/MASS code which also has harmonic loading capability but limited to linear elastic behavior. This problem was run elastically with SHELPC in order to achieve a direct comparison. Results are presented in tabular form to demonstrate the closeness of the numerical comparison. In Table 2, the displacement components from SHELPC and CLASS/MASS are compared for the harmonic loading:

$$T(\theta) = 30 \cos (4\theta)$$

Table 2: Nodal Displacements at $\theta = 0^{o}$ Due to a Single Harmonic Thermal Load $T(\theta) = 30 \cos (4\theta)$.

Node No.	SHELPC (10^{-5} inch)			CLASS/MASS (10^{-5} inch)		
	δ_R	δ_Z	δ_θ	δ_R	δ_Z	δ_θ
1	-8.947	-7.726	8.633	-8.958	-7.736	8.641
2	-8.946	7.727	8.633	-8.958	7.736	8.641
3	-0.2380	0	3.661	-0.2445	0	3.646
4	7.718	-8.767	9.678	7.719	-8.770	9.678
5	7.718	8.767	9.678	7.719	8.770	9.678

In Table 3, the individual harmonic results from SHELPC for the displacements, stresses and strains are shown. The results from a combined harmonic run are also tabulated. As can be seen from this table, the results are correctly superimposed. They also correlate well with the corresponding CLASS/MASS values.

Table 3. Nodal Displacements and Element Strains and Stresses at $\theta = 0$ Due to Combined Harmonic Thermal Load (i.e., $T(\theta) = 70 + 30 \cos 4\theta$).

Nodal Displacements (10^{-3} Inch)

Node No.	n=0			n=4			Combined		
	δ_R	δ_Z	δ_θ	δ_R	δ_Z	δ_θ	δ_R	δ_Z	δ_θ
1	0.4200	-0.2100	0	-0.08947	-0.07726	0.08633	0.3305	-0.2873	0.08655
2	0.4200	0.2100	0	-0.08946	0.07727	0.08633	0.3305	0.2873	0.08633
3	0.6300	0	0	-0.02380	0	0.03661	0.6276	0	0.03661
4	0.8400	-0.2100	0	0.07718	-0.08767	0.09678	0.9172	-0.2977	0.09678
5	0.8400	0.2100	0	0.07718	0.08767	0.09678	0.9172	0.2977	0.09678

Element Strains (10^3 Inch/Inch)

Ele. No.	n=0				n=0				Combined			
	E_r	E_Z	E_θ	$E_{\theta r}$	E_r	E_Z	E_θ	$E_{\theta r}$	E_r	E_Z	E_θ	$E_{\theta r}$
1.	0.420	0.420	0.420	0	0.174	0.155	0.187	-0.0480	0.594	0.575	0.607	0.0480
2	0.420	0.420	0.420	0	0.167	0.165	0.192	-0.0253	0.557	0.585	0.612	0.0253
3	0.420	0.420	0.420	0	0.167	0.165	0.192	-0.0254	0.587	0.585	0.612	0.0254
4	0.420	0.420	0.420	0	0.157	0.175	0.193	-0.0320	0.579	0.595	0.615	-0.0320

Element Stresses (10^3 psi)

Ele. No.	n=0				n=0				Combined			
	σ_r	σ_Z	σ_θ	$\sigma_{\theta r}$	σ_r	σ_Z	σ_θ	$\sigma_{\theta r}$	σ_r	σ_Z	σ_θ	$\sigma_{\theta r}$
1	0	0	0	0	-0.549	-1.00	-0.244	0.553	-0.549	-1.00	-0.244	0.553
2	0	0	0	0	-2.592	-0.631	-0.005	-0.292	-0.592	-0.631	-0.005	-0.92
3	0	0	0	0	-0.591	-0.631	-0.005	-0.293	-0.591	-0.631	-0.005	-0.93
4	0	0	0	0	-0.664	-0.289	0.165	-0.370	-0.664	-0.289	-0.165	-0.370

Then three more complex nonlinear comparison cases were run to demonstrate the capabilities of SHELPC. These cases demonstrate elastic/plastic comparisons for axisymmetrically loaded structures as well as harmonic summation comparisons in the elastic regime. Since no other code which does the harmonic analysis was available, a direct comparison of nonlinear harmonic analysis could not be made. This comparison will rely primarily on experimental results from actual combustors.

To compare the elastic/plastic analysis capability for axisymmetric loading, we modeled a typical axisymmetric combustor lip, as shown in Figure 5. It was modeled using 168 3-node finite elements in both SHELPC and CYANIDE 2-D programs. The axisymmetric loading conditions were run and compared satisfactorily. Figures 6 and 7 show comparisons of the effective stress and effective plastic strain, respectively, as predicted by the two programs. The plot is for the inner surface of the cooling louver around the edge from element No. 56 to element No. 136 as shown in Figure 8. As can be seen from these results, the comparison between the two programs is excellent. This case was one of those used to validate the analytical development of SHELPC where a direct comparison with axisymmetric loads (zero harmonic) could be made.

Our second example demonstrates the Fourier series capability of SHELPC under a mechanical loading situation. Figure 9 gives the particulars of the problem, a ring under a harmonic pressure distribution applied at the outer diameter. This problem was solved both elastically and plastically for the stress-strain properties shown. Figure 10 shows the SHELPC predictions for the radial displacement at the outer diameter for the two cases. The elastic results were correlated with hand calculations and CLASS/MASS results.

As a final validation example, we extended the previous comparison with CLASS/MASS to the nonlinear regime.

Figure 11 shows the problem conditions, an increased thermal loading, and the assumed stress-strain curve. The elastic solution was correlated with CLASS/MASS. The plastic solution shows the difference in effect between the pressure load of the previous example and a thermal hot streak, Figure 12. In this case, plastic flow reduces the radial displacement.

This program is continuing under development with more verification and validation cases being pursued.

REFERENCES

1. Wilson, E. L., "Structural Analysis of Axisymmetric Solids," AIAA J., Vol. 3, No. 12, pp. 2269-2274, Dec. 1965.

2. Witmer, E. A. and Kotanchik, J. J., "Progress Report on Discrete-Element Elastic and Elastic-Plastic Analyses of Shells of Revolution Subjected to Axisymmetric and Asymmetric Loading," AFFDL-TR-68-150, pp. 1341-1453, Proceedings of the Second Conference on Matrix Methods in Structural Mechanics, WPAFB, Ohio, October 1968.

3. McKnight, R. L., "Finite Element Cyclic Thermoplasticity Analysis by the Method of Subvolumes," Ph.D. Dissertation, University of Cincinnati, 1975.

4. McKnight, R. L. and Sobel, L. H., "Finite Element Cyclic Thermoplasticity Analysis by the Method of Subvolumes," Compt. Structures, Vol. 7, No. 3, 1977.

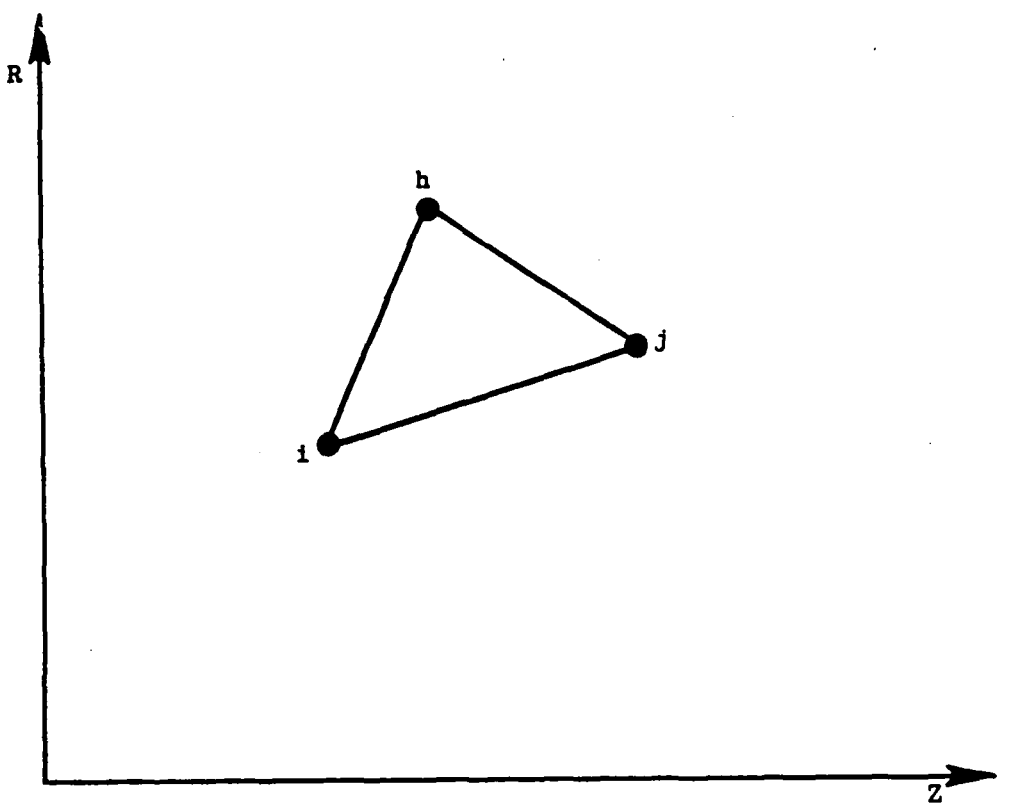

Figure 1. Finite Element Node Ordering.

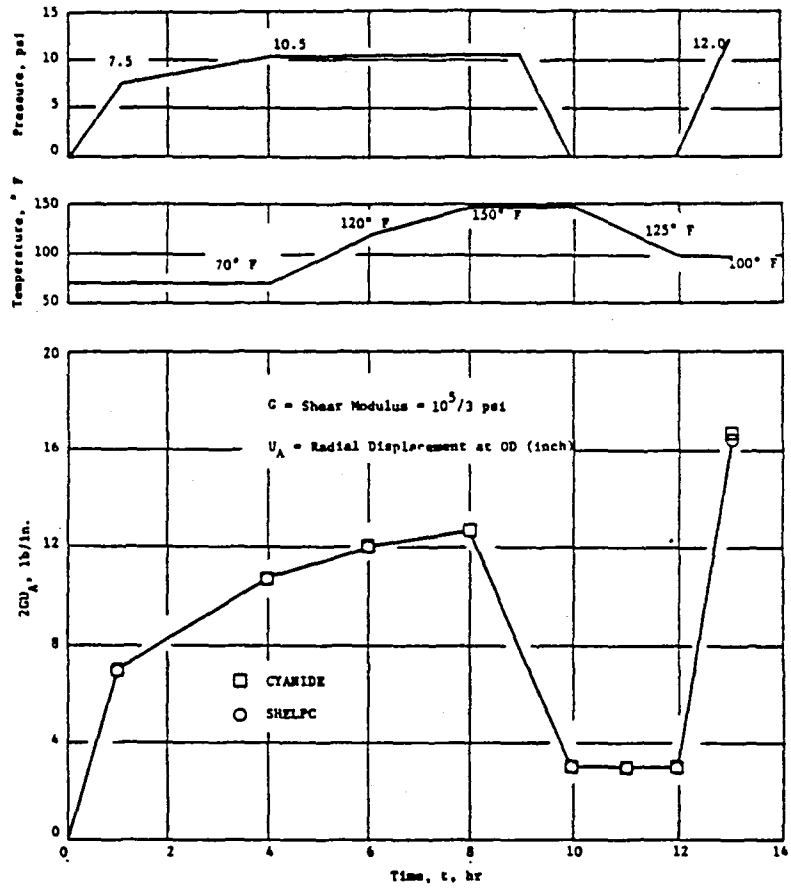

Figure 2. Load, Temperature History; Elastic-Plastic Displacement Response of a Thick-Walled Cylinder.

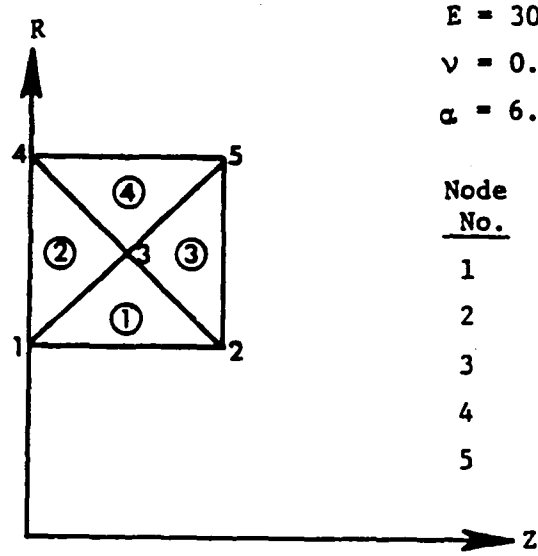

$E = 30 \times 10^6$ psi

$\nu = 0.3$

$\alpha = 6.0 \times 10^{-6}$ in/(in - ° F)

Node No.	R_i	Z_i
1	1.0	0.0
2	1.0	1.0
3	1.5	0.5
4	2.0	0.0
5	2.0	1.0

Figure 3. Thick-Walled Cyclinder Model Used for Combined Harmonic Loading Verification.

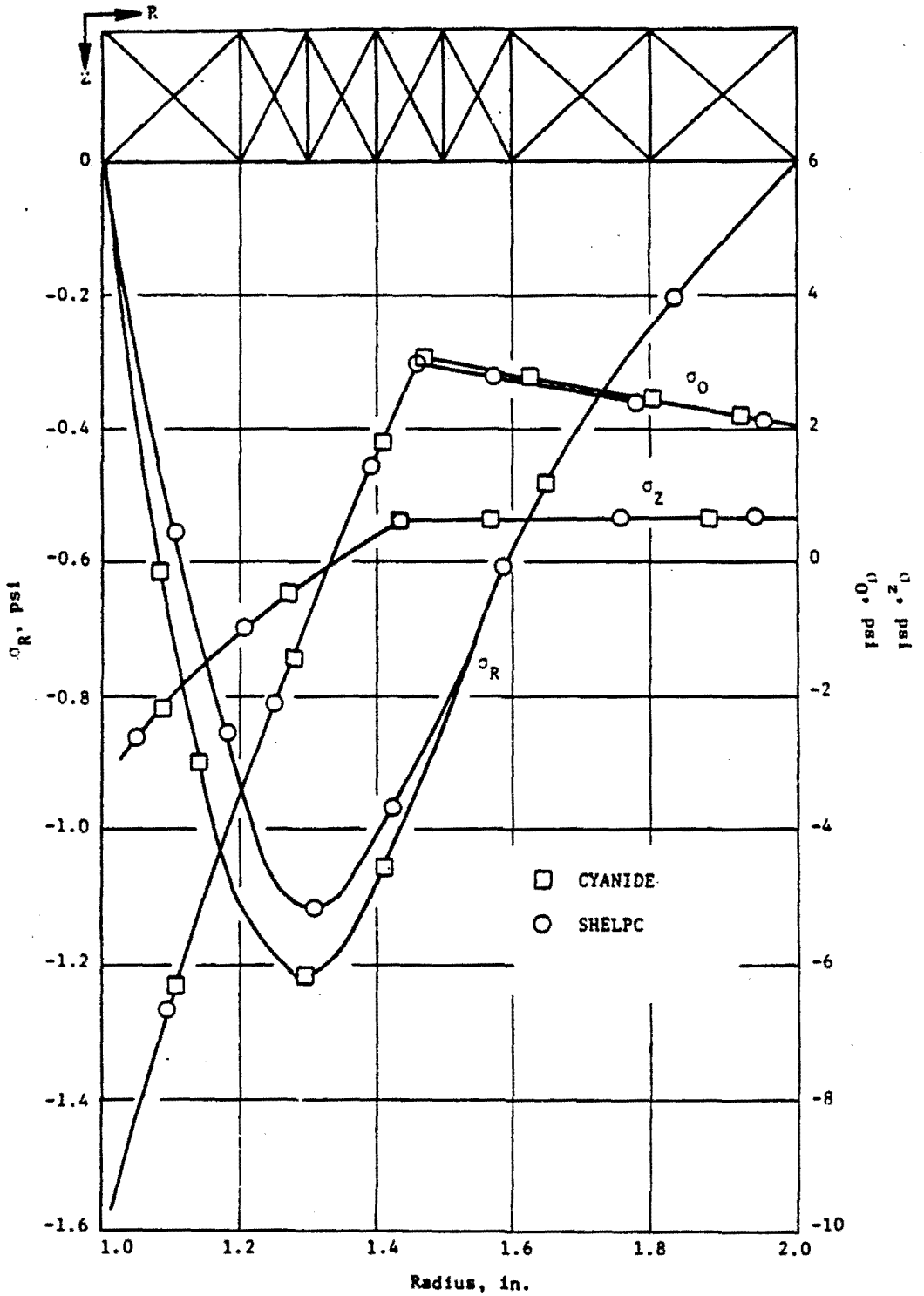

Figure 4. Residual Stress Distribution at Time = 10 hrs.

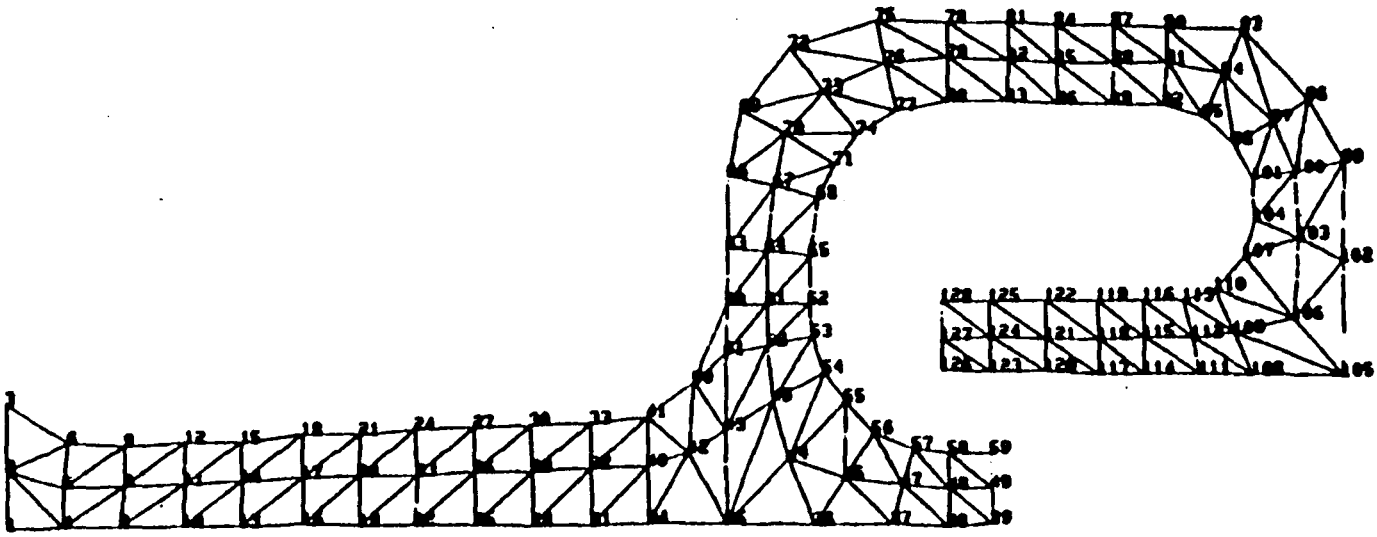

Figure 5. SHELPC Model for Combustor Lip.

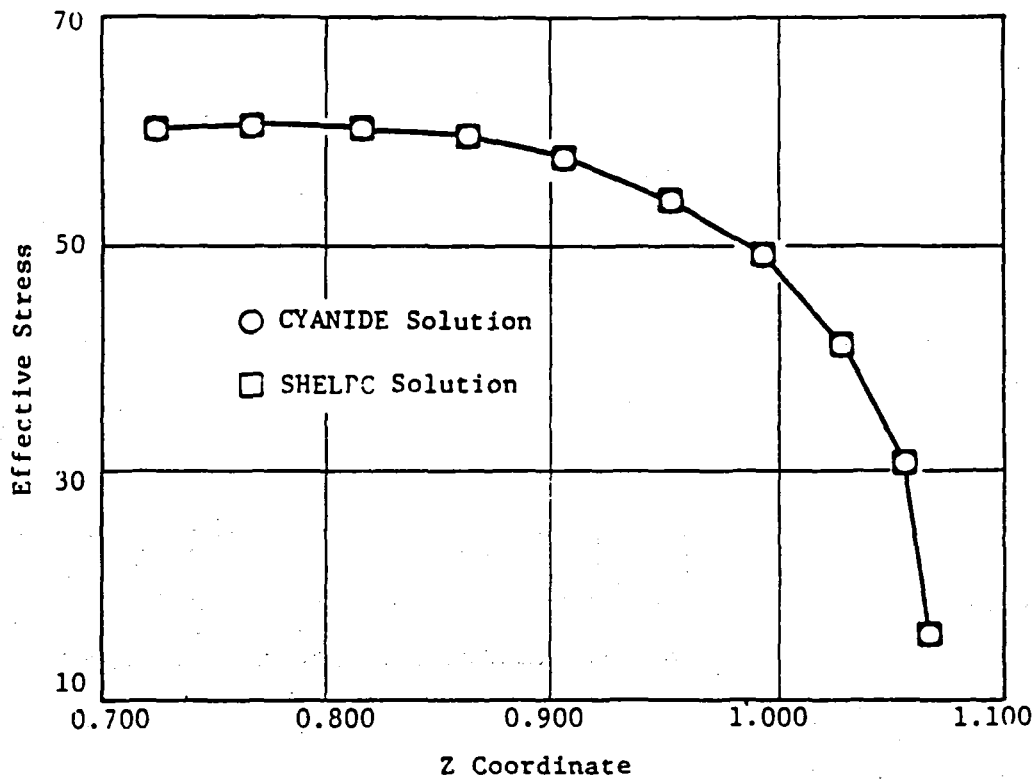

Figure 6. Effective Stress Comparison for Combustor Model.

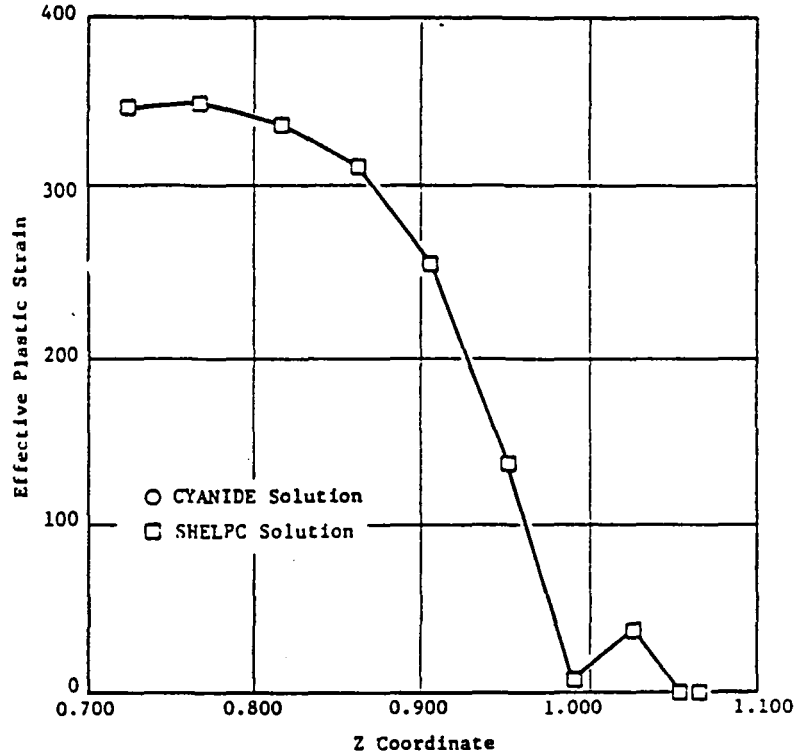

Figure 7. Effective Plastic Strain Comparison for Combustor Model.

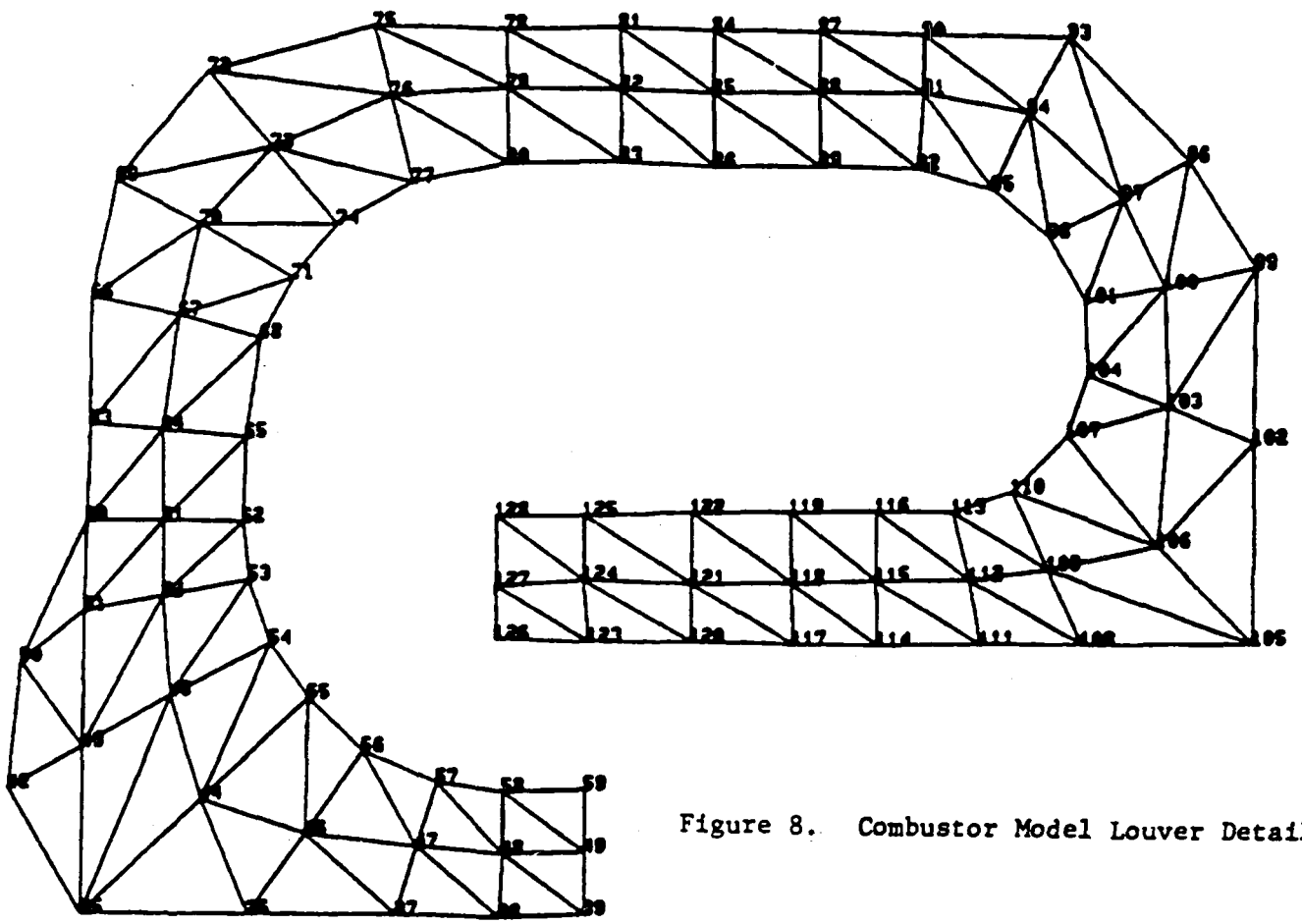

Figure 8. Combustor Model Louver Detail.

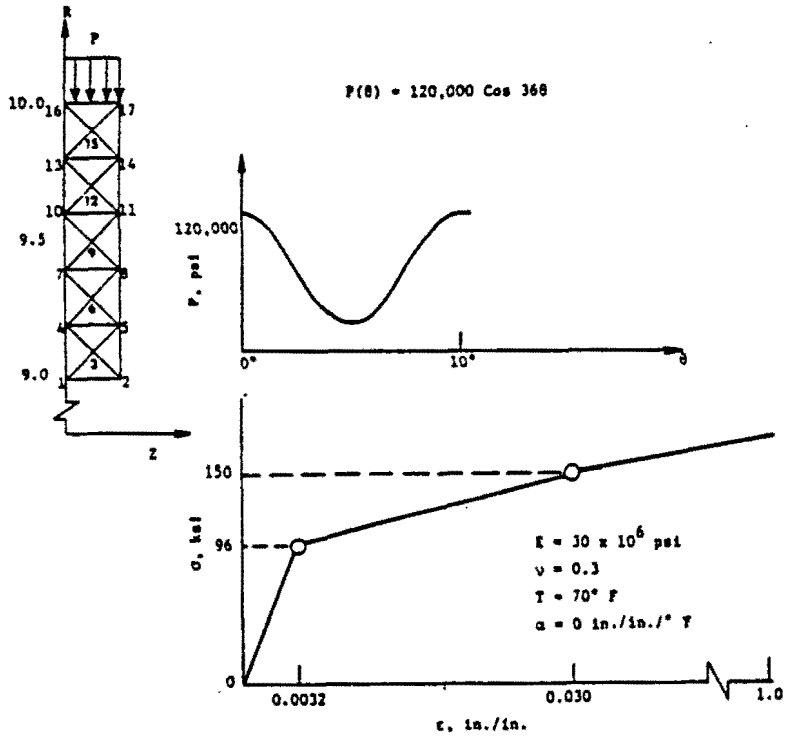

Figure 9. Ring Under Harmonic Pressure Load at OD.

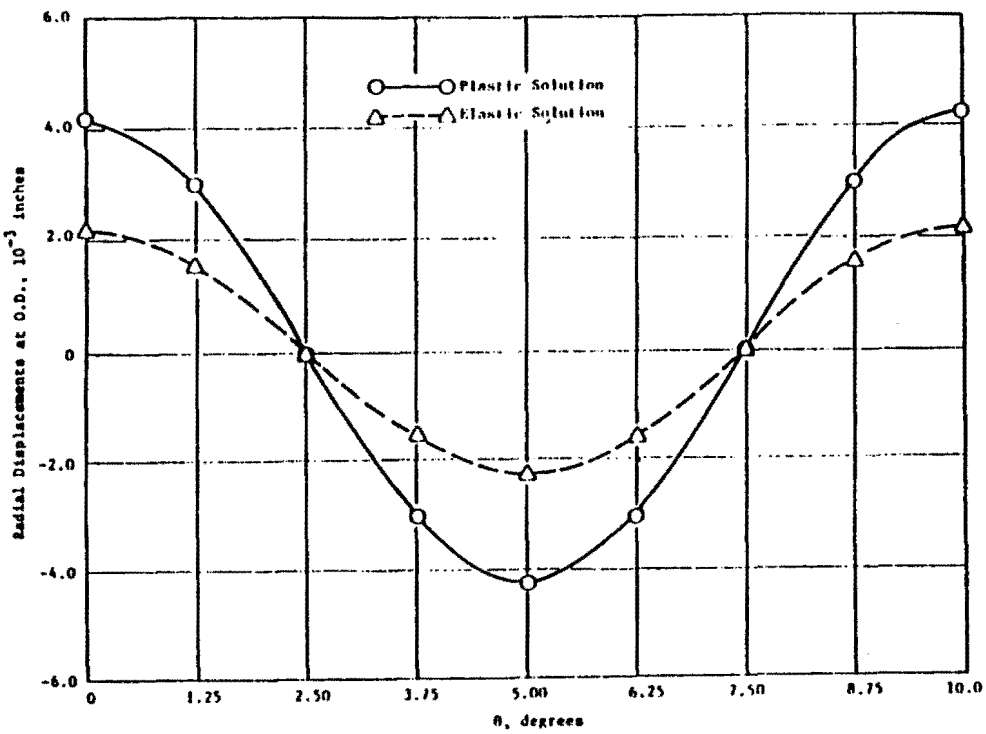

Figure 10. SHELPC Predictions of Radial Displacements.

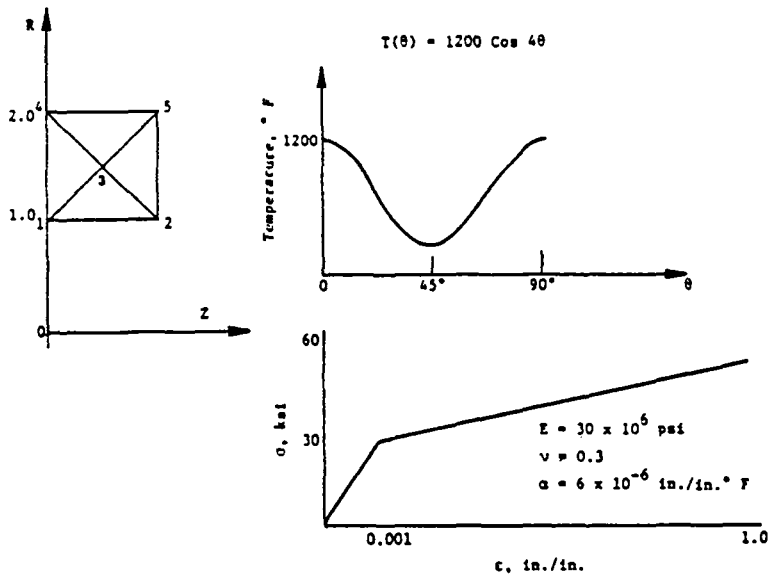

Figure 11. Cylinder Under Harmonic Thermal Load.

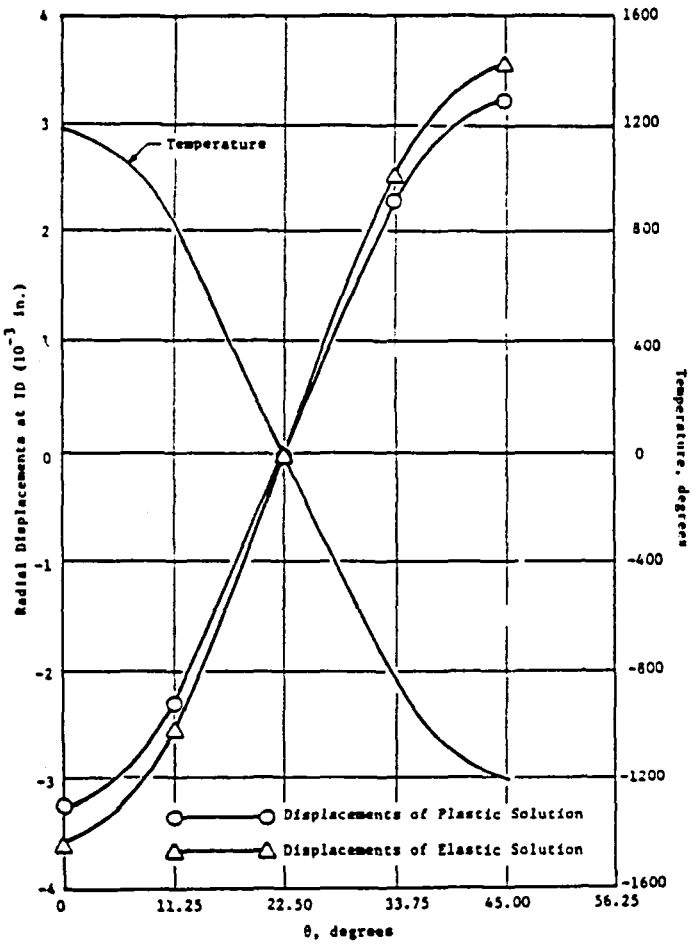

Figure 12. SHELPC Predictions for Hot Streak.

Page intentionally left blank

ANALYTICAL SIMULATION OF

WELD EFFECTS IN CREEP RANGE

A.K. Dhalla
Westinghouse Electric Corporation
Advanced Energy Systems Division
Madison, Pennsylvania 15663

The purpose of this paper is to present the inelastic analysis procedure used to investigate the effect of welding on the creep rupture strength of a typical Liquid Metal Fast Breeder Reactor (LMFBR) nozzle. The current study is part of an overall experimental and analytical investigation to verify the inelastic analysis procedure now being used to design LMFBR structural components operating at elevated temperatures. Two important weld effects included in the numerical analysis are: (a) the residual stress introduced in the fabrication process, and (b) the time-independent and the time-dependent material property variations. Finite element inelastic analysis was performed on a CRAY-1S computer using the ABAQUS program with the constitutive equations developed for the design of LMFBR structural components. The predicted peak weld residual stresses relax by as much as 40% during elevated temperature operation, and their effect on creep-rupture cracking of the nozzle is considered of secondary importance.

INTRODUCTION

A test facility was designed and built to perform thermal transient load tests on prototypic Liquid Metal Fast Breeder (LMFBR) Intermediate Heat Exchanger (IHX) inlet and outlet nozzles. Three prototypic nozzles forged from type 304 stainless steel were welded equidistantly around the circumference of the cylinder as shown in Figure 1.

All nozzles were subjected to internal pressure (p) and creep hold time (t) in a two stage creep-ratcheting test at a temperature of 1100°F (593°C): (a) Stage 1--p = 200 psi (1.4 MPa) and t = 1400 hours, and (b) Stage 2--p = 450 psi (3.1 MPa) and t = 3000 hours. One of the shell nozzles was subjected to a total of 26 thermal downshock transients; the remaining nozzles in the test article were baffled off and did not experience thermal transients. After each transient the pressure vessel was depressurized, repressurized, and uniformly heated and held at a temperature of 1100°F (593°C) for about 160 hours of creep hold time before initiating the next thermal transient. Post-test liquid dye penetrant examination revealed cracks parallel and perpendicular to the weld in the heat affected zone (HAZ) on nozzle side of all the shell nozzles. A metallurgical examination revealed that creep-rupture was the major cause of these cracks.

The investigation reported here is part of an overall experimental and analytical investigation to verify inelastic analysis procedures used to predict the creep ratcheting and the creep-rupture failure in welded structural components operating at elevated temperature. This paper presents only the analytical procedure used to investigate the weld residual stress relaxation and weld material property variation in a prototypic LMFBR-IHX shell nozzle. The following three specific areas are discussed:

1. selection of an appropriate 3-D mesh in the weld region.

2. representation of time-independent and time-dependent material response based upon uniaxial tensile and creep test data.

3. simulation of weld shrinkage due to weld cool-down.

The predicted peak effective, circumferential and longitudinal weld residual stresses relax by about 40% during elevated temperature operation, and their effect on cracking is considered of secondary importance. In subsequent discussion, the maximum weld residual stress parallel to the weld slice around the nozzle – cylinder intersection is designated as a circumferential stress, and the intermediate principal stress along the nozzle and perpendicular to the weld slice is designated as a longitudinal stress.

FINITE ELEMENT IDEALIZATION OF THE SHELL NOZZLE GEOMETRY

Three planes of symmetry were advantageously utilized to generate the refined finite element mesh shown in Figure 2 which represents the as-built nozzle geometry. The as-built nozzle sections were measured by the fabricator (Foster Wheeler Energy Applications, Inc.) after final machining but before the nozzles were welded to the cylindrical shell. The geometric dimensions of the as-built cross-sections of the nozzle were transferred via a Digitizing Tablet linked to the FIGURES-II interactive mesh generation program [1].* The finite element analysis was performed on a CRAY-1S computer using Version-4 of the ABAQUS computer program [2]. A reduced integration (2x2x2) scheme was used to obtain better accuracy at integration points than that predicted by the full (3x3x3) integration scheme [3]. The reduced integration option of the ABAQUS program uses a higher order (3x3x3) integration to form element stiffnesses and the distributed loads are integrated fully, but stresses and strains are calculated only at the reduced (2x2x2) integration points. To utilize computer resources more efficiently and to improve overall accuracy of predictions, it is preferable to use more elements in the nozzle weld region with reduced integration instead of using more integration points per element.

Boundary Conditions

In addition to the symmetric boundary conditions along the transverse, longitudinal and 60° symmetry planes shown in Figure 2, it was necessary to apply appropriate end cap pressure loadings and displacement boundary conditions to the finite element model. The pipe welded to the nozzle is

*Numerals in brackets designate references at the end of this paper.

quite flexible, hence the end cap pressure loading was applied to the pipe attachment of the nozzle without restraining the ovalization deformations of the nozzle end. In contrast, two hemispherical heads welded to the cylinder constrain free ovalization deformations of the cylinder ends. This effect was included in the analysis by constraining the circular cylinder end section to expand only axisymmetrically; end cap pressure was also applied to the cylinder end.

Convergence Study

Three elastic analyses were performed to evaluate the convergence characteristics of the 20-node isoparametric (tri-quadratic) element of the ABAQUS computer program. To select an economical mesh in the weld region internal pressure was applied to the nozzle. The three finite element models evaluated in this study are designated as:

1. I-Q1: Coarse surface mesh (72 elements), and one tri-quadratic continuum element through the thickness.

2. A-Q1: Refined surface mesh (108 elements) near the weld region, and one tri-quadratic element through the thickness.

3. A-Q3: Refined surface mesh (108 elements) near the weld region, and three tri-quadratic elements through the thickness.

The effect of weld region surface mesh refinement is shown in Figure 3. The component stress distributions predicted from the I-Q1 and A-Q1 models are in good agreement except near the weld. The surface mesh model I-Q1 is coarse and any as-built thickness variations are smoothed out. In contrast, the solid line stress distributions predicted by the A-Q1 analysis show significant irregular variation of stresses due to as-built thickness variations in the vicinity of the weld. The insert in Figure 3 shows the irregular thickness variation and slope discontinuity at the transverse section near the weld. The maximum change in thickness is from 1.19 to 1.29 inches (about 8%). The stress variations predicted by model A-Q1 near the weld are not directly proportional to the thickness because the stress distribution near the nozzle cylinder intersection is not uniform through the thickness and around the doubly curved nozzle surface.

The effects of mesh refinement through the thickness are illustrated in Figure 4, where the σ_x and σ_y stress components are plotted at the highly stressed welded location on the transverse section. The stress distributions predicted by the one and three element models (A-Q1 and A-Q3) with the same surface mesh of 108 elements are in good agreement. Similar good agreement was observed at other locations in the nozzle. Either of these two models would have been adequate for final analysis; however, the three element refined model (A-Q3) was selected for final inelastic analysis to include stress distributions through the thickness that would occur due to temperature variations during the simulated weld cool-down process.

MATERIAL MODEL FOR INELASTIC ANALYSIS

A spare nozzle forging of the same heat of material was sectioned to obtain tensile and creep material property data in circumferential and longitudinal directions from various locations in the nozzle forging. Thirteen short term tensile tests and six short term cyclic tests were performed on specimens extracted from the spare nozzle at temperatures ranging from 70 to 1100°F (21 to 593°C) to obtain time-independent stress-strain curves for elastic-plastic analysis. Twenty-two creep tests and nine relaxation tests were performed at two temperatures, 1050 and 1100°F (566 and 593°C), to obtain time-dependent creep properties. Four tensile and eight creep tests were also performed on uniaxial miniature specimens fabricated from the HAZ and the weld material. The test specimens were along the nozzle (longitudinal) and perpendicular to the circumferential weld slice.

The creep and tensile material test data indicate that properties change rapidly within a distance of 1 inch (25 mm) of the weld region of the nozzle-cylinder intersection. Although the change is continuous, from weld to HAZ to the nozzle forging base metal, in the finite element idealization it was necessary to simulate this change as a stepwise function. To simulate the observed material property variation at a reasonable computation cost, a five zone material model was developed for the nozzle side of the nozzle-cylinder intersection, where creep-rupture cracks were observed in the experiment. The creep-rupture cracks, as well as slip traces, were observed as far away as 0.5 in. (12 mm) from the weld. Material model presented in this paper reflects the nozzle material work hardening and other material property changes due to welding.

Time-Independent Material Model

The time-independent isothermal tension coupon tests conducted on the nozzle forging material at 1100°F (593°C) show a significant scatter in Figure 5. This figure displays both monotonic (first cycle) and tenth cycle test data, along with the ASME Code curves for type 304 stainless steel material. The base metal data are within the scatterband represented by the ASME minimum and average curves shown as solid lines. The curve designated as BASE METAL represents a reasonable average of specimens extracted from different locations in the nozzle forging. The nozzle weldment test results are designated as WELD and HAZ in Figure 5. To comply with the constitutive theory of linear kinematic hardening, it was necessary to bilinearize the stress strain curves obtained from the weld, HAZ and base metal of the nozzle. Figure 6 shows the decrease in bilinear yield stress with respect to the distance from the weld.

Temperature in the weld region during weld cool-down varies from room temperature to 2000°F (1093°C). Therefore, to predict residual stresses it is necessary to include temperature dependence of material properties in the analysis. The tests performed on the nozzle material were not sufficient to develop a complete temperature dependent material model. Therefore,

engineering judgment was used to utilize and extrapolate the data available in the ASME Code. The material property variations presented in [4 to 6] also provided guidance in the selection of the material model.

Temperature dependence of yield stress σ_y and plastic slope ($E_p = \Delta\sigma/\Delta\varepsilon_p$) are shown in Figures 7 and 8, respectively. The idealized variations to be used in analysis are shown as dotted lines. A finite, but small, value was assumed for both σ_y and E_p at 2000°F (1093°C). At that temperature the material is liquidus and cannot sustain significant stress. For weld and the HAZs, the variations with respect to temperature were assumed to be the same as those for the base metal up to 1500°F (816°C); thereafter, the corresponding values at 1500°F (816°C) were linearly connected to the finite value of 1 ksi (6.9 MPa) at 2000°F (1093°C). The temperature dependent material property variations of Young's Modulus E, Poisson Ratio, ν, and coefficient of thermal expansion, α are given in Table 1.

TABLE 1.-TEMPERATURE DEPENDENT MATERIAL PROPERTIES FOR TYPE 304 STAINLESS STEEL

MODULUS OF ELASTICITY (E)

$$E\ (ksi) = [28.31 \times 10^3 - 5.286\ (T-70)]\quad 70 < T < 700$$
$$= [24.98 \times 10^3 - 8.16\ (T-700)]\quad 700 < T < 1200$$
$$= [20.9 \times 10^3 - 24.88\ (T-1200)]\quad 1200 < T < 2000$$

POISSON'S RATIO (ν)

$$\nu = [0.2672 - 4.02 \times 10^{-5}\ (T-70)]\quad 70 < T < 2000$$

COEFFICIENT OF THERMAL EXPANSION (α)

$$\alpha\ (/°F) = [8.58 \times 10^{-6} + 1.82 \times 10^{-9}\ (T-70)]\quad 70 < T < 700$$
$$= [9.73 \times 10^{-6} + 1.13 \times 10^{-9}\ (T-700)]\quad 700 < T < 2000$$

Note: Temperature T is in degrees Fahrenheit.

Time-Dependent Creep Model

Twenty-two uniaxial constant load creep tests on specimens fabricated from the spare nozzle forging were conducted at stress levels ranging from 7.5 to 25 ksi (51.7 to 172.4 MPa). Eight additional creep and/or creep-rupture tests were also performed to obtain data for the HAZ and the weld region of the nozzle. Initially, attention was focused on developing an appropriate analytical representation from creep data obtained for the base metal. Thereafter, the analytical representation was extended to simulate the weld and HAZ creep data.

The experimental base metal data are compared in Figures 9a and 9b with available creep curves for type 304 stainless steel material. Typical comparisons are shown at only two stress levels: a low stress of 10 ksi (68.9 MPa) and a high stress of 20 ksi (137.9 MPa). The numerals 1 and 2 designate the single exponential (1-Exp.) and the double exponential (2-Exp.) creep equations developed for specific heats of type 304 SS material. The letters A and O designate the "ORNL ALL DATA" and "1000 HOUR DATA" creep equations developed by Oak Ridge National Laboratory for a specific heat of type 304 SS material. The letter C designates the nozzle forging base metal creep data and the letter R designates the final best-fit rational polynomial creep equation used in this study. A comparison of uniaxial creep data and the available mathematical representations show that the correlation between measured data and the analytical curve 'R' developed for the present study is quite good.

The rational polynomial creep equation form selected for the present study is as follows:

$$\varepsilon_c = \frac{Cpt}{(1 + pt)} + \dot{\varepsilon}_m t \qquad (1)$$

where, ε_c is the total creep strain in %; C is the amount of transient creep strain in %; p is the primary creep parameter in 1/hr, which relates to sharpness of curvature of primary creep region; $\dot{\varepsilon}_m$ is the minimum creep rate in %/hr; and t is the elapsed time in hr. Booker, et al., [7] have developed functional relationships for C and p in terms of $\dot{\varepsilon}_m$, with $\dot{\varepsilon}_m$ having a term C_h' (lot constant) to adjust for differences between heats of the material.

The minimum creep rate, in Equation (1), is a known quantity that is obtained from each uniaxial creep test. Based upon $\dot{\varepsilon}_m$ and the average lot constant, C_h', the primary creep parameters C and p were calculated according to the relationships presented in [7]. The creep strains predicted by the rational polynomial creep equation (1) are compared with the experimental data in Figures 10a and 10b for the low and high stress levels. The measured creep strains (designated by a letter C) are not in good agreement with the rational polynomial predictions (designated by numeral 1), which were calculated according to the procedure presented in [7]. Consequently, it was necessary to adjust constants C and p in Equation (1) to obtain a better fit to the creep data, especially to the initial primary creep strain rates, which in the analysis would determine the relaxation of residual stress due to weld effects. Various combinations of constants C and p were examined. A

reasonable fit to creep data (designated by numeral 3 in Figures 10a and 10b) was obtained by adjusting the constants C and p. That is, to obtain curve 3 from curve 1, the constant C calculated as per [7] was reduced by a factor of 3 and the constant p was increased by a factor of 9. The adjusted rational polynomial creep equation (designated as curve 3 in these figures) is adequate to represent creep response of the nozzle forging material.

The uniaxial data obtained from the HAZ and the weld material indicate that the weld region is substantially stronger (lower creep rates) than the base metal. To develop a material model for the weld region, the creep equation constants C and p were appropriately adjusted to obtain reasonably smooth variations of creep rates between the weld and the nozzle forging. The rational polynomial creep curves for five zones in the weld region are shown in Figure 11. The nozzle forging and the weld metal analytical curves are designated by numerals 1 and 5, respectively.

The rational polynomial creep model developed here is considered adequate to simulate the creep response in the nozzle analysis, however, the actual properties used in the analytical model are difficult to justify in all respects because:

1. the extent of heat affected zone (HAZ) in the as-built nozzle cannot be defined accurately,

2. the size and the number of finite elements used in the analytical model to represent the weld region require discontinuous representation of the material properties, and

3. the scatter in uniaxial material data [8] requires some approximation in the analytical representation.

THERMAL LOADING TO SIMULATE RESIDUAL STRESSES DURING WELD COOL-DOWN PROCESS

The distribution and the peak amplitude of the residual stress introduced during the welding process depend upon many variables. A few of these variables mentioned in the literature [9 to 12] are: (a) plate thickness, (b) heat input, (c) rate of cooling (heat sink, surface convection and radiation, etc., in complex geometries), (d) shift in peak temperatures during the cooling process, (e) weld repair (if any), (f) geometric configuration of the weld groove, (g) number of weld passes, and (h) geometry and size of the welded component.

Temperature Profiles Developed for the Nozzle

The purpose of the present investigation is to evaluate the relaxation and subsequent redistribution of residual stresses during creep hold time of 1100°F (593°C). Consequently, it is not necessary to simulate accurately the residual stress distribution, and predict the peak residual stress in the nozzle. An overall simulation of residual stress distribution was

accomplished by specifying temperature distributions due to the last weld pass cool-down on the outside surface. Typical weld thermal cycle charts presented in the Welding Handbook [9] show that:

1. the cooling rate of a weld and the width of the corresponding HAZ can be controlled by manipulating energy input and preheat temperature,

2. the cooling rate increases with increase in plate thickness,

3. the time at elevated-temperature decreases with increase in plate thickness, and

4. the heat flow pattern changes from a two-dimensional flow for very thin plates to a three-dimensional flow for very thick plates. The heat flow change qualitatively explains the influence of plate thickness on cooling rates.

Figure 12, taken from [10], shows the weld cool-down rate measured with respect to time and distance for a 1.3 in. (33 mm) thick 26 in. (660 mm) diameter type 304 stainless steel butt welded pipe. The weld and geometric parameters for the welded pipe, although similar, are not the same as those used to fabricate the nozzle test assembly. Temperature profiles during weld cool-down were not measured in the nozzle experiment, therefore, the temperature distributions shown in Figure 12 were used to generate temperature profiles for the nozzle weld cool-down analysis. Time dependent temperature profiles along the nozzle are shown in Figures 13a to 13c for three layers (outside, middle, and inside) through the thickness of the weld region. These nodal temperature distributions along the nozzle are assumed to be circumferentially symmetric (axisymmetric with respect to the nozzle centerline).

Figures 13a and 13c show that the temperature decreases rapidly away from the weld and within 50 seconds the highest temperature of 800°F (427°C) is below the creep range of type 304 stainless steel. Also the temperature decreases below 800°F at a distance of about 0.5 inch (13 mm) away from the edge of the weld. The analytical simulation of the nozzle weld cool-down process shown in Figures 13a to 13c is consistent with the temperature measurements presented in [9 and 10]. The metal temperatures up to a distance of about 0.8 in. (20.3 mm) from the welded hot spot decrease with elapsed time, whereas the metal temperatures at distances greater than 0.8 in. (20.3 mm) increase with elapsed time, up to about 50 seconds, before reaching a steady state uniform temperature distribution of 200°F (93°C). To further simplify the analysis, the weld deposition (heat-up) process was not simulated. The justification is that at the end of heat-up the weld would be liquidus at temperatures above 2000°F (1093°C), and would not be able to sustain significant stresses before it cools down.

Loading History for Weld Residual Stress Analysis

The following steps summarize the loading history used to perform the inelastic analysis:

1. Assume an initial stress-free state at a time less than 3 seconds for temperature distribution shown in Figures 13a to 13c, with 200°F (93°C) uniform temperature away from the weld.

2. Apply temperature distributions at times of 20 sec., 50 sec., and greater than 2000 secs. to simulate the weld cool-down process.

3. Heat-up to 1100°F (593°C) uniform operating temperature, hold at elevated temperature (without pressure) for 156 hours and cool-down to 70°F (21°C) ambient temperature.

INELASTIC ANALYSIS RESULTS

The inelastic analysis was performed in accordance with the constitutive equations recommended in [13] for the LMFBR structural components operating at elevated temperature. Figures 14a to 14c show deformations of the nozzle at the end of 156 hours of creep hold time. These deformations include free thermal deformations of the nozzle. The dotted lines in these figures represent the original nozzle geometry and the solid lines show the deformed shape, where the displacements are magnified 100 times. Figure 14a shows the overall deformations, whereas Figures 14b and 14c show two deformed sections along the length of the nozzle: (a) longitudinal section and (b) transverse section. The weld shrinkage effects are clearly seen in these figures. At distances away from the weld, free thermal expansion deformation is large but the differential thermal deformation between contiguous elements is small. Consequently, the residual stresses away from the weld region are small. Thus the stress distribution of interest is around the weld slice--a circumferential set of elements around the nozzle-cylinder intersection.

Figure 15 shows distribution of two principal stresses (circumferential and longitudinal) around the nozzle weld slice. The maximum principal residual stress is in the circumferential direction. Two curves for each principal stress in this figure show that the residual stresses decrease when the test article is uniformly heated from 200°F (93°C--cold state) to an operating temperature of 1100°F (593°C--hot state). At 200°F (93°C) the residual stresses are on the yield surface; at the 1100°F (593°C) operating temperature the yield surface shrinks and residual stresses decrease to satisfy the flow rule of the material.

Residual Stress Distribution

Figures 16 and 17 show the circumferential stress and effective plastic strain distributions along the longitudinal and transverse sections. The stress and strain predictions are plotted at the boundary of two contiguous finite elements as an average of two integration points to present smoothed stress distribution in these figures. The distributions are displayed along the inside surface of the longitudinal section in Figure 16, and along the outside surface of the transverse section in Figure 17.

The stress and strain profiles along the length of the nozzle, shown in Figures 16 and 17, indicate that the peak stress levels are predicted near the weld as anticipated. At the end of creep hold time of 156 hours the peak residual stresses near the weld region relax by as much as 40%. Longitudinal and effective peak stresses also relaxed by about the same amount. The maximum plastic strain of about 1.4% is accumulated at the transverse section of the weld slice (Figure 17). The residual stress relaxation predicted here is consistent with relaxation results presented in [14 and 15] for circumferentially welded pipes.

After completing the weld cool-down analysis, the nozzle was subjected to the internal pressure loadings and creep hold times recorded in the experiment. The creep-rupture predictions, which will be presented in a separate paper [16], indicate that the observed creep-rupture cracking parallel to weld is not due to the presence of weld residual stresses. The maximum principal residual stress is parallel and not perpendicular to the observed circumferential cracking on the outside surface. The secondary importance of residual stress on cracking can also be judged by the fact that the weld residual stresses relax rapidly during creep hold time. In contrast, the internal pressure stresses do not relax significantly and the maximum principal pressure stress is aligned perpendicular to the observed cracking. Therefore, the primary cause of cracking observed in the experiment is due to the pressure stresses [16].

CONCLUDING REMARKS

A 3-D finite element model consisting of 324 tri-quadratic elements of the ABAQUS computer program was used to predict residual stresses in a prototypic LMFBR nozzle. The weld shrinkage effects and the residual stresses were simulated numerically by specifying time-dependent temperature profiles for the nozzle weld. The variation of time-independent and time-dependent analytical material models for the weld region were established from the uniaxial tensile and creep tests of the nozzle weldment material.

The deformation plots of the nozzle after weld cool-down qualitatively show that the analysis simulated the weld shrinkage effects very well. Two highly stressed regions where cracks were observed in the experiment were correctly identified by the analysis. The maximum residual stresses occur on either side of the weld, and attenuate away from the weld region. In the absence of experimental measurements, the residual stress distributions predicted by the inelastic nozzle weld analysis are considered reasonable, especially at highly stressed nozzle locations where the residual stresses are limited by the yield surface specified for the weld, HAZ and nozzle forging material. An important conclusion from this analytical study is that the peak residual stresses relax by as much as 40% during elevated-temperature operation.

The present study is part of an overall analytical investigation undertaken to evaluate the effect of weld residual stresses on creep-rupture failure of structural components operating in creep range. In a separate

paper [16] it is shown that the residual stresses raise the total stresses predicted in the internally pressurized nozzle; however, the observed circumferential cracking (parallel to weld) on the outside surface of the nozzle is parallel to the maximum principal residual stress.

A detailed evaluation of analytical predictions in [16] show that the effect of residual stresses on creep-rupture cracking is of secondary importance. The primary reasons for nozzle weld cracking are: (a) the principal pressure stresses which are perpendicular to the observed cracks and do not relax significantly during creep hold time, and (b) the weld effect in the form of higher HAZ and weld material yield strength with about the same or slightly lower creep-rupture strength than that of the base metal.

ACKNOWLEDGEMENTS

This paper is based upon work performed for the U.S. Department of Energy under Contract DE-AM02-76CH94000. The author expresses his appreciation to Dr. D. S. Griffin for his valuable comments during the course of this investigation.

REFERENCES

[1] FIGURES II User's Guide, Westinghouse R&D Center, Pittsburgh, PA, 1983.

[2] ABAQUS User's Manuals, Vols. 1-4, Hibbitt, Karlsson and Sorensen, Inc., Providence, RI, 1982.

[3] J. Barlow, "Optimal Stress Locations in Finite Element Models," Int. J. Num. Meth. Engng., 10, pp. 243-251 (1976).

[4] E. F. Rybicki, D. W. Schmueser, R. W. Stonesifer, et al., "A Finite-Element Model for Residual Stresses and Deflections in Girth-Butt Welded Pipes," Trans. ASME, J. Press. Vessel Tech., 100, pp. 256-262 (1978).

[5] M. J. Davidson, C. W. Lawton and R. W. Loomis, "Bimetallic Weld Residual Stress Field," in Properties of Steel Weldments for Elevated Temperature Pressure Containment Applications, MPC-9, pp. 175-182, American Society of Mechanical Engineers, New York, NY, 1978.

[6] Y. Ueda, K. Fukuda, and K. Nakacho, et al. "Basic Procedures in Analysis and Measurement of Welding Residual Stresses by the Finite Element Method," in Residual Stresses in Welded Construction and their Effects, pp. 27-37, The Welding Institute, London, England, 1977.

[7] M. K. Booker and B. L. P. Booker, "New Methods for Analysis of Material Strength Data for the ASME B&PV Code," in Use of Computers in Managing Material Property Data, MPC-14, pp. 31-64, American Society of Mechanical Engineers, New York, NY, 1980.

[8] V. K. Sikka, M. K. Booker, and C. R. Brinkman, "Relationship Between Short- and Long-term Mechanical Properties of Several Austenitic Stainless Steels," in Characterization of Materials for Service at Elevated Temperatures, MPC-7, pp. 51-82, American Society of Mechanical Engineers, New York, NY, 1978.

[9] C. M. Adams, Jr., "Heat Flow in Welding," in Welding Handbook, Vol. 1, Ch. 3, 7th Ed., pp. 80-98, American Welding Society, Miami, FL, 1976.

[10] F. W. Brust and R. B. Stonesifer, "Effect of Weld Parameters on Residual Stresses in BWR Piping Systems, Final Report, " EPRI-NP-1743, March 1981.

[11] W. J. Shack, W. A. Ellingson, and L. E. Pahis, "Measurement of Residual Stresses in Type-304 Stainless Steel Piping Butt Weldments, Phase Report," EPRI-NP-1413, June 1980.

[12] A. J. Giannuzzi, D. C. Bertossa, P. P. Hallila, et al., "Studies on AISI Type 304 Stainless Steels Piping Weldments for Use in BWR Application Fifth Quarterly Progress Report for April, May, June 1976," NEDO-20985-5, August 1976.

[13] C. E. Pugh and D. N. Robinson, "Some Trends in Constitutive Equation Model Development for High-Temperature Behavior of Fast-Reactor Structural Alloys," Nucl. Eng. and Des. 48, pp. 269-276 (1978).

[14] R. Fidler, "The Effect of Time and Temperature on Residual Stresses in Austenitic Welds," Trans. ASME, J. Press. Vessel Tech, 104, pp. 210-214 (1982).

[15] S. Nair, E. Pang, and R. C. Dix, "Residual Stress Generation and Relaxation in Butt-Welded Pipes," Trans. ASME, J. Press. Vessel Tech., 104, pp. 42-46 (1982).

[16] A. K. Dhalla, "Effect of Residual Stress on Creep-Rupture Strength of a Prototypic Welded Nozzle," (in preparation).

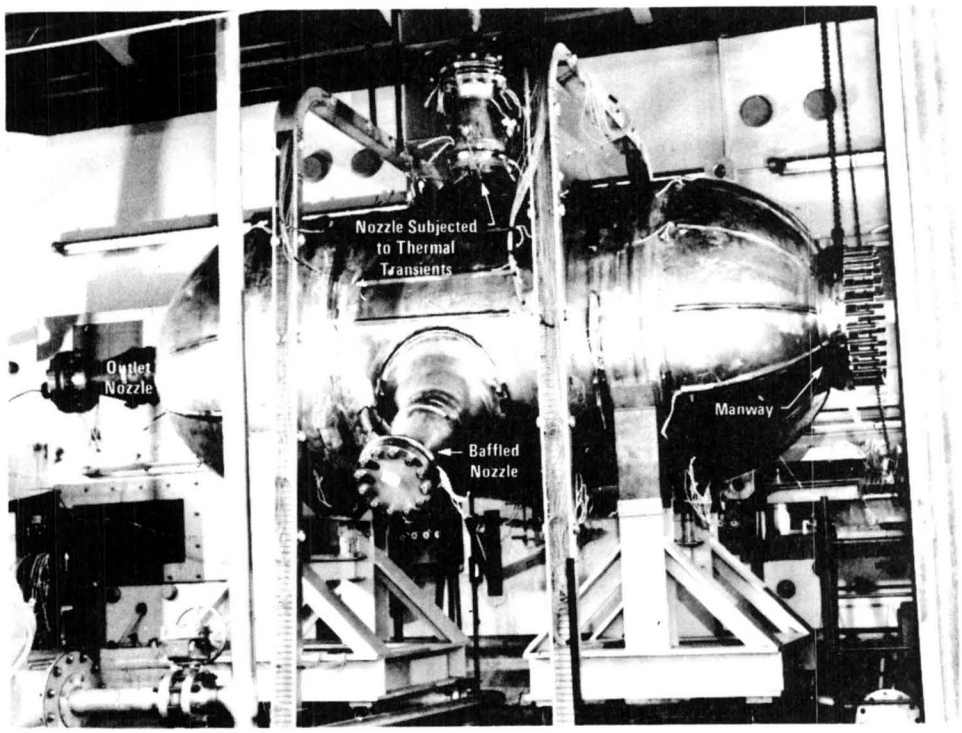

Figure 1. - Full Scale Pressure Vessel Nozzles were tested and analyzed to validate methods of analysis and design criteria

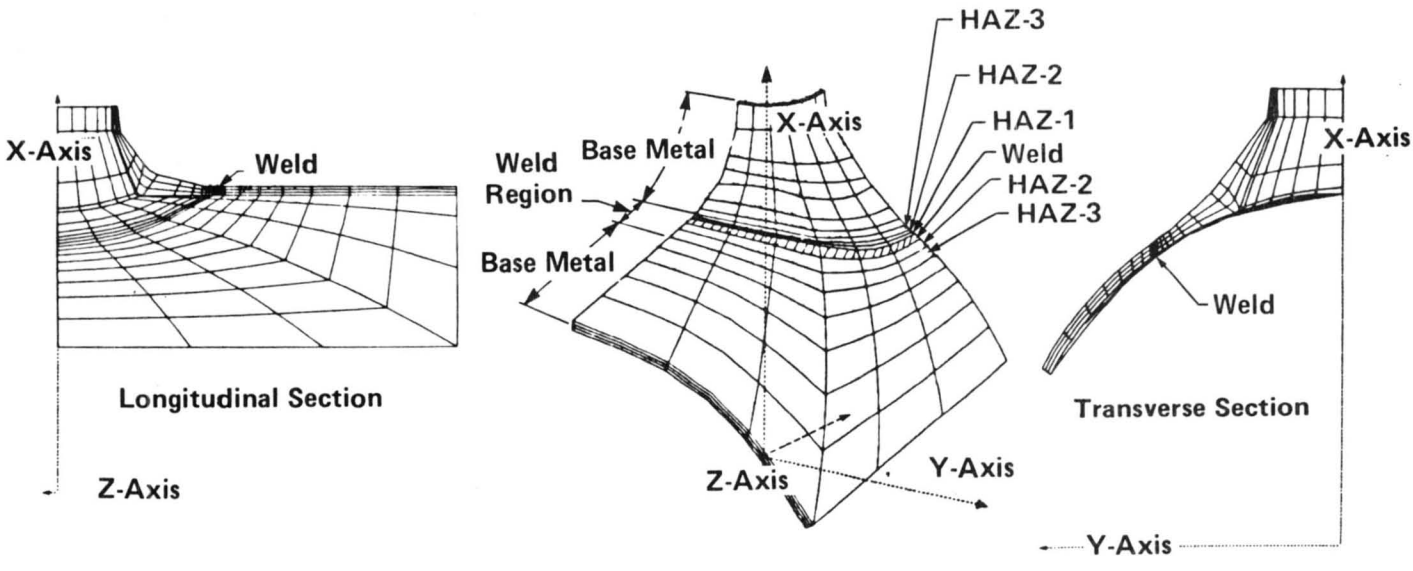

Figure 2. - Finite Element Idealization of As-Built Inlet Nozzle Geometry

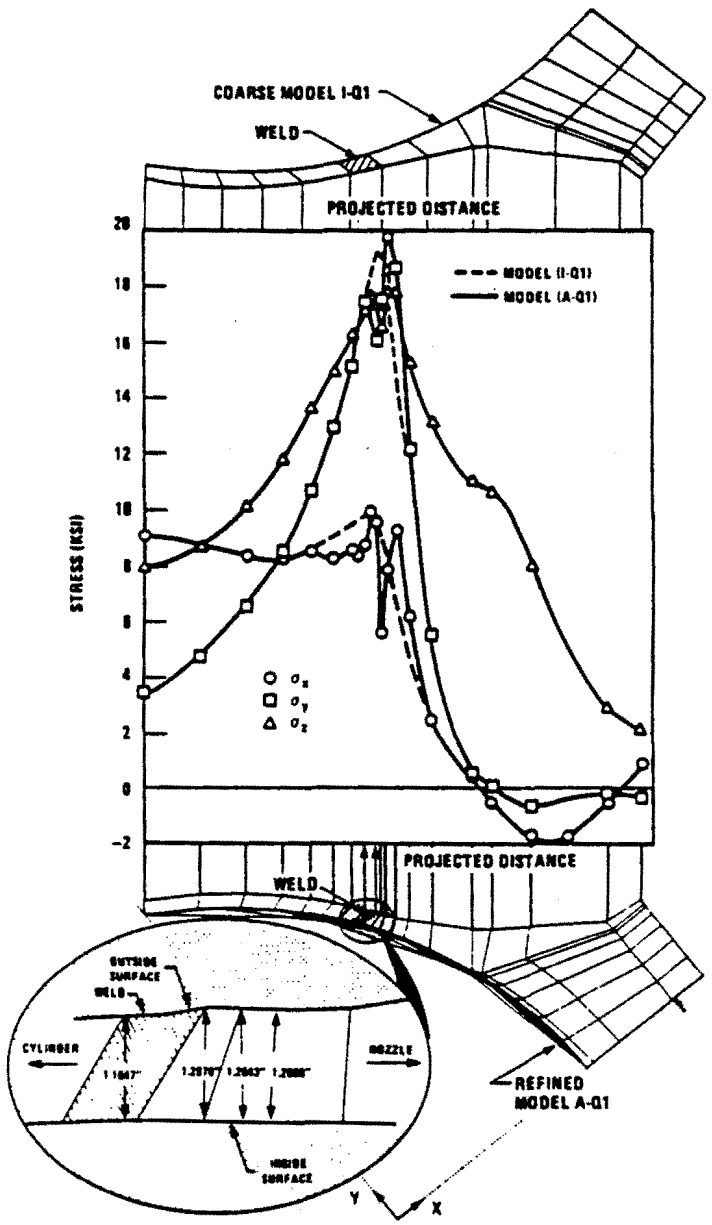

Figure 3. - Suface Mesh Refinement alters Stess Distribution near the Weld Region

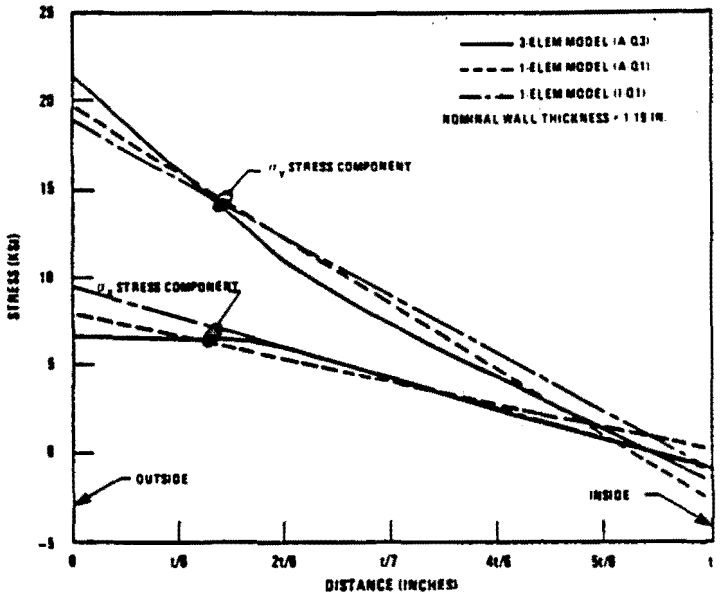

Figure 4. - Mesh Refinement through the thickness has small influence on stresses caused by internal pressure

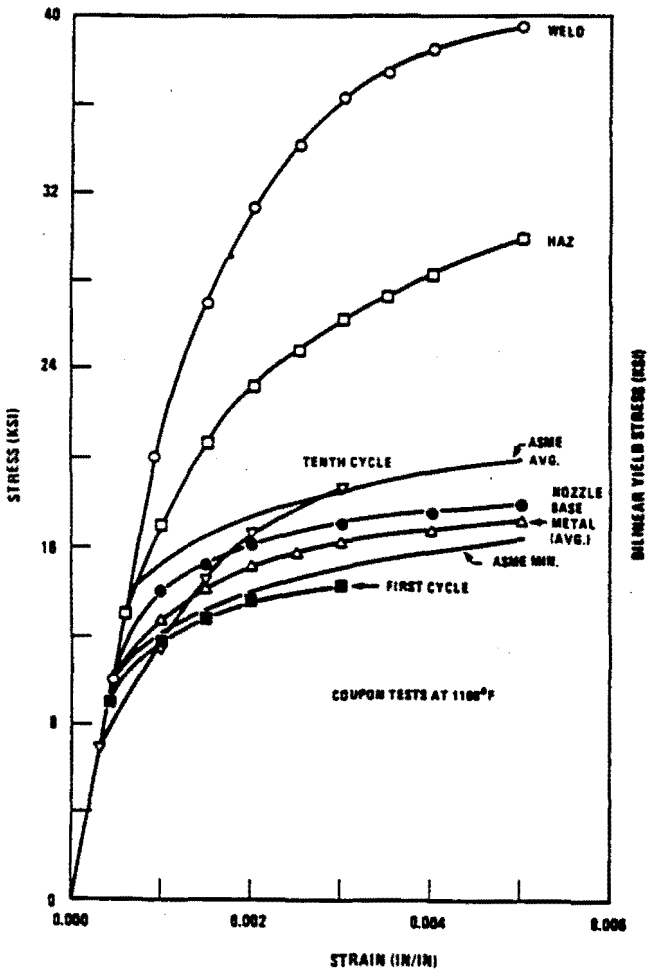

Figure 5. - Material Data obtained from Nozzle Forging

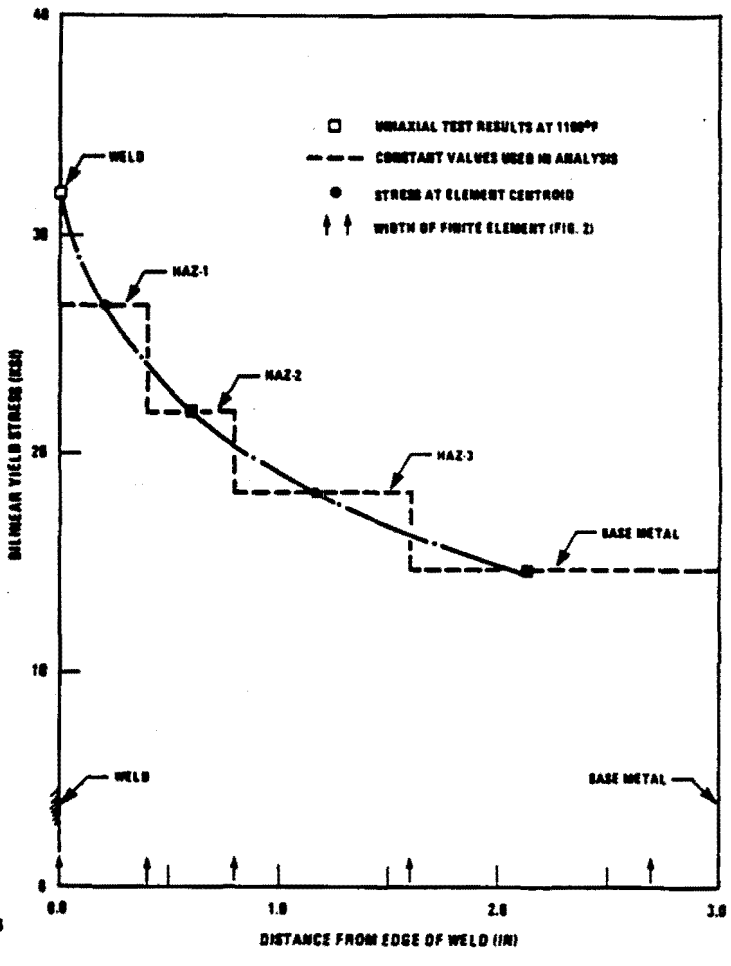

Figure 6. - Yield Stress decreases away from the Weld

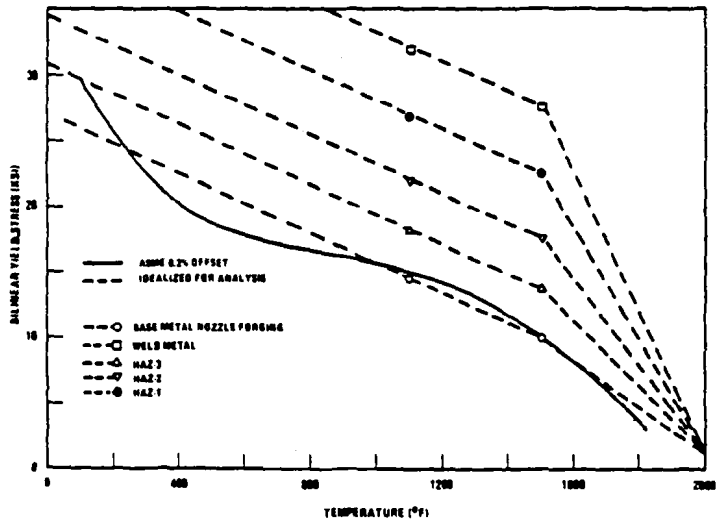

Figure 7. - Temperature Dependence of Yeild Stress, σ_y

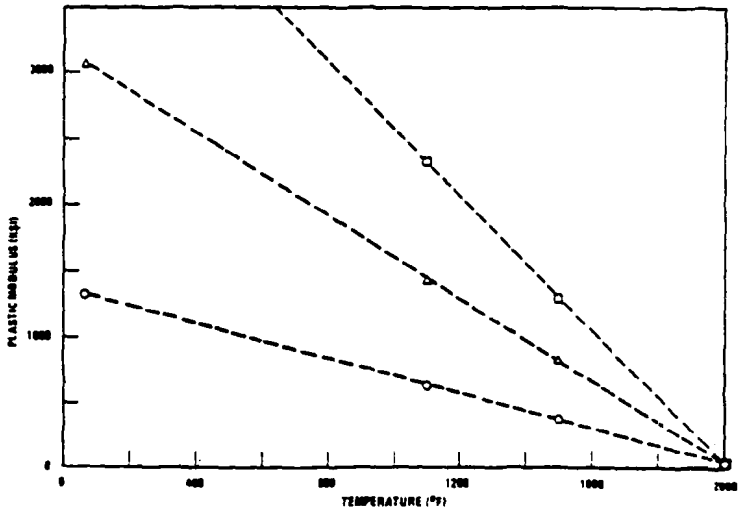

Figure 8. - Temperature Dependence of Plastic Modulus, E_p

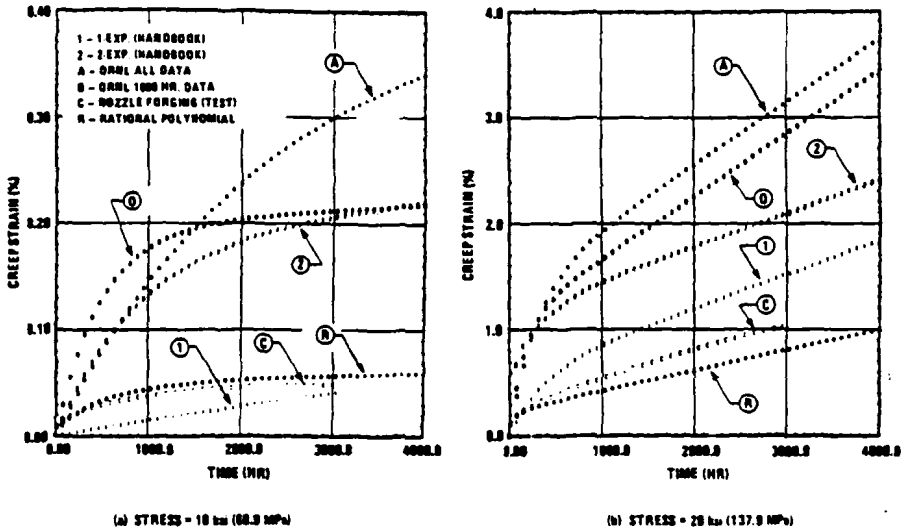

Figure 9. - Comparison of Base Metal Uniaxial Creep Test Data with 304SS Material Representations (593 ^{o}C)

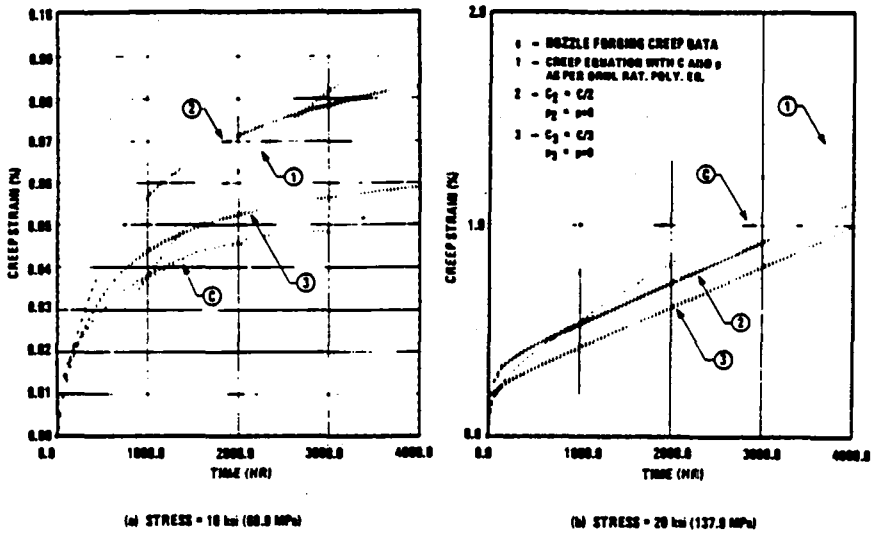

Figure 10. - Rational Polynomial Creep Equation Constants adjusted to fit Base Metal Test Data (593 °C)

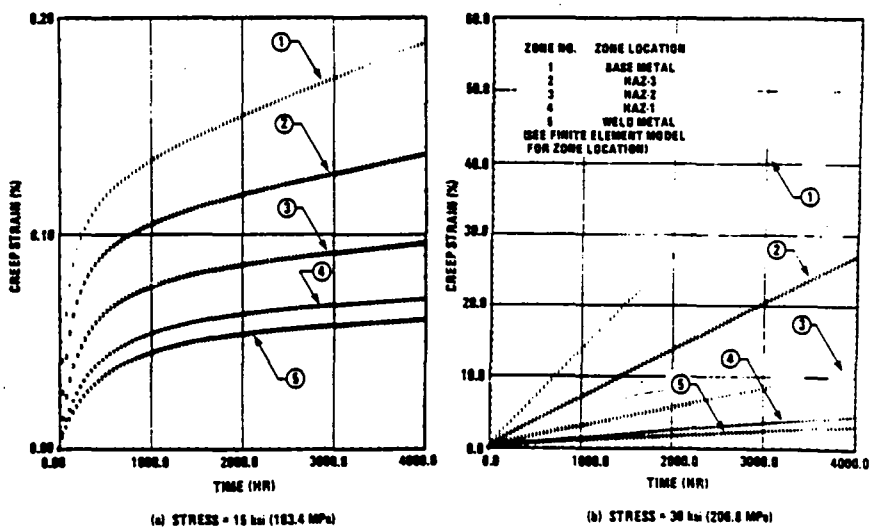

Figure 11. - A 5-Zone Rational Polynomial Creep Representation for Weld Region (593 °C)

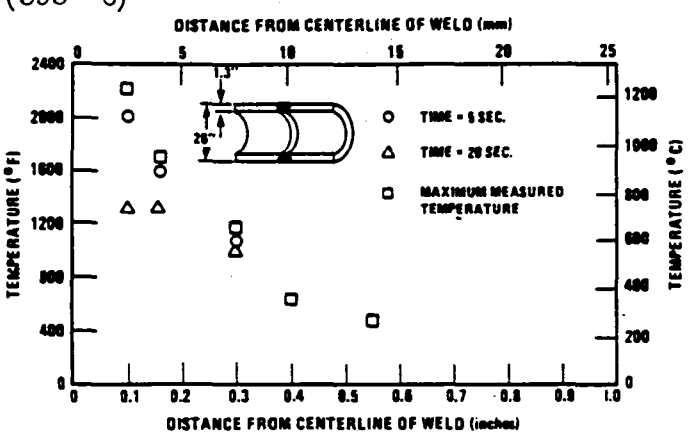

Figure 12. - Temperatures measured during Weld cool-down decrease rapidly with increase in time and distance away from Weld (ref. 10)

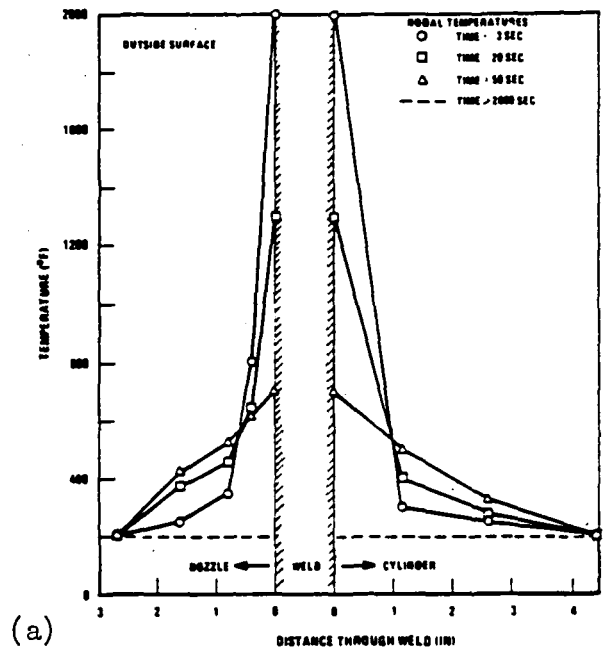

(a)

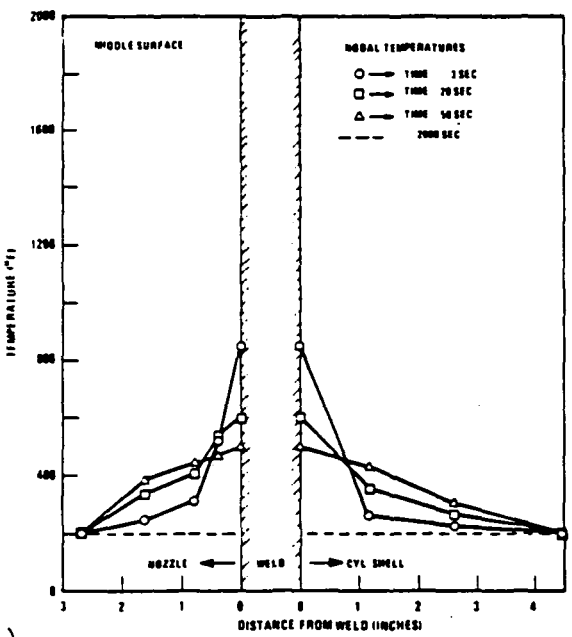

(b)

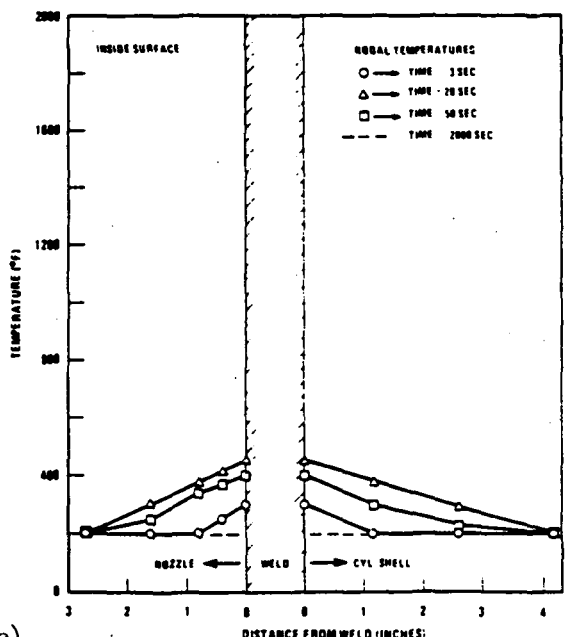

(c)

Figure 13. - Simulation of Weld cool-down temperature distribution

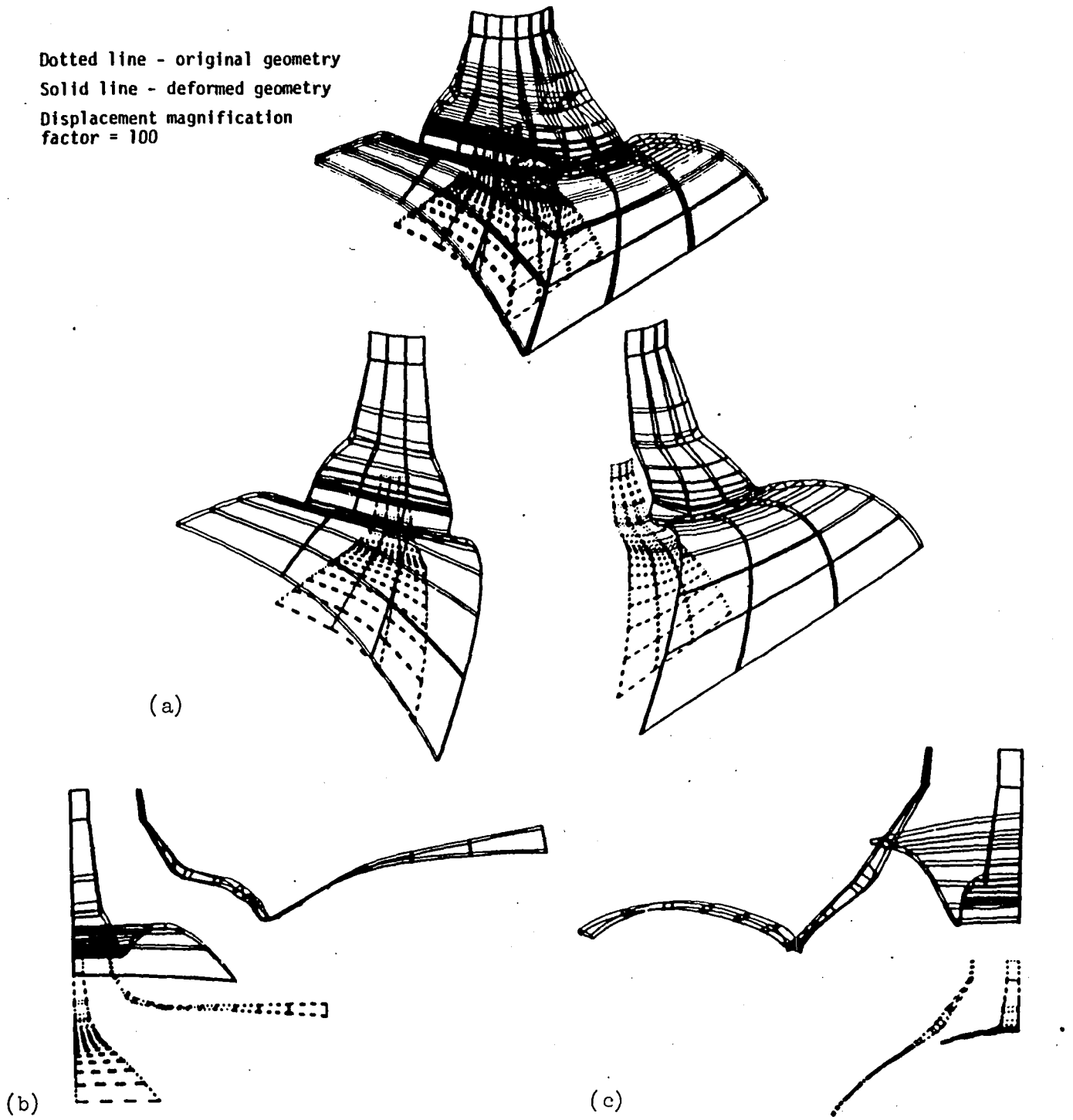

(a) Overall Weld shrinkage deformations

(b) Longitudinal section

(c) Transverse section

Figure 14. - Magnified Nozzle Deformation at the end of Weld cool-down (Includes 156 hours of Creep Hold at zero pressure)

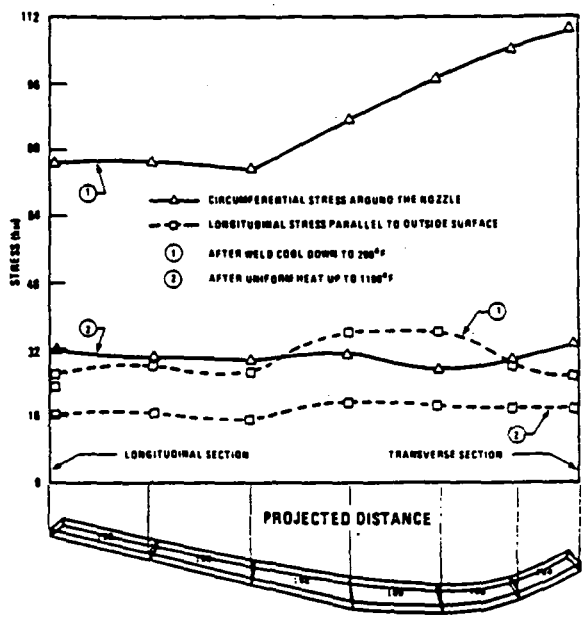

Figure 15. - Weld Residual Stress relaxes around the Circumferential Weld Slice (Nozzle HAZ Outside Surface)

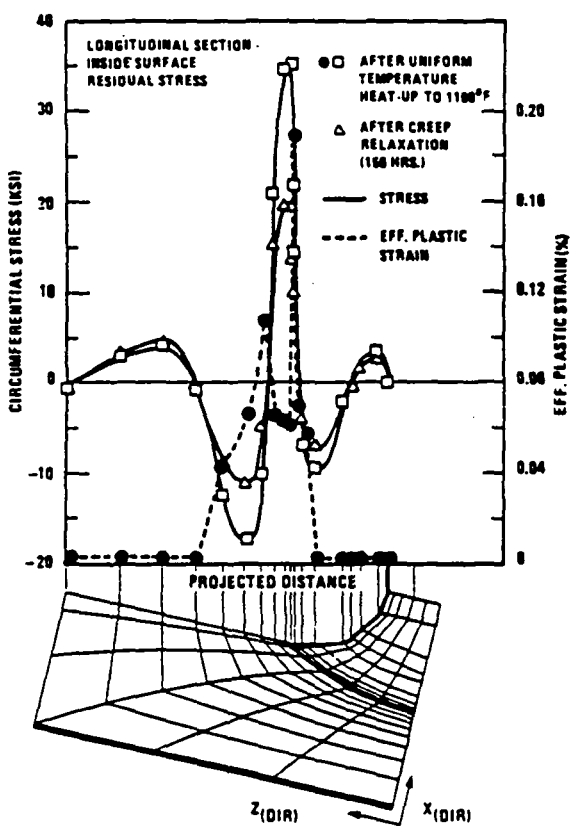

Figure 16. - Weld Residual Stress relaxes significantly during Creep Hold Time

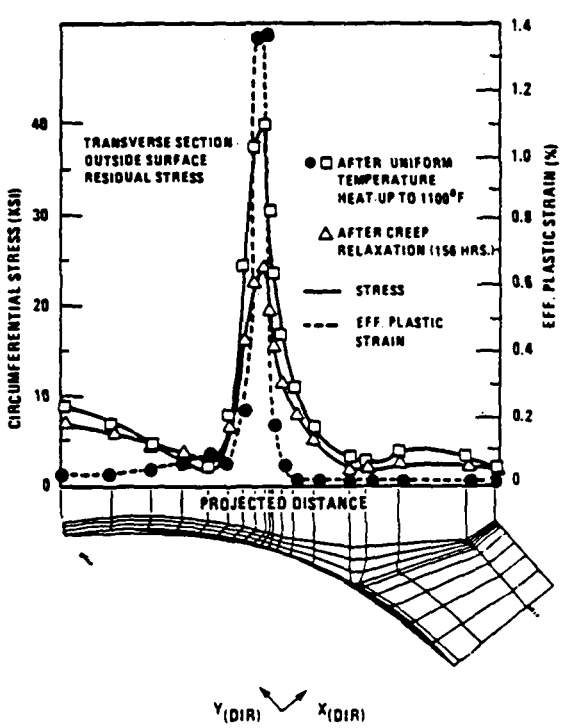

Figure 17. - Weld Residual Stress relaxes significantly during Creep Hold Time

CREEP CRACK GROWTH PREDICTIONS IN INCO 718 USING A CONTINUUM DAMAGE MODEL

Kevin P. Walker
Engineering Science Software, Inc.
Smithfield, Rhode Island 02906

Dale A. Wilson
Pratt and Whitney Aircraft
Government Products Division
East Hartford, Connecticut 06108

Creep crack growth tests have been carried out in compact type specimens of INCO 718 at 1200°F (649°C). Theoretical creep crack growth predictions have been carried out by incorporating a unified viscoplastic constitutive model and a continuum damage model into the ABAQUS nonlinear finite element program.

Material constants for both the viscoplastic model and the creep continuum damage model were determined from tests carried out on uniaxial bar specimens of INCO 718 at 1200°F (649°C).

A comparison of the theoretical creep crack growth rates obtained from the finite element predictions with the experimentally observed creep crack growth rates indicates that the viscoplastic/continuum damage model can be used to successfully predict creep crack growth in compact type specimens using material constants obtained from uniaxial bar specimens of INCO 718 at 1200°F (649°C).

INTRODUCTION

The Air Force and Pratt and Whitney Aircraft are developing technology to allow for an eventual damage tolerant design approach to turbine engine components and to retire existing components based on the detection of service initiated flaws. This approach is based heavily on the capability to predict the growth of flaws in critical structural components during the service life of the component. The majority of critical structural components operate at elevated temperatures where plasticity and time-dependent creep occur, particularly in regions of stress concentration and near the tips of fatigue cracks. Considerable research is currently being conducted on modeling crack growth behavior in engine materials. These research efforts require an understanding of crack tip behaviour in order to successfully evolve realistic crack growth criteria. Because of the complex inelastic behaviour, closed-form solutions to crack problems are not practical. An alternative approach is to use finite element methods for modeling test geometries. Such an approach, however, depends heavily on realistic constitutive models of the material behaviour as well as localized failure criteria for crack growth problems.

This paper presents some results on creep crack growth obtained under a contract [1] with the Air Force Materials Laboratory at Wright Patterson Air Force Base under the cognizance of Dr. Ted Nicholas. The Program involved the development of a constitutive model for INCO 718, a nickel-base alloy, at 1200°F (649°C) under monotonic, cyclic, and sustained loading. This model has the capability of accounting for load history effects as well as material failure or damage accumulation. The model has been incorporated into a nonlinear finite element program to simulate the crack growth behaviour in laboratory test specimens, and data have been generated to evaulate the applicability of the model. Development of the model was based on prior constitutive modeling efforts, and as such, primarily involved modifications and refinements to established approaches.

PROBLEM DESCRIPTION AND SOLUTION

At elevated temperatures the material in the vicinity of a crack tip can fail or rupture under creep (constant load) conditions due to the high stress concentration. To predict creep crack growth analytically it is first necessary to determine the stress-strain behaviour of the material in the vicinity of the crack tip. Once the stress and strain histories are known at a particular point, the time required to fail or rupture the material at that point can then be determined by a suitable failure criterion.

The theoretical effort makes use of a unified viscoplastic constitutive formulation to determine the time-dependent material behaviour in the crack tip vicinity, while a continuum damage model

is used to predict the time required to fail a particular point in the crack tip neighborhood. Both the viscoplastic constitutive model and the continuum damage model have been incorporated as a FORTRAN subroutine into the ABAQUS [2] general purpose nonlinear finite element program. When the continuum damage criterion dictates that the material at the Gaussian integration point in the finite element closest to the crack tip has failed, the node at the crack tip is released, and the crack advances to the adjacent node in the crack plane.

Under creep conditions the small amount of crack growth is difficult to determine by conventional experimental crack measuring techniques. Instead of measuring crack length as a function of time, the displacement of two points located on either side of the crack tip is monitored as a function of time by an optical interferometric displacement measurement technique. The nodes along the crack plane in the finite element model are released in such a manner that the computed displacements of the two points, due to both the viscoplastic material behaviour and the crack growth, matches the experimental displacements as time progresses. Crack length, as a function of time, then becomes a product of the finite element analysis rather than an input. Since the failure criterion under creep conditions is determined by a continuum damage model, the material constants in this model can be chosen to give a least square fit to the creep crack growth experiments in the INCO 718 compact type specimens at 1200°F (649°C) carried out under different applied loads. The material constants in the continuum damage model can also be determined to give a least square fit to the creep rupture data obtained from uncracked uniaxial specimens of INCO 718 at 1200°F (649°C). If creep crack growth is governed by creep rupture of the material directly ahead of the crack tip, then the material constants determined from the creep rupture experiments on the uncracked uniaxial specimens should coincide with those obtained from the creep crack growth experiments on the compact type specimens.

The use of combined experimental and theoretical procedures to determine crack growth criteria has been labeled the Hybrid Experimental-Numerical procedure by Kobayashi [3]. Hinnerichs and his colleagues [4] used this procedure to determine a creep crack growth criterion for IN 100 at 1350°F (732°C) from experiments carried out on a centre-cracked plate test specimen by Sharpe [5]. They found that a critical damage accumulation criterion for creep crack growth similar to that employed in the present work gave good correlation with the experiments conducted by Sharpe.

CONSTITUTIVE FORMULATION

Cyclic hysteresis loops and creep curves were generated for INCO 718 at 1200°F (649°C). Figure 1 shows a logarithmic plot of stress vs. inelastic strain rate from creep tests and cyclic hysteresis loops generated in the present work and from tests conducted by Domas, Sharpe, Ward, and Yau [6]. The plot shows the variation of secondary creep rate (or extension rate in a uniaxial hysteresis test) with applied stress. Discrepancies between the present data

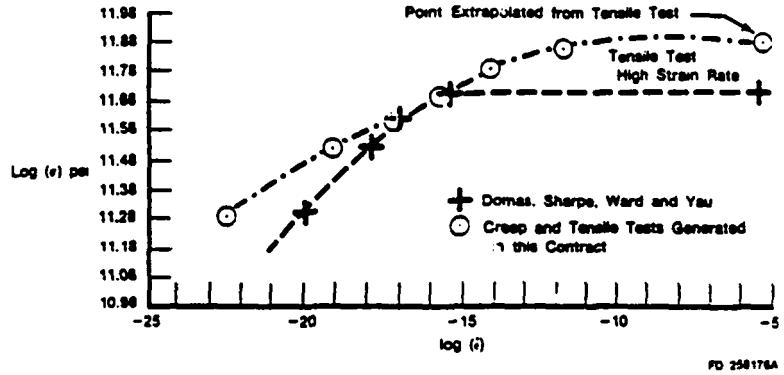

Figure 1. - Plot of Log (Stress) vs Log (Plastic Strain Rate) from Creep and Tensile Tests on INCO 718 at 649 °C.

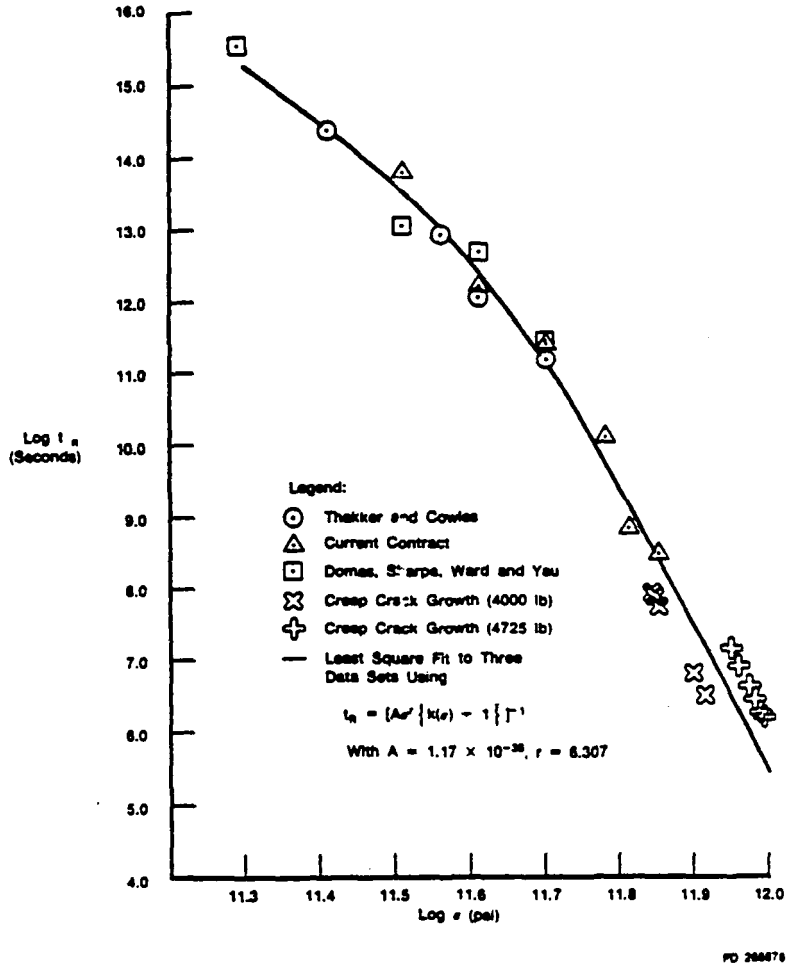

Figure 2. - Experimental Creep Rupture Data and Least Square Theoretical Fit

and that generated by Domas, et al [6], occur at both low and high stress levels. At high stress levels corresponding to the uniaxial hysteresis tests, the data points are estimates obtained by extrapolating the test data to obtain the ultimate stress values.

At high strain rates (in this context 10^{-4} to 10^{-3} per second) the material behaviour becomes insensitive to strain rate. This may be observed in the flattening of the logarithmic stress vs. inelastic strain rate curves shown in Figure 1, and is exhibited by the present data and by the data generated by Sharpe and his colleagues.

A power law expression [7] for the inelastic strain rate in terms of the applied stress and equilibrium stress was first fitted to the creep and hysteresis data. When fitting unified viscoplastic models to test data, the usual procedure is to assume that the functional form of the inelastic strain rate expression is correct, and that any deviation of the test data from the assumed functional form is due to thermal recovery of the state variables. In this manner the material constants for both rate effects and thermal recovery can be determined from the test data. A reasonable correlation of stress vs. strain rate was achieved with the power law at low to intermediate strain rates provided thermal recovery was taken into account. However, the power law may be expected to hold only over a relatively small strain rate range, and the stresses at high strain rates tend to be overestimated with a power law expression. This was clearly evident in the predicted stress results for strain rates of 5.3×10^{-4} per second and 5.3×10^{-3} per second used in the hysteresis loop testing. To obtain a better overall correlation of stress vs. strain rate, it was decided to use an exponential law for the inelastic strain rate in place of the power law. This provided a much better fit to the experimental data at all strain rates without including thermal recovery effects. Thermal recovery is present at 1200°F (649°C), but derive the current set of material constants, thermal recovery has been neglected. Table 1 shows the correlation between experiment and theory using the exponential constitutive formulation given in Appendix 1.

Table 1 *Stress vs Strain Rate With Exponential Law*

$\dot{\varepsilon}$ (Per Second)	σ (psi, Test)	σ (psi, Theory)
5.3 E-3	172000 (Extrapolated)	177536
5.3 E-4	—	164492
6.88 E-6	140000	140000
8.22 E-7	130000	127971
1.52 E-7	120000	118406
3.66 E-8	110000	110435
5.67 E-9	100000	100000
3.65 E-10	80000	86377

Table 2 *Creep Rupture Details of INCO 718 at 1200°F (649°C) Obtained in Present Contract*

Stress (ksi)	Strain on Loading: Elastic (%)	Strain on Loading: Inelastic (%)	Rupture Time (hr)	Final Elongation (%)	Reduction in Area (%)
140	0.506	0.639	1.4	8.2	12.6
135	0.610	0.607	2.0	9.0	14.2
130	0.251	0.151	6.9	7.4	12.2
120	0.279	0.056	25.5	10.5	16.2
110	0.292	0.006	56.7	8.0	13.2
100	0.286	0.0	281.1	13.4	41.9
80	0.277	0.0	Discontinued after 358 hr		

Table 3 *Creep Rupture Details of INCO 718 at 1200°F (649°C) Obtained by Domas, Sharpe, Ward, and Yau [5]*

Stress (ksi)	Rupture Time (hr)	Average Standard* Rupture Time (hr)
120	26	15
110	92	50
100	131	160
80	1583	1600

*C50TF6 Specification

Table 4 *Creep Rupture Details of INCO 718 at 1200°F (649°C) Obtained by Thakker and Cowles [8]*

Stress (ksi)	Strain on Loading: Elastic (%)	Strain on Loading: Inelastic (%)	Rupture Time (hr)	Final Elongation (%)	Reduction in Area (%)
120	0.597	0.060	20.1	12.1	15.9
110	0.581	0.012	48.3	14.8	52.3
105	0.476	0.009	116.0	23.7	56.8
90	0.450	0.005	494.8	28.0	61.3

Table 5 *Comparison of Theoretical and Experimental Creep Rupture Times*

Stress (psi)	Rupture Time Experiment (sec)	Rupture Time (sec) from $t_R=[A\,\sigma^r\{k(\sigma)+1\}]^{-1}$
140000	5040	5041
130000	24840	21000
120000	91800	85015
110000	204120	315123
100000	1011960	1011687

$A = 2.394 \times 10^{-43}$, $r = 7.22$, $k(\sigma) = 1 + 1.011E\text{-}4e^{9.446E\text{-}5\,\sigma}$

INCO 718 displays cyclic softening at 1200°F (649°C). The softening is observed in the decrease in the stress amplitude of the hysteresis loops as cycling proceeds under constant strain amplitude. It can also be observed in the increase in the width of the hysteresis loops under constant stress amplitude in fatigue testing. This cyclic softening can be modeled with the viscoplastic formulation at small cyclic strain amplitudes by allowing the drag stress state variable to decrease with cumulative inelastic strain. In the finite element creep crack growth calculations the drag stress was assumed to be constant and cyclic softening was not permitted. Material constants for the cyclic softening case and for the noncyclic softening case used in the finite element calculations are listed in Appendix 1.

Tertiary creep and creep damage accumulation have been included in the constitutive formulation by using Chaboche's continuum creep damage model [8]. Details of this model are given in Appendix 2. Experimental results of creep rupture time and creep rupture strain as a function of stress level are given in Tables 2, 3 and 4. A comparison of theoretical and experimental creep rupture times is given in Table 5.

Material constants for the creep damage model were determined from creep rupture tests on uniaxial bar specimens of INCO 718 at 1200°F (649°C). The specimens were given a standard heat treatment per specification AMS 5596C as follows:

Solution anneal at 1750°F (854°C) for one hour. Air cool to below 932°F (500°C). Age at 1325°F (718°C) for eight hours. Furnace cool to 1150°F (621°C). Age at 1150°F (621°C) for a total time of eighteen hours aging, cooling, and aging. Air cool to room temperature. The test material was furnished in the form of 0.5 in. (12.7mm.) thick flat plates having nominal dimensions 12x4 in. (305x102mm).

Figure 2 shows a logarithmic plot of stress vs. rupture time for the creep rupture tests performed in the current work and for creep rupture data generated by Domas et al [6] and by Thakker and Cowles [9]. The rupture time corresponding to an initial tensile stress level can be determined from the uniaxial form of the damage growth relation presented in Appendix 2. This relationship may be written in the uniaxial form

$$\frac{dD}{dt} = \frac{A\sigma^r}{(1-D)^{k(\sigma)}}. \tag{1}$$

Integration between the limit D=0 to D=1 gives the creep rupture time in the form

$$t_R = [A\sigma^r\{k(\sigma) + 1\}]^{-1}. \tag{2}$$

A least squares fit to the three data sets is achieved with the values

$$A=1.17\times10^{-38}, r=6.31, k(\sigma)=1+(1.011\times10^{-4})\exp(9.446\times10^{-5}\sigma).$$

This fit is shown as the solid line in Figure 2. For the data generated in the current work a least square fit is achieved with the values

$$A=2.394\times10^{-43}, r=7.22, k(\sigma)=1+(1.011\times10^{-4})\exp(9.446\times10^{-5}\sigma).$$

FINITE ELEMENT MODELING

The unified viscoplastic constitutive formulation including Chaboche's continuum creep damage model outlined in the appendices was incorporated into a FORTRAN subroutine of the ABAQUS general purpose nonlinear finite element program. The ABAQUS program solves the nonlinear finite element equilibrium equations by a Newton-Raphson iterative method. For quasistatic loading conditions the finite element equilibrium equations are solved in the form:

$$\Sigma\left(\int_{V} B^{T} J B \, dV\right) c^{k} = P(t+\Delta t) - \Sigma\int_{V} B^{T}(\sigma(t) + \Delta\sigma(\Delta u^{k}))dV, \tag{3}$$

$$\Delta u^{k+1} = \Delta u^{k} + c^{k}. \tag{4}$$

In these equations the matrix B transforms incremental nodal displacements to incremental strains according to the relationship

$$\Delta\epsilon = B\,\Delta u. \tag{5}$$

The stress increment for the unified viscoplastic constitutive formulation is a function of the strain increment, and is therefore a function of the nodal displacement increments via equation (5). Equation (3) provides the correction to the kth iteration for the displacement increment.

In order to implement the Newton-Raphson iterative method for solving the finite element equilibrium equations, it is necessary to provide the Jacobian matrix J in equation (3). This matrix is determined from the relationship

$$J = \left(\frac{\partial\sigma}{\partial\epsilon}\right)_{t+\Delta t}. \tag{6}$$

Since the differential form of the unified viscoplastic formulation results in a mathematically stiff system of differential equations, the stress increment resulting from a given strain increment must be determined by a subincrement method. The simplest method, and the one used in the present work, is to split the finite element increment into a number of equally sized subincrements and to integrate the viscoplastic equations over each subincrement with an Euler forware difference method. This can result in an unstable integration operator if the subincrement size is too large. In the FORTRAN subroutine the inelastic strain rate is determined by the forward difference representation of equation (1) of Appendix 3. If the magni-

tude of the argument of the exponential factor in equation (1) exceeds the value of thirty (30) in any subincrement, the integration procedure is stopped. The number of subincrements is then tripled and the subincrement integration procedure is restarted from the beginning. This procedure is repeated until no subincrement produces an exponential argument greater in magnitude than thirty.

Since the Jacobian matrix J cannot be obtained in algebraic form when a subincremental procedure is used, it is necessary to obtain this matrix numerically. A numerical Jacobian matrix is computed in the following manner. First the viscoplastic constitutive subroutine is entered to determine the stress increments $\Delta\sigma_{xx}$, $\Delta\sigma_{yy}$, $\Delta\sigma_{xy}$ corresponding to the strain increments $\Delta\varepsilon_{xx}$, $\Delta\varepsilon_{yy}$, $\Delta\varepsilon_{xy}$. Let $\Delta\sigma^{xx}_{xx}$, $\Delta\sigma^{xx}_{yy}$, $\Delta\sigma^{xx}_{xy}$ be the stress increments corresponding to the perturbed strain increments $\Delta\varepsilon_{xx}+0.01\Delta\varepsilon_{xx}$, $\Delta\varepsilon_{yy}$, $\Delta\varepsilon_{xy}$; let $\Delta\sigma^{yy}_{xx}$, $\Delta\sigma^{yy}_{yy}$, $\Delta\sigma^{yy}_{xy}$ correspond to the perturbed strain increments $\Delta\varepsilon_{xx}$, $\Delta\varepsilon_{yy}+0.01\Delta\varepsilon_{yy}$, $\Delta\varepsilon_{xy}$; and let $\Delta\sigma^{xy}_{xx}$, $\Delta\sigma^{xy}_{yy}$, $\Delta\sigma^{xy}_{xy}$ correspond to the perturbed strain increments $\Delta\varepsilon_{xx}$, $\Delta\varepsilon_{yy}$, $\Delta\varepsilon_{xy}+0.01\Delta\varepsilon_{xy}$. The numerical plane stress Jacobian is then determined from the matrix relation:

$$J = \begin{bmatrix} \dfrac{\Delta\sigma^{xx}_{xx} - \Delta\sigma_{xx}}{0.01\Delta\epsilon_{xx}} & \dfrac{\Delta\sigma^{yy}_{xx} - \Delta\sigma_{xx}}{0.01\Delta\epsilon_{yy}} & \dfrac{\Delta\sigma^{xy}_{xx} - \Delta\sigma_{xx}}{2(0.01\Delta\epsilon_{xy})} \\ & \dfrac{\Delta\sigma^{yy}_{yy} - \Delta\sigma_{yy}}{0.01\,\Delta\epsilon_{yy}} & \dfrac{\Delta\sigma^{xy}_{yy} - \Delta\sigma_{yy}}{2(0.01\Delta\epsilon_{xy})} \\ \text{Symmetric} & & \dfrac{\Delta\sigma^{xy}_{xy} - \Delta\sigma_{xy}}{2(0.01\Delta\epsilon_{xy})} \end{bmatrix} \quad (7)$$

Thus, the plane stress Jacobian matrix requires four calls to the viscoplastic constitutive subroutine at each Gaussian integration point in the structural model. One call is required to obtain the unperturbed stress increment, whilst three additional calls are required for each perturbed strain increment.

It is necessary to use the same number of subincrements in each of the four calls to the viscoplastic constitutive subroutine. Otherwise, the Jacobian matrix will contain components of "noise" resulting from the operation $\partial\sigma/\partial$(change in number of subincrements). For this reason it was not considered worthwhile to change the size of the subincrements by means of some self-adaptive error detecting method during the finite element integration step, since the size of each subincrement would have to be stored in order to use the same subincrement breakup in each of the perturbed strain increment calls to the constitutive subroutine. The simple procedure of

using enough subincrements to prevent the magnitude of the exponential argument from exceeding the value of thirty was therefore adopted.

In order to determine the number of subincrements to be used in the finite element integration step, the following empirical procedure was adopted. Let e denote the largest absolute value of either the xx, yy or xy components of the finite element strain increment for the case of plane stress. Numerical studies have shown that the forward difference integration procedure is generally stable provided the strain increment does not exceed the value of 10^{-4}. The number of subincrements for a given Gaussian integration point in some finite element in the structure is then determined as $e/10^{-4}$. In crack propagation experiments in a superalloy compact type specimen, the stress and strain increments are large only in the immediate vicinity of the crack tip. All other elements away from the crack tip vicinity generally experience small strain increments. Thus, in the element ahead of the crack tip, the Gaussian integration points may require 50 subincrements, while those elements further from the crack tip generally require only 2 or 3 subincrements.

If the finite element load increment is large, then all of the finite elements will require a large number of subincrements to integrate the constitutive relations. This will be the case for structures which are free of large stress or strain gradients. However, for cracked structures, the large stress and strain gradients in the vicinity of the cracks and stress risers prevent large finite element load increments from being taken. This arises from the fact that the large stress or strain gradients give a very small radius of convergence to the Newton-Raphson iteration method for solving the finite element equilibrium equations. This small radius of convergence of the iteration method for cracked structures is not peculiar to the Newton-Raphson method. During the present work a Picard, or successive substitution method (as used in the MARC program), was also used to solve the finite element equilibrium equations. For cracked structures the radius of convergence of this iteration method was also found to be very small. In addition, the rate of convergence for small increments with the Picard method is linear, whereas the rate of convergence of the Newton-Raphson method is quadratic. For this reason the Newton-Raphson iteration method for solving the finite element equilibrium equations for cracked structures appears preferable to the Picard successive substitution procedure.

The fact that small finite element increments must be used to solve the equilibrium equations for cracked structures implies that most of the structure is subjected to very small finite element strain increments. One or two subincrements are then required for most of the Gaussian points in the structure, and it is doubtful if more refined integration methods (implicit) are required for these structures.

CREEP CRACK GROWTH MODELING

Experimental creep crack growth data have been generated by loading compact type specimens of INCO 718 with applied load levels of 4000 lb. and 4725 lb. at 1200°F (649°C). It is difficult to measure crack length as a function of time on the surface of the compact type specimen with any accuracy due to the fact that the amount of crack growth is usually very small, and the crack may grow internally in the specimen without associated surface crack growth. Instead of measuring creep crack growth directly, displacements across the crack were measured as a function of time at the two points shown in Figure 3 by means of speckle interferometry. Finite element calculations were then used to determine the theoretical creep crack growth rate with computed displacements at the two speckle interferometry points which agree with the experimental measurements. Crack growth versus time is then obtained indirectly from the analytical results in the manner employed by Hinnerichs et al [4].

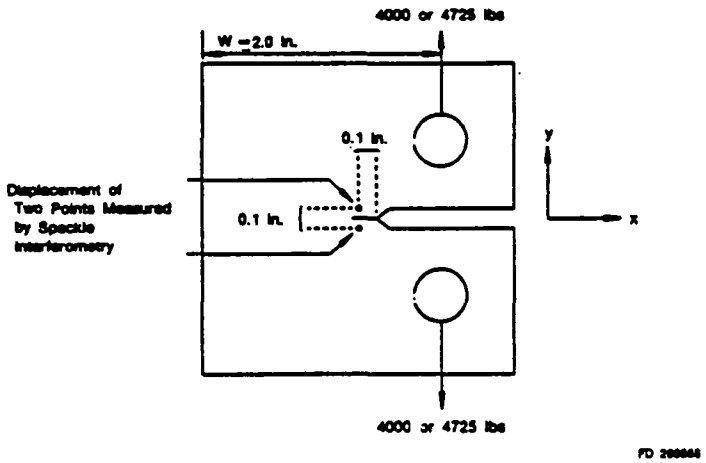

Figure 3. - Location of Two Points on Either Side of the Crack Where Displacement is Measured by Speckle Interferometry

The computations were made using plane stress assumptions. Plane stress calculations were chosen based on the analysis reported by Atluri and Nakagaki [10] where theoretical plane stress J-integral values gave the best agreement with 1.0 inch thick compact type specimen test data. The thickness of the compact type specimens used in the present work is 0.5 inches. Plane stress computations were also chosen by Hinnerichs et al [4] to analyze creep crack

growth in a centre-cracked plate which had a thickness of 0.3 inches with crack lengths as small as 0.12 inches.

Figure 4 shows the finite element mesh used to analyze one half of the compact type specimen. The mesh for the creep crack growth computations consists of 115 isoparametric 8 noded quadrilateral elements with 420 node points. Reduced integration was employed in the analysis so that the surface integrations over each element, required in the formulation of the matrices in equation (3), employed only four Gaussian integration points per element. Thirty six square elements, each of dimension 0.01 inches by 0.01 inches, are located in the area immediately surrounding the crack tip. Details of the crack tip mesh are displayed in Figure 5.

The adequacy of the mesh was checked by computing the elastic stress intensity factor generated by the finite element model under plane strain conditions. Agreement with the handbook formula [11] for the elastic stress intensity factor was achieved to within 3% accuracy.

Initially, the continuum damage model was incorporated into the unified viscoplastic constitutive formulation, and the complete constitutive/continuum damage model was coded into a FORTRAN subroutine of the ABAQUS finite element program. When the compact type specimen is initially loaded to 4000 lbs., a rapid stress redistribution occurs at the Gaussian integration points closest to the crack tip. The stress at the point closest to the crack tip relaxes (decreases) while the stresses at the points further removed from the crack tip increase slightly to preserve global equilibrium. After about 10 seconds the stress redistribution stabilizes and no further change in the state of the compact type specimen occurs until about 94 minutes have elapsed. The equivalent Von Mises stress at the Gaussian integration point closest to the crack tip, viz., point 2 in element number 83 of Figure 6, has a value of 139200 lb/in^2. The equivalent stress at integration point 1 of element 83 which is further removed from the crack tip has a much lower value of 100600 lb/in^2. After 94 minutes at the constant stabilized stress value of 139200 lb/in^2, integration point 2 in element 83 begins to rapidly accumulate creep damage and failure (creep rupture) occurs after 94.2 minutes. At this point the integration procedure becomes unstable as the damage parameter approaches values close to unity.

The constitutive equations, when written in differential form, will always tend to exhibit unstable behaviour whether or not explicit forward difference or implicit backward difference methods are used in the integration procedure. The tendency to unstable behaviour in the differential equations arises from the fact that the right hand sides of the differential equations become very large as the damage parameter approaches unity. An integral formulation of the viscoplastic model is given in Appendix 1, where it may be seen that the factor (1-D) appears on the right hand side of the equation for the stress. As D approaches unity the stress decreases to zero

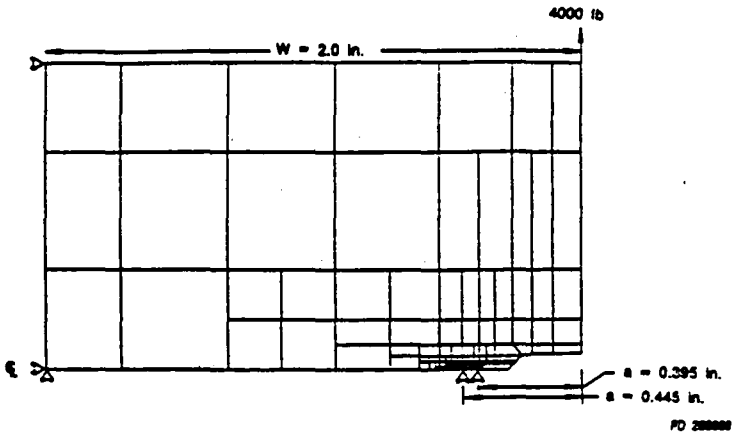

Figure 4. - Finite Element Mesh for Creep Crack Growth in Compact Type Specimen

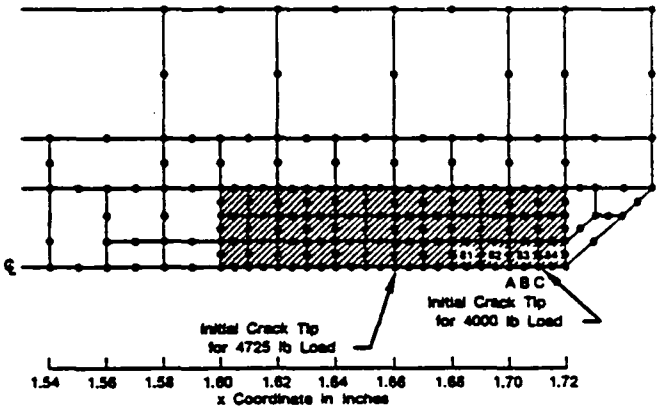

Figure 5. - Detail of Crack Tip Region in Compact Type Specimen

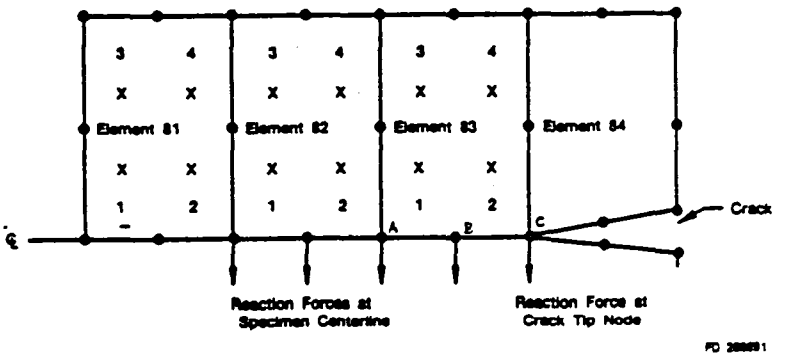

Figure 6. - Detail of Crack Tip Showing Reaction Forces and Gaussian Integration Points

and no instability should be encountered if an integral recursion procedure is used to step from the beginning to the end of the increment. This procedure was not used in the present calculations because a suitable algebraic Jacobian matrix was only developed after the present calculations were completed. Recent applications of the numerical procedure using the integral recursion relations have proved successful, and this method ought to be pursued further in an attempt to obtain a stable integration method for the coupled viscoplastic/damage equations.

Since the equivalent stress at the integration point closest to the crack tip remains constant for 94 minutes after the initial 10 to 15 second transient, and failure occurs at 94.2 minutes, it was decided to remove the damage computation from the viscoplastic FORTRAN subroutine to avoid the instability due to creep continuum damage accumulation.

The computations for creep crack growth now proceed as follows. First, the compact type specimen is loaded to either 4000 lbs. or to 4725 lbs. After a brief transient stress redistribution in the vicinity of the crack tip, the equivalent stress remains constant at the Gaussian integration point closest to the crack tip, viz. integration point 2 in element 83 of Figure 6. The time to failure for this integration point can then be determined from equation (2). From equation (5) of Appendix 3, the last two terms are responsible for decreasing the stress at the material point due to the growth of the creep damage parameter D. That is to say, as the point fails and its load carrying capacity diminishes with increasing damage, the stress at that point decreases and the load which it carries is shed onto other surrounding material points in the structure. To simulate this decrease in the load carrying capacity of the Gaussian integration point, four load increments are carried out in which the stress components are reduced by one half of their value at the beginning of each increment. Each increment lasts for 0.25 seconds, so that once failure is deemed to have occurred, the stress is reduced to about 6% of its initial stabilized value at the integration point in 1 second. In each succeeding increment the stress is further reduced by one half of its value as the analysis proceeds. Integration point 2 of element 83 in Figure 6 has now failed. The displacement boundary conditions at crack tip node C in Figure 6 are replaced by force boundary conditions. The reaction force required to hold the crack tip node C in its current location is then released in four (4) increments over a period of 1 second and the crack advances to the adjacent node B halfway through the isoparametric element.

A brief transient stress redistribution lasting for about 15 seconds again occurs, followed by a stabilized condition. The equivalent stress after stabilization is then computed at integration point 1 of element 83, and the time to rupture determined once again from equation (2). Once failure has occurred the stress is shed from integration point 1 to about 6% of its initial value in 1 second, and the crack tip node B is released in four increments over a

1 second period and the crack advances completely through the isoparametric element to the adjacent node A. This procedure is repeated for all nodes lying in the crack plane ahead of the advancing crack.

The justification for the decoupling of the viscoplastic and continuum damage constitutive models is based on the following observations:

(1). The stress falls off very rapidly in the crack plane of a compact type specimen. Consequently the stress at the integration point closest to the crack tip is large and the rupture or failure time is fairly small. The second integration point in the crack tip element and the integration points further away are subjected to such small stresses that the amount of creep damage accumulated by these points, at the time the integration point closest to the crack tip fails, is practically zero. The creep rupture time in equation (2) can then be used for each integration point in turn. Even if the damage accrued by each point is not small, the rupture time can still be determined from equation (1) by integration.

(2). The transient stress distribution after initial load up or after a node release, redistributes in a time which is much smaller than the time required to fail or rupture the integration points closest to the crack tip. Each integration point is therefore subjected to a constant stabilized stress for most of its life.

These observations are pertinent to high strength superalloy materials and are not expected to hold true for ductile materials of lower strength.

EXPERIMENTAL MEASUREMENTS

The standard compact type specimen shown in Figure 7 was used to obtain the creep crack growth rate data. Testing was conducted on a hydraulic constant load test frame. All precracking and testing was performed in accordance with the procedures outlined in ASTM 647-83. Specimen heating was provided by resistance, clamshell furnaces having windows to allow observation of the crack growth at test temperatures. The crack extension under creep loading conditions was determined by a laser heterodyne optical strain measurment system using speckle interferometry.

The concept of the heterodyne optical strain measurement system is illustrated in Figure 8. A laser beam is split into two parallel beams illuminating two closely spaced points on the object. The comparatively rough surface of the object scatters the laser light in a random manner resulting in two speckle fields reflected from the surface of the object. These two speckle fields are imaged by a lens system onto the film plane. If a photographic plate is placed at the film plane, a photographic recording of the resulting speckle interference pattern is made.

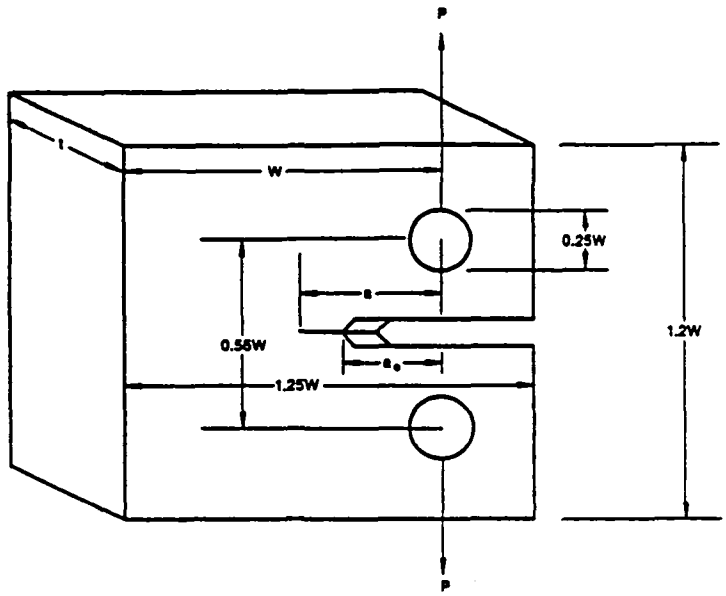

Creep Specimens	
P =4000 W =2.0 a_o = 0.275 a = 0.395 t = 0.5	P =4725 W =2.0 a_o = 0.275 a = 0.446 t = 0.5

Fatigue Specimen
P_{max} = 3069, P_{min} = 307 W = 2.5 a_o = 0.375 a = 0.505 t = 0.5

FD 268892

Figure 7. - Dimensions of Compact Type Specimens Used in Creep and Fatigue Crack Growth Experiments

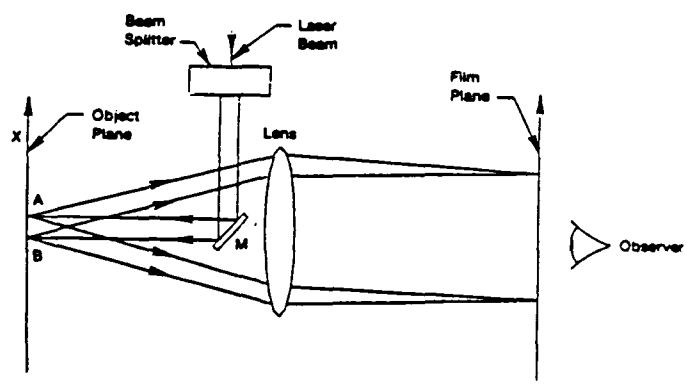

FD 268894

Figure 8. - Optical Strain Measurement Concept

The recording of the speckle interference pattern is then relocated in the same position it occupied during exposure. When the object is loaded in the X direction (Figure 8) causing points A and B on the object to separate in-plane, the spatial frequency of the fine interference fringes will change relative to the pattern previously recorded on the photographic plate with no load on the object. The effect of this change in frequency is to generate a change of phase angle between the interference pattern reflected from the object and the one recorded on the plate. The result to the observer will be the creation of a Moiré fringe pattern, each fringe of which represents a 180 degree shift in phase. The spatial frequency of these Moiré fringes is proportional to the strain on the object between points A and B.

In previous methods, the Moiré fringes were simply counted and the number of fringes directly related to strain. However, these methods have significant limitations in accurately measuring strain. For example, strain values corresponding to less than one fringe across the field of view cannot be measured; location of the fringe centres is not accurate; and no distinction is made between positive and negative strain. All of these undesirable limitations can be eliminated by the incorporation of heterodyned interferometry.

To implement heterodyned interferometry into the system shown in Figure 8, a device for constantly changing the phase of the laser beam prior to the beam splitter is added. This causes the Moiré fringes observed on the film plame to scan across the field of view in a constant direction. If the observer is replaced by a photodiode, the output of which is supplied to a phase meter, small changes in phase can easily be measured. Phase meters can accurately measure phase changes to within 0.5 degree, which is equivalent to dividing each Moiré fringe into 1000 parts. Therefore, heterodyned readout of the Moiré fringe pattern greatly increases the resolution and accuracy over typical optical techniques.

The heterodyne optical strain measurement system developed in the Materials Engineering and Technology Laboratory of Pratt & Whitney Aircraft is shown in Figure 9. A 2 watt argon ion laser is used and the heterodyne signal is provided by a $\lambda/2$ retarder plate mounted in the hollow shaft of an electric motor and by a stationary $\lambda/4$ retarder. The laser beam is split by a calcite beam displacer into two parallel beams 0.1 inches apart, which are then directed by mirrors to the specimen. Light scattered from the specimen is gathered by the strain sensor head and focused onto the photographic plate located in the plate holder. Two photodiodes are placed directly behind the plate.

The signals from the photodiodes, after being amplified and filtered, are fed into a counter that measures the phase of the signal from one of the diodes relative to the other. To conduct elevated temperature tests, an enclosure to stagnate the air between the specimen and the photodiodes is required as shown in Figure 9. An access port in the side of the furnace allows the light to reach the specimen and reflect back to the sensor head through a tunnel. The box around the sensor head helps stagnate the air and also shields the photodiodes from room lights.

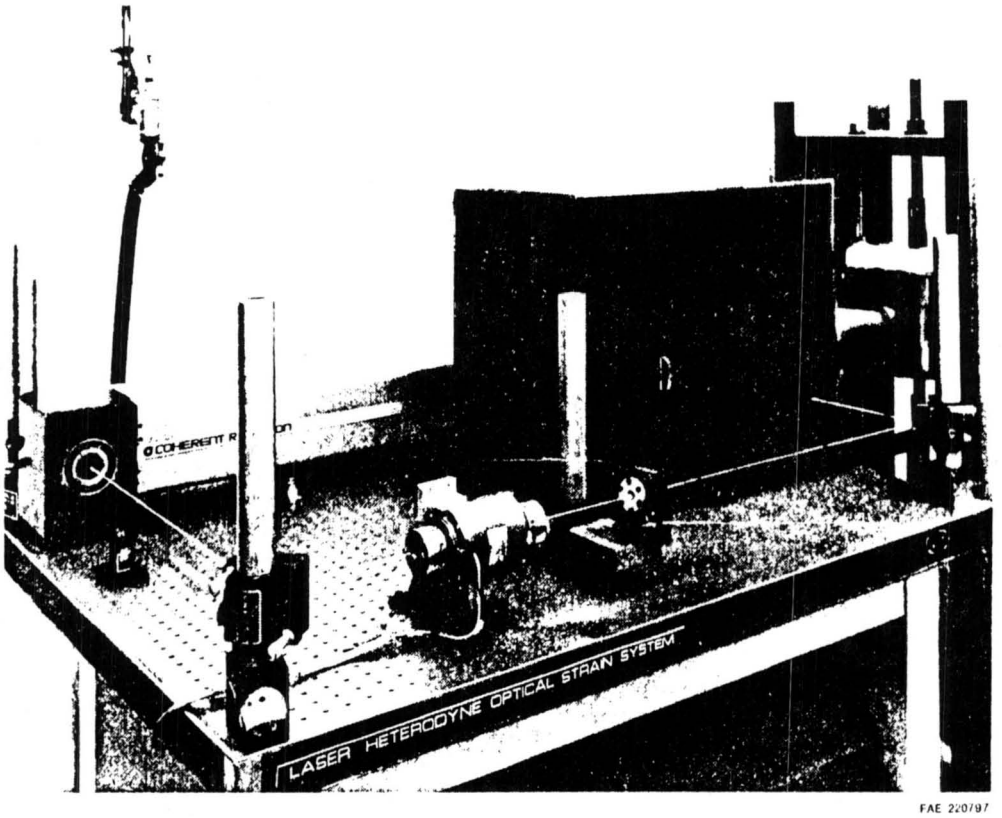

Figure 9. - Optical Strain System With Furnace, Tunnel, and Enclosure In-Place

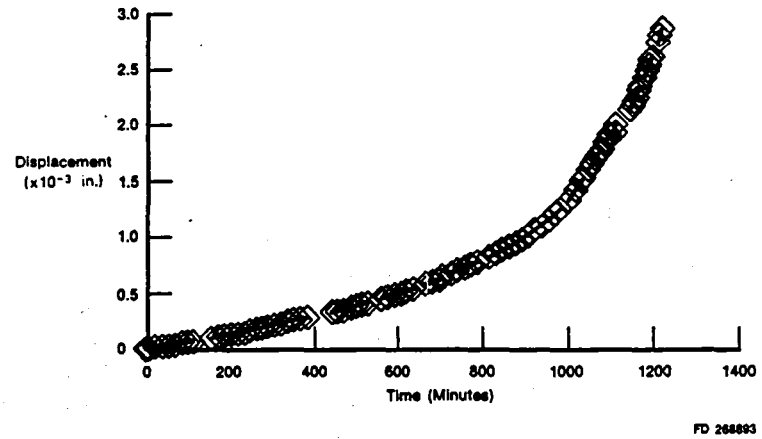

Figure 10. - Displacement from Centerline in the y-direction of Speckle Interferometry Point for Specimen Load of 4000 lbs

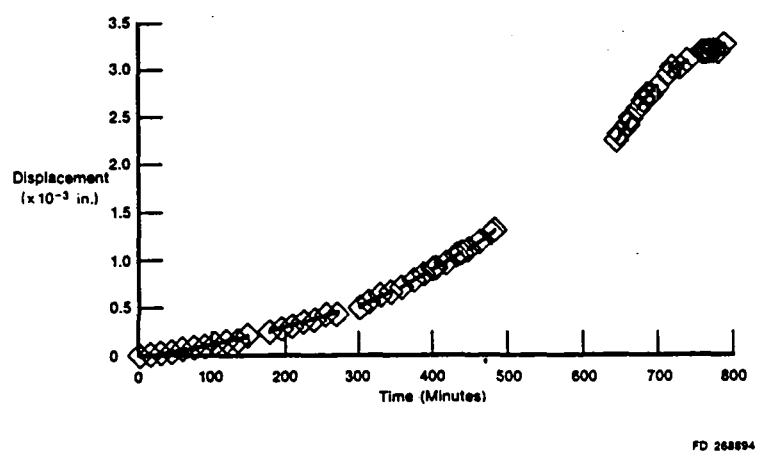

Figure 11. - Displacement from Centerline in y-direction of Speckle Interferometry Point for Specimen Load of 4725 lbs

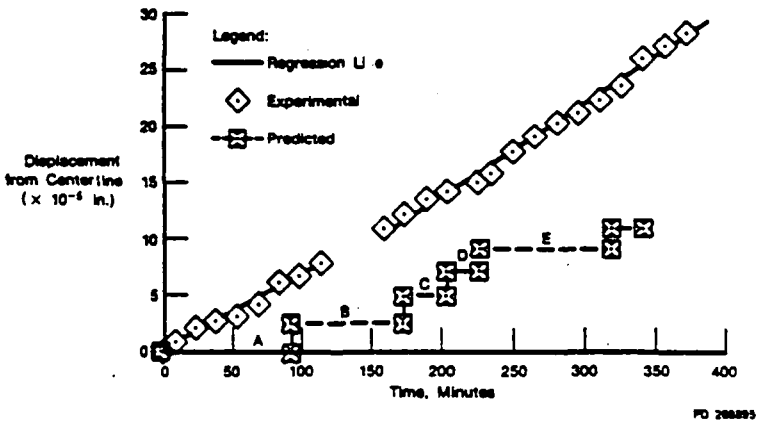

Figure 12. - Comparison of Measure and Predicted Displacements for Loads of 4000 lbs

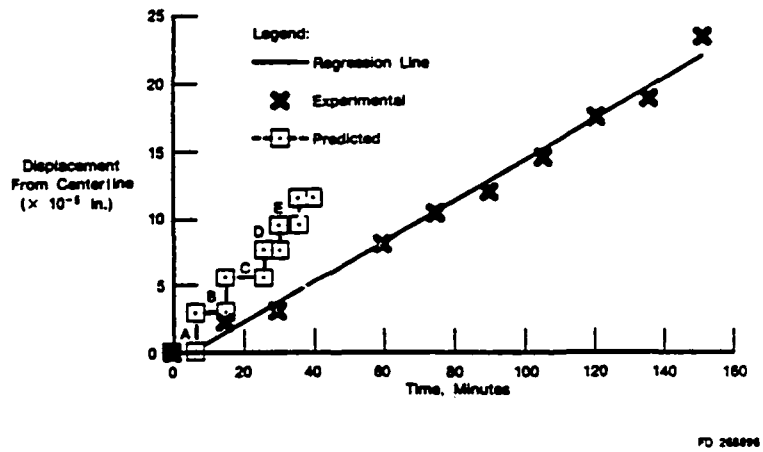

Figure 13. - Comparison of Measured and Predicted Displacements for Loads of 4725 lbs

RESULTS

The displacement of two points, located on either side of the crack tip, as shown in Figure 3, was measured as a function of time by the speckle interferometry technique described in the preceding section. Figures 10 and 11 show the experimental displacement of one of the points in the y direction (see Figure 3) as a function of time elapsed after application of load to the compact type specimen. The displacement is measured with respect to the centreline of the specimen and represents an average value for the two locations.

Theoretical and experimental results corresponding to the initial portions of these curves are displayed in Figures 12 and 13. The portions of the curves labelled A,B,C,D,E in these figures correspond to the stabilized behaviour of the compact type specimen after the 15 second transient and prior to the release of the 1st, 2nd, 3rd, 4th and 5th nodes ahead of the crack tip. The material constants A and r in the creep rupture equation (2) are chosen to give a least square fit to the uniaxial creep rupture data generated in the present work, as opposed to the values quoted in Figure 2, which correspond to a least square fit to three sets of independent data.

It is clear from Figures 12 and 13 that the computed displacement, and hence the computed initial creep crack growth rate, is too small by about a factor of two at the 4000 lb. loading level, and too large by a factor of two at the 4725 lb. loading level. Hence, the material constants generated from the uniaxial creep rupture data also give an approximate least square fit to the creep crack growth data.

Agreement between the predicted and experimental creep crack growth rates can easily be achieved simply by doubling and halving the computed creep rupture times (required to fail the Gauss points ahead of the crack tip) for the 4725 lb. and 4000 lb. load cases. A logarithmic plot of equivalent Von Mises stress at the Gauss points versus rupture time, which gives agreement between the experimental and finite element displacements at the speckle interferometry points, is given in Figure 2. As expected, the points lie on either side of the least square data line obtained from the three sets of uniaxial creep rupture data.

CONCLUDING REMARKS

Creep crack growth has been measured in compact type specimens of INCO 718 at 1200°F (649°C). Theoretical predictions of crack growth were made by employing the ABAQUS nonlinear general purpose finite element program in conjunction with a unified viscoplastic constitutive model and a continuum damage failure criterion.

The results of the current work may be summarized as follows:

(1). Initial creep crack growth rates at 1200°F (649°C) in the INCO 718 compact type specimens can be predicted by the theoretical model.

Crack growth is assumed to take place due to creep rupture of the material in the immediate vicinity of the crack tip and material constants for the continuum damage creep failure model were determined from creep rupture tests on uniaxial bar specimens of INCO 718 at 1200°F (649°C). Calculations were performed under plane stress conditions.

(2). The differential form of the unified viscoplastic constitutive model becomes very unstable when continuum damage is included in the formulation. It appears that the integral formulation of the unified viscoplastic model given in Appendix 1 should be used to obtain a stable integration algorithm.

(3). Speckle interferometry appears well suited for high temperature creep crack growth measurement.

REFERENCES

1. K.P. Walker and D.A. Wilson, "Constitutive Modeling of Engine Materials", Draft of Final Report FR-17911 to AFML Contract F33615-81-C-5040.

2. Users' Manual, Example Problems Manual, Systems Manual and Theory Manual for the ABAQUS general purpose nonlinear finite element program developed by Hibbitt, Karlsson & Sorensen, Inc. 35 South Angell St., Providence, R.I., 02906.

3. A.S. Kobayashi, "Current and Future Experimental Methods", Fracture Mechanics, Edited by N. Perrone, H. Liebowitz, D. Mulville and W. Pilkey, 10th Symposium on Naval Structural Mechanics, Washington, D.C., 1978.

4. T.D. Hinnerichs, "Viscoplastic and Creep Crack Growth Analysis by the Finite Element Method", Report AFWAL-TR-80-4140, Wright-Patterson Air Force Base, Ohio, 1981.

5. W.N. Sharpe, Jr., Unpublished Data on USAF Contract F33615-77-C-5003, Wright-Patterson Air Force Base, Ohio, 1979, (cf. Reference 4.).

6. P.A. Domas, W.N. Sharpe, M. Ward and J. Yau, "Benchmark Notch Test for Life Preditions", Final Report NASA CR-165571 on NASA Lewis Contract NAS3-22522, 1982.

7. K.P. Walker, "Research and Development Program for Nonlinear Structural Modeling with Advanced Time-Temperature Dependent Constitutive Relationships", Final Report NASA CR-165533 on NASA Lewis Contract NAS3-22055, 1981.

8. J.L. Chaboche, "Thermodynamic and Phenomenological Description of Cyclic Viscoplasticity with Damage", Translation of Publication No. 1978-3 of the Office National d'Etudes et de Researches Aerospatiales, France, by the European Space Agency Technical Translation Service, Publication No. ESA-TT-548, 1979.

9. A.B. Thakker and B.A. Cowles, "Low Strain, Long Life Creep Fatigue of AF2-1DA and INCO 718", Final Report NASA CR-167989 on NASA Lewis Contract NAS3-22387, 1983.

10. S.N. Atluri and M. Nakagaki, AIAA Journal, Vol 15, No. 7, pp. 923-931, 1977.

11. ASTM E647-83, Section 9.3.1.

Appendix 1

COUPLED CONTINUUM DAMAGE/INTEGRAL VISCOPLASTIC FORMULATION

$$\sigma_{ij}(t) = \frac{2}{3}\Omega_{ij}(t) + (\lambda(t) + \frac{2}{3}\mu(t))(1 - D(t))\,\delta_{ij}\epsilon_{kk} + \int_0^t e^{-\{Q(t) - Q(\xi)\}} \Big\{ 2\mu(\xi)(1 - D(\xi))\frac{\partial \epsilon_{ij}}{\partial \xi} - \frac{2}{3}\mu(\xi)(1 - D(\xi))\delta_{ij}\frac{\partial \epsilon_{kk}}{\partial \xi} - \frac{2}{3}\frac{\partial \Omega_{ij}}{\partial \xi} + \frac{1}{\mu(\xi)}\frac{\partial \mu}{\partial \xi}\frac{2}{3}\Omega_{ij}(\xi) \Big\} d\xi \,, \tag{1}$$

$$\Omega_{ij}(t) = \dot{\Omega}_{ij}(t) + n_1(t)c_{ij}(t) + n_2(t)\int_0^t e^{-\{G(t) - G(\xi)\}}\frac{\partial c_{ij}}{\partial \xi}\,d\xi \,, \tag{2}$$

$$K(t) = K_1(t) - K_2(t)e^{-n_7(t)R(t)} \,, \tag{3}$$

$$c_{ij}(t) = \epsilon_{ij}(t) + \frac{\lambda(t)}{2\mu(t)}\delta_{ij}\epsilon_{kk}(t) - \frac{\sigma_{ij}(t)}{2\mu(t)(1 - D(t))} \,, \tag{4}$$

$$\dot{\Omega}_{ij}(t) = -\delta_{ij}\dot{\Omega}(t) + 3\dot{\Omega}(t)\frac{c_{ik}(t)c_{kj}(t)}{c_{pq}(t)c_{pq}(t)} \,, \tag{5}$$

$$Q(t) = \int_0^t \left\{ \frac{3\mu(\xi)}{K(\xi)} \frac{1}{\log(1 + \beta\frac{\partial R}{\partial \xi})} \frac{\partial R}{\partial \xi} - \frac{1}{\mu(\xi)}\frac{\partial \mu}{\partial \xi} \right\} d\xi \,, \tag{6}$$

$$G(t) = \int_0^t (n_3(\xi) + n_4(\xi)e^{-n_5(\xi)R(\xi)})\frac{\partial R}{\partial \xi}\,d\xi \,, \tag{7}$$

$$R(t) = \int_0^t \sqrt{\frac{2}{3}\frac{\partial c_{ij}}{\partial \xi}\frac{\partial c_{ij}}{\partial \xi}}\,d\xi \,. \tag{8}$$

Appendix 2

CHABOCHE'S CREEP DAMAGE MODEL

$$\dot{D} = A \left\langle \frac{\sqrt{3/2\, S_{ij}\, S_{ij}}}{1-D} \right\rangle^{r} (1-D)^{r-k}, \tag{1}$$

$$k = 1 + (1.011 \times 10^{-4}) \exp\left(9.446 \times 10^{-5} \sqrt{3/2\, S_{ij}\, S_{ij}}\right) \tag{2}$$

The constants are chosen to have the values:

$A = 2.394 \times 10^{-43}$, $r = 7.22$.

Appendix 3

UNIFIED VISCOPLASTIC EXPONENTIAL LAW FOR UNIFIED FORMULATION

$$\dot{c}_{ij} = \frac{\exp\left(\frac{\sqrt{2/3(3a_{ij}/2 - \Omega_{ij})(3a_{ij}/2 - \Omega_{ij})}}{K(1-D)}\right) - 1}{\beta} \frac{(3a_{ij}/2 - \Omega_{ij})}{\sqrt{2/3(3a_{ij}/2 - \Omega_{ij})(3a_{ij}/2 - \Omega_{ij})}}, \tag{1}$$

$$\dot{\Omega}_{ij} = n_2\, \dot{c}_{ij} - \dot{G}_1\, \Omega_{ij}, \tag{2}$$

$$\dot{G}_1 = (n_3 + n_4\, e^{-n_5 R})\, \dot{R}, \tag{3}$$

$$K = K_1 + K_2\, e^{-n_7 R}, \tag{4}$$

$$\dot{\sigma}_{ij} = \delta_{ij}\lambda(1-D)\dot{\epsilon}_{kk} + 2\mu(1-D)\,(\dot{\epsilon}_{ij} - \dot{c}_{ij}) + \delta_{ij}\,\dot{\lambda(1-D)}\,\epsilon_{kk} + \dot{2\mu(1-D)}\,(\epsilon_{ij} - c_{ij}), \tag{5}$$

$$\dot{R} = \sqrt{2/3\dot{c}_{ij}\dot{c}_{ij}} \tag{6}$$

$$s_{ij} = \sigma_{ij} - \frac{1}{3}\,\delta_{ij}\sigma_{kk}. \tag{7}$$

The constants are chosen to have the values:

$\lambda = 1.517$ E7, $\mu = 1.012$ E7, $K_1 = 4219$, $K_2 = -1438$, $\beta = 6.203$ E9, $n_2 = 22.4$ E6, $n_3 = 269.6$, $n_4 = 0$, $n_5 = 0$, $n_7 = 14$.

For no cyclic softening $K_1 = 5657$ and $K_2 =$

☆U.S. GOVERNMENT PRINTING OFFICE:1985-537-086/ 20003 REGION NO. 4

1. Report No.	2. Government Accession No.	3. Recipient's Catalog No.
NASA CP-2369		

4. Title and Subtitle	5. Report Date
Nonlinear Constitutive Relations for High Temperature Application - 1984	June 1985
	6. Performing Organization Code
7. Author(s)	8. Performing Organization Report No. E-2368
	10. Work Unit No.
9. Performing Organization Name and Address National Aeronautics and Space Administration Lewis Research Center Cleveland, Ohio 44135	11. Contract or Grant No.
	13. Type of Report and Period Covered Conference Publication
12. Sponsoring Agency Name and Address National Aeronautics and Space Administration Washington, D.C. 20546	14. Sponsoring Agency Code

15. Supplementary Notes

16. Abstract

The second Symposium on Nonlinear Constitutive Relations for High Temperature Applications was held at the NASA Lewis Research Center in Cleveland, Ohio on June 15-17, 1984. The purpose of this symposium was to review the state-of-the-art in nonlinear constitutive modeling of high temperature materials and to identify the need for future research and development efforts in this area. Through this symposium, it was recognized that considerable research efforts are urgently needed in the development of nonlinear constitutive relations for high temperature applications. This need is further prompted by recent advances in high temperature materials technology and new demands on material and component performance. The demands for better material performance have come from the aerospace, stationary power, and automotive industries. Papers presented at this symposium are contained in the Conference Proceedings.

17. Key Words (Suggested by Author(s))	18. Distribution Statement
Viscoplastic theory; Unified theory; Constitutive theory; Nonlinear; Creep; Plasticity; Inelastic; Constitutive modeling; Material behavior; High temperature; Numerical predictions; Constitutive testing	Unclassified - unlimited STAR Category 39

19. Security Classif. (of this report)	20. Security Classif. (of this page)	21. No. of pages	22. Price
Unclassified	Unclassified	380	A17

For sale by the National Technical Information Service, Springfield, Virginia 22161